IWAIS2015 16TH INTERNATIONAL WORKSHOP ON ATMOSPHERIC ICING OF STRUCTURES

Proceedings

International Workshop on Atmospheric Icing of Structure

Swedish Energy Agency

Essential support for IWAIS 2015 has been provided by the Swedish Energy Agency

ISSN 2413-4597
ISBN 978-91-637-8552-8

ISSN 2413-4597
ISBN 978-91-637-8552-8

IWAIS 2015 PROGRAM

72 abstracts, 59 lectures, 13 electronic posters and more than 70 participants. We're now ready to launch IWAIS 2015, a world leading conference on atmospheric icing of structures.

SUNDAY JUNE 28	
18:00–20:00	ICE BREAKER AND REGISTRATION
MONDAY JUNE 29	
08:30–18:30	STUDY VISIT TO LUDVIKA
19:00–20:00	REGISTRATION EXHIBITOR STANDS AND POSTERS TO BE INSTALLED

TUESDAY JUNE 30			
TIME	EXHIBITION HALL & OTHER LOCATION	SESSION ROOM 1: GILLESALEN	SESSION ROOM 2: SWEDENBORG
08:00–08:50	Registration		
09:00–10:15		OPENING SESSION CHAIR: KATHLEEN F. JONES	
		Local organizers	
		Paul Mitten, Chairman of IWAIS	
		Determination of ice deposits thickness on overhead power lines conductors by location method, Renat Minullin, Kazan State Power Engineering University (26)	
		Coatings for protecting overhead power network equipment in winter conditions, Masoud Farzaneh, Université du Québec à Chicoutimi (15)	
10:15–10:45	BREAK		
10:45–12:15		SESSION 2 CHAIR: MASOUD FARZANEH	
		Research Condition and Capacity of Xuefeng Mountain Natural Icing Testbase (XMNIT), Jiang Xingliang (61)	
		Meteorological data for assessing climatic loads on overhead lines. Report from Cigre WG B2.28, Svein M. Fikke, Meteorological consultant (36)	
		Back to the basics: Wetting, Icing and Ice adhesion, Lasse Makkonen, VTT Technical Research Centre of Finland (2)	
12:15–13:30	LUNCH		
13:30–15:00		ANTI- / DE-ICING,COATINGS CHAIR: PAUL MITTEN	ICING MEASUREMENTS, MODELLING AND FORECASTING CHAIR: SVEIN M. FIKKE
		Optical Fiber Temperature Characteristic of OPGW during DC Ice Melting, Zhigao Meng, The State Key Laboratory of Power Transmission Equipment & System Security and New Technology, Chongqing University, Chongqing (65)	Analysis of the effect of climate change on the reliability of existing overhead transmission lines, Luc Chouinard, McGill Unviersity (1)
		Passive acoustic signal sensing approach to detection of ice on the rotor blades of wind turbines, Eugen Mamontov, Foundation Chalmers Industrial Technology (Stiftelsen Chalmers Industriteknik), Gothenburg, Sweden (21)	A Research of Icing Forecasting Algorithm Using Genetic Algorithm and Fuzzy Logic, Xin-bo Huang, College of Electronics and Information, Xi'an Polytechnic University, P.R. China (11)

		Study on Icing characteristics of Bundle Conductors under Xuefeng Mountain Natural Icing Testbase, Quanlin Wang, The State Key Laboratory of Power Transmission Equipment & System Security and New Technology, Chongqing University, Chongqing (67)	Verification of Icing-model in Finland, Karoliina Hämäläinen, Finnish Meteorological Institute (FMI), FI (13)
		On Self-cleaning and Anti-ice Performance of Double-layer-SAMs Coatings with Enhanced Corrosion Resistance on an Al Alloy Substrate, Shahram Farhadi, NSERC/Hydro-Quebec/ UQAC Industrial Chair on Atmospheric Icing of Power Network Equipment (CIGELE) and Canada Research Chair on Atmospheric Icing Engineering of Power Networks (INGIVRE), Université du Québec à Chicoutimi, QC, Canada (55)	
15:00–15:30	**BREAK & POSTER PRESENTATIONS**		
15:30–17:00	• Wet-snow activity research in Italy, Matteo Lacavalla, RSE SpA, IT (6) • Testing six wet snow models by 30 years of observations in Bulgaria, Dimitar Nikolov, National Institute of Meteorology and Hydrology - Bulgarian Academy of Sciences (NIMH-BAS), Bulgaria (33) • Effect of alkyl chain length on the hydro/ icephobic properties of SAMs coatings on aluminum alloy 6061 surfaces, Faranak Arianpour, NSERC / Hydro-Quebec / UQAC Industrial Chair on Atmospheric Icing of Power Network Equipment (CIGELE) and Canada Research Chair on Atmospheric Icing Engineering of Power Networks (INGIVRE), www.cigele.ca Université du Québec à Chicoutimi, Chicoutimi, QC, Canada (53) • How the "Steric effects" Affect Ice Repellency, UV stability and Corrosion Resistance of Dissimilar SAMs Coatings on a AA2024 Alloy, Shahram Farhadi, NSERC/ Hydro-Quebec/UQAC Industrial Chair on Atmospheric Icing of Power Network Equipment (CIGELE) and Canada Research Chair on Atmospheric Icing Engineering of Power Networks (INGIVRE), Université du Québec à Chicoutimi, QC, Canada (54)	**ANTI- DE-ICING, COATINGS** **CHAIR: SHIGEO KIMURA**	**ICING MEASUREMENTS, MODELLING AND FORECASTING** **CHAIR: LASSE MAKKONEN**
		Development and Application of Current Transferring Smart Ice Melting method and apparatus for Bundle Conductors Transmis-siuon Lines of EHV/UVU, Xingliang Jiang, The State Key Laboratory of Power Transmission Equipment & System Security and New Tech-nology, Chongqing University, Chongqing (62)	Usage of automated information system for icing control on OHL 110-500 kV, Eugeniy Satsuk, Platov South Russian State Polyechnic University (Novocherkassk Polytechnic Institute), Novocherkassk, Russia (41)
		Hydrophobic and anti-ice properties of homogeneous and heterogeneous nanoparticle coatings on Al 6061 substrates, Faranak Arianpour, NSERC / Hydro-Quebec / UQAC Industrial Chair on Atmospheric Icing of Power Network Equipment (CIGELE) and Canada Research Chair on Atmospheric Icing Engineering of Power Networks (INGIVRE), www.cigele.ca Université du Québec à Chicoutimi, Chicoutimi, QC, Canada (56)	Ice detection methods and measurement of atmospheric icing, Matthew Wadham-Gagnon, Canada (40)
		Influence of Shed Structure on Icing Characteristics of Composite Insulator Based on Natural Icing Testbase, Yang Pan, The State Key Laboratory of Power Transmission Equipment & System Security and New Technology, Chongqing University, Chongqing (66)	Observations and modeling of sea splash icing, Kathleen Jones, CRREL, USA (3)
		Research on icing behavior and ice adhesion testing of icephobic surfaces, Heli Koivuluoto, Tampere University of Technology, FI (49)	
18:30	**MINGLE & CONFERENCE DINNER, MASOUD FARZANEH AWARD BY UNIVERSITY OF QUÉBEC IN CHICOUTIMI MÅRTEN AJNE ABOUT THE SECRET LIFE OF ICE**		

WEDNESDAY JULY 1

	OUTSIDE SESSION ROOMS	SESSION ROOM 1: GILLESALEN	SESSION ROOM 2: SWEDENBORG
08:30–10:30		**OX2 - DEPLOYMENT OF LARGE SCALE WIND ENERGY IN ICING CLIMATES** **CHAIR: GÖRAN RONSTEN**	
		Lessons learned from "Large scale, cost effective deployment of wind energy in icing climates", Göran Ronsten, OX2 & WindREN (59)	
		Innovations in F-LOWICE real-time forecasts of wind power and icing effects, Erik Gregow, Finnish Meteorological Institute, FI (17)	

		Development of operational forecasting for icing and wind power at cold climate sites, Øyvind Byrkjedal, Kjeller Vindteknikk (46)	
		Vestas de-icing system, Francisco Fernandez, Vestas (71)	
10:30–11:00	**BREAK & POSTER PRESENTATIONS**		
11:00–12:30	• What we learned – Adaption and development of measurement technique and camera supervision for icing conditions, Bengt Norén, In Situ Instrument AB (58) • Wind, Ice and Snow Load Impacts on Infrastructure and the Natural Environment (WISLINE), Harold Mc Innes, The Norwegian Meteorological Institute (32) • Controller for Surface heating, Rolf Westerlund, HoloOptics (57) • Influence Analysis of Transmission Lines Insulator on the Conductor Iceshedding, Xin-bo Huang, College of Electronics and Information, Xi'an Polytechnic University, P.R.China (9)	**OX2 & ICING IN WIND ENERGY** **CHAIR: HELENA WICKMAN**	**ICING ON POWER LINES** **CHAIR: SERGEY CHERESHNYUK**
		Siemens de-icing system, Diego Levati, Siemens (72)	A severe in-cloud icing episode in Iceland 2013-2014 – Weather pattern background, Árni Jón Elíasson, Landsnet, IS (48)
		Experiences from studies of icing and production losses due to icing in OX2's Vindpilot project, Stefan Söderberg, WeatherTech Scandinavia, SE (29)	Wet snow icing - Comparing simulated accretion with observational experience, Árni Jón Elíasson, Landsnet, IS (44)
		Modelling icing conditions for a selection of Swedish wind farms during winter 2014–2015, Heiner Körnich, SMHI, SE (31)	Comparison of measured and simulated icing in 29 test spans during a severe icing episode, Egill Thorsteins, IS (45)
		Probabilistic forecasting of icing and production losses, Jennie Persson Söderman, Uppsala University, SE (28)	Automated Icing Monitoring System on the teritorry of the Czech and Slovak Republic, Jaroslav Šabata, EGÚ Brno, a.s. (70)
12:30–13:30	**LUNCH**		
13:30–15:00		**ICING IN WIND ENERGY** **CHAIR: REBECKA KLINTSTRÖM**	**ICING ON POWER LINES** **CHAIR: JAROSLAV ŠABATA**
		Case study of ice sensor using Computational Fluid Dynamics, measurements and pictures, Marie Cecilie Pedersen, Vattenfall Vindkraft A/S, Denmark (22)	Monitoring and forecasting ice loads on a 420 kV transmission line in extreme climatic conditions, Bjørn Egil Nygaard, Kjeller Vindteknikk, NOR (39)
		Supercooled Water Wettability and Freezing on Hydrophobic Surfaces: The Role of Temperature and Topography, Golrokh Heydari, KTH, Sweden (14)	Neural network approach to characterize atmospheric ice compressive strength, Hicham Farid, CIGELE/UQAC, Canada (23)
		Effect of Surface Roughness of Wind Turbine Blade on its Ice Accretion, Jian Liang, The State Key Laboratory of Power Transmission Equipment & System Security and New Technology, Chongqing University, Chongqing (64)	Multichannel radar monitoring of ice on power lines, Renat Minullin, Kazan State Power Engineering University (24)
		3-D Numerical Simulation of MWs Wind Turbine Blade's Icing, Qin Hu, The State Key Laboratory of Power Transmission Equipment & System Security and New Technology, Chongqing University, Chongqing (68)	Collapse of an Arctic Power Line due to strong Wind Gusts during Wet Snow Accumulation, Knut Harstveit, Kjeller Vindteknikk, Norway (34)
15:00–15:30	**BREAK & POSTER PRESENTATIONS**		
15:30–17:00	• Expansion of the ice deposition monitoring network in Germany, Bodo Wichura, German Meteorological Service, Climate and Environment Consultancy Potsdam, Germany (51) • The Numerical Analysis for jump height of multi-two-spans at different intervals of overhead transmission lines, Yong-can Zhu, School of Electro-Mechanical Engineering, Xidian University, Xi'an, P.R. China (12) • Development of snow accretion simulation method for electric wires in consideration of snow melting and shedding, Kazuto Ueno, Central Research Institute of Electric Power Industry, Japan (19)	**ICING ON POWER LINES AND CONDUCTORS/INSULATORS/ FLASHOVER** **CHAIR: BRIAN WAREING**	
		Technology radar monitoring of overhead power lines when detecting ice formations, Renat Minullin, Kazan State Power Engineering University (25)	
		Research on describing the icing level of porcelain and glass insulator based on icing thickness of the equivalent diameter, Zhijin Zhang, The State Key Laboratory of Power Transmission Equipment & System Security and New Technology, Chongqing University, Chongqing (69)	

	• Effect of icephobic coating on ice protection of ultrasonic anemometer with stack-type transducers, Shigeo Kimura, Kanagawa Institute of Technology (20)	Analysis of radar equipment indications and weight sensors indications during detecting ice deposits on power lines, Renat Minullin, Kazan State Power Engineering University (27)	
		Experimental research on the icing progress of insulators, Yuyao Hu, The State Key Laboratory of Power Transmission Equipment & System Security and New Technology, Chongqing University, Chongqing (63)	
17:30–19:00	IWAIS IAC COMMITTEE MEETING		
18:00–19:30	UPPSALA BY FOOT		
19:30–22:00	IWAIS IAC COMMITTEE DINNER		

THURSDAY JULY 2

		SESSION ROOM 1: GILLESALEN	SESSION ROOM 2: SWEDENBORG
09:00–10:30		**HSE & SENSORS, EQUIPMENT AND MACHINERY CHAIR: BODO WICHURA**	
		Numerical Study of Atmospheric Ice Accretion on Wind Turbines, Muhammad Virk, Atmospheric Icing Research Team, Narvik University College, Norway (7)	
		MuVi Graphene – Hybrid Atmospheric Icing Sensor, Umair Mughal, Atmospheric Icing Research Team, Narvik University College, Norway (8)	
		Methods for evaluating risk caused by ice throw and ice fall from wind turbines and other tall structures, Rolv Erlend Bredesen, Kjeller Vindteknikk, NO (38)	
		Icing forecast in GIS Meteo system, Yury Yusupov, MapMakers Group Ltd. (43)	
10:30–11:00	BREAK & POSTER PRESENTATIONS		
11:00–12:30	• Comparison of three different antiand de-icing techniques based on SCADA-data, Sandra Kolar, Uppsala Universitet/OX2 (52) • Review of icing related failures of wind masts in Bulgaria, Dimitar Nikolov, National Institute of Meteorology and Hydrology - Bulgarian Academy of Sciences (NIMH-BAS), Bulgaria (42) • The recognition and detection technology of ice-covered insulatorsunder complex environment, Xin-bo Huang, College of Electronics andInformation, Xi'an Polytechnic University, Xi'an, P.R.China (10)	**CONDUCTORS / INSULATORS / FLASHOVER CHAIR: XINGLIANG JIANG**	**TESTING FACILITIES, ICING ON MASTS, TOWERS AND BUILDINGS CHAIR: ALAN B. PEABODY**
		Anti-icing tests on La Farga CAC copper, Lluis Riera, La Farga, Spain (5)	Icing Measurements at Berlin TV Tower: A case study of a falling ice situation on 23rd December 2012, Bodo Wichura, German Meteorological Service, Climate and Environment Consultancy Potsdam, Germany (50)
		Relation between test span measured ice loads and conductor size, Brian Wareing, United Kingdom (4)	Investigation of Using Icephobic Coatings on a Cable Stayed Bridge, Douglas Nims, University of Toledo, Toledo, USA (37)
		Comparison of ice accumulation on simplex and duplex conductors in parallel overhead transmission lines in Iceland, Pétur Thór Gunnlaugsson, IS (47)	Isotopic Mass Balance Measurements of Spray Ice, Toshihiro Ozeki, Hokkaido University of Education (30)
		Advanced test methods for full-scale ice tests of DC insulators strings intended for ±350 kV, Andreas Dernfalk, STRI (18)	A prediction method of slide snow/ice load applied to roofs, Xuanyi Zhou, State Key Laboratory of Disaster Reduction in Civil Engineering, Tongji University, Shanghai, China (60)
12:30–13:30	LUNCH		
13:30–15:00		**SESSION 16 - CLOSING SESSION CHAIR: MATTHEW WADHAM GAGNON**	
		Ripples on Icicles, Lasse Makkonen, VTT (16)	

THURSDAY JULY 2

		Fault statistics on overhead transmission lines in Russia because of icing, Sergey Chereshnyuk, Research and Development Center at Federal Grid Company of Unified Energy System (R&D Center @ FGCUES), Moscow, Russia (35)	
15:00–15:30	**BREAK**		
15:45–17:45	**TRAVEL TO NYNÄSHAMN**		
18:35–22:00	**BOAT TO GOTLAND**		

FRIDAY JULY 3

	ACTIVITY	LOCATION	
09:00–16:00	SMART GRID GOTLAND	GOTLAND	

SATURDAY JULY 4

	ACTIVITY	LOCATION	
09:00–17:00	VISIT TO N. GOTLAND	FÅRÖ	

SUNDAY JULY 5

	ACTIVITY	LOCATION	
09:00–16:00	VISIT TO S. GOTLAND	NÄSUDDEN	
18:00	DEPARTURE FOR VISBY HARBOR	VISBY	
19:10–22:30	BOAT TO NYNÄSHAMN	VISBY	
23:30	ARRIVAL TO C STOCKHOLM	STOCKHOLM	

Table of content

Back to the basics: Wettability, icing and ice adhesion

Lasse Makkonen
VTT Technical Research Centre of Finland
lasse.makkonen@vtt.fi

***Abstract*: Icing in the wet growth regime is caused by water drops on a surface, the dynamics of which are determined by external forces, such a gravity and wind drag. However, the drop dynamics also depend on the wetting characteristics of the surface material. The static contact angle determines the area of a drop that is in contact with the solid, and the difference between the advancing contact angle and receding contact angle, i.e., the contact angle hysteresis, determines the critical external force at which the drop begins to slide. Many studies have been made on the contact angles and their relation to runback icing and ice adhesion, but no quantitative theory for the contact angle hysteresis exists. Here, the contact angle hysteresis is explained by a first principles theory, and good quantitative agreement between the theory and experimental data is found. The implications of the theory to icing and ice adhesion are outlined.**

Keywords: icing, wettability, hydrophobicity, contact angle

INTRODUCTION

Freezing of runback water is a significant concern during wet growth icing, and also during dry growth icing when thermal ice prevention is applied. Freezing of drops causes aerodynamically dangerously rough ice accretions [1] and initiates icicle growth [2,3]. The dimensions and dynamics of the drops on a solid surface are determined by external forces that include gravity, wind drag and, in the case of rotors and wind turbines, the centrifugal force.

In addition to external forces, the drop dynamics depend on the wetting properties of the surface material, characterized by the solid-liquid contact angles. When a drop slides on a surface, its contact angle at the advancing and receding side of the drop no longer corresponds to the static equilibrium contact angle. The difference between the advancing contact angle and receding contact angle, called the contact angle hysteresis, determines the external force at which the drop begins to slide. These relations are vital in understanding of the icing process, because the rate of freezing of the drops during sliding depends on the liquid-solid contact area and contact time [4-6]. Furthermore, bouncing of impacting drops [7,8] and eventual shedding of the unfrozen water [9,10] are closely related to the receding contact angle.

Many studies have been made in order to estimate the critical external force that causes water to be removed from various surfaces [9,11-17]. In the simplest case, the critical tilt angle of a plane, at which a drop starts to slide, has been studied for different drop sizes and surfaces [14-17]. However, the fundamentals of wetting have not been fully resolved. In fact, the classical theory of wetting does not predict any contact angle hysteresis on a homogenous smooth surface. Experimental studies have been made on the dynamic contact angles and their relation to runback icing [7,10,18,19] and ice adhesion [20-27], but no quantitative theory exists. This has considerably hampered the selection of optimal surface materials for the applications that include icing due to runback drops.

Wetting of solid surfaces by a liquid is a classical and familiar physics problem [28,29]. When a drop does not spread completely, it forms a specific angle of contact with the solid at the three-phase contact line (Figure 2). This Young's equilibrium angle [30], i.e. the static contact angle θ measured on a horizontal surface, is widely used as a measure of the wetting characteristics of surfaces.

Figure 1: Drop of water sliding on an inclined polymer surface.

Under the influence of an external force, a drop becomes asymmetric in shape, and upon a sufficient force being exerted, it begins to slide (Figure 1). At that time, there is a difference between its front (advancing) contact angle θ_a and back (receding) contact angle θ_r. This is called contact angle hysteresis. Here, the contact angle hysteresis, H, is specified as $H = \cos\theta_r - \cos\theta_a$. Since a liquid does not transfer stress at low flow rates, the external force on the drop manifests itself as the force vector of the magnitude H. Accordingly, H determines the external force at which drops are removed from the surface.

Numerous experimental and theoretical studies have been made on the contact angle hysteresis, and were reviewed by De Gennes [28] and more recently by Eral et al. [29]. The origin of contact angle hysteresis has been explained by surface roughness and heterogeneities, surface deformation, liquid adsorption and retention, viscous dissipation, molecular rearrangement upon wetting, and interdiffusion [29]. However, there is no consensus on the origin of the contact hysteresis, and no quantitative theoretical models for it exist.

In the following, the fundamental origin of contact angle hysteresis is revealed and a first-principles physical theory of it is presented. The theory is the quantitatively compared with experimental data.

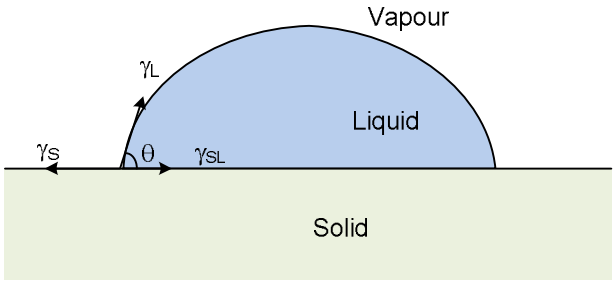

Figure 2: Young's equilibrium of surface tensions at a three-phase line of a droplet on a solid surface.

I. Theory

The balance of tensions at a contact line was proposed in 1805 by Thomas Young [30]. Formally, this is

$$\gamma_S = \gamma_{SL} + \gamma_L \cos\theta \quad (1)$$

Here γ_S, γ_{SL} and γ_L are, respectively, the solid-vapor, solid-liquid, and liquid-vapor interfacial tensions (Figure 2). In this classical construction, the three mechanical surface tensions γ_S, γ_{SL} and γ_L are at equilibrium in the direction parallel to the solid surface.

Equation (1) has been understood as the mechanical balance of the three surface tensions, but also as a result of minimizing the total free energy. In the latter interpretation γ_S, γ_{SL} and γ_L in figure 2 represent scalar thermodynamic surface energies Γ_S, Γ_{SL} and Γ_L, instead of mechanical tension vectors.

While the surface tensions involving a liquid phase can be interpreted either way, the mechanical surface tension of a dry solid, γ_S, is a contentious concept [32-35]. In particular, it is hard to explain how the solid could do work in moving the drop laterally, considering that the net atomic imbalance of forces is perpendicular to the interface. A perpendicular force can do work laterally only when the molecules are free to move, i.e. at an interface that involves a liquid. Thus, we conclude that only the surface energy interpretation of Young's Equation is valid. Then, the tension γ_S is a passive force that can only resist, but not cause, motion of a contact. Using the energy interpretation, Young's equation is written as

$$\Gamma_S = \Gamma_{SL} + \Gamma_L \cos\theta \quad (2)$$

Taking that γ_S is a passive force, on the left side of Figure 2, there is no force on the solid that could move the contact line to the left. On the other hand, moving the contact line to the right at a constant θ would increase the free energy of the system, since $\Gamma_S > \Gamma_{SL}$. Hence, the equilibrium contact line of a drop on a solid surface is pinned and an external force is required to make it move in either direction.

The fundamental mechanism that controls θ by surface energies is nevertheless valid here. Due to the pinning, the surface chemical potential at the contact line is

$$P = [\Gamma_S - (\Gamma_{SL} + \Gamma_L \cos\theta)] / \rho \quad (3)$$

where ρ is the surface particle density, can be reduced only by the adjustment of the free coordinate θ. At equilibrium, P equals zero, i.e., θ adopts the value given by Eq. (2).

Equation (2) describes the selection of the contact angle due to minimizing the chemical potential at the contact line that is pinned. However, when the drop is forced to move, a mechanical balance must exist in the direction of the motion. Since an interface involves surface energy, work is spent when new solid-liquid surface is being created. Hence, when the contact line on the left side of Figure 2 moves to the left, an additional tension, γ_{SL}, arises. The disappearing solid-vapor interface at the advancing contact line does not affect the mechanical balance, as long as γ_S has no such interpretation that it could do mechanical work laterally. The additional tension, initiated by the motion and resisting it, must equal the change in the tension exerted to the contact line via the drop. This change can occur only by adjusting the contact angle. We thus have the mechanical balance at the advancing contact line as

$$\gamma_{SL} = \gamma_L \cos\theta - \gamma_L \cos\theta_a \quad (4)$$

Noting that $\Gamma_L = \gamma_L$ and $\Gamma_{SL} = \gamma_{SL}$, Eq. (4) can be written as

$$\Gamma_{SL} = \Gamma_L \cos\theta - \Gamma_L \cos\theta_a \quad (5)$$

We next consider the receding contact line, i.e. the situation when the left side of the drop in Figure 2 moves to the right. This motion brings in an additional tension, γ_S, owing to the work spent in creating new solid-vapor interface behind the receding contact line. The disappearance of the solid-liquid interface at the receding contact line does not affect this mechanical balance, because the surface tension of the liquid-solid interface is fixed at the value γ_{SL}. We thus obtain the mechanical balance at the receding contact line as

$$\gamma_S = \gamma_L \cos\theta_r - \gamma_L \cos\theta \quad (6)$$

Since γ_S in Eq. (6) represents the tension that arises due to creating new solid-vapor surface, its scalar value equals Γ_S and Eq. (6) can be written as

$$\Gamma_S = \Gamma_L \cos\theta_r - \Gamma_L \cos\theta \quad (7)$$

We next employ Berthelot's rule [36], which provides the solid to liquid surface energy ratio as a function of the equilibrium contact angle as

$$\Gamma_S / \Gamma_L = [(1 + \cos\theta) / 2]^2 \quad (8)$$

Inserting Eq. (8) into Eqs. (5) and (7) gives analytical expressions for the contact angles of a sliding drop as a function of the static contact angle.

For the advancing contact angle we have

$$\cos\theta_a = [-(\cos\theta)^2 + 6\cos\theta - 1] / 4 \quad (9)$$

The maximum contact angle is 180°, so that $\cos\theta_a$ has a lower limit at -0.464 ($\theta = 117.7^o$), below which $\cos\theta_a = -1$ and H is determined by θ_r alone.

For the receding contact angle we have

$$\cos\theta_r = [(\cos\theta)^2 + 6\cos\theta + 1] / 4 \quad (10)$$

The minimum contact angle is 0°, so that $\cos\theta_r$ has an upper limit at $\cos\theta = 0.464$ ($\theta = 62.3^o$), above which $\cos\theta_r = 1$ and H is determined by θ_a alone.

II Discussion

According to the theory above, θ_a and θ_r and H depend on θ only. The theory thus explains the empirically observed features that the contact angle hysteresis is inherent to all surfaces, and independent of the contact line velocity [37] and the effective vertical force [38].

Quantitative predictions of the theory are in good agreement with the experimental data that are available from experiments

on relatively smooth surfaces [39,40]. This is encouraging considering that the data cover many different liquid-solid combinations, and that the theoretical model here is purely physical, i.e. it includes no experimental ingredients or fitting parameters.

The model presented cannot be directly applied to a rough solid. This is because the contact angles depend on the surface morphology at the contact line in a complicated way, especially when the surface texture is directionally non-isotropic [41-44]. However, the understanding of the process that determines the contact angle hysteresis on a rough surface H^R, is important when developing superhydrophobic materials by surface modification. To that end, it is noteworthy that, for isotropic surfaces, when applied to the Wenzel state, the theory gives $H^R = r\,H$, where r is the ratio of the total surface area of the solid to its apparent surface area ($r > 1$). This shows that increasing the roughness increases the contact angle hysteresis in the Wenzel state, i.e. on a hydrophilic material.

In the Cassie state, i.e. on a hydrophobic material, the roughness affects via air entrapment and the fraction Φ_s of the apparent interface where a true solid-liquid contact exists. Then, the dynamic balances in Eqs. (5) and (7) become

$$\cos\theta_a = \Phi_s\,(\cos\theta - \Gamma_{SL}/\Gamma_L) - 2(1-\Phi_s) \qquad (11)$$

$$\cos\theta_r = \Phi_s\,(\cos\theta + \Gamma_S/\Gamma_L) - (1-\Phi_s) \qquad (12)$$

It follows from Eqs. (10) and (12) that the apparent advancing contact angle θ_a^R gets to 180^o at all angles θ when the surface roughness factor is $\Phi_s < 0.5$. Thus, the equation for the contact angle hysteresis H^R on a reasonably rough hydrophobic and isotropic solid becomes

$$H^R = \Phi_s\,[((\cos\theta)^2 + 6\cos\theta + 5)/4] \qquad (13)$$

This shows that under these conditions, making the surface rougher decreases the contact angle hysteresis. This effect is linear with respect to the true solid-liquid contact area, and is in agreement with the recent experiments [45, Figs. 7 and 11]. Equation (13) can also be expressed in terms of the intrinsic contact angle on the rough surface θ^R by inserting into it the Cassie relation, $\cos\theta = (\cos\theta^R + 1 - \Phi_s)/\Phi_s$. The resulting values of H^R are in good agreement with the data by Morrow [46, Fig. 11].

Thus, the theory provides new insights into drop dynamics also on a rough surface, and removes many misunderstandings in the literature. A particular implication of the theory is that hydrophobicity should not be defined in a simple way. For example, the critical tilt angle may be smaller in a situation where the static contact angle is higher.

The implications of this theory to the adhesion of ice can be outlined as follows. The thermodynamic work of adhesion W_a is defined as

$$W_a = \Gamma_S + \Gamma_L - \Gamma_{SL} \qquad (14)$$

whereas the contact angle hysteresis from Eqs. (5) and (7) is

$$H = \Gamma_S + \Gamma_{SL} \qquad (15)$$

This shows that the relations between the dynamic contact angles and the work of adhesion are not straightforward. However, they are solvable by the theory, since the surface energies, and thus both W_a and H, are all functions of θ. Furthermore, the theory shows that making a surface superhydrophobic by increasing its roughness may either decrease or increase its adhesion strength, as recently observed [47,48].

Acknowledgments

This work was supported by the Academy of Finland, the TopNano project funded by Norden, and the FrontLines project.

References

[1] M.B. Bragg, A.P. Broeren and L.A. Blumenthal, 2005. Iced airfoil aerodynamics. *Prog. Aerospace Sci.* 41, 323-362.

[2] L. Makkonen, 1998. Modelling power line icing in freezing precipitation. *Atmos. Res*. 46, 131-142.

[3] L. Makkonen, 2000. Models for the growth of rime, glaze, icicles and wet snow deposits on structures. *Phil. Trans. Roy. Soc. London A*, 358, 2913-2939.

[4] K. Fumoto and H. Yamagishi, 2005. A study on freezing of supercooled water droplet impacting on solid surfaces. Proceedings, 11th International Workshop on Atmospheric Icing of Structures (IWAIS), Montreal, 13-16 June 2005, 6 p.

[5] P. Tourkine, M. Le Merrer and D. Quere, 2009. Delayed freezing on water repellent materials. *Langmuir* 25, 7214-7216.

[6] S. Jung, M.K. Tiwari, N.V. Doan & D. Poulikakos, 2012. Mechanism of supercooled droplet freezing on surfaces. *Nature Comm.* 3, 615.

[7] V. Bahadur, L. Mishchenko, B. Hatton, J.A. Taylor, J. Aizenberg and T. Krupenkin, 2011. Predictive model for ice formation on superhydrophobic surfaces. *Langmuir* 27, 14143-14150.

[8] C. Antonini, F. Villa, I. Bernagozzi, A. Amirfazli and M. Marengo, 2011. Drop rebound after impact: The role of the receding contact angle. *Langmuir* 29, 16045-16050.

[9] A.J.B. Milne and A. Amirfazli, 2009. Drop shedding by shear flow for hydrophilic to superhydrophilic surfaces. *Langmuir* 25, 14155-14164.

[10] D. Mangini, C. Antonini, M. Marengo & A. Amirfazli, 2015. Runback ice formation mechanism on hydrophobic and superhydrophobic surfaces. *Cold Regions Sci. Technol.* 109, 53-60.

[11] P. G. De Gennes, F. Brochard-Wyart, and D. Quéré, 2004. *Capillarity and Wetting Phenomena* (Springer).

[12] H.B. Eral, D.J.C.M. 't Mannetje, and J.M. Oh, 2013. Contact angle hysteresis: a review of fundamentals and applications. *Colloid Polymer Sci.* 291, 247-260.

[13] F.J. Montes Ruiz-Cabello, M.A. Rodriguez-Valverde and M. A. Cabrerizo-Vilchez, 2011. Contact angle hysteresis on polymer surfaces: An experimental study. *J. Adhesion Sci. Technol.* 25, 2039-2049.

[14] D. Quéré, 2008. Wetting and roughness. *Ann. Rev. Mater. Res.* 38, 71-99.

[15] C.W. Extrand and Y. Kumagai, 1995. Liquid drops on an inclined plane: The relation between contact angles, drop shape, and retentive force. *J. Colloid Interface Sci.*170, 515-521.

[16] B. Krasovitski and A. Marmur, 2005. Drops down the hill: Theoretical study of limiting contact angles and the hysteresis range on a tilted plate. *Langmuir* 21, 3881-3885.

[17] E. Pierce, F.J. Carmona and A. Amirfazli, 2008. Understanding of sliding and contact angle results in tilted plate experiments. *Colloids Surfaces A* 323, 73-82.

[18] F. Wang, C. Li, Y. Lv, F. Lv and Y. Du, 2010. Ice accretion on superhydrophobic aluminium surfaces under low-temperature conditions. *Cold Regions Sci. Technol.* 62, 29-33.

[19] R. Liao, Z. Zuo, C.Guo, A. Zhuang, Y. Yuan, X. Zhao and Y. Zhang, 2015. Ice accretion on superhydrophobic insulators under freezing condition. *Cold Regions Sci. Technol.* 112, 87-94.

[20] W.D. Bascom, R.L. Cottington and C.R. Singleterry, 1969. Ice adhesion to hydrophilic and hydrophobic surfaces. *J. Adhesion* 1, 246-263.

[21] C. Laforte, J-L. Laforte, and J-C. Carriere, 2002. How a solid coating can reduce the adhesion of ice on a structure. Proceedings, 10th International Workshop on Atmospheric Icing of Structures (IWAIS), Brno, 17-21 June 2002, 6 p.

[22] S.A. Kulinich and M. Zarzaneh, 2009. Ice adhesion on super-hydrophobic surfaces. *Appl. Surf. Sci.* 255, 8153-8157.

[23] S.A. Kulinich and M. Zarzaneh, 2009. How wetting hysteresis influences ice adhesion strength on superhydrophobic surfaces. *Langmuir* 25, 8854-8856.

[24] A.J. Meuler, J.D. Smith, K.K. Varanasi, J.M. Marby, G.H. McKinley and R.E. Cohen, 2010. Relationships between water wettability and ice adhesion. *ACS Appl. Mater. Interfaces* 2, 3100-3110.

[25] L. Makkonen, 2012. Ice adhesion – theory, measurements and countermeasures. *J. Adhesion Sci. Technol.* 26, 413-445.

[26] O. Gohardani and D.W. Hammond, 2013. Ice adhesion to pristine and eroded polymer matrix composites reinforced with carbon nanotubes for potential usage on future aircraft. *Cold Regions Sci. Technol.* 96, 8-16.

[27] V. Hejazi, K. Sobolev and M. Nosonovsky, 2013. From superhydrophobicity to icephobicity: forces and interaction analysis. *Sci. Rep.* 3, 2194.

[28] P.G. De Gennes, F. Brochard-Wyart and D. Quéré, 2004. *Capillarity and Wetting Phenomena* (Springer).

[29] H.B. Eral, D.J.C.M. 't Mannetje and J.M. Oh, 2013. Contact angle hysteresis: a review of fundamentals and applications. *Colloid Polym. Sci.* 291, 247-260.

[30] T. Young, T., 1805. An essay on the cohesion of fluids. *Phil. Trans. R. Soc. London* 95, 65.

[31] P.G. De Gennes, 1985. Wetting - statistics and dynamics. *Rev. Mod. Phys.* 57, 827-863.

[32] J.W. Gibbs, 1993. The Scientific Papers of J. Willard Gibbs, Thermodynamics Vol. 1. (Ox Bow).

[33] J.J. Bikerman, 1978. Surface energy of solids. *Topics Curr. Chem.* 77, 1-66.

[34] L. Makkonen, 2012. Misinterpretation of the Shuttleworth equation. *Scripta Mater.* 66, 627-629.

[35] L. Makkonen, 2014. Misconceptions of the relation between surface energy and surface tension on a solid. *Langmuir* 30, 2580-2581.

[36] D. Berthelot, 1898. Sur le Mélange des Gaz. *Compt. Rendus* Vol. 126, 1703-1706.

[37] H. Tavana, D. Jehnichen, K. Grundke, M.L. Hair and A.W. Neumann, 2005. Contact angle hysteresis on fluoropolymer surfaces. *Adv. Colloid Interface Sci.* 134/135, 236–248.

[38] J.V.I. Timonen, M. Latikka, O. Ikkala and R.H.A. Ras, 2013. Free-decay and resonant methods for investigating the fundamental limit of superhydrophobicity. *Nature Comm.* 4, 2398.

[39] M. Miyama, Y. Yang, T. Yasuda, T. Okuno and H.K. Yasuda, 1997. Static and dynamic contact angles of water on polymeric surfaces. *Langmuir* 13, 5494-5503.

[40] C.N.C. Lam, R. Wu, D. Li, M.L. Hair and A.W. Neumann, 2002. Study of the advancing and receding contact angles: liquid sorption as a cause of contact angle hysteresis. *Adv. Colloid Interface Sci.* 96, 169-191.

[41] E. L. Decker, B. Frank, Y. Suo and S. Garoff, 1990. Physics of contact angle measurement. *Colloids Surf. A* 156, 177-189.

[42] D. Quéré, 2008. Wetting and roughness. *Ann. Rev. Mater. Res.* 38, 71-99.

[43] A. Marmur, 2009. Solid-surface characterization by wetting. *Ann. Rev. Mater. Res.* 39, 473-489.

[44] W. Cho, A.Tuteja, J.M. Marby, R.E Cohen and G.H.A. McKinley, 2009. Modified Cassie–Baxter relationship to explain contact angle hysteresis and anisotropy on non-wetting textured surfaces. *J. Colloid Interface Sci.* 339, 208-216.

[45] B.M.L. Koch, A. Amirfali and J.A.W. Elliott, 2014. Modeling and measurement of contact angle hystcresis on textured high-contact angle surfaces. *J. Phys. Chem.* C 118, 18554-18563.

[46] N. R. Morrow, 1975. The effect of surface roughness on contact angle with special reference to petroleum recovery. *J. Can. Petrol.* 4, 42-52.

[47] S.A. Kulinich, S. Farhadi, K. Nose and X.W. Du, 2011. Superhydrophobic surfaces: Are they really ice-repellent. *Langmuir* 27, 25-29.

[48] G. Momen, R. Jafari and M. Farzaneh, 2015. Ice repellency behavior of superhydrophobic surfaces: Effects of atmospheric icing conditions and surface roughness. *Appl. Surf. Sci.* 349, 211-218.

Observations and modeling of sea splash icing

Kathleen F. Jones and Keran J. Claffey
Cold Regions Research and Engineering Laboratory, Hanover, New Hampshire, U.S.A.
kathleen.f.jones@usace.army.mil

Abstract: Stationary offshore structures are subject to icing from sea spray and from run-up and splash. Sea spray is created by the bursting of bubbles in whitecaps and, at very high wind speeds, by water sheared from the crest of waves by the wind. The relatively large drops in this spindrift can result in significant ice accretion on any offshore structure in cold temperatures with wind speeds greater than about 20 m/s. For offshore structures with significant area at the waterline, waves running up on the side of the structure create large quantities of splash even at lower wind speeds. The relatively warm splash keeps ice from forming on the structure near the ocean surface even in subfreezing temperatures. The water content in the splash decreases with elevation and if the air is cold enough there may be sufficient cooling to freeze some or all of the water. In this paper we present observations of splash icing on a mast on Mt. Desert Rock in January-February 2014. We also develop a simple model of run-up and splash based on wave tank experiments and field observations. We compare the icing profile on the mast with model results using local observations of wind speed, air and water temperature, and significant wave height and period.

Keywords: icing, run-up, splash, off-shore structure

NOMENCLATURE

c_s	scatter coefficient= $\pi D/\lambda$
d	water depth (m)
D	diameter (width) of structure (m)
fr	splash fraction
g	acceleration of gravity (m/s^2)
H	wave height (m)
k	wave number= $2\pi/\lambda$ (m^{-1})
m	run-up and splash parameter
R	run-up height (m)
s_0	wave steepness = $2\pi H/gT^2$
S	splash height (m)
T	wave period (s)
u	water particle velocity at η_{max} (m/s)
U	wind speed (m/s)
W	liquid water content (g/m^3)
z	height above mean sea level (m)
η_{max}	height of wave crest (m)
ω	wave frequency= $2\pi/T$ (s^{-1})
λ	wave length (m)
π	3.14159
ρ_w	density of water
χ	tide height relative to mean sea level (m)

INTRODUCTION

Stationary offshore structures are subject to icing from sea spray and from run up and splash. Sea spray is created by the bursting of bubbles in whitecaps and, at very high wind speeds, by water sheared from the crest of waves by the wind. Icing may also occur as a result of wave interaction with a structure. For offshore structures with significant area at the waterline, waves running up on the side of the structure can create large quantities of splash even at wind speeds less than 20 m/s.

In this paper we present observations of icing on a mast at the water's edge on a small rocky island in the Gulf of Maine. Run-up and splash on the mast occurred as waves hit the near-vertical rock wall seaward of the mast. In the next section we present our observations of icing on Mt Desert Rock during the second Winter Rock Experiment (WREx2) in January-February 2014. In Section III we develop a model for run-up and splash icing on structures where that may be significant, namely those with significant area at the waterline. The model is based on observations of run-up and splash in wave tank experiments and at a breakwater. We relate splash and run-up height to the scatter coefficient, and suggest a simple variation for the splash liquid water content with height above the mean water surface. In Section IV we apply this model to measurements from WREx2.

I. BACKGROUND

Wave run-up on offshore structures is given as a function of the scatter coefficient $c_s = \pi D/\lambda$ in [1] based on observations in a wave tank of run-up on a partially submerged cylinder. The maximum run-up from mean sea level is given by

$$R_{\max} = 0.5H_{\max}\left(2.06 + 2.33c_s - 1.32c_s^2\right) + 0.5H_{\max}.$$

where H_{max} is the maximum wave height. Note that for c_s>0.9, the run-up height decreases as the ratio of structure width to wavelength increases. At the point of maximum wave force on the structure, which also depends on c_s, the numerical model N_RIGICE ejects droplets from the wave. The mass of water in the surface of each wave that is ejected as drops is specified by the code, but not described in [1] , and can be adjusted by a user-specified calibration parameter. N_RIGICE also includes a module for wind-generated spray, with a user-specified minimum wind speed for spray generation, using W from [2]. Small changes to these two user-specified parameters can drastically change the model results [1].

Forest et al [3] develop an equation for liquid water content in spray as a function of the significant wave height for their model RIGICE04. The liquid water content is based on measurements from the man-made Tarsuit Island, a drilling caisson structure with walls made of concrete boxes. They compare results from this model with N_RIGICE using weather data from the 2-year deployment of the Rowan-Gorilla III rig (Figure 1) near Sable Island, Nova Scotia. That rig has minimal area at the waterline so little tendency to generate run-up and splash. Based on the two models, they expected significant icing on the rig in more than a dozen weather events. However, the only event in which the icing sensors mounted on the rig showed any indication of ice accretion was also the only event with winds exceeding 20 m/s. This indicates that the source of the ice was probably sea spray generated over the open ocean, rather than splash from the interaction of the waves with the structure.

Kulyakhtin and Tsarau [4] use the Mitten [1] run-up equation but with a maximum run-up equal to the significant wave height H_s for $c_s \geq 0.9$. The sea spray flux in their icing model for fixed offshore structures depends on wind speed, wave period, significant wave height, and height above mean

sea level, but includes nothing to characterize the interaction of the structure with waves. Run-up is calculated only to determine the portion of the structure that is washed by waves and kept free of ice.

In this paper we follow Mitten [1], treating run-up and splash together—splash as a continuation of the run-up of green water on the structure—for structures with significant area at the waterline. Our model is simpler than N_RIGICE and has no user-specified parameters.

Figure 1: Rowan Gorilla III drill rig.

II. Observations

We observed splash icing on a mast near the water's edge on Mt. Desert Rock in the Gulf of Maine during the second Winter Rock Experiment (WREx2) in January and February 2014. The average salinity in this part of the Gulf of Maine was 33 psu. On days when the rock at the base of the mast was above the waves, we collected ice samples from the mast for salinity measurements. When the air temperature was below freezing, the surface of the accreted ice was hard and shiny with features that appeared to have been formed by rivulets of water flowing down and around toward the lee side of the mast under the influence of wind and gravity (Figure 2). Cleats, blocks, shackles, and ropes wrapped around the mast interrupted this water flow at about 0.5 m above the base. There was typically no ice below this level and many small icicles on the ropes and gear (Figure 3).

We collected small samples for salinity measurements by chipping ice from the accretion on the mast or by breaking off sometimes dripping icicles on 11 days between 23 Jan and 18 Feb. The ice in all of our 40 non-icicle samples was solid, with

Figure 2. Profile of splash icing on the mast on Mount Desert Rock, 17 Feb 2014.

Figure 3. Icicle formation on the ropes and gear on the mast on Mt. Desert Rock, 23 Jan 2014.

no entrapped water. The samples had a median salinity of 12 psu, with 25th and 75th percentile values of 10 and 19 psu. The icicle salinity was higher, with a median salinity of 29 psu for the 20 samples, and 25th and 75th percentile values of 21 and 33 psu. The highest icicle salinity was 65 psu.

Photographs of the mast taken almost every day from 22 Jan to 18 Feb shown in Figure 4 illustrate the evolution of the ice accretion on the mast from run-up and splash.

III. Run-up and splash model

The height of the run-up and the height of splash in our model are based on the formulation in De Vos et al [5], extended to encompass the wave tank observations of splash by Ramirez et al [6] and the observations of splash caused by wave interaction with a breakwater by Yamashiro et al [7].

De Vos et al [5] were interested in wave run-up on wind turbine foundations that could damage the platform and boat landing facilities that provide access to the turbine. They carried out small-scale wave tank tests and characterized the 2% run-up using a velocity head stagnation model with a parameter *m* that depends on the shape of the foundation and the steepness of the wave, with run-up decreasing with steepness:

$$R_{2\%} = \eta_{\max} + m\frac{u^2}{2g} \tag{1}$$

where u is the water particle velocity at the wave crest $\eta_{\max}$, both given by second order Stokes theory:

$$\eta_{\max} = \frac{H}{2} + k\frac{H}{2}\frac{H}{8}\frac{\cosh(kd)}{\sinh^3(kd)}\left(2+\cosh(2kd)\right)$$
$$u = \frac{Hgk}{2\omega}\frac{\cosh\left(k\left(\eta_{\max}+d\right)\right)}{\cosh(kd)} + \frac{3H^2k\omega}{16}\frac{\cosh\left(2k\left(\eta_{\max}+d\right)\right)}{\sinh^4(kd)} \tag{2a}$$

In deep water ($kd \to \infty$) these relationships can be simplified and provide lower bounds on u and $\eta_{\max}$:

$$\eta_{\max} = \frac{H}{2} + k\frac{H^2}{8}$$
$$u = \frac{Hgk}{2\omega}. \tag{2b}$$

To calculate $R_{2\%}$ in (1), the 2% wave height $H_{2\%}$, which can be estimated by $H_{2\%} = 1.4H_s$ is used in (2a) and (2b).

Ramirez et al [6] did the same kind of wave tank tests as [5] and used high-speed video to determine the run-up height of both green water and splash on slender piles. Keeping the

Figure 4. Icing on the mast on Mt. Desert Rock during WREx2.

formulation in terms of 2nd order Stokes theory for simplicity (rather than stream function theory used in [8] results in the following relationships between m and wave steepness s_0

$$m_g = -66.67 s_0 + 4.53 \text{ for } s_0 < 0.035$$
$$= 2.2 \quad \text{for } s_0 > 0.035 \tag{3a}$$

for run-up R and

$$m_s = -200 s_0 + 13.6 \text{ for } s_0 < 0.035$$
$$= 6.6 \quad \text{for } s_0 > 0.035 \tag{3b}$$

for splash S. While some offshore platforms have slender piles supporting the platform, others such as Molikpaq (Figure 5) have significant area at the waterline. To extend the formulation above to those sorts of structures, we used observations of splash generated by wave interaction with a vertical-sided breakwater. Yamashiro et al [7] used high-speed video to document the height of splash. The breakwater is 140 m wide with a top at 6.4 m above mean sea level. Splash from wave interaction with breakwater went as high as 57 m above the top of the breakwater with winds in the 9 to 12 m/s range and significant wave heights between 2 and 3 m. Using the splash height histograms in [7] along with histograms from the other observations (personal communication, Masaru Yamashiro) for the five periods when a) the breakwater had the original vertical sides, and b) the significant wave height and period are available, we calculated the 2% splash heights above mean sea level. In this calculation we assumed that the occurrence frequencies of splash at 2 and 4 m above the breakwater (which were not documented) were the same as the frequency at 6 m. Using the five cases from [7] and the three cases from [6],

Figure 5: Molikpaq drill rig.

shown in Table 1, we determined a relationship between m_s and c_s and between the fraction of time with splash *fr* and c_s:

$$m_s = 4.7 + 24.1c_s$$
$$fr = 0.055 + 0.0878c_s \le 0.78 \quad (4)$$

In our run-up and splash model, the m_s function of the c_s in (4) replaces the m_s function of s_0 in (3b). However there are no measurements of run-up on the breakwater to replace (3a). Run-up is limited by the height of the obstacle. If the calculated run-up from (3a) is greater than height of the obstacle, the splash height is decreased by the excess, as the waves interacting with the structure are not constrained to move vertically above the top of the structure.

Table 1. Splash data from [6] and [7]

D m	H_s m	c_s	s_0	*fr*	*S* m
0.56	1.05	0.072	0.033	0.026	1.57
0.56	1.1	0.052	0.02	0.032	2.22
0.56	1.1	0.058	0.02	0.080	3.52
140	1.66	8.34	0.04	0.617	25.4
140	2.2	6.75	0.036	0.648	41.4
140	2.33	6.49	0.04	0.706	31.4
140	1.78	7.62	0.038	0.767	33.4
140	1.78	7.3	0.04	0.782	26.4

To characterize the occurrence rate of various splash heights as a function of the 2% height, we combined all five breakwater cases to remove the effects of the variation in wind direction and the steadiness of the wind on the shape of the splash height distribution. This combined cumulative distribution of splash heights up to the 2% height is fit by

$$F = 1.01 - 1.197\exp\left(-0.118S_{\max}\right) \quad (5)$$

with a maximum splash height S_{max}=40 m.

What is the liquid water content in the splash plumes? We assume that there is green water at the significant wave height z=0.5H_s, so the liquid water content at that height above the current tide level is the density of water ρ_w. From that level the liquid water content decreases exponentially to W_s at the apparent top of the splash plume. This results in

$$W(z) = W_s\left(\frac{\rho_w}{W_s}\right)^{\frac{S-z}{S-0.5H_s}}. \quad (6)$$

with the plume extending above *S* with decreasing *W*(*z*). We take W_s=10 g/m^3, high enough for the splash above the breakwater to be visible at *S*.

For each time interval in the analysis, we calculate η_{max} and *u* from $H_{2\%}$, m_g from (3a), m_s from (4), and then $R_{2\%}$ and $S_{2\%}$ from (1). The splash plume liquid water content at height *z* is made up of superposed plumes with maximum heights above the tide level varying from 0.5H_s to $S_{2\%}$. The total splash in the time interval is the plume liquid water content multiplied by the fraction of time with splash from (4).

Examples of liquid water content profiles for the conditions in WREx2 are shown in Figure 6 for a 4-m wide obstacle (the approximate width of the rock face below the mast). The weather and ocean data and calculated splash parameters *S* and *fr* for these cases are in Table 2, in order of decreasing wind speed. Notice that the liquid water content in the plume depends on the dominant wave length and tide as well as on wind speed and significant wave height. For lower tides the impacting wave is carried higher above the obstacle as splash rather than flowing over it.

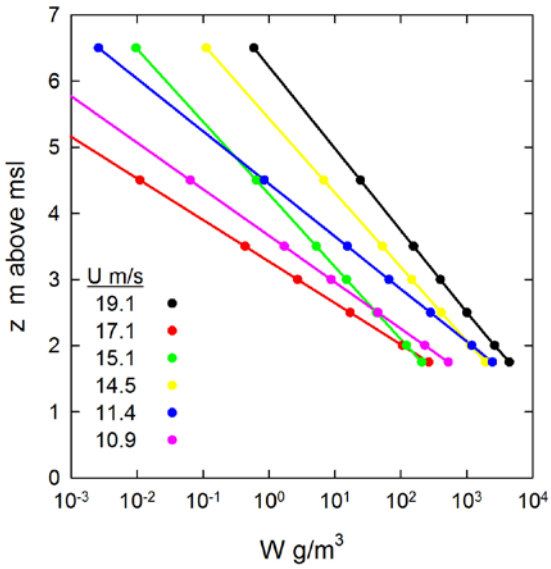

Figure 6. Examples of splash plume liquid water content from WREX2 weather and ocean data and a 4-m-wide rock face.

Table 2. Wind and ocean data and calculated splash parameters for the splash liquid water content profiles in Figure 6.

U m/s	H_s m	λ m	χ m	*fr*	*S* m
19.1	3.0	43.9	-0.5	0.08	7.7
17.1	3.0	64.0	-1.0	0.07	4.7
15.1	2.0	33.0	-1.4	0.09	6.4
14.5	1.9	25.0	-0.2	0.10	6.4
11.4	1.2	20.2	0.2	0.11	4.6
10.9	1.2	20.2	-0.1	0.11	4.0

IV. SPLASH ICING

We assume that splash drops are large enough that the collision efficiency is 1.

The seawater temperature is above freezing and the liquid water content at lower elevations in the splash plume is relatively high, so unless the air is cold, splash may not freeze on the structure and may even remove previously accreted splash ice. We assume that no ice accretes at elevations below $z = \chi + 0.5H_s$. Above this height, we use a simple heat balance algorithm, taking the salinity of the water into account by assuming a freezing temperature of -1.6°C, rounded up to compensate for ignoring any cooling of the splash plume. In the heat balance calculation, we consider convective and evaporative cooling and heat released by cooling the seawater to -1.6°C and by the latent heat of fusion. Depending on air temperature and humidity, wind speed, ocean temperature, and splash liquid water content, splash may accrete as ice or previously accreted ice may melt. The relatively fresh accreted ice (see section II) is also allowed to melt in periods without splash if the air temperature is above 0°C.

Splash icing on the leg of a wind turbine platform fixed to the bottom in 40-m deep water in the Baltic Sea is shown in Figure 7. Using the rung spacing for scale indicates a leg diameter of about 3 m. As access to the platform is by boat, the ice covering the ladder denied access. There is some weather and ocean data associated with that icing episode available (personal communication, Jacob Royle) but it has not been published. Mizuno et al [9] show splash icing on an experimental structure with 0.5-m diameter legs set on the bottom in the Sea of Japan in 7-m deep water. Weather and ocean data and photographs of the structure were collected from 1988 through at least 1990, but are no longer available (personal communication, Mitsunari Hirasawa).

Figure 7: Ice-covered leg of wind turbine platform in the Baltic Sea

V. Results and Discussion

The mast in WREx2 provides an example of splash icing, but with the splash generated by a rock face rather than by an engineered structure. The rock face is essentially vertical, but it bends over to horizontal near the top, and becomes jumbled large rocks where the point of land merges with the rest of the island. Depth of water at the rock face is about 5m. Weather and ocean data for WREx2 are shown in Figure 8. Air temperature and wind speed are measured from the lighthouse. Water temperature, significant wave height, and wavelength are measured at a buoy 15 km north. Note the 3 to 4 m tidal range. The bottom panel shows the modelled ice mass on the mast, assuming splash ice accreted with a uniform thickness and a density of 900 kg/m^3 on the windward half of the mast. The 6-day tick spacing on the horizontal axis matches the 6-day-long rows of photographs in Figure 4.

Splash data to fill in between values from the breakwater and the slender pile wave tank tests would better define the variation of both run-up and splash for the range of configurations of fixed offshore structures. It would also be useful to determine the effect of cross-sectional shape on splash. A field test in relatively deep water with structure widths of 5, 10, 25, 50, and 100 m, with both curved and flat sides would be ideal. Splash heights would be documented by high speed video, as in [6] and [7], with atmosphere and ocean measurements made from an instrumented buoy.

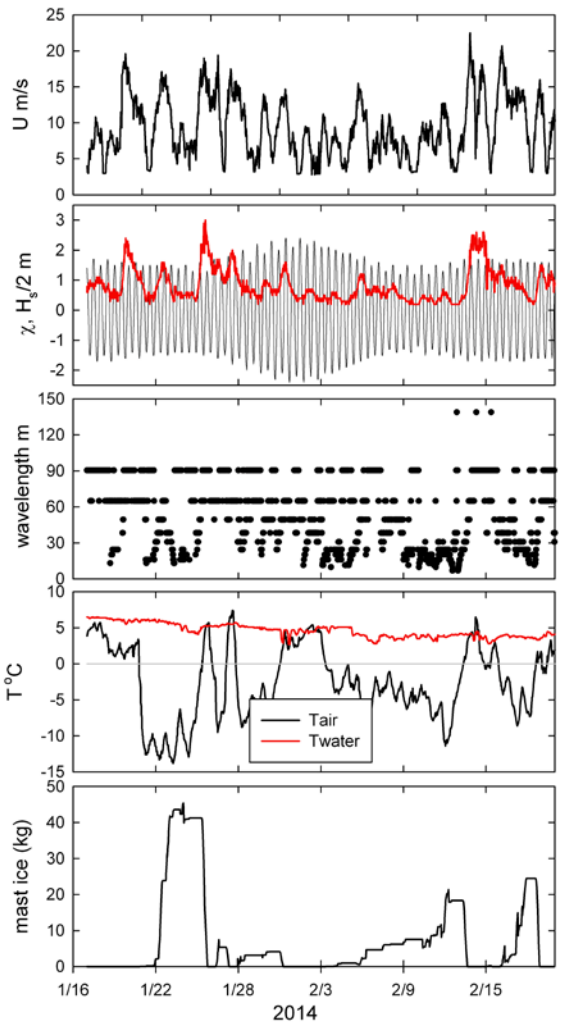

Figure 8. Mt. Desert Rock weather and ocean conditions and modelled ice mass on mast 17 Jan to 20 Feb 2014.

Acknowledgments

ONR Award Number N0001412MP20085 supported this work. We thank College of the Atlantic, Chris Tremblay, and Tanya Lubansky for providing logistics for WREx2.

References

[1] P. Mitten, Measurement and modeling os spray icing on offshore structures-Final report for Atmospheric Environment Service (1994) 70 pages.

[2] L. Horjen and S. Vensmo, Mobile platform stability (MOPS) subproject 02-icing, MOPS Report No. 15, Norwegian Hydrodynamic Laboratories, STF60 A 284002 (1984) 45 pages.

[3] T.W. Forest, E.P. Lozowski, R. Gagnon, Estimating marine icing on offshore structures using RIGICE04, *Proceedings of IWAIS XI* (2005).

[4] A. Kulyakhtin and A. Tsarau, A time-dependent model of marine icing with application of computational fluid dynamics, *Cold Regions Scince and Technology* **104-105** (2014) 33-44.

[5] L. De Vos, P. Frigaard, and J. De Rouck, Wave run-up on cylindrical and cones shaped foundations for offshore wind turbines, *Coastal Engineering* **54** (2007) 17-29.

[6] J. Ramirez, P. Frigaard, T. Lykke Andersen, L. De Vos, Large scale model test investigation on wave run-up in irregular waves at slender piles, *Coastal Engineering* **72** (2013) 69-79.

[7] M. Yamashire, A. Yoshida, Y. Nishi, Effects of wave dissipating blocks on reduction of salinity in the air generated at a vertical breakwater based on field observations, *Coastal Engineering Journal* **54**, 3 (2012) 1250019, 24 pages.

[8] T. Lykke Andersen, P. Frigaard, M.L. Damsgaard, L. DeVos, Wave run-up on slender piles in design conditions-Model tests and design rules for offshore wind, *Coastal Engineering* **58** (2011) 281-289.

[9] Y. Mizuno, M Hirasawa, K. Yano, K. Tokikawa (1991) Investigation of sea spray icing on offshore structure, *Proceedings of 1st International Offshore and Polar Engineering Conference* (1991) 543-547.

Results of the application of a hydrophobic coating base polymer on stranded OHL Cu cable

Background

The project to apply an hydrophobic coating developed by LFL has its origin in a blizzard, which took place on 9 and 10 March 2010 in the NE area of Spain: the region of Catalonia as shown in Fig. 01.

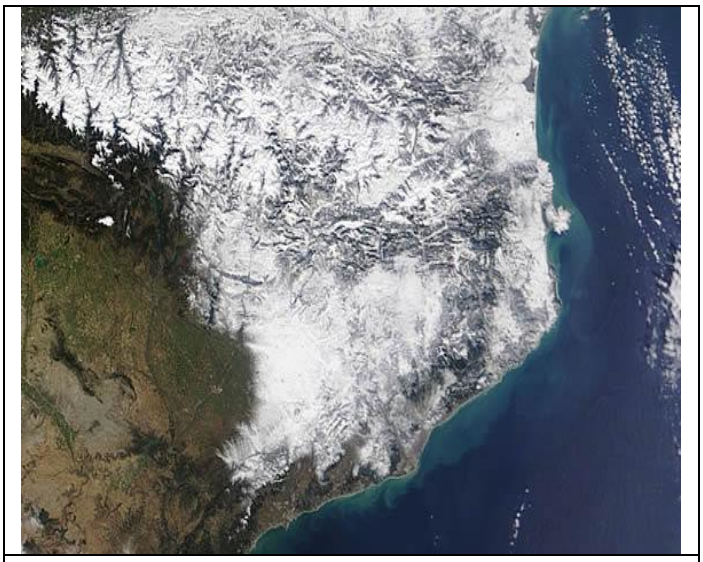

Fig 01: satellite image of the area affected by the snowstorm of March 2010

As the weather situation of 03/09/2011 described in Fig. 02 shows there was an ingress of a cold air mass from Eastern Europe. This air mass, before reaching the eastern coasts of the Iberian peninsula, went across the waters of the Gulf of Lion, in the NW Mediterranean and became saturated with moisture because of the always relatively high temperature of the Mediterranean surface waters (12 / 13 ° C at the beginning of March). Once the cold and moist air mass thus formed came in contact with the mountain ranges arranged along the NE Mediterranean coast of the Iberian peninsula it produced an intense and abundant snow fall at all heights in a way that areas close to the coast (offshore areas < 500 m above the sea level) had snow precipitation at temperatures between - 1 to 2 ° C which means that it was a very sticky wet snow.

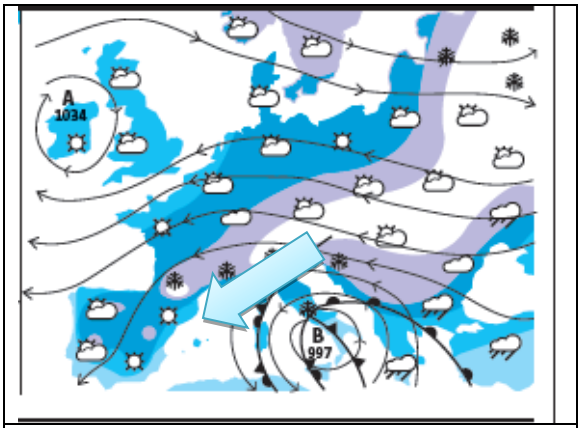

Fig 02: 03/10/2010 meteorological situation producing triggering the snow storm

During this episode in the geographical area shown in Fig. 03 a snowfall of 500 mm (equivalent to 50 mm of rainfall) of wet snow occurred over a period of time of 1.5 h, this resulted in the accumulation of layers of snow with a thickness of up to 300 mm on almost the entire 45 kV, 25 kV and lower voltages electrical distribution network, which jointly with winds of 50-70 km/h , produced the collapse of a large number of towers. This occurred area shown in Fig. 03 which includes populated and tourist areas such as the Costa Brava. I n total there were 11 days without electric service in the area with resulted in heavy economical losses both for the local D.S.O and its customers.

The standards applicable to electrical lines of medium and high voltage in the area affected didn't take into account the possibility of snow loads at altitudes below 500 m.

Analysis of the archives shows that the area affected by this snow storm have a history of other large snowfall incidents in the years: 1947, 1962, 1971, 1983,1985,2001,2010. The 1947 snow storm was the largest but at that time the grid was not as developed as it is today and the damage had less impact. In total there is an average recurrence period of 9 years during the studied time period.

Fig 03 Detail of the most affected area, highlighted in yellow the affected set of distribution lines

Figures 04 and 05 exhibit some of the damage caused by the accumulation of snow and ice weight on the distribution lines in the area shown in Fig. 03.

The development of a new type of cable for OHL lines with a polymer type coating overlay whose purpose is to act as passive protection against accumulation of wet snow and the further ice on OHL cables as a possible solution to this recurring problem has been made by the company LFL.

The result of such action is the CAC cable which is a hydrophobic polymer-coated copper stranded wire

Fig 04 : Tower line 110kv, 2 circuit , bent by the combined action of wind and snow

Fig 05 : Tower of 25kV line , 2 circuit, collapsed by the weight of the snow

Coating:

The solution adopted includes coating each stranded wire of hydrophobic polymer material

This solution presents the main challenge of being outdoors which may deteriorate the coating for several reasons; mainly:

- Action of the UV RAYS from the Sun
- Corrosion
- Variations in temperature both for meteorological environment or for the cable heating by electrical current flow

Fig 06 : CAC coated section

Tests on the coated wire have determined that the coating keeps its properties for a minimum period of 7 years. The exact number depends on the environmental conditions of the power line deemed: if it is a more or less sunny or for a highly corrosive area.

The maximum working temperature is established to 170 ° C which is a temperature only occasionally reached in an overhead electric line (usually in N-1 or N-2 situations).

Fig 07 : Quality test of coating: the "tie" test

In Fig. 07 can be seen one of the quality procedures conducted to check the coating adherence to the wires to be stranded , this test ,known as "tie" , winds the yarn around a equivalent diameter to itself : in practice between 2.0 and 2.5 mm; the coating must remain perfectly bonded to copper surface as can be see in Fig. 07.

Until now only polymeric coating adhesion has been achieved on the polished surface of freshly drawn copper; in the case of the aluminum the constant existence of an Aluminum oxide layer on the surface gives a lower adherence of the coating on the Aluminum surface and as a consequence the "tie" test failure .

A basic concept in hydrophobicity is the contact angle or angle which a drop of water has when placed on a flat surface; this angle must always be higher than 90 ° to be considered an hydrophobic surface.

Blaock polimer	test 01	test 02	test 03	test 04	test 05
1	129,0	136,8	138,7	141,2	129,1
2	128,8	151,0	136,6	138,4	129,0
3	122,9	125,4	136,4	119,5	131,6
4				129,4	
Average	**126,9**	**137,7**	**137,2**	**132,1**	**129,9**

Table 01 : contact angles found with the black polymer coating .

The results obtained from contact angle measures are in a range of 125 to 137 °which gives the hydrophobicity propriety to the treated surface.

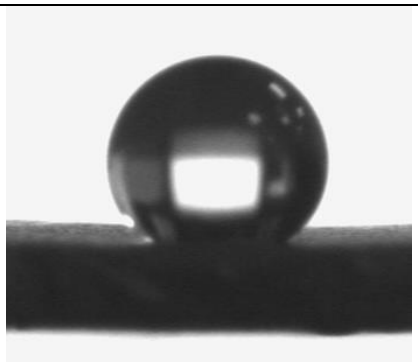

Fig 08 : Angle of contact obtained on polymer coated surface

Tests carried out on Dead Water Fell

Tests conducted on Dead Water Fell facilities in the UK during the winter of 2013-2014 were designed to test the behavior of the polymer coating on CAC HLS-95 and 150 cables (95 and 150 mm^2 cross-sections) against a non-coated ACSR-180 cable

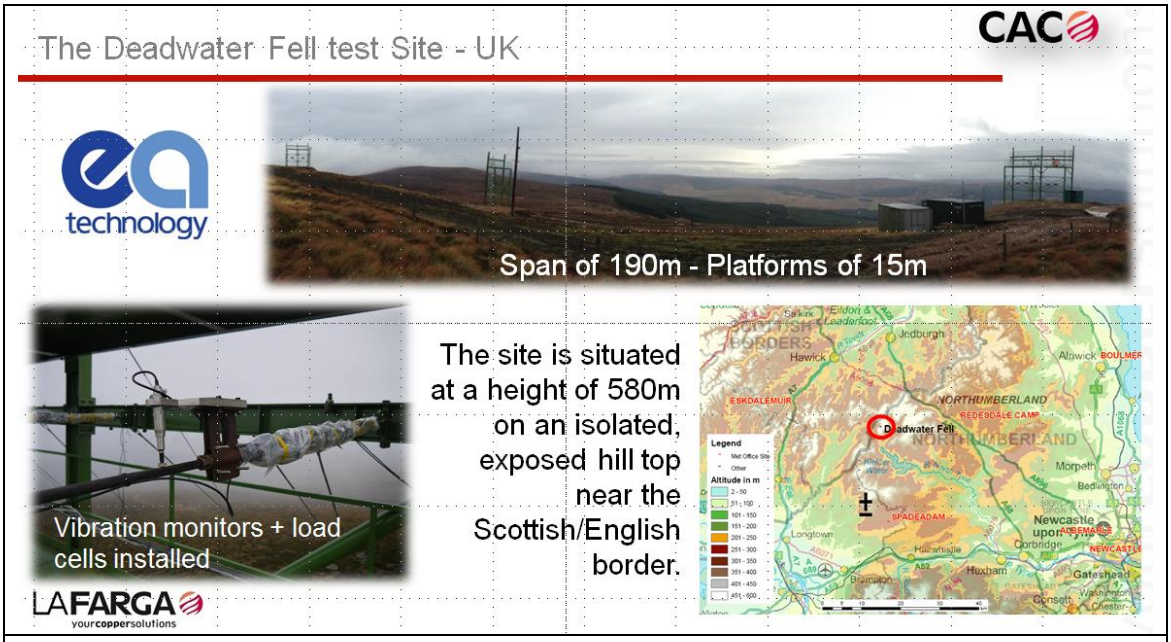

Fig 09 : Dead Water Fell facilities to test OHL cables against real whether conditions

The 2013-14 winter turned out to be one of the less harsh recorded on the location of Dead Water Fell, with only 7 episodes of snow between November 2013 and March 2014.

	CAC-HLS 95	CAC-HLS 150	ACSR LA-180
Material type	copper	copper	aluminium + steel
Conductor greased weight (kg/Km)	846	1335	676
Conductor diameter (mm)	12,6	15,9	17,5
Conductor strand size (mm diameter)	2,5	2,25	2,5 (Al) and 2,5 (Steel)
Number of strands	19	37	30 (Al) and 7 (steel)
Coefficient of linear expansion (10-6/degree °C)	16,8	16,8	18,6
Modulus of elasticity (kN/mm^2)	50	50	75
UTS (kN)	47,5	75	63,9

Table 02 : Properties of the cables tested

In any case and because of the relative mildness of the winter, snowfall took place in conditions very similar to those outlined in the **background** point of this paper

The graphs displayed in figs 10, 11 and 12 give a synopsis of the behaviour

found. The color code is:

- Dark blue : ACSR-180
- Red : CAC-HLS 150
- green : CAC-HLS 95
- Light blue: ambient temperature evolution

The most outstanding fact is that the cables coated with polymer facing ambient temperatures in the range: - 2 to - 3 ° C take much longer to put on stress as a result of snow or ice accretion; Furthermore it is also observed that cable ACSR-180 has a much higher mechanical stress than the cable CAC-HLS-150 despite the fact that the copper cable is significantly heavier than the aluminum cable.

Fig 10 presents the behaviour of the 3 cables under conditions of wet snow: temperature while the snow was falling was close to 0^0 C . In this case the effect of snow on coated wires is practically negligible compared to the great increase of ACSR cable mechanical stress. The data presented in Fig. 11 was acquired in colder conditions and the increase in mechanical stress due to the ice load is bigger in the ACSR cable and remains for longer than on the coated cables.

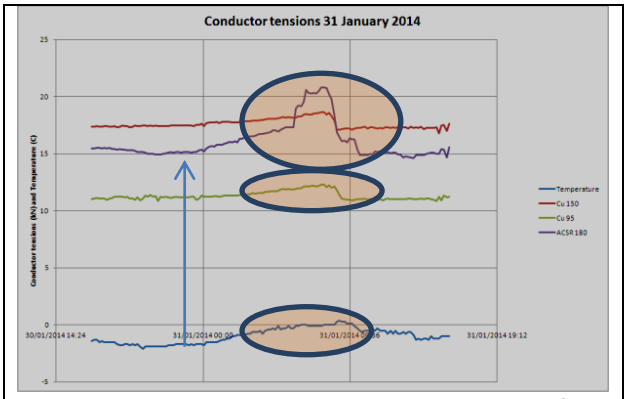

Fig 10 cables CAC behaviour in comparison of a ACSR 180 in wet snow conditions

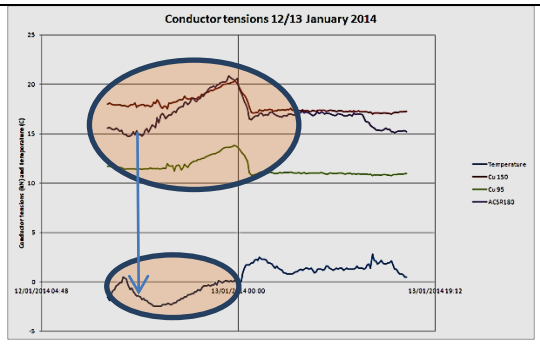

Fig 11 : CAC cables behaviour front ACSR 180 in wet snow conditions

Fig. 12 is a summary of the results obtained in the 7 episodes reported; the graph shows the maximum increases in mechanical stress recorded in each cable in each event. As shown in the graph there is a dependency between the ambient temperature and the increase of stress in such a way that at temperatures close to 0°C CAC coated cables hardly register increments of mechanical stress, unlike the ACSR cable that displays substantial increases in mechanical stress : more than double that of the CAC cables . When the temperature is lower than - 3 °C CAC cables have higher mechanical stress increases but, anyway, they are always lower than the uncoated ACSR-180 cable

Conclusions

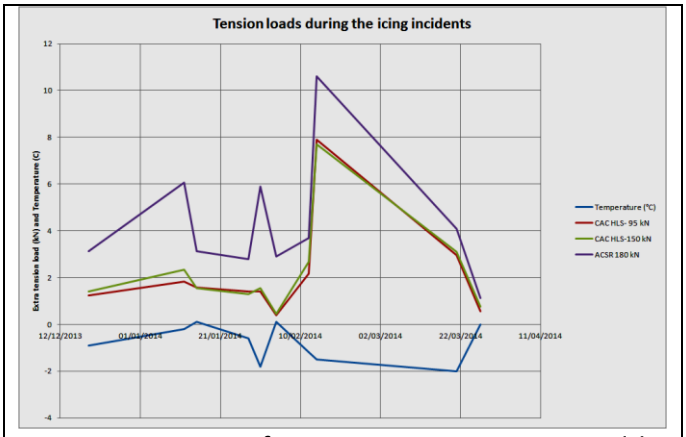

Fig 12 : Overview of stress increases experienced by strand coated CAC and uncoated ACSR..

- Coated Copper stranded yarn that shape copper cables have shown that snow and ice adheres less on it when temperature conditions are close to the 0 ° C which meets the aim of preventing collapses in OHL located in coastal areas not exceeding 500 meters above sea level located along the northern shores of the Mediterranean and other areas of similar climate.
- It can be seen that in case of lower temperatures: < - 3 ° C snow accretion increases but is always less than a non-coated cable.
- The time that the ice remains on the cable is less if it is coated: see Figure 11 in which it can be seen that a certain layer of ice remains on the cable ACSR-180 for ½ day while CAC wires lose the layer of ice accreted when the temperature reaches 0°C. Also, the ice accretion starts later in coated cables than on the uncoated. ***Then the ice layer is smaller and it remains less time over a polymeric coated copper cable***.

Further test and improvements to be carried out

A test conducted on Dead Water Fell facilities does not properly cover the area of ice and snow accretion at temperatures below - 5 ° C for long periods of time.

Tests performed are only related to one of the possible coatings whose hydrophobicity is moderate; it is of interest, to try a super hydrophobic coating: with a contact angles > 150 ° having good behaviour in the face of UV, corrosion and thermal cycles

WET-SNOW ACTIVITY REASERCH IN ITALY

Matteo Lacavalla[1], Pietro Marcacci[1], Andrea Freddo[2]
[1] RSE SpA, Research on the Energy System, via R. Rubattino 54, 20134 Milan, Italy
[2] TERNA SpA, - Via Egidio Galbani, 70 - 00156 Rome - Italy
matteo.lacavalla@rse-web.it

Abstract: **The power grid infrastructure is vulnerable to some extreme meteorological phenomena and this could create some difficulties in the safe management of the power system. The wet-snow accretion on overhead lines is well-known to the Transmission and Distribution System Operators. The problem affects much of Europe, with an annual number of wet-snow type steadily increasing over the total number of snowfalls. The problem imposes a greater attention to this phenomenon, either through a focused weather forecast both through active and passive mitigation strategies. RSE has developed WOLF (Wet snow Overload aLert and Forecasting) for overhead lines warning on the transmission power grid. The weather forecast system is already being tested at the Italian TSO. WOLF, together with wet-snow load, provides an estimation of the ant-icing current necessary to keep OHL free of wet-snow sleeve formations, supporting operators in adopting mitigation active strategies. In synergy with WOLF, an automatic station named WILD (Wet Snow Ice Laboratory Detection) has been installed in the municipality of Vinadio in the west Alps, at an altitude of 950 m asl, for the verification of the forecasts system. Through WILD measurements, it is possible to analyse in detail the weather conditions most critical for the wet-snow sleeve formation and, at the same time, to make the "tuning" of the parameters in the models of accretion and anti-icing. A prototype of an active anti-icing circuit is able to maintain snow-free the surface of a typical cable in any condition of wet-snowfall and a rotating system allows to measure and compare the sleeve accretion on different type of conductors. In the terms of the passive mitigation, a qualitative test is being carried out at WILD station on innovative conductors materials provided by Italian TSO, characterized by different surface hydrophobic and ice-phobic treatments. The wet-snow accretions on new cables are compared, although qualitatively, in the same weather conditions with those on conventional conductors. This experimentation may be an important test to get a selection of materials to be used in the areas most exposed at wet-snow risk.**

Keywords: wet snowfall, overhead lines, winter blackouts, weather forecast, wet snow sleeve accretion monitoring.

LEGEND AND ABBREVIATIONS

OHL	*Overhead Lines*
HV	*High Voltage*
MV	*Medium Voltage*
TSO	*Transmission System Operator*
DSO	*Distribution System Operator*
WOLF	*Wet-snow Overload aLert and Forecasting*
WILD	*Wet-Snow Ice Laboratory Detection*
NWP	*Numerical Weather Prediction*
RAMS	*Regional Atmospheric Modeling System*
WRF	*Weather Research and Forecasting*
AI	*Anti-Icing current*
ACSR	*Aluminium Conductor Steel Reinforced*
ACSR-Z	*ACSR with Trapezoidal Wire*
ACCC	*Aluminium Composite Core Conductor*
TACIR	*Aluminium Conductor Invar Steel Reinforced*
MAE	*Mean Absolute Error*
RMSE	*Root Mean Square Error*
R^2	*Coefficient of determination*

INTRODUCTION

The heavy wet snowfall events are responsible for several and harmful winter blackouts on Italian electrical networks of HV and MV power lines due to the formations of ice and snow on OHL conductors [1]. It is estimated that every year, in Italy, the cost of damages from these particular snowstorms is greater than 200 million euros. For this reason, it is important to develop and define different strategies to limit the risk on overhead power lines. Efforts are made to establish and improve standards and methodologies for handling the impact of wet snow accretion in the most economical and rational manner. Over the past 30-50 years, such knowledge was built up from field observations and measurements, laboratory studies and model development [2,3]. However, despite this better understanding, actual severe weather conditions at a remote location are always a critical question for overhead power lines [4,5].

Figure 1: broken MV conductor on ground due to strong wet-snowfall event in central part of Italy.

In order to approach the problem, RSE and the Italian TSO TERNA, have developed two primary strategies:

- **Predictive system**. WOLF [5] is the forecast system based on the output of different NWP models (RAMS,WRF) in combination with:

i. the wet-snow accretion model proposed by Makkonen [6,7] for the estimation of snow load and sleeve thickness on cylindrical conductor;

ii. the mathematical thermal model proposed by Shurig and Frick [8,9] for the estimation of AI current to prevent from ice formations on OHL.

- **Wet-snow test site**. WILD is the first outdoor remote station in Italy, entirely developed by RSE, in which it is possible to:

i. monitor the wet-snow accretion on different types of conductors by using a special rotating test-span weighted by two load cells;
ii. test innovative super-hydrophobic and icephobic coatings of ACSR and ACCC conductors;
iii. verify the weather and accretion forecast by using instruments able to operate in extreme weather conditions;
iv. test the effect of AI current on ACSR conductors.

I. WET-SNOW TEST SITE

The IEC 61774 rules [10] and the activity of CIGRE WG B2.28 advise a strategy for collecting different data sources in order to obtain the best possible information basis to evaluate the maximum design load. The experimental research in Iceland has been also considered in this work [11,12,13]. WILD has been developed taking into account these recommendations. The wet-snow test site has been installed in the west part of the Alps in the municipality of Vinadio, at an altitude of 950 m asl. This area is particularly subjected to strong wet-snowfall events due to intense humid fronts coming from the Ligurian sea.

The measurements acquired from the WILD station are of different types and can be grouped as follows:

- principal meteorological parameters as air temperature, wind speed and its direction, snow accumulation, snow water equivalent of precipitation;
- physical measurements and characterization of the snowfall: droplet size, snowflakes velocity, number of particles;
- mechanical measurements on conductors exposed to snowfall: weight, size, diameters of ice sleeve;
- electronic measurements related to the control of the anti-icing current;
- pictures of the wet-snow event by using two web-cameras.

A scheme of wet-snow test site is shown in Figure 2. The weather and accretion measurements converge in a central acquisition system. The acquisition system allows the sending of data to RSE server, through a scheduling by internet connection.

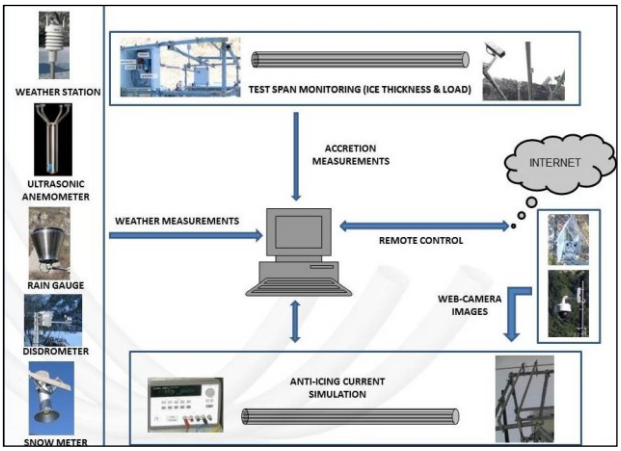

Figure 2: scheme of all measurements collected at the experimental station.

A. *The monitoring system of test spans*

WILD, in the current configuration, allows the installation up to seven test spans of about 14 meters in length to carry out qualitative comparative test of different type of conductors exposed to the same environmental condition. Figure 3 shows the set-up of test span installed at WILD station. Starting from the left of the image, the first two conductors have been treated with black varnish, the first one is a conductor ACSR-Z Ø19.04mm, the second one is the *low-sag* type TACIR Ø18.99mm. At the center of image, the two not treated conductors are respectively ACCC Ø24mm and ACSR Ø22mm. The last two conductors are ACSR-Z Ø19.04mm with two different of hydrophobic coatings.

Figure 3: test span installed at the experimental station.

B. *The accretion monitoring system*

Two other pieces of ACSR conductors with a length of 3 meters have been mounted on a system that allows them a slow rotation, according to ISO12494. The rotation is necessary for two reasons: principally because the rotation system is able to efficiently capture the total flow of snowfall and in this way it is more correct the comparison with the simulated values obtained by the accretion model which assumes a conservative growth on conductor. The second reason is because especially at the center of a span of overhead power line, the load of snow sleeve causes a little torsion/rotation of conductor. One of these two pieces of ACSR conductor has been treated on the surface with an hydrophobic coating. The not treated ACSR conductor is weighted through two load cells placed under them and two ultrasonic sensors measure the thickness of snow-sleeve during the wet-snowfall event.

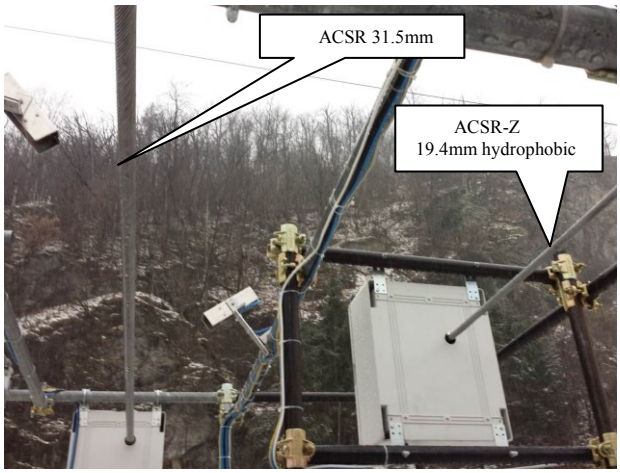

Figure 4: ACSR conductors subjected to slow rotation. The left conductor of the image is weighted and ultrasonic sensors measure the thickness of snow sleeve.

C. *The AI current system*

Two ACSR Ø31.5mm conductors of 1.5m in length are devoted to the simulation of the AI current. A previous experimental campaign has already shown that a skin temperature set to 2°C is sufficient to prevent from ice formation in all snowfall conditions. For this reason, in order to minimize the AI current for the power line, the surface temperatures of two conductors have been reduced respectively to 1°C and 1.5°C through a specific circuit. The simulation of AI current is allowed by a resistance wire inside each conductor, able to produce a Joule-effect up to 40 W/m as shown in Figure 5. To maintain the skin temperature at the set points in all environmental conditions, a PC acquires every minute the surface temperature measured by thermal sensors and regulates the power sent to the conductors by a programmable power supply.

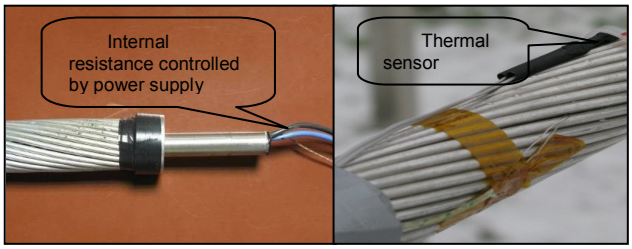

Figure 5: ACSR conductors intended for the simulation of AI current. The internal resistance reproduces the Joule effect and the thermal sensor measures the skin temperature.

II. FUNDAMENTAL OF WET-SNOW MODELS

Unfortunately, there is no specific accretion model that can well simulate all physical and mechanical processes involved in wet-snow accretion. This statement is particularly true for wet snow. There are different models proposed in the literature for wet snow icing accretion [14,15,16,17], but all of them are based on the basic equation (1) for ice accretion described in the ISO standard for icing of structures [7]:

$$\frac{dM}{dt} = \alpha_1 \alpha_2 \alpha_3 * w * A * V \qquad (1)$$

where α_1 is the collision efficiency; α_2 is the sticking efficiency, and α_3 is the accretion efficiency; w is water content (kg/m^3); A is the cross-sectional area (m^2) perpendicular to object; V is the particle impact speed perpendicular to object (m/s).

For the wet-snow precipitation, the atmospheric water content can be considered as the sum of solid (snow and graupel phases) an liquid precipitation. The terminal vertical velocity of snowflakes V_s is assumed to be 1.5 m/s, obtained by three years measurements of a disdrometer during wet-snowfall events. For wet-snow conditions it can be assumed that the collision efficiency and the accretion efficiency is unity (α_1=1 and α_3=1). The sticking efficiency α_2 may be inferred from some field observations. In particular, α_2 depends on the liquid water content of snowflakes and the impact speed. One of α_2 approximation has been proposed by Admirat approach.

Regarding to the density of snow sleeve ρ_s, there is a strong dependence from the wind intensity, because higher snowflake impact speed will tend to produce a more compact snow deposit. For a cylindrical conductor, the sectional area *A* has been approximated to the diameter, considering the mass accreted per unit length.

In general, considering meteorological data given at a temporal resolution Δt, the equation (1) can be integrated forwarding in time [18], assuming that the weather variables are constant for each time step *i*:

$$M_i = M_{i-1} + I_i D_{i-1} \Delta t \qquad (2)$$

where I is the intensity of accretion per unit area and expressed by the following equation (3):

$$I = \alpha_2 I_0 \sqrt{1 + \left(\frac{U \sin\theta}{V_s} \right)^2} \qquad (3)$$

where I_0 may be considered the intensity of precipitation at a given time step; U is the wind intensity (m/s); θ is the angle between the wind direction and the conductor supposed horizontal; V_s is the terminal vertical velocity of snowflakes.

Considering a cylindrical wet-snow accretion on conductor, the corresponding snow sleeve diameter is given by (4):

$$D_i = \left[\frac{4(M_i - M_{i-1})}{\pi \rho_s} + D_{i-1}^2 \right]^{1/2} \qquad (4)$$

The empirical parameters have been deduced from measurements of WILD station collected over the past three winters. Below the methods considered for the algorithm are briefly described.

- Wet-snow condition if air temperature T_{2m} is in the range of -0.5°C to 2°C.
- Precipitation is the sum of solid -snow and graupel- and liquid precipitation.
- Sticking coefficient $\alpha_2 = 1/U^{1/2}$; 0.1 if U>10m/s
- Density of snow sleeve $\rho_s = 300 + 30U$; $\rho_s = 600$ kg/m^3 if U>10m/s.
- Vertical velocity of snowflakes V_s = 1.5 m/s.

For dry-snow condition, when the temperature is lower than -0.5°C , the snow accretion is limited by the empirical coefficient α_2 =0.1 and ρ_s =100 kg/m^3.

III. FUNDAMENTAL OF ANTI-INCING MODELS

The literature proposes different thermal models for estimating the temperature of a conductor subject to Joule effect [9]. The thermal model proposed by Shurig and Frick [8] has been used to estimate the AI current necessary to maintain the conductor at a specific skin temperature in order to keep it free from snow accretion. The mathematical model considers the conductor in steady state and the heat balance equation is given by (5):

$$P_j + P_s = P_r + P_c \qquad (5)$$

where P_j and P_s represent the heat gain, P_r and P_c the heat losses. P_j is the Joule heating due to current flow, P_s is the solar radiation heating, P_r is the radiative cooling and P_c is the loss for convective cooling. This equation doesn't consider if the conductor is wetted. But in wet-snow condition, the conductor is affected by a flow of snowfall. For this reason, another loss term P_w must be considered in (1) due to wetted conductor (6).

$$P_j + P_s = P_r + P_c + P_w \qquad (6)$$

Considering the new formulation of heat balance (6), the joule effect produced can be expressed by (7):

$$I^2 * R_T = P_c + P_r + P_w - P_s \quad (7)$$

where R_T is the resistance at the temperature of conductor. The term P_r depends on the emissivity of conductor, the ambient temperature and the conductor surface temperature. The convective cooling P_c is caused mainly by the wind and the difference temperature of the conductor and the air. Whereas, the term P_s is related to the solar irradiation and to the absorptivity of conductor surface. In wet-snow conditions, P_s can be ignored. Finally, the AI current may be expressed as:

$$AI = 5.6 * \sqrt{\frac{(P_r + P_c + P_w - P_s) * 10^4 * D}{R_T}} \quad (8)$$

where D is the conductor diameter. In order to verify the Joule effect produced by the internal resistance of the ACSR conductor at WILD station, the thermal model proposed by Shurig and Frick has been applied for dry weather condition[1] observed. The conductor surface temperature has been maintained from the electronic circuit around 2°C. The current reproduced by the circuit is in according to the current calculated by the Shurig and Frick thermal model, Figure 6.

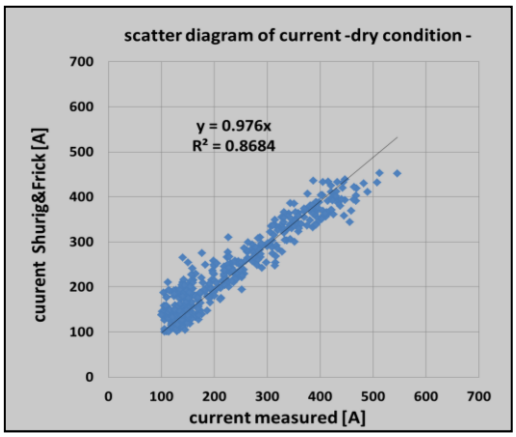

Figure 6: correlation between AI current calculated by using the thermal model and AI measured on ACSR conductor.

The same simulation has been conducted in wet-snow condition, where the surface conductor was wetted. By using the (5), it is notable the underestimation ($BIAS_{model}$=-130A) of the current given by thermal model respect to measured current (Figure 7). The energy debt is mainly due to the cooling of wetted conductor and can be expressed by the P_w term.

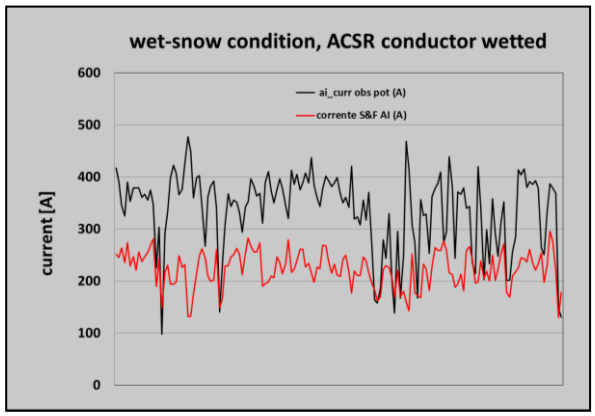

Figure 7: underestimation of current calculated through the model in wet snow condition (red line) respect to observed data (black line).

[1] This condition refers to the absence of precipitation and air temperature lower than 3°C. In this condition, the surface conductor is dry.

The P_w term, that represents the cooling for surface unit, can be calculated by (9):

$$P_w = P_j + P_s - (P_r + P_c) \quad (9)$$

The wet cooling effect is mainly related to the intensity of snow precipitation, as shown in Figure 8.

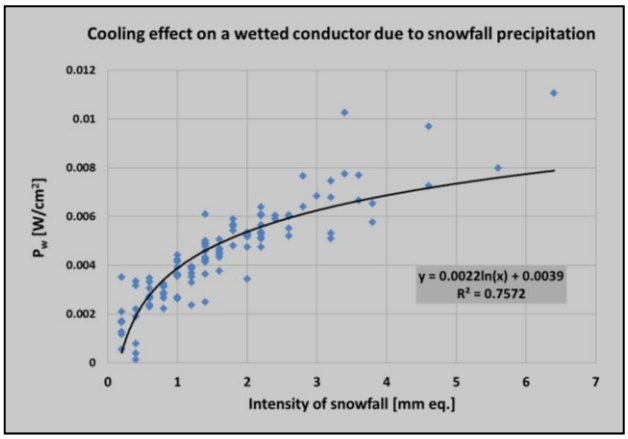

Figure 8: logarithmic relationship between the intensity of snowfall and the term P_w.

The loss due to snowfall precipitation can be expressed by the following empirical equation:

$$P_w = 0.0022 * \ln(prec) + 0.0039 \quad (10)$$

where *prec* is the observed water equivalent of snowfall. Using the empirical P_w term into (8) for the calculation of AI current, it is possible to obtain a new AI current very close to experimental data as shown in Figure 9 ($BIAS_{model}$=4A).

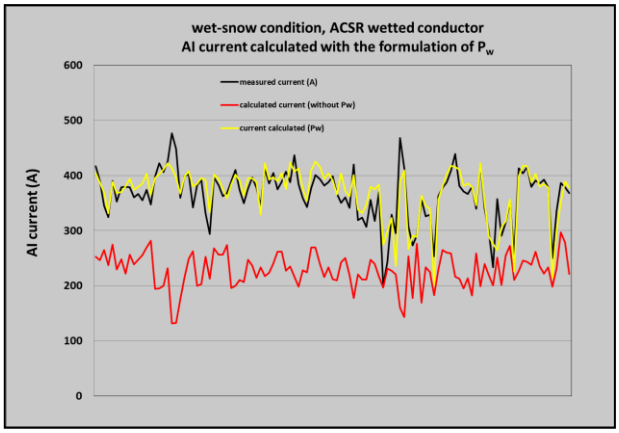

Figure 9: AI current calculated in wet-snow condition with the empirical term P_w deduced by experimental data (yellow line).

IV. WET-SNOW SIMULATION

Two wet-snow events occurred at WILD station last February 2015, are simulated with 2 non-hydrostatic NWP models, RAMS v6.0 developed by ATMET[2] and WRF ARW - V3.4.1. The simulation of both NWP models are done at a resolution of 0.05° with 40x41 grid points in the 2-way nested domains, Figure 10. Both models use terrain-following vertical coordinate with 36 vertical levels. The models are initialized and forced at their boundaries with ECMWF forecast with a

[2] Atmospheric, Meteorological and Environmental Technologies.

grid resolution of 0.125°. The structure of the atmospheric water content is given by the Thompson scheme. The predicted phases graupel, snow and rain have been converted to total mass of precipitation.

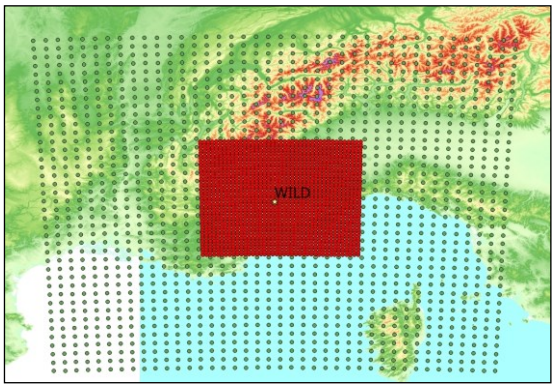

Figure 10: NWP two-way nested domains. WILD station is located at the center of two domains.

The models are run for the whole accretion period as indicated by the wet-snow observation with a forecast horizon of +84h, 1-hour time step. For these simulations, some improvements have been introduced to better represent the complex orography of the domain. The enhancement can be summarized in an improved land-use classification based on the Corine-dataset and in a better representation of orography based on SRTM-dataset with a resolution of 90m. These changes lead to a more accurate surface temperatures and a better representation of the surface winds. The two case studies analysed concern the snowfall events occurred on 5-6 and on 15-16 of February 2015. In the next three paragraph, all simulations of weather forecast, wet-snow accumulation prediction on rotating ACSR conductors and AI current simulation has been described, together with images of webcam installed at the experimental station.

A. Simulation of weather

The simulations of NWP models have been compared with the observation registered at the WILD station. Figure 11 represents very typical conditions favourable for wet-snow accumulation determined by a low pressure in the Rhone-Alps region for both snowfall events. The low pressure is capable of activating high wind speed against Italian west-Alps (*stau effect*), and heavy precipitation near the alpine ridge where the experimental station is located (Figure 12). The air temperature is slightly below 0°C and the typical duration of these events is 24-36 hours with important wet-snow accumulation on OHL.

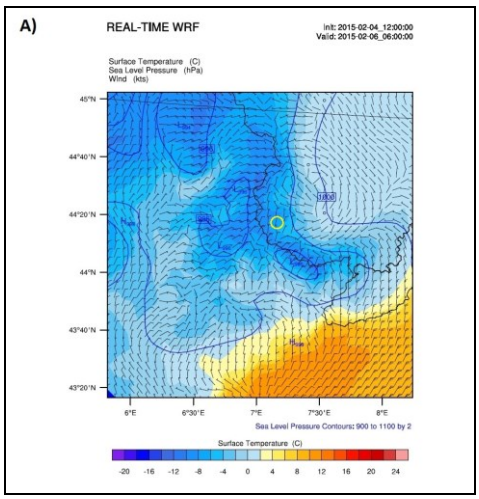

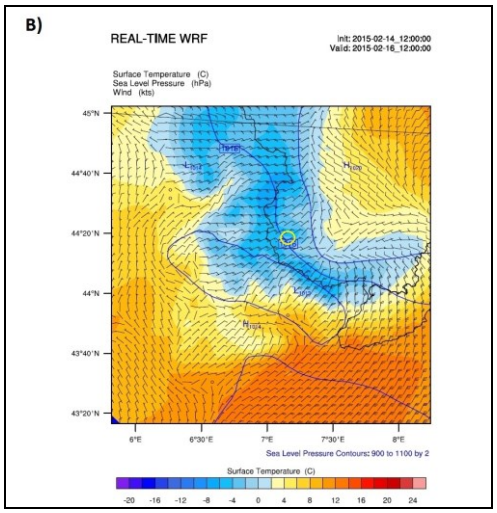

Figure 11: simulated surface air temperature (°C), 10 meter wind speed (half-barb 5 kts, full-barb 10 kts, flag 50 kts) and direction at a horizontal resolution of 5 km at 06 UTC on 6 February (A) and at 12 UTC on 16 February (B). The yellow circle line in both images indicates the position of WILD station.

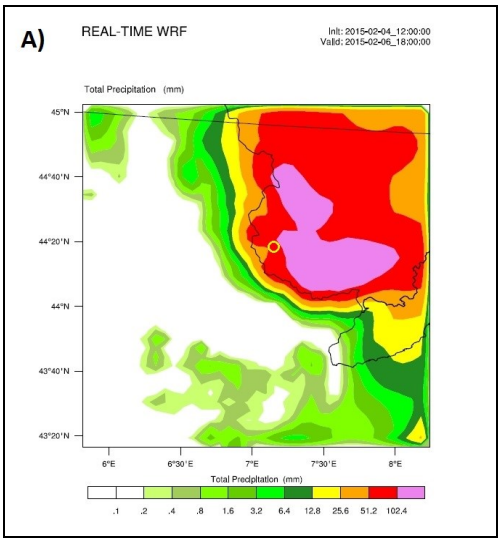

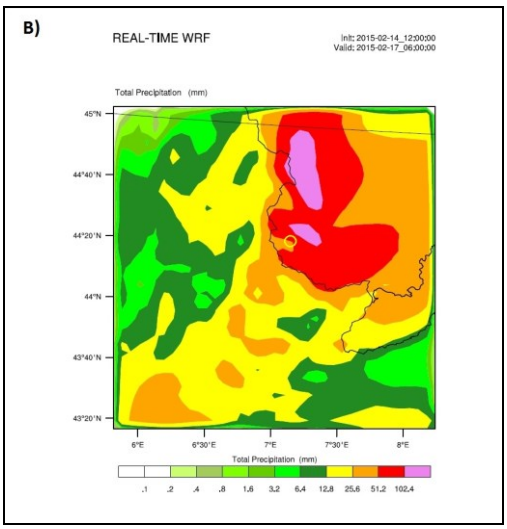

Figure 12: simulated total precipitation (mm) at the end of snowfall forecast period at 18 UTC on 6 February (A) and at 06 UTC on 17 February (B). For both events, WRF simulation indicates heavy snowfall in the west part of the Alps, especially in the area near the WILD station (yellow circle line).

Since the air temperature is a critical parameter to predict in complex orography [12,19], two grid points of WRF models has been considered for the simulation of air temperature. The first one (WRF1) is the nearest point to the station. The air temperature at the altitude of WRF1 (1548 m asl) has been attributed to the elevation of WILD station (944m asl) by using a low vertical lapse rate Γ of 0.3°C/100m, deduced from some observation in wet-snow condition in the Alps. The second grid point (WRF2) is located in the same valley at an altitude of grid point of 1082 m asl very close to the elevation of the station. Whereas, only one grid point of RAMS has been chosen at an altitude of 1559 m asl, because the resolution of topography does not allow to find a grid point with an elevation close to the station. Figure 13 details the simulated air temperature and precipitation for WILD location. The best prediction of the air temperature has been obtained by using WRF2 for both events (Table 1). For these cases, the models tend to underestimate temperature (-1°C WRF2, -2.2°C RAMS -2°C WRF1). The bias of 1°C is within the typical uncertainty of a prediction model, the other values can be affected by an error due to the use of vertical lapse rate that is very difficult to determine in complex orography. Other tests have been performed using a square box of grid points centered on station, but the performance of the forecast has not changed significantly. The reason is that the points of the box are always at a higher altitude than the elevation of the station and the average air temperature of the box must be recalculated through the vertical lapse rate Γ.

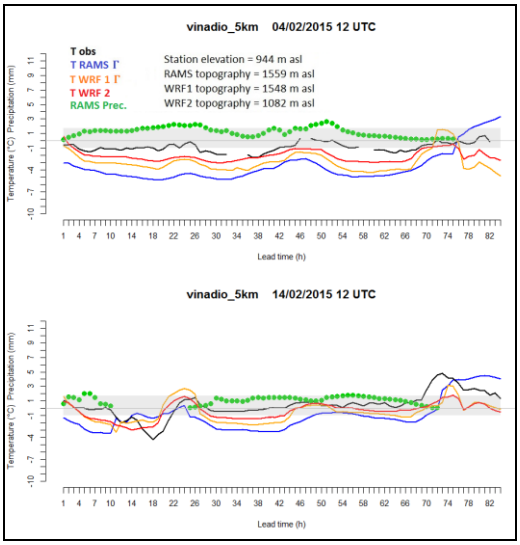

Figure 13: measured (black line) and simulated air temperature for both case studies. Blue curve represents temperature of RAMS, orange and red lines respectively WRF1 and WRF2 simulations. Green dots represents the intensity of precipitation (mm/h) expected from RAMS.

Regarding to the total precipitation, both models tend to overestimate the precipitation observed at the experimental station (Figure 14). For the first event 5-6 February, the observed precipitation was 65 mm, respect to 92 mm predicted by RAMS and 113 mm with WRF. In the second case, the precipitation was 50 mm, 66 mm predicted by RAMS, 61 mm simulated with WRF. It is evident the best prediction both in terms of temperature and precipitation for the second case study. The statistical indices have been summarized in Table 1 and Table 2. The analysis was not performed on the intensity of the wind, because the station is located in an area particularly sheltered from the wind. In the wet-snow conditions observed, the intensity of the wind measured was always less than 2 m/s, instead of wind forecast generally greater than 6-7 m/s.

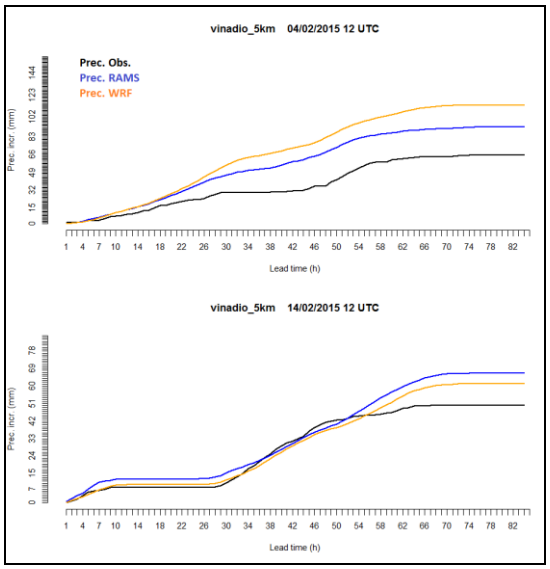

Figure 14: measured (black line) and simulated total precipitation expected from WRF (orange line) and from RAMS (blue curve) for both wet-snowfall events.

Table 1: statistical indices for air temperature.

	4-6 February 2015			14-16 February 2015		
Temp. (°C)	RAMS	WRF1	WRF2	RAMS	WRF1	WRF2
RMSE	3	2.5	**1.4**	2.5	1.7	**1.5**
MAE	3.1	2.2	**1.2**	2	1.4	**1**
BIAS	-2.2	-2	**-1**	-1	-0.8	**-0.7**

Table 2: statistical indices for total precipitation.

	4-6 February 2015		**14-16 February 2015**	
Prec. (mm)	RAMS	WRF	RAMS	WRF
RMSE	**20**	35	10	**5**
MAE	**18**	31	7	**4**
BIAS	**19**	33	6	**3**

B. Wet-snow accumulation

Observation and simulation of wet-snow accumulation are presented for the two case studies occurred on 4-6 February and on 15-16 February. The measurements of wet-snow accumulation were obtained from a load cells that were in operation in support of the ACSR Ø31.5mm rotating conductor. Figure 15 shows the most intense phase of snowfall on 5 February, when the sleeves of snow formed on the test spans.

Figure 15: test span during the heavy wet-snowfall event occurred on 05 February 2015.

The next image (Figure 16) reveals a significant wet-snow accretion on the two rotating conductors. It is important to notice that the conductor with hydrophobic coating (on the right part of the image), has a similar sleeve and therefore, the treatment was not appropriate for the wet-snow condition. In the same picture, in the upper left part of the image, the simulation of AI current worked properly and the conductors don't show any wet-snow accretion. Just before the snow shedding, the measured thickness of sleeve was 14 cm and its load 2.7 kg/m, compared to the expected load of 2.4 kg/m (Figure 18).

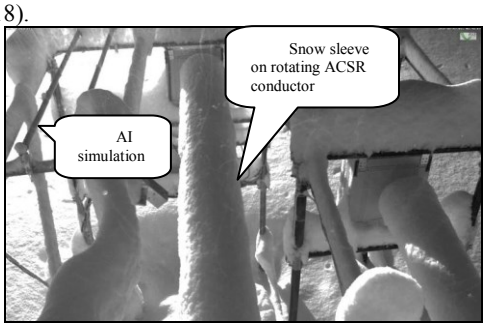

Figure 16: wet-snow accretion on the rotating conductors (photo taken 1-hour before snow shedding, 05-02-2015 06 UTC). In the upper left of image, the two AI conductors are free of snow sleeve.

Figure 17 shows an image captured by the webcam at the end of snowfall occurred on 15-16 February. The snow formation are noticeable for all test spans. The measured load on ACSR conductor was 5kg/m and the thickness of sleeve was 11 cm. The wet-snow load expected on the same conductor was 4.2 kg/m and, also for this event, the two cables with the AI current simulation had no growth of sleeve.

Figure 17: Photo of test spans with snow accretion at the end of the event occurred on 15-16 February 2015.

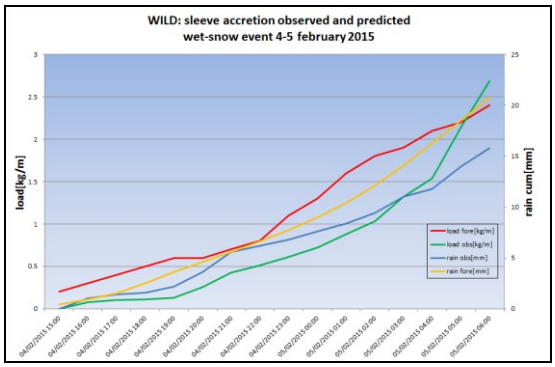

Figure 18: measured (green line) and evaluated wet-snow load (red line) on the ACSR rotating conductor during the event of 4-5 February 2015.

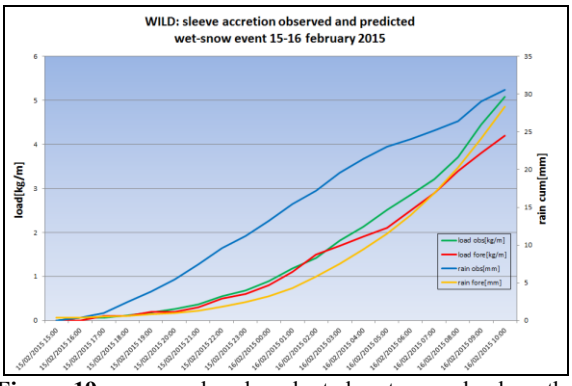

Figure 19: measured and evaluated wet-snow load on the ACSR rotating conductor (15-16 February 2015).

C. *AI current simulation*

During the last winter 2014-2015, 11 snowfall affected the WILD station, but only the two heavy wet-snowfall occurred on February have been considered for the simulation. During these events, the AI circuit described on I.C, worked properly and the accretion of snow has not occurred on both ACSR conductors. In correspondence to these strong wet-snowfall, WOLF has provided an estimation of the AI current necessary to keep OHL free of wet-snow sleeve formations in the expected weather conditions. Thus, it is possible to compare the observed AI current on the ACSR Ø31.5mm used at the WILD site, and the predicted values. The first event has been presented in Figure 20, in which it is possible to notice a variability of the measured AI current, instead of the simulated one. This fact is due to the parameterization of P_w considered in the AI model, while the AI current registered at the station is clearly dependent on the variability of weather conditions. In any case, especially for the second event (Figure 21), there is a good agreement between the predicted and measured data, both in terms of duration of the events, and in the maximum values assumed by the current.

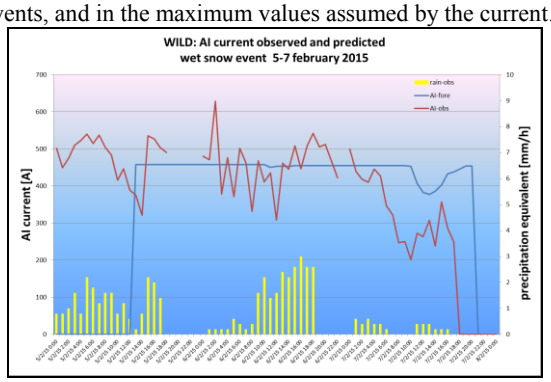

Figure 20: comparison from AI current predicted (blue line) and observed at WILD station (red line) during the wet-snow event on 5-6 February.

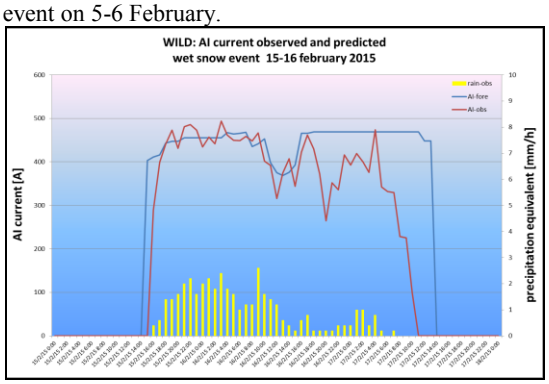

Figure 21: comparison from AI current predicted (blue line) and observed at WILD station (red line) during the wet-snow event on 15-16 February.

V. CONCLUSION

RSE, in collaboration with the Italian TSO TERNA, is carrying out a research activity on issues of prediction, monitoring and mitigation of the wet-snow formations for the overhead power lines. In this paper, two wet-snow events in the west Alps have been described and analyzed using the observation of weather conditions and wet-snow accretion measurement collected at the WILD station. The wet-snow load on the rotating ACSR conductor was respectively of 2.7 kg/m with an equivalent diameters greater than 30 cm for the first event and an accumulation of 5 kg/m with a diameter of 25 cm for the second one. Both the transmission and distribution systems were subject to disruptions close to the WILD station with several blackouts. The new type of conductors, treated on the surface with hydrophobic varnish, were tested with rather poor results.

Two high resolution numerical meteorological models, RAMS and WRF, have been adopted for the atmospheric simulation. The most critical parameter is the air temperature, especially in complex orography. The Γ vertical lapse rate of 0.3°C/100m introduced in the simulations, in some cases revealed to be in a good accordance with the observations, but in other cases is inadequate to represent the vertical profile of the wet-air. The statistical indices for air temperature indicate a better prediction for the WRF model compared to the RAMS simulation with the tendency of both models to underestimate the air temperature. Regarding to the precipitation, the performances of the two models are not so different with a general overestimation of the total amount. It is clear that the successful simulation of wet snow accumulation is critically dependent on detailed and correct atmospheric input data, and detailed and accurate wet-snow model. Considering the experience acquired at the WILD station, the sticking coefficient is too much dependent from the wind. The effect of the wind has been reduced in the estimation of sticking through the square root of its intensity.

The Joule effect simulation on the two ACSR conductors demonstrates that the circuit is able to preserve the cables from snow formation keeping the surface temperature of conductor close to 2°C. The predicted values of AI current obtained through the input of weather forecast in the thermal model [8] correct with the terms P_w, are very close to those simulated. In the next experimental winter season, the set-point will be reduced to 1.5°C in order to limit the simulated AI current.

Other surface treatments of cables will be tested next winter, with the possibility of installing conductors from collaborations with other international research centers.

ACKNOWLEDGMENT

This work has been financed by the Research Fund for the Italian Electrical System under the Contract Agreement between RSE S.p.A. and the Ministry of Economic Development – General Directorate for Nuclear Energy, Renewable Energy and Energy Efficiency in compliance with the Decree of March 8, 2006.

REFERENCES

[1] Bonelli P., Lacavalla M. – "Trend in snow deposition on overhead electric lines: using synoptic data to investigate the relationship black-out risk/climate change. " Management of Weather and Climate Risk in the Energy Industry. NATO Science for Peace and Security Series – C. Environmental Security- Edited by Troccoli A., January, 2010 (ISSN: 1874-6519).

[2] Fikke, S., et al. (2007), COST 727: Atmospheric icing on structures, measurements and data collection on icing: State of the art, Publ. MeteoSwiss 75, MeteoSwiss, Zurich, Switzerland.

[3] Farzaneh M. : Atmospheric Icing of Power Networks. Edit. by Farzaneh M., 2008 Springer Science.

[4] P. Admirat, "Wet snow accretion on overhead lines," *Atmospheric Icing of Power Networks,* pp. 119-169, 2008.

[5] Bonelli,P., Lacavalla,M., Marcacci,P., Mariani,G., and Stella,G.: Wet snow hazard for power lines: a forecast and alert system applied in Italy, Nat. Hazards Earth Syst. Sci., 11, 2419-2431, doi:10.5194/nhess-11-2419-2011,2011.

[6] L. Makkonen, "Models for the growth of rime, glaze, icicles and wet snow on structures," *Phil. Trans. R. Soc.,* no. 358, pp. 2913-2939, 2000.

[7] ISO/TC98/SC3/WG6, Atmospheric icing of structures, International Standard, ISO 12494, 2000.

[8] Schurig, O.R. and Frick, C.W.: Heating and Current-Carrying Capacity of Bare Conductors for Outdoor Service. Gen. Elec. Rev., 33, No. 3, Mar., 1930, pages 141-157.

[9] Mathematical Model for Evaluation of Conductor Temperature in The Steady (or Quasi-Steady) State (Normal Operation), CIGRE, ELECTRA No. 144, Oct. 1992, pp. 109-115.

[10] IEC: Overhead lines – Meteorological data for assessing climatic loads. International Electrotechnical Commission Technical Report 61774, 1997.

[11] Á. J. Eliasson and E. Thorsteins, "Ice load measurements in test spans for 30 years," in 12th IWAIS, Yokohama, Japan, October 2007.

[12] J. Elíasson, H. Ágústsson and G. M. Hannesson, "Wet-Snow accumulation - A study of two severe events in complex terrain in Iceland," in 15th IWAIS, St. John's, Newfoundland and Labrador, Canada, 2013.

[13] Á. J. Elíasson, H. Ágústsson, G. M. Hannesson and E. Thorsteins, "Modeling wet snow accretion - Comparison of cylindrical model to field measurements," in 15th IWAIS, St. John's, Newfoundland and Labrador, Canada, 2013.

[14] Y. Sakamoto, "Snow accretion on overhead wires," *Philos. Trans. Roy. Soc. A,* no. 358, pp. 2941-2970, 2000.

[15] G. Poots, "Aspects of a Model of Wet-Snow Accretion on an Overhead Line Conductor," in *8th IWAIS*, Reykjavik, 1998.

[16] L. Makkonen, "Estimation of wet snow accretion on structures," *Cold regions science and technology,* no. 17, pp. 83-88, 1989.

[17] L.Makkonen and B. Wichura, "Simulating wet snow loads on power line cables by a simple model," *Cold Regions Science and Technology*, Vols. 2-3, no.61, pp. 73-81, 2010.

[18] B. E. K. Nygaard, H. Ágústsson and K. Somfalvi-Tóth, "Modeling Wet Snow Accretion on Power Lines: Improvements to Previous Methods. Using 50 Years of Observations," J. Appl. Meteor. Climatol., in press, 2013.

[19] Fikke, S. M., J. E. Kristjansson, and B. E. K. Nygaard (2008), Modern meteorology and atmospheric icing, in Atmospheric Icing of Power Networks, edited by M. Farzaneh, pp. 1‑29, Springer, Dordrecht, Netherlands,doi:10.1007/978-1-4020-8531-4_1.

Influence Analysis of Transmission Lines Insulator on the Conductor Ice-shedding

Xin-bo HUANG[1], Guan-hua XU[2],Yong-can ZHU[3], Ming-jin LIAO[1],Xin-xin ZHENG[1]
[1]College of Electronics and Information, Xi'an Polytechnic University, Xi'an 710048, China;
[2]College of Mechanical and Electrical Engineering, Xi'an Polytechnic University, Xi'an 710048,China;
[3]College of Mechanical and Electrical Engineering, Xidian University, Xi'an 710071,China)
(hxb1998@163.com)

Abstract: **Conductor strenuous exercise will be caused by the ice-shedding. It is easy to cause the occurrence of electrical or mechanical accident of transmission line. Therefore, Conductor-insulator finite element model has been established through the ANSYS, and it is the analysis of the dynamic characteristics for the wire type, material properties and the length of the insulator string under different ice shedding. The influence of insulator has been separately analyzed from the jump height, unbalanced tension etc. for the conductor ice-shedding. The results showed that: It I type insulator on ice-shedding unbalanced tension impact is about 0.9 times smaller than the V type insulator. It is not significant for ice-shedding unbalanced tension effects about the composite and ceramics materials. The ice-shedding jump height will be unchanged for the V type or I type insulator with the length increase of insulator string, but ice-shedding unbalanced tension will be decreased. The related results provide a reference for the subsequent study on conductor ice-shedding and lines structure design.**

Keywords: icing; ice-shedding; FEM; insulator; ice-shedding jump height; unbalanced tension

INTRODUCTION

Ice-shedding recently caused mechanical or electrical accidents by a serious threat to the safe and stable operation of power system. Overhead transmission lines in our country is affected by the terrain, line structure and natural disasters, part of the line will inevitably through the heavy ice areas, there is an urgent need for ice-shedding problem in-depth analysis[1].

The some research of domestic and foreign scholars on the conductor ice-shedding. Foreign, Jamaledding et al [2] to simulate the conductor length of 3.22 m in a variety of ice-shedding in the artificial climate chamber. Kalman T et al [3] by establishing the finite element model, considering the dynamic response under various conditions of icing conductor. In China, under the tower-line system dynamic response simulation of ice-shedding of ABAQUS for different numerical Yan Bo et al [4] use, and gives the influence of wind load on the ice-shedding the maximum transverse swing. Yao Chen-guo et al [5] by using the finite element analysis method, analysis of different wind speed for dynamic response characteristics of ice-shedding. Yang Feng-li et al [6] of ice shedding model, study of different factors on the dynamic response of the tower. Jiang Xing-liang et al [7] in the icing experiment station of DC ice melting, recording and observation of ice-shedding process. The above research is mainly concentrated in the ice-shedding of transverse swing, lead stress, study of tower line system of unbalanced tension and the jump amplitude less.

ANSYS to establish the finite element model of ice-shedding in this paper, the additional force simulation of icing simulation method, a sudden withdrawal load simulation method for dynamic characteristics of ice-shedding, insulation substring type, material properties and the length of ice-shedding, in-depth study the ice jump height and ice-shedding from the unbalanced tension of

conductors, the research results have been completed.

Ⅰ. CALCULATION CONDITION

A. Finite element modal

Ice-shedding model includes two parts: transmission line, insulator string. ANSYS establishes the conductor insulator coupled finite element model used in this article, as shown in figure 1. According to the conduct and grounding line in accordance with Hooke Law, only by the properties of tension can not be compressed, the bar element Link10 simulation, the unit can only bear the axial tension or compression, with geometric nonlinearity, in order to simulate the cable or clearance. The bar element Link8 simulation of insulator string, the unit has the stress stiffness, large deformation characteristics. Between conductor and ground and insulator string is connected by hinge. Figure A, B, C, D were the conductor suspension point.

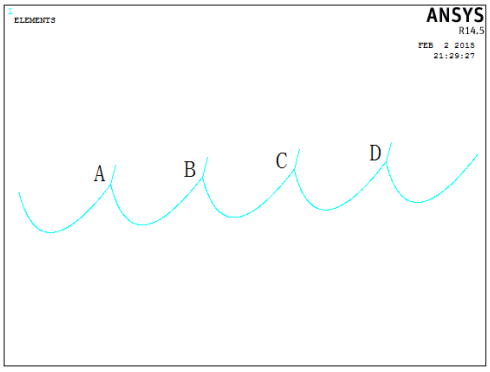

Figure 1 Finite element model of conductor-insulator

B. Analysis method

Nonlinear dynamic process of conductor ice-shedding of large displacement and small deformation, to solve the problem, literature [8] by using the central difference explicit direct integral algorithm to solve the problem, but this method is too complicated and the accuracy is not high. In this paper using the finite element method is solve.

By using the finite element transient dynamics method of ice-shedding are numerical simulation. It is used to determine the dynamic response analysis method of structure change with time under arbitrary load. It can analyze the structure change with time under static load, transient load, harmonic load under the action of the random combination of the displacement, strain, stress, etc.

C. Meteorological condition

The temperature of -5oC, does not consider the effect of the wind speed. The jumping height is increase with the increasing ice thickness. So the paper consider is 15mm of the ice thickness.

D. Material parameters

In this paper, the conductor type is LGJ-630/45, and its mechanical parameters are shown in Table1. Insulator adopts composite insulator. Ice-shedding analysis is simplified of insulator. It main consideration is insulator core, the other components as the added mass of core. The ice load of the insulator string is equivalent to the vertical load of the insulator string. It is applied on the insulator.

Table1 Mechanical parameters of conductor LGJ-630/45

Parameters	LGJ-630/45
Aluminum / steel root number	45/7
The total cross section /mm^2	666.55
Outer diameter /mm	33.60
Linear density /（kg/km）	2060
Pull off force /kN	48.7
EX/MPa	63000
The coefficient of linear expansion /10^{-6}	20.9

E. Icing load simulation

Assuming that the conductor is uniformly coated with circular cross-section, the load is simulated by the additional force simulation method, and the ice load is simulated by the method of abrupt withdrawal. It assuming that the quality of each spacing concentrated load is M of simulation icing load, see (2) [9]

$$\begin{cases} m=\rho\pi b(D+b) \\ M=mL/n \end{cases} \quad (2)$$

Type: m: conductor icing quality on per unit length, kg/m; ρ : ice density, 900 kg/m^3; D: conductor outside diameter, mm; b: ice thickness, mm; L: conductor length, m; n: divide the number of elements.

F. De-ice simulation

In order to facilitate the calculation, the ice-shedding analysis usually abbreviated to along the span direction uniform coating of ice, as shows in

figure 2(a). This paper analyzes the method of uniform ice-shedding in middle span, as shows in figure 2(b).

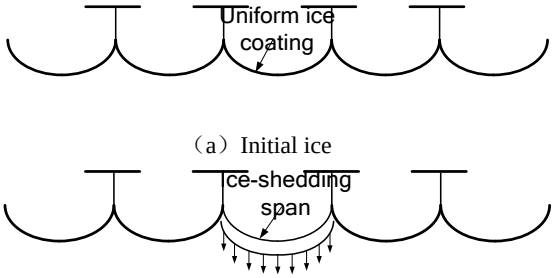

（a）Initial ice

（b）Middle Span Uniform Ice-shedding

Figure 2 Ice-shedding Span Location of Conductors

II. CALCULATION RESULT AND ANALYSIS

A Conductor ice-shedding dynamic characteristics

Ice-shedding is easy to cause the mechanical or electrical accident. Due to the change of the load will vibrate of de-icing span conductors. It is adjacent span the insulator strings and conductors will change. This section will analyze the dynamic response of ice-shedding in conductors. Analysis of ice-shedding is a strain section within the period of continuous span of calculation model. It is L-L-L-L-L and L is 400m. It is ice thickness 15mm and ice-shedding rate is 50%. Middle span happens to ice-shedding. The length of the insulator string is 5m. Conductor type is LGJ-630/45. It is not considering the influence of altitude difference and wind speed. Figure 3 for conductor vertical displacement of the middle span nodes time-history curve. From figure 3 shows that the jumping height of middle span nodes is 5.471m. Since the middle span of ice-shedding, left and right sides of the symmetrical reverse, so only take one side, as shows in Figure 4. Figure 4 for the longitudinal unbalanced tension time-history curve.

From figure 3 and figure 4 shows that when conductors is ice-shedding, its a low frequency motion. The longitudinal unbalanced tension is also low frequency synchronization, and not the instantaneous generation of the conductors icing.

B Impact analysis insulator material properties on ice-shedding of iced conductor

Conductors ice-shedding analysis is consider insulator composite and ceramics materials of unbalance tension influence. It is other calculation the conditions of the 2.1 sections, the results are shown in Table 2.

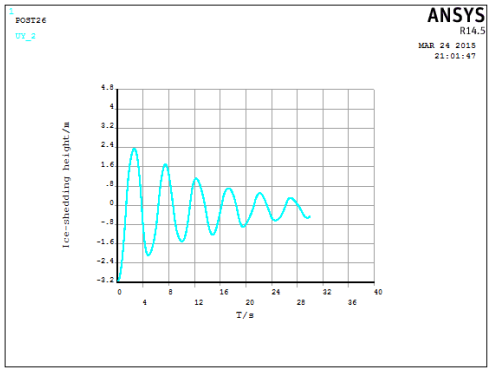

Figure 3 The jumping height of ice-shedding time-history curve

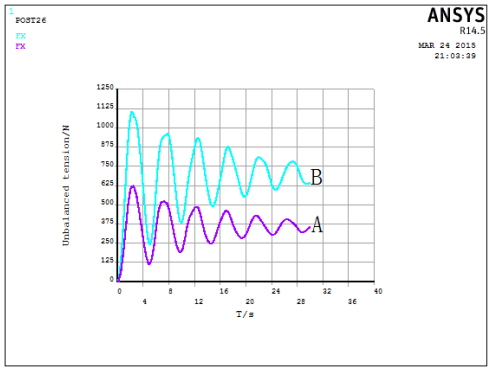

Figure 4 The longitudinal unbalanced tension time-history curve

Table 2 The longitudinal unbalanced tension of ice-shedding with different materials of insulator

Span/m	materials	
	composite	ceramics
200	169.169	166.505
300	589.036	581.477
400	1508.88	1485.264
500	2915.520	2878.105
600	5019.826	4940.774

From table 2 shows that composite and ceramics materials to de-ice longitudinal unbalanced tension had no significant influence, its error within the allowable range. In the following chapters selected composite as the research object.

C Impact analysis insulator on the jumping height of ice-shedding of iced conductor

Analysis of consider insulator string type and length of the jumping height of ice-shedding the

influence for ice-shedding. The insulator string type consists of I and V. The length is respectively 3m, 5m, 8m, 10m, 15, 20m. It is the other calculation the conditions of the 2.1 sections, the results are shown in Figure 5 and Figure 6.

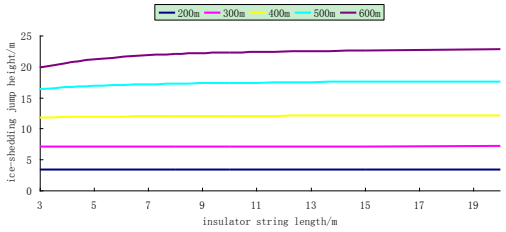

Figure 5 The jumping height of ice-shedding under the length of I different insulator

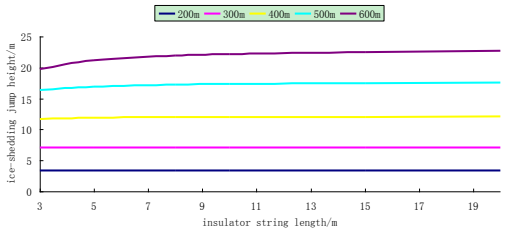

Figure 6 The jumping height of ice-shedding under the length of V different insulator

From figure 5 and figure 6 shows that the influence of the V insulator string on the jumping height of the conductors is slightly lower than the I insulator string. Whether it is V type insulator or I type insulator, with the increase of insulator string length, the jumping height of ice-shedding has no influence. When insulator string length must be, the jumping height of ice-shedding is probably linear increase with increasing the ice-shedding span.

D Impact analysis insulator on ice-shedding unbalanced tension of iced conductor

Conductors ice-shedding analysis are consider insulator string type and length of the influence unbalance tension, and calculate the conditions of the 2.2 sections, the results are shown in Figure 7 and Figure 8.

From Figure 7 and figure 8 shows that V type and I type insulator string on conductors ice-shedding unbalanced tension effect trend of approximately same, but I type insulator the influence of conductors ice-shedding unbalanced tension than the V type insulator on small about 0.9 times. Whether it is V type insulator or I type insulator, with the increase of insulator string length, conductors ice-shedding unbalanced tension decreases. When insulator string length must be, conductors ice-shedding unbalanced tension is increase with increasing the span.

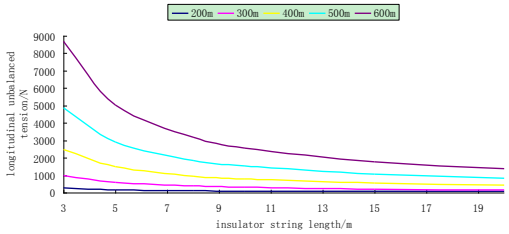

Figure 7 I type insulator longitudinal unbalanced tension

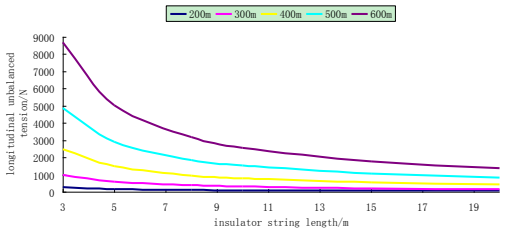

Figure 8 V type unilateral longitudinal unbalanced tension

III. CONCLUSION

(1)Composite and ceramics materials to de-ice longitudinal unbalanced tension had no significant influence, its error within the allowable range.

(2)The influence of the V insulator string on the jumping height of the conductors is slightly lower than the I insulator string, but I type insulator the influence of conductors ice-shedding unbalanced tension than the V type insulator on small about 0.9 times.

(3)Whether it is V type insulator or I type insulator, with the increase of insulator string length, the jumping height of ice-shedding has no influence, but the unbalanced tension of ice-shedding decreases.

(4)When the length of insulator string must be, whether it is V type insulator or I type insulator, ice-shedding unbalanced tension and jumping height are increase with increasing the ice-shedding span.

REFERENCES

[1] HUANG Xinbo, MA Longtao, XIAO Yuan, et al, “Form-finding analysis based on finite element method for line with uniform ice-coating”, Electric Power Automation Equipment, 2014, pp. 72-76.

[2] A.Jamaleddine, G.McClure, J.Rousselet, et al, “Simulation of ice shedding on electrical transmission

lines using ADINA", Computers & Structures, 1993, pp. 523-536.

[3] Kalman T, Farzaneh M, McClure G, "Numerical analysis of the dynamic effects of shock-load-induced ice shedding on overhead ground Wires", Computers & Structures, 2007, pp. 375-384.

[4] Yan Bo, Chen Kequan, Xiao Hongwei, et al, "Horizontal amplitude of iced conductor after ice-shedding under wind load", Chinese Journal of Applied Mechanics, 2013, pp. 913-919.

[5] YAO Chenguo, ZHANG Rufang, ZHANG Lei,et al, "Influence of Wind Vibration of Overhead Transmission Tower-line System on Ice Shedding", High Voltage Engineering, 2014, pp. 381-387.

[6] Yang Fengli, Yang Jingbo, "Analysis on Loads Form Ice Shedding Conductors in Heavy Icing Areas", Journal of Vibration and Shock, 2013, pp. 10-15.

[7] Jiang Xingliang, Bi Maoqiang, Li Zhenyu, et al, "Study on DC Ice Melting and Ice Shedding Process Under Natural Condition", Power System Technology, 2013, pp. 2626-2631.

[8] HUAG Xinbo, CHEN Ronggui, WANG Xiaojing, et al, "Online Monitoring System and Fault Diagnosis of Overhead Transmission Line", Beijing: China Electric Power Press, 2008, pp.157-196.

[9] WANG Zhangqi, QI Lizhong, YANG Wen-gang, et al, "Research on the applicability of Lumped Mass Method for Cable's Dynamic Tension in the Ice Shedding Experiment", Proceedings of the CSEE, 2014, pp. 1982-1988.

[10] A. Jamaledding, et al, "Weigh-dropping Simulation of ice-shedding effects on an overhead transmission line model", Proeeedings of 7th IWAIS (International Workshop on atmosphereic Icing of Struetures), Canada, 1996, pp.44-48.

[11] Laszlo E. Kollar and Masoud Farzaneh, "Vibration of Bundled Conductors Following Ice Shedding", IEEE Transactions On Power Delivery, 2008, pp.1097-1104.

[12] CHEN Yong, HU Wei, WANG Liming, HOU Lei, "Research on Ice-shedding Characteristic of Icing Conductor", Proceedings of the CSEE, 2009, pp. 115-120.

[13] ZHAO Yuzhe, LI Li, DENG Wei, "Numerical Simulation of Dynamic Response of Ice-shedding on Transmission Line", Resources and Power, 2013, pp. 205-209.

[14] YANG Fengli, YANG Jingbo, "Analysis on loads form ice shedding conductors in heavy icing areas",Journal of Vibration and Shock, 2013,pp. 10-15.

[15] HOU Lei, WANG Liming, ZHU Puxuan, et al, "Dynamic Behavior Computation of Ice Shedding of UHV Overhead Transmission Lines", Proceedings of the CSEE[J], 2008, pp. 1-6.

[16] MENG Xiaobo, WANG Liming, HOU Lei, et al, "Dynamic characteristics of ice-shedding on UHV overhead transmission lines", J Tsinghua Univ (Sci & Tech), 2010, pp. 1631-1636.

[17] HE Qing, LV Xifeng, ZHAO Xiaotong, "Research on Application of De-icing Technology on High Voltage Transmission Line Under the Condition of Incentive", Proceedings of the CSEE. 2014, pp. 2997-3003.

The Recognition and Detection Technology of Ice-covered Insulators under Complex Environment

Xin-bo Huang[1], Ju-qing LI[1], Ye Zhang[1] Fei Zhang[1]
[1] College of Electronics and Information, Xi'an Polytechnic University, Xi'an, 710048, P.R.China
huangxb1975@163.com

Abstract:**In order to avoid the impacts of outer factors on the ice-covered insulators recognition, such as weather, seasons, outside illumination changes, acquisition time, image background and image contrast, a general algorithm which can recognize and detect the ice-covered insulator accurately in a complex environment is put forward in this paper. With the video monitoring device, the image information of insulators with or without covered ice can be acquired. The ice-covered insulator images under complex environment are regarded as the research objects. Morphological closing operation is conducted on the ice-covered insulator images firstly. Then the high frequencies in the image are removed by the Wavelet Domain. A kind of invariant background quotient image can be acquired by dividing the processed images and the original images, then after the camera calibration on the quotient images, the edge contours of insulators can be extracted using the wavelet edge detection method, and the icing thickness of insulator can be obtained by using template matching algorithm and geometric model. The method is verified in an artificial climate chamber, the results show that this method can eliminate the interference of the complex background weather, accurately identify icing insulators and calculate the insulator icing thickness. This method can be applied to recognition and detection of ice-covered insulators under complex environment.**

Key Words**: *icing insulators; monitoring device; quotient image; contour feature; template matching; geometric model***

INTRODUCTION

Extreme weather conditions, such as freezing rain, heavy snow will cause insulators icing phenomenon. If the phenomenon is serious ,the transmission line will be pulled down ,threating the safe operation of power network and even cause huge economic losses and casualty accident . So it will be particularly important to recognize the situation of insulator icing timely and accurately. Under complex conditions, how the situation of transmission line insulators icing can be mastered real-timely in order to take measures to avoid the accident is a hotspot of current research [1-3]. The existing main recognition technologies of insulator icing are recognizing the transmission lines icing automatically through image processing technology[4], using the mechanical analysis method to identify the icing[5],online monitoring method for transmission line icing based on 3D reconstruction[6]. All the methods mentioned above are for the recognition of transmission line and insulators icing which are under single weather and background. It is difficult to recognize the ice-covered status of the insulators under complex environment for all-weather accuratly and effectively. Therefore, it's essential to propose a universal technology which can accurately detect the isulators icing conditions under complex environment.

In this paper, a general algorithm of morphological closing operation wavelet quotient image is proposed for accurately identify the icing conditions of insulators under complex environment. It can realize the accurate identification of the ice cover conditions of the insulator under the conditions of weather, season and image background, and has the advantages of simple principle, convenient operation, high accuracy and reliability. It has important significance to improve the reliability of the electric network operation for predicting the icing conditions of insulators.

I ALGORITHM IMPLEMENTATION PROCESS

In order to improve the monitoring accuracy of iced insulator under complex environment, the algorithm of morphological closing operation quotient image is used to process the collected insulator image, reducing the influence of complex environmental factors .The ice thickness of insulator is calculated, forecasting accurately and alarming timely.

II GRAY-SCALE PROCESSING

By gray scaling image, the influence of color depth difference on the wavelet domain and its inverse transform image is discarded, improving the speed of image recognition and reducing the computational quantity. By finding the point of a color in the RGB space, the projection of the origin to the point vector is calculated and the gray value of the color is obtained. In this paper, r, g, b components are represented by 8 bits, the value range is [0,255], gray value calculation formula is as follows [7]:

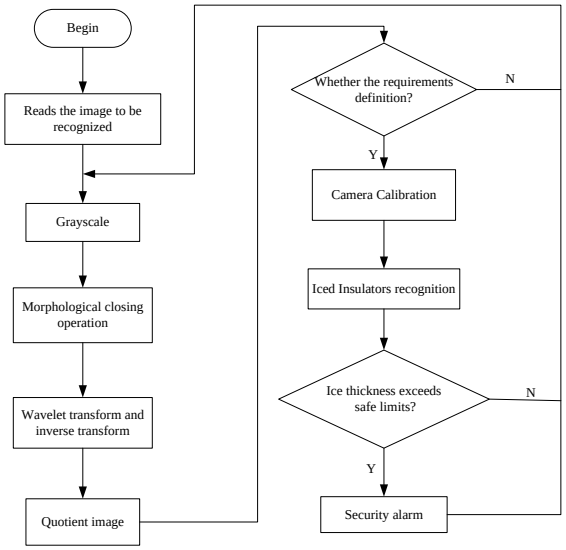

Figure 1: Algorithm flowchart

$$y = \frac{(r,\ g,\ b)\bullet(255,255,255)}{\left|(255,255,255)\right|} \tag{1}$$

In the formula, (r, g b) represents the coordinate vector of a color in the color space, (255,255,255) represents the vector of the diagonal in the color space, $|\bullet|$ is the modulus of the vector.

After the vector operation, the formula (1) can be simplified to:

$$Y = \frac{r+g+b}{\sqrt{3}} \tag{2}$$

According to the formula (2), the insulator icing images on the scene of the fog day, cloudy day, sunny day are shown in Figure 2 (a) (b) (c), their corresponding gray processing results as shown in Figure 2 (d) (e) (f).

The color of each pixel in the insulator's color image is determined by R, G, B three components, each component has 255 values, and a pixel can have the changing range of 255^3 colors. After grayscal processing, the pixel points of the changing range of a image is reduced to 255. By contrasting the images unprocessed and processed, the same as color image, the gray image also reflects the distribution and feature of an image's whole and local

color and intensity grade accurately. The color's intensity information of the insulator image is removed by grayscal processing, reducing the amount of the original data, diminishing the amount of the follow-up calculation remarkably.

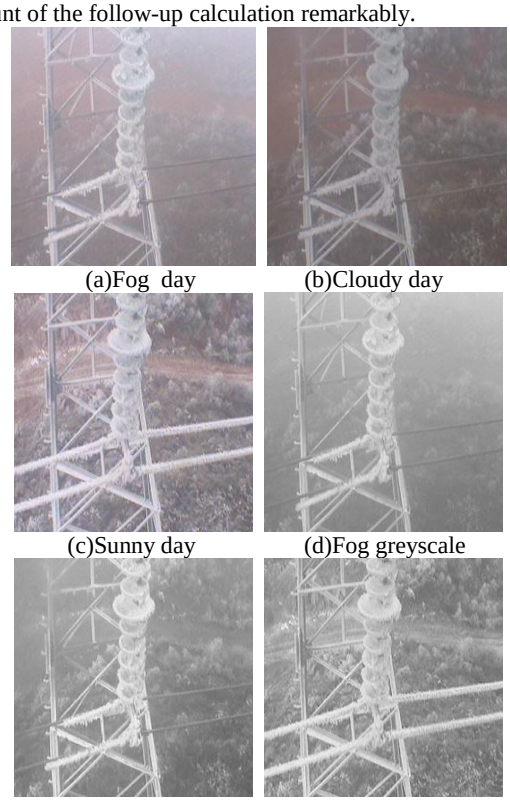

(a)Fog day (b)Cloudy day

(c)Sunny day (d)Fog greyscale

(e) Cloudy greyscale (f)Sunny greyscale

Figure 2: Greyscale comparison photograph

III WAVELET DOMAIN QUOTIENT IMAGE

Based on the gray closing processing, wavelet transform is introduced [8]. In the frequency domain, the high frequency information of the greyscale image is filtered. Through the inverse transformation to the space domain， clear background of ice-covered insulators image can be obtained by quietening with the original image

A. *Gray-closing operation*

In this paper, to solve the problems such as holes, no cohesion which are produced in the process of photographing and transmission, the gray closing operation(X•S) in morphology is used to process the acquired images, doing the pre-treatment for wavelet transform and quotient image acquisition.

The definition of the gray-closing operations [9]: firstly using the structural element S_1dilatate image X to obtain the image X_1,then using the structural element S_2 erode image X_1, gray-closing operation is represented by a symbol $X \bullet S^+$ and its formalized definition is:

$$X \bullet S^+ = (X \oplus S_1) \Theta S_2 \tag{3}$$

In order to improve the resolution of target, two different structural element S_1 、 S_2 are used in the two gray operations , $S^+ : \{S_1, S_2\}$;the relationship between S_1、 S_2 is S_1>S_2 the structural element S_1 is larger than S_2.

B. *Wavelet domain transformation*

In the aspect of digital image processing, wavelet transform is used to transform the image signal in the spatial or temporal domain into the wavelet domain, making it the multi-level wavelet coefficients. In the view of the feature that the energy distribution of ice-covered insulator greyed image is concentrated, after the secondary decomposition of wavelet coefficient, the inverse transformation method is used to improve the image contrast. Processing procedure is shown in figure 3.

Figure 3: Wavelet analysis diagram

Two-dimensional wavelet transform is used to analysis the iced insulator gray image at the frequency domain [10].First, the first wavelet decomposition of the original image is carried out to obtain horizontal low frequency vertical low-frequency information LL1, horizontal low frequency vertical high-frequency information LH1, horizontal high frequency vertical low-frequency information HL1, horizontal high frequency vertical high-frequency HH1. The LL1 low-frequency sub-image shows the main features of the image; and then the secondary LL1 wavelet decomposition of LL1 is carried out. The corresponding image after two times decomposition coefficient matrix is shown in Figure 4 (b) (c) The decomposition effect of the original gray image is shown in Figure 4 (e) (f).

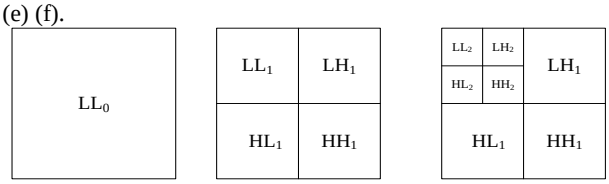

(a) Original image (b) A decomposition (c) Two decomposition

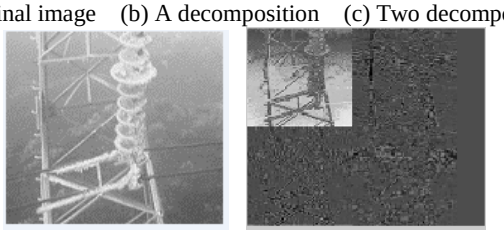

(d) Original greyscale image (e) A decomposition image

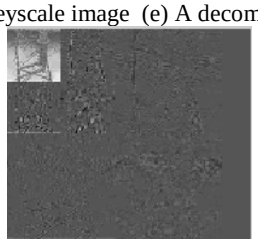

(f) Two decomposition image

Figure 4: Wavelet transform decomposition

By the decomposition diagram, the distribution of wavelet coefficients in space has good correspondence with the original image. The energy will be re allocated in the frequency space after the wavelet transform [11]. The low frequency sub-band contains the low-frequency information of the image, but part of the edge details are lost .These missing details was assigned to the other three sub-diagrams, so the upper left corner sub-diagram is blurred than the original image, and the dimensions of length and width also dropped to 1/4 of its original with its resolution down to 1/16 of the original. The displayed sub-band image is reconstructed by decomposing the low frequency after the inverse transformation, figure 5 is the reconstruction of three cases renderings.

C. *Quotient image*

Based on the Algorithm of Morphological Closing Operation Quotient Image is proposed in this paper. After the ice insulator image is processed by the gray closing operation, the high-frequency sub band of the image is removed at wavelet domain, and the results are estimated as the background of the icing insulator image [12]. By wavelet domain transformation, the image is 2D image, the original image must be converted into 2D image and then can be processed by quotient image processing. The background estimation images and the original image after processing the 2D image dividing, and a higher resolution target image is obtained by the method of synthesis.

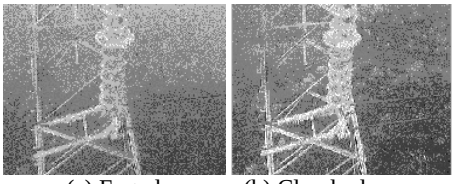

(a) Fog day (b) Cloudy day

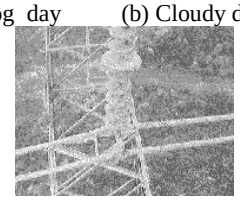

(c) Sunny day

Figure 5: Wavelet transform renderings

The definition of the wavelet quotient image of the morphological gray level close operation is:

$$MWQI = \frac{Gray(I)}{IDWT(LPF(DWT(Close(Gray(I)))))} \quad (4)$$

In the formula, Gray represents grayscal processing; Close represents gray closing operation; DWT represents discrete wavelet transform; LPF represents low pass filter; IDWT represents inverse discrete wavelet transform; division operation is between pixels by dividing.

The algorithm of morphological gray closing operator wavelet image can be described as follows:

(l)The original image is carried out by gray closing operation according to the 4 type; (2) Wavelet transform is carried out on the basis of (1); (3) Threshold is selected making the high frequency sub-band coefficients below the threshold value are set to zero; (4) Through the wavelet inverse transformation，the result image is regarded as a background image.(5) the background image is divided by the original image obtaining the gray closing operation quotient image. Treatment effect is shown in figure 6.(Clarity refers to the clarity of the detail in the image and its boundaries .By looking at the clear degree of the image to compare the image quality.)

(a) Haze days quotient image (b) Cloudy quotient image

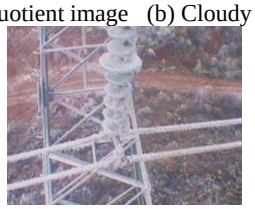

(c) Sunny quotient image

Figure 6: Compare before and after image effects processing

Table 1: Comparison of sharpness of the image before and after processing

	Fog Day %	Cloudy Day %	Sunny Day %
Before treatment	30	35	50
After quotient image processing	75	80	85

Insulator image clarity has obvious enhancement by quotient image processing results figure, the contour lines of ice insulators are more obvious relatively to the background. From the table 1we can see, the processed image clarity has an obvious enhancement, improving the highest is the fog days 45%, the lowest is sunny day, also achieved 35%. The background of gray closing operation quotient image is relatively stable and clear. Compared to a single processing algorithm, this gray closing operation quotient image can better identify ice insulator image information under complicated conditions, and has high clarity.

IV ICED INSULATOR RECOGNITION

A. *Camera calibration*

The research of camera calibration technology is mainly on the positioning cameras in computer vision system and the problems of parameter recognition of internal and external [13]. Computer stereo vision system used in this paper obtained image information from the camera, calculating the position and shape of 3D environment insulator geometry information. Producing and the inherent character of the information carried by the image is through the 2D image formed from the 3D scene by the geometrical model, the imaging model is shown in 7 below.

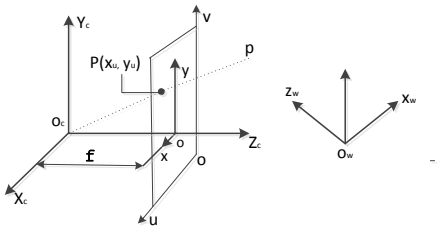

Figure 7: Camera imaging geometry

To recognize and detect the un-iced and iced insulator using camera calibration not only can correct the camera distortion, but can realize conversion between image coordinate and world coordinate, so that the actual ice thickness of the transmission line insulator can be accurately recognized under the Metric unit of the world coordinate system. .

B. *Recognition Algorithm*

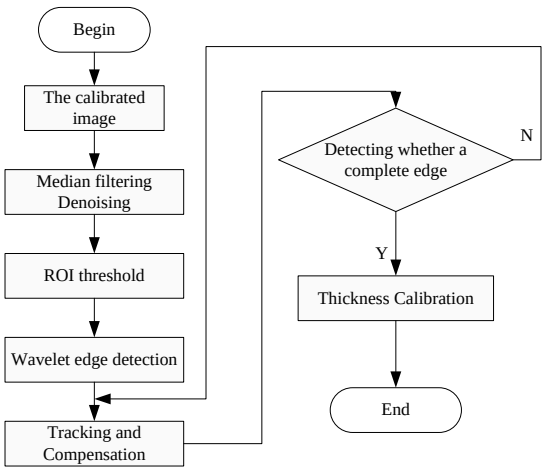

Figure 8: Algorithm recognition flowchart

The image noise is eliminated by the median filtering method with nonlinear smoothing technology. The noise is generated in the collection, transmission and the change process of closing operation quotient image

The region of interest ROI is extracted by local adaptive segmentation algorithm. The processing unit of the algorithm is generally based on the pixel or sub-block, each pixel or sub-block in the image is to strike a threshold [14-15], in order to construct a threshold value plane of the entire image, denoted as T(x, y). Then, the ROI region is segregated by the threshold value plane, the formula is expressed as:

$$g(x,y) = \begin{cases} black & if \quad f(x,y) \le T(x,y) \\ white & if \quad f(x,y) > T(x,y) \end{cases} \quad (5)$$

By calculating the mean $m(x,y)$ and standard deviation $s(x,y)$ of the current points in the window of w×w obtain the corresponding threshold. .

Then, the edge of iced insulator is extracted by wavelet edge detection [16]. By multi-scale characteristics of wavelet, the noise

can be suppressed in the large-scale of wavelet, identifying the edge reliably; positioning in the small-scale of wavelet accurately. Extraction results are obtained integrating the edge image of different scales. According to the feature that the edge of the image is local feature discontinuity, using the wavelet transform of the mutation signal sensitivity, and it has good localization performance in the time domain and the frequency domain, the detection of wavelet can be used to analyze the singularity and realize the location of singular points, so as to achieve the purpose of edge detection. The wavelet edge extraction is superior to other methods in improving the edge location accuracy and reducing the noise.

Finally, by edge tracking and compensation, the weak edges which are not detected can be further detected. The module value of the weak edges is less than the threshold which is set at the edge detection. These values are lost in edge detection at selecting edge points. But compared to the surrounding pixels, a local peak of the weak edge can be detected.

V EXAMPLES AND RESULTS ANALYSIS

The recognition method in this paper is verified in the artificial simulate iced laboratory. In indoor condition, by simulating the insulator at a humidity of and a temperature of under sunny, cloudy, fog and snowy four kinds of situations' insulator icing status and monitoring real-timely. Then the ice thickness identification method mentioned in this paper is used to recognize the insulator icing image. The thickness of the ice through experiment measured and algorithm identified are shown in Table 2 .Taking the icing status of the insulator in sunny days as an example and the recognition diagram is shown in Figure 9.

Obtaining from Figure 9, when sunny, the edge information of the iced insulator can be judged accurately by the algorithm. The thickness of the iced insulator can be recognized accurately by the algorithm. From Table 2, the maximum relative error of the thickness of the iced insulators in the four cases is the snowy day4.8 %, and the lowest is the sunny day, only1.5 %. This fully shows that the algorithm of this paper can adapt to all kinds of complex environment, and can recognize the ice thickness of insulator accurately.

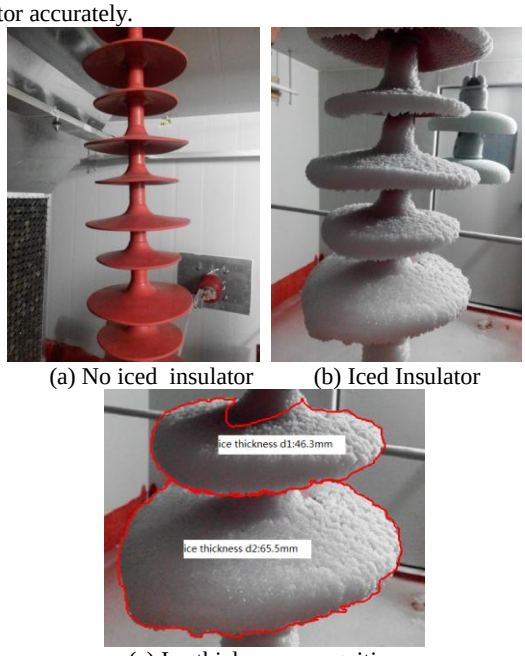

(a) No iced insulator (b) Iced Insulator

(c) Ice thickness recognition

Figure 9: Recognition of insulator on sunny day

Table 2: Measurement values and Recognition values of the icing insulators' thickness /mm(20mm)

Experimental conditions	Insulation sheet (up)			Insulation sheet (down)		
	Measurement values	Recognition values	Δ/%	Measurement values	Recognition values	Δ/%
Sunny Day	45.9	46.3	1.5	64.4	65.5	1.7
Cloudy Day	45.8	47.1	2.8	64.6	66.5	2.9
Fog Day	46.9	48.7	3.8	65.1	67.7	3.9
Snowy Day	47.1	49.2	4.4	65.4	68.6	4.8

VI CONCLUSION

1) The grayscal closing operation quotient image used in this paper can process the complex background of a image into relatively uniform background mode, solving the problem existing in the traditional methods that need to use different recognition algorithms under different backgrounds. This algorithm is simple and feasible, and has the characteristic of low cost. Besides, it can save a lot of human resources cost and improve the utilization rate of the on-line monitoring system.

2) This recognition method can recognize the icing status of the insulator under different conditions accurately, and the maximum relative error of the recognition method is only4.8 %.This recognition method is feasible and accurate.

REFERENCES

[1] HUANG Xinbo, etc, "Line monitoring and fault diagnosis Transmission Line", China Electric Power Press, October 2008, pp.197-217.

[2] HUANG Xinbo, etc, "Thickness measurement of transmission line icing thickness based on image processing", Electric Power Automation Equipment, October 2011,pp. 76-80.

[3] http://www.chinanews.com/gn/2011/01-07/2772723.shtml.

[4] ZHANG cheng, JIANG xiucheng, etc, "Automatic recognition based Insulators image processing technology", East China Electric Power, Jan 2009, pp.146-149.

[5] ZHU Yukun, "Transmission Line Icing Based on Image Processing", China Southern Power Grid Technology, June 2010, pp. 106-110.

[6] YANG Hao, WU Wei, etc, "Icing image monitor three-dimensional reconstruction based insulator", Electric Power Automation Equipment, February 2013, pp. 92-98.

[7] CHEN Duansheng, SONG Fengfei, ZHANG Qun, "A color image to gray adaptive global mapping method", Computer Systems & Applications, September 2013.

[8] YANG Wenyu, YANG Junjie, FAN Yue, etc, "Study on icing on-line monitoring system of high voltage transmission lines", China International Conference on Electricity Distribution CICED 2008, Dec. 2008,pp.1-4.

[9] CHANG Dakun, LUO Sanming, "Morphology extended its application closing operation function", Computer Engineering and Applications, September 2013, pp. 185-187.

[10] S. M. Berlijn etc, "Laboratory Tests and Web Based Surveillance to Determine the Ice- and Snow Performance of Insulators", IEEE Transactions on Dielectrics and Electrical Insulation, June 2007, pp.1373-1380.

[11] LIU Lihua, WANG Yinhui, DENG Fangan, "Face illumination compensation based on wavelet image of people", Computer Engineering and Design, July2009,pp. 3402-3406.

[12] F.Russo and G .Ramponi, " An Image Enhancement Technique based on the FIRO Operator ",In IEEE International Conference on Image Processing(ICIP-95),Washington DC,USA,Oct1995, pp.155-158.

[13] Wei O.Ma S, "Complete two-Plnae camera calibration and experimental comparisons", Pore.IEEEInt.Conf. On Computer Vision. Los Almaitos:IEEE, 1993, pp.439-446.

[14] Rafael C Gonzalez. Digital image processing. Beijing, China: Publishing House of Electronics Industry, 2009: 423-429.

[15] Kapur J N, Sahoo P K, Wong A K C,"A new method for gray2level picture thresholding using the entropy of the histogram", Compture Vision Graphics Image Processing, October 1985,pp.273-285.

[16] Y.Y.Tang,L.Yang, J.Liu, "Characterization of Dirac-Structure Edges with Wavelet Transform", IEEE Trans.Sys.Man Cybernetics-Part B:Cybernetics, Jun 2000, pp.93-109. .

A Research of Icing Forecasting Algorithm Using Genetic Algorithm and Fuzzy Logic

Xin-bo HUANG[1], *Yu-xin WANG[1], Yong-can ZHU[2], Hong-bo Li[1], Yi-ge WANG[1]
[1]College of Electronics and Information, Xi'an Polytechnic University, Xi'an 710048, China;
[2]School of Electro-Mechanical Engineering, Xidian University, Xi'an 710071, China
huangxb1975@163.com & wangyuxin_ac@sina.com

***Abstract*: According to the icing forecasting problems of transmission line, an icing forecasting fuzzy system was optimized by using genetic algorithm to get a better results. Firstly, a combined fuzzy rules base was established by using a learning algorithm, and combined with the expertise experience fuzzy rules in the field data. Secondly, the parameters of icing forecasting model such as the input-output domain fuzzy division、combined fuzzy rule base and membership function, etc. were optimized by genetic algorithm, moreover, the theory mix of genetic algorithm and fuzzy logic was studied and discussed further. Finally, the monitoring data acquired from transmission line online monitoring system on Guizhou Power Grid of China in 2014 was selected to compare the predicted effects of icing forecasting model before and after optimization.**

Keywords: transmission line; icing; icing forecasting; genetic algorithm; fuzzy logic

INTRODUCTION

Since January 2008, many provinces in southern China suffered a large area, long sleet freezing weather, which leading to a number of transmission line accidents, such as break line, pole collapse, tower collapse, ice flashover and ice-shedding and so on. A large area of the grid in a paralyzed state and the direct economic losses of more than 100 billion yuan. Therefore, it has great engineering practical significance to ensure the safe operation to develop a transmission line online monitoring system, remote real-time monitoring lines icing conditions, establish icing forecasting algorithm which based on monitoring data, and provide ice alarming [1]-[5].

Ice growth prediction model was established previously by the author [6], the dynamic and static performance and control effect of fuzzy system are decided by the fuzzy rules and correct choice of the membership functions. Upon the fuzzy system is established, the fuzzy rules were fixed, the implicit control process does not produce significant changes beyond the control. If the fuzzy rules can't cover all cases, the fuzzy system control effect is likely to be poor. In addition, it is difficult to determine the fuzzy rules on the basis of experience in multidimensional space when the number of input and output variables increase or decrease, and if the number of variables was increase, the number of fuzzy rules to choose space will increase sharply, which is difficult to judge the system control effect [7]-[10]. GA (*genetic algorithm*) is a global search algorithm, according to a set of control effect of fitness function evaluation algorithm, less dependence on the problems, so that can avoid falling into local optimum, and very suitable for optimization design of fuzzy control system [11].

In this paper, firstly a combined fuzzy rules base was established by using a learning algorithm combined with the expertise experience fuzzy rules in the field data. Then GA is used to optimize the parameters of icing forecasting model, such as the input-output domain fuzzy division; combined fuzzy

rules base and membership function, etc. Finally, the monitoring data acquired from transmission line online monitoring system on Guizhou Power Grid of China in 2014 was selected to compare the predicted effects of icing forecasting model before and after optimization.

I. COMBINED FUZZY RULES BASE

Assuming the value pairs for the formula (1), x_1 and x_2 are the input, and y is the output. The domain of x_1 and x_2 respectively are: $[x_1^-,x_1^+]$、$[x_2^-,x_2^+]$; the range of y is $[y^-,y^+]$.

Step 1: The fuzzy division for the range of x_1, x_2 and y are used by triangular membership functions. As shown in figure 1 , successively named: Nn, N1, O, P1, Pn. Determining the membership degree of $x_1^{(i)}$、$x_2^{(i)}$、$y^{(i)}$ in the different fields, and assigning the $x_1^{(i)}$、$x_2^{(i)}$、$y^{(i)}$ in a certain field where they have the maximum membership degree.

$(x_1^{(1)},x_2^{(1)};y^{(1)})$, $(x_1^{(2)},x_2^{(2)};y^{(2)})$,… (1)

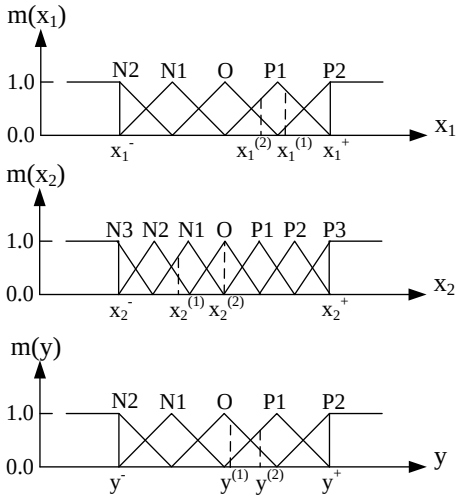

Figure 1: Fuzzy partition of x1、x2、y universe

From the picture 1: for the value pairs of $(x_1^{(1)},x_2^{(1)};y^{(1)})$ and $(x_1^{(2)},x_2^{(2)};y^{(2)})$ are:

$(x_1^{(1)},x_2^{(1)};y^{(1)})$ → $[x_1^{(1)}$(0.8 in P1,max),$x_2^{(1)}$(0.7 in N1,max);$y^{(1)}$(0.9 in O, max)]→Rule 1;

$(x_1^{(2)},x_2^{(2)};y^{(2)})$ → $[x_1^{(2)}$(0.6 in P1,max),$x_2^{(2)}$(1 in O, max);$y^{(2)}$(0.7 in P1, max)]→Rule 2.

Step 2: Every generated rule was given a strength so that can solve the problems of conflicting among rules. If x_1 is A，x_2 is B，y is C，intension should define as D. The intension of Rule1 and Rule2 respectively are：

$$D(Rule)=m_A(x_1)m_B(x_2)m_C(y) \quad (2)$$

$$D(Rule1) = m_{P1}(x1)\ m_{N1}(x2)\ m_O(y) = 0.8\times0.7\times0.9=0.504 \quad (3)$$

$$D(Rule2) = m_{P1}(x_1)\ m_O(x_2)\ m_{P1}(y) = 0.6\times1\times0.7=0.42 \quad (4)$$

Step 3: Combine generated fuzzy rules and expertise ecperience fuzzy rules, and then set up combined fuzzy rules base.

II. OPTIMIZE FUZZY CONTROL SYSTEM WHICH BASED ON GA

Select the appropriate coding method to unified coding for the parameters of membership function and the combined fuzzy rules base , which form a chromosome, to improve the genetic operation and set the objective function, thus optimize the ice fuzzy system.

A. Encoding parameters

1) The selection of coding mode

Common GA coding mode contains binary coding, decimal coding, real coding, matrix coding, symbol coding and so on [12]-[14]. The advantages of binary encoding are the simple encoding and decoding operation. The disadvantages are that for some problems of multi-dimensional, high-precision, chromosome encoded string is longer, the search space increases sharply with dimension increases which leads to a large computation. Real coding greatly reduces the string length and improves the efficiency of the algorithm without frequent coding and decoding genetic operation which make its interpretability strong.

2) Membership function coding

To ensure the increasing order of chromosome and generate invalid code string, the distance between its base end is selected as the optimization target. The width of the base of triangular membership function is defined to ensure that adjacent fuzzy partition is not isolated and has little overlap after genetic manipulation.

3) Combined fuzzy rules base coding

All the elements in combined fuzzy rules base were encoded in symbols while 1 to 5 integer values correspond to five fuzzy languages N2, N1, O, P1, P2.

The symbol coding is generated transforming the digitized combined fuzzy rules base to one-dimensional. Combined with membership function and combined fuzzy rules base coding to form a chromosome encoding string.

B. Improvements of genetic operation

1) Improvements of selection

N chromosomes randomly selected to form a new population based on individual fitness and new populations were crossover and mutation in the population of a certain generation. In order to ensure complete population, improve population diversity, expand the search space and prevent the loss of useful gene, we calculated the fitness of each chromosome of the new population, the population operated by crossover and the population by mutation, then selected the best n chromosomes from 3n chromosomes as the next generation population. Which can ensure that the integrity of group, and improve the population diversity, expand the search space and prevent the loss of effective gene.

2) Improvements of crossover

From the perspective of the whole population, for there were large individual differences among populations in the early running GA, choose a larger crossover probability to highlight the role of crossover, thus speeding up the speed of the algorithm. At the same time choose a smaller crossover probability to reduce the likelihood of outstanding individuals destroyed in the late running algorithm because of the small individual differences.

3) Improvements of mutation

Similarly, a smaller mutation probability conducive to the evolution of population in the initial period of running. A greater probability could enhance the diversity of the population and avoid algorithm catching in local optimum in the late running algorithm.

With the above operation, not only the diversities of population could be maintained but also the convergence capabilities of the system.

III. ICE FUZZY SYSTEM WAS OPTIMIZED BY USING GA

In this paper, the monitoring data of ice online monitoring systems of eight transmission lines installed in Guizhou Power Grid in China was selected, mainly includes the ice of IT (*ice thickness*); ET (*environmental temperature*); EH (*environmental humidity*); EW (*environmental wind speed*); CT (*conductor temperature*), which were real-time monitored.

A. Establish an icing fuzzy system

Selecting ET; EH; EW and CT, which transmission line online monitoring system had been monitored as input variables of the ice growth prediction model, the ice thickness of the corresponding value (IT) as the output variable.

The range of input and output variables respectively: ET was -10~10℃, EH was 80~100%, EW was 0~10m/s, CT was -10~10℃, and IT was 0~30mm. And fuzzy division was five level well-distributed triangles.

B. Establish a combined rules base

First of all, the field data of ET; EH; EW; CT and IT were extracted and preprocessed. Then, determining the membership degree of the input and the output in the different universes, and then distributed the maximum membership degree of the input and the output in one universe. Next, generating fuzzy rules with the field data, and calculating the intensity of each fuzzy rule D, counting of the number of the same fuzzy rules and calculating the average strength of the same fuzzy rules. Finally, Using expert experience rules and fuzzy rules which had higher average strength to establish combined fuzzy rules base, as shown in table 1. Selecting higher strength rules when compare the fuzzy rules with expert experience rules, and the strength of the expert experience rules was 0.8.

C. System was optimized by using GA

From the picture 2: Flowchart of icing fuzzy system optimized by GA.

1) Initialize the population

Setting 800 as the population size, 200 as

termination evolutionary generation, 0.7 and 0.001 as the crossover probability and mutation probability were respectively.

Table 1: Combined fuzzy rules base

ET	EH	EW	CT	IT	Strength
NB	NB	O	O	NS	0.8000
NB	NS	NB	PS	NB	0.6011
NB	PS	NB	NB	NS	0.8000
NB	PS	NS	O	NS	0.8000
NB	PS	O	O	O	0.4241
NB	PB	NB	NB	PB	0.8000
NS	NS	NS	O	NB	0.8000
NS	NS	PS	O	NB	0.3328
NS	O	NS	O	NS	0.8000
NS	O	O	NS	NS	0.8000
NS	O	O	O	NB	0.2632
NS	O	PS	O	NB	0.8000
NS	PS	NB	NB	NS	0.8000
NS	PS	NB	O	NB	0.4167
NS	PS	NB	NB	O	0.8000
NS	PS	NS	NB	NS	0.8000
NS	PS	NS	O	O	0.8000
NS	PS	O	O	NS	0.8000
NS	PB	NB	NS	PB	0.8000
NS	PB	NS	NS	PS	0.8000
NS	PB	NS	O	O	0.8000
NS	PB	O	NS	NB	0.8000
NS	PB	O	O	PS	0.8000
O	NB	NB	O	NB	0.4445
O	NB	NB	PS	NS	0.8000
O	NB	NB	PB	NB	0.5231
O	NB	NS	PS	NB	0.6823
O	NB	O	O	NB	0.8000
O	NS	NB	PS	NB	0.4721
O	NS	O	PS	NB	0.3348
O	O	NB	NB	NS	0.8000
O	PS	NB	O	NB	0.3840
O	PS	NS	NS	NS	0.8000
O	PS	NS	O	O	0.8000
O	PS	O	O	O	0.8000
O	PB	NB	O	NB	0.2746
O	PB	NB	PS	O	0.8000
O	PB	NS	O	NB	0.8000
O	PB	NS	PS	NS	0.8000
O	PB	PS	O	NS	0.4569
PS	NB	NB	PS	NS	0.5681
PS	NS	NB	PS	NS	0.6466
PS	NS	NS	PS	NB	0.3114
PS	NS	O	PB	NB	0.2467
PS	O	NB	O	NS	0.6374
PS	PS	NB	O	NB	0.4685
PS	PS	NB	PS	NS	0.8000
PS	PS	NS	PS	O	0.8000
PS	PS	O	PS	NS	0.8000
PS	PS	PB	PS	NB	0.8000
PS	PB	NB	O	NS	0.8000
PS	PB	NS	O	NB	0.8000
PS	PB	O	O	O	0.8000
PB	NB	NB	PS	NB	0.3050
PB	NB	NS	PB	NB	0.3391
PB	NS	NS	PS	NB	0.1686
PB	O	NS	PS	NS	0.8000
PB	PS	NS	PB	NS	0.8000
PB	PS	O	PS	NS	0.8000
PB	PB	O	PB	NB	0.8000

2) Coding

There were 60 fuzzy rules and 300 element numbers in the combined fuzzy rules base shown in table 1. Agreeing 1 to 5 integer values correspond to five fuzzy languages NB; NS; O; PS; PB, while limiting code in the range of {1,2,3,4,5}.

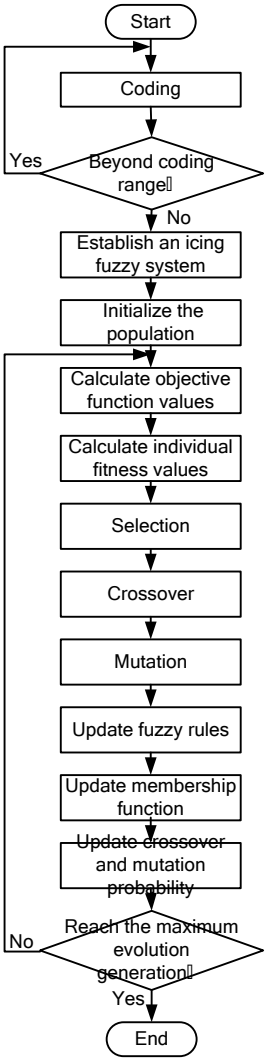

Figure 2: Flowchart of icing fuzzy system optimized by GA

Ice fuzzy system's membership function was coded, for example, the membership function of ET, which coding ranges of the distance between the

bottom end were respectively: $a_1 \in (-11,-5]$, $a_2 \in (-5,0]$, $a_3 \in (0,5]$, $a_4 \in (5,10]$. Agreed scope of the distance between the bottom edge end points was [0.8d,1.2d], where d=(10-(-11))/w. Based on first-order inertial time-delay model simulation system, when w was 4 the division of triangular membership functions was feasible [15]. Joint membership function and combined fuzzy rules base coding to form a chromosome encoding string, which length was (4×5)+(5×n)=20+5n, n was the number of rules in combined rules base.

3) The probability of crossover and mutation

The adaptive genetic proposed by M. Srinivas uses a crossover and mutation probabilities with adaptive capacity [16]. In this method, if contemporary adaptation fitness is equaled to the maximum degree, the crossover and mutation probabilities evaluate is 0. Preferred individual almost does not change and outstanding individuals were not the optimal solution for the global optimal solution in the early evolution of the population. So it was easy to fall into local optimization algorithm that this method was very unfavorable for the early evolution. This paper improved adaptive crossover and mutation probabilities, which is calculated as follows:

$$p_c = \begin{cases} 0.8 - \frac{(0.8-0.5)(f' - f_{avg})}{f_{max} - f_{avg}}, & f' \geq f_{avg} \\ 0.8, & f' < f_{avg} \end{cases} \quad (5)$$

$$p_m = \begin{cases} 0.1 - \frac{(0.1-0.001)(f_{max} - f)}{f_{max} - f_{avg}}, & f \geq f_{avg} \\ 0.1, & f < f_{avg} \end{cases} \quad (6)$$

In formula, f_{max}—The largest group fitness value in group;

f_{avg} — The average fitness value of each generation group;

f' — The maximum fitness value of each generation individuals performing crossover operation;

f—The maximum fitness value of each generation individual performing mutation operation.

4) Objective function

Using the minimum value of the sum of the difference between fuzzy system output values of ice and ice monitoring data as objective function, namely:

$$J = \sum_{i=1}^{N} \left| Y_{fuzzy} - Y_{data} \right| \quad (7)$$

In formula, Y_{fuzzy} was ice thickness of ice fuzzy system's output, Y_{data} was monitoring data of icing, N was the number of monitoring data.

5) Individual fitness value

$$Fit(y) = \begin{cases} Cmax - J, & J < Cmax \\ 0, & other \end{cases} \quad (8)$$

In formula, Cmax was the maximum individual fitness value in population.

D. Case study

Selected monitoring data acquired from transmission line online monitoring system on Guizhou Power Grid in 2014, as shown in figure 3, extracting some data and using GA to optimize ice fuzzy system, in another part of the data to validation. Figure 4 is membership function of icing fuzzy system optimized by GA, the membership function of fuzzy partition was no longer homogeneously, more practical. Figure 5 is output surface of icing fuzzy system optimized by GA. Figure 6 is forecasting effect of icing fuzzy system which is optimized by GA, the ice thickness in 0 to 18 mm have higher prediction ability, high accuracy and small error.

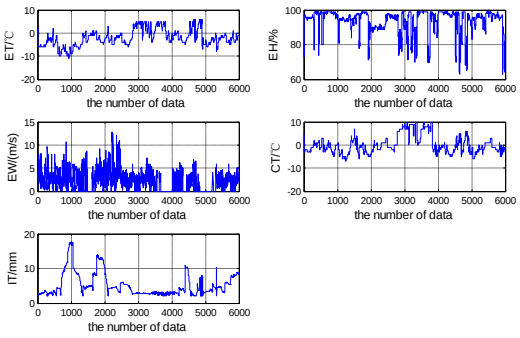

Figure 3: Monitoring data acquired from transmission line online monitoring system on Guizhou Power Grid in 2014

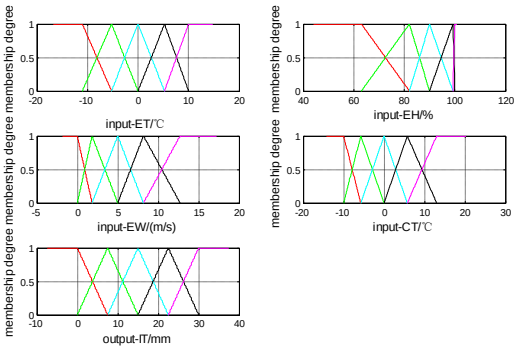

Figure 4: Membership function of icing fuzzy system

optimized by GA

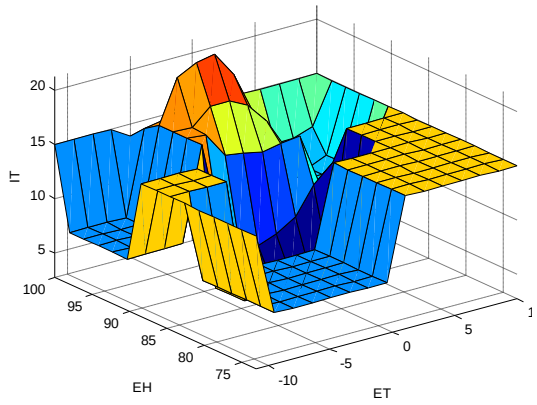

Figure 5: Output surface of icing fuzzy system optimized by GA

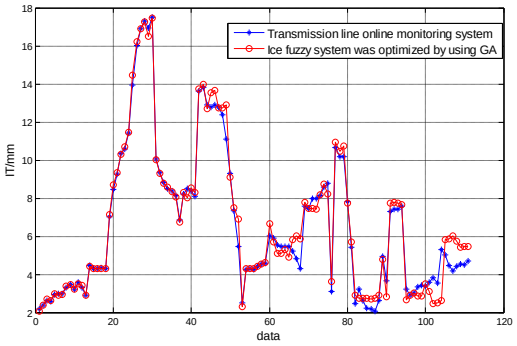

Figure 6: Forecasting effect of icing fuzzy system optimized by GA

IV. CONCLUSION

In this paper, ice prediction model which based on genetic algorithm and fuzzy logic fusion is established, which had the following advantages: (1) having self-study habits, which can automatically generate fuzzy rules according to on-line monitoring data, and monitoring also had the applicability for unknown;(2) having the self-adaptability, which can be adjusted automatically by the GA ice fuzzy system parameters;(3) having higher prediction accuracy for line ice, which had a certain practical significance.

REFERENCES

[1] ZHANG Wen-liang, YU Yong-qing et al, "Investigation and Analysis of Icing and Snowing Disaster Happened in Hunan Power Grid in 2008", Power System Technology, April 2008, pp. 1-5.

[2] HUANG Xin-bo，ZHANG Guan-jun et al, "Relation of transmission line icing and local meteorology", High Voltage Apparatus, August 2008, pp. 289-294.

[3] WANG Li-ming, LI Hai-dong et al, "Review of On-line Monitoring System of Ice Coating on Transmission Lines", High Voltage Apparatus, June 2013, pp. 48-56.

[4] LI Licheng, YANG Lin, HAO Yanpeng, "Review of On-line Monitoring of Ice Coating on Overhead Transmission Line", Power System Technology, February 2012, pp. 237-243.

[5] Yi Luo， Yi Yao et al, "Research on Power Transmission Line Ice Prediction System", 2012 International Conference on Measurement, Information and Control(MIC), May 2012, pp. 817-820.

[6] HUANG Xin-bo，LI Jia-jie et al, "Icing Thickness Prediction Model Using Fuzzy Logic Theory" High Voltage Engineering, May 2011, pp. 1245-1251.

[7] YING Hao, "Some Issues in Fuzzy Control Theory and Applications", ACTA AUTOMATICA SINICA, July 2011, pp. 591-592.

[8] ZHANG Xiaohui, DAI Guanzhong, XU Naiping, "The Study on Drawing and Filtering Fuzzy Control Rules by Using Genetic Algorithms", CONTROL THEORY AND APPLICATIONS, Jun 1998, pp. 379-384.

[9] WANG Li-xin, "Fuzzy Systems: Challenges and Chance- My Experiences and Perspectives", July 2001, pp. 585-590.

[10] MENG Xiang-hai, ZHENG Lai, QIN Guan-ming, "Traffic Accidents Prediction and Prominent Influencing Fcators Analysis Based on Fuzzy Logic", Journal of Transportation Systems Engineering and Information Technology, April 2009, pp. 87-92.

[11] JIN Yaochu, Jiang Jinping, "Two Approaches to Optimal Fuzzy Control", Proceedings of the CSEE, May 1996, pp. 201-204.

[12] ZHANG Chao-qun, ZHENG Jian-guo, QIAN Jie. "Comparison of coding schemes for genetic algorithms", Application Research of Computers, May 2011, pp. 819-822.

[13] YE Chen-zhou, YANG Jie, HUANG Xin, CHEN Nian-yi, "The Drawback of Real-Valued GA and Its Remedy", CIMS, May 2001, pp. 28-32.

[14] ZHU Can, LIANG Xi-ming, YAN Dong-huan, "The Mechanism Reasearch of a Novel Genetic Algorithm Based Species Selection", International Conference on Computer Science and Software Engineering, June 2008, pp. 462-266.

[15] XIN Ming-ying, LIU Feng, SUN Dalie, ZHANG Jian-guo, "The optimized design of the fuzzy controller (Ⅱ)- The disquisition of optimized triangle subjection function", Journal of Northeast Agricultural University, September 2002, pp. 296-299.

[16] M. Srinivas, L.M. Patnaik. "Adaptive Probabilities of Crossover and Mutation in Genetic Algorithms" IEEE Transactions on Systems, Man and Cybernetics, April 1994, pp. 656-667.

[17] Rudolph,G. "Convergence analysis of canonical genetic algorithms", IEEE Transactions on Neural Networks, May 1994, pp. 86-101.

The Numerical Analysis for Jump Height of Multi-two-spans Ice-shedding at Different Time Intervals of Overhead Transmission Line

Yong-can ZHU[1], *Xin-bo HUANG[2], Xin-xin ZHENG[2], Yu-xin WANG[2]

[1]School of Electro-Mechanical Engineering, Xidian University, Xi'an 710071, China

[2]College of Electronics and Information, Xi'an Polytechnic University, Xi'an 710048, China;

286844943@qq.com & huangxb1975@163.com

Abstract: **Transmission line ice-shedding is the typical fault inducement. The decreasing of the electric clearance and increasing of the dynamic tension are usually caused by ice-shedding vibration of overhead transmission line. Flashover, fittings damaged, or even wire breakage and tower collapses may be occurred if the ice-shedding vibration is serious which pose a threat to the safe operation of power equipment. According to different parameters of transmission line such as spans, span length, ice thickness, a finite element analysis model of wire-insulator was established, and the simulation of ice-shedding from overhead transmission line was adopted by additional force method. Then, the jump height of multi-two-spans at different time intervals can be got. The result shows that the amplitude of jump height decreased when the same time of ice-shedding on multi-two-spans which effect was equivalent to unilateral strain tower. The amplitude of previous ice-shedding spans is easily exceeded by the later spans when the vibration cycle of multi-two-spans interval was about 5/8. Besides, it was great impact on spans coupling such as the weight of the ice, spans, span length, damp and other factors. When the mass of the ice and spans is larger, the jump height of previous ice-shedding spans can easily passed by the later spans, but the effect of damp, span length is just the opposite.**

Keywords: transmission line; ice-shedding; jump height; ice-shedding interval; spans coupling

INTRODUCTION

Icing caused serious impact on the safe operation of overhead line worldwide by the influences of climate. In early 2008, the ice disaster in southern China caused 10kV overhead line tower damaged 140000, 220kV tower damaged more than 1500 and economic losses of billions. According to post-survey, 90% tower collapses accidents related to the ice-shedding vibration of overhead line [1]-[2]. Overhead line covered ice chunks fall off causing the overhead line vibration and horizontal swing subject due to weather conditions (temperature, wind) or artificial mechanical deicing, the typical dynamic impact effect can easily cause the overhead line fault. Transmission line de-icing fault mainly include mechanical and electrical: First, the vibration of overhead line results in a significant change in dynamic tension which cause additional impact load on fittings, it will lead to more serious fittings damage, line break, tower breakage, tower collapses and other mechanical accidents; Second, a significant jump of overhead transmission line, causing the wire-wire, wire-ground electrical clearance reduction and the transmission line flashover, transmission line burning and other issues[3]-[4]. The dynamic response of overhead transmission line ice-shedding has important theoretical and practical value.

Under natural conditions, transmission line ice-shedding with great unpredictability and unrepeatable, it is difficult to achieve the desired effect through natural observation. Overhead transmission line ice-shedding is difficult to carry out by artificial icing limited to the phytotron venue requirements. The current overhead transmission line ice-shedding experimental study simulated through lumped mass method or overhead line miniatures method. Jamaleddine [5]-[6], Kollár [7]-[8] built a miniature model of overhead line, simulated the dynamic response of overhead line ice-shedding by artificial icing and concentrated load. Morgan [9], Meng Xiao-bo [10] preformed separated span and continuous spans ice-shedding experiment to research jump height amplitude, dynamic tension vibration attenuator rate and other dynamic response by concentrated load on real transmission line span to simulate overhead line icing. Zhangqi Wang [2] conducted comparative experiments

between concentrated load method and artificial real de-icing on isolation overhead transmission line model, he got the overhead line tension curve under different conditions by changing the ice thickness, suspended span ratio, amount of de-ice and shedding location. Most of these studies focus on the relationship between de-ice dynamic response and factors such as tower line parameters, spacers, ice thickness and ice-shedding rate on one single overhead line span, and lack of research on continuous spans situation. In this paper, the wires-insulator finite element analysis model was established by professional software; the additional force method was used to simulate the response process of overhead transmission line ice-shedding and got the ice-shedding jump height at different time intervals on two continuous spans. At last we analyzed the influence of ice thickness, span length, spans, the damping, height and other parameters on the ice jump amplitude during ice-shedding occurred at two continuous spans non-simultaneous.

I. NUMERICAL SIMULATION METHOD ON ICE-SHEDDING OF OVERHEAD LINE

A. *Wires-insulator finite element analysis model*

Based on relevant studies about the finite element model of conductor-insulator, the structure of tower ignored because of little effect to the ice-shedding of overhead line, that only need to establish the finite element model of wires-insulator is shown in figure 1. Link 10 be used for simulate transmission line due to the characteristic of tensioning without pressure to the wires and ground line. This unit has the stress stiffening, large deformation function and geometric nonlinearity, which is very suitable for the simulation cable or chain. Insulator structure is relatively complex, but the insulator type and material have little impact on dynamic characteristic of ice-shedding, It is possible that by modeling and analyzing the insulator mandrel only. In addition, the insulator adapts to link 8 to simulator and hinged connection with overhead line.

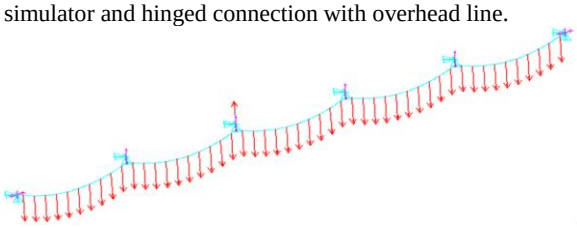

Figure 1: Finite element model of conductor-insulator

The overhead transmission line is multi-gear combination, tension tower on both sides, suspension point is equivalent to a fixed point and suspension insulator on straight tower in the middle, the suspension insulator was set at 5m, sectional area was 2500mm2 and the elastic modulus was 63000Mpa with swing degrees of freedom in the middle towers. Meanwhile, LGJ-400/50 ACSR conductor is selected as analysis object, which has some features such as wire diameter of 27.63 mm, the total sectional area of 451.55mm2, the quality of per unit length of 1511kg/km, tension force of 123.4KN and the elastic modulus of 69000Mpa. It is 400m for the span of overhead line and 24KN for the operator tension, and its thickness is 15mm.

B. *The FEA process of the ice-shedding process*

The transmission line elastic potential energy can get release in the ice-shedding process, rapid rebound oscillation, running tension rapid change. Influenced by wire damping and other factors, the ice-shedding oscillation gradually tends to rest. The numerical simulation of the transmission line ice-shedding is based on the three, which are the additional concentrated force method, the element birth and death method, the density change method, and the better accuracy is obtained [12]. The main steps of the finite element analysis of the ice-shedding are:

(1) The transmission line form finding, catenary equilibrium calculation of overhead transmission line in operation under the action of self weight and tension;

(2) The catenary equilibrium calculation overhead line with ice loads;

(3) The ice cover in the overhead line at a certain time is detached in some form, and the process is mainly simulated by the additional concentrated load method, the element birth and death method or the changing density method.;

(4) The response of the tower line after the ice-shedding.

C. *Overhead transmission line finite element form finding*

The overhead transmission line is a typical cable structure, with a catenary shape under self weight and ice load. Overhead transmission line form finding is calculated catenary weight and run under the action of the tension of the equilibrium state, the equilibrium state is the premise and basis of the calculation of transmission line galloping, ice-shedding, aeolian vibration model, the correct calculation will directly affect the dynamic analysis accuracy. Generally use the professional software, The analysis of overhead line form finding will be formed with and without the icing, get the overhead line sag value, the maximum tension value, the length of the wire, hanging points stress value, the calculation error is within the scope of the engineering [13]-[14]. Figure 2 shown the direct iteration method for overhead line form finding, first set the wire diameter, cross-sectional area, the gravity load numerical, running tension, elastic modulus, Poisson's ratio, linear expansion coefficient and initial strain and other parameters and create overhead line finite element model, applied value from a heavy load and solving the overhead line state, get the overhead transmission line horizontal tension value iteration for convergence condition, until meet the set of horizontal tension convergence conditions, the output is the state of overhead transmission line under the self loading.

D. *Calculation of additional force*

Overhead transmission line icing and snowing is a uniformly distributed along the span of the vertical load, the additional force method is that the uniform of ice quality to a plurality of discrete points. With the number of additional force points increases, the single concentrated load value decreased, and the overhead line static and dynamic response for additional force method is very similar to uniformly distributed load, the calculation precision can meet the needs of the engineering. As shown in Figure 3, according to the thickness of the hollow cylindrical transmission line icing considered, additional force method only needs the space overhead line icing load of the equivalent load. The calculation formula is shown as [2]:

$$F=\rho g\pi bL\,(D+b)\,/n \quad (1)$$

Where F is overhead line concentrated load, ρ is ice density, in this paper ρ=900kg/m^3; D is wire outside diameter; b is ice thickness; L is the actual length of transmission line; n is dividing unit number. In this paper, the finite element model is set for each meter as an analysis unit, and each element of the load equivalent of ice load is equivalent to an additional force.

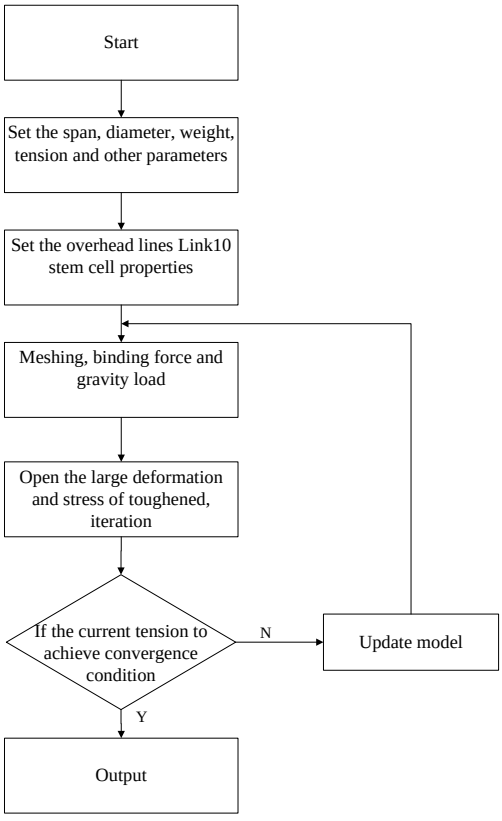

Figure 2: Basic steps of overhead line finite element form finding

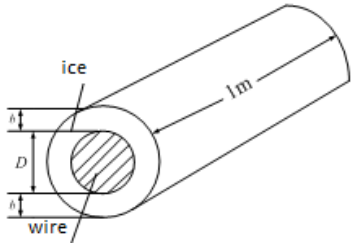

Figure 3: Calculation of ice thickness

II. THE EFFECT OF THE DIFFERENT TIME INTERVALS FOR TWO-SPAN ICE-SHEDDING JUMP HEIGHT

After the free combination with different time, different mass of ice-shedding and different tower -line system, ice-shedding form is varied. At different time intervals for two-span ice-shedding model is shown in Figure4.

The setting pattern of 7 tower 6 spans overhead transmission line is shown in figure 5. The middle two spans are the span of ice-shedding (span A ice-shedding firstly, followed by B) and the rest is not. 1 #, 7 # for tension insulator is equivalent to fixed point, don't have swinging degrees of freedom. 2-6# for suspension insulators have the swinging degrees of freedom.

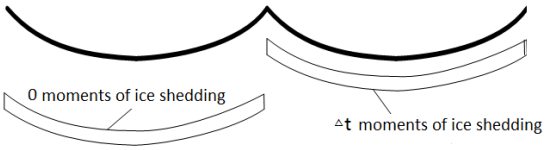

Figure 4: The way at different intervals times for adjacent two-span ice-shedding on overhead line

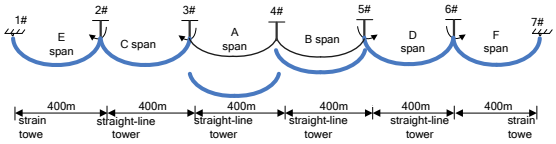

Figure 5: Transmission line with 7 tower and 6 span

When the damping coefficient is 0.1, maximum ice-shedding jump height on the A single span is 11.98 m and oscillation period T is 15.2 s. Based on the periodic T, time history of displacement responses at midpoints of span B of the different time intervals combined ice-shedding is obtained, as shown in Figure 6.

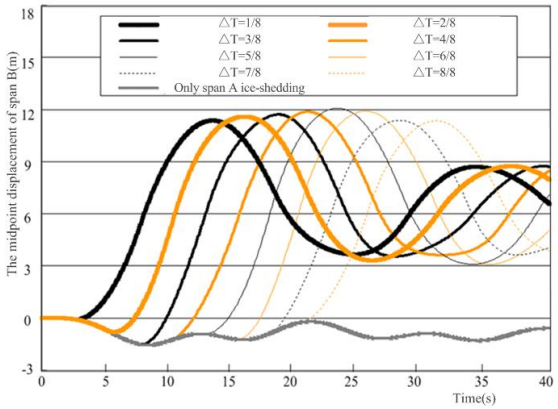

Figure 6: Time history of displacement responses at midpoints of span B for two-span assembling ice-shedding

As shown in Figure 6, after span A ice-shedding about 2s, the oscillating wave propagates to the midpoint of span B, with shift direction is negative, and the elastic potential energy of the span B is increased. By shock wave transmission delay and overhead line damping effect, in the time intervals range of 0 and 5T/8, the span B ice-shedding wire elastic potential energy with ΔT increased, and it is the same with the ice-shedding bounce height. The opposite effect is obtained when the ΔT is between 5T/8 and 1T, overhead transmission line maximum bounce height decreases with the ΔT.

Ice-shedding jump amplitude of two-span ice-shedding at different times intervals is shown in Table 1. When ΔT is equal to 0, the adjacent two spans ice-shedding at the same time, 4# insulator on both sides of the overhead line vibration offset each other, the insulator can be kept stationary state, unbalanced tension is null, The dynamic response process of A, B span is similar to the unilateral tension tower ice-shedding and maximum bounce height less than single span condition. The B span bounce height reached the maximum when 4T/8< ΔT <6T/8, B span midpoint ice jump amplitude is close to or more than A. When 0<ΔT<4T/8, ice-shedding process of span B leads to reduce the rising trend of span A, the jump height of span A not yet reached the point of the maximum displacement for the single span ice-shedding. When 4T/8< ΔT <1T, the midpoint of span A reached maximum displacement followed by span B ice-shedding. Influence by span B ice-shedding and damping conductor, the effect on span A

maximum ice jump amplitude does not increase any more.

Table 1: Ice jump amplitude of two-span ice-shedding at different times

ΔT (T)	A jump amplitude (m)	B jump amplitude (m)	B > A
0	10.97	10.97	
1/8	11.28	11.35	
2/8	11.85	11.57	
3/8	11.96	11.70	
4/8	11.98	11.87	
5/8	11.98	12.08	YES
6/8	11.98	11.91	
7/8	11.98	11.37	
8/8	11.98	11.34	

III. ANALYSIS OF THE INFLUENCE FACTORS IN TWO-SPAN ICE-SHEDDING JUMP HEIGHT

A. Impact of ice weight for two-span ice-shedding jump height

Transmission line ice weight is the important influential factor of ice-shedding, which increased jump height of overhead line. Holding section 2 model parameters unchanged, respectively to simulate dynamic response of ice-shedding in 10 mm, 15 mm, 20 mm three different ice thickness. In order to analysis the impact of ice weight for two-span ice-shedding jump height at different time course, the numerical simulation results are shown in table 2.

Same as section 2, the largest ice jump amplitude of span B still appeared on the ΔT = 5 T / 8 for the asynchronous ice-shedding. When the ice thickness is 10 mm, the span B midpoint bounce height is less than span A in the time intervals of 4 T / 8, 5 T / 8, 6T/ 8. The dynamic response of span A ice-shedding results in the decrease of span B to ice jump height. When ice thickness is 20 mm, B span midpoint bounce height is more than span A on 5T/ 8, 6 T / 8 two time intervals, the dynamic coupling of the A span ice-shedding caused by the ice increases the jump height of the B.

Table 2: Ice jump amplitude of two-span ice-shedding at different weight

ΔT (T)	Icing thickness (mm)	A jump amplitude (m)	B jump amplitude (m)	B > A
0	10	7.4	7.4	
4/8	10	8.35	8.19	
5/8	10	8.35	8.21	
6/8	10	8.35	8.02	
0	15	10.98	10.98	
4/8	15	12.04	11.87	
5/8	15	12.04	12.08	YES
6/8	15	12.04	11.91	
0	20	14.2	14.2	
4/8	20	15.28	15.03	
5/8	20	15.28	15.54	YES
6/8	20	15.28	15.51	YES

B. Impact of span length for two-span jump height

It is report that the span length significantly affected ice-shedding jump height. When the span length increased, the Ice-shedding jump height also increased. In order to analysis the influence of overhead line span length for jump amplitude of two-span ice-shedding, holding Section 2 model parameters unchanged, the overhead transmission line were set up to 300m,400 m,500m. Ice-shedding jump height numerical simulation results are shown in table 3.

The span B bouncing height decreases with span length. The midpoint bounce height of span A were higher than span B at 4 t / 8, 5 t / 8, 6 t / 8, while the span length is 500m. When overhead line distance is 300 m and 400 m, ΔT = 5 T / 8, span B bounce height is greater than span A, the coupling caused by span A ice-shedding increases the jump amplitude of span B, the longer the length of span, the weaker the coupling effect, the jump height of previous ice-shedding spans hardly passed by later ice-shedding spans.

Table 3: Ice jump amplitude of two-span ice-shedding at different span length

ΔT (T)	span length(m)	A jump amplitude(m)	B jump amplitude(m)	B > A
0	300	6.94	6.94	
4/8	300	7.55	7.44	
5/8	300	7.55	7.61	YES
6/8	300	7.55	7.52	
0	400	10.98	10.98	
4/8	400	12.04	11.87	
5/8	400	12.04	12.08	YES
6/8	400	12.04	11.91	
0	500	15.21	15.21	
4/8	500	17.12	16.63	
5/8	500	17.12	16.81	
6/8	500	17.12	16.53	

C. Impact of spans for two-span ice-shedding jump height

The actual number of span have a significant impact on the bounce height off the ice, the dynamic response of isolated tower-line system is much smaller than that of multiple tower-line system after ice-shedding. The jump height of ice-shedding slight increases with the number of transmission line spans. The jump height of intermediate span ice-shedding is an isolated value when the span number is greater than five. Holding Section 2 model parameters to analysis the impact of spans number for two-span ice-shedding jump height .The dynamic response of ice-shedding are simulated for span 4, 6 and 8 of overhead transmission line. The results of numerical simulation are shown in table 4.

The bounce height of span B is less than A when the spans number is 4 and the interval is 4T/8, 5T/8, 6T/8, the dynamic response caused by the previous span reduced the jump height of the latter ones. When the span number are 6 and 8, and ΔT equal to 5T/8, the maximum amplitude of ice shedding of B span is larger than A span. The coupling effect enhanced with the increase of the span number and the ice-shedding height of the latter span increased.

D. Impact of height difference for two-span ice-shedding jump height

Ice-shedding jump height is affected by height difference very little. Numerical simulation shows that the ice-shedding height reduced with the increased of height difference. Maintaining the parameters of Sections 2 model unchanged, 40 meters height difference of overhead transmission line was set. The results of dynamic response for two-span asynchronous ice-shedding as shown in table 5. The height difference makes the overhead transmission line span coupled weakened, the jump height of previous ice-shedding spans can easily passed by later ones.

Table 4: Ice jump amplitude of two-span ice-shedding at different spans

ΔT (T)	spans (m)	A jump amplitude(m)	B jump amplitude(m)	B > A
0	4	10.01	10.01	
4/8	4	11.66	11.29	
5/8	4	11.66	11.48	
6/8	4	11.66	11.15	
0	6	10.98	10.98	
4/8	6	12.04	11.87	
5/8	6	12.04	12.08	YES
6/8	6	12.04	11.91	
0	8	11.33	11.33	
4/8	8	12.2	12.09	
5/8	8	12.2	12.29	YES
6/8	8	12.2	12.14	

Table 5: Ice jump amplitude of two-span ice-shedding at different height difference

ΔT (T)	height difference(m)	A jump amplitude(m)	B jump amplitude(m)	B > A
0	0	10.98	10.98	
4/8	0	12.04	11.87	
5/8	0	12.04	12.08	YES
6/8	0	12.04	11.91	
0	40	11.26	11.26	
4/8	40	11.96	11.59	
5/8	40	11.96	11.68	
6/8	40	11.96	11.44	

E. Impact of damp coefficient for two-span ice-shedding jump height

The structural damping coefficient of transmission line is mainly derived from the axial friction of the twisted wire during the process of the ice-shedding. Roshan Fekr [15] and others put forward in the study of mathematical model for overhead transmission line to proposed iced conductors damping coefficient of 0.1, the bare wire damping coefficient is 0.02, then McClure [16], Chen Kequan [17] and other people in their own research using the parameter values. In order to analyze the overhead line damping effect two-span asynchronous ice-shedding jump amplitude. Set the structural damping coefficient to 0.02, 0.06, 0.1, the numerical simulation results of overhead transmission line ice-shedding jump height as shown in table 6.

The midpoint of span B jump height was greater than span A in 4T / 8, 5T / 8, 6T / 8 three time intervals when overhead line damping coefficient was 0.02, the ice-shedding response of second span had obvious enhancement; With the increase of damping coefficient, the maximum jump height of span B slow decline compared to span A, on the condition of damping coefficient equal to 0.06 and time intervals equal to 5T / 8, 6T / 8, span B overhead transmission line jump height is greater than the midpoint of span A; When the damping coefficient is 0.1, only when time intervals is 5 T / 8, span B bounce height just greater than A's . With the increase of the damping coefficient of overhead transmission line, the elastic potential energy absorbed by overhead transmission line is more, and the amplitude of the ice-shedding decreases as well.

Table 6: Ice jump amplitude of two-span ice-shedding at different damp

ΔT (T)	damp	A jump amplitude(m)	B jump amplitude(m)	B > A
0	0.02	12.61	12.61	
4/8	0.02	13.76	13.88	YES
5/8	0.02	13.76	14.53	YES
6/8	0.02	13.76	14.26	YES
0	0.06	11.74	11.74	
4/8	0.06	12.84	12.806	
5/8	0.06	12.84	13.17	YES
6/8	0.06	12.84	12.95	YES
0	0.1	10.98	10.98	
4/8	0.1	12.04	11.87	
5/8	0.1	12.04	12.08	YES
6/8	0.1	12.04	11.91	

IV. CONCLUSION

(1) Tower has little effect on the dynamic response of overhead transmission line ice-shedding, the conductor-insulator finite element analysis model is built in this paper by additional force, and the jump height of ice shedding was obtained with different time intervals and other parameters for multi-two-spans overhead transmission line;

(2) Dynamic response process on overhead transmission line ice-shedding is similar to the unilateral strain tower conditions, the maximum jump height is less than single span ice-shedding, when the multi-two-spans ice-shedding at the same time, the insulator will be kept stationary state, and unbalanced tension is 0 .

(3)Base on period of oscillation T of single span ice-shedding. The jump height of first ice-shedding spans may be exceeded by later spans when the multi-two-spans interval was about 4T/8-6T/8.

(4)It was great impact on spans coupling such as the weight of the ice, spans, span length, damp coefficient and other factors. When the mass of the ice and spans is large, the jump height of previous ice-shedding spans can easily surpassed by the later spans, but the effect of damp, span length is just the opposite.

REFERENCES

[1] HU Yi, "Analysis and Countermeasures Discussion for Large Area Icing Accident on Power Grid", High Voltage Engineering, 2008, pp.215-219.

[2] WANG Zhangqi, QI Lizhong, YANG Wengang, et al,

"Research on the applicability of Lumped Mass Method for Cable's Dynamic Tension in the Ice-shedding Experiment", Proceedings of the CSEE, 2014, pp.1982-1988.

[3] CHEN Yong, HU Wei, WANG Liming, et al, "Research on Ice-shedding Characteristic of Icing Conductor", Proceedings of the CSEE, 2009, pp.210-217.

[4] SHEN Guohui, YUAN Guanghui, SUN Bingnan, et al, "Dynamic Impact Effects on Tower-line System Due to Ice-shedding", Engineering Mechanics, 2010, pp. 210-217.

[5] Jamaleddine A, McClure G, Rousselet J, "Simulation of ice-shedding on electrical transmission line using ADINA", Computers & Structures, 1993,pp.523-536.

[6] Jamaleddine A, McClure G, Rousselet J, "Physical and numerical simulations of ice-shedding effects on a reduced-scale model of overhead transmission line", Proceedings of the International Symposium on Cable Dynamics. Belgium, Institute of Electrical and Electronics Engineers, 1995, pp.45-52.

[7] Kollár L E, et al, "Natural wet-snow shedding from overhead cables", Cold Regions Science and Technology, 2010, pp.40-50.

[8] Kollár L E, Farzaneh M, "Modeling Sudden Ice-shedding From Conductor Bundles", IEEE TRANSACTIONS ON POWER DELIVERY, 2013, pp. 604-611.

[9] Morgan V T，Swift D, "Jump height of overhead-line conductors after the sudden release of ice loads", Proceedings of the Institution of Electrical Engineers, 1964，pp.1736-1746.

[10] Meng Xiaobo，Wang Liming，Hou Lei，et al, "Dynamic characteristic of ice-shedding on UHV overhead transmission line", Cold Regions Science and Technology ，2011,pp.44-52.

[11] Bo Yan，Chen Kequan，Guo Yueming，et al, "Numerical Simulation Study on Jump Height of Iced Transmission Line After Ice-shedding ", IEEE Transaction on Power Delivery，2013，pp.216-225.

[12] SHEN Guohui, XU Xiaobin, LOU Wenjuan, et al, "Applicability Analysis of Finite Element Methodologies to Simulate the Ice-accreting and Ice-shedding on Transmission Line ", Engineering Mechanics, 2011, pp.9-15.

[13] HUANG Xinbo, Ma Longtao, Xiao Yuan, et al, "Form-finding analysis based on finite element method for line with uniform ice-coating", Electric Power Automation Equipment, 2014,pp.72-76.

[14] HUANG Xinbo, Ma Longtao, Xiao Yuan, et al. "Simulation research on the amplitude factors of ice-shedding of transmission line", Journal of Xi'an Polytechnic University, 2014, pp.525-531.

[15] M. R. Fekr and G. McClure, "Numerical modelling of the dynamic response of ice-shedding on electrical transmission line", Atmospheric Research, 1998, pp.1-11.

[16] G. McClure, M. Lapointe, "Modeling the structural dynamic response of overhead transmission line", Computers and Structures, 2003, pp.825-834.

[17] CHEN Kequan ,"Study on Dynamic Responses of Iced Transmission Line after Ice-shedding and the Mechanical De-icing Method", Chongqing: Chongqing University, 2012.

Verification of Icing-model, in Finland.

Karoliina Hämäläinen[1], Sami Niemelä[1]
[1] Finnish meteorological institute, Helsinki, Finland
karoliina.hamalainen@fmi.fi

***Abstract*: Icing-model used at FMI gets its input from the numerical weather prediction model AROME. The AROME uses traditional observations in verification and assimilation purposes. However, the absence of daily icing measurements makes the verification of Icing-model challenging. In this paper we present the methods and results of the verification of Icing-model.**

Keywords: icing, modelling, verification, icing rate

ABBREVIATIONS

LWC	*Liquid Water Content*
MVD	*Median Volume Diameter*
FMI	*Finnish Meteorological Institute*
NWP	*Numerical Weather Prediction*
CLW	*Cloud Liquid Water*
agl.	*Above ground level*

I. INTRODUCTION

Icing causes many difficulties to wind energy and creates challenges to operators. Financial loss can be expected at the electricity markets, when the promised electricity amount is not produced. Detailed day-a-head icing forecasts could provide help to this situation by enabling better power production estimates.

In our study we use combined modelling system. The post-processing tool Icing-model gets the input from numerical weather prediction (NWP) model AROME [1]. AROME uses many different kinds of observations in assimilation, from satellites to ground observations. AROME is also used as the operational weather forecasting model at Finnish meteorological institute (FMI). However, measuring of atmospheric icing is not part of FMI's daily routine. Due to this the amount of icing measurements available is quite limited. Yet, there are some observations from different field campaigns. And more or less regular daily measurements are made at Puijo measurement station.

The lack of operational icing measurement data made us to perform sensitivity tests to understand how the Icing-model behaves. In this work we present the results from observation comparison and sensitivity tests. The results of sensitivity test are presented as hours of active icing per month, which corresponds to frequency of the events. This is due to the fact that we were interested on how large is the uncertainty in the results of Finnish Icing Atlas, published by FMI.

II. OBSERVATIONS AND MODELLING METHODS

A. Observations

We collected five different types of icing measurements from FMI's observation archives for three sites to validate our Icing-model. The observations available were from Puijo (continental area in Eastern-Finland) and Luosto (Lapland) measurement stations. In addition to FMI measurements, data from one wind turbine site at Riutunkari (west coastal are) was also used.

From Puijo we had data from Labkotec's LID-3300IP and Vaisala's FD12P instruments. The Vaisala FD12P instrument is not actually icing measurement instrument, but a visibility sensor. Together with temperature measurement and wind speed we used the correlation relation defined by Hirvonen et al. [2].

Labkotec data was also available from Riutunkari wind farm provided by Labkotec Oy. LID-3300IP instrument gives ON-OFF type of information if it is icy or not.

From Luosto we had two different types of measurements. ON-OFF data from Rosemount instrument and mass measurements form Combitech IceMonitor.

With AROME we created weather datasets to cover the periods from which we had observations. These dataset were post-processed by Icing-model. We tested each site and the observations from each instrument separately against the model results.

B. Icing-model

The input for the Icing-model is taken from NWP model AROME. From the AROME we get wind speed, temperature and liquid water content. AROME has advanced microphysics scheme in which it is able to divide hydrometeors into five categories: rain, snow, graupel, cloud water and cloud ice. In our setup only liquid water content (rain and cloud water) is used in icing calculations.

AROME has a 3D-Var assimilation system, in which it uses wide spread of different kind of observations. The horizontal grid-size of AROME is 2.5 km with 60 levels in vertical. Consequently, the icing results are calculated for whole Finland by using the same resolution.

The Icing-model was developed for climatological applications such as for creating the new Finnish Icing Atlas. The Icing-model is based on physics described in ISO Standard 19494 [1], so called Makkonen model. In this method ice is accumulated over standard cylinder. It takes into account the surface area *A* seen by the wind *V*, *LWC* and three coefficients. These coefficients describe sticking, collision and accretion efficiencies. The icing rate is:

$$\frac{dM}{dt} = \alpha_1 \alpha_2 \alpha_3 \cdot LWC \cdot A \cdot V$$

In addition to *LWC*, the Icing-model needs to know the cloud particle number concentration. In our work we use constant value 100 cm^{-3}. From literature we discovered that ~70 cm^{-3} responds to clean marine air [4] and 300 cm^{-3} to forested area [5]. It is clear that constant value is not the best option for all conditions. Therefore, we performed sensitivity test to evaluate magnitude of possible errors due to constant number concentration approach.

C. *Sensitivity tests*

We tested how sensitive the Icing-model itself is for the input it gets from the weather model. Input variables such as wind speed, temperature, liquid water content and cloud particle number concentration were perturbed in order to see the effects of these parameters. The motivation for this was to understand the effect on icing results if we mis-forecast the parameter. The test period is February 2006. Monthly mean values of icing intensity were calculated and compared to original Icing Atlas results.

The perturbations are following:

- Temperature by ±2˚C, the average temperature bias of AROME during Wind Atlas.
- Wind speed by ±2m/s, average difference between calm and windy month during Wind Atlas.
- Liquid water content by ±20%, if water content is wrongly divided between different water phases.
- Cloud particle concentration by ±30%, and even with 300 cm^{-3}.

III. RESULTS

D. *Observation comparison*

According to Icing-model observation comparison the Icing-model has the skill to detect icing events (Fig. **1**). However, the ability to estimate accumulated ice mass is very poor (Fig. **2**). The model results did not seem to be greatly dependent on used instrument. However, we trusted the Puijo and Luosto observations more, because from these stations we had maintenance information available.

From Figure **1** we see that the modelled and observed temperatures are very close to each other, during the test period November 2005. We can recognize that modelling error in 23rd of November is due to temperature error in the NWP-model. In the observations the temperature is below zero, but the model is just above 0˚C. This is why the Icing-model does not produce ice. The other modelling error can be identified during 18th of November. In this case the NWP-model predicts the temperature right, but does not have CLW to produce ice. Altogether it seems that the Icing-model is very sensitive to temperature and CLW input from NWP-model.

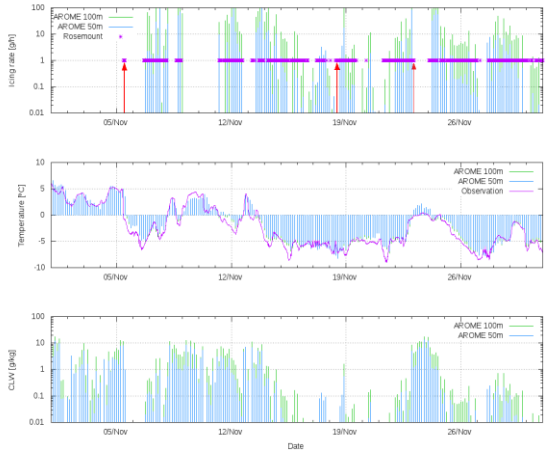

Figure 1. Luosto observations against model results, in November 2005. At the upper panel icing observations with purple stars and icing intensity from the model with green and blue respect to 100m and 50m heights. At the middle panel observed temperature (purple) and modelled temperature (green and blue). At lower panel cloud liquid water in the Icing-model.

In figure **2** we show example of the ice mass comparison from Luosto. We can see that the start of the ice mass accumulation is quite accurately simulated. However, the mis-forecasted temperature in the model launches melting almost four hours too early even if there would be enough liquid water available. The amount of ice mass is also far too low.

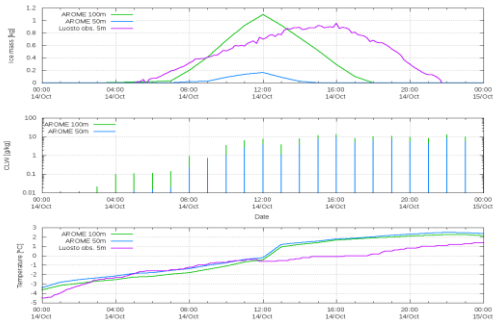

Figure 2. Ice mass observation comparison from Luosto measurement station in 14th of October 2007. At top panel ice mass. In the middle panel CLW content by the Icing-model. At lower panel: temperature. Purple values are presenting the observations from 5m height. And the green and blue are presenting the Icing-model results respect to 100m and 50m heights.

E. Results of sensitivity tests

The results are strongly dependent on how well the wind speed, temperature and liquid water content are forecasted. The results presented here are monthly mean values of hours of active icing. The original model results, to which we are comparing the test setup, is from Finnish Wind Atlas dataset.

Effects of temperature perturbations were as expected. Most radical changes are seen when the original temperature is close to zero degrees, like at coastal areas if the sea is not frozen. However, when the temperature is just below zero it seems not to have an effect on how much ice is accumulating. In Northern highland areas where the temperature can drop so low that the liquid water particles does not exist any longer the icing is reduced. From figure **3** we can see that by decreasing and increasing the temperature, the strongest effects are found on coastal areas and highlands. The most radical changes are seen at the south-west coastal areas, when temperature is increased by 2˚C. In this area the absolute values are already higher in original model run and rising of temperature causes significant reduction in monthly mean values.

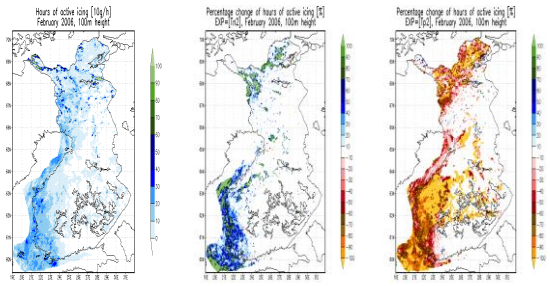

Figure 3. Effects of air temperature to hours of active icing during February 2006. On a left hand side: original model result. At the middle temperature decreased by 2˚C and on a right hand side temperature increased by 2˚C.

Perturbation of wind speed had largest relative changes [%] in the areas where the original values were small (from 0 to 10 hours per month). In these areas the changes were about 80-100%. However, the absolute changes in monthly mean values of icing were rather small. The modelled wind speed do not seem to have an effect on frequency of icing-events, but it has an effect on icing rate and how much ice is accumulated.

Changes in liquid water content has an effect on ice mass accumulation but not so much on when the accumulation is detected. Hence, the perturbation has a modest effect on hours of active icing. The largest changes are seen in the areas where the original values are small. Altogether the changes in absolute icing hours are small, when perturbing the liquid water content by 20%.

The Icing-model results were not sensitive to changes in cloud particle number concentration if the amount of LWC was kept as in original model run. In other words the droplet size distribution did not seem to have a great effect on ice mass or icing-rate, when studying the monthly averages.

IV. CONCLUSIONS

In general, the comparison between observations and icing-model results are very promising. However, the Icing-model has no or low skill to predict ice mass accumulation correctly. One problem in the ice mass comparison was that the observations were from 5m agl., but the lowest model level is at 30m height from the ground seen by the model. In Luosto's case the observations are made at top of a hill which cannot be seen by the weather model in such detail, causing a shift about 130m. Nevertheless, the Icing-model is suitable to predict the existence of icing events, but to estimate the severity of the event cannot be estimated accurately enough.

AROME is used as operational weather forecasting model at FMI. The daily verification results show that AROME has the skill to predict the temperature and the wind speed reliably. So the errors in icing results caused by temperature and wind speed should be in general rather small.

In the beginning of the study we were more concerned about the errors caused by LWC and cloud particle number concentration. Especially the cloud particle concentration raised some concerns, because we do not have tools to measure the concentration and create local maps. However, the sensitivity tests show that constant cloud particle number concentration assumption do not seem to cause significant error relative to other sources. However, predicting the clouds and the liquid

water content temporally and spatially correctly still remains as challenge. For more accurate icing-forecasts we need to improve the microphysics in the NWP-model to cast clouds more accurately.

ACKNOWLEDGEMENT

The author would like to thank Finnish agency for Technology and Innovation for funding the project Finnish Icing Atlas (project 40477/09). In addition thanks to Helsinki University by providing the Chancellor's Travel Grand, which made it possible to take part in IWAIS 2015 conference.

REFERENCES

[1] Y. Seity et al. “The arome-france convective-scale operational model” Monthly Weather Review, 2011. pp. 976-991.

[2] J. Hirvonen et al. “Comparison of visibility observations at a meteorological tower to cloud base height observations from nearby weather stations.” The 14th International Workshop on Atmospheric Icing of Structures (IWAIS): Chongqing, China, 2011. (May 8 - May 13).

[3] International Standard, ISO 12494 – Atmospheric Icing of Structures. July 2000.

[4] Korolev and Mazin. ”Zones of increased and decreased droplet concentration in stratiform clouds.” Journal of Applied Meteorology, 1993. 32(4): pp. 760–773.

[5] P. Bechtold et al. “The Meso-NH Atmospheric Simulation System: Scientific Documentation. Part III: Physics.” Available: http://mesonh.aero.obs-mip.fr/mesonh/dir_doc/book1_m49_22nov2011/scidoc_p3.pdf (Accessed: 8.10.2014).

Innovations in F-LOWICE Real-Time Forecasts of Wind Power and Icing Effects

Ben C. Bernstein[1], Erik Gregow[2] and Ian Wittmeyer[1]
[1] Leading Edge Atmospherics, Longmont, Colorado, USA
[2] Finnish Meteorological Institute, Helsinki, Finland
email: [1]ben@icingweather.com, [2]erik.gregow@fmi.fi

***Abstract*: Recent enhancements to F-LOWICE have been made to improve real-time, HIRLAM-based forecasts of temperature and wind speed at wind farms, as well as the downstream effects on both "clean" and "iced" power estimations from the F-LOWICE algorithms. A method to communicate the uncertainties in wind power forecasts and the effects of icing upon them is also described.**

Keywords: icing, wind power, models, probability

LEGEND AND ABBREVIATIONS

FMI	*Finnish Meteorological Institute*
LAPS	*Local Analysis and Prediction System*
LWC	*Liquid Water Content (TNR 8 pt)*
MVD	*Median Volume Diameter*
T	*Temperature*
U	*Wind Speed*

INTRODUCTION

In recent years, numerous systems have been developed for the diagnosis and prediction of wind power and the effects of icing conditions thereon. These include two systems developed in partnership between Leading Edge Atmospherics ("LEA") and the Finnish Meteorological Institute ("FMI") called "LOWICE" and "F-LOWICE". Respectively, these systems produce diagnoses and forecasts of icing and wind power. As part of the Swedish Energy Agency's Wind Pilot Program, LOWICE, F-LOWICE and forecast systems from several other agencies were run over Sweden for several icing seasons.

Output from these systems have been compared with observations of temperature, wind speed, power and icing at wind farms and the results have proven that these systems provide reasonably realistic information. Of course, the systems are not perfect and errors and biases have been identified. Among the LEA-FMI systems, the LAPS analysis-based diagnostic system LOWICE clearly outperformed the HIRLAM-forecast based F-LOWICE system, especially in terms of temperature and wind speed. Model forecast errors promulgated downstream causing errors in icing presence, and both "clean" and "iced" power predictions. Additional errors inherent in models include mis-timing of weather features, such as fronts, wind maxima/minima, presence and strength of inversions, structure of wind profiles, plus natural variability of meteorological phenomena, especially in complex terrain.

In an effort to improve real-time F-LOWICE forecasts for the final seasons of the Wind Pilot Program, two improvements to the system were put in place. The first was an attempt to identify errors and biases in the first six hours of HIRLAM model forecasts of temperature (T) and wind speed (U) at wind farms via comparison with wind farm observations and high-quality diagnostics from the LAPS model, then apply those corrections to the remainder of the forecast run.

The second approach was to communicate to users some of the uncertainties in power forecasts that are associated with local variability as well as mis-forecasting of meteorological features that are relevant to wind turbine icing and power.

I. DIAGNOSITCS, FORECASTS AND OBSERVATIONS

LEA and FMI have been running two real-time systems to assess the potential for wind turbine icing across Scandinavia for several years. The longest running system is "LOWICE", which provides hourly diagnoses, while the newer "F-LOWICE" system (forecast version of LOWICE) has been providing forecasts out to +48 hours for the last two years.

A. LAPS-based LOWICE

Beyond the direct measurement of icing at a given location, there are numerous sources of meteorological data that can be used to estimate near-surface icing conditions indirectly. In particular, observations from satellites, surface stations and radars provide a great deal of useful information, especially when paired with forecasts from numerical weather models. Each of these data sources has its strengths and weaknesses for the diagnosis and forecasting of icing, and the information from each must be considered carefully in the context of the meteorological environment in order to use them effectively. For example, significant radar reflectivity can be a strong indicator of glaze icing when freezing rain is occurring, but it can also be a strong indicator of the depletion of liquid water in icing clouds when snow is occurring.

It is with these concepts in mind that a real-time version of the "LOWICE" system was developed using the Finnish Meteorological Institute's Local Analysis and Prediction System (LAPS) model to produce hourly assessments of the likelihood and severity of icing over Scandinavia [1,2]. LAPS-Scandinavia combines ECMWF model forecast grids with Meteosat geostationary satellite data, reflectivity from a network of radars, and surface observations across the domain to create hourly, 3-D analyses of the state of the atmosphere in the domain. LAPS grids of pressure, temperature, winds, relative humidity, cloud fields and precipitation provide essential input fields to the LOWICE system. A map of the LAPS domain and the model's representation of terrain of Scandinavia are given in Fig. 1.

At each grid point, LOWICE examines the satellite and surface observations to determine whether or not the grid point is "cloudy", and then tests to see whether the vertical level of interest (e.g. a wind farm) is vertically located within the clouds and/or within a layer of liquid precipitation. If either is the case and temperatures are suitable, then icing conditions may exist. The likelihood of icing is then assessed through examination of the physical structure present (e.g. a single layer cloud), applying fuzzy-logic interest maps to icing-relevant fields (e.g. temperature, cloud top temperature), and testing for the presence of certain precipitation types (e.g. snow, freezing rain) nearby. Using this same information, liquid water content is estimated and combined with wind speed to estimate icing rates, ice loads and most importantly, both "clean" (ice-free) and "iced" power for individual turbines and entire wind farms.

B. *HIRLAM-based F-LOWICE*

A forecast version of LOWICE, known as "F-LOWICE" was developed to produce 0-48 hour forecasts of the same fields and outputs described above, based primarily on numerical model forecasts from the HIRLAM model [3]. Of course, observations of the presence of clouds, cloud structures, cloud phase, precipitation presence, intensity and type, as well as other highly relevant fields for icing and wind power are not available for future times. However, surrogates of these fields can be derived from 4-D model forecasts of temperature, wind speed, relative humidity, explicit cloud microphysics, and precipitation. Though imperfect, these fields can be used to simulate the expected presence of relevant meteorological features in the atmosphere and passed through algorithms similar to those applied in LOWICE to estimate icing- and wind-power in the future. A map of the HIRLAM sub-domain used by F-LOWICE and the model's representation of terrain of region are given in Fig. 1.

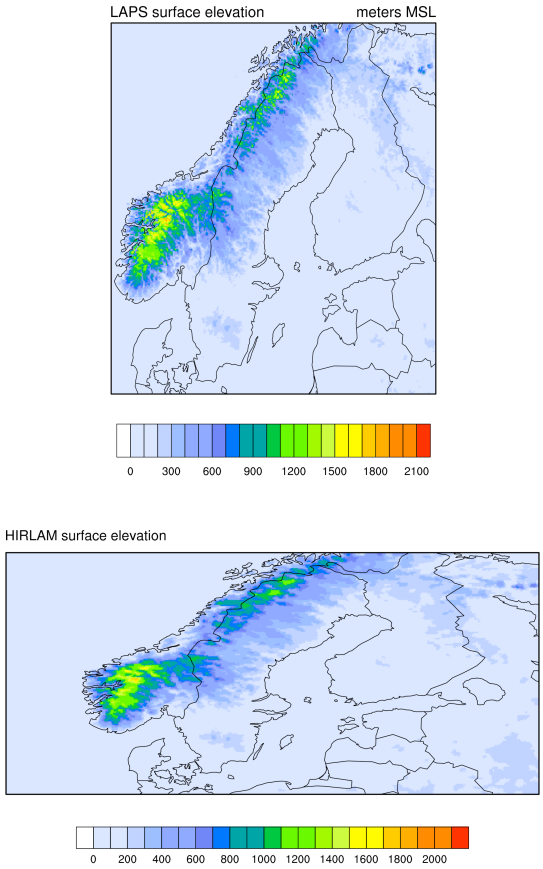

Figure 1: LAPS (top) and HIRLAM subset (bottom) grids used by LOWICE and F-LOWICE, respectively. The height of the model terrain is shown here.

C. *"GROUND TRUTH" OBSERVATIONS*

Real-time data from wind turbines and co-located meteorological and icing instruments provided "ground truth" observations for comparison with LOWICE and F-LOWICE system output. Turbine data included temperature, winds, and measured power production, while the meteorological instruments provided independent measurements of temperature, winds, and in some cases ice load, visibility and/or ceiling height. Webcam images were also available at some sites (Fig. 2). Such imagery proved very helpful for documenting events and corroborating instrumentation measurements with things like visible ice growth or depletion over time.

Figure 2: Example of iced instrumentation package on top of a wind turbine. Another turbine and some low-altitude icing clouds are evident in the background.

II. ADJUSTMENTS TO RAW HIRLAM MODEL FORECASTS

In an effort to correct for systematic over-forecasts of wind speed (U) and under-forecasts of temperature (T) coming from raw, interpolated HIRLAM model grids, a rudimentary correction scheme was developed. It was based on comparison of the first six hours of each HIRLAM model run with both a) turbine-observations and b) LAPS gridded diagnoses of T and U. Differences and ratios were calculated then weighted to estimate appropriate corrections to raw HIRLAM forecasts for hours 1-6, then those same corrections were applied to forecast hours 7-48, covering the remainder of the forecast run. Comparisons between observations and both the original and adjusted output at longer forecast times (12+ hours) have been made. Although statistics have not yet been calculated, visual inspection of daily output have indicated that predictions of T, U, icing and iced power have improved.

An example of the difference between the original (left) and adjusted wind speeds (right) and their effect on power forecasts is shown in Fig. 3. It is clear that for this case, wind speed and power estimates were far too high in the original version. These are greatly improved in this adjusted version for this case, with the over-estimation of wind speed and power essentially eliminated. However, due to some issues with the handling of air density effects on the power curve (January application of September-derived power curve), the adjusted result now gives a slight under-estimate of power production.

In the absence of a correction to the air density issue (which should be easy), adjusted values of ice power only resulted in a slight improvement in the power estimation for this case. Still, the adjustments to both wind speed and power have put the latest version of F-LOWICE in a better position to accurately predict the presence of icing, ice growth and decay, the clean power and the effects of icing on power production (power loss due to ice), once issues like the air density have been resolved.

It is important to note, however, that differences found between observations and forecasts over the first six hours are not always representative of the differences that will occur in the hours that follow, especially at times well beyond +6 h. To this end, climatological biases are also being considered as an additional ingredient to the HIRLAM adjustment scheme. In concept, differences between the 1-6 hour forecasts and recent observations should be more meaningful for forecast times that immediately follow (e.g. 7-12 hours), but should become less meaningful with forecast length. In contrast, long-term errors (e.g. a persistent cold bias) may become more meaningful with

forecast length. Thus, we are considering applying a gradual transition from the observation-based adjustments to the climatological adjustments with forecast length. This would be handled by applying time-adjusted weight to the different adjustment parameters.

Though visual inspection of daily HIRLAM/F-LOWICE forecasts and corresponding observations from wind farm appears to indicate that the method described above has yielded improvements in forecast quality, the adjusted forecasts have yet to be verified. A head-to-head comparison of original and adjusted T, U and power forecasts is planned in the coming months.

III. Probabilistic forecast information

It is well understood that numerical model forecasts of even basic parameters such as temperature and wind speed are prone to errors and that those errors tend to increase with increasing forecast length. Mis-timing of fronts, wind maxima/minima, the presence and strength of wintertime inversions and complex vertical wind profiles can make even the simple aspects of forecasting wind power quite difficult at times. Moisture parameters, especially forecasts of microphysical fields, take these challenges a step further, as the prediction of relative humidity, let alone saturation, cloud phase, liquid water content and drop size are far more difficult, especially as forecast length increases.

Thus, there is inherent uncertainty in not only the basic parameters of T and U, which are pivotal to wind power production forecasts, but quite significant uncertainty in forecasts of the presence, intensity and downstream effects of icing on power production. Despite this, single values of all of these parameters are typically provided to wind power forecast users, such as power traders. These values are considered to be representative of the icing at a particular wind turbine, both in 3-D space and in time (e.g. for a given hour).

In an effort to convey a sense of the uncertainty that is inherent in such forecasts, LEA-FMI began to experimentally provide wind power trading companies with graphics showing not only the baseline, single-point forecasts of clean power and three unique estimates of iced power for specific wind farms, but also a "cloud" of clean and iced power forecasts for data points immediately surrounding the wind farms in 3-D space. With these data presented in time series (e.g. Fig. 4), it is possible to get an indication of the level of uncertainty in both space and time.

During the 2014-15 icing season, the probabilistic plots began to include the adjustments that were described in the previous section, helping to improve upon over-forecasts of power production that were present in earlier versions of both standard and "probabilistic" output from F-LOWICE.

IV. Future work

The methods described above represent improvements in both the quality of F-LOWICE forecasts of icing and power and the communication of the inherent uncertainties in such forecasts to highly sensitive users such as power traders. Though these are steps in the right direction, there is a great deal of work left to be done. One of the most important items for the advancement of LOWICE and F-LOWICE is the adjustment of power curves to include air density. Currently, their power curves are derived during ice-free periods of early autumn, and they have been held constant throughout the icing season. This approach ignores the fact that greater air density during colder periods causes power curves to change, generally becoming steeper and shifting slightly to the left, allowing greater power generated at the same wind speed. If this were corrected, the underproduction of power shown in Fig. 3 should be improved upon. Further improvements to the linear approximations of the power curves may also help.

Acknowledgment

The authors would like to express our sincere thanks to Göran Ronsten of Windren AB, for his steadfast support of the meteorolological "participant" groups throughout the life of the Wind Pilot Program. Though the program has had many challenges, he has proven to be both a staunch supporter of the work being done and a leader who asks necessary and difficult questions in a congenial way. Furthermore, he has also fostered a good relationship among the participants, encouraging us to learn from one another and build our capabilities in concert (pun intended).

We would like to thank the other participants (WeatherTech, SMHI and Kjeller Vindteknikk) for their contributions to this program and for the opportunity to work alongside them. We would also like to thank the Swedish Energy Agency for their support of the Wind Pilot Program, OX2 for graciously sharing their wind farm data with the participants, the members of the "reference group" for their great efforts to examine, validate and verify the varied output from the four participant groups, while providing good quality feedback with the underlying goal of helping all of the participant groups produce better products. Finally, we wish to thank InSitu and Combitech for their hard work trying to keep instrument packages running in such harsh environments.

References

[1] Gregow, E., B.C. Bernstein, I. Wittmeyer and J. Hirvonen, 2015: LOWICE: A real-time system for the assessment of low-level icing conditions and their effect on wind power. Journal of Atmospheric and Oceanic Technology, In Press.

[2] Albers, S. C., J. A. McGinley, D. L. Birkenheuer, and J. R. Smart, 1996: The local analysis and prediction system (LAPS): Analyses of clouds, precipitation, and temperature. Wea. Forecasting, 11, 273-287.

[3] Undén P. et. al., 2002. HIRLAM-5 Scientific Documentation, HIRLAM-5 Project, Norrköping, SWEDEN , 144 p.

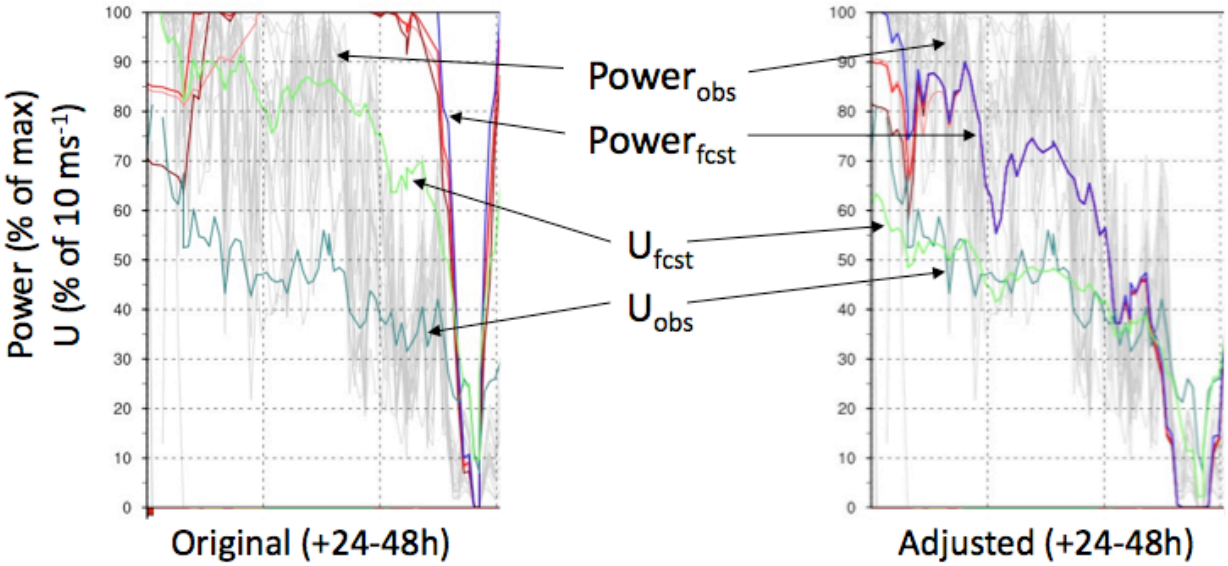

Figure 3: Wind speed and power data for 3-day period in January. Observed power production (grey) and median observed wind speeds (dark green) from multiple turbines are shown in both panels. In the left panel, the original HIRLAM forecast wind speeds (light green) and associated F-LOWICE "clean" (blue) and "iced" (red and tan) power are shown. In the right panel, adjusted HIRLAM wind speeds and F-LOWICE power are shown. All forecasts are from forecast times +24 to +48 h.

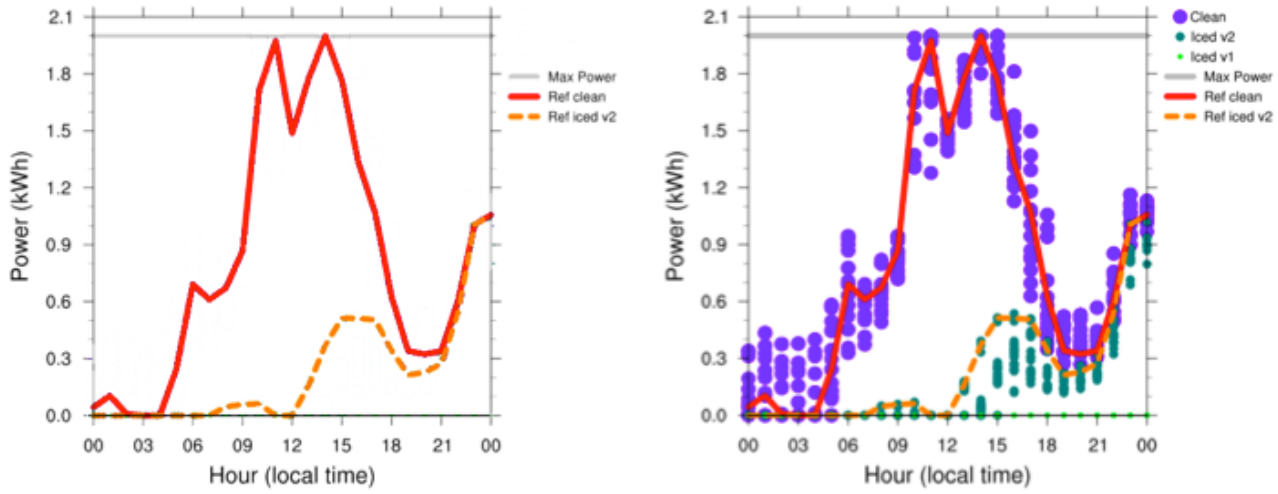

Figure 4: Standard (left) and "probabilistic" (right) plots of forecast clean and iced power from F-LOWICE for an example 24-hour period. The original clean (red) and iced (dashed tan) lines are included in both panels. Forecasts shown are for one wind turbine based on forecast times from +24 to +48 h.

Advanced test methods for full-scale ice tests of DC insulators strings intended for ±350 kV

A. Dernfalk[1], J. Lundengård[1], E. Petersson[1], I. Gutman[1], K. Tucker [2], S. Banerjee [3]
[1] STRI (Sweden), [2] Nalcor (Canada), [3] Kinetrics (Canada)
andreas.dernfalk@stri.se

***Abstract*: A new ±350 kV HVDC transmission line is planned from Muskrat Falls to Soldiers Pond in Canada. Along the route, two areas were considered as potential challenges for dimensioning with respect to pollution and ice; one characterized as coastal area and another one characterized as mountainous area. Three basic possible service cases were identified to be simulated by representative laboratory testing: polluted insulator covered by rime ice; polluted insulator covered by glazed ice; polluted insulator covered by glazed ice accreted under full-scale voltage. The insulator string consisted of standard DC glass cap-and-pin insulators and the performance was verified by withstand test during melting phase of ice. For each test case, four insulator strings were first subjected to the specified ice/pollution conditions, and thereafter subjected to a voltage withstand test. This required development of a sophisticated set-up providing automatic application of ice without voltage and later with voltage on the relatively long insulator strings. The paper presents details on testing philosophies and practical principles for all three possible service cases, listed above.**

Keywords: ice, insulator testing, pollution, test facilities

LEGEND AND ABBREVIATIONS

SDD	*Salt Deposit Density (IEC 60507)*
NSDD	*Non-Soluble Deposit Density (IEC 60507)*

INTRODUCTION

A new ±350 kV HVDC transmission line is planned in Canada from Muskrat Falls to Soldiers Pond. Along the route, two areas were considered as potential challenges for dimensioning with respect to pollution and ice; one characterized as coastal area and another one as mountainous area. Based on the previous work and investigations it was decided to use DC glass cap-and-pin insulators for the new design. To verify DC pollution/icing performance of full-scale 350 kV HVDC overhead line glass insulator strings a number of withstand tests were decided and performed simulating typical service cases. Three basic possible service cases were identified to be simulated by representative laboratory testing:

- Polluted insulator covered by rime ice
- Polluted insulator covered by glazed ice
- Polluted insulator covered by glazed ice accreted under full-scale voltage

These cases required development of a sophisticated set-up providing a combination of pollution and ice accretion on insulators. This in turn required creation of advanced automatic system for the application of ice without voltage and later with voltage on the relatively long insulator strings.

I. TEST SET-UP

For each test case, four insulator strings were first subjected to the specified ice/pollution conditions, and thereafter subjected to a voltage withstand test. In order to be able to meet the test requirements for simultaneous pollution and ice testing sophisticated set-up providing automatic application of ice without voltage and later with voltage on the relatively long insulator strings was developed. The schematic view of the set-up for ice accretion in de-energized state is shown in Figure 1 for three insulators and its final arrangement is shown in Figure 2.

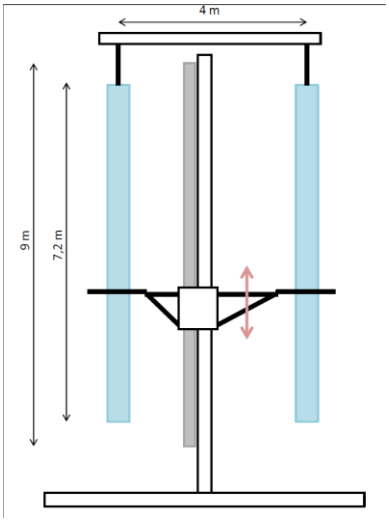

Figure 1: Schematically shown test set-up for insulators in parallel (ice accretion without voltage).

Figure 2: Final set-up for four insulators in parallel during ice accretion without voltage (rime ice).

II. CREATION OF POLLUTION

In all test cases the insulators were contaminated at room temperature prior to subsequent ice accretion in cold conditions. Pollution was applied by the standard IEC procedure (IEC 61245), i.e. dipping the insulators into a standard suspension prepared from water, salt (NaCl) and kaolin. The required pollution levels, characterized by standard pollution parameter

Salt Deposit Density (SDD) were obtained in the range from about 0,05 mg/cm^2 to about 0,15 mg/cm^2 and were achieved by varying the amount of salt. Another standard pollution parameter, the Non-Soluble Deposit Density (NSDD) was targeted to be approximately 0,1 mg/cm^2. Pollution levels were checked by measurements on sample insulators not included in the following ice accretion and voltage test. Example of contamination procedure by dipping is presented in Figure 3.

Figure 3: Example of application of pollution by dipping of the insulators (IEC 61245).

III. CREATION OF ICE (WITHOUT VOLTAGE)

After application of pollution, four complete insulator strings were assembled in parallel in the climate test hall. In this part of the investigation ice was accreted onto the de-energized insulator strings through spraying of fog by sophisticated automatic system of nozzles, see Figure 4.

Figure 4: Example of application of ice without voltage application by sophisticated automatic system of nozzles.

For all test cases the ice was formed either from water similar to standard IEC rain from the tap water. During all ice applications the air temperature in the test hall was kept between -7°C and -8°C. Water was sprayed towards the four insulators without additional air flux (no wind simulation).

To avoid removal of the firstly applied pollution layer, small amounts of water were first sprayed onto the insulators in a cyclic manner (using nozzles moving up and down along insulator with adjustable pause length after each sweep). According to the test program both rime ice and glaze ice were simulated. The required type of ice was achieved by use of different nozzles and different distances from the nozzles to the test objects.

The nozzles were moving with a velocity of about 0,1 m/s. By smart combination of the water flow, distances and number of nozzles the water froze more or less instantly when hitting the insulators and no icicles were accreted and no free water could dissolve the pollution layer.

Ice thickness and ice distribution were specified to be measured by rotating rod in some parts of the agreed test program, see examples in Figure 5 and Figure 6. However, the visual criterion for bridging was the dominant criterion to make a decision when the target ice accretion is accomplished. Typically, ice accretion was continued until the "complete bridging" was achieved (according to the agreement additional criterion was that about 50% of the diameter of the insulator should be covered by ice); this was defined by visual observation and recorded by photography. The rotating rod was installed at the bottom of one of the strings in case of ice accretion without voltage application; while it was installed at the top of the arrangement in case of ice accretion with voltage application.

Example of complete ice accretion for the rime ice is presented in xxx and for the glazed ice in xxx.

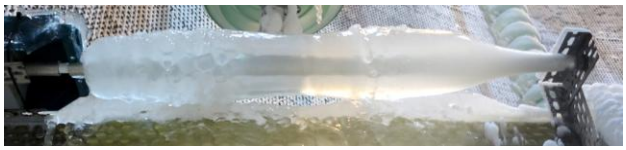

Figure 5: Example of ice accretion at the rotating rod when the rod was installed under the insulators.

Figure 6: Example of ice accretion at the rotating rod, when the rod was installed on top of the insulators.

Figure 7: View of the insulator string covered by rime ice.

Figure 8: View of the insulator string covered by glazed ice.

IV. Creation of Ice (with Applied Voltage)

Insulators were contaminated and after pollution and drying the ice was accreted at the insulators during about 24 hours. The main specifics in this test in comparison to previous ones were that the ice accretion was performed under full DC voltage of 361 kV. For the ice accretion under voltage a certain distance was needed to prevent flashover. Thus in this case nozzles spraying larger droplets (which reach longer) were used. The nozzles were moving up and down with a velocity of about 0,15 m/s. One nozzle was spraying on each string. The water was pre-cooled to a temperature just above 0 degrees C. After the ice accretion time of 24 hours there was bridging of a large part of the insulator strings and the amount of ice was agreed to be sufficient, see Figure 9 and Figure 10.

Figure 9: View of the insulator strings covered by glazed ice accreted under full DC voltage 361 kV.

Figure 10: Close view of the insulator covered by glazed ice accreted under full DC voltage 361 kV. Note long icicles developed along the E-field lines.

V. Important Parameters to be Checked During the Test

The following important parameters were measured during the tests (see summary in Figure 11):

- Temperature in the climate hall
- Humidity in the climate hall
- Ice density
- Melted ice water conductivity via collection of melt water during voltage test
- Melted ice water volume via collection of melt water after voltage test
- DC test voltage
- Leakage current
- Ice temperature by non-contact IR measurements (see example of measurements in Figure 12).

Parameter	Target value if applicable
Temperature in the climate hall during ice accretion	Stable, about -7÷-8°C
Temperature in the climate hall during the voltage test	Increased to about +1°C
Humidity	NA
Ice density	Rime ice or glaze ice according to IEEE
Melted ice water conductivity	NA
Melted ice water volume	NA
DC test voltage	-361 kV DC
Leakage current	NA
Ice temperature	NA
Dew point*	NA

Figure 11: Parameters measured during the test and their target values.

The following procedure was used for the measurements of ice weight per unit of insulator length and further calculations. The total amount of ice and dripping water were collected from the insulators of the full length during and after the voltage test. The weight of the collected samples was measured by a scale

and the melted ice water conductivity was measured in specially cleaned boxes.

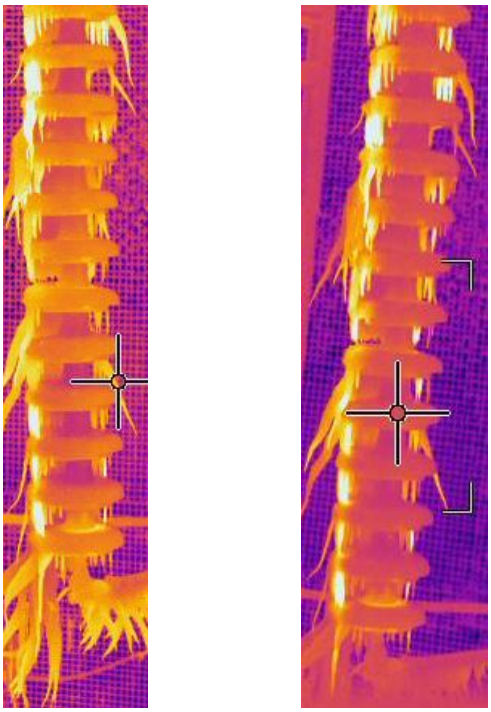

Figure 12: Examples of IR camera measurements of ice temperature (surface temperature is influenced by partial discharge activity).

VI. Summary

To verify DC pollution and icing performance of 350 kV HVDC full-scale glass insulator strings chosen by Nalcor, withstand tests defined by Nalcor according to the principles of IEC 61245, IEEE 1783 [1] and IEEE position paper [2] were performed at STRI. Three basic service cases included pollution and rime ice; pollution and glazed ice and pollution and glazed ice accreted under full voltage. Special sophisticated and automated arrangements of nozzles made this possible and also different levels of pollution and ice were feasible to achieve, see examples in Figure 13.

Figure 13: Examples of different levels of ice created during the test: left – low level; right – high level.

According to the test program, after the pollution and ice accretion was finished, the voltage withstand tests were performed in "melting regime" mode according to the principles of IEEE 1783 [1]. This was achieved by increase of temperature in the climate test hall after finalized ice accretion for each case. The door of the chamber was opened and additional flow of warm air was created by the fans evacuating air through the roof of the chamber.

Due to the size of the test objects, and due to the amount of ice, the test objects could not be moved after ice accretion. Thus, the insulators could not be tested one by one. Therefore, for all cases insulators were tested in the same position as during ice accretion phase; i.e. four insulators in parallel. This arrangement simulated IEC standard withstand procedure, where it is allowed to treat as withstand test either no flashovers after three tests or one flashover after four tests. If flashover occurs on two parallel test objects of four, then the test in this project was treated as failed to confirm the withstand level.

The results of voltage tests will be reported in the separate contribution from Nalcor at the 2015 World Congress & Exhibition on Insulators, Arresters & Bushings to be held in Germany in October 2015.

Acknowledgment

The authors would like to acknowledge the whole team of engineers from Nalcor, STRI and Kinetrics for their great contribution in the various aspects of this investigation, especially in the development and verification of new test methods and undertaking the tests. Their dedication and flexibility have contributed remarkably to the success of this project.

References

[1] M. Farzaneh, E.A. Cherney, W.A. Chisholm, A.C. Baker, R.A. Bernstorf, J.T. Burnham, A. Carreira, R.S. Gorur, T. Grisham, S. Grzybowski, S. Gubanski, I. Gutman, G. Karady, S. Marra, A. Schwalm, V. Sklenicka, G.A. Stewart, R.Sundararajan, "IEEE Guide for Test Methods and Procedures to Evaluate the Electrical Performance of Insulators in Freezing Conditions", IEEE Std 1783TM-2009, 17 October 2009.

[2] M. Farzaneh, T. Baker, A. Bernstorf, K. Brown, W.A. Chisholm, C. de Tourreil, J.F. Drapeau, S. Fikke, J.M. George, E. Gnandt, T. Grisham, I. Gutman, R. Hartings, R. Kremer, G. Powell, L. Rolfseng, T. Rozek, D.L. Ruff, D. Shaffner, V. Sklenicka, R. Sundararajan and J. Yu., "Insulator Icing Test Methods and Procedures", IEEE Transactions on Power Delivery, Vol. 18, No. 4, October 2003, pp. 1503-1515.

Development of snow accretion simulation method for electric wires in consideration of snow melting and shedding

Kazuto Ueno, Yuzuru Eguchi, Takashi Nishihara, Soichiro Sugimoto, Hisato Matsumiya
Central Research Institute of Electric Power Industry (CRIEPI)
k-ueno@criepi.denken.or.jp

***Abstract*: In order to quantitatively clarify the process from the start of snow accretion to overhead transmission lines until snow shedding, we have developed a numerical code, SNOVAL®(Ver.3) (Snow accretion simulation code for overhead transmission lines). SNOVAL consists of meteorological data as input, a snow accretion model, a thermodynamic model for snow melting, and a snow shedding model. In the snow accretion model, dynamic effect of an electric wire rotation by external moments due to gravitational and aerodynamic forces on snow deposit is considered. The shape of accreted snow produced by SNOVAL is not necessarily to maintain cylindrical shape as in simple cylindrical accretion models. In contrast to the existing snow accretion models in which the snow deposit is always oriented normal to the wind speed, SNOVAL is applicable to snow accretion on electric wires under calm to strong wind in any direction. In the thermodynamic model with heat exchanges between the air, electric wire and snow deposit, the liquid water content in the snow deposit is introduced by taking into account the melting of snow deposit as well as the melting of snowflakes prior to impact. The sticking efficiency (accretion factor) and density of the accreted snow in the snow accretion model are parameterized based on the liquid water content and the shape of accreted snow. In the snow shedding model, the adhesive force between the surface of electric wire and ice granules is estimated as a function of the liquid water content. Wet snow shedding is numerically evaluated based on the balance of forces and its related moments exerted on the accreted snow. SNOVAL is applied to natural wet snow accretion to conductor samplers supported by wires, and the quantitative comparisons between numerical and observational results are made.**

Keywords: Snow accretion simulation, Accretion factor, Liquid water content, Adhesive force, Snow shedding

INTRODUCTION

In order to prevent snow related damage to overhead transmission facilities, a great deal of research has been done to understand wet-snow accretion to overhead transmission lines and to improve the accuracy in predictions on accreted snow load. However, physical model explaining all processes from the start of snow accretion, growth, until snow shedding is still not satisfactory, research efforts continue in many countries [1-4]. On the other hand, computer aided simulations for snow accretion across the span of the conductor have been developed since 1970, taking into account the effect of conductor rotation on the snow accretion process [1,5]. CRIEPI also has developed a snow accretion simulation code, named SNOVAL(Ver.2), which can evaluate numerically the temporal change of three dimensional accreted snow shape, mass and electric wire rotation under calm to strong wind in any direction [6,7].

SNOVAL(Ver.2) has been improved to incorporate a model of snow accretion to electric wires and snow melting. This model enables us not only to calculate the liquid water content of snow deposit by taking into account the melting process due to heat exchanges between the air, electric wire and snow deposit, but also to give density of snow deposit and accretion factor based on the liquid water content. Adhesive force between the surface of electric wire and snow deposit is also estimated based on the liquid water content. Furthermore, a snow shedding model is incorporated in the improved version, in which the time of snow shedding is quantitatively evaluated based on the balance between the adhesive force and gravitational, aerodynamic forces exerted on snow deposit, or the balance of moments related to these forces. The extended version, SNOVAL(Ver.3), is thus able to reproduce the process from the start of snow accretion until snow shedding [8].

In this paper, we give a brief outline of physical models developed in [8] with some modifications of parameterization for density of snow deposit and accretion factor. Numerical results obtained from SNOVAL(Ver.3) are compared with observations for a wet snow event in Japan.

I. MODELS

As shown in Fig. 1, SNOVAL(Ver.3) is an extended version based on SNOVAL(Ver.2), and consists of an input of meteorological data of surface and atmosphere (top), model of snow accretion growth and wire rotation (left), model of snow accretion and melting (right), and model of snow shedding (bottom).

A. Dynamical model of snow accretion growth and electric wire rotation

Snow accretion growth and shape at the position (x, ψ) at time t is determined by solving the following equation of thickness $h(x, \psi, t)$ of snow layer attached to a smooth cylindrical conductor (Fig.2):

$$\frac{\partial h(x,\psi,t)}{\partial t} = -\frac{\sigma(t)(\mathbf{S}\cdot\mathbf{n_e})}{\rho_s(t)(\mathbf{N}\cdot\mathbf{n_e})} \quad (1)$$

where $\sigma(t)$ is the accretion factor (the fraction of snow that sticks to the snow deposit after collision), $\rho_s(t)$ the density of the accreted snow, and $\mathbf{n_e}$ and $\mathbf{N}$ the outward unit normal to the accreted surface and to the conductor, respectively. The quantities $\sigma(t)$ and $\rho_s(t)$ are unknown and need to be parameterized. $\mathbf{S} = G_0\mathbf{v_s}$ is the accretion intensity per unit area due to the mass concentration G_0 of falling wet snow in the air multiplied by impact speed of snowflakes $\mathbf{v_s}$. Here G_0 is given by

$$G_0 = \rho_w P(t) \times 10^{-3}/(600 v_f) \text{ for } P[\text{mm}/10\text{min}] \quad (2)$$

where ρ_w is the density of water and v_f is the terminal speed of snowflakes corresponding to the precipitation rate P. Snowflakes follow rectilinear paths in the wind direction prior to impaction because of their large inertia. Therefore, $\mathbf{S} = G_0\mathbf{v_s}$ can be approximated as $\mathbf{S} = G_0\mathbf{v}$, where $\mathbf{v} = (v_x, v_y, v_z)$ is the wind velocity. Using the horizontal wind speed $w_v(t) = \sqrt{v_x^2 + v_y^2}$, wind direction $\theta_d(t)$ and azimuth θ_c (Fig.3), and

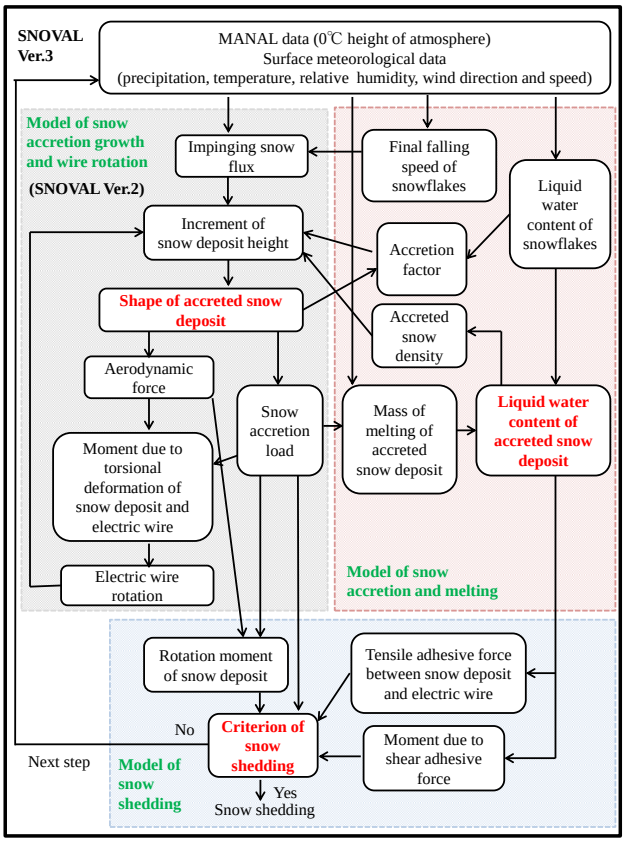

Fig.1. Framework of SNOVAL Ver.3.

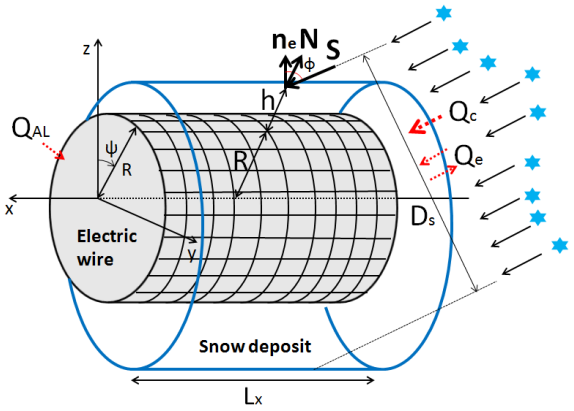

Fig.2. Snow accretion on a smooth cylindrical electric wire of finite length.

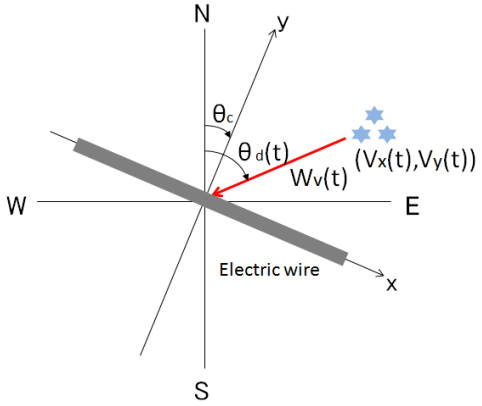

Fig.3. Wind direction relative to an electric wire.

considering the case of absence of up and down blow, $v_z = 0$, $\mathbf{S}$ can be expressed as

$$\mathbf{S} = \begin{pmatrix} S_x(t) \\ S_y(t) \\ S_z(t) \end{pmatrix} = G_0 \begin{pmatrix} -w_v(t)\sin(\theta_d(t) - \theta_c) \\ -w_v(t)\cos(\theta_d(t) - \theta_c) \\ -v_f \end{pmatrix} \quad (3)$$

The accumulated snow mass per unit length of a conductor with L_x in length is estimated from

$$m(t) = \frac{\rho_s(t)}{2L_x} \int_0^{L_x} \int_0^{2\pi} \left\{ \left(R + h\,(x,\psi,t)\right)^2 - R^2 \right\} d\psi dx \quad (4)$$

The equation for the rotation angle φ due to the torsional deformation of electric wire is given by

$$I \frac{\partial^2 \varphi}{\partial t^2} = GJ \frac{\partial^2 \varphi}{\partial x^2} + M_s' + M_w' \quad (5)$$

where I is the moment of inertia of electric wire and accreted snow, G the shear modulus and J the polar moment of inertia. M_s' and M_w' are moments due to gravitational and aerodynamic forces exerted on accreted snow, respectively. Since M_s' and M_w' depend on φ, (5) is a nonlinear equation with respect to φ.

B. *Snow deposit melting*

The rate of production of melt water within snow deposit is

$$\frac{dm_w(t)}{dt} = \left(Q_c(t) + Q_e(t) + Q_{Al}(t)\right)/L_f \quad (6)$$

where $m_w(t)$ is the mass of melt water per unit length and L_f the latent heat of fusion. $Q_c(t)$ is the convective heat flux from the airstream:

$$Q_c(t) = h_c(t)(T_a(t) - T_s) \times l(t) \quad (7)$$

where T_a is the air temperature, T_s the fusion temperature (0℃ for wet snow deposit mixing of ice and water), and $l(t)$ arc length of the outside of accreted snow. h_c is the heat transfer coefficient defined by

$$h_c(t) = K_a Nu(t)/D_s(t) \quad (8)$$

where K_a is the thermal conductivity of air, $Nu(t)$ the Nusselt number averaged over the circumference of the snow deposit, and D_s the distance of cross section of the snow deposit perpendicular to the snowflake impact speed (Fig.2). Using the Reynolds number defined by $Re(t) = D_s(t)|v_y(t)|/\nu_a$ with the kinematic viscosity of air ν_a, the following $Nu(t)$ is employed:

$$Nu(t) = \begin{cases} 0.891Re^{0.296} & (0.1 \le Re < 1) \\ 0.891Re^{0.330} & (1 \le Re < 4) \\ 0.821Re^{0.385} & (4 \le Re < 40) \\ 0.615Re^{0.466} & (40 \le Re < 4{,}000) \\ 0.174Re^{0.618} & (4{,}000 \le Re < 40{,}000) \\ 0.0239Re^{0.805} & (40{,}000 \le Re < 250{,}000) \end{cases} \quad (9)$$

$Q_e(t)$ is the evaporation/condensation heat flux for the accretion surface:

$$Q_e(t) = \frac{0.622 h_c(t) L_e \left(\frac{RH(t)}{100} e_w(T_a(t)) - e_w(T_s)\right)}{C_p \times P_a} \times l(t) \quad (10)$$

where $RH(t)$ is the relative humidity, L_e the latent heat of evaporation over water, C_p the specific heat of air at constant pressure, P_a the atmospheric pressure, and $e_w(T)$ the saturation vapor pressure at temperature T[℃],

$$e_w(T) = 6.112 \times 10^{7.5T/(T+237.3)} \quad (11)$$

$Q_{Al}(t)$ is heat transfer from the environment by conduction across the conductor to the root of snow deposit:

$$Q_{Al}(t) = -K_{Al} \int_{\psi_1}^{\psi_2} \left.\frac{\partial T}{\partial r}\right|_{r=R} R d\psi = h_c(t)(T_a(t) - T_0) \times \tilde{l}(t) \quad (12)$$

where K_{Al} is the thermal conductivity of Aluminum, T_0 the temperature of the surface of electric wire, and $\tilde{l}(t)$ arc length of electric wire exposed to the atmosphere. Since the thermal conductivity of Aluminum is very large compared to that of air, it is a good approximation to put $T_0 = 0$℃ during snow accretion.

C. *Liquid water content*

The liquid water content (LWC) of accreted snow is defined as follows:

$$\Lambda(t) = \frac{\int_0^t \lambda(t) dm(t)}{m(t)} + \frac{m_w(t)}{m(t)} \quad (13)$$

where λ is the LWC of snowflakes before impact. The first term is the ratio of total mass of water due to snowflakes before impact to the mass of snow deposit, and the second term is the ratio of the mass of melt water produced form (6) to the mass of snow deposit. λ is calculated based on a micro-physical model of melting of snowflakes in the atmosphere, in which the effects of air temperature, relative humidity, and snowflakes size and density on the process of melting of snowflakes is estimated [9].

D. Density of accreted snow and snow accretion factor

Taking into account that the density of wet snow is closely related to wind speed [2,3] and the LWC of snow sample [10], we parametrize the density of accreted snow in terms of these variables:

$$\rho_s(t) = \frac{\rho_0+\frac{550c}{550-\rho_0}|v_y|}{1+\frac{c}{550-\rho_0}|v_y|} \times (1 + \Lambda(t) + \Lambda(t)^2 + \cdots) = \frac{\rho_0+\frac{550c}{550-\rho_0}|v_y|}{1+\frac{c}{550-\rho_0}|v_y|} \times \frac{1}{1-\Lambda(t)} \quad (14)$$

where $|v_y|$ is wind speed perpendicular to electric wire and snow deposit and $c = -\rho_0/25 + 35$. c was determined from the fact that the slope $d\rho_s/d|v_y|$ gradually decreases as ρ_0 increases in the experiment [11] (Fig.4). In case of dry density of $\Lambda = 0$ and $|v_y| = 0$, (14) gives ρ_0 which must be determined according to local conditions [4]. As $|v_y|$ increases, the first term of (14) approaches 550[kg/m³] at which snow densification due to rearrangement of ice particle changes to that due to both rearrangement and plastic deformation. Furthermore, the first term of (14) gives approximately $\rho_0 + b|v_y|$ for small $|v_y|$, where b is the slope in the vicinity of $|v_y| = 0$ in Fig.4. This linear dependence of density on wind speed was adopted by many authors [1-4]. The second term of (14) comes from the experimental fact that the density increases as Λ increases [10]. Λ increases with increasing temperature, relative humidity, falling snowflakes speed, wheras Λ decreases with increasing precipitation rate and wind speed. In particular, Λ is very sensitive to temperature variation [8].

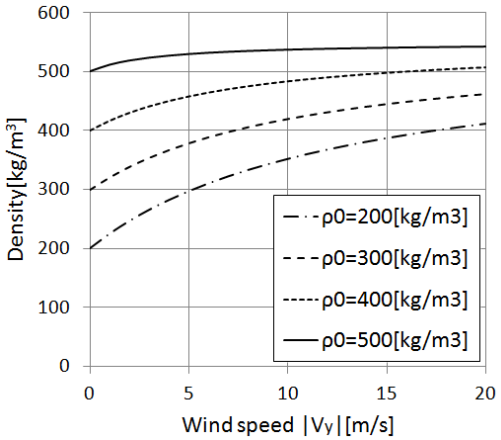

Fig.4. Dependence of the first term of (14) on the wind speed $|v_y|$ for various ρ_0.

We propose a local accretion factor which is a function of both meteorological conditions and the shape of three-dimensional snow accumulation:

$$\sigma(t) = \begin{cases} \frac{1+\cos\{10.5(\lambda(t)-0.1)\}}{2\left(\sqrt{1+(|v_y|/v_f)^2}\right)^A} \times \left(\frac{-\mathbf{S}\cdot\mathbf{n_e}}{|\mathbf{S}|}\right)^{\alpha(t)} & (-\mathbf{S}\cdot\mathbf{n_e} > 0) \\ 0 & (-\mathbf{S}\cdot\mathbf{n_e} < 0) \end{cases} \quad (15)$$

The numerator of the first term of (15) achieves a maximum at $\lambda = 0.1$ and this is based on the idea that the accretion factor σ

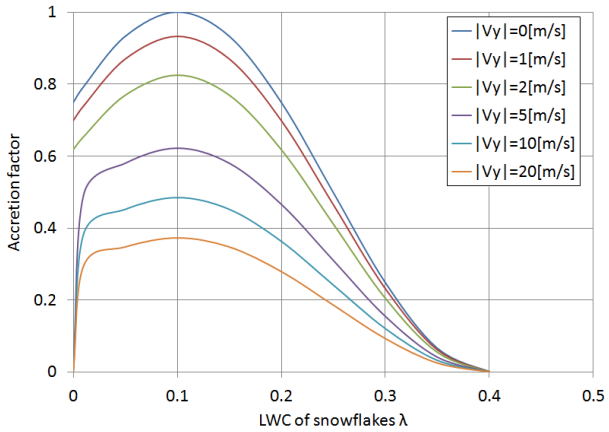

Fig.5. The first term of snow accretion factor (15) as a function of LWC of snowflakes for various wind speed $|v_y|$ [m/s].

is highest at a LWC of incoming snowflakes corresponding to the stickiest snow [4]. In case of dry snow, it is observed that snow accretion does not occur if $|v_y|$ is greater than 3[m/s][12] and hence $\sigma = 0$ in the vicinity of $\lambda = 0$ (Fig.5).

The second term of (15) is powers of a cosine $\cos\emptyset = -\mathbf{S}\cdot\mathbf{n_e}/|\mathbf{S}|$, where ∅ is the angle between the impacting trajectory and the normal to the surface of the snow deposit (Fig.2). This factor means that the probability of snow accretion is highest at the stagnation point (line) of snow deposit where shear force due to wind is zero and adhesive force between snow particles is dominant. On the other hand, far from the stagnation point (line), when shear stress is over adhesive force, the probability of the exfoliation of snow particles is high and then the accretion factor is decreased. Using the cosine low proposed by Poots [1], i.e. $\alpha = 1$, however, the calculated accreted mass underestimates the observations when the wind speed is small. On the other hand, when the wind speed is over 15[m/s], the calculated accreted mass overestimates the observations [12]. This suggests that the accretion factor is not necessary to obey the cosine law, and hence we propose the dependence of α on wind speed and diameter of snow deposit such that

$$\alpha(t) = B|v_y|^{1.5} D_s^{0.5} \quad (16)$$

which comes from the fact that shear force due to wind around the surface of snow deposit is proportional to $|v_y|^{1.5} D_s^{0.5}$ [13]. As α increases, the second term of (15) leads to more streamline shapes in contrast to the bluff shapes (Fig.6). The effect of wind speed on the accretion factor σ is controlled by the factor A in the denominator of the first term of (15) and B in (16). The latter does not exist in the cylindrical-sleeve accretion models [1-4]. We employ an empirical calibration method in finding the appropriate values of A and B, allowing for the best agreement between calculated and observed mass of snow deposit. Applying to some Japanese wet snow events, the best agreement was found with $A = 0.38$ and $B = 0.15$. The value of A is close to 0.4 used in a cylindrical-sleeve accretion model [4].

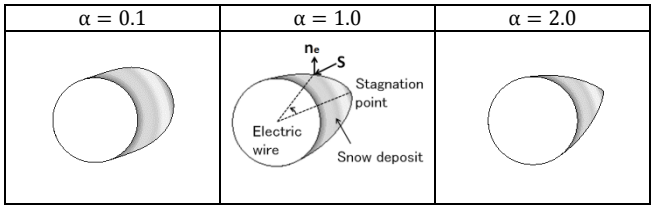

Fig.6. Accreted snow shapes for different α.

E. Wet snow shedding

Gravitational and aerodynamic forces exerted on snow deposit per unit lengh are, respectively,

$$f_g(t) = mg \quad (17)$$

$$f_w(t) = \frac{1}{2}\rho_a |v_y(t)|^2 C_d D_s(t) \quad (18)$$

where ρ_a is the air density and C_d the drag coefficient. Integrating the component of an infinitesimal tensile adhesive force parallel to the gravity over the surface between the electric wire and snow deposit (dashed red line in Fig.7 (a)), the total tensile adhesive force is

$$f_{tad}(t) = \int_{\pi/2}^{\psi_0} \sigma_{tad}(t)\cos(\pi - \psi)\, R d\psi \quad (19)$$

where R is the radius of electric wire and the tensile adhesive strength σ_{tad} depends on the LWC and density of snow deposit as well as the surface roughness of electric wire. Once the lower part of the electric wire is completely covered with snow, ψ_0 in (19) is $3\pi/2$ and $f_{tad}(t) = \sigma_{tad}(t) \times 2R$. According to the experiments [10,14,15], σ_{tad} has a maximum $(\sigma_{tad})_{max}$ at a LWC of snow sample, which is around $\Lambda = 0.1 \sim 0.2$. However, it should be noted that $(\sigma_{tad})_{max}$ varies depending on the strength of initial compression force applied to the snow sample [15] and increases as the initial compression force increases. We employ the following σ_{tad} obtained for a small initial compression force [14,15],

$$\sigma_{tad} = \begin{cases} (10.0(\sigma_{tad})_{max} - 278.0)\Lambda + 27.8 & (0.0 \le \Lambda < 0.1) \\ -90.0\Lambda + (\sigma_{tad})_{max} + 9.0 & (0.1 \le \Lambda < 0.3) \\ -1045.5\Lambda + (\sigma_{tad})_{max} + 295.5 & (0.3 \le \Lambda < 0.4) \\ 0 & (0.4 \le \Lambda \le 1.0) \end{cases} \quad (20)$$

Figure 8 shows that σ_{tad} increases as Λ increases when $\Lambda < 0.1$ and achieves a maximum $(\sigma_{tad})_{max} \sim 350[N/m^2]$ at $\Lambda = 0.1$, and then gradually decreases as Λ increases, and finally $\sigma_{tad} = 0$ when $\Lambda > 0.4$. The criterion of snow shedding corresponding to the shape of accreted snow in Fig.7(a) is that gravitational force exceeds the tensile adhesive force,

$$f_g(t) > f_{tad}(t) \quad (21)$$

The moment due to gravity and wind force are, respectively,

$$M_g(t) = f_g r_{cg} \sin\theta_{cg} \quad (22)$$

$$M_w(t) = -f_w r_{cg} \cos\theta_{cg} \quad (23)$$

and we denote their sum as $M_{gw}(t)$, where r_{cg} is the center of gravity of snow deposit and θ_{cg} is the angle from the zenith of electric wire and snow deposit (Fig.7(b)). Integrating shear adhesive strength σ_{sad} along the surface between the electric wire and snow deposit (dashed red line in Fig.7 (b)), the moment due to shear adhesive strength is

$$M_{sad}(t) = R\int_{\psi_1}^{\psi_2} \sigma_{sad}(t) R d\psi \quad (24)$$

We assume that the dependence of σ_{sad} on LWC of snow deposit has a similar behaviour as that of the tensile adhesive strength σ_{tad}. However, its maximum $(\sigma_{sad})_{max}$ is different from $(\sigma_{tad})_{max}$. Since the tensile strength does not exceed twice the shear strength for most other materials, we assume that $(\sigma_{tad})_{max}/2 \le (\sigma_{sad})_{max} < (\sigma_{tad})_{max}$. The criterion of snow shedding corresponding to the shape of accreted snow in Fig.7(b) is that the moment due to gravity and wind force exceeds the moment due to shear adhesive force,

$$M_{gw}(t) > M_{sad}(t) \quad (25)$$

The time of wet snow shedding is numerically determined from the point where either (21) or (25) is satisfied. Here, we treat $(\sigma_{tad})_{max}$ and $(\sigma_{sad})_{max}$ as parameters and investigate the effect of these parameters on snow shedding time.

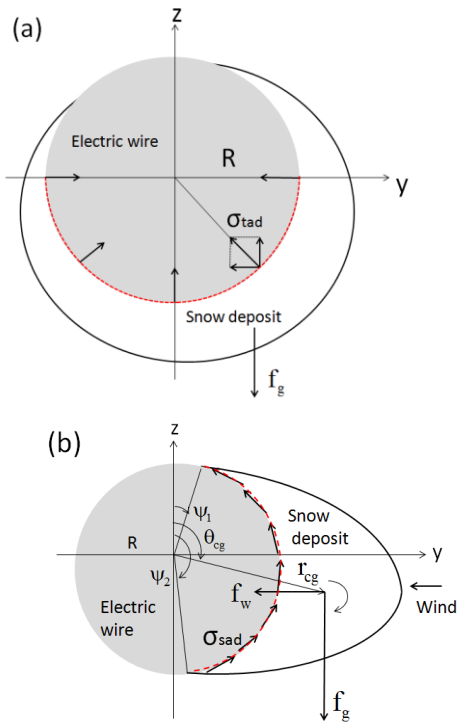

Fig.7. Snow shedding for different shape of accreted snow.

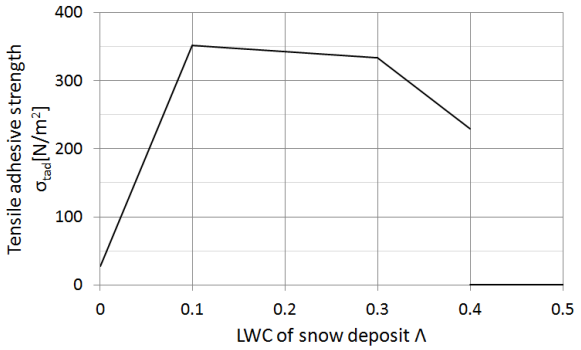

Fig.8. Tensile adhesive strength as a function of LWC of snow sample.

II. RESULTS AND DISCUSSION

We installed conductor samplers with different size, torsional stiffness, and orientation in Kushiro, where is located at east area of Hokkaido island in Japan, and have continued observations to clarify meteorological condition for wet snow events since 2010. Figure 9 shows the snow accretion process on different conductor samplers for a wet snow event at Kushiro on April 21, 2013. Each edge of a conductor sampler is supported by a short wire whose length and thickness control conductor rotation. The torsional spring constant k_s for sampler conductors is given by $k_s = 4GJ \times L_x/L^2$ so that the torsion of conductor sampler is equivalent to that in the middle of the span of actual transmission lines [16]. Here GJ is the torsional stiffness of actual electric wire with the same size as sampler conductor, L_x a half of length of conductor sampler, and L a half of span length equivalent to actual transmission line. Table 1 shows the specification of sampler conductors in Fig.9 and the value of a half of k_s for each conductor sampler is indicated.

The meteorological data on April 21, 2013 is shown in Fig. 10. Temperature, relative humidity, wind speed and direction were obtained at the observational location, whereas precipitation was observed at the weather station in the neighbourhood of the observational location. Precipitation was observed from 14:50 at both the weather station and the observational location. However, snow accretion to conductor samplers started at 15:40 after which temperature and relative humidity appropriate for snow accretion continued until 22:00. During this wet snow event, wind speed varied in the range 2~7[m/s], wind direction was almost perpendicular to conductor samplers, and mean precipitation rate was 0.6 [mm/10min].

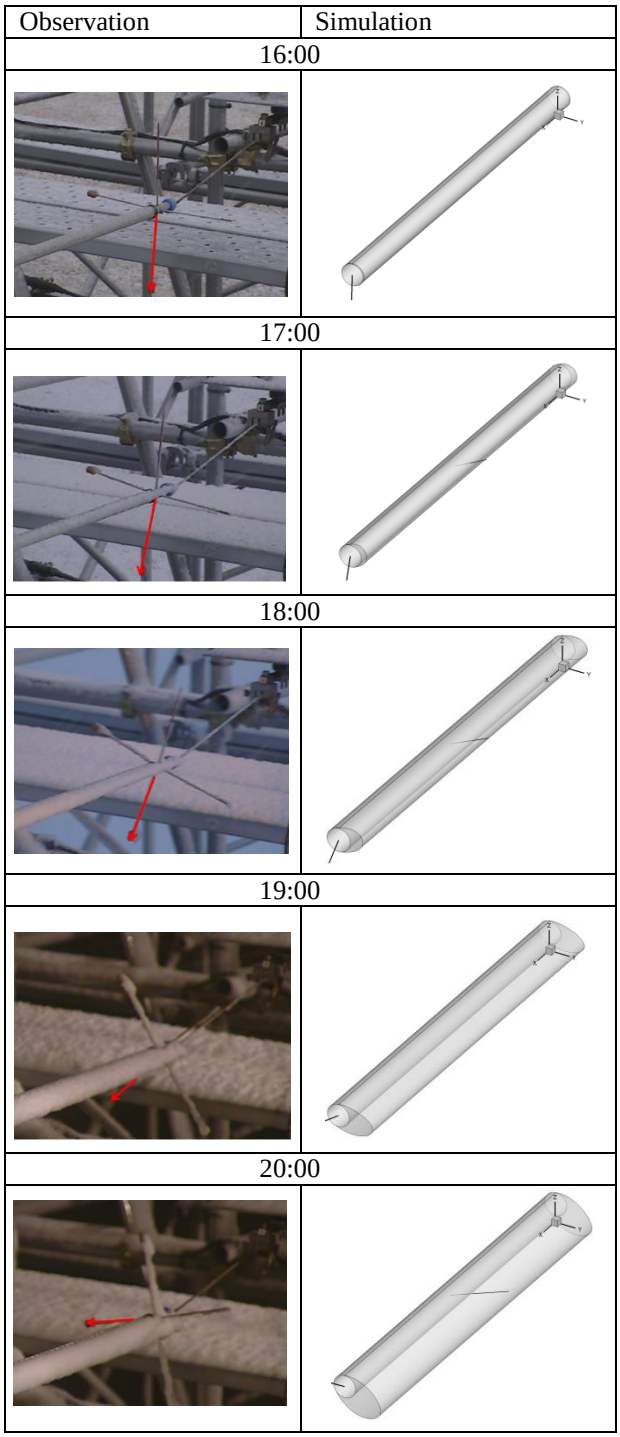

Fig.9 (a). Snow accretion process on sampler 1.

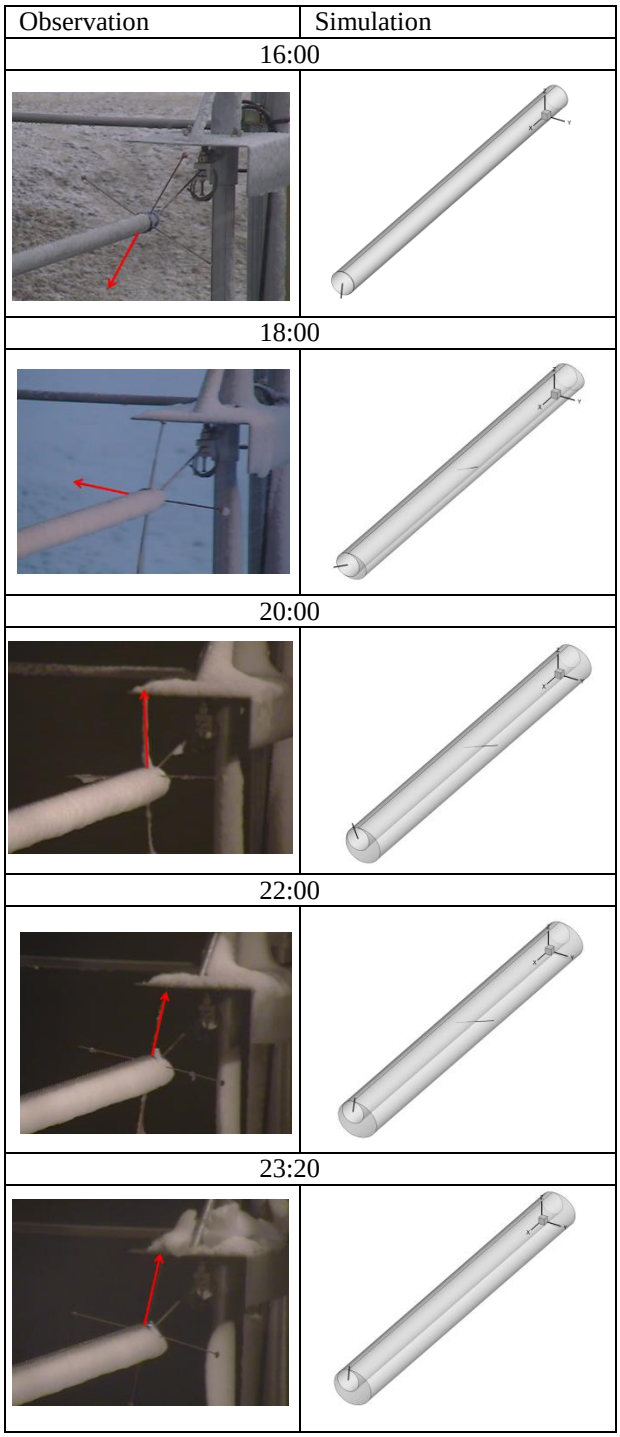

Fig.9 (b). Snow accretion process on sampler 2.

Analytical condition for numerical simulation using SNOVAL(Ver.3) is shown in Table1. The simulation was conducted for above conductor samplers with different size and torsion, but with the same direction relative to wind. Figure 11 shows the comparison of accreted snow mass numerically estimated with observations, as well as the cross section of calculated snow deposit. It is found that the growth rate of mass by simulation is consistent with the observations, especially the mass increased during 18:00~20:00 because of large impinging snow flux due to increased wind speed and precipitation rate.

The bold line on the section of snow deposit in Fig.11 indicates electric wire rotation from the initial position of 6 o'clock. This corresponds to conductor rotation which is estimated by measuring rotation angle of a rod attached on each side of a conductor sampler, as highlighted in red in Fig.9. Since the torsional spring constant of sampler 1 is greater than that of sampler 2, sampler 1 is hard to rotate and snow accumulation develops on the windward side. On the other hand, sampler 2 rotates easily compared to sampler 1 and the resulting accretion shape is close to a cylindrical-sleeve, except the top of electric wire is not completely covered with snow. The accreted mass on each sampler achieves a maximum, then the calculated rotation angle is roughly 90 [deg] for sampler 1, whereas 180 [deg] for sampler 2, which are agreement with the observations (see the rods highlighted in red in Fig.9).

The dashed and solid lines in Fig. 11 (a) are temporal change of accreted snow mass for different shear adhesive strength, $(\sigma_{sad})_{max} = 150[N/m^2]$ and $(\sigma_{sad})_{max} = 220[N/m^2]$,

Table1. Analytical condition

	Sampler 1	Sampler 2
type	ACSR 240 mm^2	ACSR 810mm^2
Sampler length L_x[m]	2	
Sampler diameter D_0[m]	0.0224	0.0384
Torsional stiffness GJ[Nm^2/rad]	68.8	588
Equivalent span length 2L[m]	90	300
Tosional spring constant $k_s/2$ [Nm/rad]	0.0680	0.0523
Azimuth θ_c [rad]	$\pi/8$	
Drag coefficient C_d	1.0	
Space division	Axial direction: 10 Circumferential direction: 720	
Time division [s]	1	
Time step	36000	
0℃ height of atmosphere [m]	250	
Initial radius of snowflake [m]	0.005	
Parameter in snow density ρ_0 [kg/m^3]	500	
Parameters in accretion factor A, B	0.38, 0.15	
Maximum of tensile adhesive strength $(\sigma_{tad})_{max}$ [N/m^2]	300, 360	
Maximum of shear adhesive strength $(\sigma_{sad})_{max}$ [N/m^2]	150, 220	

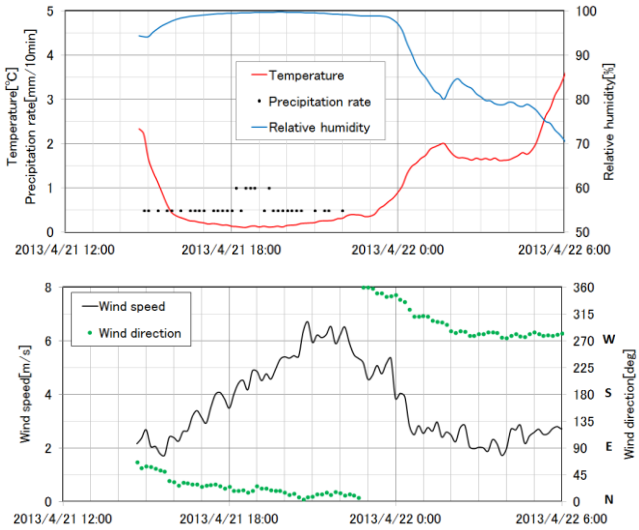

Fig.10. Meteorological data (top: temperature [℃], relative humidity [%], precipitation rate [mm/10min], bottom: 10min mean wind speed and direction).

respectively. The time of shedding for the latter coincides with the observation. However, the snow shedding model in SNOVAL(Ver.3) is based on shedding all at once, therefore, cannot explain a gradual decrease of accreted snow due to partial shedding after 20:30, as shown in the red line in Fig. 11 (a). The dashed and solid lines in Fig. 11 (b) are temporal change of accreted snow mass for different tensile adhesive strength, $(\sigma_{tad})_{max} = 300[N/m^2]$ and $(\sigma_{tad})_{max} = 360[N/m^2]$, respectively. The time of snow shedding in the former case is

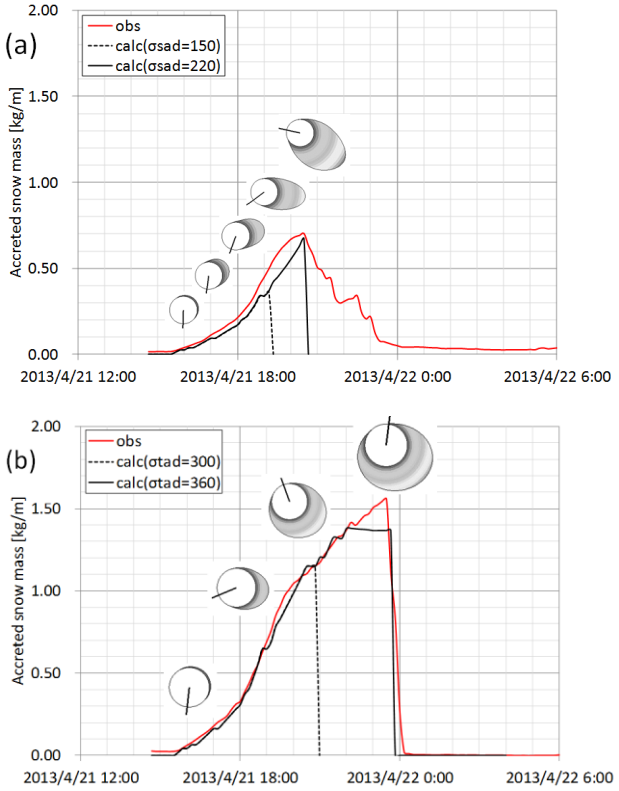

Fig.11. Comparison of observed with numerically estimated of accreted snow mass for different adhesive strength: (a) sampler 1, (b) sampler 2.

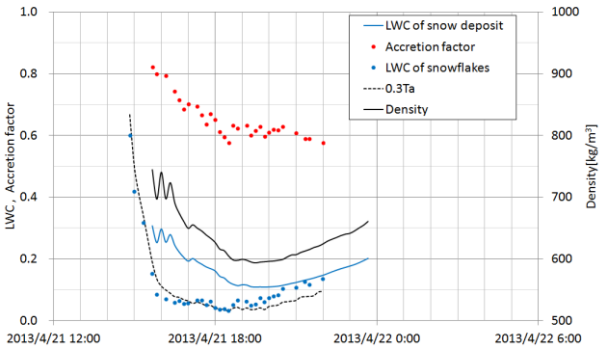

Fig.12. Temporal change of LWC of snowflakes before impact, accretion factor, LWC and density of snow deposit.

faster than the observation, whereas in the latter case, the time of shedding occurs at around the time of observed shedding.

Using the surface meteorological data and MANAL data on April 21, 2013, we calculate the LWC of snowflakes with initial radius of 5 mm and 0℃ height of atmosphere of 250m. Since the LWC of snowflakes and snow deposit is very sensitive to temperature variation, these temporal changes are reflected in Fig. 12. Indeed, the temporal change of LWC of snowflakes can be well approximated as $0.3T_a$. Mean LWC of snowflakes during 15:40~22:00 is about 0.08 and hence snowflakes prior to impact is expected to be sticky. Precipitation at observational location starts at 14:50. However, snow accretion does not occur until 15:40 because the LWC of snow deposit is over 0.4 and then adhesion force is zero (see Fig.8). Accordingly, SNOVAL(Ver.3) incorporating the model of snow accretion and melting can predict the start time of snow accretion. The temporal change of accretion factor and density of snow deposit is shown in Fig.12. It is found that the density is dominated by

the change of LWC of snow deposit rather than that of wind speed. On the other hand, accretion factor decreases with decreasing the LWC of snowflakes and with increasing wind speed until 19:00, but after that the change is slightly suppressed due to the increase in the LWC of snowflakes. Mean values of accretion factor and density during snow accretion are 0.65 and $630[\mathrm{kg/m^3}]$, respectively. The latter is close to $660[\mathrm{kg/m^3}]$ estimated from the last image on Fig. 9(b).

III. Conclusion

The start time of snow accretion and the temporal change of mass and shape of accreted snow, wire rotation are evaluated using SNOVAL(Ver.3). They are consistent with field observations for conductor samplers supported by wires. However, the time of wet snow shedding strongly depends on the tensile and shear adhesive strength. It is necessary to estimate these strength experimentally for various LWC and density of snow deposit, and to consider the surface roughness of actual stranded wire. The findings from the analysis with SNOVAL (Ver.3) will be utilized to improve the accuracy in the estimation of accreted snow mass predicted by cylindrical-sleeve models and to predict snow deposit shape necessary for galloping analysis. In order for that, employing many wet snow events, the versatility of proposed accretion factor and density must be enhanced.

Acknowledgment

We would like to thank the Federation of Electric Power Companies of Japan for permitting us to use data obtained in the research for snow damage to overhead transmission and distribution facilities.

References

[1] G. Poots, *Ice and snow accretion on structures*, Research Studies Press, 1996.

[2] P. Admirat, “Wet snow accretion on overhead lines,” *Atmospheric Icing of Power Network*, Ed. M. Farzaneh, Springer, pp.119-169, 2008.

[3] Y. Sakamoto, “Snow accretion on overhead wires,” Phil. Trans. Roy. Soc. Lond. A., Ed. G. Poots, 358, pp.2941-2970, 2000.

[4] B. E. K. Nygaard et al., “Modeling Wet Snow Accretion on Power Lines: Improvements to Previous Methods Using 50 Years of Observations,” Journal of Applied Meteorology and Climatology, pp.2189-2203, 2013.

[5] K. Goto, “A Simulation Computation of Twist of De-Snowing Electric Wires due to Snow Accretion,” Seppyo, 38, pp.127-137, 2013.

[6] Y. Eguchi et al., “Development of simulation code SNOVAL for snow accretion on overhead transmission line-Formulation of snow accretion and growth models under oblique wind condition-” CRIEPI Research Report, No. N11016, pp.1-22, 2012.

[7] Y. Eguchi et al., “Development of a snow-accretion simulation method for transmission line under calm wind condition,” JSME annual meeting 2013, G01102.

[8] K. Ueno et al., “Development of models for snow accretion on electric wires and snow shedding with melting process,” CRIEPI Research Report, No. N15001, pp.1-29, 2015.

[9] T. Matsuo and Y. Sasyo, “Melting of snowflakes below freezing level in the atmosphere,” J. Meteorol. Soc. Jpn. 59, pp.10-25, 1981.

[10] R. Hefny et al., “Adhesion of wet snow to different cable surfaces,” Proc of the 13th International Workshop on Atmospheric Icing of Structures, Andermatt, Switzerland, 2009.

[11] K. Sato, “Snow cap and accretion phenomena due to wet snow,” Workshop of reserch for radar and numerical model on precipitation, 2014.

[12] T. Nishihara et al., “Study of Damage to Overhead Trasmission Facilities Caused by Wind, Snow and Salt -Research results in fiscal years 2007－2011-,” CRIEPI Research Report, No. N19, pp.1-130, 2013.

[13] H. Schlichting and K. Gersten, *Boundary Layer Theory*, Springer, 1999.

[14] A. Sato and G. Wakahama, “Adhesion force of wet snow,” The Japanese Society of Snow and Ice autumn meeting, p.111, 1974.

[15] Y. Mizuno and G. Wakahama, “Adhesive Strength of Wet Snow,” Low Temperature Science, Ser. A, 35, pp.133-145, 1977.

[16] T. Nishihara et al., “Development of a simple device for observing snow accretion by using a short dummy conductor supported by wire ropes,” CRIEPI Research Report, No. N11030, pp.1-17, 2012.

Effect of icephobic coating on ice protection of ultrasonic anemometer with stack-type transducers

S. Kimura[1], K. Sato[2] , H. Morikawa[3] , J. Hietanen[4] , Y. Yamagishi[1] , T. Kojima[3] , T. Saito[1]
[1] Kanagawa Institute of Technology, [2] National Research Institute for Earth Science and Disaster Prevention,
[3] Meteorological Research Institute for Technology, [4] Vaisala Oyj
skimura@me.kanagawa-it.ac.jp

***Abstract*: In cold climates, ultrasonic anemometers with stack-type heated transducers sometimes record extraordinarily higher instantaneous wind speeds than average wind speed during short periods in long series of measurements. A successive record of wind speed measured at a high sampling frequency indicates that those high-speed winds are not gusts because they suddenly jump from the speeds fluctuating around a certain value to a far higher speed and immediately return to almost the same value before the events of sharp increase. We have identified the cause of such abnormal measurement by repeatedly performing snowing wind tunnel tests; it is because of the formation of ice-bridge on transducers. The surface of a transducer is heated by an electric heating element in the longitudinal center. However, very narrow upper and lower parts of the transducer remain unheated because of inner structural constraints. Therefore, ice or snow accretion may occur on the upper part when the anemometer operates under icing or snowing conditions. When the condition is prolonged, the accretion grows downward and covers the transducer like a canopy. In the central part of the transducer, the temperature is kept constant at a certain positive value even in subzero environments such that snowflakes colliding with the surface melt upon impact. The meltwater runs down along the surface to the unheated lower end and then to the upper arm. Because the upper arm of the anemometer is unheated, water begins to freeze on the surface immediately below the transducer. As water continuously flows down and freezes, the ice grows upward. As a result, the accretions of ice growing downward from the upper end and upward from the lower end meet each other at the center of the transducer. However, because the middle region of the transducer is heated and maintained at a prescribed temperature regardless of ambient conditions, the ice melts and forms a gap at the interface between the ice and the transducer surface. Consequently, an ice bridge is formed, and it disturbs the normal transmission of ultrasonic waves between the transducers. Based on this finding, we applied a superhydrophobic coating to the unheated upper arm in order to accelerate the removal of molten water by wind force. The results from a snowing wind tunnel test showed that the coating imparted a low-wettability characteristic to the upper arm for preventing ice growth, and measurements could be taken without any missing or unusual data. In the present research, to further verify the effectiveness of coating on icing prevention, another snowing wind tunnel test was conducted using the same anemometer with extended superhydrophobically coated areas including the transducer, lower arm, and top cover of the body. Prior to the test, an acoustic impedance analysis was performed using a covering of silicon rubber to examine the transmissivity of the ultrasonic waves through the coating film and the ice deposit on the transducer. Moreover, an immersion test of the covering that was inherently attached to the transducer was carried out in accordance with the guidance of the Japanese Industrial Standard (in a short duration only for the wind tunnel test) in order to evaluate the influence of paint thinner on the covering.**

Keywords: snowing, ultrasonic anemometer, snowing wind tunnel test, ice/snow protection

INTRODUCTION

Wind measurements under cold climate conditions have become increasingly important for wind energy applications. Severe weather events can impose measurement challenges even for heated wind sensors. Therefore, there is a strong need to improve data availability, which requires improvements to the sensor's de-icing design. Regarding ultrasonic anemometers that have cylindrical transducer stacks, we have identified the ice-bridge forming process even on the heated transducer stack in wind tunnel tests during snowing. The surface of the transducer stack is heated by an internal electric heating element. However, the very narrow upper and lower parts of the transducer remain less heated because of inner structural constraints. Thus, the temperature profile is not uniform. Therefore, ice or snow accretion may occur on the upper part under harsh icing or snowing conditions. When the condition is prolonged, the accretion grows downwards and covers the transducer like a canopy. If this ice-bridge forms, it might disturb the normal transmission of ultrasonic waves between the transducers[1,2]. Based on this finding, we applied a superhydrophobic coating to the unheated upper arm in order to accelerate the removal of molten water by wind force. The results from a snowing wind tunnel test showed that the coating imparted a low-wettability characteristic to the upper arm in preventing ice growth, and measurements could be taken without any missing or unusual data[3]. In the present research, in order to further verify the effectiveness of coating on icing prevention, another wind tunnel test was conducted in the presence of snow using the same anemometer with extended, superhydrophobically coated areas, including the transducer, lower arm, and top cover of the body. Prior to the test, an acoustic impedance analysis was performed using a covering made of silicon rubber in order to examine the transmission of the ultrasonic waves through the coating film and the ice deposit on the transducer. Moreover, an immersion test of the covering that was inherently attached to the transducer was carried out in accordance to the guidance of the Japanese Industrial Standard (only for a brief time interval during the

wind tunnel test) in order to evaluate the influence of the paint thinner on the covering.

I. TRANSMISSIVITY

A. Acoustic impedance and transmissivity

As known, the mechanism of wind measurement of an ultrasonic anemometer is based on the difference of the arrival time of the ultrasonic waves propagating between two transducers in the airflow. When the acoustic waves travel through the boundary between the different media some may be reflected, and the rest pass through, similar to light propagation under the same conditions. The tranmissivity is the ratio of the transmitted to the incident sound pressure at the interface of the media. It can be determined using the acoustic impedance of the respective media in accordance to the following equation[4].

$$t = \frac{2Z_2}{Z_1 + Z_2} \qquad (1)$$

where t denotes the transmissivity, and Z_1 and Z_2 the acoustic impedances of an incident and transmitted materials, respectively. It is clear from the equation that the transmissivity tends to become less if Z_1 of the transmitted side is greater than Z_2 in the incident side. The media through which the ultrasonic wave propagates between the two transducers are the surface coverings made of silicon rubber and with air in between. When ice accretes on the transducer surface, it has to be taken into account in regard to the existing media under normal conditions. If the air gap forms at the interface of the surfaces of the transducer stack and the ice, the total number of the media becomes equal to seven. The transmissivity can also constitute a measure to evaluate the applicability of the icephobic coating to the transducer stacks for ice protection. The acoustic impedance is a function of the density and acoustic speed of a material, and is defined as the product of these two parameters. The acoustic impedances used for the present calculation are shown in Table.1. The icephobic paint used for the present research was HIREC100, the product of Japanese Manufacturer NTT Advanced Technology.

Table 1 Acoustic impedance

Material	Acoustic impedance [Ns/m^3]
Air	4.13e+2
Ice	3.53e+6
Silicon	1.50e+6
PTFE	4.00e+4

B. Analyses results

Fig.1 shows a schematic of a situation for the VAISALA WMT 703 transducers where ice adheres to the coated transducer surfaces that face each other. In this case, the ultrasonic waves transmitted from one side travel to the receiver of the other successively through the silicon covering, ice accretion, air, ice accretion, and silicon covering.

The transmissivities calculated for all conceivable cases that may be considered in iced conditions are summarised in Table 2. In the table, the symbols S, A, I, and C, respectively denote the silicon covering, air, ice, and the coated film. For instance, Eq. 1 calculates the transmissivity to be approximately 3.5e-4 for the case shown in the figure. The surface which is clean, as expressed by the code S-A-S in an abbreviated form, is approximately 1e-3.

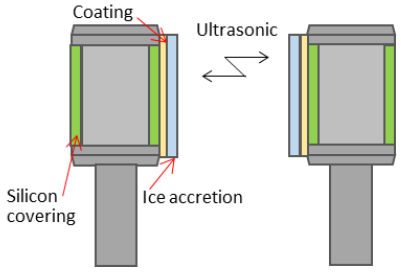

Fig.1 Schematic of ultrasonic transmission/reception between iced coated transducers

Table 2. Transmissivity

Conditions of transducer	Media	Transmission coefficient
Ice free	S-A-S	1.10e-03
Iced/ Iced + gap	S-I-A-S	1.96e-04
	S-I-A-I-S	3.92e-04
	S-A-I-A-I-S	5.16e-07
	S-A-I-A-I-A-S	2.41e-10
Coated	S-C-A-C-S	1.54e-03
	S-C-I-A-I-C-S	3.50e-04

For the cases of the ice-free state and the tight adhesion of ice to the surface, it can be found that the values of the transmissivity are of the order of magnitude of -3 or -4. From the results of the previously conducted tests with an imitated ice accretion, it can be deduced that wind speed can be normally measured, as long as ice attaches tightly to the transducer surface and there is no gap, even if ice accretion occurs on the transducer. This finding validates the deduction drawn from the analysis that the tight ice accretion may influence the wind measurement in a minor way. When the irregular wind speeds are measured, namely in the cases where an ice bridge forms on the transducer, the order of magnitude of the transmissivity tends to become considerably less, as indicated in the table. In regard to the two types of coating, the transmissivities between the two coated transducers have values that can be in the same order of magnitude as those at the ice-free state, regardless of the presence of the ice accretion. Accordingly, this suggests the applicability of the icephobic coating to the transducer in terms of the proper functionality of the ultrasonic anemometer and its protection from ice.

II. PRELIMINARY TESTS

A. Covering test

A wind tunnel test was conducted on the ultrasonic anemometer at room temperature using a substitute of the coating in order to ensure that the coating film on the transducers exerts no negative influences on the evoked measurement. The thin membrane of the polyvinyl chloride resin, the impedance of which was close to that of the icephobic paint, was used as the substitute as shown in Fig.2. Wearing the membrane covering on the transducer was conducted very carefully in order to remove any air present inside the covering. The test was first started with the membrane-covered ultrasonic anemometer, and was then carried out with the uncovered anemometer successively, so that the environmental conditions were kept constant.

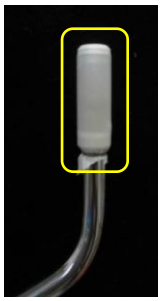

Fig.2 Transducer stack covered with a thin membrane made of vinyl chloride

The comparison of the measured wind speeds developed by the ultrasonic anemometer under the two different transducer surface conditions can be seen in Fig.3. The red curve shows the wind speed of the covered anemometer, while the blue curve shows the uncovered anemometer. The normalised absolute difference of the averaged wind speeds measured by these two ultrasonic anemometers in the range of the constantly regulated wind is 0.85%. This suggests that correct wind measurements using the ultrasonic anemometer with icephobically-coated transducers are feasible.

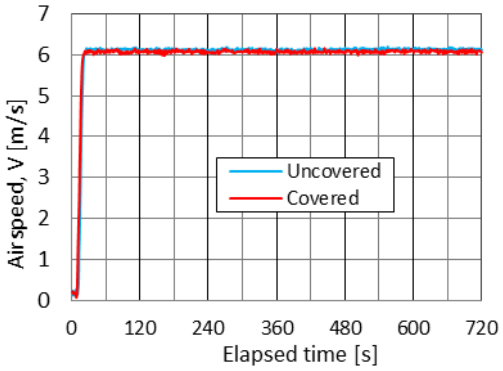

Fig. 3 Wind speeds measured by covered and original anemometers

B. Immersion test

The icephobic paint used for the present research was HIREC100. The paint thinner of butyl acetate was used to make a coated film on the surface of the body. Therefore, for the application of this paint to the ultrasonic anemometer, the chemical influences of the thinner on the properties of the silicon covering of the transducer were examined using the immersion test since the materials used for the coating of other surfaces were metallic, and are thus not subjected to a chemical change by the thinner. The immersion test was carried out in accordance with the guidance of the Japanese Industrial Standard k 5600-1 (ISO 2812-1) as shown in Fig.4[5]. The duration of the process was shortened to 21 d for the snowing wind tunnel test. The test results showed that no damage of the silicon-made covering was observed in terms of the thickness and surface conditions. We then applied the paint to the transducers, upper and lower arms, and to the top cover of the ultrasonic anemometer.

C. Wind tunnel test at room temperature

At the next stage, another wind tunnel test was conducted at room temperature in order to confirm the function of the anemometer equipped with the transducers that had a thin coated-film on their surfaces. The test was carried out by changing the airspeed in the test section of the wind tunnel. During the test, the flow started from a rest (calm) state and was then increased in speed. It was successively maintained at four

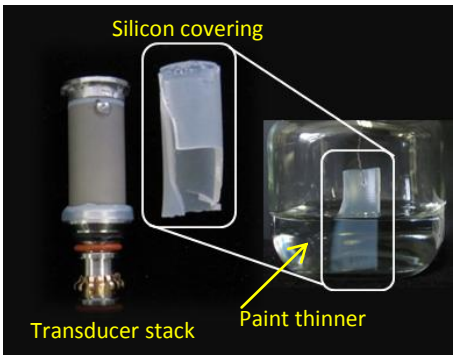

Silicon covering peeled off from the transducer surface

Silicon covering immersed in the paint thinner for 21 days

Fig.4 Immersion test (shortened duration)

different wind speeds equal to 3, 6, 12, and 19 m/s. Based on this procedure, the ability of the anemometer to follow the changing wind speed could be examined at the same time. For comparison, the wind tunnel airspeed was measured by the pitot-tube and digital-manometer (P-M) system during each test run. The variations of the wind tunnel airspeed measured by the anemometer and the P-M system are shown in Fig.5. The chart indicates that negligible discrepancies exist between the two wind speeds not only at steady state but also in the ascending and descending modes. This outcome can be interpreted as a capability of the coated anemometer to conduct highly reliable wind speed measurements.

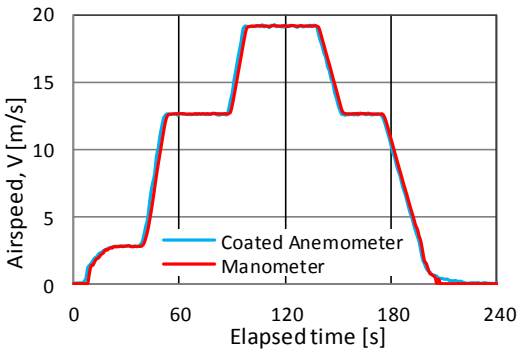

Fig.5 Wind speeds measured by coated anemometer and Pitot-tube manometer system

III. SNOWING WIND TUNNEL TEST

A. Facility, devices, and test conditions

The snowing wind tunnel test was conducted at the wind tunnel placed inside the Cryospheric Environment Simulator (Fig.6) of the Shinjo Cryospheric Environment Laboratory of the National Research Institute for Earth Science and Disaster Prevention. The aim of the test was to evaluate the effectiveness of the icephobic coating for snow/ice prevention in the case of the heated ultrasonic anemometer equipped with stack-type transducers, which are the original versions of the VAISALA WMT-703. The heating elements were embedded in the middle part of the transducers and the lower arms. As mentioned earlier, the paint was applied to the transducers, to the upper and lower arms, and to the top cover of the anemometer (Fig.7). Fig.8 depicts the schematic of the snowing wind tunnel test. The snowfall device was placed on the ceiling of the test section from which snowflakes were supplied into the test section. The ultrasonic anemometer was placed in the leeward side of the snowfall device at a distance that was determined in accordance to the airflow speed in the test section in order to optimally create the snowing environment around the anemometer.

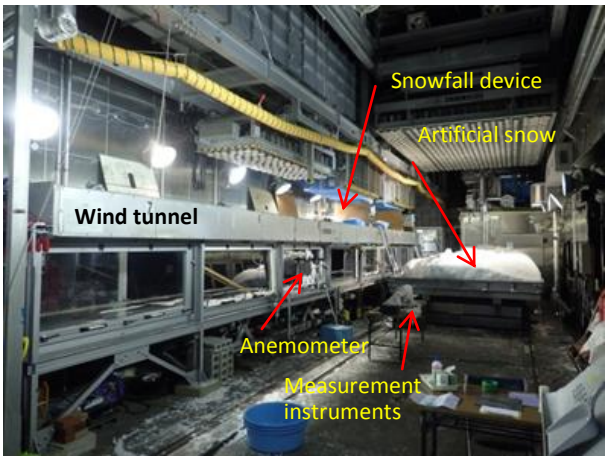

Fig.6 Snowing wind tunnel facility
at Shinjo Cryospheric Environment Laboratory

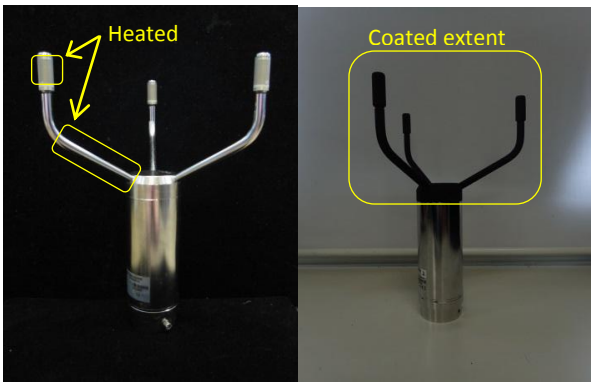

(a) Uncoated ultrasonic anemometer (b) Coated ultrasonic anemometer

Fig.7 Heating parts and coated extent of the ultrasonic anemometer VAISALA WMT 703

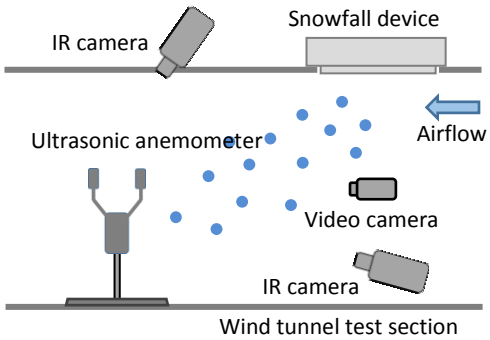

Fig.8 Schematic of snowing wind tunnel test

All tests were carried out at -12°C. The airflow speed was set at values between 1 and 6 m/s. In each test, the surface conditions were monitored using two video cameras set up in the windward location and outside of the wind tunnel test section. With the use of the video cameras, the frontal and side views of the anemometer were recorded throughout the test. For reference, two infrared(IR) cameras were used to measure the surface temperature. One IR camera was placed on the ceiling of the test section and the other besides the video camera in the windward. The measured wind data were transferred to the personal computer and stored in the hard disc. However, the wind data were not used for the evaluation of the effectiveness of the coating for ice/snow protection for two reasons: one was the inherent shortcoming of the characteristics of the snowing wind tunnel test for the wind sensors because ice and/or snow accretion occurs in the limited area of the transducer stack due to the stable, one-directional airflow. The other reason was in reference to the particular conditions of the present test where the video and IR cameras were placed in the windward section of the anemometer, disturbed the airflow inside the test section, and produced strong turbulence behind them.

B. Results and discussion

B-1. Weak wind condition

The duration of the snowfall test under the weak wind condition of 1 m/s was 30 min for the uncoated ultrasonic anemometer and 20 min for the coated one. In this wind condition, snowflakes fell from the ceiling at an angle that was approximately 45°. Figs.9 and 10 show the change of the surface condition along with the elapsed time of the test for the uncoated and coated transducers, respectively. It is clearly understood from Fig.9 that secondary icing occurred within a 10 min interval after the onset of the snowfall even if the transducer was heated. Ice grew to the windward side, spreading the covering area on the transducer frontal surface. At 30 min, snow largely accumulated on the ice deposit and covered the entire frontal area of the transducer. It has to be noted that even in a snowfall environment, ice accreted on the heated surface of the transducer through the secondary icing process, in the early stage of the icing event.

The middle part of the transducer was heated and regulated for temperature maintenance at 30°C regardless of the ambient temperature, so that a contact surface of an ice deposit totally covered the windward side of the transducer surface. This was shaped like an arch, maintaining a gap at the interface. As explained earlier, the presence of an air gap decreased the transmisivity of ultrasonic waves. Hence, the ice formation, as seen in Fig.9, led to incorrect wind measurements.

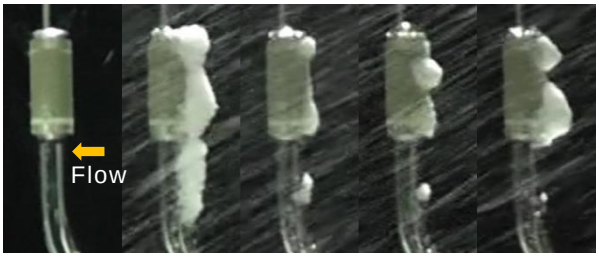

Fig.9 Original transducer stack at 1 m/s

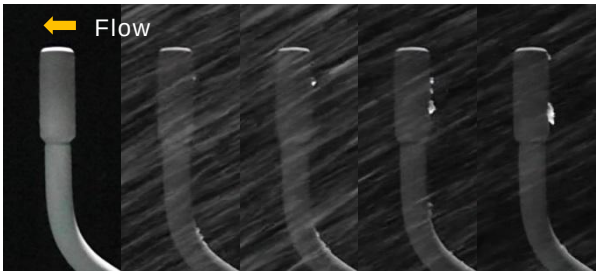

Fig.10 Superhydrophobically coated transducer stack at 1 m/s

In contrast, the surface of the transducer had been kept clean during the 20 min test run even though a minute quantity of ice deposit was found on it. In Fig.10, which was obtained at 10 min, although one small ice deposit was found on the heated middle part, it disappeared in 10 min. However, interestingly, another thin layer of an ice deposit that was larger than the ice that was previously accreted was observed at a location different than the location of the transducer in the picture at 20 min. Nonetheless, in all cases, no obvious ice accretion was

formed on the coated surface, which resulted in the deduction that the superhydrophobic coating was dramatically effective in preventing the transducer from accumulating ice/snow accretion. Moreover, absence of ice accretion ensured the correct and stable wind measurement of the ultrasonic anemometer.

B-2. Higher wind condition

Ice accretion on the coated and the uncoated transducers at the wind speed of 6 m/s are shown in Figs.11 and 12. In this wind condition, the snowflakes travel and collide with the transducer surface almost horizontally.

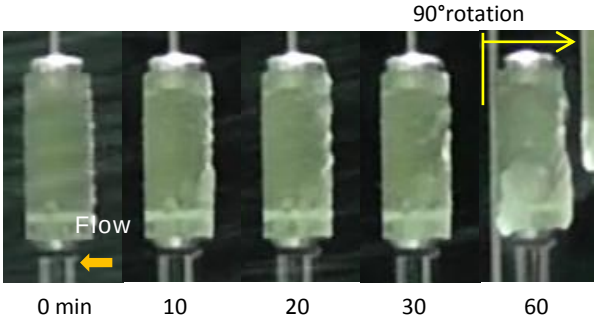

Fig.11 Uncoated transducer stack at 6 m/s

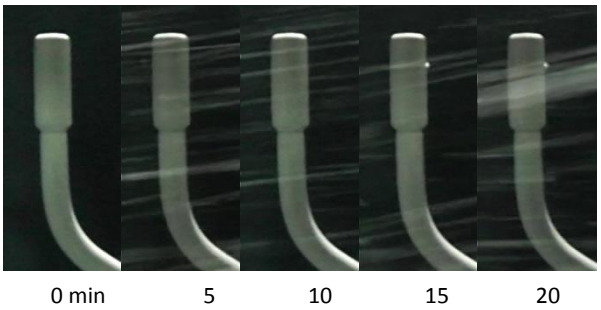

Fig.12 Superhydrophobically coated transducer stack at 6 m/s

For the uncoated anemometer, the total test duration was 60 min. After the first half of this time interval, the ultrasonic anemometer was rotated by 90° for widening the icing area on the transducer surface. Since the values of the snow flux and the speed in the weak and higher wind conditions were different from each other, the growth and range of ice accretion may undergo a different process. Therefore, the comparison between the higher and weak wind conditions in terms of the shape of the ice accretion cannot be simply conducted. Even so, as shown in Fig.11, ice grows on the surface as time elapses.

For the coated transducer, Fig.12 indicates that nothing happens on the transducer surface even though, as in the weak wind condition, a very small ice deposit like a frozen droplet is found at 20 min. From the video analysis, it is observed that the ice was blown off shortly after its formation. In addition, the small ice deposit formed on the transducer surface at almost the same area as in the weak wind condition. This implies that the surface roughness in the area was a bit different from the other area. Hence it would be required that painters have to carefully make a coating film on the surface since it should be as uniform as possible.

In regard to snow accumulation on the top cover of the anemometer, under the higher wind conditions, no snow was left on it after the 20 min test. This led to the suggestion that no heating would be needed for the superhydrophobically coated top cover as long as the wind speed was higher than some threshold, and that a better heating scheme has to be considered for energy saving.

IV. Concluding Remarks

As indicated by this research study, the secondary icing is the primary cause of incorrect measurements in a heated ultrasonic anemometer with stack-type transducers (VAISALA WMT-703) in areas subject to snowing and/or icing. The secondary icing under the snowy condition is a physical phenomenon where icing occurs through the process of refreezing of the meltwater from accumulated ice or from ice accreted on a surface, produced by artificial heating or by a localised temperature increase due to solar radiation. Therefore, enhancing the removal of meltwater from the surface would be considered the most effective way to prevent the secondary icing. The most promising measure to shape this concept is an icephobic coating applied to a surface of interest, and in particular, to superhydrophobic paint.

Prior to the actual application of such paint to the existing ultrasonic anemometer, and in order to ensure the capabilities of wind measurements after coating, several tests and analyses were implemented. The transmissivities of the ultrasonic waves is the most definitive measure for evaluation of the influence of ice accretion on the transducer in regard to wind measurements for the conceivable cases at which incorrect wind measurements were elicited by the ultrasonic anemometer due to snow and/or ice accretion. These were obtained by the acoustic impedance analysis. Moreover, the transmissivity was calculated when the superhydrophobic film was formed on the transducer surface. It was indicated from the analysis that the ice-bridge formation that had an air-gap at the interface between the ice and the transducer surface reduced dramatically the values of the transmissivity compared to the values when no icing occurred. More importantly, the coating film exerted no negative influence on the measurement.

At the next stage, the chemical damage to the transducer's silicon covering due to the thinner of the superhydrophobic paint NIREC-100 was evaluated using the immersion test, in accordance to the Japanese Industrial Standard and within a shorter testing period just for the snowing wind tunnel test. The result was favorable since no damage was found. Additional wind tunnel tests were carried out at room temperature using the same anemometer, with the transducers covered by a thin membrane of vinyl chloride that had an acoustic impedance value at the same impedance level as that of the superhdrophobic paint and the coated transducers, in order to examine the influences of a film on wind measurement. Consequently, it was suggested that the coated anemometer would work properly, regardless of the presence of the thin coating film.

The effectiveness of the coating of the superhydrophobic paint on the wind measurement of the heated ultrasonic anemometer equipped with the stack-type transducers was examined by carrying out the snowing wind tunnel test under weak and higher wind conditions, and at the temperature at -12ºC. The coating was applied to the upper half of the anemometer, and included the transducers, with an embedded electric heater in the middle part. It can be mentioned that the coated surfaces of the anemometer were kept clean throughout each test run in the higher wind condition. In contrast, in the weak wind condition, while the transducers and the arms were free from snowing or icing, snow accumulated on the superhydrophobically coated top cover of the body because snowflakes fell almost vertically and were not blown away by the weak airflow. As a result, it could be concluded that the superhydrophobic coating application to the ultrasonic anemometer equipped with the stack-type transducers would be effective for stable and accurate wind measurements in snowing and dangerous areas.

ACKNOWLEDGMENT

Special thanks go to Mr. S. Mochizuki and Mr. M. Ohkawa of the Shinjo Cryospheric Environment Laboratory of National Research Institute for Earth Science and Disaster Prevention for their dedicated contribution to the snowing wind tunnel test.

REFERENCES

[1] Kimura, S., H. Morikawa, T. Sato, T. Yamagishi, T. Kojima, T. Yoshioka and K. Kawakami: Mechanism of incorrect measurement by ultrasonic anemometer, Proc. of 26th Cold Region Technology Symposium, 2010, pp.33-37

[2] Kimura, S., H. Morikawa, T. Sato, T. Yamagishi, T. Kojima, T. Yoshioka and K. Kawakami: Experimental examination for invalid signal output from ultrasonic anemometer, Proc. of 27th Cold Region Technology Symposium, 2011, pp.76-79

[3] Kimura, S., H. Morikawa, K. Sato, T. Yamagishi, T. Kojima, T. M. Koyata, H. Miyagi, H. Endo and S. Mochizuki: Modification and verification of ice prevention scheme for ultrasonic anemometer, Proc. of 29th Cold Region Technology Symposium, 2013, pp.93-97

[4] Udagawa, Y.: Introduction to ultrasonic wave technique, Nikkan Kogyo Shimbun, 2010

[5] Japanese Industrial Standards Committee: Japanese Industrial Standard www.jisc.go.jp/eng/ (2015)

Passive acoustic signal sensing approach to detection of ice on the rotor blades of wind turbines

Eugen Mamontov [1], Viktor Berbyuk [2]
[1] Department of Research and Development, Foundation Chalmers Industrial Technology,
SE-412 88 Gothenburg, Sweden,
[2] Department of Applied Mechanics, Chalmers University of Technology
SE-412 96 Gothenburg, Sweden
eugen.mamontov@cit.chalmers.se

***Abstract*: In cold seasons, irregular layers of atmospheric ice (AI) are usually accreted on the rotor blades of operating wind turbines. For smart, energy-efficient deicing, ice-detection systems should not only detect the AI-layer on the blade skin (BS) but also provide the "landscape" of the material parameters of this layer over the BS surface, which generally vary in time. The work considers a passive sensing with wireless lowpass single-axis accelerometers, which are located at the centers of the mutually non-intersecting low-curvature disk-shape regions on the inner surface of the BS and measure acoustic accelerations normal to the surface. They include the acoustic component caused by the operational load in the BS. The work deals with this component only, and develops acoustic model and method for identification of the AI-layer parameters. The model is based on the third-order acoustic PDEs originating from the derived acoustic partial integro-differential equation, which includes the Boltzmann superposition integral with the related stress-relaxation function. The method can identify the following eight parameters: the thickness, volumetric mass density, bulk and shear moduli, stress-relaxation time, porosity, as well as volume and shear viscosities. The identification method is computationally efficient and can be suitable for implementation in the real-time mode. The proposed identification model and method enrich the scope of structural health monitoring of systems with the identification of material parameters of the thin-layer components. The work also suggests a few directions for future research.**

Keywords: blade of the operating wind turbine rotor, atmosheric ice, ice detection for smart deicing, third-order acoustic partial differential equation, parameter identification

LEGEND AND ABBREVIATIONS

AI	*Atmosheric Ice*
IDS	*Ice-Detection System*
BS	*Blade Skin*
SRT	*Stress-Relaxation Time*
NEC	*Non-Equilibrium Component*
ANS	*Average Normal Stress*
TPD	*Thin Planar Disk*
PC	*Personal Computer*
FD	*Finite Difference*
PDE	*Partial Differential Equation*
SRF	*Stress-Relaxation Function*
ODE	*Ordinary Differential Equation*

INTRODUCTION

In cold seasons, irregular layers of atmospheric ice (AI) are usually accreted on the outer surfaces of the wind turbine rotor blades. These layers can cause unexpected down times and increase the maintenance cost, thereby reducing the energy-production efficiency. AI presents an unpredictable mixture of crystalline and amorphous ice including such forms as dense snow frozen to the surface, soft rime, hard rime, clear ice, and glaze (e.g., [1], [2]). The parameters of the AI-layer (e.g., the thickness, mass volumetric density, porosity, elastic moduli, viscosities, and stress-relaxation time) vary from a half on order to a few orders depending on the parameter (e.g., [3]–[5]).

For smart, energy-efficient deicing, ice-detection systems (IDSs) should not only detect the AI-layer on the blade skin (BS) but also provide the "landscape" of the material parameters of this layer over the BS surface, which generally vary in time. Consequently, the IDS development should deal with the following main features.

(1) The operational load in a BS creates irregular space-time distributions of material variables (e.g., strain, stress, and displacement) which depend on the acceleration, deceleration, speed of rotation of the rotor, the blade-pitch angle, the wind, the presence of the AI layer on the skin, and other factors. The corresponding experimental data are well documented (e.g., [6, Figs. 6–9], [7, Fig. 8 and Fig. 10(b)]).
(2) The BS-layer is of a complex, curvilinear shape that, in the course of the rotor operation, varies in space and time. This feature is also well documented (e.g., [6], [7]).
(3) The AI stress-relaxation time (STR) can be in an interval of a few orders (e.g., [3]–[5]).
(4) The aforementioned time-varying "landscape" of the AI-layer parameters should be identified with an appropriate acoustic model from the results measured by the IDS sensors, which are located on the inner BS surface and wirelessly controlled by a computer and gateways in the real-time mode.

Thus, the model and identification method are in the focus of the IDS development. The present work proposes acoustic model and method for identification the AI-layer parameters. The method uses the results of [8] and can estimate the following eight parameters: the thickness, mass density, bulk and shear moduli, STR, porosity, and volume and shear viscosities.

Due to the above Point (1), the identification method presumes passive rather than active sensing. The method is based on measurements of the acoustic accelerations at different points on the inner surface of the skin. (The acoustic acceleration is understood as, loosely speaking, the difference between

the total acceleration and the acceleration of the macroscopic motion.) The challenge in Point (2) is met by the extending the thin-planar-disk approximation introduced in [8] from a single solid layer to the two-layer sys-tem of the BS/AI layers. The features in the above Points (3) and (4) are allowed for by the corresponding generalization of the viscoelastic model developed in [8] and preceded in [9]. The model is based on a partial integro-differential equation for the non-equilibrium component (NEC) of the average normal stress (ANS) derived in [8, Sections 2 and 3]. The proposed identification method is computationally efficient and suitable for the use indicated in Point (4).

1. ACOUSTIC MODEL FOR THE BS/AI-LAYER SYSTEM

The model developed in [8] and generalized below is based on the thin-planar-disk (TPD) approximation, which is introduced in [8, Section 3] for the case of a single layer. This approximation presumes that:

- a major part of the space-time varying curvilinear skin of the operating blade with the AI layer accreted on its outer surface can be approximated with a set of mutually non-intersecting planar disk-shaped cylinders, briefly, disks;
- in each disk, the thicknesses of the BS- and AI-layers h_s and h are independent of the location on the disk surface;
- each disk is thin in the sense that

$$[(h_s+h)/R]^2 << 1 \tag{1.1}$$

where R is the radius of the disk. Thus, the radiuses of all disks should be sufficiently small in order to allow the above planar-disk approximation and sufficiently big in order to enable inequality (1.1) for each disk to hold.

At the center of each disk on the inner surface of the BS layer, one attaches a wireless lowpass single-axis acoustic accelerometer measures the acoustic acceleration, which is normal to the surface. This acceleration is caused by the operational load in the layer. The accelerometer network can wirelessly be controlled by a personal computer (PC) and a gateway in the real-time mode. For better energy efficiency, this network should be endowed with wireless acoustic energy harvesters. The time developments of the accelerations measured at the point of the accelerometer locations are transmitted to the PC where the acoustic accelerations form the time-varying "landscape" of the data over the entire part of the two-layer-system surface represented with the TPD approximation. The PC by means of the acoustic model and identification method described below transforms these data into the space-time heterogeneous values of the AI-layer parameters

The model and method are the same for each disk. They apply the input data listed in Table 1.1.

Remark 1.1. As is well known, physical quantities at equilibrium are independent of time. The present work only considers materials, which are at equilibrium also independent of space. The equilibrium versions are denoted with the sign "overline" applied to the notation of the corresponding quantity (e.g., see the related notations in Table 1.1). □

As is shown in [8, Section 3], the above TPD approximation allows reduction of the model for a thin planar disk in three spatial dimension to the model in one spatial dimension, along the axis perpendicular to the disk, say, the x-axis. Without a loss of generality, one can consider that the inner surface of the BS-layer corresponds to value $x = 0$ and the x-axis has the origin at the center of the disk. Then the single-layer model of work [8] in the present case of the two-layer system can be written as the third-order partial differential equations (PDEs)

$$\bar{\theta}_s \partial^3\Pi_s/\partial t^3 + \partial^2\Pi_s/\partial t^2 = \bar{s}_s^2\left[\partial^2\Pi_s/\partial x^2 + 2\bar{\theta}_s\partial(\partial^2\Pi_s/\partial x^2)/\partial t\right], \quad 0 \le x \le h_s, \tag{1.2}$$

$$\bar{\theta}\,\partial^3\Pi/\partial t^3 + \partial^2\Pi/\partial t^2 = \bar{s}^2\left[\partial^2\Pi/\partial x^2 + 2\bar{\theta}\,\partial(\partial^2\Pi/\partial x^2)/\partial t\right], \quad h_s \le x \le h_s+h, \tag{1.3}$$

with boundary conditions

$$\Pi_s(0,t) = 0, \tag{1.4}$$

$$\Pi_s(h_s,t) = \Pi(h_s,t), \tag{1.5}$$

$$-\bar{\rho}_s^{-1}\,\partial\Pi_s(h_s,t)/\partial x = -\bar{\rho}^{-1}\,\partial\Pi(h_s,t)/\partial x, \tag{1.6}$$

$$\Pi(h_s+h,t) = 0, \tag{1.7}$$

and expression

$$a(t) = -\bar{\rho}_s^{-1}\,\partial\Delta\Pi_s(0,t)/\partial x \tag{1.8}$$

for acoustic acceleration $a(t)$ (cp., Row 11 in Table 1.1). In the

Table 1.1. The input data for the model and method for each disk in the TPD approximation.

The characteristics in Rows 2–8 and 11 generally dependent on the parameter in Row 1. The characteristics in Rows 1–8 are the same for each disk. They are assumed to be independent of time in each interval comprising any three successive time points (see Row 9). The data in Rows 9 and 10 can be specific to each disk. The data in Row 11 are specific to each disk.

	Notation	Meaning
1	$\bar{T}$	absolute temperature of AI
2	$\bar{\rho}_a$	volumetric mass density of air (used as described in Remark 1.2); it is 1.2 kg / m^3 at sea level
3	$\bar{\rho}_i$	volumetric mass density of a continuous, non-porous AI (used as described in Remark 1.2); it is 916.7 kg / m^3 at zero °C
4	h_s	thickness of the BS layer
5	$\bar{\rho}_s$	volumetric mass density of the BS
6	$\bar{K}_s$	bulk modulus of the BS
7	$\bar{\theta}_s$	stress-relaxation time in the BS
8	$s^*(\bar{\rho})$	dependence of the speed of the bulk acoustic waves in the AI layer (e.g., see (1.14))
9	N	number of the successive time points, at which the acceleration was measured; $N \ge 4$; this inequality allows to evaluate the third-order time derivatives with the help of finite-difference (FD) formulas
10	$t_1,\dots,t_N$	successive time points, $t_1<\dots<t_N$, at which the acceleration values were measured
11	$a_1,\dots,a_N$	values of acoustic acceleration $a(t)$ at time points t_k, $k=1,2,\dots,N$; value a_k is the one at time point t_k; values a_k , $k=1,2,\dots,N$, correspond to the NEC of the *operational-load-caused* stress force in the BS layer normal to the inner surface of the layer (cp., (1.8))

above relations, $\Pi_s = \Pi_s(x,t)$ and $\Pi = \Pi(x,t)$ are the NECs of the ANS in the BS and AI layers, h, $\bar{\rho}$, and $\bar{K}$ are the thickness, volumetric mass density, and bulk modulus of the AI layer, $\bar{\theta}_s$ and $\bar{\theta}$ are the SRTs of the BS and AI layers, and parameters

$$\bar{s}_s = \sqrt{\bar{K}_s/\bar{\rho}_s}, \qquad \bar{s} = \sqrt{\bar{K}/\bar{\rho}} \tag{1.9}$$

are the speeds of the bulk acoustic waves in these layers. Inequality

$$\bar{\rho} > 0 \tag{1.10}$$

holds because AI or, if it is absent, air, is not a vacuum. Note that the bulk waves in a medium are understood in the present

work as the waves related to *uniform* compressions/rarefactions. Also note that scalar PDE (1.2) or (1.3) can be quantitatively adequate only if the material is isotropic and the ratio of its shear modulus to the bulk one is sufficiently small (or, equivalently, the corresponding Poisson coefficient is not very far from 0.5).

A necessary condition for the applicability of linear quasi-equilibrium continuum-mechanics models such as acoustic equations (1.2) and (1.3) are relations (e.g., [8, (2.3)])

$$|\Delta p_s|/\bar{K}_s << 1, \qquad |\Delta p|/\bar{K} << 1, \tag{1.11}$$

respectively, where Δp_s and Δp is the NECs of the pressures, which correspond to Π_s and Π, respectively, and are coupled with the latter by relations [8, (2.15)]

$$\Delta p_s = \Pi_s - \bar{\theta}_s \partial \Pi_s/\partial t - 2\bar{\theta}_s^2 \partial^2 \Pi_s/\partial t^2 + 4\bar{\theta}_s^2 \bar{s}_s^2 \partial^2 \Pi_s/\partial x^2. \tag{1.12}$$

$$\Delta p = \Pi - \bar{\theta}\, \partial \Pi/\partial t - 2\bar{\theta}^2 \partial^2 \Pi/\partial t^2 + 4\bar{\theta}^2 \bar{s}^2 \partial^2 \Pi/\partial x^2. \tag{1.13}$$

Expressions (1.12), (1.13), and inequalities (1.11) endow PDEs (1.2) and (1.3) with the self-testing capabilities [8, pp. 5-6].

It is shown in [8, Section 2] that, in PDE (1.2) (or (1.3)), the first term on the left-hand side and the multiplier "2" instead of "1" on the right-hand side result from the stress-relaxation function (SRF) in the Boltzmann superposition integral included in a more general, partial integro-differential equation derived in [8] (see [8, (2.10)]). The present forms of these terms correspond to the simplest, exponential approximation for the SRF.

Equation (1.2) and boundary conditions (1.4)–(1.6) form the boundary-value problem for the BS layer. Equation (1.3) and boundary conditions (1.5)–(1.7) form the boundary-value problem for the AI layer. These problems are mutually coupled because of the coupling of the layers with (1.5) and (1.6). Thus, (1.2)–(1.7) present a system of boundary-value problems. The solution of this system is the steady-state one because the operational load is long-lasting or, in modeling terms, defined in the entire time axis. Note that a steady-state solution of an asymptotically stable ordinary differential equation (ODE) in Euclidian space or a function Banach space is, loosely speaking, its unique solution with an initial condition in the limit case as the initial time point tends to $-\infty$ (e.g., see [11] for the details). This solution is specified with function $a(t)$ in (1.8).

Remark 1.2. If the AI-layer parameters $\bar{\rho}$, $\bar{K}$, and $\bar{\theta}$ are available, then the layer porosity $\bar{\varphi}$ ($0 \le \bar{\varphi} \le 1$), volume viscosity $\bar{\eta}$, shear modulus $\bar{G}$, and shear viscosity $\bar{\mu}$ can be estimated as $\bar{\varphi} = (\bar{\rho}_i - \bar{\rho})/(\bar{\rho}_i - \bar{\rho}_a)$, $\bar{\eta} = \bar{K}\bar{\theta}$, $\bar{G} = [s_T^*(\bar{\rho})]^2/\bar{\rho}$, and $\bar{\mu} = \bar{G}\bar{\theta}$, respectively, where $s_T^*(\bar{\rho})$ is the $\bar{\rho}$-dependence of the speed of the transverse acoustic waves in the AI layer. The speed of the longitudinal acoustic waves in the AI layer, $s_L^*(\bar{\rho})$, as a function of $\bar{\rho}$, can also be available. An experimental example of both the dependences for dense snow (including AI) can be found in [1, Fig. 2]. These data are related to the values of $\bar{\rho}$ in the entire dense-snow interval, i.e. from 300 kg/m^3 up to the value in Row 3 of Table 1.1. Functions $s_L^*(\cdot)$ and $s_T^*(\cdot)$ enable one to describe $s^*(\cdot)$ in Row 8 of Table 1.1. Indeed, due to (e.g., [10, (2.12), (2.14)])

$$s^*(\bar{\rho}) = \sqrt{[s_L^*(\bar{\rho})]^2 - (4/3)[s_T^*(\bar{\rho})]^2}. \tag{1.14}$$

The aforementioned value $\bar{s}$ can be determined as

$$\bar{s} = s^*(\bar{\rho}) \tag{1.15}$$

in terms of function (1.14). □

In view of Remark 1.2, the rest of the present work concentrates on identification of parameters h, $\bar{\rho}$, $\bar{K}$, and $\bar{\theta}$. This is carried out on the basis of boundary-value problem (1.2)–(1.7) and relation (1.8).

2. Separation of the boundary-value problem for the BS layer from the one for the AI layer

The treatment of the above boundary-value problem can be simplified if one separates the BS-layer subproblem from the AI-layer subproblem. This can be achieved by the following change of variables

$$\Pi_s(x,t) = Y_s(x,t) - hW(t)\,x, \qquad 0 \le x \le h_s, \tag{2.1}$$

$$\Pi(x,t) = Y(x,t) + h_s W(t)\,[x - (h_s + h)], \quad h_s \le x \le h_s + h, \tag{2.2}$$

where $Y_s(x,t)$ and $Y(x,t)$ are the new variables, and

$$W(t) = (\bar{\rho}_s h_s + \bar{\rho}\, h)^{-1}\left[\bar{\rho}\, \partial Y_s(h_s,t)/\partial x - \bar{\rho}_s\, \partial Y(h_s,t)/\partial x\right] \tag{2.3}$$

is an auxiliary function. Boundary conditions (1.4)–(1.7) for Π_s and Π correspond to zero boundary conditions for Y_s and Y,

$$Y_s(0,t) = Y_s(h_s,t) = 0, \tag{2.4}$$

$$Y(h_s,t) = Y(h_s + h,t) = 0. \tag{2.5}$$

In view of (1.8) and (2.1),

$$h\,W(t) = f_0(t) \tag{2.6}$$

where

$$f_0(t) = \bar{\rho}_s\, a(t) + \partial Y_s(0,t)/\partial x. \tag{2.7}$$

In the limit case as the AI-layer thickness h tends to zero, limit relation

$$\lim_{h \downarrow 0} f_0(t) = 0 \tag{2.8}$$

holds because of (2.1), (2.3), and (2.6).

Importantly, relations (2.3) and (2.6) enables one to express a certain characteristic of the AI layer in terms of the related characteristics of the skin layer, namely

$$\bar{\rho}_s h \frac{\partial Y(h_s,t)}{\partial x} = \bar{\rho}\, h \frac{\partial Y_s(h_s,t)}{\partial x} - (\bar{\rho}_s h_s + \bar{\rho}\, h) f_0(t)$$
$$= -\bar{\rho}_s h_s f_0(t) + \bar{\rho}\, h f_1(t) \tag{2.9}$$

where

$$f_1(t) = \partial Y_s(h_s,t)/\partial x - f_0(t). \tag{2.10}$$

Application of (2.1) and (2.2) to PDEs (1.2) and (1.3), as well as allowing for (2.6) lead to the BS and AI-layer PDEs

$$\bar{\theta}_s \frac{\partial^3 Y_s}{\partial t^3} + \frac{\partial^2 Y_s}{\partial t^2} = \bar{s}_s^2 \left(\frac{\partial^2 Y_s}{\partial x^2} + 2\bar{\theta}_s \frac{\partial}{\partial t} \frac{\partial^2 Y_s}{\partial x^2} \right)$$
$$+ \left[\bar{\theta}_s \frac{d^3 f_0(t)}{dt^3} + \frac{d^2 f_0(t)}{dt^2} \right] x, \qquad 0 \le x \le h_s, \tag{2.11}$$

$$\bar{\theta} \frac{\partial^3 Y}{\partial t^3} + \frac{\partial^2 Y}{\partial t^2} = \bar{s}^2 \left(\frac{\partial^2 Y}{\partial x^2} + 2\bar{\theta} \frac{\partial}{\partial t} \frac{\partial^2 Y}{\partial x^2} \right)$$
$$- \frac{h_s}{h} \left[\bar{\theta} \frac{d^3 f_0(t)}{dt^3} + \frac{d^2 f_0(t)}{dt^2} \right] [x - (h_s + h)], \quad h_s \le x \le h_s + h. \tag{2.12}$$

One can see that the change of variables (2.1), (2.2) allows achieving the separation of the BS-layer boundary-value problem from the AI-layer. Indeed, in terms of new variables Y_s and Y, the BS-layer boundary-value problem (2.11), (2.7), (2.4) is independent of the AY-layer boundary-value problem (2.12), (2.7), (2.5).

Consequently, one can first reconstruct the solution of the first problem by using already known function $a(t)$ in (2.7), and then apply this function and the obtained solution to determine the solution of the second problem, which will allow to regard equation (2.12) as the equation for identification of the parameters h, $\bar{\rho}$, $\bar{K}$, and $\bar{\theta}$.

The first and second parts of this program are considered in Sections 3 and 4. The latter one uses the following three equations related to (2.12). In view of (2.1), the versions of PDE (2.12) at $x = h_s$ and $x = h_s + h$ are

$$\bar{s}^2\left\{\partial^2 Y(h_s,t)/\partial x^2 + 2\bar{\theta}\, d[\partial^2 Y(h_s,t)/\partial x^2]/dt\right\} + h_s\left[\bar{\theta}\, d^3 f_0(t)/dt^3 + d^2 f_0(t)/dt^2\right] = 0, \quad (2.13)$$

$$\bar{s}^2\left[\partial^2 Y(h_s+h,t)/\partial x^2 + 2\bar{\theta}\, d[\partial^2 Y(h_s+h,t)/\partial x^2]/dt\right] = 0. \quad (2.14)$$

Also, differentiating (2.12) with respect to x and substituting value $x = h_s$ into the resulting equality, one obtains equation

$$\bar{\theta}\frac{d^3}{dt^3}\frac{\partial Y(h_s,t)}{\partial x} + \frac{d^2}{dt^2}\frac{\partial Y(h_s,t)}{\partial x} = \bar{s}^2\left[\frac{\partial^3 Y(h_s,t)}{\partial x^3} + 2\bar{\theta}\frac{d}{dt}\frac{\partial^3 Y(h_s,t)}{\partial x^3}\right] - \frac{h_s}{h}\left[\bar{\theta}\frac{d^3 f_0(t)}{dt^3} + \frac{d^2 f_0(t)}{dt^2}\right].$$

Multiplication of it by $\bar{\rho}_s h$ and substitution of (2.9) into the left-hand side of the resulting equality lead to

$$\bar{\rho}\left[\bar{\theta}\frac{d^3 f_1(t)}{dt^3} + \frac{d^2 f_1(t)}{dt^2}\right] = \bar{\rho}_s \bar{s}^2\left[\frac{\partial^3 Y(h_s,t)}{\partial x^3} + 2\bar{\theta}\frac{d}{dt}\frac{\partial^3 Y(h_s,t)}{\partial x^3}\right], \quad h > 0. \quad (2.15)$$

By introducing an appropriate approximation for the term in the brackets on the right-hand side of (2.15), one can obtain a time-varying algebraic equation for parameters to be identified, i.e., h, $\bar{\rho}$, $\bar{K}$, and $\bar{\theta}$. This is considered in Section 4.

3. Reconstruction of the Steady-State Solution of the Boundary-Value Problem for the BS-Layer

Change of variables (2.1), (2.2) not only allows the separation discussed in Section 2 but also provides homogeneous boundary conditions (2.4), (2.5). Relations (2.4) enables one to reconstruct the solution of the BS-layer boundary-value problem (2.11), (2.7), (2.4) by means of the Fourier method (e.g., [12, Chapters VIII and IX]). It provides expansions of solutions of linear PDEs, which are based on the Laplace operator, in the operator eigenfunctions (e.g., [13, Chapter V]).

The Laplace operator in the BS-layer PDE (2.11) is differential expression $\partial^2/\partial x^2$ endowed with boundary conditions (2.4). The eigenvalues and eigenfunctions for this operator are well known (e.g., [12, pp. 118-119], [13, Chapter V, Section 22.4, (21)]. The eigenvalues are $-\kappa_{s.i}^2$, $i = 1,2,\ldots$, where

$$\kappa_{s.i} = (\pi/h_s)\, i, \qquad i = 1,2,\ldots, \quad (3.1)$$

and the orthonormal eigenfunctions are

$$X_{s.i}(x) = \sqrt{2/h_s}\sin(\kappa_{s.i}x), \quad 0 \le x \le h_s, \quad i = 1,2,\ldots. \quad (3.2)$$

According to the Fourier method, solutions of boundary-value problem (2.11), (2.4) is presented in the form

$$Y_s(x,t) = \Sigma_{i=1}^{\infty}\Theta_{s.i}(t)X_{s.i}(x), \quad 0 \le x \le h_s, \quad (3.3)$$

where $\Theta_{s.i}(t)$ are the time-dependent coefficients of the expansion. Combining (3.1)–(3.3), one obtains

$$\partial Y_s(0,t)/\partial x = \sqrt{2/h_s}\,(\pi/h_s)\,\Sigma_{j=1}^{\infty} j\,\Theta_{s.j}(t), \quad (3.4)$$

$$\partial Y_s(h_s,t)/\partial x = \sqrt{2/h_s}\,(\pi/h_s)\,\Sigma_{j=1}^{\infty}(-1)^j j\,\Theta_{s.j}(t). \quad (3.5)$$

Since (2.11) includes the source function, which is linear and homogeneous in x, one also needs to consider the corresponding expansions for these functions. By using (3.1), (3.2), and the well-known results (e.g., [13, Sections 21.4 and 22.3 of Chapter V], [14, 430.11]), one can show that the expansions are the following:

$$x = \sum_{i=1}^{\infty}\left[\sqrt{2/h_s}\int_0^{h_s} x_*\sin(\kappa_{s.i}x_*)\,dx_*\right]\left[\sqrt{2/h_s}\sin(\kappa_{s.i}x)\right] = \sum_{i=1}^{\infty}\sqrt{2h_s}\,\frac{(-1)^{i-1}}{\kappa_{s.i}}\left[\sqrt{2/h_s}\sin(\kappa_{s.i}x)\right] = \sum_{i=1}^{\infty}\sqrt{2h_s}\,h_s\frac{(-1)^{i-1}}{\pi i}X_{s.i}(x), \quad 0 \le x \le h_s. \quad (3.6)$$

Remark 3.1. The terms in the series in (3.6) contribute to both the shape and integral over the corresponding x-interval of the function on the left-hand side. However, it appears that these contributions are qualitatively different.

In view of (3.2), the terms in (3.6) with odd and even values of i are even and odd functions of $x - h_s/2$, respectively. This means that the even terms substantially contribute to the correspondence of the shape of the x-dependence on the right-hand side of (3.6) to function x on the left-hand side.

Moreover, as follows from (3.6),

$$\int_0^{h_s} x\,dx = \frac{h_s^2}{2} = 2\sum_{i=1}^{\infty}\frac{(-1)^{i-1}}{\kappa_{s.i}}\int_0^{h_s}\sin(\kappa_{s.i}x)\,dx = \frac{h_s^2}{2}\frac{8}{\pi^2}\sum_{i=1}^{\infty}\frac{1-(-1)^i}{2}\frac{1}{i^2}. \quad (3.7)$$

The sum of the series on the right-hand side of (3.7) can be evaluated as follows (e.g., [14, (48.12)])

$$\Sigma_{i=1}^{\infty}[1-(-1)^i]/(2/i^2) = \pi^2/8. \quad (3.8)$$

Relations (3.7) and (3.8) show that the terms with even values of i do not contribute to the integral at all. They only, so to say, correct the shape of the approximation formed by the preceding terms of the series. This means that, if the series is approximated with the finite sum corresponding to the values of i from unit to, say, $J \ge 1$, it is reasonable to do that at even J.

One can also check that the integral can be approximated with a very small relative error, say, of 5% when at least eight terms of the series are taken into account. This indicates that J should be not only even but also not less than eight. □

Since PDE (2.11), by means of (2.7), involves not only $a(t)$ but also $\partial Y_s(0,t)/\partial x$, which a value of the solution of the BS-layer boundary-value problem, it is necessary to rewrite (2.11) in the corresponding form, i.e.,

$$\bar{\theta}_s\frac{\partial^3 Y_s}{\partial t^3} + \frac{\partial^2 Y_s}{\partial t^2} = \bar{s}_s^2\left[\frac{\partial^2 Y_s}{\partial x^2} + 2\bar{\theta}_s\frac{\partial}{\partial t}\left(\frac{\partial^2 Y_s}{\partial x^2}\right)\right] + \left\{\bar{\rho}_s\left[\bar{\theta}_s\frac{d^3 a(t)}{dt^3} + \frac{d^2 a(t)}{dt^2}\right] + \left[\bar{\theta}_s\frac{d^3}{dt^3}\frac{\partial Y_s(0,t)}{\partial x} + \frac{d^2}{dt^2}\frac{\partial Y_s(0,t)}{\partial x}\right]\right\}x, \quad 0 \le x \le h_s. \quad (3.9)$$

Substitution of (3.3), (3.4), and (3.6) into (3.9) results in

$$\bar{\theta}_s\left[\frac{d^3\Theta_{s.i}(t)}{dt^3} + \frac{(-1)^i 2}{i}\Sigma_{j=1}^{\infty} j\frac{d^3\Theta_{s.j}(t)}{dt^3}\right] + \left[\frac{d^2\Theta_{s.i}(t)}{dt^2} + \frac{(-1)^i 2}{i}\Sigma_{j=1}^{\infty} j\frac{d^2\Theta_{s.j}(t)}{dt^2}\right] + \bar{s}_s^2\frac{\pi^2}{h_s^2}i^2\left[\bar{\theta}_s\frac{d\Theta_{s.i}(t)}{dt} + \Theta_{s.i}(t)\right] = \frac{\bar{\rho}_s\sqrt{2h_s}\,h_s}{\pi}\frac{(-1)^{i-1}}{i}\left[\bar{\theta}_s\frac{d^3 a(t)}{dt^3} + \frac{d^2 a(t)}{dt^2}\right], \quad i = 1,2,\ldots. \quad (3.10)$$

Thus, coefficients $\Theta_{s.1}(t), \Theta_{s.2}(t), \ldots$ of the Fourier expansion (3.3) are described with infinite-dimensional ODE system (3.10). In practice, one can solve it in the finite-dimensional approximation. More specifically, at any $J \ge 1$, the Jth-approximation versions of (3.3)–(3.5) and (3.10) are

$$Y_s(x,t) = \Sigma_{i=1}^{J}\Theta_{s.i}(t)X_{s.i}(x), \qquad 0 \le x \le h_s, \quad (3.11)$$

$$\frac{\partial Y_s(0,t)}{\partial x} = \sqrt{\frac{2}{h_s}}\frac{\pi}{h_s}\Sigma_{j=1}^{J} j\,\Theta_{s.j}(t), \quad (3.12)$$

$$\frac{\partial Y_s(h_s,t)}{\partial x} = \sqrt{\frac{2}{h_s}}\frac{\pi}{h_s}\Sigma_{j=1}^{J}(-1)^j j\,\Theta_{s.j}(t), \quad (3.13)$$

$$\bar{\theta}_s\left[\frac{d^3\Theta_{s.i}(t)}{dt^3}+\frac{(-1)^i 2}{i}\sum_{j=1}^{J} j\,\frac{d^3\Theta_{s.j}(t)}{dt^3}\right]$$
$$+\left[\frac{d^2\Theta_{s.i}(t)}{dt^2}+\frac{(-1)^i 2}{i}\sum_{j=1}^{J} j\,\frac{d^2\Theta_{s.j}(t)}{dt^2}\right]$$
$$+\bar{s}_s^2\frac{\pi^2}{h_s^2}i^2\left[\bar{\theta}_s\frac{d\Theta_{s.i}(t)}{dt}+\Theta_{s.i}(t)\right]$$
$$=\frac{\bar{\rho}_s\sqrt{2h_s}h_s}{\pi}\frac{(-1)^{i-1}}{i}\left[\bar{\theta}_s\frac{d^3a(t)}{dt^3}+\frac{d^2a(t)}{dt^2}\right],\quad i=1,2,\ldots. \quad (3.14)$$

According to Remark 3.1, number J should be even and such that $J\geq 8$.

As follows from Table 1.1, acoustic acceleration $a(t)$ in (3.14) is available in the form of values $a_1, a_2, \ldots$ measured in a set of successive time points t_k, $k=1,\ldots,N$, $N\geq 4$. Accordingly, at each $i=1,\ldots,J$, one can consider values $\Theta_{s.i.k}$ of $\Theta_{s.i}(t)$ at the mentioned time points and express the time derivatives of functions $a(t)$ and $\Theta_{s.i}(t)$ by means of the corresponding FD formulas. This will result in the system of NJ linear algebraic equations with constant coefficients for NJ values $\Theta_{s.i.k}$, $i=1,\ldots,J$, $k=1,\ldots,N$. Assuming that the matrix of this system is nonsingular, one can uniquely solve the system for the mentioned values.

Remark 3.2. The output data of the above solution procedure are values $d^{(l)}f_0(t)/dt^{(l)}$ and $d^{(l)}f_1(t)/dt^{(l)}$, $l=0,1,2,3$, at points $t=t_k$, $k=1,\ldots,N$, which are evaluated as scalars $f_{0.k}^{(l)}$ and $f_{0.k}^{(l)}$ by means of (2.7), (2.10), measured acoustic-acceleration values a_k, expressions (3.12), (3.13), and the FD formulas based on the obtained values $\Theta_{s.i.k}$. □

Remark 3.2 is used in the method described below.

4. Equation and Method for Identification of the Four Parameters of the AI-Layer

Equality (2.15) can be used for identification of the AI-layer parameters h, $\bar{\rho}$, $\bar{s}$, and $\bar{\theta}$ provided that one estimates the term in the brackets on the right-hand side by means of available acoustic acceleration $a(t)$ or the parameters to be identified. In order to do that, one can apply the approach developed in [8, Section 4] for a single layer to the present case of the AI layer in the two-layer, skin/AI system.

According to this approach, it can be sufficient to approximate $Y(x,t)$ with the fourth-order polynomial

$$Y(x,t)\approx[b_2(t)(x-h_s)^2+b_1(t)(x-h_s)+b_0(t)][(x-h_s)^2-h(x-h_s)]$$
$$=b_2(t)(x-h_s)^4+[b_1(t)-b_2(t)h](x-h_s)^3$$
$$+[b_0(t)-b_1(t)h](x-h_s)^2-b_0(t)h(x-h_s),\quad h_s\leq x\leq h_s+h, \quad (4.1)$$

which has two t-independent roots $x=h_s$ and $x=h_s+h$ according to (2.5), and a pair of real or complex conjugate roots that need not be t-independent. In order to obtain the above estimation, one can involve relations (2.9), (2.13), and (2.14), and, thus, the x-derivatives of (4.1) of the first, second, and third orders. (The third-order derivative is used in (2.15).)

Differentiation of (4.1) three times in x and combining the obtained derivatives of the first, second, and third orders with relations (2.9), (2.13), and (2.14), one derives expression

$$\bar{s}^2\left\{\partial^3 Y(h_s,t)/\partial x^3+2\bar{\theta}\,d\left[\partial^3 Y(h_s,t)/\partial x^3\right]/dt\right\}$$
$$=(1/h)\left\{12(\bar{s}/h)^2\left[h_s[f_0(t)+2\bar{\theta}\,df_0(t)/dt]\right.\right.$$
$$\left.-(\bar{\rho}h/\bar{\rho}_s)[f_1(t)+2\bar{\theta}\,df_1(t)/dt]\right]$$
$$\left.+5h_s\left[\bar{\theta}\,d^3f_0(t)/dt^3+d^2f_0(t)/dt^2\right]\right\}. \quad (4.2)$$

Application of (4.2) to the right-hand side of (2.15) transforms the latter into

$$\bar{\rho}h\left[\bar{\theta}\,d^3f_1(t)/dt^3+d^2f_1(t)/dt^2\right]$$
$$+12(\bar{s}/h)^2\left[\bar{\rho}h[f_1(t)+2\bar{\theta}\,df_1(t)/dt]\right.$$
$$\left.-\bar{\rho}_s h_s[f_0(t)+2\bar{\theta}\,df_0(t)/dt]\right]$$
$$-5\bar{\rho}_s h_s\left[\bar{\theta}\,d^3f_0(t)/dt^3+d^2f_0(t)/dt^2\right]=0,\quad h>0, \quad (4.3)$$

This is the equation for identification of the AI-layer parameters h, $\bar{\rho}$, $\bar{s}$, and $\bar{\theta}$.

One can emphasize the different roles of terms $f_0(t)$ and $f_1(t)$ in (4.3) by moving the related terms to the right- and left-hand sides, respectively. This results in

$$\bar{\rho}h\left\{\bar{\theta}\,d^3f_1(t)/dt^3+d^2f_1(t)/dt^2+12(\bar{s}/h)^2[f_1(t)+2\bar{\theta}\,df_1(t)/dt]\right\}$$
$$=\bar{\rho}_s h_s\left\{5[\bar{\theta}\,d^3f_0(t)/dt^3+d^2f_0(t)/dt^2]\right.$$
$$\left.+12(\bar{s}/h)^2[f_0(t)+2\bar{\theta}\,df_0(t)/dt]\right\},\quad h>0, \quad (4.4)$$

The form of this relation, as well as notations (2.7) and (2.10) confirm that it is a relation for the two-layer system. Equation (4.4) is a generalization of a single-layer equation [8, (4.2)] obtained by means of the fourth-order-polynomial approximation (4.1) (or [8, (4.1)]). Indeed, equation (4.4) regarded as an ODE for $f_1(t)$ is analogous to the single-layer ODE [8, (4.2)]. The structure of the left-hand side of (4.4) coincides with the one of the left-hand side of [8, (4.2)]. However, in contrast to the single-layer ODE, which is homogeneous, the two-layer ODE (4.4) is nonhomogeneous: it is driven with the right-hand side determined by term $f_0(t)$.

The identification method based on equation (4.3) described below.

Dividing (4.3) by $\rho_s h_s$, one reduces it to the following more compact form

$$q\left[\bar{\theta}\,d^3f_1(t)/dt^3+d^2f_1(t)/dt^2\right]$$
$$-12c\left[[f_0(t)+2\bar{\theta}\,df_0(t)/dt]-q[f_1(t)+2\bar{\theta}\,df_1(t)/dt]\right]$$
$$-5\left[\bar{\theta}\,d^3f_0(t)/dt^3+d^2f_0(t)/dt^2\right]=0,\quad h>0, \quad (4.5)$$

where

$$c=(\bar{s}/h)^2>0, \quad (4.6)$$
$$q=(\bar{\rho}h)/(\bar{\rho}_s h_s)>0. \quad (4.7)$$

The inequalities in (4.6) and (4.7) follow from (1.10) and the inequality in (4.5). Equation (4.5) is the equation for identification of parameters $\bar{\theta}$, c, and q. The input data for (4.5) are the output data specified in Remark 3.2.

If parameters c and q are available, then parameters $\bar{\rho}$, $\bar{s}$, and h can be determined uniquely. Indeed, as follows from (4.6) and (4.7), $\bar{\rho}\bar{s}=(\bar{\rho}_s h_s)q\sqrt{c}$. Since $\bar{s}$ can be presented with dependence $\bar{s}^*(\bar{\rho})$ (see the text on (1.14) and Row 8 of Table 1.1), which is monotonically increasing, the indicated equality enables one to determine $\bar{\rho}$ as the unique solution of equation

$$\bar{\rho}\,\bar{s}^*(\bar{\rho})=(\bar{\rho}_s h_s)q\sqrt{c}. \quad (4.8)$$

As soon as $\bar{\rho}$ is available, $\bar{s}$ and h are calculated with (1.15) and (4.6) or (4.7), respectively. In turn, after the AI-layer parameters h, $\bar{\rho}$, $\bar{s}$, and $\bar{\theta}$ are identified, the other parameters of the layer can be determined in the way described in Remark 1.2.

Note that, as follows from the inequality in (4.5), the equation in (4.5) is applicable at any $h>0$. However, in view of notations (4.6), (4.7), and relation (2.8), the equation becomes an identity in the limit case as $h\downarrow 0$ and, thus, remains valid in this limit case as well.

The left-hand side of (4.5) is a polynomial of the degree not greater then three of three variables, parameters c, q, and $\bar{\theta}$. Thus, it is in general a tri-linear function, i.e., linear in each of the three variables. In general, the parameters can be identified

with the help of equation (4.5) in different ways. The simplest one is evaluation of them from the equation system consisting of the three versions of equation (4.5) at three successive time points, say, t_{k-2}, t_{k-1}, and t_k, $k=3,...,N$, where, in each version, the time derivatives are replaced with the FD formulas mentioned in Remark 3.2. This presumes that parameters c, q, and $\bar{\theta}$ are t-independent in interval $[t_{k-2},t_k]$ and, thus, are represented with their values c_k, q_k, and $\bar{\theta}_k$ specific to this interval. These values are determined as the unique solution of the mentioned system of the three tri-linear equations. This solution is suitable only if (see (4.6) and (4.7)) $c_k>0$, $q_k>0$, and $\bar{\theta}_k \geq 0$. The determined values present the parameters identified in interval $[t_{k-2},t_k]$.

Applying this procedure to the intervals corresponding to each of $k=3,...,N$, one obtains the piecewise-constant t-dependent approximations for the identified AI-layer parameters. These t-dependences include the influence of the operational load upon the parameters.

In view of the approximate nature of the FD formulas used in the proposed method, the t-dependences can be rather irregular. Consequently, they, in general, need to be "smoothed" in order to provide the component, which is caused by the operational load rather than the quantitative FD errors. The "smoothing" method can be a topic for future research.

At each $k=3,...,N$, the coefficients of the corresponding system of three tri-linear equations completely determine many of the properties of the system, for instance, the following.

- Does it have at least one suitable (see above) solution?
- If yes, how many solutions of this type exist?
- If more than one, how can one choose the most suitable?

These questions also present topics for future study. Some of them can be contributed with practical methods. Tri-linear systems are nonlinear. They can be solved with direct, non-iterative techniques or iterative techniques. Direct methods are not often applied to nonlinear systems because the corresponding analytical treatments are available in exceptional cases only. For this reason, it is much easier to use iterative methods. Book [15] provides a comprehensive introduction in this field.

However, iterative methods are difficult to use in the real-time computing because of at least two still unanswered questions.

- How can one assure unquestionable convergence of the iterations to a solution of the nonlinear system?
- How can one choose the initial approximation such that the resulting iterative approximations converge to the solution of interest?

The related difficulties usually presume intervention of an expert (e.g., a user) in the computational process. But these interventions are inappropriate to the real-time mode. Due to that, one can more closely consider direct methods. For example, one of them can be based on the procedure similar the one described in [8, the text on (4.5) and (4.6)]. The resulting identification can be computationally efficient and relevant for implementation in the real-time mode.

One more topic for future research is a calibration of the proposed identification method with respect to the related experimental data.

5. Conclusion

The present work generalizes the approach to a thin single solid layer (documented in one of the previous papers of the authors) for the case of a thin two-layer system, which comprises the BS and AI layers. They are assumed to be isotropic and isothermal. The work considers a passive sensing with wireless lowpass single-axis acoustic accelerometers, which are located at the centers of the mutually non-intersecting low-curvature disk-shape regions on the inner surface of the BS and measure acoustic accelerations, which are normal to the surface and caused by the operational load in the BS. The work develops the acoustic model based on the third-order PDE and the resulting from it method for identification of the following eight parameters of the AI-layer: the thickness, volumetric mass density, bulk and shear moduli, SRT, porosity, and volume and shear viscosities. The identification method is computationally efficient and can be suitable for implementation in the real-time mode. The proposed identification model and method enrich the scope of structural health monitoring of systems with the identification of material parameters of the thin-layer components. The work also suggests a few directions for future research.

Acknowledgement

The authors thank the Swedish Energy Agency for a partial support of the present work via the project 37286-1.

References

[1] R.A. Sommerfeld, "A review of snow acoustics", Rev. Geophys. & Space Phys., 20(1), 1982, 62-66.

[2] H. Gao, J.L. Rose, "Ice detection and classification on an aircraft wing with ultrasonic shear horizontal guided waves", IEEE Trans. Ultrasonics, Ferroelectrics, & Frequency Control, 56(2), 2009, 334-344.

[3] b. R.M. Deeley, "The viscosity of ice", Proc. Royal Soc. London. Series A 81(547; Sep. 11), 1908, 250-259.

[4] P.P. Kobeko *et al.*, "Plastic deformation and viscosity of ice", J. Tech. Phys., 16(3), 1946, 263-272.

[5] P.V. Hobbs, Ice Physics, Clarendon Press, Oxford, 1974.

[6] K. Schroeder *et al.*, "A fibre Bragg grating sensor system monitors operational load in a wind turbine rotor blade", Meas. Sci. Technol. 17, 2006, 1167–1172.

[7] J.R. White *et al.*, "Operational load estimation of a smart wind turbine rotor blade", Proc. of SPIE 7295, 2009, 72952D/1-72952D/12.

[8] E. Mamontov, V. Berbyuk, "Identification of material parameters of thin curvilinear viscoelastic solid layers in ships and ocean structures by sensing the bulk acoustic signals", VI Int. Conf. Comput. Meth. Marine Engrng, MARINE 2015, (F. Salvatore, R. Broglia, and R. Muscari, Eds.) 15-17 June 2015, Rome, Italy, 12 pp.

[9] E. Mamontov, V. Berbyuk, "A scalar acoustic equation for gases, liquids, and solids, including viscoelastic media", J. Appl. Math. & Phys, 2, 2014, 960-970.

[10] H.F. Pollard, Sound Waves in Solids, Pion, London, 1977.

[11] E. Mamontov, "Dynamic-equilibrium solutions of ordinary differential equations and their role in applied problems", Appl. Math. Lett., 21(4), 2008, 320-325.

[12] N.S. Koshlyakov, M.M. Smirnov, E.B. Gliner, Differential Equations of Mathematical Physics, North-Holland Publishing, Amsterdam, 1964.

[13] V.S. Vladimirov, Equations of Mathematical Physics, Mir, Moscow, 1984.

[14] H.B. Dwight, Tables of integrals and other mathematical data, McMillan, New York, 1961.

[15] J.M. Ortega, W.R. Rheinboldt, Iterative Solution of Nonlinear Equations in Several Variables, Acad. Press, New York, 1970.

Case Study of an Ice Sensor using Computational Fluid Dynamics, Measurements and Pictures - Boundary displacement

Marie Cecilie Pedersen
Dept. of Energy Technology
Aalborg University &
Vattenfall Vindkraft A/S
Kolding, Denmark
email: mcpe@et.aau.dk

Henrik Sørensen
Dept. of Energy Technology
Aalborg University
Aalborg, Denmark

Benjamin Martinez
Vattenfall Vindkraft A/S
Kolding, Denmark

Thomas Condra
Dept. of Energy Technology
Aalborg University
Aalborg, Denmark

***Abstract*—This paper presents an icing model developed using Computational Fluid Dynamics (CFD). One key part part of the model development is the surface boundary displacement due to the accumulated mass of ice. The paper presents the development of a boundary layer displacement method to be included in the CFD icing model using ANSYS-FLUENT.**

***Keywords:* ice accretion, surface boundary displacement, Computational Fluid Dynamics, dynamic-mesh, cold climate**

I. Introduction

Icing on wind turbines has been studied over the last 20 years and modelling of icing is a discipline, which has been approached by different methods and for different applications. Nevertheless, utility companies wish to improve and develop new and more precise turbine icing tools and production loss assessment models. The need for solving the energy and mass balance for droplets impinging on an object and to obtain the mass of accumulated ice over time is common for most of the tools. Within the wind power industry the model by Makkonen [1], originally developed for power line icing, has been widely used and is part of the iso standard iso-12494:2001 [2]. In recent work by Davis [3] the impact of icing on wind turbines was studied using Numerical Weather Prediction (WRF[1]) in combination with an icing model based on Makkonen's model [1], to forecast production losses due to icing. The original model [1] is empirically tuned for a cylinder but not a wind turbine. Thus, to improve on this fact [3] represents the turbine by a 1m long blade segment represented as a cylinder with a diameter based on the leading-edge radius of the given airfoil, and this showed promising results [4].

The power of the methodology by Davis [3] is the ability to study icing on an annual basis and the forecasting application provided by using the numerical weather models. However, details of a smaller time-scale from each individual icing event might be lost or not available. For future improvements of the methodology, a 3D CFD icing model specifically designed for wind turbines is put forward as a solution [3]. The methodology used by Vattenfall is similar to the overall approach seen in [3], but without any modifications to the Makkonen model. Similar to the conclusions from [3] experience have shown that changes to the ice model are essential to improve the overall production loss assessment methodology. Thus, this work aims to clarify whether a detailed CFD model can bring value into the current methodology for production loss assessment.

CFD models have met resistance in the wind power industry because of the computation time, the use of constant meteorological conditions and finally it has been questioned, if the accuracy gained from the micro-physics of a CFD simulations is necessary. In [5] an icing event of 17 hours was modelled using FENSAP-ICE based on data collected at a wind farm in Gaspé, Québec, Canada. The computational time was reduced by using a multi-shot approach of 34 steady-state simulations of 0.5 hours of icing, dividing the turbine blade into 9 stations and running the simulation in 2D. FENSAP-ICE is an commercial CFD code, which was originally developed for aircraft icing and is based on Messinger's model from 1953 [6]. The simulations were fed with observed values of temperature and wind speed and to obtain the power output a BEM-code was included. Another example of FENSAP-ICE being used for wind turbine application is seen in [7] and the [8], where performance degradation and power losses were studied and the possibilities of the design of an anti-icing system was proposed. The drawback of FENSAP-ICE is the strong link to the aircraft industry and that the model does not include shedding, which allows exaggerated ice horns to form [3]. Production loss assessment methods driven by numerical weather models [3] are typically fed with 1 hour based data. Such data can also be used in CFD simulations, as well as data of a much smaller time-scale. Furthermore, distributions of the Median Volumetric Diameter (MVD) can be included, which completely eliminates the issue of constant meteorological conditions.

A challenge when studying icing is the accessibility to observed and measured data. One problem is the reliability of the measurement equipment, as pointed out in [9]. Another is the complexity related to measuring and observing icing directly on the turbine itself, as seen at the TechnoCentre éolien, Quebec, Canada [10]. Thus, to circumvent the issue an ice sensor, installed at Vattenfall's Swedish wind farm, Stor-Rotliden, has been chosen as the foundation of the develop-

[1]Weather Research and Forecasting

ment of an CFD-based icing model for wind turbines. The ice sensor is combitec IceMonitor, which is a 0.5m long freely rotating cylinder with a diameter of 3cm. It is installed on a met mast together with other measurement equipment, as seen in Figure 1. From the CFD model development based on the IceMonitor, including testing and validation, the approach will be applicable to any geometry such as a turbine blade or a blade section. As the numerical platform of the study ANSYS-FLUENT has been used.

(a) (b)

Fig. 1. The IceMonitor to the left in the pictures at Stor-Rotliden wind farm with limited ice (a) and fully iced (b).

Other studies using ANSYS-FLUENT for icing applications are seen in [11] and [12]. In [11] the flow field around three different iced airfoils based on the airfoil (NACA 63-415) are simulated. The three geometries were obtained from experiments using in-fog icing conditions in a refrigerated wind tunnel. The k-ω SST turbulence model was used to study and compare numerical and experimental values of the lift, drag and pressure coefficients. A similar study was carried out in [12]. Another icing related study carried out using ANSYS-FLUENT is presented in [13], where the droplet collection efficiency (β) was calculated using an Eulerian frame, by employing the User-Defined-Scalar-Transport framework in ANSYS-FLUENT. In the Eulerian frame the collection efficiency was defined as:

$$\beta = \frac{\alpha_n(\mathbf{u}\cdot\mathbf{n})}{U_\infty} \quad (1)$$

where $\mathbf{n}$ is the unit surface normal vector, α_n is the normalised droplet volume fraction on the surface and U_∞ is the free-stream velocity. This approach, of calculating the collection efficiency, is equivalent to the approach by FENSAP-ICE presented in [14]. Common for the previous work carried out using ANSYS-FLUENT is:

- decoupling of the iced geometry obtained and studying the aerodynamic changes of the iced geometry
- decoupling of the impingement model and ice model with the geometry change of the iced object

However, this study aims to combine the entire process into a full icing model capable of:

1) Impingement model (multiphase flow and collection efficiency)
2) Ice model including runback
3) Generation of new geometry of iced object
4) Study of the aerodynamic changes and the ability to add a heat source for de-icing applications

This paper focuses on the generation of the new geometry of the iced object. This is an essential step, which has to be robust and able to handle any kind of ice accumulation on the surface. From a CFD point of view, two approaches are suitable for this purpose:

- variable porosity
- surface boundary displacement

If taking a look at fouling deposition modelled in various CFD-combustion applications, the underlying methodology is similar to the accumulation of ice. An example is the work seen by Knudsen [15], where a porosity model is developed in ANSYS-CFX to account for the geometry change due to ash deposition. Using porosity approach in CFD simply means prescribing a porosity to each cell and updating the porosity according to the accumulated mass. Thus, if the given cell is completely covered by mass of for example ash slag, the cell will be included as completely blocked in the CFD flow solution. In this way, the geometry change is taken into account. The advantage of this approach is that a complex mesh-update algorithm is avoided and the computational time is kept low. The drawback could be the need for a very fine mesh to account for smaller-scale geometry changes, which might be interesting to include in an ice accretion model.

The other way to account for the accumulated mass is to update the surface boundary mesh and generate a new iced geometry. In [16] a method to predict ice on an airfoil is presented using a 2D panel method and Messinger's model as the thermodynamic model. From the calculated mass of accumulated ice, the ice thickness is found as $h = \frac{\dot{m}_{ice}\Delta t}{\rho_{ice}\Delta s}$ (m), where ρ_{ice} is the ice density [16] [17]. The new surface is generated by first placing the new nodes at the corresponding thickness in a perpendicular direction to the old surface followed by connecting the nodes by average points between the nodes. To account for shape distortion and twisting of the grid, for example, glaze ice conditions, a smoothing algorithm is included, which can delete and renumber nodes. In [18] heat and mass transfer is studied with in improved roughness model for aircraft applications using a the 2D CIRAMIL code, which is a combination of a 2D potential flow solver and a thermodynamic solver. The panels are updated by using the bisection-method, which insures that the ice grows continuously in the normal direction to the surface. The panels are calculated based on the old nodes and the ice sections are limited by the bisection of angles with adjacent neighbouring panels. In FENSAP-ICE the mesh is updated similar to [16] by a surface displacement vector $\Delta h = \frac{\dot{m}_{ice}\Delta t}{\rho_{ice}}$, which is obtained from the ice accretion speed vector normal to the surface [19]. The ice accretion speed vector is used as an input to an Arbitrary Lagrangian-Eulerian (ALE) formulation to displace the surface in time [19] [20].

II. Method

The model is set-up in the environment of ANSYS-FLUENT following a preliminary modelling study [21]. The Euler-Euler multiphase model [22] is employed to express the two-phase droplet laden flow of air and super-cooled water droplets in combination with the k-ω SST turbulence model [11], assuming no coalescence or break-up of particles and

no heat or mass transfer between the phases. As mentioned previously two methods are suitable for taking the accumulated mass of ice into account. In this study it was chosen to use the surface boundary displacement method. The surface boundary displacement are addressed by employing User Defined Functions. The entire method is illustrated by the flow-diagram in Figure 2.

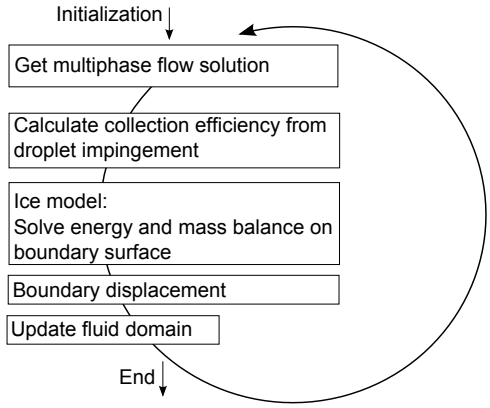

Fig. 2. Flow diagram of the modelling structure

A. Ice Model

In this study a simplified rime ice situation is modelled, since the surface boundary displacement is the main objective of the paper. Under rime ice accretion it is assumed, that all particles which hit the surface will freeze instantly and turn into ice. In fact, the complete model is based on a set of partial differential equations (PDEs), originally presented in [6]. The PDEs will be integrated in the model frame by the User-Defined-Scaler-Transport framework in ANSYS-FLUENT [23]. The mass of ice $\dot{m}_{ice}$ initiates the mesh update algorithm and is explained in the following section.

B. Boundary displacement

To insure a reliable and robust surface boundary displacement, the accumulated mass of ice has to be conserved, the ice growth is continuous and normal to surface and the displacement must be mesh independent. The surface boundary displacement is initialised by the Dynamic-mesh package by ANSYS-FLUENT [22], from where the DEFINE_GRID_MOTION macro is used, which is linked to an ANSYS-FLUENT node position algorithm. The macro is transient and by an iterative process the node points can be updated. The approach of this study is inspired by work using the ice height Δh_{ice} to displace the node points.

From the instantaneous accumulated mass of ice the mesh is updated by calculating a node displacement vector $\vec{v}_{n,i}$ giving an (x,y,z) coordinate of the new location of the node. The node displacement vector is obtained by a face-looping approach as follows:

1) Obtain face cell centre position displacement vector ($v_{f,i}$), see Equation 2
2) Relate/convert face cell centre position to new node positions
3) Move node point location by node displacement vector by an iterative mesh update process

$$v_{f,i} = \frac{\dot{m}_{ice}}{\rho_{ice}}\mathbf{n} \tag{2}$$

where, ρ_{ice} is the density of ice and $\mathbf{n}$ is the surface normal. Figure 3 illustrates the boundary displacement only based on the face centre displacement vectors. The shaded grey area is the area from each boundary cell, which is occupied by accumulated ice according to the face centre displacement vector. The red circle shows the inconsistent distribution of the accumulated mass of ice between the faces, which challenges the creation of the new surface boundary.

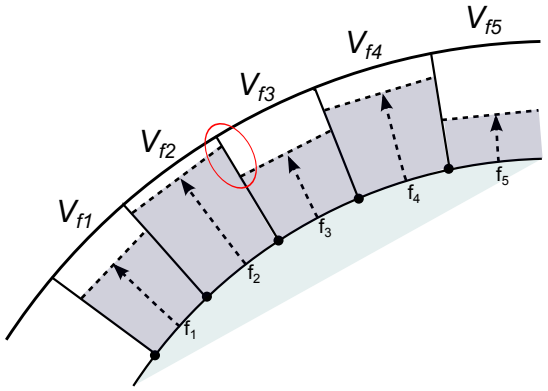

Fig. 3. Boundary displacement by face centre displacement vectors.

To circumvent the issue illustrated in Figure 3, corresponding node displacement vectors are found by liner interpolation, as illustrated in Figure 4. From this method, the total accumulated mass of ice in each boundary cell will be distributed evenly to created the new surface boundary of the object, illustrated by the dashed line.

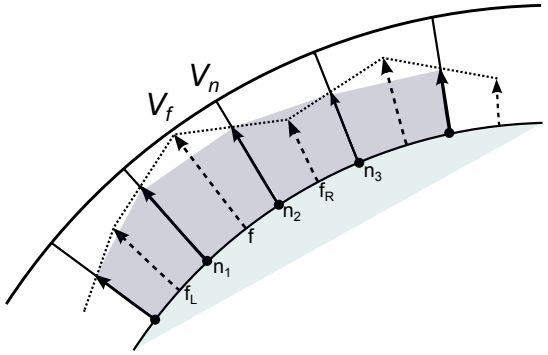

Fig. 4. Boundary displacement by converting face centre displacement vectors to node displacement vectors.

By the linear interpolation the contribution from the node neighbouring face, f_L and f_R , to the node displacement vector is enabled. The nodes are updated according to the following expression:

$$p_{n,i}^{t+\Delta t} = p_{n,i}^{t} + v_{n,i}^{t}\Delta t \tag{3}$$

where $p_{n,i}$ is the current node positions, t is the current time and Δt the time step. The boundary layer displacement is fully transient, which means that the mesh is updated every time step.

III. Results

Two 2D situations were studied, one with an angle of attack(aoa) of 0° and one with an aoa of 16°. The C-grid topology was used to generate the grid, which consist of an outer unstructered part and an inner structured part surrounding the cylinder, as seen in Figure 5.

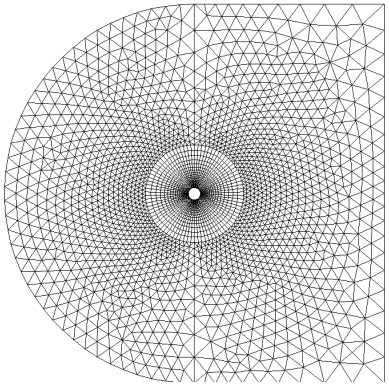

Fig. 5. Computational domain.

The conditions of the simulations are shown in Table I.

TABLE I. Test case settings. * = number of cells at boundary

Parameter:		
Total no. cells	5013	mixed cells
BC cells*	82	no. cells
Time step size	0.01	(s)
Simulation time	15	(min)
aoa	0, 16	^{o}
U_∞	20	$\frac{m}{s}$
T_∞	-10	C^o
$\alpha_{d,\infty}$	$3.33{\cdot}10^{-7}$	$-$
LWC	0.3	$\frac{g}{m^3}$
MVD	10	μm

In the simulation it is assumed that $\dot{m}_{ice} \approx \dot{m}_{imp} = U_\infty LWC\beta$. This implies that all mass, which hit the object will freeze and accumulate on the boundary. The assumption is close to assuming rime ice accretion. The collection efficiency (β) at t = 0 min, for the two cases are seen in Figure 6. As expected the maximum collection is shifted to the left for the case of aoa = 16°.

Figure 7 and Figure 8 shows the geometry change over 15 minutes of ice accretion, divided into intervals of 5 minutes. The ice growth is seen on the front of the cylinder around the stagnation point, which seems reasonable because of small MVD which results in the particles following the airflow and being deflecting around the object.

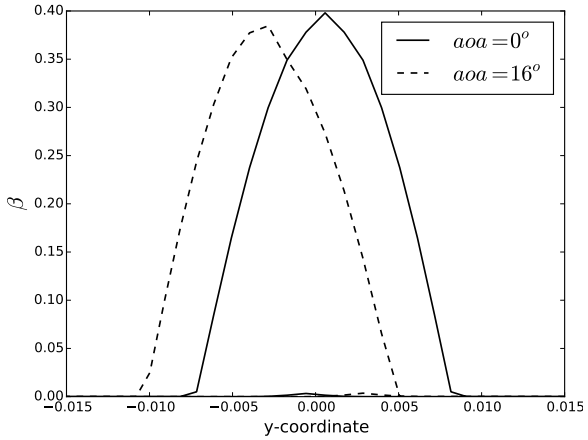

Fig. 6. Collection efficiency before ice accretion.

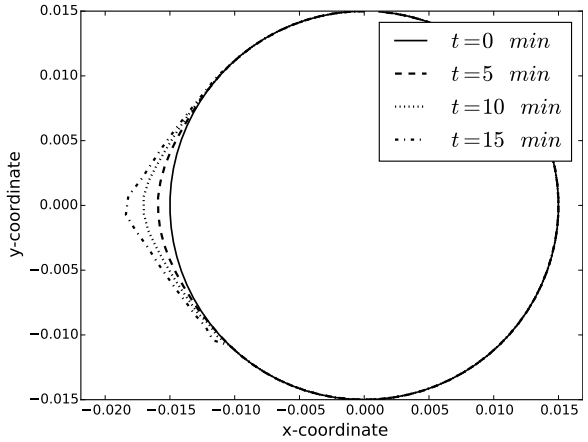

Fig. 7. Ice accretion shapes during 15 minutes of ice accretion at aoa of 0°.

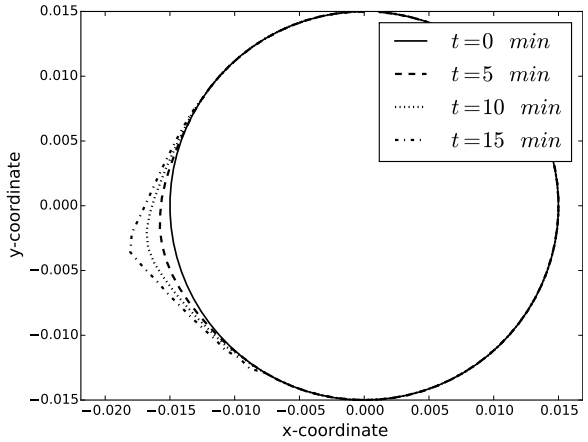

Fig. 8. Ice accretion shapes during 15 minutes of ice accretion at aoa of 16°.

IV. Discussion and Conclusion

In this study it was found, that updating the mesh using the dynamic-mesh frame in ANSYS-FLUENT by applying a node displacement algorithm was feasible. A test case of 15 minutes of ice accretion was simulated successfully. To improve the mesh update a higher order discretisation scheme will be tested, such as the spline method. Furthermore, since the mesh update is fully transient it is time consuming especially for more dense mesh. Thus, for simulating longer icing events it is considered to let the model run in a so-called *quasi-steady* mode, similar to the 17 hours icing event in [24]. To improve on the ice model, a thermodynamic model will be included, which enables the study of glaze ice accretion and, for example, de-icing conditions.

Acknowledgement

Marie Cecilie Pedersen would like to thank Vattenfall R&D in Kolding and the Danish Agency for Science, Technology and Innovation for their financial support of the industrial PhD project.

References

[1] L. Makkonen, "Models for the Growth of Rime , Glaze , Icicles and Wet Snow on Structures," *Philosophical Transactions: Mathematical, Physical and Engineering Sciences*, vol. 358, no. 1776, pp. 2913–2939, 2000.

[2] T. S. S. Institute, "Athmospheric Icing on strutures, SS-ISO 12494," The Swedish Standards Institute, Tech. Rep., 2001, technical report.

[3] N. Davis, "Icing Impacts on Wind Energy Production," *PhD diss., Vestas Wind Systems A/S and The Technical University of Denmark, DTU Wind Energy*, 2014.

[4] N. Davis, A. N. Hahmann, N.-E. Clausen, and M. Žagar, "Forecast of Icing Events at a Wind Farm in Sweden," *Journal of Applied Meteorology and Climatology*, vol. 53, no. 2, pp. 262–281, 2014.

[5] D. Switchenko, W. G. Habashi, G. Baruzzi, and I. Ozcer, "FENSAP-ICE Simulation of Complex Wind Turbine Icing Events, and Comparison to Observed Performance Data," in *32nd ASME Wind Energy Symposium*, 2014.

[6] B. L. Messinger, "Equilibrium Temperature of an Unheated Icing Surface as a Function of Air Speed," *Journal of the Aeronautical Sciences (Institute of the Aeronautical Sciences)*, vol. 20, no. 1, pp. 29–42, 1953.

[7] T. Reid, G. Baruzzi, I. Ozcer, D. Switchenko, and W. Habashi, "FENSAP-ICE Simulation of Icing on Wind Turbine Blades, Part 1: Performance Degradation," in *51st AIAA Aerospace Sciences Meeting including the New Horizons Forum and Aerospace Exposition 07-10 January 2013, Grapevine (Dallas/Ft. Worth Region), Texas*, 2013.

[8] ——, "FENSAP-ICE Simulation of Icing on Wind Turbine Blades, Part 2: Ice Protection System Design," in *51st AIAA Aerospace Sciences Meeting including the New Horizons Forum and Aerospace Exposition*, 2013.

[9] H. Wickman, "Evaluation of Field Tests of Different Ice Measurement Methods for Wind Power," Uppsala University, Sweden, Tech. Rep., 2013, master Thesis.

[10] M. Wadham-Gagnon, "Wind Energy in Cold Climate," TechnoCentre éolien, Gaspe, Quebec, Canada, Tech. Rep., 2015, internal presentation at Vattenfall.

[11] F. Villalpando, M. Reggio, and A. Ilinca, "Numerical study of flow around iced wind turbine airfoil," *Engineering Applications of Computational Fluid Mechanics*, vol. 6, no. 1, pp. 39–45, 2012.

[12] X. Chi, B. Zhu, T. Shih, H. Addy, and Y. Choo, "CFD analysis of the aerodynamics of a business-jet airfoil with leading-edge ice accretion," *AIAA Paper*, vol. 560, 2004.

[13] S. Wirogo and S. Srirambhatla, "An Eulerian Method to Calculate the Collection Efficiency on Two and Three Dimensional Bodies," *AIAA paper*, vol. 1073, 2003.

[14] Y. Bourgault, Z. Boutanios, and W. G. Habashi, "Three-Dimensional Eulerian Approach to Droplet Impingement Simulation Using FENSAP-ICE, Part 1: Model, Algorithm, and Validation," *Journal of Aircraft*, vol. 37, no. 1, pp. 95–103, 2000.

[15] S. K. Kær, "Numerical Investigation of Deposit Formation in Straw-fired Boilers," *PhD diss., Aalborg University*, 2001.

[16] C. Son, S. Oh, and K. Yee, "Quantitative analysis of a two-dimensional ice accretion on airfoils," *Journal of Mechanical Science and Technology*, vol. 26, no. 4, pp. 1059–1071, 2012.

[17] Y. Cao, C. Ma, Q. Zhang, and J. Sheridan, "Numerical simulation of ice accretions on an aircraft wing," *Aerospace Science and Technology*, vol. 23, no. 1, pp. 296–304, 2012. [Online]. Available: http://dx.doi.org/10.1016/j.ast.2011.08.004

[18] G. Fortin, J.-L. Laforte, and A. Ilinca, "Heat and mass transfer during ice accretion on aircraft wings with an improved roughness model," *International Journal of Thermal Sciences*, vol. 45, no. 6, pp. 595–606, 2006.

[19] NTI, "User Manual FENSAP-ICE, Version 2012 release 1.1," Newmerical Technologies International, Montreal, Quebec, Canada, Tech. Rep., 2012, manual.

[20] W. Habashi, J. Dompierre, Y. Bourgault, M. Fortin, and M.-G. Vallet, "Certifiable computational fluid dynamics through mesh optimization," *AIAA journal*, vol. 36, no. 5, pp. 703–711, 1998.

[21] M. C. Pedersen and C. Yin, "Preliminary modelling study of ice accretion on wind turbines," *Energy Procedia*, 2014. [Online]. Available: http://dx.doi.org/10.1016/j.egypro.2014.11.1102

[22] ANSYS Inc, "ANSYS Fluent Theory Guide," ANSYS, Tech. Rep. Relaese 15.0, November 2013.

[23] Ansys Inc, "ANSYS Fluent UDF Manual," ANSYS, Tech. Rep. Relaese 15.0, November 2013.

[24] C. N. Aliaga, M. S. Aubé, G. S. Baruzzi, and W. G. Habashi, "FENSAP-ICE-UNSTEADY: Unified In-Flight Icing Simulation Methodology for Aircraft, Rotorcraft, and Jet Engines," *Journal of Aircraft*, vol. 48, no. 1, pp. 119–126, 2011.

Neural network approach to characterize the atmospheric ice compressive strength

Farid H[1], Farzaneh M [1], A. Saeidi [1], F. Erchiqui [2]

Canada Research Chair on Engineering of Power Network Atmospheric Icing (INGIVRE)
University of Quebec in Chicoutimi, Quebec, Canada

[2] Laboratoire de Bioplasturige et Nanotechnologie, Université du Québec en Abitibi-Témiscamingue, Rouyn-Noranda, Québec, Canada
hicham.farid1@uqac.ca

Abstract:

Atmospheric icing of structures is a phenomenon that hampers human activities in cold climate regions. Coupled with environmental effects such as wind and temperature fluctuations, accumulated ice can shed, which may lead to serious damage to equipment.

Characterizing the compressive strength of atmospheric ice is important to understand the ice shedding phenomenon. For this purpose, several tests were carried out in order to study the behavior of atmospheric ice under compression, and under different environmental and structural parameters.

In order to simulate the natural processes of atmospheric icing, ice was accumulated in the closed loop wind tunnel of CIGELE (*Industrial Chair on Atmospheric Icing of Power Network Equipment*), , Three temperatures were considered (-20 ^{o}C, -15 ^{o}C and -5 ^{o}C) in this experiment. The wind speed inside the tunnel was set to 20 m/s in order to obtain a mean volume droplet diameter of 40µm and a water liquid content of 2.5 g/m^3. Each type of ice was tested at the same temperature at which it had been accumulated. A tomographic analysis was carried out on a small specimen (cylinder of 1 cm diameter × 2 cm length) for each temperature in order to quantify the porosity and determine the grain size and their distribution.

The neural network approach was used to predict the compressive strength of atmospheric ice as function of strain rate and temperature. Four strain rates ($10^{-4}s^{-1}$, $10^{-3}s^{-1}$, $10^{-2}s^{-1}$ and $10^{-1}s^{-1}$,) and three temperatures (-20°C, -15°C and -5°C) were considered. The obtained results show the capability of the used neural networks to reproduce the compressive behavior of atmospheric ice under different conditions.

Keywords: ***Atmospheric ice, ice shedding, compressive strength, neural networks, brittle failure.***

INTRODUCTION

The study of ice accretion on structures is an issue of paramount importance in cold climate regions. Coupled with wind, accumulated ice on structures may impair their operation, and result in significant damage, [1]–[3]. The accumulation of ice on the power transmission lines may create a variety of problems: collapse of transmission towers under excessive load, breaking of electrical cables and wires due to dynamic loading (fatigue), ice-covered insulator flashover, etc.[1], [4].

Atmospheric icing is a meteorological phenomenon that is manifested by a deposition of water drops or snowflakes on a cold surface exposed to the ambient air [2], [4], [5].Although the dangers caused by ice accretion on structures are considerable, ice shedding is as much important. This mechanism, which corresponds to the reduction of accumulated ice on a surface, is the source of several dynamic and structural instabilities on the power lines network[6]. The understanding of this phenomenon imposes a deep knowledge of the structural and rheological properties of atmospheric ice.

Unlike other types of ice such as fresh water ice or sea ice[7], few works on the mechanical properties of atmospheric ice have been reported in the literature, [8], [9]. The compressive strength of atmospheric ice is considered to be the most significant property of icing engineering, especially as concerns the understanding of ice shedding by mechanical breaking which is affected by environmental and structural parameters such as strain rate, temperature, wind speed, porosity, liquid water content, etc.[10].

In order to characterize the ice fracture under different types of loading, researchers have proposed different failure criteria[11]. However, the explicit expression of these laws is complex, most of the time not including some basic environmental and structural parameters.

Algorithms associated with the artificial neural networks can prove to be an interesting alternative to the classical algorithms, as they can model and predict systems behavior without the necessity of explicit relationships between its components. The neural networks have been recently used in many engineering fields[12], and showed their capacity to adapt to problems of different nature.

In this paper, the backpropagation neural network is used to predict the compressive strength of atmospheric ice as function of strain rate and temperature. The experimental data is used to train and test the neural network. A comparison with other sets of experimental data shows the good predictive capacity of the proposed model.

I. ATMOSPHERIC ICE COMPRESSIVE STRENGTH EXPERIMENTAL DATA

Mechanical properties of atmospheric ice are subject to changes under several parameters such as temperature, strain rate, anisotropy and porosity. Therefore, one of the mean objectives of the present study is to elucidate the effect of those parameters by carrying out compressive tests on cylindrical ice specimens prepared under different laboratory conditions.

Atmospheric ice was prepared under specific conditions in the atmospheric icing research wind tunnel.

The following technique was used to simulate the natural atmospheric icing process. Warm water was injected into a cold airstream through the nozzles located at the trailing edge of a spray bar. Three independent supply lines provide air and water to the nozzles. Using a computer program allowing to control the flux and velocity of airflow inside the tunnel, air speed was controlled to have a mean volume droplet diameter (MVD) of 40 μm and liquid water content (LWC) of 2.5 g/m^3. Atmospheric ice was accumulated on a rotating aluminum cylinder (diameter 78 mm and length 590 mm). The cylinder was carefully cleaned with hot water and soap before each set of experiment, placed in the middle of the test section of the wind tunnel, and fixed by each edge against a rotor making 1 rpm, the rotation of the aluminum cylinder making the thickness distribution of ice uniform as illustrated in Figure 1. The distance between the cylinder and spray nozzles is large enough for the droplets to reach kinetic and thermodynamic equilibria.

Figure 1 Accumulated atmospheric ice on the rotating cylinder

Depending on accumulation conditions such as air velocity and liquid water content, the time needed to grow a sufficient thickness of ice on the cylinder varied from 2 to 4 hours, sometimes up to 8 hours.

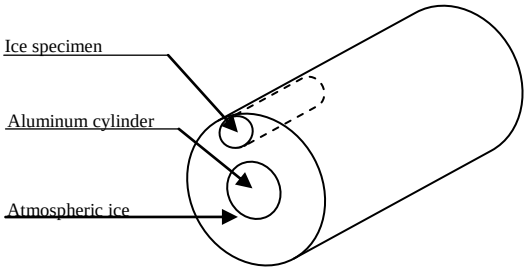

Figure 2 Schematic illustration of accumulated atmospheric ice and the specimen cut

Figure 2 shows the specimen orientation according to the accumulated ice. Once a thickness of 60 mm was obtained, prismatic blocks were cut using a warm aluminum blade in order to avoid any mechanical stress, and then machined into a cylindrical shape with a diameter of 40 mm and a length of 100 mm.The specimen dimensions are chosen in order to avoid any influence of grain size on the compressive behavior of ice[13].

The atmospheric ice specimen were prepared at three different temperatures; -20, -15 and -5 °C. A closed-loop electrohydraulic testing machine was used to carry out all the compressive tests. The machine had two load cells of capacity 250 KN and 25 KN, the latter chosen for ice testing. The whole system was located inside a controlled cold room, with temperature ranging from -40 °C to 0 °C, with an accuracy of ±0.5 °C.

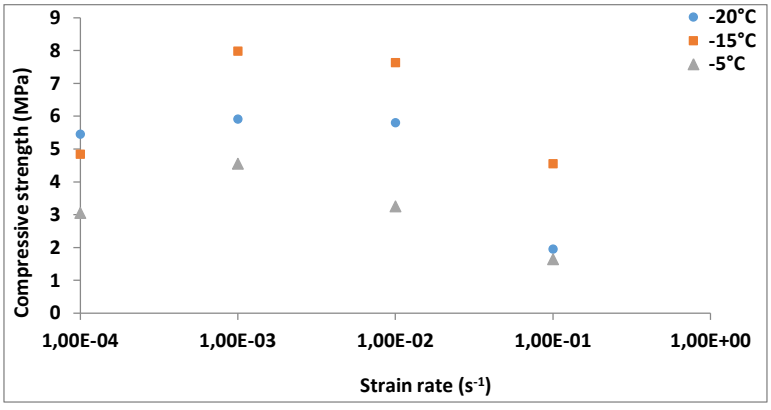

Figure 3 Compressive strength evolution versus strain rate for different temperatures

In each test, the compressive stress versus strain was recorded as function of time, temperature and strain rate. Figure 3 shows the evolution of ice compressive strength versus strain rate for the three different temperatures.

II. COMPRESSIVE STRENGTH MODELING USING NEURAL NETWORKS

A. The neural networks approach

Recently, neural networks have been used in many areas including classification, pattern recognition, speech synthesis, diagnosis, identification and control of dynamic systems[14].

The use of neural networks is justified by the fact that they can approximate nonlinear functions without having to specify explicit relationships between different variables. Their performance keeps improving continuously while relying on dynamic learning, which provides a robust neural identification towards the parametric variations and disturbances that can affect the operation of the studied system.

In the present work, neural networks are exploited the reproduce and predict atmospheric ice compressive strength as function of temperature and strain rate. The well-known multilayer perceptron is used for this application.

B. Type, structure and training algorithm

The used neural network is composed of one input layer, many hidden layers, and one output layer. The input layer contains two neurons (temperature and strain rate), the output layer contains one single neuron, while the number of the hidden layers varies depending on the experimental set and the needed modeling accuracy.

Figure 4 illustrates the architecture of the used neural network: 60% of the experimental data is used for training, 20% is used for validation, while 20% is kept for testing purposes. In order to minimize the error between the desired value and the network output, a back propagation learning algorithm is used, combined with the Levenberg-Marquardt optimization algorithm. In addition, the sigmoid function is selected as activation function of the hidden layers.

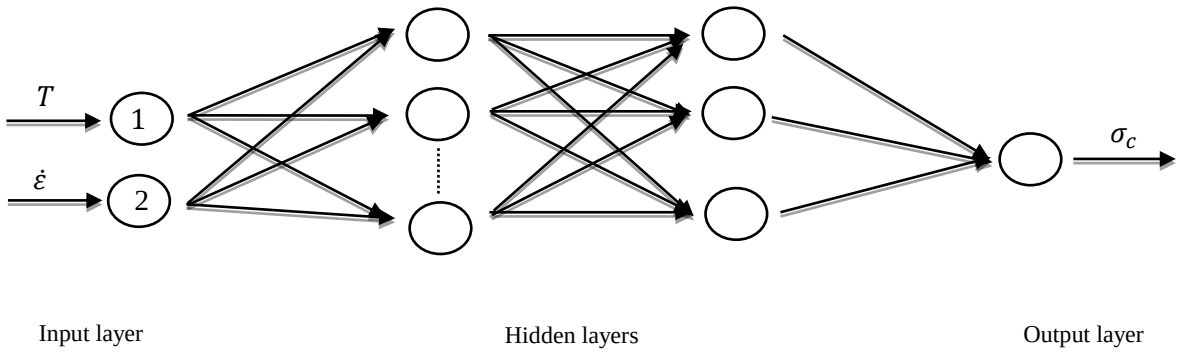

Figure 4 The architecture of the neural network model

III. ICE COMPRESSIVE STRENGH PREDICTION USING NEURAL NETWORKS

The training of the neural network involves three stages: the feed forward of the input training pattern, the back propagation of the associated error, and the adjustment of the weights. After the training completes, the convergence tests is carried out. To avoid overtraining, the convergence criterion used in this study is the root mean-square error of the testing data.

A comparison was made between the experimental values of the compressive strength and those obtained by the artificial neural network model. The results obtained before the training phase are shown as well in Figures 5, 6 and 7, below.

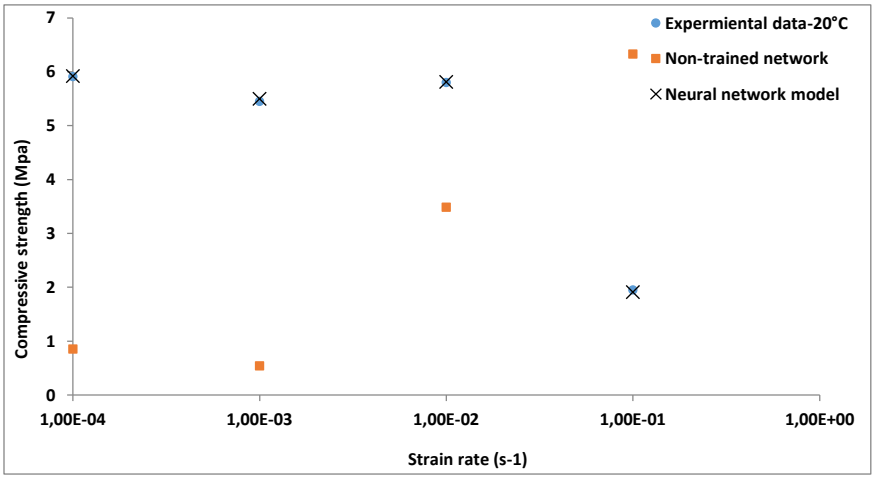

Figure 5 Predicted compressive strength at -20°C

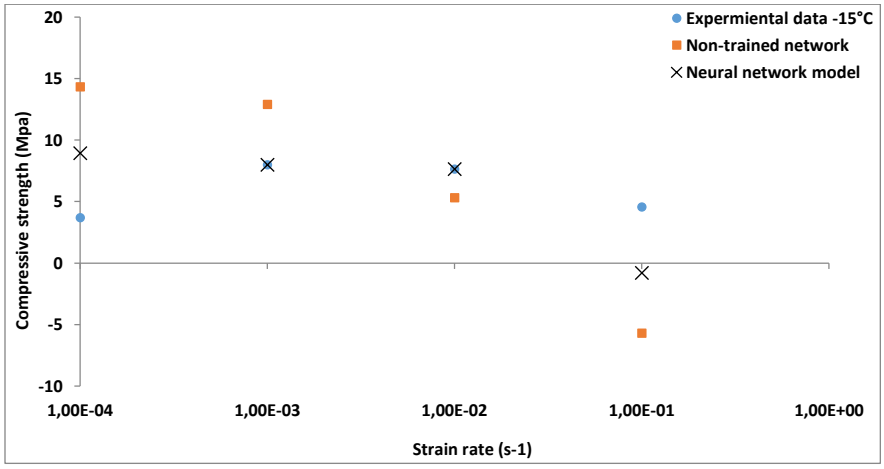

Figure 6 Predicted compressive strength at -15°C

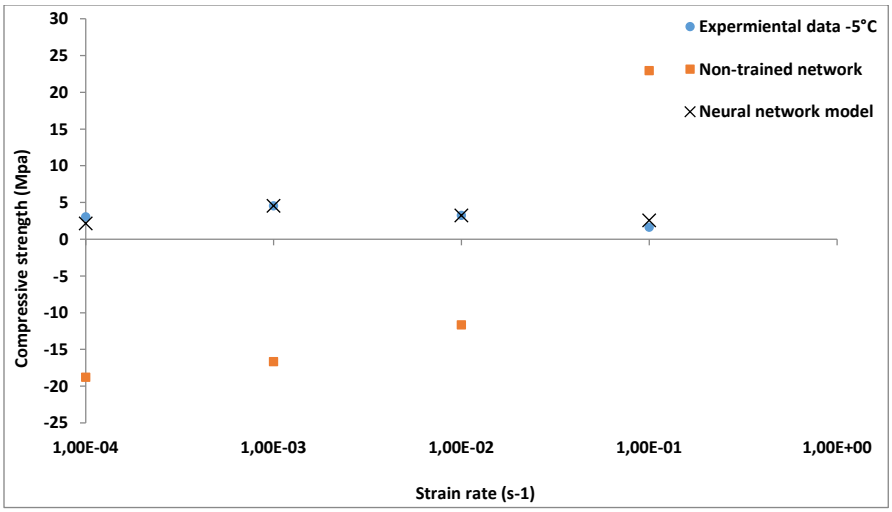

Figure 7 Predicted compressive strength at -5°C

In Figures 5, 6 and 7, results from experiments, non-trained and trained networks are compared. The accuracy level of the learning algorithm is also shown.

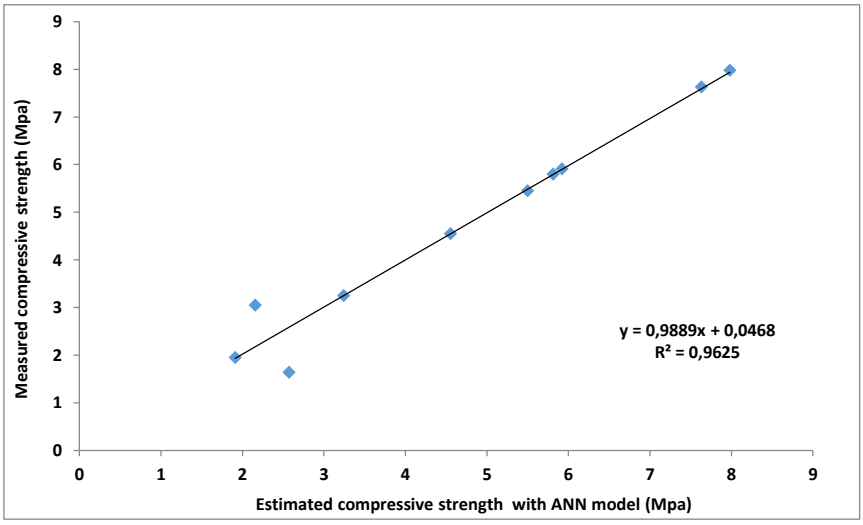

Figure 8: Comparison of the measured compressive strength and the estimated values by the ANN model

In Figure 8, the measured values of the ice compressive strength and estimated values by the neural network model are compared. It is to be noticed that the compressive strength values used do not belong to the data base used to train the network.

The estimated values by the ANN model show a very good correlation with $R^2 = 0.9625$, where R is the linear correlation coefficient. The relative error is 1.71% for -20 °C, 5.37 % for -15 °C and 0.22 % for -5 °C.

CONCLUSION

The objective of this study was to investigate the compressive strength of atmospheric ice as function of different parameters such as temperature and strain rate. It was shown that the predictive accuracy of the neural network approach used for that purpose was very good for compressive strength of atmospheric ice. The relative error was 1.71 % for 20 °C, 5.37 % for -15 °C and 0.22 % for -5 °C.

ACKNOWLEDGEMENT

The present work was carried out within the frame work of the Canada Research Chair on Power Network Icing Engineering (INGIVRE) and the NSERC/Hydro-Quebec/UQAC Industrial Chair on Atmospheric Icing of Power Network Equipment (CIGELE). The authors would like to thank all the sponsors of the project (Hydro-Québec, Hydro One, Réseau Transport d'Électricité (RTE), Alcan Cable, K-Line Insulators, Tyco Electronics, Dual-ADE, and FUQAC) whose financial support made this research possible. The authors also thank Mr Pierre Camirand for the experimental apparatus and Mr Xavier Bouchard for the pictures.

REFERENCES

[1] M. Farzaneh, *Atmospheric Icing of Power Networks*. Springer Science & Business Media, 2008.

[2] M. Farzaneh and W. a. Chisholm, *Insulators for Icing and Polluted Environments*. 2009.

[3] G. Poots, *Ice and Snow Accretion on Structures*. Research Studies Press, 1996.

[4] M. Farzaneh, "Ice accretions on high-voltage conductors and insulators and related phenomena," *Philos. Trans. R. Soc. A Math. Phys. Eng. Sci.*, vol. 358, no. 1776, pp. 2971–3005, Nov. 2000.

[5] J. F. Lozowski, E.P. Gayet, "The atmospheric icing: a review," in *4th IWAIS*, 1988, pp. 1–5.

[6] H. Fuheng, F. Shixiong, "Icing on overhead the transmission lines in cold mountainous district of Southwest China and its protection," in *IWAIS*, 1988, pp. 354–357.

[7] B. Michel, *Ice mechanics*. Presses de l'université Laval, 1978.

[8] M. Eskandarian, "Ice shedding from overhead electrical lines by mechanical breaking," 2005.

[9] A. M. A. Mohamed and M. Farzaneh, "An experimental study on the tensile properties of atmospheric ice," *Cold Reg. Sci. Technol.*, vol. 68, no. 3, pp. 91–98, Sep. 2011.

[10] M. Kermani, M. Farzaneh, and R. Gagnon, "Compressive strength of atmospheric ice," *Cold Reg. Sci. Technol.*, vol. 49, no. 3, pp. 195–205, Sep. 2007.

[11] E. M. Schulson, "Brittle failure of ice," *Eng. Fract. Mech.*, vol. 68, no. 17–18, pp. 1839–1887, Dec. 2001.

[12] H. Adeli, "Neural Networks in Civil Engineering: 1989–2000," *Comput. Civ. Infrastruct. Eng.*, vol. 16, pp. 126–142, 2001.

[13] J. Schwarz, R. Frederking, V. Gavrillo, I. G. Petrov, K.-I. Hirayama, M. Mellor, P. Tryde, and K. D. Vaudrey, "Standardized testing methods for measuring mechanical properties of ice," *Cold Reg. Sci. Technol.*, vol. 4, no. 3, pp. 245–253, Jul. 1981.

[14] M. H. Palmer-BrownD., Draganova C., Pimenidis E., "Engineering Applications of Neural Networks - 11th International Conference, | Springer," 2009.

Multichannel radar monitoring of ice on power transmission lines

Minullin R.G.[1], Goryushin Yu.A.[2], Chereshnyuk S.V.[3], Kasimov V.A.[1], Yarullin M.R.[1]
Borschevskiy A.I.[4]
[1] Kazan State Power Engineering University, [2] OJSC "Federal Grid Company of Unified Energy System",
[3] Research and Development Center at Federal Grid Company of Unified Energy System,
[4] OJSC "Scientific-industrial enterprise "Radioelektronika" named after V.I. Shimko"
Minullin@mail.ru

***Abstract*: A unique technology and technique as radar method and ice detecting apparatus on overhead power transmission lines, which were firstly introduced in substations in Russia are represented here.**

Keywords: overhead power transmission lines, ice on the wires, ice location detection, measuring methods, radar equipment sets, systems operation, observation of ice deposits, advantage of radar detection of ice.

LEGEND AND ABBREVIATIONS

KSPEU	*Kazan State Power Engineering University*
PTL	*Power Transmission Lines*

Currently, there are two ways of ice detection wires of PTL:

1) Forecasting the probability of icing on basis of meteorological data of environment around the wire, taking into account the technical parameters of transmission line.
2) Immediate control of icing with sensors and ice detection devices [1].

Ice forecasting based on meteorological environmental data, is used in many countries where icing on transmission lines is an urgent issue to mitigate or avoid its impact on effectiveness of these lines.

Formation of ice on wires on overhead lines depends on the climatic region and is subject to certain meteorological laws: depends on the humidity and ambient air temperature, wind conditions. Formation of ice also depends on wire diameter, suspension height, mounting inflexibility, twists on wire, current flowing through the load.

Unfortunately till now there is no specific model of ice deposit formation on power transmission lines, which can reliably take into account all these factors, so in such kind of forecast number of false alarms is sufficiently high. In addition, the forecast data may not be specifying indications at the beginning of ice melting, formed on the wires of overhead lines.

Now a days immediate control of icing on power transmission lines is being performed by two methods: method of weight sensors and radar sensing method.

The method of weight sensors is based on comparing the weight of the wires in a passage in absence and presence of ice deposits. The value of wire tension is determined by ice load, wind, as well as ambient temperature. Assessment of the stress state of the wire and comparing it with the maximum permissible value, are carried out with strain sensors. The sensors detect the weight of glaze deposits close to one pillar, their data is transmitted to the receiving station using means of remote control.

Radar detection method of ice on wires of power transmission lines is an alternative method of strain sensors. Radar method is being developed in the KSPEU over 15 years since 1998 [1]. This method is unique in the world according to all available information of last 40 years.

During this period of theoretical and experimental work, methods and sensing apparatus of power transmission lines have been developed, and methods of interpretation of results of sensing ice deposits detection have been established.

Formation of ice on wires represents as impure dielectric, reducing the speed of spreading signal along the line causes additional attenuation due to dielectric losses of electromagnetic wave energy that is consumed in heating of ice layer coating. Radar method allows to determine the occurrence of icing on a transmission line by comparing the propagation time of the reflected signals and their amplitudes in presence and in absence of ice formation.

To probe line with pulse radar (reflectometer), which is a simplified diagram of the connection to the line is shown in Figure 1, *a* totality of the reflected pulses forms a trace. The appearance of ice deposits on line causes a change in trace. If, from the standard (reference) trace (Figure 1, *b* – green line) to deduct the current trace (Figure 1, *b* – blue line), the difference changes are reliably detected by the appearance of a signal corresponding to the end of the line (Figure 1, *b* – red line). The more the characteristic impedance of the line will change under the influence of thickness of ice deposits due to changes of dielectric constant between the wires of the line, the more will be the difference between the traces, the more will decrease pulse amplitude ΔU and will increase pulse delay $\Delta\tau$ (Figure 1, *b*).

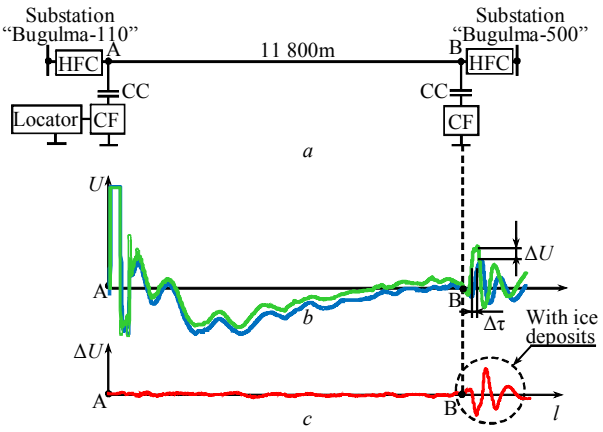

Figure 1. Detection of ice on the line 110 kV "Bugulma-110–Bugulma-500": a – line diagram; b – trace of line without ice (green line) and in presence of ice (blue line); c – difference (red line) line traces without ice and in the presence of ice with fluctuations in the signal at point B due to the presence of ice deposits (HFC – high-frequency choke, CC – coupling capacitor; CF – connection filter, locator - locating the device)

Figure 2 shows as an example of daily bases changes of amplitude *U* (top) and the delay $\Delta\tau$ (lower graph) of the reflected pulses of 110 kV PTL "K Bukash-R Sloboda".

In presence of ice deposits the amplitude U and delays $\Delta\tau$ change synchronously, as shown in Figure 2 (marked by dashed ovals). Using two criteria's U (or ΔU) and $\Delta\tau$ increase the reliability and accuracy of ice detection on wires of power transmission lines.

Except ice deposits, weather conditions, changes in ambient temperature (dashed line in Figure 3, the temperature scale on the right side of the figure), wind effects, and so on can effect on reading on amplitude U and reflected pulse delay $\Delta\tau$.

Hardware-software complex of ice monitoring system consists of the following components:

- radar sensing device;
- communicatation device;
- a computer with a wireless modem and operator interface;
- central server.

Commutation device is designed to connect output/input of radar with one of 16 wires of overhead transmission lines of substation.

The computer along with wireless modem and interface control the operation of radar device, transmit data to the central server, and form the operator interface.

The central server performs as an archiver.

Recently, employees of KSPEU designed and manufactured a small series of radar system for sensing power transmission lines, which are being successfully used to control icing on existing power transmission lines.

In 2012, employees of KSPEU together with employees of OJSC "Scientific-industrial enterprise "Radioelektronika" named after V.I. Shimko" by the order from OJSC "Federal Grid Company of Unified Energy System" designed, manufactured and tested a prototype of an autonomous and automatic ice monitoring system with 16 channels. The complex has a desk-wall mounted version as showed in Figure 3.

Control of icing on power transmission lines has been carrying out since 2009 in lines of 35-110 kV substation "Bugulma-110" (the Volga region), on lines of 110 kV substation "K Bukash" (Volga region), and from 2013 on lines of 110 kV substation "Shkapovo" (Ural) and on the lines of 330 kV substation "Baksan" (North Caucasus). The complex operates continuously in an automatic sensing mode and transmits data every 30 (60) minutes to the control center of KSPEU. Ice deposit data can be transmitted via GSM channel or internet to control room at any distance, providing a user-friendly interface to monitor the dynamics of icing and melting of ice on wires of power transmission lines.

In all substations preliminary diagnosis of condition of transmission lines was performed before control, defined their configurations, measured standard traces, identified channels and high-frequency interfering communication network, set probing mode and took measures to isolate reflected pulses of interference.

Currently in substation "Bugulma-110" radar complex is serving 7 power transmission lines, out of then six are of 110 kV and one in of 35 kV.

A schematic arrangement of controlled power transmission lines in relation with substation "Bugulma-110" is shown in Figure 4.

Figure 5 shows an example of changing parameters ΔU and $\Delta\tau$ of transmission line "Bugulma-110–Bugulma-500" for January 2011-2014.

According to Figure 5 largest ice formation was observed in 1 Jan 2014, when U decreased to 25 relative units, and $\Delta\tau$ increased to 2 microseconds. These values U and $\Delta\tau$ were below to critical, like others, so the melting of ice on power transmission lines "Bugulma-110–Bugulma-500" in the period under consideration did not happen.

As radar measurements are integral measurements, in same ice condition, ΔU and $\Delta\tau$ of long lines are overvalued in relation to short lines. Therefore, more objective parameters are specific

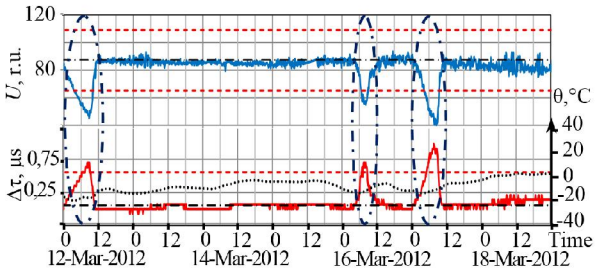

Figure 2. Daily bases change of amplitude U (top) and the delay $\Delta\tau$ (lower graph) of the reflected pulses of 110 kV power transmission line "K Bukash-R Sloboda"; ovals designated registration of ice formations [12.03-18.03.2012]

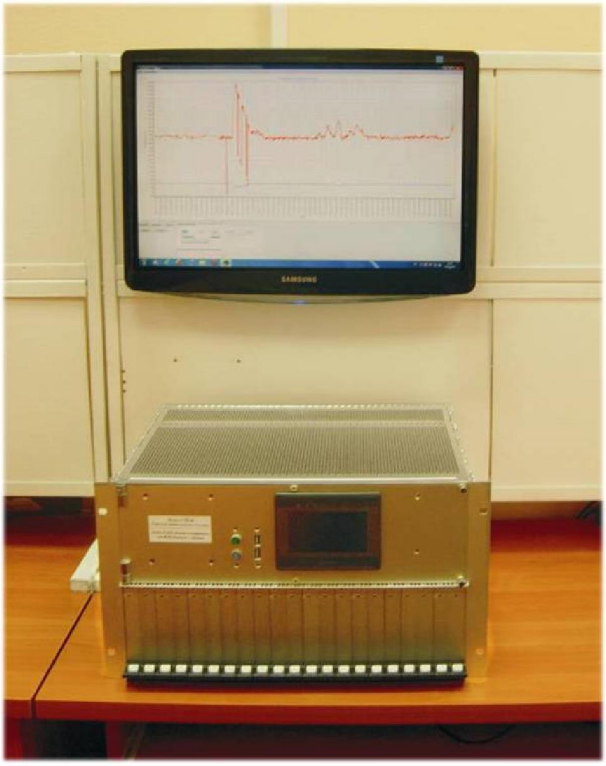

Figure 3. Desktop version of ice detection radar on power transmission lines with 16 wires [2012]

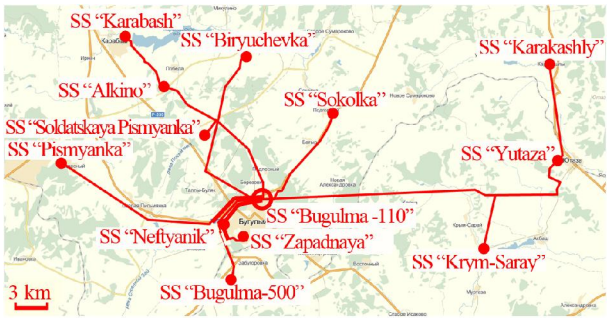

Figure 4. A schematic arrangement of seven power transmission lines of substation "Bugulma-110" controlled by radar complex

attenuation values δK (dB/km) and the delay $\delta\tau$ (μs/km), given to a unit length of the line, in this case length is 1 km.

Examples of multi-channel sensing results in substation "Bugulma-110" for the period November-December 2014 with measurements of specific values $\delta\tau$ are shown in Figure 6. According to the data of Figure 6 largest ice deposit was found

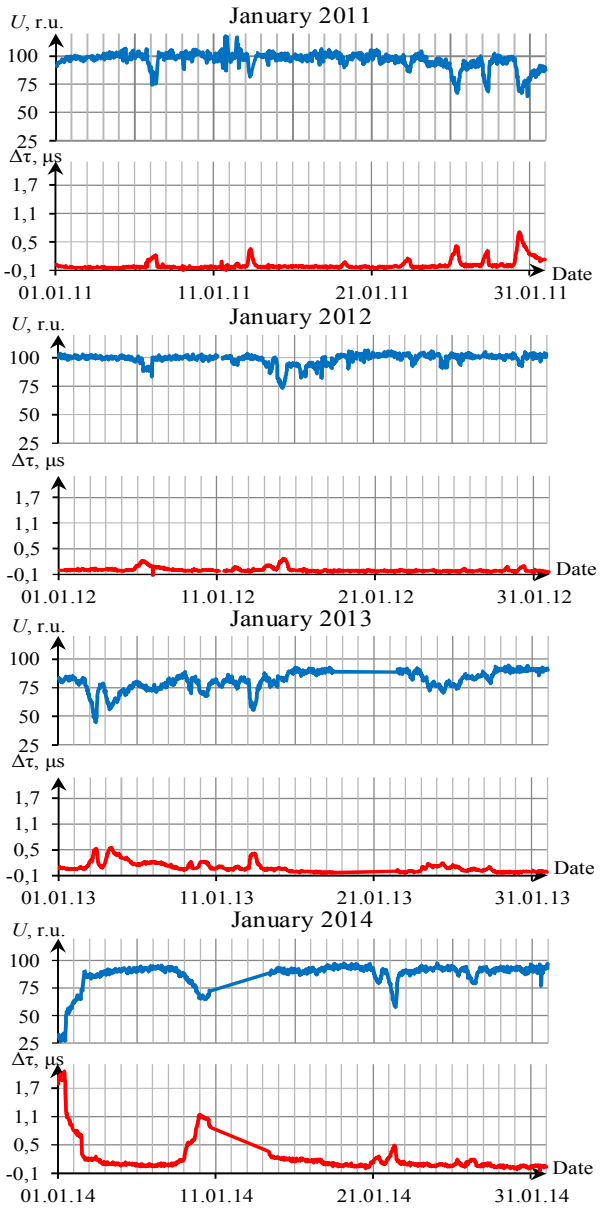

Figure 5. An example of change of the measured amplitude U and delay Δτ reflected radar signals in presence of ice deposits on transmission line "Bugulma-110–Bugulma-500" for January 2011-2014

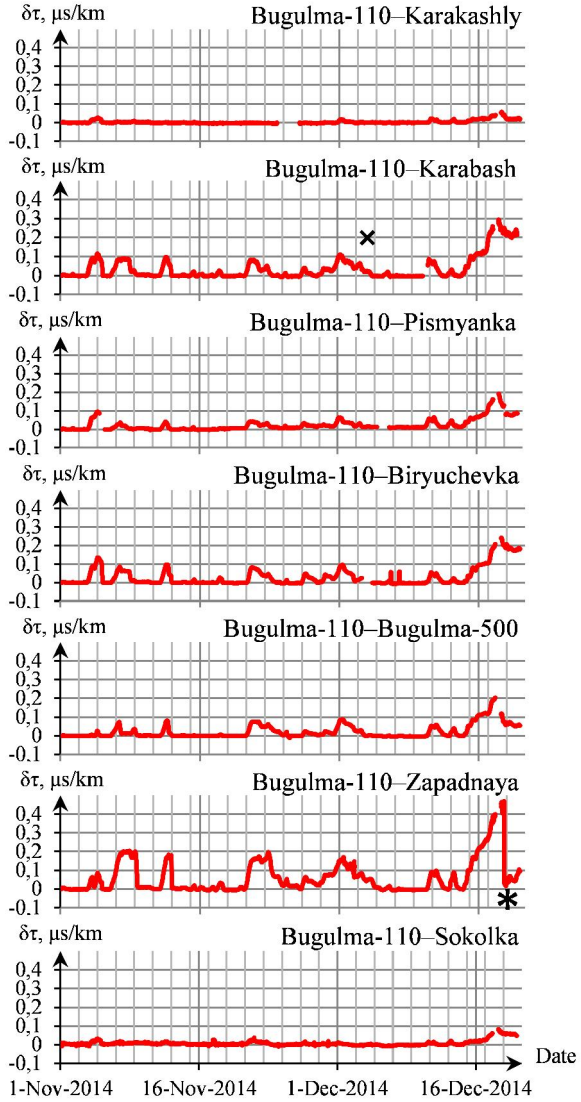

Figure 6. Example of changing the specific delay of reflected radar signals during formation of ice deposit on controlled transmission lines of substation "Bugulma-110" [1.11-20.12.2014]

on the line "Bugulma-110–Zapadnaya", where a breakage was made to prevent wire in December 18, 2014 , ice melting (marked *) at values δK = 1.2 dB/km and δτ = 0.48 μs /km.

Figure 7 shows a photograph of frost formation on wires of transmission line "Bugulma-110–Karabash" December 1, 2014 at 10 o'clock 16 minutes, which corresponded δK = 0.3 dB/km and δτ = 0.1 μs/km (snapping time is marked on Figure 6 with a cross). Naturally, this ice formation could cause breakings power line wires.

Thus, radar ice detection system has been developed and introduced into service to detect ice formation on the 35-330 kV overhead transmission lines. Complexes can reliably monitor the dynamics of ice formation on the wires and clearly define the beginning of time required for melting ice deposits in real time.

Figure 7. Frost formation on wire lines "Bugulma-110–Karabash" December 1, 2014 at 10 o'clock 16 minutes, which corresponded δK = 0.3 dB/km and δτ = 0.1 μs/km (snapping time is marked in Figure 5 with cross)

ACKNOWLEDGMENT

The authors would like to thank OJSC "Federal Grid Company of Unified Energy System" (Moscow), Academy of Science of the Republic of Tatarstan, and OJSC "Setevaya Kompania" (Grid Company of the Republic of Tatarstan) for their financial and technical support.

REFERENCES

[1] Minullin R.G., Petrushenko Yu.Ya., Fardiev I.Sh. Sounding of Air Power Transmission Lines by the Location Method // Russian Electrical Engineering. New York: Allerton Press, Inc., 2008. Vol. 79 (№ 7). PP. 389–396.

Technology radar monitoring of overhead power lines when detecting ice formations

Minullin R.G.[1], Yarullin M.R.[1], Kasimov V.A.[1]
[1] Kazan State Power Engineering University
Minullin@mail.ru

***Abstract*: Radar monitoring technology on overhead power transmission lines for detecting ice deposits formation on wires is described here. The results of using this technology at existing power transmission lines are shown.**

Keywords: ice deposits on wires, power transmission line, radar sensing technology, electromagnetic impulse, optimum impulse

LEGEND AND ABBREVIATIONS

PTL	*Power Transmission Line*
HF	*High Frequency*

Sensing impulses reflected from any available heterogeneous wave resistance from the end of line carry information about appearing ice deposits in radar detecting method.

Formation of ice on wires represents as heterogeneous dielectric, reducing the speed of signal along the line causes additional attenuation due to dielectric losses of electromagnetic wave energy that is consumed in heating of ice layer coating. Radar method allows to determine the occurrence of icing on a transmission line by comparing the propagation time of reflected signals and their amplitudes in presence and in absence of ice formation.

When probing line with pulse radar (reflectometer), totality of the reflected pulses forms a trace. The appearance of ice deposits on line causes change in trace. The more the characteristic impedance of the line will change under the influence of thickness of ice deposits due to changes of dielectric constant between the wires of the line, the more will increase pulse delay $\Delta\tau$ and decrease pulse amplitude U.

Radar sensing technology of ice deposits formation for power transmission line is developed. It includes the following steps:

1. Trial traces are taken and digitally precessed to extract the desired signal from noise in controle line.

2. By using impulse reflectometer length of line is determined. Attenuation in line is calculated to determine the amplitude of sensing source impulse.

For calculation method [1] and software module “attenuation” are used.

As for example, Figure 1 shows the calculation result of signal attenuation in the HF tract of lines with length of 16 630 m and 45 700 m.

According to preliminary calculations of attenuation, the amplitude of radar sensing output signal is estimated. That allows reliably and accurately detect impulses reflected from heterogeneity of the line, with oscillation background in HF tract of PTL.

However, this calculations method has wide assumptions, which is unacceptable in some cases as describing complex process like spreading radar sensing impulses through short-band transmission lines. Especially discrepancies between the

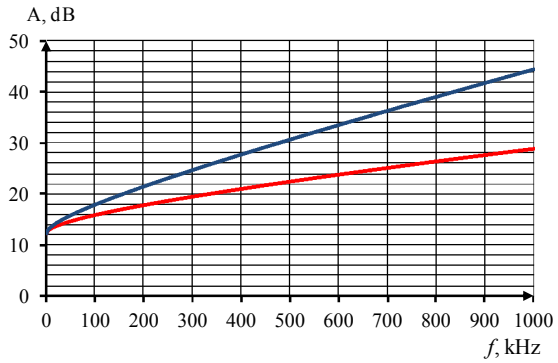

Figure 1. Relation of attenuation with frequency in HF tract, got from lines with length of 16 630 m (red line) and 45 700 m (blue line)

calculated and actual values are observed during formation of rime-ice deposits on wires.

More accurate values of attenuation of each HF tract can be determined individually, as well as combinedly by experiments using special diagnostic apparatus. But measuring of frequency response of HF tract experimentally is not always possible.

In such cases, modeling of HF tract of PTL with special packages such as Matlab Simulink gives more reliable values of calculation.

Shape of reflected pulses from the end of line are also determined. Optimum duration of sensing impulse is selected. Shape of sensing pulse transforms by increasing duration, but the main impulse retains its shape and amplitude, providing a stable measurement of reflected pulse delay (Figure 2).

Reference trace is measured and saved in memory.

3. Interfering condition of controlled line is studied in detail.

4. Sensing mode is defined, parameters of sensing impulse are set.

5. Taste traces are taken and sensing modes are adjusted to optimize them.

6. The value of delay $\Delta\tau$ obtained by measuring and reducing the impulse amplitude ΔU are used to recalculate the thickness of ice deposits. If the line consists of several radar areas then weight and thickness of the ice are calculated for each of them separately.

7. The calculated values of ice deposits are transferred to controle room of power distribution company where these are displayed in user friendly format. In case of detecting ice deposits which can cause accident in power transmission lines, melting decisions is taken.

Over 7 years of experimental research, this technology is proved as a useable. Comparison of radar monitoring device readings and direct observations of ice on power transmission lines is a proof. As an example in Figure 3 shows the dynamics of changes traces in regular intervals of 5-6 December 2011, during the beginning of the intensive growth of snow layer on wires of power transmission lines.

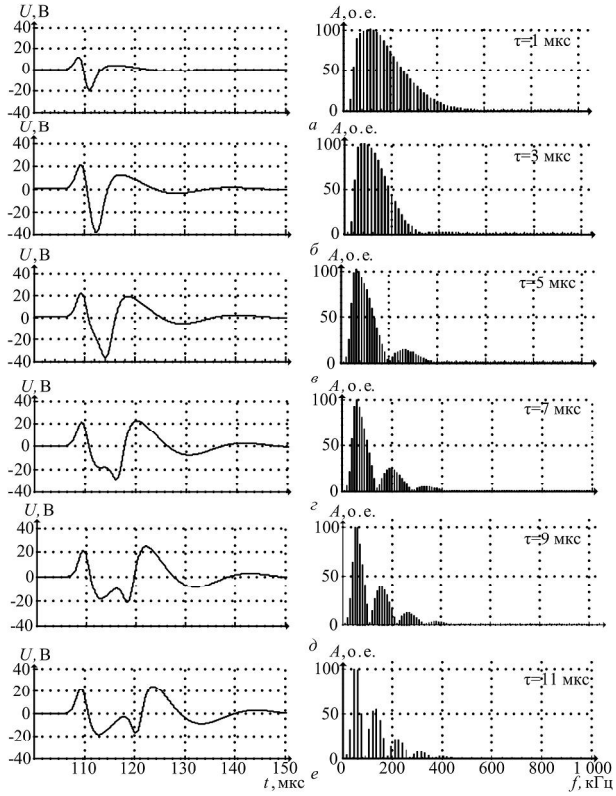

Figure 2. The shape of rectangular impulse with different durations and corresponding spectrums through HF tract of PTL

Fragments of traces with detailed changes in shape of reflected impulses from the HF stopper mounted on PTL at a distance of 40 300 m (left column) and 70 000 m (right column) during formation and growth of ice-snow deposits are shown in Figure 3

Figure 3 shows a clear tendency of reducing amplitude of first oscillations U and increasing its delay $\Delta\tau$ at reflection points according to growth of thickness of snow layer.

Synchrono-proportional decrease of U and increase of $\Delta\tau$ for impulses indicate that the ice-rime layer throughout the entire length (70 000 m) has the same thickness.

In presence of snow clutch with diameter of 2 cm, which is not harmful for integrity of wires, reflected impulses on line are reduced in amplitude U, and delay $\Delta\tau$ increases by 5-6 μs, which is a stable and reliable sign to appear deposits on wires of PTL.

Thus, radar monitoring system and developed technology provide reliable early detection of rime-ice formation on wires of overhead power transmission lines.

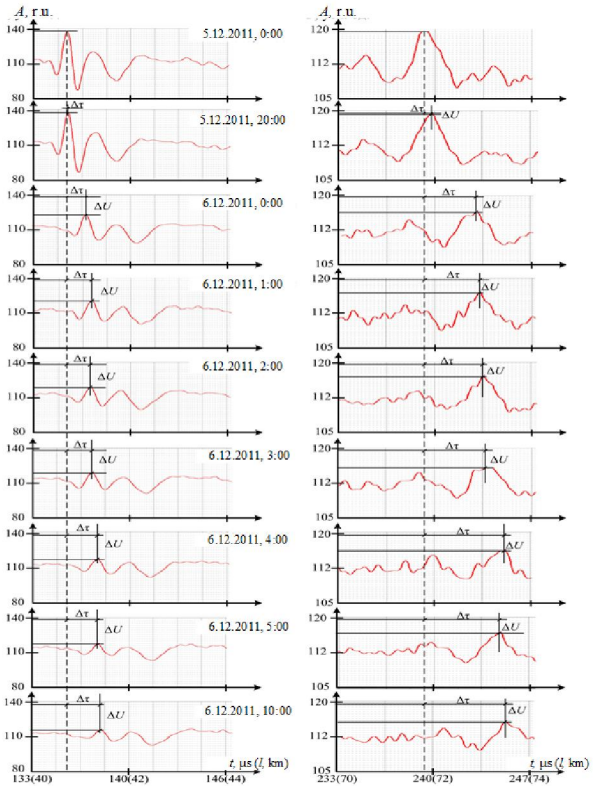

Figure 3. Detailed dynamics of changing fragments of traces of overhead PTL with length of 40 300 m, followed by HF bypass on overhead PTL with length of 29 700 m during period 5.12.2011 - 6.12.2011

ACKNOWLEDGMENT

The authors would like to thank OJSC “Federal Grid Company of Unified Energy System” (Moscow), Academy of Science of the Republic of Tatarstan, and OJSC “Setevaya Kompania” (Grid Company of the Republic of Tatarstan) for their financial and technical support.

REFERENCES

[1] Yu. P. Shkarin “High frequency tracts of communication channel over power transmission lines” — Moscow: NTF "Energopress", 2001. — 72 p.

Determination of ice deposits thickness on overhead power lines conductors by location method

Minullin R.G.[1], Kasimov V.A.[1], Yarullin M.R.[1]
[1] Kazan State Power Engineering University
Minullin@mail.ru

***Abstract*: This abstract describes the location method of ice deposits detection on overhead power lines. The researchers examine influence of ice deposits on parameters of reflected location signals. The method of ice deposits thickness determination on overhead power lines by analyzing the location signal attenuation and delay is offered in the article. The method of subdividing power lines into location probing segments to identify the ice deposits thickness is considered.**

Keywords: overhead power lines, ice deposits on the wires, pulsed signal location probing, attenuation and delay of the reflected signal, thickness of ice deposit, distribution of ice deposit formations according to the thickness along the line.

LEGEND AND ABBREVIATIONS

HF	*High Frequency*
GID	*Glass-Ice Deposition*
OPL	*Overhead Power Lines*

Glaze-ice and rime depositions on overhead power lines may result in damaging of wires and transmission towers. Monitoring of ice formation is necessary in order to prevent these damages. One of the methods to control ice depositions is pulsed signal location method [1, 2]. Pulsed signal location probing device is connected to high frequency channel of transmission line.

According to the pulsed signal location method for power lines diagnostics, information is sent by the pulses, which are reflected from existing obstacles of a line surge-impedance. End of lines, attach areas of taps to power lines, junctions of overhead lines with intermediate cables, as well as deliberately inserted obstacles in the form of HF stopper circuit cause significant changes of self-surge impedance. Studies of sensitivity and stability [3] of pulsed signal location method have shown that due to digital signal processing it is possible to discover even minor changes of the line impedance, a priori existing in the line.

Ice deposition on wires cause changes on location signal parameters: amplitude U and propagation velocity v get reduced, i.e. additional signal attenuation $\Delta\alpha$ and delay $\Delta\tau$ in a line link occur due to the dielectric properties of GID. If the surface of a power line is covered with ice deposits then the electromagnetic wave propagates in an imperfect dielectric, and a portion of the wave energy goes for the heating of ice coating. The biggest change in the signal is caused by pure ice coating, as it forms the densest deposit. Increase of attenuations and delays, caused by ice deposition, depends on ice thickness and length of icing area.

Thus, signal location method allows controlling the whole power line. At the same time, average ice thickness is determined along the line. In this case, it is impossible to differentiate between slight-thickness ice deposition of the whole overhead power line and dangerous concentration of ice on its separate areas. The method of subdividing power lines into location segments with spotted imperfections is used to prevent this drawback.

When considering modal components according to source [4], attenuation of line link with due regard to ice depositions is increased mainly because of attenuation change in the principal mode. Variations of attenuation coefficient $\Delta\alpha$ (dB/km) and phase coefficient $\Delta\beta$ (rad/km) for non-symmetrical line with identical wires, covered with ice, comparing to coefficients for the lines with identical wires ice-free are determined by the following formulas [4]:

$$\Delta\alpha \approx \frac{2\pi 10^{-7} f 10^3 \operatorname{tg}\delta_{Ice} 10^3 K \ln(1+b/r)}{0.115\left(Zp - 60K\ln(1+b/r)\right)\varepsilon'_{Ice}(1+\operatorname{tg}^2\delta_{Ice})};$$

$$\Delta\beta \approx \frac{2\pi 10^{-7} f 10^3 \cdot 10^3 K \ln(1+b/r)}{\left(Zp - 60K\ln(1+b/r)\right)}\left(1 - \frac{1}{\varepsilon'_{Ice}(1+\operatorname{tg}^2\delta_{Ice})}\right);$$

where Z – wave impedance of the principal mode, defined reference to losses caused by ice depositions; p – number of wires in bundled phase; r – radius of bundled phase component; K – coefficient, that takes into account number of wires in bundled phase; ε'_{Ice} – real part of complex ice dielectric constant; and $\operatorname{tg}\delta_{Ice}$ – dielectric loss tangent.

According to the source [4], attenuation for line links in OPL phases is determined for the mode 1 (Z_1 = 360 Ohm), and for intraphase and internal ground wire links – intraphase and internal ground wire modes (respectively Z_{IPh} = 200 Ohm, Z_{IGW} = 240 Ohm).

Signal delay is determined according to max correlation of reflected signals. In order to calculate GID influence on signals it is necessary to use group velocity. Ice has abnormal dispersion in terms of frequency index of location device functioning. Group velocity of signal propagation is calculated as follows:

$$v_{gr} = \left(\frac{1}{v} - \frac{f\mathrm{d}v}{v^2\mathrm{d}f}\right)^{-1};$$

$$v \approx \left(\frac{10^{-7}\cdot 10^3 K\ln(1+b/r)}{Zp - 60K\ln(1+b/r)}\left(1 - \frac{1}{\varepsilon'_{Ice}(1+\operatorname{tg}^2\delta_{Ice})}\right) + \frac{1}{v_0}\right)^{-1},$$

where v is phase velocity when GID is occurred on wires, in km/sec; v_0 – velocity without GID on wires, for principal mode $v_0 \approx$ c (velocity of light).

For example, Figure 1 shows projected reliance for steel aluminium wires (brand-names AS 120/19 and AS 150/19) with

amplitude U and signal delay $\Delta\tau$ from ice deposition walls b (Figure 1, *a*, *b*), from the length of wires covered by ice deposition l (Figure 1, *c*, *d*) and from frequency f (Figure 1, *e*, *f*).

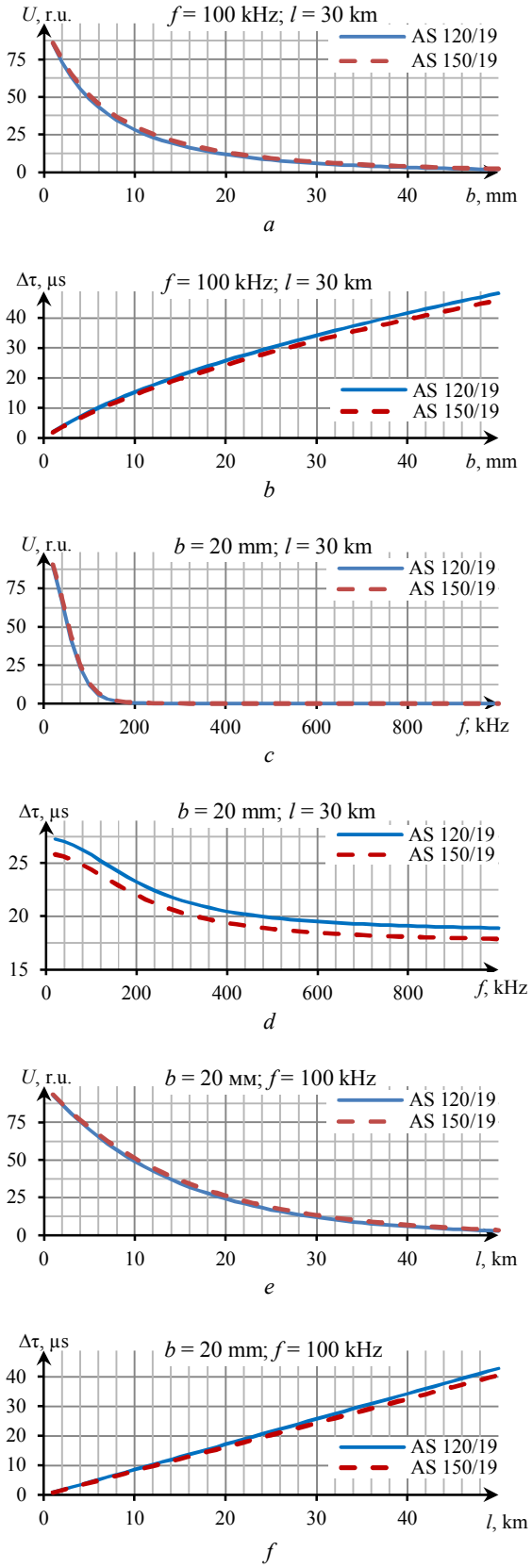

Figure 1. Correlation of amplitude U (*a*, *c*, *e*) and delay $\Delta\tau$ (*b*, *d*, *f*) of location signal from ice thickness deposition b (*a*, *b*); from the lengths of wires covered by ice deposition l (*c*, *d*); from frequency of pulsed probing signal f (*e*, *f*)

Besides, additional delays cause wires stretching due to the ice depositions weight and wind loads. However, they have little impact on total delay, thus they could be ignored. Signal attenuation increases due to reduction in wire diameter and augmentation of signal frequency (Figure 1, *c*), while delay is decreased when frequency grows (Figure 1, *d*). augmentation of ice thickness wall, and length of wires covered by ice leads to attenuation growth (Figure 1, *a*, *e*) and delays growth (Figure 1, *b*, *f*) of location signal. Linear dependence between delay index and length of ice coating (Figure 1, *f*) allows to bring lineal delay, which simplifies calculation of operating values for the lines with different length.

Hereinabove it was described definition of location signals parameters U and $\Delta\tau$ for ice deposition with the wall b and ice cover length l_{ice} on wires OPL. In order to define ice walls using U and $\Delta\tau$ indexes it is necessary to solve inverse problem – i.e. finding system roots of two equations with two unknowns:

$$\begin{cases} U(b,l) = U_{ice}; \\ \Delta\tau(b,l) = \Delta\tau_{ice}. \end{cases}$$

Unfortunately, it is difficult to define walls thickness and ice length using parameters U and $\Delta\tau$ of the reflected signal because equation could have numerous solutions, as well as no solutions at all. Hence, l and b could not be determined uniquely. According to some observations, it is also necessary to record length of the area, most likely covered by ice depositions l, and then calculate thickness of ice walls by each of the parameters, thus defining range of possible values for ice thickness b.

Results of calculations using developed method, algorithm and computer program [5] to define U and $\Delta\tau$ by ice thickness b as of January 2013 are depicted on Figure 2. Maximum value of ice deposition equal to 3 mm was observed on January 4, 2013. Those ice depositions could not make any harm to the coherence of overhead power wires.

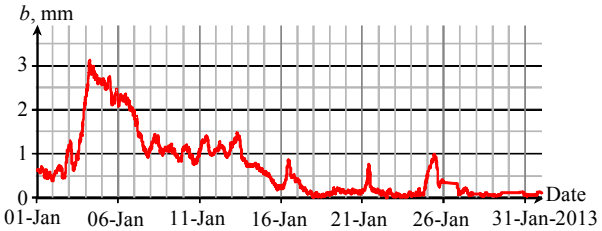

Figure 2. The location method to control thickness of ice depositions on 110 kV wires OPL within a month "K Bukash–R Sloboda" [1–31 Jan 2013]

As was already mentioned above, drawback of location method is failure to differentiate between slight-thickness ice deposition of the long overhead power line and dangerous concentration of ice on its separate small areas. The method of subdividing power lines into location segments with spotted imperfections is used to prevent this drawback.

Due to the spotted imperfections, it is possible to subdivide the 40 000 m "K Bukash–R Sloboda" line into 5 areas. Graph of ice thickness b behavior could be depicted for each of the line as shown on Figure 3.

By comparing dependence of ice thickness from time on different areas (Figure 3, blue curves) with the curve of average ice thickness values variations (Figure 3, dashed line), which was calculation without line-splitting, it is evident that ice thickness b (in mm) varies on different areas. It is obvious that maximum risk of wires breakage is observed at maximum values of b. Within the observation period, maximum wall

thickness was recorded on the area between towers № 99 and 134 (7.12.2011), and minimum thickness value between № 40 and 99 (10.12.2011).

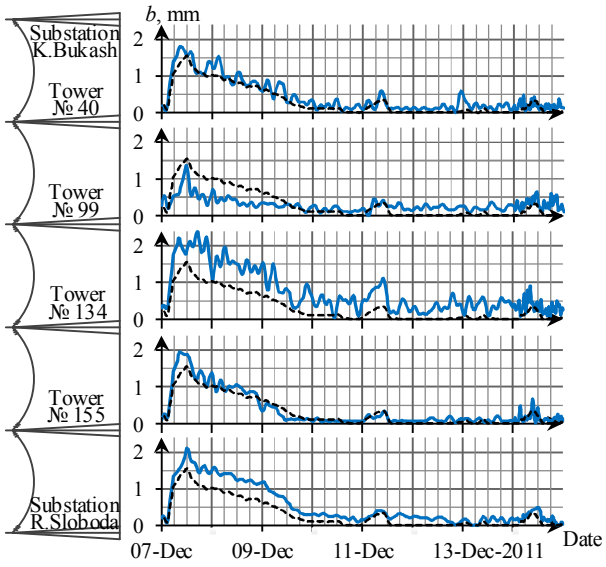

Figure 3. Time history of ice thickness *b* on "K Bukash–R Sloboda" line for five areas (blue curves) and for the whole line (dashed curve) [7–14 Dec 2011]

Figure 4 depicts graphs of ice thickness behavior along the "K Bukash–R Sloboda" line. The first two graphs show propagation of ice depositions, which started to be formed on December 30, 2013, and completely faded away on January 1, 2014. The first graph, calculated as of 19:00, December 30, 2013, corresponds to the maximum ice load per this icing incident. The thickest ice wall reached 2.9 mm value and was recorded on the 4th area (between towers №134-155). Later, ice coating started to come off from the wires, which corresponds to the moment of partial vanishing on second graph. As shown on 2nd graph Figure 4, ice thickness decreased along the most part of the line (except 2nd area): it decreased almost in half on the 4th area from 2.9 mm to 1.5 mm, however grew on the second area (between towers №40-99) from 2.5 mm to 2.8 mm.

The last two graphs on Figure 4 correspond to the icing incident as of January 11-12, 2014. Maximum values of ice depositions are indicated on January 11 at 21:40. Thickness of ice wall on the 4th area reached 4.1 mm value. Since then ice depositions started to decrease; in 2 hours ice thickness was reduced to 2.5 mm on the 4th area, though it stayed the same on 1, 3 and 5 areas. However, by 4:00 on January 12, 2014, the line was totally cleaned off the ice.

This method of line subdivision allows eliminating drawback of the location method, which is determination of integral ice thickness value along the whole line length. Thus, it will help to prevent accidents on small but highly affected to the icing areas.

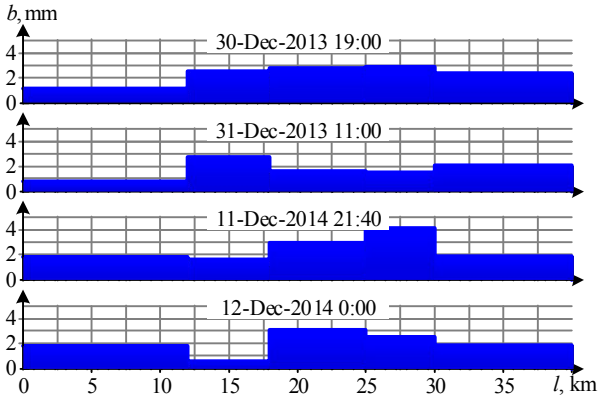

Figure 4. Propagation of ice deposition on wires along 110 kV line on "K Bukash–R Sloboda" line during different observation days

Given examples decisively demonstrate capabilities of the location method for ice deposition detection on OPL wires, and confirms its high sensitivity to earlier detection of ice coating, starting from 0.1 mm ice thickness and even less.

Algorithm, methodology and computer program to calculate thickness of ice coating deposition were developed and probe-tested in order to help estimating weight of ice-forming coupling in a span. If it exceeds allowed values, a signal to start ice melting is given. In the above mentioned cases, ice melting was not needed.

ACKNOWLEDGMENT

The authors would like to thank OJSC "Federal Grid Company of Unified Energy System" (Moscow), Academy of Science of the Republic of Tatarstan, and OJSC "Setevaya Kompania" (Grid Company of the Republic of Tatarstan) for their financial and technical support.

REFERENCES

[1] Minullin R.G., Fardiyev I.Sh., Petrushenko Yu.Ya., Gubayev D.F.., Mezikov A.F., Korovin A.V. Sposob obnaruzheniya poyavleniya gololyoda na provodah linii elektroperedachi. RU 2287883 C1, 20.11.2006.

[2] Minullin R.G., Gubayev D.F. Obnaruzheniye gololednyh obrazovaniy na liniyah elektoperedachi lokatsionnym zondirovaniyem Kazan: Kazan.gos.energ.un-t (Kazan State Power Engineering University), 2010. 207 p.

[3] Minullin R.G., Kasimov V.A., Yarullin M.R., Filimonova T.K. Issledovaniye parametrov vysokochastotnogo trakta linii elektroperedachi lokatsionnym metodom v shtatnyh usloviyah pri otsutstvii gololeda // Energetika Tatarstana (Power Engineering of Tatarstan). 2012. № 4(28). p. 44-50.

[4] Kostenko M.V, Perelman L.S., Shkarin Yu.P. Volnoviye processy I elektricheskiye pomehi v mnogoprovodnyh liniyah vysokogo napryazheniya. – M.: Energiya, 1973.

[5] Kasimov V.A.. Minullin R.G. Programmniy modul dlya rascheta stenki gololednyh otlozheniy na provodah liniy elektroperedachi po rezultatam lokatsionnogo zondirovaniya. Certiifcate of state registration of the software № 2013661783. Registered 16.12.2013.

Analysis of radar equipment readings and weight sensors indications during ice deposits detection on power transmission lines

Minullin R.G.[1], Kasimov V.A.[1], Yarullin M.R.[1]
[1] Kazan State Power Engineering University
Minullin@mail.ru

***Abstract*: The possibility of two methods of ice deposits detection on power transmission lines are being described here, their advantages and disadvantages are being reted. In particular results of measurements of existing overhead power transmission lines, the advantages of radar method to detect ice deposits over strain sensors method.**

Keywords: overhead power transmission lines, ice on wires, method of strain sensors, method of radar detection of ice, measuring technique, comparative experiments to detect icing and melting, advantage of radar detection method of ice.

LEGEND AND ABBREVIATIONS

PTL *Power Transmission Lines*

Control of icing on power transmission lines now a days are carried out by two methods: the method of strain sensors and radar sensing method.

The method of weight sensors is based on comparing the weight of the wires in a passage in absence and presence of ice deposits. The value of wire tension is determined by ice load, wind, as well as ambient temperature. Assessment of the stress state of the wire and comparing it with the maximum permissible value, are carried out with strain sensors. The sensors detect the weight of glaze deposits close to one pillar, their data is transmitted to the receiving station using means of remote control.

In radar sensing method locator pulses are fed through the control line and determined the time to get reflected signal. Locator pulses are fed into power line through coupling filter and coupling capacitor in presence of high frequency line trap. Amplitude U reduces by increasing the absorption of electromagnetic energy, and delay $\Delta\tau$ increases by reducing the speed of impulse propagation [1, 2] for reflected radar pulses in case of ice formation.

The technique of converting values of reflected pulse amplitude and delay into equivalent weight of ice deposits on wires was developed. This technique allows us to compare the results of measurements obtained by location and weight methods on a comparable basis by weight ice deposits.

Experimental studies to detect ice on power transmission lines with radar systems developed by employees of KSPEU, carried out since 2009 in substations “Bugulma-110” and “K Bukash” (the Volga region). From 2012 prototype radar complex, designed and manufactured by employees of KSPEU together with employees of JSC “Scientific-industrial enterprise “Radioelektronika” named after V.I. Shimko” ordered by JSC “Federal Grid Company of Unified Energy System”.

Comparison of data obtained by radar sensing method and by strain sensors have been carring out since 2013 in areas of substations “Baksan” (North Caucasus) and “Shkapovo” (the Urals). The complexes operate continuously in an automatic sensing mode and transmit data every 30 (60) minutes to the control center of KSPEU.

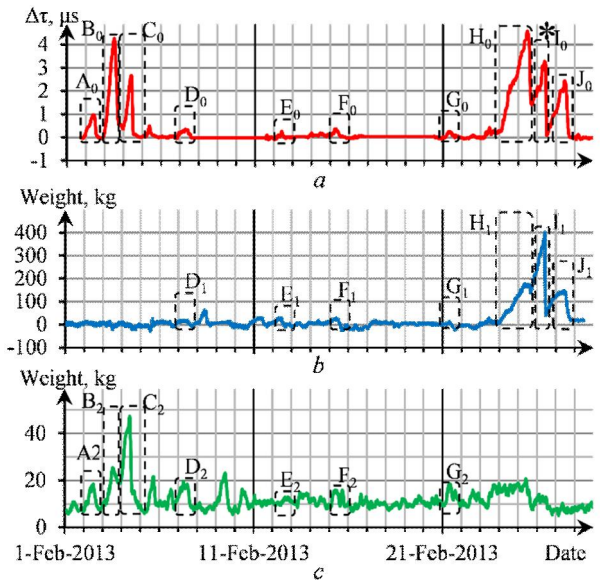

Figure 1. Comparison of registrations ice deposits on line 330 kV (North Caucasus): *a* – by radar sensing (measured delay $\Delta\tau$); *b*, *c* – by strain sensors method (measured ice weight P in one passage); registration ice formations are marked by dashed ovals; * – the beginning of ice melting [1.02-28.02.2013]

Figure 1, *a* shows the changes of reflected pulse during time delay $\Delta\tau$ for sensing 330 kV PTL (North Caucasus) with radar complex, developed in KSPEU.

In Figure 1, *b*, *c*, corresponding readings P of strain sensors located at distances of 1.3 km (pillar number 243) and 29.3 km (pillar number 134) from the beginning of the 330 kV line are shown.

As shown in Figure 1, *a* by radar data, a large ice formed on the line 2.02-4.02.2013 caused maximum pulse delay $\Delta\tau_{max} = 4.5$ ms.

Close to pillar number 243 on line 2.02-4.02.2013 ice was not detected by strain sensors (Figure 1, *b*).

On pillar number 134 (Figure 1, *c*) on line 2.02-4.02.2013 ice of maximum load $P_{max} = 40$ kg was detected by strain sensors.

In the interval 5.02-23.02.2013 (Figure 1, *a*, *b*, *c*) shows a small quantity of ice while using radar method (D_0, E_0, F_0, G_0) and strain sensors method on pillar 243 (D_1, E_1 F_1, G_1) and on pillar 134 (D_2, E_2, F_2, G_2).

Following cases of large ice deposits was observed during the period of 24.02-27.02.2013. According to radar sensing (Figure 1, *a*) ice deposits on line peaked at midday of

25.02.2013 (H_0) with $\Delta\tau_{max}$ = 4.5 ms. Then in some sectors ice was fallen down, and again the growth of ice continued til midday of 02.26.2013 (I_0) with $\Delta\tau_{max}$ = 3.3 ms. At this time ice began melting (Figure 1 and indicated by an asterisk). Throwing of ice deposits as a result of the melting occurred in the afternoon of 26.02.2013. However, growth of ice deposits lasted until noon of 27.02.2013 (J_0) with $\Delta\tau_{max}$ = 2.5 ms. Then there was a natural ice deposits throwing occurred and the line returned to its staffing condition.

According to strain sensors data, on the pillar number 243 (Figure 1, *b*) ice deposits gradually increases until it melts in the afternoon 02.26.2013 (I_1). After melting ice deposits slowly continued to increase (J_1). Then, in the afternoon of 27.02.2013 deposits disappeared naturally.

As seen from a comparison of Figure 1, *a*, *b* the overall dynamics of the ice deposits formation in both registrations are the same. But there are differences in details, as radar sensing monitors the entire line and strain sensors monitor only one flight line.

Comparison of sensors readings on pillar number 243 and number 134 in Figure 1 *b*, *c* show ice deposits, detected by the sensor on pillar number 243, is not detected by the sensor on pillar number 134 (and vice versa) due to uneven deposition of ice.

In radar sensing all resulting ice deposits A_0 – J_0 are fixed precisely without loss (Figure 1, *a*).

Comparative experiments were performed to detect ice deposits in winter 2013-2014 on 110 kV PTL (Urals).

Figure 2 is a graph of weight changes of ice on wire phase *A*, obtained by using radar sensing techniques (Figure 2, *a*) and by the strain sensors, which are mounted on phase conductors *A*, *B* and *C* close to pillar number 23 (Figure 2, *b*-*d*).

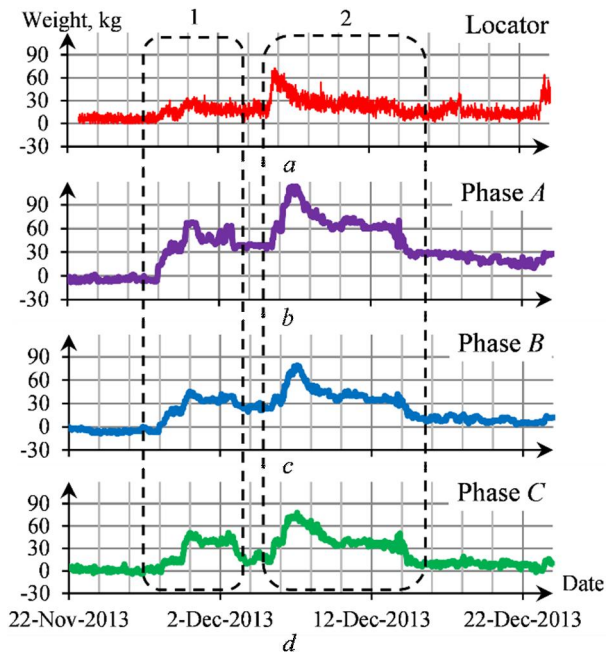

Figure 2. Changes ice deposits weight according to radar device connected to phase *A* (*a*) and according to strain sensors on phases *A*, *B* and *C* (*b*-*d*) on wires of 110 kV line", where the dashed outline 1 - period 28.11-4.12 2013 .; 2 bar loop - 5.12-15.12.2013 period of [22.11-23.12.2013]

Figure 2 shows how formation of ice deposits began with increasing weight on all three phases on 28.11.2013 (dotted outline 1). According to strain sensors on 30.11.2013 on the wires of the three phases was observed 45-65 kg ice deposits in one passage (Figure 2, *b*, *c*, *d*).

Corresponding readings of radar method, figured out by using modal theory of high-frequency signals propagation through overhead lines, give a figure about 30 kg for a single span (Figure 2, *a*).

The discrepancy reading of radar method and strain sensor method prove the fact that the distribution of the ice along the power line was uneven, i.e. in areas not monitored by strain sensor icing can be less than the place close to pillar number 23 where strain sensor is mounted.

The second period of icing began 5.12.2013 (dashed circuit 2 in Figure 2). According to the sensor reading of wire of phase *A*, were the most susceptible ice deposits. In the two half spans close to pillar number 23 ice deposits reached upto 75-110 kg (Figure 2, *b*-*d*). According reading of radar system average weight of ice deposits on the wire of phase *A* in one span reached upto 70 kg (Figure 2, *a*). Weight of ice deposits formation on line 14.12.2013 was shortly reduced naturally without interference and ice melting was not required.

By comparing the curves in Figure 2, *a*-*d* it is evident that the dynamics of wire weight changes with ice deposits during icing is detected by strain sensors as well as by radar sensing quite objectively. However, there are differences in details readings and these devices have different operating principles.

Registration of dynamics of ice deposits weight changes on 110 kV line (Ural) with subsequent melting shown in Figure 3. Intensive ice deposits on wires began in evening, 26.12.2013, the weight of ice reached upto 375-400 kg on 28.12.2014 in the same span according to readings of radar system, and strain sensors on the wire phase A.

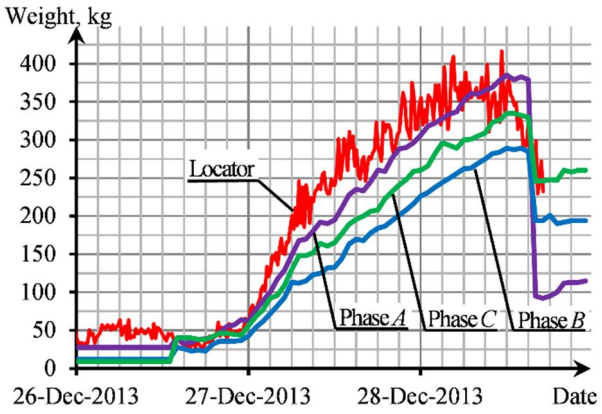

Figure 3. Changes of ice deposits weight according to radar device connected to Phase *A*, and according to strain sensors mounted on wire close to pillar number 23 of 110 kV line [26.12-28.12.2013]

To prevent accident ice melting on wires three phases line was performed. As a result of ice melting on 28.12.2013 wire weights were reduced to permissible values, as shown in Figure 3.

According to readings of strain sensors ,weight of ice deposits on phase lines do not match with each other according to absolute value, as shown in Figure 3. The same phenomenon is observed in the 330 kV line, which can be explained by varying degrees of tension when they were mounted, and all strain sensors are not with similar sensitivity. Mismatching of data of strain sensors by absolute vale mounted on different phase wires of transmission line, reduces the reliability of their redings, causes difficulty to determine the critical weight of ice deposits that can cause an accident on the power transmission lines, and causes uncertainty in taking operational decisions about the beginning of the melting of ice deposits.

Radar method can reliably monitor in real time the dynamics of icing on wires, allows clearly identifying the

starting time of ice melting, which is necessary to prevent wire breakage on power lines. In addition, radar method allows monitoring ice melting process.

Radar method has the following advantages compared to the method of weighing conductors that are currently used in rare cases on some power lines:

1) pulse signal simultaneously serves as a sensor and a carrier of information about icing on wire, so there is no need to install separate sensors and data transmitters on wires, which would have collected data from sensors and then transmit data to control center, so is used small, simple and cheap structure of the equipment;

2) it ensures control of the entire line, not just a single span;

3) installation of radar equipment does not require intervention in the power line structure, because radar equipment is placed in the indoor substation, which increases reliability and simplifies its exploitation for operating personnel;

4) commissioning of radar equipment takes a few minutes if the power line has a high-frequency channel;

5) it is possible to monitor all lines outgoing from the substation using periodical switching.

ACKNOWLEDGMENT

The authors would like to thank JSC "Federal Grid Company of Unified Energy System" (Moscow), Academy of Science of the Republic of Tatarstan, JSC "Setevaya Kompania" (Grid Company of the Republic of Tatarstan), LLC "Bashkirenergo" (Ural) and "MES South" (North Caucasus) for their financial and technical support.

REFERENCES

[1] Minullin R.G., Fardiev I.Sh., Petrushenko Yu.Ya., Mezikov A.K., Korovin A.V. et al. Location method for the detection of the appearance of glaze ice on the wires of power transmission lines. //Russian Electrical Engineering. New York: Allerton Press, Inc., 2007. Vol. 78. № 12. PP. 644–648.

[2] Minullin R.G., Petrushenko Yu.Ya., Fardiev I.Sh. Sounding of Air Power Transmission Lines by the Location Method // Russian Electrical Engineering. New York: Allerton Press, Inc., 2008. Vol. 79 (№ 7). PP. 389–396.

Isotopic mass balance measurements of spray ice

Toshihiro Ozeki[1], Kyohei Yamane[1], Satoru Adachi[2], Shigeru Aoki[3]
[1] Sapporo Campus, Hokkaido University of Education, [2] Snow and Ice Research Center, NIED,
[3] Institute of Low Temperature Science, Hokkaido University
ozeki.toshihiro@s.hokkyodai.ac.jp

***Abstract*: Spray ice is frozen ice formed from sea or lake spray water in cold regions and accreted on ships, offshore structures, and trees in lakeside, developing into a massive ice form. Freezing spray is the main cause of spray icing; however, spray ice accretion often occurs under intense snowfall. We investigated the contribution of snow to spray icing. We collected samples of spray ice, snow, and water on the west coast of Hokkaido Island and in Lake Inawashiro and Lake Towada of Main Island, Japan. The structural characteristics of the spray ice were analyzed using conventional thin-section and NMR imaging. The observed layer structure in the samples depends on the growth history of the spray ice. Additionally, the spray ice was composed of two ice types with different crystal structures: granular ice with uniform, rounded smaller grains and columnar ice. The differences in ice composition may be influenced by snow accretion. The snow mass fraction of the spray ice samples was calculated from the isotopic mass balance. The oxygen isotopic composition of the melted samples was analyzed using a standard mass spectrometer. The oxygen isotopic composition values of spray ice were higher than that of the sea or lake water supply. This difference suggests that isotope fractionation has occurred during the wet growth of spray ice. We verified the isotope fractionation during the wet growth of artificial spray ice produced in cold room experiments. The snow mass fraction of spray ice responds to icing events and the oxygen isotopic composition values of granular ice layers tend to be lower than the other layers, suggesting the contribution of snow accumulation. High snow fractions in the samples demonstrate that snow contributed significantly to the growth of spray ice.**

Keywords: spray icing, snow accumulation, isotopic mass balance, $\delta^{18}O$

INTRODUCTION

Spray ice is ice formed from the spray of sea or lake water in cold regions that accumulates on ships, offshore structures, or trees at the waterside, and develops into a massive ice form. Coast of Hokkaido Island on the Sea of Japan is characterized by extreme sea-water spray icing. Marine disasters caused by ice accretion occur frequently, however, even today, deicing continues to be a manual operation that usually involves the use of a hammer. On the other hand, "spray ice" is an interesting ice phenomenon in natural lakes, also observed around Lake Inawashiro and Lake Towada, Japan. It is a popular motif for photographs, and a tourist attraction.

Several recent studies have investigated the feature of sea-water spray ice. [1] developed a theoretical model of salt entrapment in sea-water spray ice; a thin liquid-water film on the icing surface runs off from the surface and consequently traps liquid in the spray ice matrix. [2] studied the microstructural features of spray ice on ships and demonstrated the presence of a channelized network of brine. [3] measured the three-dimensional microstructure of sea-water spray ice using the Nuclear Magnetic Resonance (NMR) imaging technique, and confirmed the presence of such a channelized network of brine in natural sea-water spray ice samples. Numerous researchers estimated sea-water spray icing. A ship-icing prediction algorithm [4] is used operationally by the National Oceanic and Atmospheric Administration office (NOAA). The factor used to estimate the severity of potential spray icing is derived from a simplified heat balance of the icing surface. [5] investigated the growth rate of sea-water spray icing using telephotographs recorded in intervals and found that the growth rate of the cross sectional area of the spray icing increases monotonically with the product of air temperature and wind speed (i.e., the heat loss by convective heat flux). In addition, [6] reviewed computer simulations of marine ice accretion and discussed the US Coast Guard's Cutter Midgett model and a three-dimensional time-dependent vessel-icing model.

Freezing spray is the main cause of spray icing; however, spray ice accretion often occurs during intense snowfall. It is important, therefore, to estimate the contribution of snow to the growth rate of spray icing. [7] investigated the characteristics of lake-water spray ice. The structural characteristics of the ice were analyzed using thin sections of the samples, while the snow mass fraction of the ice samples was calculated from the isotopic mass balance. They suggested that the high snow fraction in the samples indicates a significant contribution of snow.

In this study, the contribution of snow to spray icing is investigated using field observations and laboratory experiments.

I. OBSERVATIONAL SITES AND ICE SAMPLES

We collected samples of spray ice, snow, and water on the west coast of Hokkaido Island and in Lake Inawashiro and Lake Towada of Main Island, Japan (Figure 1).

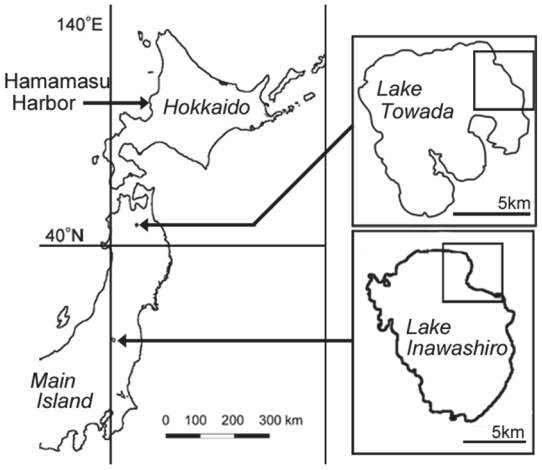

Figure 1: Locations of observational sites. Hamamasu harbor in Hokkaido Island, Lake Inawashiro and Lake Towada of Main Island, Japan.

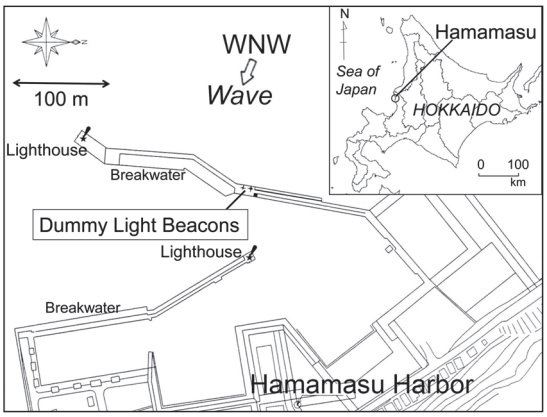

Figure 2: Schematic view of Hamamasu Harbor.

Figure 3: Dummy light beacons on breakwater at Hamamasu Harbor. Stormy weather often generated not only heavy spray jets but intense snowfall.

Figure 4: Massive ice forms on trees. upper: Lake Inawashiro, lower: Lake Towada.

A. West coast of Hokkaido Island

The observations of sea-water spray ice were conducted at the Hamamasu Harbor, located at the west coast of Hokkaido. Figure 2 shows the location of the observational site. Two dummy light beacons were set up at the northern breakwater extending from the north to the south: one consisted of fiber-reinforced plastics (FRP) and the other one consisted of steel coated with acrylic silicon resin. The height of both dummy light beacons was approximately 4 m. The breakwater line was chosen perpendicularly to the primary wind direction during the winter season. High waves caused by north-westerly wind often generated a heavy spray jet at the dummy light beacons. The spray icing grew under heavy sea-water spray and during low temperatures [5]. Additionally, stormy weather often generated not only heavy spray jets, but also intense snowfall (Figure 3).

B. Spray icing on trees beside lake

Lake Inawashiro and Lake Towada are located on the main island of Japan (Figure 1). Lake Inawashiro, situated at 514 m a.s.l., has an area of approximately 100 km2 and an average depth of 50 m. Lake Towada, situated at 400 m a.s.l., has an area of approximately 60 km2 and an average depth of 70 m. Because of the depth of both lakes, almost the entire water surface is ice free, even in the middle of winter, when spray ice is usually formed along the shore. The exception is a narrow area at the northeast shore of the lakes that is covered with very thin ice.

Spray ice accumulates on trees at the lakeside, and often develops into a massive ice form (Figure 4). The samples of spray ice were collected on the east side of the lakes.

II. METHODS

The contribution of snow to spray ice formation is important to consider when estimating the growth rate of spray ice. In this study, we focused on the isotopic mass balance in sea-water, snow, and spray ice. Generally, the concentration of the heavy stable isotope ^{18}O varies with phase changes, and depends on the temperature of the phase changes [8]. The oxygen isotopic composition $\delta^{18}O$ can be calculated using the following equation:

$$\delta\,^{18}\mathrm{O} = \frac{R - R_{SMOW}}{R_{SMOW}} \times 1000\ [‰] \qquad (1)$$

where R is the isotopic ratio $H_2{}^{18}O$ / $H_2{}^{16}O$ in the sample and R_{SMOW} is the isotopic ratio in Standard Mean Ocean Water.

The snow mass fraction of the spray ice samples is calculated from the isotopic mass balance. [9] [10] used an isotopic mass balance to estimate the contribution or fraction of snow in sea ice, where the snow ice consists of a mixture of snow and sea-water. The stable oxygen isotopic composition $\delta^{18}O$ in an ice segment (δi) can be estimated using the $\delta^{18}O$ values of sea-water (δw) and of snow (δs) in the following equation:

$$\delta\, i = (1 - f_s) \times (\delta w + f) + f_s \times \delta s \qquad (2),$$

where f_s is the snow mass fraction in the ice segment and f is an effective fractionation coefficient associated with the freezing of sea-water. For the effective fractionation coefficient f, a value of 3.0 ‰ [11] or 2.9 ‰ [12] is used. Both values are empirical values for ice grown relatively slowly from pure water.

Figure 5: cross section of a sea spray ice sample.

III. Observational results

The structural characteristics of the spray ice are analyzed using conventional thin-section and NMR imaging. Figure 5 shows the layered structure of a sea-water spray ice sample in cross section. The observed layering in the samples depends on the growth history of the spray ice. Additionally, the spray ice is composed of two ice types with different crystal structures: a granular layer with uniform, rounded smaller grains and an ice layer with columnar ice. The differences in the ice composition may be caused by snow. The granular structure is similar to rounded polycrystals in a seasonal snow layer on the ground. On the other side, the columnar ice layer is similar to ice layers in icicles [2] [13], although the ice layer included brine. NMR imaging indicates that these layers have brine drainage channels. NMR imaging of a lake-water spray ice indicates the absence of a channelized network within the columnar grains. The crystal shape is similar to that of sea-water spray ice, but its structure differs from the structure of sea-water spray ice due to the presence of brine.

The oxygen isotopic composition of the melted samples is analyzed using a standard mass spectrometer. Table 1 and Table 2 show the results of the average $\delta^{18}O$ values for the ice, snow, and water samples. In event 1, an average $\delta^{18}O$ value of -10.80 ‰ was calculated for the snow samples, while the average $\delta^{18}O$ value of the sea-water samples is -0.11 ‰. We could not obtain $\delta^{18}O$ values for the snow and sea-water samples of event 2, here we assume the same average values as for the samples of event 1. It is remarkable that almost all oxygen isotopic composition values of spray ice are higher than the values of the sea- or lake-water supply.

Table 1: Observed δ18O values of sea spray ice samples together with snow and sea-water samples. The values of some spray ice samples are shown divided into two ice types, i.e. granular grains and ice layer.

Sample	Ice type	$\delta^{18}O$ (‰)
Event 1		
1A-1	Average	1.38
1A-2	Average	0.83
1A-3	Ice	1.09
1A-4	Granular	1.16
1B-1	Ice/Granular	0.42
1B-2	Ice	-0.24
1B-3	Granular	-0.09
1C-1	Ice/Granular	1.15
1C-2	Ice	1.13
1C-3	Granular	1.22
1D	Average	0.26
Event 2		
2A	Ice/Granular	–0.55
2B	Granular	–0.75
2C	Granular	–3.53
Snow		–10.80
Sea water		–0.11

Table 2: Observed $\delta^{18}O$ values of spray ice samples in lake together with snow and lake-water samples.

Sample	Ice type	$\delta^{18}O$ (‰)
Lake Inawashiro		
Spray ice	Average	–8.2
Snow		–9.6
Lake water		–9.6
Lake Towada		
Spray ice	Average	–6.8
Snow		–12.5
Lake water		–8.1

IV. Laboratory experiment

A. Equipment and Method

The oxygen isotopic composition values of spray ice were higher than that of the sea or lake water supply. This difference suggests that isotope fractionation has occurred during the wet growth of the spray ice. It is conceivable that the fractionation coefficient of sea ice, i.e. $f = 3.0$, is over-estimated. Since this value decreases with an increment in the growth rate as suggested in sea ice study of [14], f of spray ice might be lower than these values.

To verify the f value, we investigated the isotope fractionation during the wet growth of spray ice through laboratory experiments. The experimental apparatus was set in a cold room at Hokkaido University of Education (Sapporo). The textile, Sky Clear Coat (SCC), was set on a cylinder (height: 2 m; diameter: 0.3 m). SCC (Taiyo Kogyo Corp., Tokyo, Japan) comprises polyester cloth and polyvinyl chloride coated with a T_iO_2 film; it exhibits hydrophilic behavior with a water contact angle of less than 30° owing to the photoinduced effect on the T_iO_2 surface [15]. A schematic view of the apparatus is shown in Figure 6. The air temperature in the cold room was maintained at approximately -20 °C. Small water droplets with a diameter of approximately 0.3-0.5 mm were supplied by a fan-shaped spray nozzle; they were sprayed on the cylindrical test specimen. The distance of the specimen from the spray nozzle was 1.1 m.

B. Experimental Results of Isotope Fractionation

Under the aforementioned conditions, wet growth of ice occurred on the windward side of the specimen. Spray water formed a thin fluid film flowing on SCC, which has a hydrophilic surface. Part of the water froze into spongy ice as it flowed down

the textile surface. The surface gradually began to be covered by sheet-like ice. The duration of spray supply was 30 min. The maximum thickness of ice was 10 mm.

We carried out the experiments 6 times. Oxygen isotopic composition of the melted samples was analyzed using a standard mass spectrometer. From the results, the average $\delta^{18}O$ value of the spray ice was calculated as -10.52 ‰ with a standard deviation of 0.24. The average $\delta^{18}O$ value of the water supply was -11.92 ‰. The difference between the spray ice and the water was 1.41.

To decrease the growth rate of icing, the room temperature was raised to -10 °C, and an additional four experiments were conducted. The result of the average $\delta^{18}O$ value of the spray ice is -10.20 ‰ with a standard deviation of 0.18. The average $\delta^{18}O$ value of the water supply was -11.96 ‰. The difference between the spray ice and the water is, therefore, 1.76. As a result, the fractionation coefficient of -10 °C experiments is higher than the fractionation coefficient of the -20 °C experiments. This tendency agrees with the sea ice study [14].

Air temperature, wind speed, and growth rate of the spray ice fluctuates from hour to hour in nature, therefore the effective fractionation coefficient is not settled. In this study, we assumed an effective fractionation coefficient *f* of 1.5 for the calculation of the snow mass fraction. Lake Inawashiro was excluded from the calculation because the $\delta^{18}O$ value of snow was close to the value of lake-water.

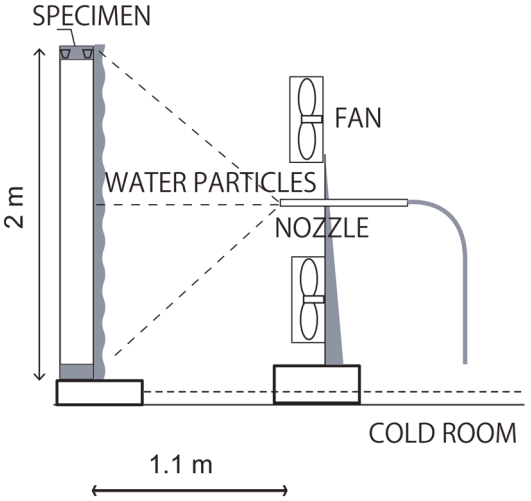

Figure 6: Apparatus for laboratory experiment.

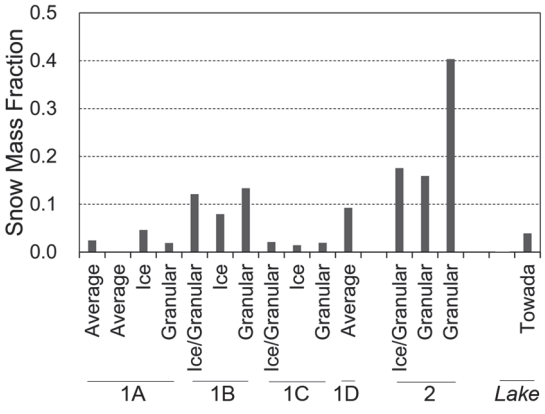

Figure 7: Snow Mass Fraction of Spray Ice.

V. Discussion ot the results

Figure 7 indicates the snow mass fraction of the spray ice samples in Table 1 and Table 2. The snow mass fraction of spray ice corresponds to icing events and ice samples. The snow mass fraction of spray ice responds to icing events and the oxygen isotopic composition values of granular ice layers tend to be lower than in other ice layers, suggesting the contribution of snow accumulation. High snow fractions in the samples demonstrate that snow contributed significantly to the growth of spray ice.

The values of granular ice layers tend to be higher than in other layers, suggesting the contribution of snow accumulation. High snow fractions in the samples demonstrate that snow contributed significantly to the growth of spray ice.

[7] investigated the structural characteristics of the spray ice in detail using the samples from Lake Inawashiro. They suggested that the ice structure consists of two different types of ice, a uniform orbicular granular type and a columnar type with large elongated grains. The characteristic granular structure is similar to snow ice in sea ice. They further suggested that the granular segment is composed of a mixture of snow and water spray tossed up on the beach, produced by penetration of water into the snow layer, which froze within such a structure.

VI. Conclusions

The contribution of snow to spray icing was investigated through field observations and laboratory experiments. The samples of sea-water spray ice and lake-water spray ice were analyzed using a conventional thin-section, NMR imaging and oxygen isotopic composition.

The observed layer structure in the samples depends on the growth history of the spray ice. Additionally, the spray ice consists of two ice types with different crystal structures: granular ice with uniform, rounded smaller grains and columnar ice. The differences in ice composition may be influenced by snow accretion.

The oxygen isotopic composition of the melted samples was analyzed using a standard mass spectrometer. The oxygen isotopic composition values of spray ice are higher than the values of the sea or lake water supply. This difference suggests that isotope fractionation has occurred during the wet growth of spray ice. We verified the isotope fractionation during the wet growth of artificial spray ice produced in cold room experiments.

The oxygen isotopic composition of the artificial spray ice indicates that the $\delta^{18}O$ values of the spray ice is higher than the value of the water supply. The difference between the values of spray ice and of water depends on the air temperature. The result suggests that the fractionation decreases with an increment in the growth rate of spray ice. We suggest an effective fractionation coefficient of 1.5 for the spray ice event.

The snow mass fraction of the spray ice samples is calculated from the isotopic mass balance. The snow mass fraction of spray ice responds to icing events and ice samples. The values of granular ice layers tend to be higher than for the other layers, suggesting the contribution of snow accumulation.

Acknowledgment

We wish to express our gratitude to Prof. H. Yamaguchi of University of Tokyo, and Dr. T. Kawamura of Hokkaido University for their useful discussion about spray icing. We would like to thank to Dr. S. Matoba and Ms. M. Kitagawa of Hokkaido University for their support of isotope ratio measurements. We are grateful to 1st Regional Coast Guard Headquarters for their support in the field observation. The field observation was supported by JSPS KAKENHI Grant Number 22310110. The laboratory experiment was supported by the

research program of the Green Network of Excellence, MEXT, Japan.

REFERENCES

[1] L. Makkonen, "Salinity and growth rate of ice formed by sea spray", Cold Regions Sci. Technol., 14, pp. 163-171, 1987.

[2] C. C. Ryerson and A. J. Gow, "Crystalline structure and physical properties of ship superstructure spray ice", Phil. Trans. Roy. Soc. Lond., A358, pp. 2847-2871, 2000.

[3] T. Ozeki, K. Kose, T. Haishi, S. Nakatsubo and Y. Matsuda, "Network images of drainage channels in sea spray icing by MR microscopy", Mag. Res. Imag., 23, pp. 333-335, 2005.

[4] J. E. Overland, "Prediction of Vessel Ising for Near-Freezing Sea Temperature", Weather and Forcasting, 5, pp. 62-77, 1990.

[5] T. Ozeki, Y. Tamate, S. Adachi, K. Izumiyama and T. Tazawa, "Field observation of sea spray icing on lighthouses and ice adhesion test of superhydrophilic pliable sheet for deicing", Proc. 13th Int. Workshop Atmos. Icing Structures, 2009, 4 pp.

[6] E. P. Lozowski, K. Szilder and L. Makkonen, "Computer simulation of marine ice accretion", Phil. Trans. Roy. Soc. Lond., A358, pp. 2811-2845, 2000.

[7] T. Kawamura, T. Ozeki, H. Wakabayashi, M. Koarai, "Unique lake ice phenomena observed in Lake Inawashiro, Japan: Spray ice and ice balls", J. Glaciol., 55, pp. 939-942 (2009).

[8] W. Dansgaard, S. J. Johnsen, H. B. Clausen and N. Gundestrup, "Stable Isotope Glaciology", Meddelelser om Gronland, 197, pp 1-53, 1973.

[9] M. A. Lange, P. Schlosser, S. F. Ackley, P. Wadhams and G. S. Dieckmann, "18O Concentrations in sea ice of the Weddell Sea, Antarctica", J. Glaciol., 36(124), pp. 315-323, 1990.

[10] M. O. Jeffries, A. P. Worby, K. Morris and W. F. Weeks, "Seasonal variations in the properties and structural an isotopic composition of sea ice and snow cover in the Bellingshausen and Amundsen Seas, Antarctica", J. Glaciol., 43(143), pp. 138-151, 1997.

[11] J. R. O'Neil, "Hydrogen and oxygen isotope fractionation between ice and water", J. Phys. Chem., 72, pp. 3683-3684, 1968.

[12] M. Lehmann and U. Siegenthaler, "Equilibrium oxygen- and hydrogen-isotope fractionation between ice and water", J. Glaciol., 37(125), pp. 23-26, 1991.

[13] T. Tabata and N. Ono, "On the crystallographic study of several kinds of ices", Low Temperature Science, A20, pp.199-213, 1962. (in Japanese with English résumé)

[14] H. Eicken, "Factors determining microstructure, salinity and stable-isotope composition of Antarctic sea ice: Deriving modes and rates of ice growth in the Weddell Sea", AGU Antarctic Research Series, 74, pp. 89-122, 1998.

[15] T. Ozeki, R. Yamamoto, K. Izumiyama and T. Sakamoto, "Ice Adhesion Tests on Pliable Polymer Sheets for Protection against Sea Spray Icing", J. Adhesion Sci. Tech., 26, pp. 651-663, 2012.

Wind Ice and Snow Load Impacts on Infrastructure and the Natural Environment (WISLINE)

Harold Mc Innes[1], Jan Erik Haugen[1], Jón Egill Kristjánsson[2], Bjørn Egil K. Nygaard[3], Roy Rasmussen[4], Svein Solberg[5], Kristina Blennow[6], Ole Einar Tveito[1]

[1] The Norwegian Meteorological Institute, [2] University of Oslo, [3] Kjeller Vindteknikk, [4] The National Center for Atmospheric Research, [5]The Norwegian Forest and Landscape Institute, [6] Swedish University of Agricultural Sciences, harold.mcinnes@met.no

***Abstract*: Atmospheric icing is a major weather hazard in many mid- to high-latitude locations in the winter, including Norway. There are mainly three types of atmospheric icing; in-cloud icing due to liquid cloud droplets at sub-freezing temperatures; icing due to supercooled rain droplets, and icing caused by wet snow or sleet at temperatures just above freezing point. In-cloud icing and icing caused by wet snow have together with strong wind caused damage to overhead power lines in Norway on several occasions, leaving people without electricity and the power companies with large expenses.**

The main objective of WISLINE is to quantify climate change impact on technical infrastructure and the natural environment caused by strong winds, icing and wet snow. In order to investigate future ice and snow loads, an extensive knowledge about such loads in the present climate is required. This will be provided by improving the description of the cloud microphysical processes of the AROME weather prediction model, which is run operationally by several European forecasting centres. The improved model will be combined with routines for ice accretion in order to produce an icing climatology for the present climate, which will be verified against measurements of ice loads on power lines as well as measurements of cloud water. The next step is then to apply the improved model to downscale data from climate models in order to produce a future icing climatology.

As damage is often caused by icing accompanied with heavy wind, wind loads in present as well as future climate will be investigated in the project. Techniques for downscaling wind data in complex terrain will be studied in order to provide a dataset for wind in both present and future climate. Wind and heavy snow may also cause damage to forests such as up-rooting and stem breakage, and we will hence combine wind, icing and snow damage data for forests with the datasets from WISLINE in order to produce a risk model for forest damage for both present and future climate. All datasets and results of the project will be open to end-users as well as the public.

Keywords: icing, snow loads, power lines, AROME, microphysics

Legend and Abbreviations

NWP	*Numerical Weather Prediction Model*
WRF	*Weather Research and Forecasting Model*
LAM	*Limited Area Model*

Introduction

Atmospheric icing is a major weather hazard in many mid- to high-latitude locations in the winter, including Norway. There are mainly three types of atmospheric icing; (1) 'freezing fog', i.e., in-cloud icing due to (supercooled) liquid cloud droplets at sub-freezing temperatures (Figure 1); (2) 'freezing rain', i.e., icing due to supercooled rain drops at sub-freezing temperatures; (3) 'wet-snow icing', which is caused by heavy precipitation in the form of of snow or sleet at temperatures just above freezing (Figure 2). All three types are common in central and northern Europe and North America, with (1) and especially (2) mainly occurring in continental air masses in inland regions, while (3) is most common in coastal regions, such as Iceland, the U.K., Japan and parts of Germany (Nygaard et al., 2013). Icing has been known to cause significant problems for many sectors of society, in particular for power transmission lines, wind turbines, aviation, telecommunication towers and road traffic. An extreme example of (2) is the ice storm that hit eastern North America in January 1998 with more than 100 mm of freezing rain observed in some areas (Gyakum and Roebber, 2001). This resulted in more than 4 million people in Canada and the United States losing power for days to weeks, or even months and a total economic damage estimated at 4.4 billion U.S. dollars.

Figure 1: In-cloud icing on a power line (Photo Ole Gustav Berg/Statnett)

A recent major icing event in Europe was the wet-snow event in Münsterland in Germany in November 2005, in which 82 transmission towers collapsed, leaving 250 000 people without electricity for several days (Frick and Wernli, 2012).

During the winter of 2013/2014 two 420 kV transmission lines in Southern Norway suffered severe damage due to ice loads exceeding their design values, i.e. observations indicated ice loads four to five times the design value at one location.

Values for extreme wind- , ice- and snow loads with corresponding return periods are used to design technical infrastructure such as bridges, telecommunication towers, and electricity transmission lines. Historically, the design estimation approach in Norway has been based on simple empirical relations developed from a limited number of in-situ observations, and therefore involves considerations that are subjective and based on individual experience. Recent damages on the electric grid show that the traditional approach has problems in predicting representative values in areas with rough and complex topography combined with the advection of warm and moist air masses in the winter season. There is therefore an urgent need to develop a methodology for estimation of such design values in a more objective and consistent way.

Preliminary studies within the frame of COST action 727 "Atmospheric Icing of Structures" showed that reasonable ice loads could be obtained by using the microphysical fields from an early version of the Weather Research and Forecasting (WRF) model (e.g. Harstveit et al. 2009; Nygaard 2009). Ice loads calculated from an updated WRF based model archive developed at Kjeller Vindteknikk have made it possible to reproduce and estimate the return periods of the 2013/2014 winter's icing events. There is however a large potential to further develop these objective methods, and use the tools within a consistent NWP model framework for quantification of changes in the icing climate in Norway.

Figure 2: Snow load on power line (Photo Hallingdal Kraftnett)

In forests wind and heavy loads of snow, rime and ice can cause wind-throw or stem breakage (Figure 3). Wind-throw has been the most damaging agent in Europe's forests during the last 150 years, and it has increased considerably during the last 50 years in Europe (Schelhaas et al. 2003), mainly driven by changes in forest management (Nilsson et al. 2004, Bengtsson and Nilsson 2007). The risk for such damage is expected to increase further with climate change due to a slight increase in windiness, reduced root anchorage due to more rain and wetter soils during the storm season (Kamimura et al. 2012), a reduction in the depth and extent of frozen soil (Kellomaki et al. 2010) and increased frequency of heavy snow fall (Gregow et al. 2011). The Gudrun storm may serve as an illustration of possible future damage events. When it hit Sweden on 8th January 2005, it followed a period of 2 weeks with heavy rain.

Increased attacks by the spruce bark beetle can be expected after wind and snow damage, in particular with increasing temperatures (Schlyter et al. 2006). Falling trees or tree tops generate considerable damage on infrastructure, mainly roads, railways and power lines. The damage risk can be decreased through appropriate forest management, and scenarios make up an important basis for decisions on altered management. This includes changing tree species, providing the trees generous space at low age (increasing 'single tree stability'), avoidance of late and heavy thinning (increasing 'social stability'), and careful placement of stand edges after clear-cut in the landscape (Nielsen 2001, Albrecht et al. 2012).

Figure 3: Wind damage from the storm Dagmar in 2011 (Photo Jon Eivind Vollen/Skogkurs)

Design of robust infrastructure and management of natural resources require quantitative information about climate loads in the future. In order to investigate future ice, snow and wind loads, an extensive knowledge about such loads in the present climate is required. The basic idea of the WISLINE project is to improve the methods for calculating ice and wind loads, apply these methods for the present climate and verify the data against observations. When this is done successfully, we will have methods that are capable of simulating climate loads at high resolution, and the next step is then to downscale data from climate models in order to produce wind and ice datasets for a future climate. We can then fulfil the main objective of WISLINE: To quantify climate change impact on technical infrastructure and the natural environment caused by strong winds, icing and wet snow.

I. THE PROJECT

The Research Council of Norway has granted the project Wind Ice and Snow Load Impacts on Infrastructure and the Natural Environment 6.5 millions Norwegian kroner for the period 2015 – 2018. In addition to the previously mentioned main objective, they also stated the following sub objectives for the project:

-To improve the description of cloud microphysical processes of importance for simulating atmospheric icing.
-To quantitatively assess future wind and ice design loads on electric transmission lines in different geographical regions in Norway.
-To establish risk assessment models for weather hazard induced damages on forests.

The grant from the Research Council and the stated objectives are a result of a proposal from The Norwegian

Meteorological Institute and several partners. These are The Department of Geosciences at The University of Oslo, National Center for Atmospheric Research (NCAR) in Colorado, Kjeller Vindteknikk (KVT), Norwegian Forest and Landscape Institute (NFLI) and Swedish University of Agricultural Sciences (SLU). These different institutions have competence in various fields such as cloud micro physics, wind modelling, downscaling of climate data and forestry, which is necessary to fulfil the ambitious objectives of the project. The project also has a user group consisting of Skogbrand (insurance company owned by Norwegian forest owners), Statnett (system operator, the Norwegian energy system) and the Directorate for Emergency Communication (agency for public safety network) who conveyed their support for project proposal to the Research Council, contributing to it's success. In addition to this Statskog (The Norwegian state-owned land and forest enterprise) has joined the user group, and it might be extended further.

A. The partners

The Norwegian Meteorological Institute (MET Norway) is the meteorological service for both The Military and the Civil Services in Norway, as well as the public. The mission of the institute is to contribute to protection of life, property and the environment as well to provide the meteorological services required by society. MET Norway operates an extensive network of meteorological observations in Norway, its adjacent seas and the polar areas and performs research for both private and public sector.

Founded in 1811 as the first in Norway, the University of Oslo is the country's leading public institution of research and higher learning with 27 000 students and 6000 employees. Department of Geosciences at the University of Oslo was formed in 2003 as a merger between the three earth sciences departments: the Geology Department, the Department of Physical Geography and the Department of Geophysics. The merger resulted in the widest ranging earth sciences department in Norway, covering a wide range of disciplines from deep mantle processes to atmospheric sciences.

The National Center for Atmospheric Research (NCAR) is a federally funded research and development center devoted to service, research and education in the atmospheric and related sciences. NCAR's mission is to understand the behavior of the atmosphere and related physical, biological and social systems; to support, enhance and extend the capabilities of the university community and the broader scientific community – nationally and internationally; and to foster transfer of knowledge and technology for the betterment of life on Earth. The National Science Foundation is NCAR's primary sponsor, with significant additional support provided by other U.S. government agencies, other national governments and the private sector.

Kjeller Vindteknikk (KVT) was established in 1998 in Kjeller, Norway, as a spin-off from the Institute for Energy Technology (IFE). With the increasing number of customers in Sweden, a subsidiary was open in Stockholm in 2009. Today, KVT is one of the leading companies in wind measurement and analysis in Norway and Sweden. The staff consists of meteorologists, physicists, engineers and technicians. Kjeller Vindteknikk has extensive experience from a large number of wind power projects in Sweden, Norway and other countries such as Iceland, Bulgaria and Macedonia.

The Norwegian Forest and Landscape Institute (NFLI) is one of Norway's foremost scientific institutions regarding the use of forest resources, forest ecology and the environment. The institute is also responsible for a range of national mapping programs and resource inventories related to land cover, forestry, agriculture, landscape and the environment. The institute provides knowledge to the authorities, the business community and the general public in order to contribute to the sustainable management of and value creation based on land resources through research and data management.

The Swedish University of Agricultural Sciences (SLU) is a university focusing on the sustainable use of biological natural resources, as well as on environmental and life sciences. The activities span from genes and molecules to biodiversity, animal health, bioenergy and food supply. Urban and regional planning, sustainable urban and rural development and global issues such as climate change are also on the agenda.

B. How the project is organised

A project involving a variety of competence from different institutions should be divided into sub projects addressing the different fields, and for WISLINE we identified 5 sub projects or work packages (WPs). These are presented in Figure 4, which shows the project structure. While WP1 mainly addresses the microphysics of the AROME model, and hence the scientific basis of the project, WP2 will together with WP3 apply the results from WP1 by simulating climate loads such as ice, snow and wind, and produce datasets for both present and future climate. As WP4 addresses forest damage from wind and snow, it will apply data from WP2 and WP3 directly by combining wind and snow data with forest damage data. The activities of WP5 are related to data storage and availability, which is essential as WISLINE is under obligation to provide open access to data. The different WPs will be described more in detail below.

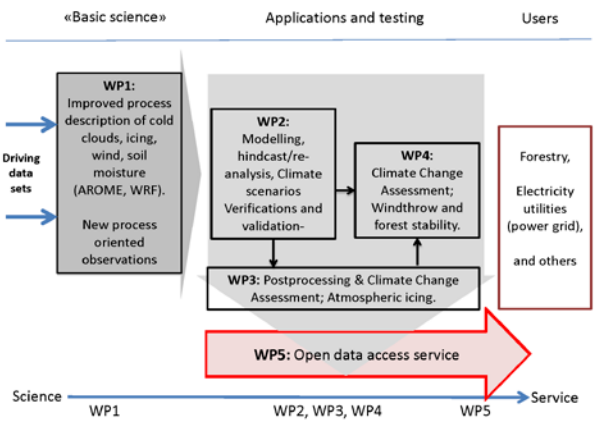

Figure 4: The project structure

The end users of the methods and data from WISLINE will be agencies and private companies connected to forestry, power supply, telecommunication and aviation. The user group will be invited to take active part in the project in order to assure that the results of WISLINE will benefit planning of robust infrastructure and protection of natural environment in a changing climate.

II. THE WORK PACAKGES OF WISLINE

The activities that are necessary in order to meet the objectives of WISLINE have been placed under the different WPs according to academic field and need for competence. This section provides a brief presentation of each WP.

A. WP1 – Improved predictions of atmospheric icing by upgrading the cloud microphysics scheme in the AROME NWP model

The NWP model AROME is a LAM run operationally at MET Norway as well as several other European forecasting centers. The current AROME cloud microphysics scheme is based upon Cohard and Pinty (2000), which when followed backward through the literature, has physical processes similar to Ferrier (1994), Rutledge and Hobbs (1984), and Lin et al (1983). The recent study by Liu et al. (2011) showed how the schemes with roots in Lin et al. (1983) all predicted too much ice and too little liquid and resulted in too much surface precipitation compared to observations. In contrast, the Thompson et al (2008) and Morrison et al (2009) schemes predicted much more liquid and less ice with surface precipitation that very closely matched the observations. The objective of WP1 is to improve the microphysics scheme of AROME and hence its ability to simulate cloud droplet distribution and precipitation processes.

A realistic distribution of cloud ice and supercooled droplets is essential if the model is used for simulating cloud icing on infrastructure such as power lines, and the model will be verified against icing observation from Statnett's test span at Ålvikfjellet in Western Norway. We also plan to purchase a Thies distrometer for validation purposes, and place it at Gaustatoppen (Figure 5), which is a mountain in Eastern Norway, 1883 m above sea level. As part of the project Development of a toolbox for assessing Frost and Rime ice impact on overhead Transmission Lines (FRonTLINES), Kjeller Vindteknikk and Statnett plan to set up a second test span, which will be available for WISLINE for validation purposes. Furthermore FRonTLINES activities on forecasting atmospheric icing and hoar frost will benefit from the improvements of AROME's microphysics.

Figure 5: Gaustatoppen (Photo Ole Jørgen Østby / MET)

WP1 will be led by Jón Egill Kristjánsson from The University of Oslo, and the co leader will be Roy Rasmussen from NCAR. Greg Thompson from NCAR will also contribute to this work. Major parts of WP1 will be carried out as a PhD project by Bjørg Jenny K. Engdahl at the Norwegian Meteorological Institute, supervised by professor Kristjánsson. The activities of WP1 will increase AROME's ability to predict precipitation and icing events, which will benefit both planning and operation of infrastructure such as power lines, public roads and air ports. This will also make the AROME a robust tool for downscaling data from climate models to investigate ice and snow loads in a future climate.

B. WP2 –Establish high-resolution datasets for present and future climate

The design of infrastructure with respect to climate loads not only requires adequate modelling tools but also datasets of sufficient length. The objective of WP2 is to establish both a high resolution hindcast archive and a dataset for future climate based on the AROME model with the improved micro physics scheme from WP1. Design values are mainly based on extreme value analysis e.g. one need to design for ice loads that have a return period of 150 years, which means that the length of the dataset should be three to four decades. To provide datasets of such lengths is beyond the scope of WISLINE, which will demonstrate the use of AROME to produce high resolution datasets of approximately one decade for present and future climate. The datasets from AROME will have a spatial resolution of 2.5 km, but we also plan to apply a surface model to downscale data further to 1 km.

WP2 will be led by Jan Erik Haugen at The Norwegian Meteorological Institute with contribution from at least three other scientists from MET Norway. The work will be done in close collaborations with WP3, which will focus on wind and icing climatology and WP4, which addresses forest damage.

C. WP3– Climate change influence on the geographical distribution of wind and icing design loads in Norway

Ice loads on infrastructure such as power lines are calculated by applying a postprocessor on data from NWP models. The postprocessor will calculate ice load (kg ice per meter line) based on variables such as precipitation, wind speed, temperature, liquid water content and droplet distribution. We plan to develop existing postprocessors further and apply these on data from WP2 in order to create datasets for atmospheric icing in both present and future climate. Theses activities will be carried out in collaboration with FRonTLINES.

Although WP2 will provide wind data, further work on the data is required since a horizontal resolution of 2.5 km is not sufficient to describe wind loads in complex terrain. Methods for further downscaling will be tested and validated against observations, and recommended methods will be demonstrated and applied to both hindcast data as well as data from climate projections.

WP3 will be led by Bjørn Egil K. Nygaard from KVT, and Greg Thompson from NCAR as well as scientists from MET will contribute to the work. The work on wind in complex terrain will be supervised by Knut Harstveit from KVT.

D. WP4– Forest damage from wind and snow

Damage to forest by wind and snow occurs if the load from wind and/or snow exceeds the resistance of the forest to this load. The vulnerability of the forest to this kind of damage also depend on soil wetness and the surrounding topography as this strongly influences the local wind conditions, and we plan to estimate an index for wind speed by combining downscaled wind data with an elevation model. We will then fit a statistical model for forest damage based on wind, snow and soil data and validate it against a forest damage database. Based on this model and datasets from WP2 and WP3, a risk map for weather induced forest damage in both present and future climate will be created.

WP4 will be led by Svein Solberg at NFLI with contributions from scientists at NFLI and MET as well as Kristina Blennow from SLU.

E. WP5– Data Services

According to the conditions for R&D projects issued by the Research Council, we are under obligation to provide open access to the datasets produced by WISLINE. During the project period WP5 will prepare, manage and publish the data sets through relevant portals and servers, assuring that end user will benefit from the datasets as soon as they are considered suitable for publication. WP5 will be led by Harold Mc Innes at MET Norway.

ACKNOWLEDGMENT

The authors would like to thank The Research Council of Norway for the funding of WISLINE (Project No. 244106/E10).

REFERENCES

[1] Albrecht, A., et al. (2012). "How does silviculture affect storm damage in forests of south-western Germany? Results from empirical modeling based on long-term observations." European Journal of Forest Research 131(1): 229-247.

[2] Bengtsson, A. and C. Nilsson (2007). "Extreme value modelling of storm damage in Swedish forests (vol 7, pg 515, 2007)." Natural Hazards and Earth System Sciences 7(5): 615-615.

[3] Cohard, J.-M., and J.-P. Pinty, (2000) A comprehensive two-moment warm microphysical bulk scheme. Part I: Description and selective tests. Q. J. R. Meteorol. Soc., 126, 1815-1842.

[4] Ferrier, B. S., (1994). A double-moment multiple-phase four-class bulk ice scheme. Part I: Description. J. Atmos. Sci., 51, 249–280.

[5] Frick, C., and H. Wernli, (2012). A Case Study of High-Impact Wet Snowfall in Northwest Germany (25–27 November 2005): Observations, Dynamics, and Forecast Performance. Wea. Forecasting, 27, 1217-1234.

[6] Gregow, H., et al. (2011). "Combined Occurrence of Wind, Snow Loading and Soil Frost with Implications for Risks to Forestry in Finland under the Current and Changing Climatic Conditions." Silva Fennica 45(1): 35-54.

[7] Gyakum, J. R., and P. J. Roebber, (2001). The 1998 Ice Storm—Analysis of a Planetary-Scale Event. Mon. Wea. Rev., 129, 2983-2997.

[8] Harstveit K, Ø Byrkjedal and E. Berge (2009). Validation of Regional In-Cloud Icing Maps in Norway. IWAIS XIII, Andermatt, September 8 to 11, 2009

[9] Kamimura, K., et al. (2012). "Root anchorage of hinoki (Chamaecyparis obtuse (Sieb. Et Zucc.) Endl.) under the combined loading of wind and rapidly supplied water on soil: analyses based on tree-pulling experiments." European Journal of Forest Research 131(1): 219-227.

[10] Kellomaki, S., et al. (2010). "Model Computations on the Climate Change Effects on Snow Cover, Soil Moisture and Soil Frost in the Boreal Conditions over Finland." Silva Fennica 44(2): 213-233.

[11] Lin, Y.-L., R. D. Farley, and H. D. Orville, (1983). Bulk parameterization of the snow field in a cloud model. J. Climate Appl. Meteor., 22, 1065–1092.

[12] Liu, C., K. Ikeda, G. Thompson, R. Rasmussen, and J. Dudhia, (2011). High-Resolution Simulations of Wintertime Precipitation in the Colorado Headwaters Region: Sensitivity to Physics Parameterizations. Mon. Wea. Rev., 139, 3533-3553.

[13] Morrison, H., G. Thompson, and V. Tatarskii, (2009). Impact of cloud micrpohysics on the development of trailing stratiform precipitation in a simulated squall line: Comparison of one- and two-moment schemes. Mon. Wea. Rev., 137, 991-1007.

[14] Nielsen, C. N. (2001). "Veiledning i styrkelse af stormfasthed og sundhed i nåletræbevoksninger." Dansk Skovbruks Tidsskrift(4/01): 216-263.

[15] Nilsson, C., et al. (2004). "Recorded storm damage in Swedish forests 1901-2000." Forest Ecology and Management 199(1): 165-173.

[16] Nygaard, B. E. K. (2009). "Evaluation of icing simulations for the COST 727 icing test sites in Europe." IWAIS XIII, Andermatt, Switzerland (2009).

[17] Nygaard, B. E. K., H. Ágústsson, and K. Somfalvi-Toth, (2013). Modeling Wet Snow Accretion on Power Lines: Improvements to Previous Methods Using 50 Years of Observations. J. Appl. Meteorol. Climatol., 52, 2189-2203.

[18] Rutledge, S. A., and P. V. Hobbs, (1984). The mesoscale and microscale structure and organization of clouds and precipitation in midlatitude cyclones. XII: A diagnostic modeling study of precipitation development in narrow cold-frontal rainbands. J. Atmos. Sci., 41, 2949-2972.

[19] Schelhaas, M. J., et al. (2003). "Natural disturbances in the European forests in the 19th and 20th centuries." Global Change Biology 9(11): 1620-1633.

[20] Schlyter, P., et al. (2006). "Assessment of the impacts of climate change and weather extremes on boreal forests in northern Europe, focusing on Norway spruce." Climate Research 31(1): 75-84.

[21] Thompson, G., P. R. Field, W. R. Hall, and R. M. Rasmussen, (2008). Explicit forecasts of winter precipitation using an improved bulk microphysics scheme. Part II: Implementation of a new snow parameterization. Mon. Wea. Rev., 136, 5095-5115.

TESTING SIX WET SNOW MODELS BY 30 YEARS OF OBSERVATIONS IN BULGARIA

Dimitar Nikolov[1], Lasse Makkonen[2]
[1] National Institute of Meteorology and Hydrology – Bulgarian Academy of Sciences, [2] VTT - Finland
dimitar.nikolov@meteo.bg

***Abstract*: Six simple wet snow accretion models are applied for simulations of well documented historical severe wet snow events in Bulgaria for the period 1969-1998. The data base consists of information about the diameters and masses, and thereof about the densities, of wet snow depositions in cases of damages on power lines. These measurements were taken soon after each of the damage. For all cases is checked if the meteorological conditions correspond to the wet snow accretion criterion of Makkonen. The models used in this study are: the model of Admirat and Sakamoto (Admirat et al., 1986a,b, Admirat and Sakamoto, 1988a), the model of Finstad et al. (1988), two model suggestions of Sakamoto and Miura (1993), the model of Makkonen (1989) and its improvement (Makkonen and Wichura, 2010) and one with the latest suggestion for the sticking efficiency by Nygaard et al. (2013).**

The estimated density of the wet snow depositions varied between 700 and 400 kg/m^3 and these measured values are used in the calculations instead of the experimental relationships proposed in some of the models. Working with known densities allows us to make conclusions for the approximations of the sticking efficiency and the snow concentration in air. The models are tested with two data sets – the original one consisting of standard three and six hourly synoptic measurements and its transformation into hourly values.

The sensitivity of some of the models to the meteorological parameters is also demonstrated.

Keywords: wet snow accumulation and model assesments, sticking efficiency and fall velocities of snowflakes

ABBREVIATIONS OF THE USED WET SNOW MODLES

AS	*Admirat and Sakamoto*
Finstad	*Finstad, Fikke and Ervik)*
SM	*Sakamoto and Miura*
LM	*Makkonen*
BEN	*Nygaard et al.*
α_2	*sticking efficiency*

INTRODUCTION

Wet snow accretion affects many regions located not only in cold climates. The phenomenon is common in France [3, 5, and 8], Japan [3, 15, and 16], Norway and Iceland [6] but also in parts of Central or South Europe [4]. Severe wet-snow storms are common even in Southeast Europe, e.g. the central south and southeast regions of Bulgaria. In this area, especially in the mountainous regions (the mountain Rodopes), wet snow causes damage almost every year [11 and 12]. In winter 2011-2012 alone four damages happened there. The most recent case is that from 6 to 7 January 2012 but now the affected regions were not limited only to the Rodophes - they encompassed almost the whole country. More than 200 poles collapsed and several overhead conductors were broken, more than 500 000 residents were affected, some of them for up to 6 days. Some reports of wet snow depositions with diameter up to 20 cm appeared in the public, but no official information is still available, except few photos at the disposal of the Electricity System Operator. No quantitative measurements from that event are available.

The models used in this study are: the model of Admirat and Sakamoto [1-3], the model of Finstad et al. [7], two model suggestions of Sakamoto and Miura [14] for the sticking efficiency, one with the latest suggestion of Nygaard et al. [13] and the model of Makkonen [9] and its improvement [10].

The models have been applied to 10 past severe wet snow events so far. The estimated density of the wet snow depositions varied between 700 and 400 kg/m^3 and these measured values have been used in the calculations instead of the experimental relationships proposed in the models. In the few cases, where no density measurements were available or they were not trustworthy, we have estimated the density indirectly. Working with known densities has allowed us to make conclusions for the approximations of the sticking efficiency and the snow concentration in air. The proposed density formulas have been also roughly evaluated.

I. SHORT DESCRIPTION OF THE USED MODELS

The above mentioned six simple wet snow accretion models have been used in this study. These models use only the available meteorological data as input information and some theoretical or experimental assumptions and relationships. The six models could be divided into two groups according to the method utilized for parameterization of the mass concentration of snow in air. The first group estimates this quantity using the precipitation rate and the assumption that the fall velocity of the snow particles is 1 m/s – the first five of the used models belong to this group. Actually they differ from each other only in the approximation of the sticking efficiency.

In the second group is only the model of Makkonen (the first version and its improvement). This model uses the horizontal visibility during snowfall for estimation of the snow concentration in air. It was utilized in a case study simulation of the severe wet snow event in Münsterland, Germany in 2005, showing good results [10].

All of the models have the following same assumptions, which are true in a wet snow process: cylindrical form of the depositions and unity collision efficiency. All calculations have been made for diameter of the conductor 2 cm. For determination of the beginning and ending of wet snow accretion process the criterion of Makkonen [9, 10], namely the web bulb temperature to be above - 0.1 ^{o}C, has been applied.

A. The sticking efficiency in the different models

Admirat et al. [1] proposed the sticking efficiency to be approximated by the inverse value of the wind speed, assuming that the fall velocity of the snowflakes is 1 m/s. Finstad et al. [7] suggested the following formula for the sticking efficiency,

trying to reflect its dependency on the air temperature (T_a) and the diameter of the obstacle (D):

$$\alpha_2 = \frac{0.038\ T_a}{VD} \qquad (1)$$

They also set up ranges of validity, which are $0^oC \le Ta \le 4\ ^oC$, $5 \le V \le 15$ m/s, and $0.01 \le D \le 0.04$ m and all values of α_2 above 1 are taken to be just 1. According to this expression this coefficient will increase with the temperature and will have its maxima at the end of the accepted temperature range.

Sakamoto and Miura [14] emphasized the reasonable dependence of α_2 on the conductor diameter, but criticized its constant increasing with the air temperature. They pointed out, that according to their observations, there should be a temperature point where the coefficient achieves its maximum and decreases in both sides and proposed the following approximations, which are based on wind tunnel experiments and observations of few natural wet snow events:

$$\alpha_2 = \exp(-1.01 + 4.37\ T_r - 6.89\ T_r^2 - 0.0168\ P\ V\ t), \qquad (2)$$

where t is the time step, V is the wind speed, P is the precipitation rate, $T_r = T/T_d$, T is the air temperature and T_d is the upper temperature limit above which snow turns into rain. In our calculations with this model the value of 4^oC is used. The proposed expression for this coefficient possess the expected behaviour with a maximum at certain temperature point, which depends also on the chosen upper temperature limit. At fixed other conditions the maximums are shifting into direction of the positive temperatures, the curves are becoming wider and more flat at the top but the maximum values are almost the same. This is presented on the figure 1.

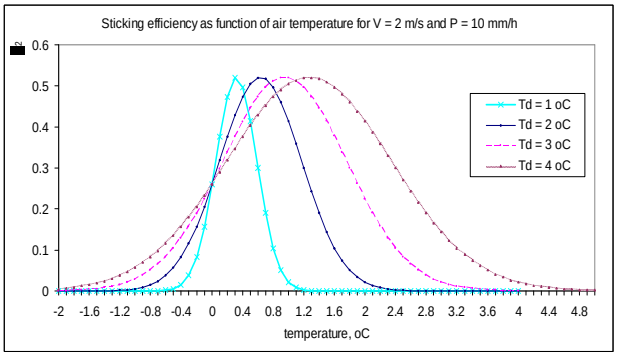

Figure 1: The curves for α_2 according to equation (11) for four different upper temperature limits

The accretion efficiency according to equation (2) decreases with increasing wind speed and precipitation rate but it is independent of the diameter of the obstacle. It has its absolute maximum in the corresponding temperature points for low precipitation rates and low wind speeds. However high wind speeds and/or precipitation rates may compensate the decreasing of the efficiency and may lead to an increase of the total ice load with increasing the values of these both parameters up to a certain level before decreasing. This was pointed out by the authors themselves, who stated that according to their calculations the estimated snow mass begins to decrease when the total precipitation exceeds 30 and 60 mm for wind speed 16 and 8 m/s correspondingly. It should be noted that for very small precipitation rate i.e. 1 mm/h the maximum values of α_2 are very high even for strong wind speeds – they remain above 0.5 up to 23 m/s – see figure 2.

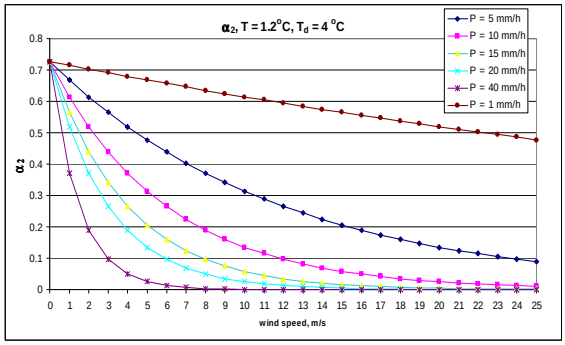

Figure 2: Change of α_2 according to equation (2) with the wind speed for different precipitation rates, Td = 4 ^oC and fixed air temperature T = 1.2 ^oC

The whole behaviour of α_2, proposed by the authors, seems quite reasonable except the independence of the diameter of the conductor. In order to overcome this Sakamoto and Miura [14] joined the advantages of their model with the model of Finstad et al. and recommended for α_2:

$$\alpha_2 = 4.5\ \frac{\exp\left[-6\,(T/T_d - 0.320)^2\right]}{V^{0.2} D} \qquad (3)$$

According to this formula α_2 has its maximum always at the same temperature as equation (2) but are much lower. Certainly this underestimation of α_2 results also in lower ice loads and diameters of the depositions as will be shown in the next paragraph. It should be also noted that although the dependence on the diameter is now included in the formula, the dependency on the precipitation rate is excluded.

Recently Nygaard et al [13] proposed for the sticking efficiency an expression based again only on wind speed:

$$\alpha_2 = V^{-0.5} \qquad (4).$$

The model of Makkonen uses for the sticking efficiency the approximation of Admirat and Sakamoto. Description of this model and its improvement can be find in Makkonen [9] and Makkonen and Wichura [10].

II. DATA TRANSORMATIONS AND INPUT CHANGES

In order to better investigate and compare the selected models in regard to all their peculiarities the following transformations and transitions of the input data and quantities have been made:

1. *Time scale transformation of the input data (transformation of the short data set into long data set)*

This transformation is determined by the fact that the measurements in the used stations are the standard surface meteorological observations, which means that most of them are three hourly and those of the precipitation amounts three or six hourly, and it is reasonable to expect that hourly intervals should represent an event better. For the assessment of the hourly values the following simple assumption has been made – the values of the air temperature, the wind speed and the visibility have been assumed to be the same in the hours before and after the SYNOP observations, except in cases where rapid changes occurred – then additional adjustments have been made. The precipitation amounts have been divided equally in the measurement intervals. In addition to the described transformation some corrections concerning the precipitation data have been also performed - when simultaneous snow and rain was observed, appropriate reduction of the total precipitation amount has been made in order to derive the part only from snow.

2. *Change of the upper temperature limits*

This transformation concerns only both models of Sakamoto and Miura (1993) because only they possess such dependence. Four different upper temperature limits have been tested in this study - Td = 1, 2, 3, and 4 ^{o}C.

III. MODEL RESULTS

In figure 3 an example of the results from the model simulations for the case 2 are shown. It can be seen that in this case the models of Admirat and Sakamoto (AS) and of Makkonen show the best fit to the measured data (given as a box plot). The second model of Sakamoto and Miura (S-M-2) and the model of Finstad underestimate significantly, while the models of Björn Egil Nygaard et al (BEN) and the first one of Sakamoto and Miura (S-M-1) overestimate very much the measured values of the radius of the depositions. This pattern is similar in all the cases investigated.

All results, except those for the model of Finstad, are summarized graphically in the following six scatter plots (Figures 4 – 8). This concerns mostly the results with the long data set. Only the results for S-M-1 model are presented with two graphics and this will be explained later. The results for the Finstad model are similar to those of S-M-2.

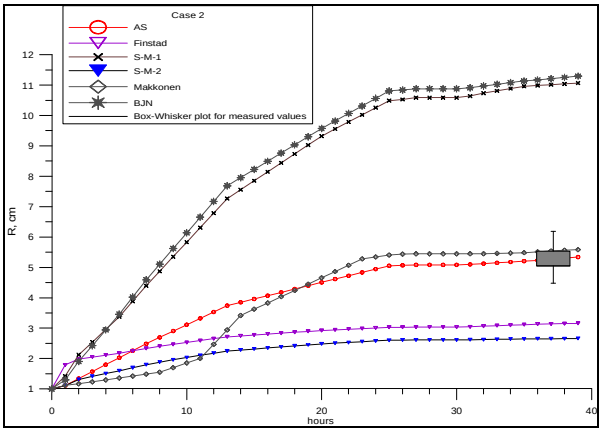

Figure 3: Model results for case 2, 06-07.03.1984

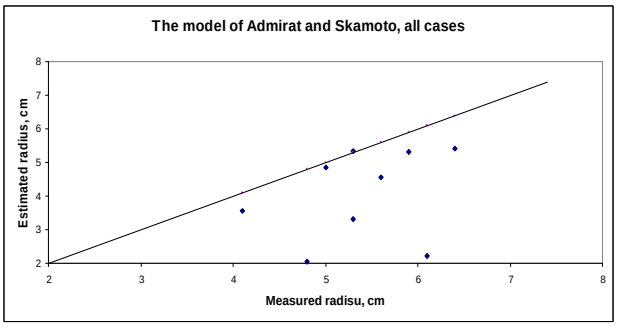

Figure 4: Scatter plot for the results of the model of Admirat and Sakamoto (the black solid line represents the true values)

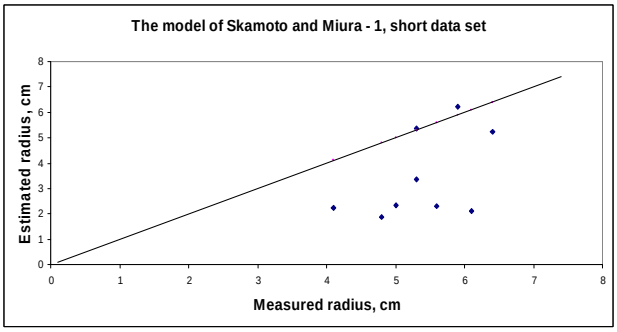

Figure 5a: Scatter plot for the S-M-1 model, short data set

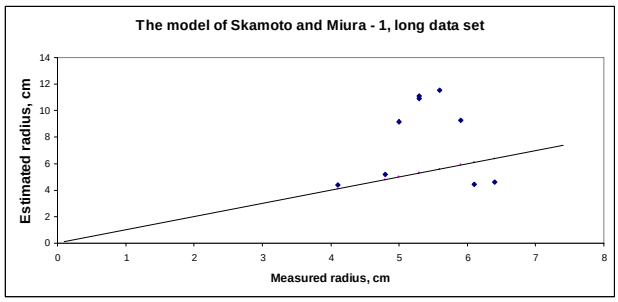

Figure 5b: Scatter plot for S-M-1 model, long data set

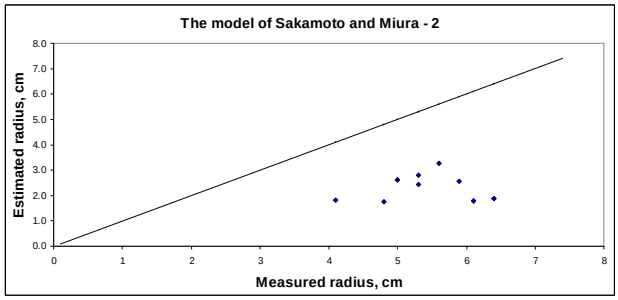

Figure 6: Scatter plot for S-M-2 model

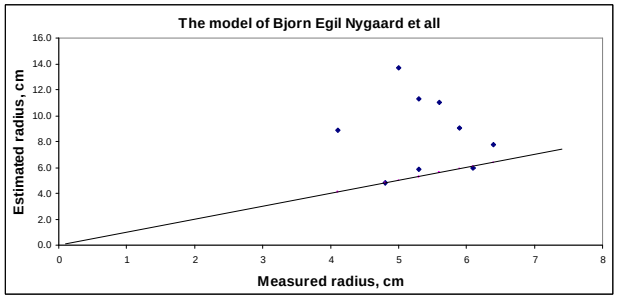

Fig. 7: Scatter plot for the BEN model

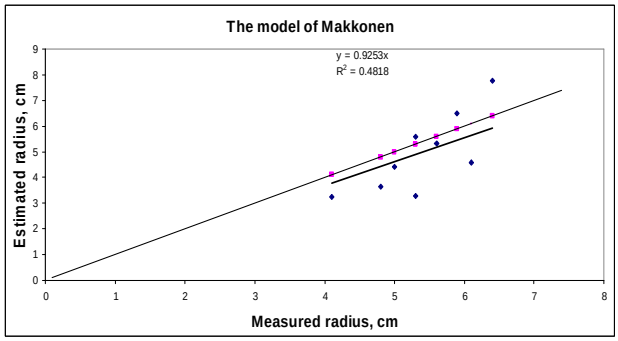

Fig. 8: Scatter plot for the model of Makkonen

At first sight it seems that all models, but that of Makkonen, either underestimate or overestimate the measured values. Indeed only the LM model shows narrow spread of the points close to the true values (Fig. 8). The S-M-2 model (Fig. 6), as well as the Finstad model, always vastly underestimates the true values with both data sets. The S-M-1 model shows change of front when changing the time scale of the input data. The usage of short data set leads to significant underestimation with exception of three cases (Fig. 5a). The transformation of the short data set into a long one (hourly input data) always results in serious increase of the model estimations (Fig. 5b). The BEN model demonstrates significant overestimation in more than the half of the cases but fits well to the measured values in three of them (Fig. 7). Figure 4 for the AS model also depicts low underestimation. However, it has been found that this underestimation is mainly connected with the cases with high

wind speeds (above 10 m/s). When we remove these cases, the following picture appears – Fig. 9.

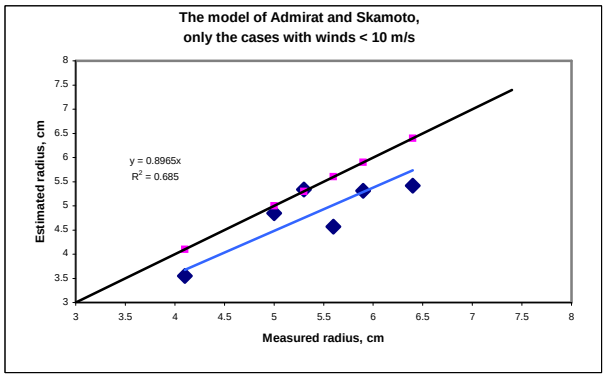

Figure 9: Scatter plot for the results for the model of Admirat and Sakamoto only for the cases with wind speed below 10 m/s.

Because the AS and BEN models are very similar, we have investigated closer the BEN results and we reveal that its three good estimations describe cases with high wind speeds. This was most evident in the last calculated case – the event from 02-03.02.1986 in Southeast Bulgaria - one of the most severe cases ever happened. The mean measured value for the radius of the deposition was 6.1 cm and the mean ice load 6.5 kg/m. The BEN model has estimated 5.8 cm and 6.1 kg/m. No one from all other models approaches so close to these values. The LM and AS yield 4.63 and 4.43 cm correspondingly.

On the next two figures are presented two pictures from that event, which illustrate the situation, as well as the measuring procedure.

Figure 10: Sampling and measuring procedure from the event on 02-03.02.1986

Figure 11: Sampling and measuring procedure form the event on 02-03.02

Table 1 summarizes the results from the investigation of the influence of the data transformation. It can be seen that all models, except for the S-M-1, undergo very low change with this transformation and the AS model even not any. This means that these models could be used directly with the three or six hourly measurements. The strong increase (in the first case up to 100%) in the results of the S-M-1 model is due to the sensitivity of the sticking efficiency and hence the model itself to the meteorological variables. As mentioned above α_2 has very high values when the precipitation rates are small and the air temperature is close to the points of extrema.

Table 1 Relative changes between the short and long data sets for the first four cases (values in %)

AS	Finst.	S-M-1	S-M-2	BEN	LM
0.0	- 3.9	48.1	- 3.4	- 0.9	2.3

Moreover – the model of SM1 features high dependence not only in regards to the transformation of the time scale of the input data but also on the choice of the upper temperature limit. This is shown on Fig. 12a representing the increasing of the calculated with four different upper temperature limits radiuses of the wet snow depositions from the first event. The used temperature limits are 1, 2, 3 and 4 ^{o}C and the corresponding curves reveal significant differences. The greatest results are yielded with Td = 4 ^{o}C and this is determined mostly by the favourable combination of low precipitation rate (mean value of 0.8 mm/h) and air temperature around 1.3 ^{o}C, which is exactly the point where the sticking efficiency has its absolute maximum for Td = 4^{o}C (see Fig. 1).

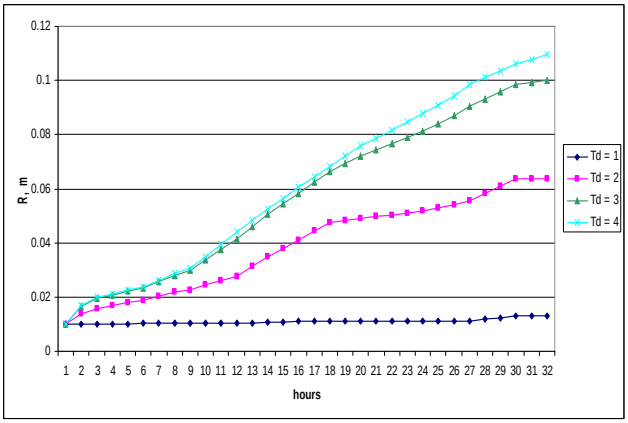

Figure 12a: Estimated radiuses of the deposited wet snow in case 1 with the SM1 model for different upper temperature limits – Td = 1, 2, 3 and 4 ^{o}C; long data set

Figures 12b and 12c compare the radii for the four selected temperature limits and their relative change in regards to the data transformation from short to long data set for the first case. As mentioned above the greatest values of the radii are obtained for Td = 4^{o}C for both data sets. The data transformation yields to an increment in the radii of more than 100 % for all temperature limits except for the lowest one. For Td = 1 ^{o}C the increase is only 24.3 %.

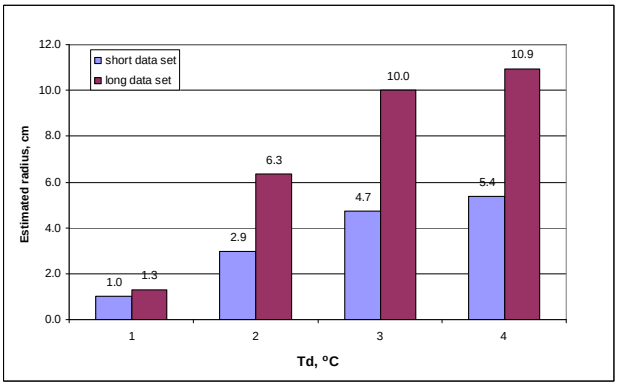

Figure 12b: Comparison of the estimated radiuses after the S-M-1 model by the transformation from the short to the long data set for the different upper temperature limits

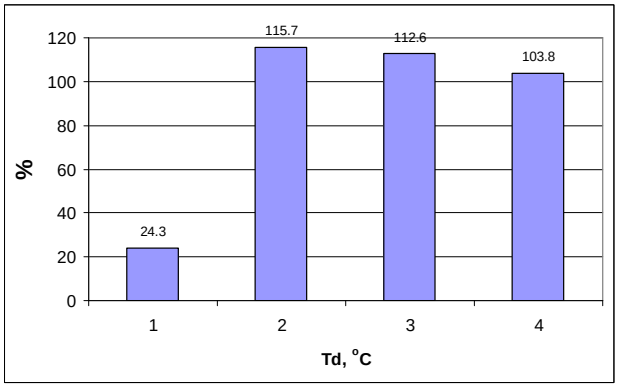

Fig. 12c: Relative change in the estimated radiuses by the transformation from the short to the long data set for the different upper temperature limits

The same investigation for the influence of the temperature limits has been done also for the sticking efficiency α_2. In summary, the S-M-1 model is very sensitive to transformation of the input data, because, on the one hand, this transformation divides the 3 or 6 hourly precipitation amount into low one hourly quantities and on the other hand it most often retains the high wind speeds for the hours between the observations (were there is no significant change in the wind speed between the three-hourly observations). These both operations act in direction of common enhancement of the sticking efficiency, especially when the air temperature is close to the point of the maximum for the selected Td. The location of these points depends on the chosen upper temperature limit, and this is another important sensitivity of the model.

IV. Conclusions

The models with best performance seem to be AS and LM – they both have relative good estimations of the measured values; both ate not sensitive to the data transformation and they always have close results. However, they have their own limitations. It may be assumed that the AS model gives not so good results for high wind speed cases. Above 10 m/s it underestimates the depositions – for such wind speeds the BEN models seems more appropriate. The LM should be used carefully when fog is presented together with the snowfall. However such combination seems to be rare except for the mountain regions.

The BEN model usually gives overestimation but yields very good results for wet snow conditions accompanied by high wind speed. Actually a combination of the two parameterisations – the one of AS for wind speed up to about 10 m/s and the one from BEN for wind speeds above – might be the best way.

The S-M-1 model sometimes gives good results but is very sensitive to the meteorological input information and to the chosen temperature limit.

The other two models (S-M-2 and Finstad) always underestimate the depositions, probably due to the very high assumed dependency on the wet snow radius.

References

[1] Admirat, P., Sakamoto, Y., De Goncourt, B., 1986a. Calibration of a Snow Accumulation Model Based on Actual Cases in Japan and France. Proc. Fourth Int. Workshop on Atmospheric Icing of Structure. IWAIS, Paris, France, pp. 129-133.

[2] Admirat, P., Sakamoto, Y., Lapeyre, J.L. and Maccagnan, M., 1986b. Quantitative results and proposed mechanisms on wet snow accretion in the Ishiuchi wind tunnel facilities. Third Int. Workshop Atmospheric Icing of Structures, Vancouver, B.C.

[3] Admirat, P. and Y. Sakamoto, 1988a. Calibration of a wet-snow model on real cases in Japan and France. Proc. Fourth Int. Workshop on Atmospheric Icing of Structures. IWAIS, Paris, France.

[4] Bonelli P., M. Lacavalla, P. Marcacci, G. Mariani, and G. Stella, 2011. Wet snow hazard for power lines: a forecast and alert system applied in Italy. Nat. Hazards Earth Syst. Sci., 11, 2419-2431, 2011

[5] Dalle, B. and P. Admirat, 2011. Wet snow accretion on overhead lines with French report of experience, Cold Regions Science and Technology 65: 43-51.

[6] Eliasson, A.-J., Thorsteins, E., Olafsson, H., 2000. Study of Wet Snow Events on the South Coast of Iceland. Proc. IX Int. Workshop on Atmospheric Icing of Structure. IWAIS, Chester, U.K.

[7] Finstad K., S. Fikke and E. Magnar, 1988. A comprehensive deterministic model for transmission line icing applied to laboratory and field observations. Proc. IV Int. Workshop on Atmospheric Icing of Structures. IWAIS, Paris, France

[8] Gland, H. and Admirat, P., 1986. Meteorological conditions for wet snow occurrence in France, Calculated and measured results in a recent case study on March 5th, 1985, Proc. Third Int. Workshop on Atmospheric icing of Structures. IWAIS, Vancouver, Canada.

[9] Makkonen, L., 1989. Estimation of wet snow accretion on structures. Cold Regions Science and Technology, 17(1): 83-88.

[10] Makkonen L. and B. Wichura, 2010: Simulating wet snow loads on power line cables by a simple model. Cold Regions Science and Technology, 61: 73-81.

[11] Moraliiski, E. and A. Gocheva, 1991. Estimation of the conductor icing in Bulgaria, Energetic, vol. 3-4 (in Bulgarian).

[12] Nikolov, D. and E. Moraliiski, 1999. Icing and damages on technical equipment on the territory of Bulgaria, Proc. of IV ECAM, Norrköping, Sweden.

[13] Nygaard, B.E.K., Ágústsson, H., Somfalvi-Tóth, K., 2013. Modeling wet snow accretion on power lines: Improvements to previous methods using 50 years of observations. J.Appl. Meteorol. Climatol. 52 (10), 2189–2203.

[14] Sakamoto, Y. and A. Miura, 1993. Comparative study of wet snow models for estimating snow load on power lines based on general meteorological parameters. Proc. Sixth Int. Workshop on Atmospheric Icing of Structures. IWAIS, Budapest, Hugary.

[15] Shoda, M. 1953. Studies on snow accretion. Res. Snow and Ice, 1:50-72 (in Japanese).

[16] Wakahama, G., Kuroiwa, D. and Goto, K., 1977. Snow accretion on electric wires and its prevention. J. Glaciol., 19(81): 479-487

Fault statistics on overhead transmission lines in Russia caused by icing

Sergey CHERESHNYUK, Vladimir LUGOVOI, Larisa TIMASHOVA

Research and Development Center at Federal Grid Company of Unified Energy System (R&D Center @ FGC UES)
Russia
e-mail: lione2000@mail.ru

Introduction

Icing events make a significant impact on normal operation of overhead transmission lines. During OHL operation, technical failures can occur. In the article, an attempt has been done to assess failure rate caused by icing. The analysis of the failure rate of overhead line components (towers, conductors, ground wires, insulators and line hardware) at 110-750 kV was done for the period from 1997 up to 2007.
The main goal of fault statistics analysis was to mark out elements of OHL and substations most suffering from icing events.

Accidents and incidents.

Depending on the character and heaviness of failure, it is possible to distinguish *accident* and *incident*. Accident it is an event when there is equipment damage or power outage for a long time. Incident it is an event when there is no or small equipment damage or power outage for a short time. According to Russian standards after every accident or incident happened, a special investigation commission is organized.

Investigation results are formalized with the "Technical failure investigation act". This act contains the following main sections:

- Address section – with main info on failure: day and time of failure beginning, location, damage, etc.
- Description section – with network operating conditions before failure, failure beginning and development, failure causes, damages description;
- Damaged equipment description section – with information on damaged equipment type, brand and technical parameters.

Fault statistics for substation equipment

During the period 1997-2007 at 110-750 kV substations were recorded nearly 6.500 events of substations' equipment failures. Main portion of failures happened with switchers (46,2%) and disconnectors (30,4%), less with transformers (12,9%). Icing events do not have a noticeable effect on damage statistics to main substation's equipment. So out of all the examined cases, no more than 2-3% ones occurred due to icing events.

Fault statistics for OHL and it's elements

During theperiod 1997-2007 at 110-750 kV OHL 9948 events of overhead line's components failures happened, including:

- 110 kV – 7953 (84,2%) events;
- 220 kV – 1185 (12,5%) events;
- 330 kV – 110 (1,2%) events;
- 500 kV – 164 (2,0%) events;
- 750 kV – 7 (0,1%) events.

Main failure causes as follow:

- outside interference (influence) (trees falling, running-down accidents, vandalism, etc.) – 26,2%;
- ice loads and combined ice-wind loads – 17,6%;
- lightning overvoltages – 15,2%;
- failures caused by technical condition of overhead line components – 13,8%.

During the period 1997-2007 occurred 324 events of tower damages.

Main causes for metal towers are:

- tower elements, conductors and ground wires stealing – 26,2%;
- climatic loads – 25,7%;
- corrosion and aging – 19,2%;
- building and mounting defects – 14,7%;
- outside interference (influence) – 13,9%.

Main causes for concrete towers are:

- climatic loads – 38,7%;
- building and mounting defects – 24,0%;
- outside interference (influence) – 15,4%.
- natural disasters – 13,8%.

During the period 1997-2007 happened 4755 event of conductor damages. Main causes are:

- Mounting defects – 10,7%;
- Icing – 10,2%;
- Trees and young growth – 11%;
- Corrosion, aging and strength loss – 10,4%;
- Outside interference – 13,1%.

During the period 1997-2007 occurred 1305 events of ground wires damages. Main causes are:

- Corrosion, aging and strength loss – 32,9%;
- lightning overvoltages – 21,1%;
- Icing – 17,9%.

Conclusion

Icing events have a significant impact on the reliability of power supply. The most damaged and vulnerable elements include conductors and ground wires. For these elements icing events are one of the major causes of damage.

Meteorological data for assessing climatic loads on overhead lines. Report from Cigré WG B2.28

Svein M. Fikke
Meteorological Consultant
fikke@metconsult.no

***Abstract*: Cigré has over the last decades published several reports on extreme weather actions, including loadings due to atmospheric icing, on electric overhead power lines. The last report was completed by WG B2.28 early 2015. For atmospheric icing the report describes a new approach for applying high resolution numerical meteorological weather prediction models where the cloud physics parameters are incorporated. Current operating test sites are presented, and some anticipated consequences of global climate change on icing are roughly discussed.**

Keywords: icing, wind, power lines, models, topgraphical influence, icing maps, icing measurements, climate change.

Legend and Abbreviations

Cigré	*International Council on Large Electric Systems*
SC B2	*Study Committee B2"Overhead Lines"*
WG	*Working Group*
IEC	*International Electrotechnical Commission*
NWP	*Numerical Weather Prediction model*
NNA	*National Normative Annex*

Introduction

The purpose of this report is to summarize new information relevant for assessing climatic loads on electric overhead lines. Such information has appeared in several publications from Cigré SCB2, as well as from other sources, after the publication of the Technical Report IEC 61774 "Overhead lines – Meteorological data for assessing climatic loads" in 1997 [1]. Later, Cigré WG B2.16 issued in 2006 the report "Guidelines for meteorological icing models, statistical methods and topographical effects" [2].

A new WG was set up by Cigré SC B2 in 2010 on "Meteorological data for assessing climatic loads. Update of IEC Technical Report (TR) 61774". According to its "Terms of Reference" WG B2.28 should: "compile and restructure updated meteorological knowledge for the purpose of application in international standards, especially on:

a) Turbulent wind enhancement behind steep terrain
b) Application of numerical weather prediction models
c) Measurements and observations of ice loads on overhead line components

Probably the most important reasons for reviewing meteorological data and assessment procedures concerning climatic loads and other adverse weather impacts on electric power overhead lines are the rapid developments in data availability for the atmosphere, better knowledge of physical processes relating to cloud physics and precipitation, and the capacities of modern computers. These factors have dramatically improved the reliability of modern weather forecasts. However, the same factors have also enhanced the ability to describe details in adequate weather parameters in local topography down to spatial scales relevant to the span length of electric power transmission lines, even in rough and complex terrain, by using standard NWPs.

Also, the concern on the effects of global warming due to anthropogenic emissions of greenhouse gases, mainly CO_2, has led to more specific attention on potential threats to electrical installations due to increased rates of extreme weather events, such as storms, floods, mud slides, rising sea level, foundations in melting permafrost, etc. A number of examples are given from many countries where pro-active mitigation actions are already taken or considered.

The final report from WG B2.28 is now in press [3]. This paper gives a short review of the part of the report with updated information on icing models, using weather forecasting models for the purpose of creating icing maps, and updated information on operating test sites for ice accretions.

Some anticipated effects from changes in the global climate on atmospheric icing, as well as a review of anti-icing and de-icing technologies are briefly mentioned.

A couple of wind issues are mentioned first however, as this may be relevant for wind on ice calculations.

I. Wind

Most common wind standards and design codes contain well accepted models for wind turbulence, therefore such models are not described in detail here. However, there are certain properties linked with some strong wind systems which are not always generally known or described in such wind codes. In particular this relates to vortex generation behind steep mountain sides. There are many examples that this kind of turbulence has occurred unexpectedly and caused damage to buildings and infrastructure in mountainous terrain.

A particular concern for wind engineering and overhead power line design has been the various transitions between wind gusts and mean winds of different averaging time for extra-tropical conditions. Therefore this aspect is analysed as well.

As these aspects are not a particular topic for IWAIS, the reader is instead referred to the Cigré WG B2.28 report [3].

II. Atmospheric Icing

A. A new approach to mapping of ice loadings

Atmospheric icing is already described in detail in Cigré TB 291 "Guidelines for meteorological icing models, statistical methods and topographical effects" [2]. The current brochure [3] updates some information concerning ice load measurements and modelling, especially, of wet snow accretion, and the application of NWP models for analyses of wet snow and rime ice accretions on electric overhead line conductors. However, NWP models are so far only adequate for individual case studies. For long term extreme value calculations it is necessary to run the wet snow model on long time series of regular meteorological data from weather stations. For rime ice a NWP is the only way to study this

phenomenon over a large area where no relevant data are available.

It has been found that the previously used accretion models for wet snow did not sufficiently explain a number of wet snow events in nature, in most cases the traditional model gave a systematic under-estimate of the actual wet snow loads. The model presented in this report is compared in particular with a great number of cases in Iceland where such loadings have been measured in great detail over many years. Therefore it was possible to revise the accretion model for wet snow on overhead lines to obtain a better fit with observations of such loads from the field.

Probably the biggest challenge with calculating ice loadings from any icing type is to obtain good quality input data. In the case of wet snow it is extremely important to ensure high quality measurements of precipitation. This may not be obvious in many cases, where, for instance, the "tipping bucket" method is used at regular weather stations. Snow measurements are always difficult as wind may blow the snow away from the gauge, even when it is equipped with a wind shield. But with a tipping bucket wet snow may accrete around the edge of the catchment part and hence disturb the catchment conditions for snow. Therefore such measurements must be given special attention.

In the case of rime ice there has been in principle no realistic way of getting "in situ" measurements of the fundamental cloud parameters like liquid water content and size distributions of cloud droplets, and indeed not from historic extreme rime ice events where the ice loadings should be re-analyzed. This situation has changed dramatically over the last years, when it has become possible to calculate such parameters from numerical models for the cloud atmosphere. In combination with digital information of the surface properties of the Earth, it has now become possible to calculate realistic high resolution values of rime icing in complex terrain by using advanced numerical weather prediction models.

As a demonstration of the potential of such modelling of both wet snow and rime ice, a recent map of ice loadings for Great Britain is presented in Figure 1. This map will be incorporated in the revision of EN 50341-1 [4] for the UK National Normative Annex (NNA). The inherent data in this map contains information on wet snow loads, rime ice loads and combined ice and wind loads, all provided in grid squares of 500 m x 500 m.

Wet snow loads are calculated with a return period of 50 years from regular weather stations. Due to the dense network of such stations in the UK it was possible to establish excellent correlation between individual stations and hence it was also possible to find good correlation functions with altitude and latitude over the whole UK.

In the case of rime icing a NWP model was run all through one selected winter season, and accordingly it was possible to identify relations with altitude and exposure for rime icing in the highlands. In order to evaluate rime ice loadings with a return period of 50 years standard procedures given in [4] were used. However, it was emphasized that whenever in the future new infrastructure should be built in these areas, a revision of the rime ice load assessments are strongly recommended.

If needed, other information, both meteorological and technical, can be gridded into the same system. The same grid boxes may contain other meteorological data, such as extremes for wind speeds, temperatures, snow depths on ground and lightning intensity. Also, they may contain operational and fault history of the overhead lines running through these grids.

In accordance with EN50341 requirements, the data is provided as wind only, ice only and combined wind and ice in the NNA.

Figure 1. Combined wet snow and rime ice loading map for Great Britain

B. Icing measurements

Atmospheric icing is monitored and measured manually or automatically using various instruments as described in [5] and [6]. The only standard reference for icing measurements is given in ISO 12494 "Atmospheric icing on structures" [7]. According to this standard the overall design of the measurement device should be in principle as follows:

A cylinder with a diameter of 30 mm is placed with the axis vertical and slowly rotating around the axis. The cylinder length should be minimum 0.5 m, but if heavy ice accretion is expected, length could be 1 m. The cylinder is placed 10 m above terrain.

Measurements of icing and ice accumulations have been widely performed in many countries to collect information to be used for especially design of overhead power lines. As there have been no generally accepted standard or method for such measurements, most countries have designed their own systems, mostly as test spans or racks of various types. Such measurements are discussed in Cigré TB 291 [2].

- However, there are some general difficulties with such measurements, especially for remote places. There are multiple reasons for this:
- Icing comprises, by itself, a hostile environment for any type of instrument, especially those based on electronic sensing and recording
- Instruments for on/off-measurements of icing are not feasible for measuring accumulated loads, and vice versa
- The accretion rate of icing on any sensor depends strongly on the mechanical design of the sensor itself
- Each individual icing type sets limitations on the manner ice accretion can be measured
- The icing rate, or efficiency of droplet or snow collection, varies with the dimensions and shape of the accreted ice itself.

Several systems should be mentioned because of their systematic use and extensive data bases. These are

1. The "Passive Ice Meter (PIM)" as used in Canada
2. Test spans as used in Iceland
3. Measuring rigs used in Russia.

4. Also some operating test sites (as per 2014) are indeed important and mentioned (Iceland, Hawke Hill (Newfoundland, Canada), Deadwater Fell (UK)).

Further details on ice measurements in Europe (except Iceland) can be found in the State-of- art report from COST Action 727 "Atmospheric icing on Structures" [5].

The influence on rime icing from topography is emphasized in the report. This is particularly important along coastal areas dominated by significant mountain areas. A descriptive image of such effects on rime icing is presented in Figure 2.

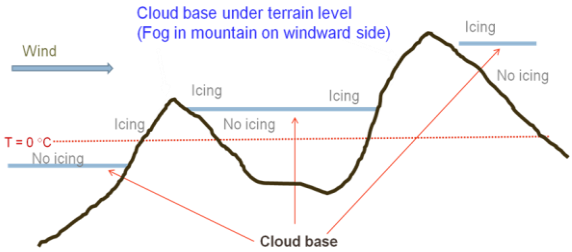

Figure 2. Schematic influence on cloud base and rime icing from upwind mountain topography.

A more comprehensive and detailed model for the macro-, meso- and microscale icing dependency of local and remote topography is developed in Russia and outlined in the report. The Russian procedures are here presented for the first time in English.

III. Changes in Global Climate

Although the question on climate change was not included in the tasks for this WG, some general comments are considered relevant for general information.

There are no longer any doubts that the global atmosphere is getting warmer mainly due to emissions of the greenhouse gases CO_2 and methane. This warming of the atmosphere will accordingly increase the total amounts of humidity in the atmosphere. But there is, at this point, very little evidence as to how this will in turn affect wet snow and rime ice loads for electric overhead lines. However, based on the available information on climate developments the following reasonings are found to be relevant for atmospheric icing in different areas:

- *Coastal areas*. As the sea temperature is also expected to rise, there may be fewer days of temperatures close to 0 °C along the coastal sides of continents, especially in northern latitudes. This may mean less frequency of wet snow incidents. However, higher intensity of short time wet snow precipitation may lead to higher loads when combined with low temperatures.
- *Continental inland*. Further inland from the coast where subfreezing temperatures are more frequent, higher wet snow loads in absolute values may be expected, although less frequent than at present. In predominant continental areas in northern latitudes the frequency and magnitude of wet snow loads are likely to increase.
- *Mountains*. In the mountain areas and continental highlands it is expected that the 0°C isotherm will be lifted on average, and hence lead to less frequent rime icing, at least at lower elevations. More humidity in clouds will contribute to higher rime ice loads whenever the conditions are favourable.
- *Extreme values*. It is not possible to make any sort of conclusions as to how the above arguments will influence the ice loadings with a given return period in local areas.
- For *freezing rain* there is at this point no strong indicator for significant change in either frequency or absolute load values following from the most likely scenarios for climate change.

However, a report published in 2014, from the Royal Society (UK) and National Academy of Sciences (US) [8], states:

Earth's lower atmosphere is becoming warmer and moister as a result of human-emitted greenhouse gases. This gives the potential for more energy for storms and certain severe weather events. Consistent with theoretical expectations, heavy rainfall and snowfall events (which increase the risk of flooding) and heatwaves are generally becoming more frequent. Trends in extreme rainfall vary from region to region: the most pronounced changes are evident in North America and parts of Europe, especially in winter.

Acknowledgment

The author would like to thank all members of the WG B2.28 for their active contributions. The main authors are:

S. M. Fikke, Convenor (NO), S. Chereshnyuk (RU), H. Ducloux (FR), A. J. Elíasson (IS), M. Farzaneh (CA), B.E.K. Nygaard (NO), and J. B. Wareing (UK).

Other contributors are: F. Jakl (SI), J. Toth (CA) and N. Sugawara (JP).

However, I hope this is not unfair for any others, but a particular tribute should be paid to Dr Bjørn Egil Kringlebotn Nygaard for his fundamental work on improving the wet snow accretion model and the implementation of icing models into regular NWPs, Sergey Chereshnyuk for sharing the long-awaited Russian methods and work in this field for the first time in the English language, and to Hervé Ducloux who did some new studies on average wind speed transformations. Hervé was also a great help during final editing phase of the report.

The officially appointed reviewers from Cigré SC B2 were P. Dulhunty (AU), L. Kempner (US) and A. Haldar (CA). Their comments and suggestions indeed enhanced the content and quality of this report.

References

[1] IEC TR 61774 "Overhead lines – Meteorological data for assessing climatic loads". Reference nubmer CEI/IEC 61774: 1997, Geneva, Switzerland.

[2] Cigré WG B2.16 TB 291 "Guidelines for meteorological icing models, statistical methods and topographical effects", Cigré, April 2006, Paris, France.

[3] Cigré WG B2.28 "Meteorological data for assessing climatic loads on overhead lines", In press. Cigré, Paris, France.

[4] EN 50341-1: Overhead electrical lines exceeding AC 1 kV - General requirements - Common specifications, 2012.

[5] S. Fikke, G. Ronsten, A. Heimo, S. Kunz, M. Ostrolizlik, P. Persson, J. Sabata, B. Wareing, B. Wichura, J. Chum, T. Laakso, K. Säntti et L. Makkonen, COST 727: Atmospheric icing on structures - Measurements and data collection on icing - State of the art, Publication of MeteoSwiss, Switzerland, 2006.

[6] A. Heimo et al., COST 727 - Final Report: Atmospheric Icing on Structures, WMO/CIMO, In press.

[7] ISO 12494: Atmospheric icing on structures, ISO, 2000.

[8] Royal Society (UK) and the National Academy of Sciences (US), «Climate Change - Evidence & Causes,» 2014. Available: https://royalsociety.org/policy/projects/climate-evidence-causes/.

Investigation of Using Icephobic Coatings on a Cable Stayed Bridge

Ahmed Abdelaal[1], Clinton Mirto[1], Douglas Nims[1], Tsun-Ming Ng[1], Kathleen Jones[2], Charles Ryerson[2], Arthur Helmicki[3], Victor Hunt[3]

[1]University of Toledo, USA, [2]US Army Cold Regions Engineering and Research Laboratory, [3]University of Cincinnati, USA

Douglas.Nims@utoledo.edu

ABSTRACT: **Icing is a significant challenge that affects structures in many countries. Bridges are an example of structures that may be severely affected by atmospheric icing. The Veterans' Glass City Skyway (VGCS) is a single pylon cable stayed bridge with a main span of 375 m in Toledo, Ohio which was opened to traffic in 2007. The VGCS is owned by the Ohio Department of Transportation (ODOT). Six major icing events have occurred on the bridge which led to the closure of bridge lanes and damaged cars. Therefore, over 80 anti-icing/de-icing technologies were investigated. In addition to considering active and passive technologies, bridge management was considered as an approach to assist the bridge operators.**

Tests on icephobic coatings were conducted at the University of Toledo (UT). An icing tunnel was used to conduct experiments with conditions similar to natural icing scenarios. Three different coatings were tested in the icing tunnel. Based on the results of the icing tunnel test, one coating was selected for testing outdoors in simulated icing events. The stay cable sheaths of the VGCS are made of stainless steel, which offers aesthetic and life cycle cost advantages. Because the stay appearance is important, in addition to preventing ice build-up, being durable enough to last through several winters, and being economical, the coating must not alter the appearance of the stays.

None of the coatings tested performed the anti-icing function effectively. Under the same conditions and over the same duration, the ice layer accumulated on the coated specimen was thicker than that on the uncoated specimen. The results showed that water would bead on the coating, which initially prevented ice from forming directly on the stainless steel surface. However, rather than running off the coating, the water droplets would freeze rapidly on top of the coating. This resulted in a craggy, uneven surface that trapped water effectively, which in-turn led to an increase in ice accumulation rate compared to an uncoated specimen.

Other techniques such as chemicals and internal heating were also tested in this project. Overall, no technique, active or passive, met the operational requirements for the bridge. Therefore, ODOT elected to monitor the conditions on the bridge and protect the traveling public by closing traffic lanes when there is a risk of ice fall. An automated real time monitoring system (dashboard) was built to identify possible icing conditions.

Keywords: icing, bridges, coatings, anti-/de-icing

INTRODUCTION

Icing is a worldwide problem that many structures suffer from. In the United States and lower part of Canada, 36 cable stayed bridges are open to traffic, under construction or proposed, and 32 located in or near regions where damaging ice storms have been reported historically. Furthermore, suspension bridges or other bridges with above deck superstructure are prone to the icing problem [1]. As ice accumulates on the stays, it may resist falling for days until the right condition for ice shedding occurs, which will lead to either the closure of lanes or the whole bridge to protect travellers from ice falling. Lane closure not only results in inconvenience to motorists, but economic loss as well. Therefore, several anti-icing/de-icing technologies were investigated in order to solve this problem.

In this study, three icephobic coatings were tested, (1) aliphatic petroleum distillates with proprietary additives, (2) epoxy polymers, silicate mesh with new melt-point-depressants, and (3) fluorocarbon polymer and aliphatic, moisture-cure, three-part polyurethane. Experiments were conducted at the University of Toledo's (UT's) icing wind tunnel and icing experiment station.

I. VETERANS' GLASS CITY SKYWAY BRIDGE AND WEATHER HISTORY

The Veterans' Glass City Skyway (VGCS) is a large single pylon cable stayed bridge in Toledo, Ohio, USA with a main span of 375m and carries three lanes of traffic in each direction with average daily traffic count of 50,000. The stay sheaths are brushed stainless steel, which was chosen because of its lower life cycle cost and aesthetics. It is owned and operated by the Ohio Department of Transportation (ODOT).

Since the opening of VGCS in July 2007, six major icing events have occurred. Examples of precipitation types that may occur during icing events include rain, freezing rain, ice pellets, and snow, or a mix [2][3]. The main cause for five of the six events was freezing rain. Table 1 shows a summary of all icing events.

Because the icing events posed a potential threat to the traveling public and have a significant economic impact, a broad investigation was conducted in order to review all the identified anti/de-icing technologies. Based on this investigation, both active and passive technologies were identified as having some potential according to their efficiency, cost, and environmental friendliness[4][5].

Table 1: VGCS Icing Event History[6]

Ice Event	Ice Accretion	Ice Shedding Trigger	Ice Persistence	No. of Lanes	Damaged Vehicles
December 2007	Freezing rain and fog	Rain with temperature above freezing	2	2	Yes
March 2008	Snow, rain, and fog	Sun with temperature above freezing	1	2	Yes
December 2008	Snow and fog; freezing rain and fog	Rain, gusty winds and temperatures above freezing	7	2	No
January 2009	Freezing rain and fog	Gusty winds, temperature above freezing	10	1	No
February 2011	Freezing rain, clear	Light wind, overcast, and temperature above freezing	4	All	No
January 2015	Freezing rain and snow.	Gusty winds and overcast, remaining ice sublimated/melted of stays following day when ambient air temperature was above freezing	4	All	No

II. UNIVERSITY OF TOLEDO TESTING FACILITIES

A. Icing tunnel

In order to conduct experiments with scenarios similar to a natural environment, an icing tunnel was designed and built by the University of Toledo. The icing tunnel consists of two main parts, i.e. freezing room and a tunnel system. All the icing tunnel parts are shown in Figure 1[7].

Figure 1: UT Icing Tunnel

The icing tunnel is a closed loop system. The cooling unit is capable of keeping the temperature constant as low as -20°C. A multispeed fan was installed for adjusting the wind speed. The test section is made from a clear tube to allow for photography. The test section has a misting system to simulate rain and mounting system to support the specimen.

B. UT Icing Experiment Station (Scott Park)

An icing experiment station was set up at the University of Toledo's Scott Park Campus in order to better understand the nature of icing events, to conduct icing experiments regardless of the natural precipitation, and to minimize the risks to the investigators. Three

full scale sheath specimens were used for the experiments. The specimens were positioned to simulate the stays' orientation with respect to the sun.

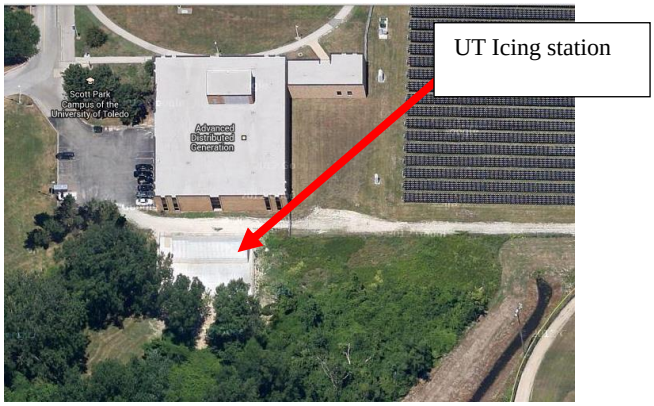

Figure 2: UT Icing experiment station (Google earth)

Figure 3: Three specimens with different orientations

III. COATING EXPERIMENT INSIDE ICING TUNNEL

In this experiment, the air speed was 8.8 m/s and the cooling unit was turned on until the temperature reached to -5.5 °C, as these conditions were reported as typical conditions for a freezing rain storm. Moreover, the misting system was turned on to simulate freezing rain. This experiment was done for all three coatings as well as the uncoated specimen. For each case three different nozzle sizes, i.e., 40, 42, and 50 microns, were used to simulate different rain droplet sizes. In this report, however, only pictures of the 40 microns nozzle size will be presented. The duration of each experiment was 10 minutes [8].Figure 4 shows the specimen before and after 10 minutes for the 40 micron nozzle system for all of the cases. Table 2 summarizes the results of all the experiments.

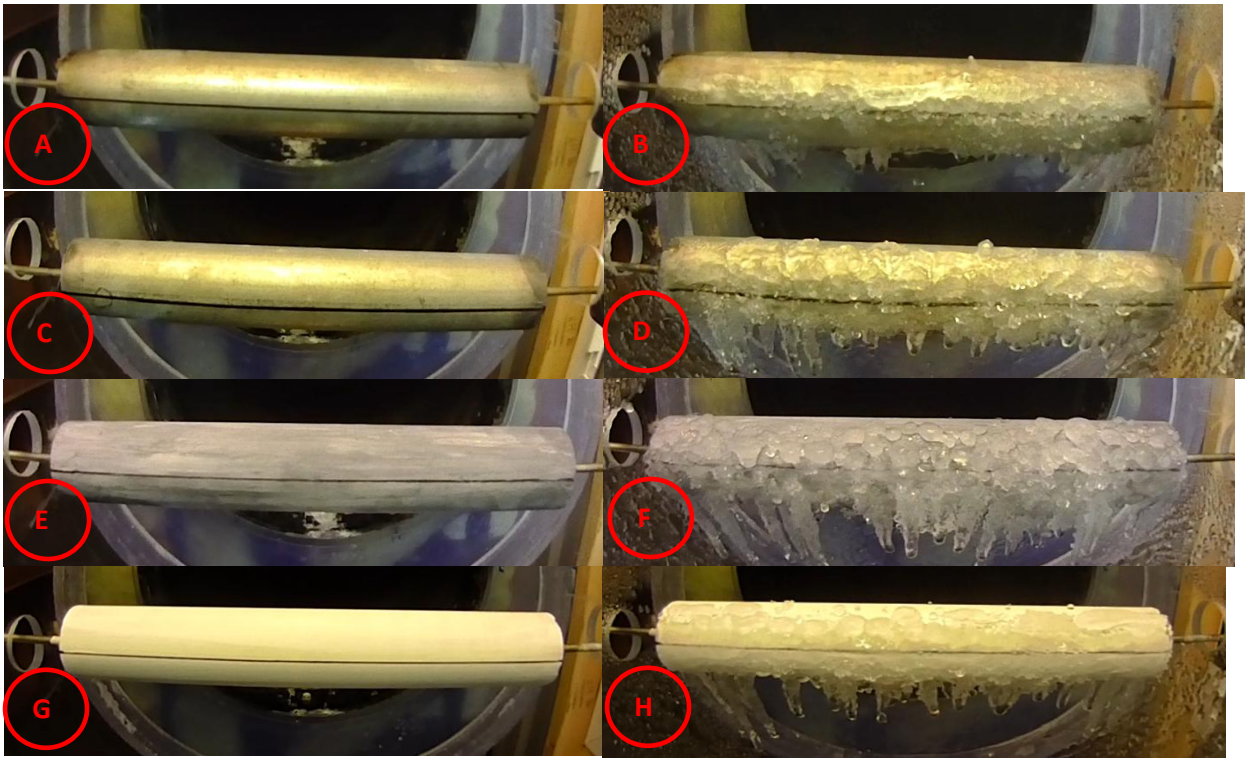

Figure 4: A) Uncoated - 40 Micron - 0:00 min, B) Uncoated - 40 Micron – 10:00 min, C) Aliphatic petroleum distillates with proprietary additives – 40 Micron – 0:00 min, D) Aliphatic petroleum distillates with proprietary additives – 40 Micron – 10:00 min, E) Epoxy polymers, silicate mesh with new melt-point-depressants – 40 Micron – 0:00 min, F) Epoxy polymers, silicate mesh with new melt-point-depressants – 40 Micron – 10:00, G) Fluorocarbon polymer and aliphatic, moisture-cure, three-part polyurethane – 40 Micron – 0:00 min, H) Fluorocarbon polymer and aliphatic, moisture-cure, three-part polyurethane – 40 Micron – 10:00 min

For the coated specimen experiment, three different coatings were used: the aliphatic petroleum distillates with proprietary additives (Coating 1); epoxy polymers, silicate mesh with new melt-point-depressants (Coating 2); and fluorocarbon polymer and aliphatic, moisture-cure, three-part polyurethane (Coating 3). In the case of aliphatic petroleum distillates specimen, the water began to show on the specimen's surface as small droplets, then these smaller droplets combined together forming bigger droplets that moved to the top and the bottom of the specimen. The frozen droplets continued to accumulate, covering the whole surface and forming icicles due to gravity. The thickest part of the ice approximately 10 mm. Similarly, for epoxy polymers and fluorocarbon polymer the same process occurred. However, the sizes of the water droplets on the specimens were smaller, and the icicles became longer and oriented downstream. The thickest part for the epoxy polymers was 10 mm, while the thickest part for the fluorocarbon polymer was 8 mm.

Table 2: Approximated ice thickness comparison of coatings and droplet sizes [1][8]

Coating / Droplet Size	None	Coating 1	Coating 2	Coating 3
40 micron	6.5 mm	10.0 mm	10.0 mm	8.0 mm
42 micron	5.5 mm	6.5 mm	6.5 mm	9.5 mm
50 micron	5.0 mm	6.5 mm	5.5 mm	9.5 mm

As can be seen from the table, none of the coating types prevented ice from accumulating. Instead, the ice accumulation became larger. The reason for this situation was the rapid freezing of the water droplets on the specimen's surface. Additionally, the surface of the ice on the specimen was uneven which trapped water and increased the freezing rate. The table shows that the smaller the droplet sizes, the higher the ice accumulation except for coating 3 which may be due to the different chemical composition of the coating.

IV. COATING EXPERIMENTS AT THE ICING EXPERIMENT STATION

The aliphatic petroleum distillates with proprietary additives was selected for testing on a full scale stay because it is clear and will not affect the color or shine of the stays. The coating was applied to one side of half of the specimen, then a mist of water was sprayed onto the entire specimen. The coating caused water to bead into small droplets. Due to the brushed surface of the sheath, small water droplets did not roll and/or blow off the coated surface, but rather suddenly turned to ice. Figure 5 shows the stay before and after the mist was sprayed[8].

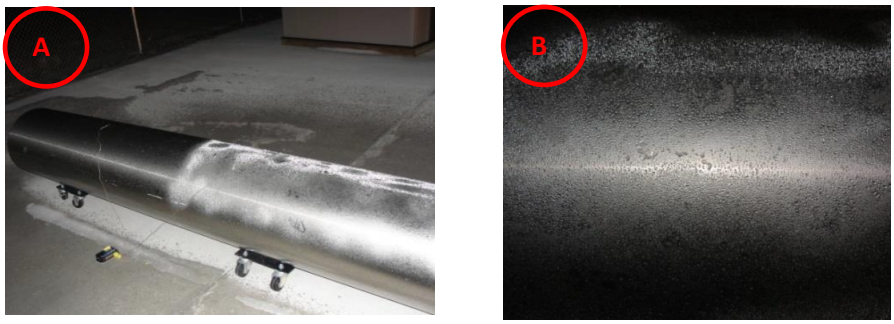

Figure 5: A) Aliphatic petroleum distillates with Proprietary additives Sprayed on half of the Specimen, B) Water Droplets due to aliphatic petroleum distillates with Proprietary additives

Therefore, it can be concluded that after conducting the coating experiments in both laboratory and field, the build-up of ice was not be prevented. Another concern was that the coating tested outdoors developed a gummy appearance on the stays after one month.

V. OTHER TECHNOLOGIES

A. Thermal de-icing/anti-icing (internal heating)

The VGCS stays are hollow with the structural elements occupying roughly 50% of the internal volume, therefore, it would be possible to blow hot air up the stays. To test this idea, internal heating experiments were conducted with a 70,000 BTU forced air space heater as a heat source.

A de-icing and an anti-icing experiment were conducted. For the de-icing experiment, the stay had a 12 mm thick layer of ice accumulated and hot air was blown inside the pipe until the ice melted. Figure 6 shows the melting pattern in the thermal de-icing test. Results of this experiment showed that the heating system successfully melted the accumulated ice without shedding.

The second test was an anti-icing thermal experiment. Initially, the stay was clear with no ice accumulation and it was heated just above freezing, then a mist of water was sprayed onto the specimen. Results showed that after a period of time ice began accumulating on the stay, which is shown in Figure 7.

Figure 6: De-icing Pattern in Thermal Test

Figure 7: Accumulated Ice in Anti-icing Thermal Test

It was found that the hot air was effective in de-icing, but not in anti-icing where the ice still accumulated, which means that more heat is needed to prevent ice from accumulating. Also, the cost for heating a large bridge would be too high[8].

B. Fluid Chemical De-icer

Experiments were conducted using chemicals to determine the efficacy as anti/de-icing technology and also the effect on the stay appearance. The material used was an organic based fluid made of refined molasses carbohydrate, NaCl, CaCl2, KCl, and MgCl2, and the efficacy of the chemical for de-icing of pavements was proven by ODOT[9]. Similar to the internal heating technique de-icing and anti-icing experiments were conducted. For the de-icing chemical experiment, a 1/8 inch thick layer of ice was accumulated on the specimen, and then the fluid was dripped onto the ice layer through a drip tube system. As shown in Figure 8, the chemical was only able to melt down a narrow rivulet through the ice due to its low viscosity [8]. For the anti-icing chemical experiment, the fluid was applied with a manual sprayer on half of the specimen and a mist of water was sprayed onto the specimen to see the efficacy of that anti-icing strategy. Figure 9 shows how ice accumulated on the specimen in the presence of the chemical. This chemical could neither prevent the ice from accumulating nor remove existing ice.

Figure 8: Drip Tube System used in Chemical De-icing Test

Figure 9: Formation of Ice in Chemical Anti-icing Test

VI. REAL TIME MONITORING SYSTEM (DASHBOARD) AND SENSOR DEVELOPMENT

The results showed that none of the technologies were suitable for application on the bridge. Thus, an automated real time monitoring system was built to observe the conditions on the bridge. The dashboard shows data from the sensors (stay temperature, ice accumulation, precipitation, solar radiation) that have been set up on the bridge. In addition, the dashboard shows data that were gathered from local airports and Road Weather Information System (RWIS) stations. An algorithm was developed based on the weather data that were derived from the bridge. This algorithm allows ice accumulation, ice shedding, and clear conditions on the bridge to be identified[1][2]

Figure 10, a screen shot of the dashboard, shows various tabs that allow the operator to view data in many ways. The Dashboard tab, which is the primary tab, provides the current status of VGCS stays with a speedometer-like indicator, a legend of the indicated state of transition, and a running history of the last 48 hours of recorded icing conditions. The Map tab shows weather data at locations where the weather stations exist. The History tab shows records of the weather stations and sensor readings, and finally the Documentation tab shows information about the accumulation, shedding algorithms, and criteria[1][2]. This information will help the operators in monitoring the bridge status and assist them in making the right decision to protect the motorists.

Furthermore, two new sensors have been developed, i.e. ice presence and state sensor and ice thickness sensor. The ice presence and state sensor is a resistance based sensor that is used in detecting the state of the water on the stay or if it is clear. This sensor is very essential in detecting ice accumulation and shedding events. The ice thickness sensor is used to measure the thickness of the ice on the stay by utilizing a laser and camera. The camera is used in detecting the line generated by the laser. By taking pictures during an event, the thickness can be measured with the aid of image processing software. These sensors have been tested successfully both in the lab and field, and will be deployed on the VGCS in 2015.

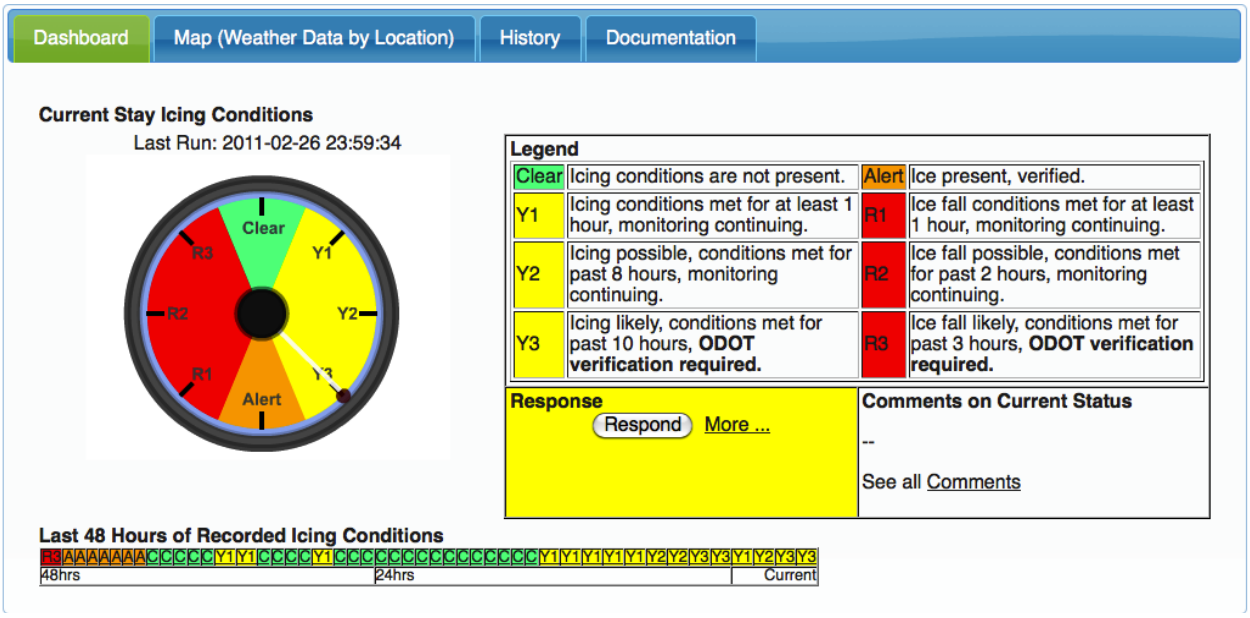

Figure 10: Screenshot of dashboard tab of the monitoring system[10].

VII. CONCLUSION

Three anti-icing/de-icing techniques - coating, chemicals, and hot air - were examined. None of these techniques were appropriate for implementation on the VGCS due to the lack of efficiency in preventing icing, high cost, altering the aesthetic features of the stay, or due to various environmental concerns. An automated real time monitoring system was developed in order to obtain the current conditions of the stays, which will assist the operator in the decision making process based on the information that resulted from the developed algorithms. Moreover, two new sensors were developed, ice presence and state sensor and ice thickness sensor, in order to detect the ice accumulation and ice shedding events, and measuring the ice thickness on the stay. This measured data can be added to the dashboard in order to give precise information to the operator about the stay conditions

REFERENCES

[1] C. Mirto, A. Abdelaal, D. K. Nims,T. Ng,,V. J. Hunt, A. J. Helmicki,C. C. Ryerson, K. Jones, " Icing Management on the Veterans' Glass City Skyway Stay Cables. Transportation Research Record 15-5605, 2015 (In press)

[2] D. K. Nims, V. Hunt, A. Helmicki, T. Ng, “Ice Prevention or Removal on the Veteran’s Glass City Skyway Cables”, Final Report. Ohio Department of Transportation Office of Research and Development, State Job Number 134489, 2014.

[3] K.F. Jones,” Toledo weather conditions associated with ice accumulation on the Skyway Stays”, Cold Regions Research and Engineering Laboratory, Hanover, NH 03755, 2010.

[4] J. Belknap,” Designing an Ice Management System for the Veteran’s Glass City Skyway”, M.S. Thesis University of Toledo, December 2011.

[5] A. Arbabzadegan, “Ice Prevention or Removal of Veteran’s Glass City Skyway Cables”, M.S. Thesis, University of Toledo, December 2013.

[6] C. Mirto, “A Sensor for Ice Monitoring on Bridge Superstructures”, M.S. Thesis University of Toledo, May 2015.

[7] D.L. Whitacre, “Development of an Icing Research Wind Tunnel at The University of Toledo”, MS Thesis University of Toledo, December 2013.

[8] K. Likitkumchorn,” Ice Prevention and Weather Monitoring on Cable Stayed Bridges”, M.S. Thesis University of Toledo, May 2014.

[9] Trademarkia, 2011, www.Trademarkia.com/beet-heat-85179043.html. (December 2011)

[10] D. K. Nims, “Ice Prevention or Removal on the Veteran’s Glass City Skyway Cables”, Interim Report. Ohio Department of Transportation Office of Research and Development, State Job Number 134489, 2010.

Methods for evaluating risk caused by ice throw and ice fall from wind turbines and other tall structures

Bredesen, Rolv Erlend[1], Refsum Helge Ausland[2]
[1] Kjeller Vindteknikk, [2] Lloyds Register Consulting
rolv.bredesen@vindteknikk.no

***Abstract*:**

IceRisk, a state-of-the-art method for assessing site specific risk caused by ice fall or throw from turbines or other tall structures, has been developed in close collaboration between Kjeller Vindteknikk and Lloyd's Register Consulting. The method consists of a detailed meteorological simulation resulting in maps of ice throw probability zones and safety distances for the considered site, followed by a risk assessment. The approach results in a map showing safety zones, i.e. what type of activities are acceptable within the vicinity of the wind turbine or similar installation.

Guidelines for acceptable risk levels, both for facility operating personnel and for third parties, are proposed. The calculated risk for any specific site may take into account local risk reducing measures, and calculate individual risk for different exposure, such as pedestrians and vehicle passengers, separately.

The IceRisk methodology has so far been applied for met masts, tall towers, power lines and wind turbines in Norway. Since 2013, validation work has been performed by ongoing inspections on and around a 209 m telecom mast at Tryvann, Oslo.

Keywords: IceRisk, ice throw, ice fall, turbines, telecom masts, power lines, wet snow icing, rime ice, risk assessment, risk mitigation, forecast, warning systems .

LEGEND AND ABBREVIATIONS

a	*height of ice piece, e.g.: $(L/rho)^{0.5}$*
b	*width of ice piece*
c	*length of ice piece*
Cd	*Drag coefficient, taken as 1.0*
A	*Effective frontal ice piece area: 0.5*(ab+ac+bc)*
ρ	*Density ice, typical value hard rime: 500 kg/m^3*
ρ_{air}	*Density air, typical value 1.22 kg/m^3*
M	*Mass ice piece: rho*a*b*c*
g	*Gravitational acceleration: 9.81 m/s^2*
CdAoM	*Form factor icefall: Cd*A/M*
Vt	*Terminal velocity: $(2*g/rho\_air/CdAoM)^{0.5}$*
E	*Impact kinetic energy ~ 0.5*M*Vt^2*
LIRA	*Localized individual risk, Outer safety zone at level <1e-6 [fatalities/year]*
H	*Hub height wind turbine*
D	*Rotor diameter wind turbine*
dZ	*Overheight*
L	*Ice load [kg/m], typically accreted on a rotating vertical cylinder of diameter 30 mm*
DSB	*Norwegian Directorate for Civil protection*

INTRODUCTION

The IceRisk-methodology is used to assess risks associated with being hit by ice pieces shedded from a fixed or moving structure. A typical result is at what distances the risks for being struck by a falling ice debris are acceptable for different exposures such as facility workers, occasional 3rd persons present, or vehicle passengers given none or different considered risk mitigation efforts. The methodology is also suited for assessing the damage potential on structures and property.

The methodology presented in this article is primarily based on a ballistic ice throw model [1] coupled with a detailed meteorological study and a risk assessment as well as our own experiences [2][3][4] and others experiences of ice throw modelling and observed distances of ice throw and ice fall [5][6][7][8][9][10][11].

In this article the IceRisk methodology is presented with results from a selection of our own studies in Norway regarding the associated risk from telecom towers, power lines and wind turbines [2][3][4][21][22][23][25][26][27] .

I. METHODOLOGY

The IceRisk-methodology consists of several parts; First a detailed longterm meteorological modeling of the wind and icing condition at the site is performed. Then the aggregation [13] of ice in the construction is calculated before we consider under which conditions ice pieces are shedded from the construction. E.g. how is the shedding related to melting conditions and/or stronger wind episodes when dangerous amounts of ice are present. An ice fall size distribution is calculated and classified by analyzing the ice amounts that is accreted and shed above associated ice load thresholds. Given the wind conditions with dangerous ice amounts present (e.g. L > 1-2 kg/m) and the size distribution one can use a ballistic trajectory model [1] to calculate the impact position and kinetic energies of the ice pieces (assumed shaped as freely rotating ice cubes). For wind turbines one also has to consider the angular and radial distribution functions for ice throw release positions [6]. Here, we consider ice pieces with impact kinetic energies above 40 J and with weights above 100 g, as dangerous (fatal) [2][4][18]. A combination of the statistics are then performed resulting in probability maps and tables. Finally a risk assessment study is performed yielding the safety zones around the facilities where different exposures are allowed. When risks are above threshold values [2][3][4] one should incorporate risk mitigations efforts if re-siting is not possible. Based on model validation we consider ice fall drift distances calculated with a high degree of accuracy [23].

II. ICE FALL CALCULATIONS

The parameters describing the impact position and velocities for a shed ice piece are the release position, release velocity, wind velocity, wind shear, terrain and combined form parameter C_d*A/M[1]. Here, C_d is the drag coefficient[2], takes as 1.0, while A and M are the effective frontal area for the ice piece (the side oriented against the wind and fall direction) and the mass of the ice piece. If we know the precise form, orientation and weight for an ice piece we can calculate the Cd*A/M parameter to find the associated drift distance and impact kinetic energy for a falling ice piece. The equivalent cross-sectional area for a freely rotating ice cube is 50 % larger than if the ice cube is falling with the smallest face kept oriented against the wind and fall direction. Note that this corresponds to setting an effective drag-coefficient of 1.5 considering the smallest face of the cube as the frontal area. Also note that the combinations of Cd=1 and ρ = 500 kg/m^3, Cd=1.2 and ρ=600 kg/m^3, and Cd=1.4 and ρ=700 kg/m^3 all yield the same form factor Cd *A/M.

A. *Smallest ice piece with kinetic energy above 40 Joule*

Lighter ice pieces drift further than denser ones. From a sensitivity analysis [26] we found that the smallest dangerous ice cube released from 209 m is between 150 and 200 g during calm wind conditions for the respective ice cube densities of 800 and 500 kg/m^3. For 30 m/s wind speeds the lower mass for a freely rotating ice cube is around respectively 100-120 g in the 40 J energy limit for the given densities. Note that these values are valid for ice fall where the terminal velocity is reached from below. For ice throw the terminal velocity is reached from above with time if the initial relative wind velocity is exceeding the terminal velocity.

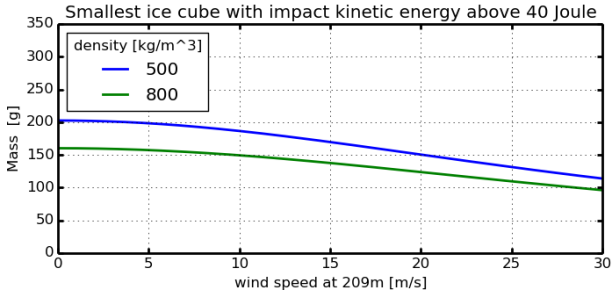

Figure 1 Smallest ice cube at given wind speeds with an impact kinetic energy above 40 J for the respective ice densities of 500 kg/m^3 (blue) and 800 kg/m^3 (green).

B. *Comparison of calculated safety distance for freely rotating ice cube with safety distance rule for stopped turbine*

The safety distance curve for the 40 J ice piece released from 209 m (seen in Figure 14) is nonlinear and can be fitted with the following representation: D = A+B*C*(exp(WS/B)-1). Here WS is the wind velocity at 209 m, A=-3.4, B=63.5, C=8.1, and D is the safety distance. If we compare this safety distance with a general safety rule for a stopped wind turbine: H*vh/15, where H is total height and vh is wind speed at hub height we compare with previous results. With a wind shear of 0.18, a total height of 209, hub height taken as 155 m, and a hub height wind speed of 15 m/s, we get a safety distance of 140 m. This means that the general safety rule distance (209 m for vh=15m/s) can be reduced with 33 % to match our results at this distance.

C. *Sensitivity analysis on form - plates and rods vs ice cubes*

Both freely rotating plates and rods can drift further than cubes in 40 J limit [26]. With wind speeds of 9.5 m/s at 209 m.a.g.l. the horizontal drift distance for ice cubes of density 500 kg/m^3 is 80 m. For plates which are shrunk by a factor 4 on one side the safety distance for the worst size ice plate is approximately 10 m further. For rods a stretch factor of 4 also gives longer drift distances but not as long as for plates.

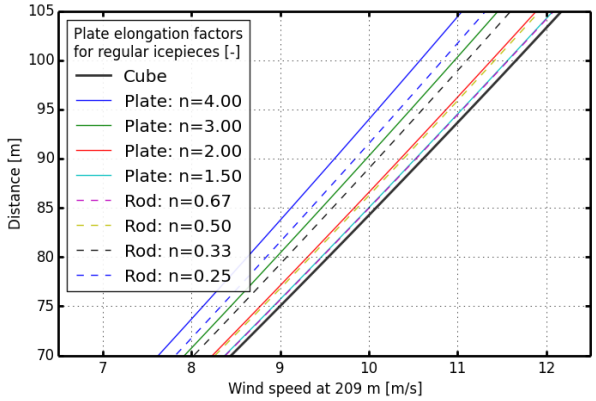

Figure 2: Safety distances for ice cubes with the ratio given in the legend between the height/width and the length of the freely rotating regular ice piece in the 40 J limit.

Calculations with elongation factors above 4 is not shown as the assumption of freely rotating ice pieces might become invalid. At calm wind conditions and a elongation factor of 4 (plate) the ice piece have size of 3.1 x 12.5 x 12.5 cm, weighing 240 gram in the 40 J energy limit. With 35 m/s winds this size is reduced to 2.5 x 9.5 x 9.5 cm with a weight of 110 g. For ice pieces with a density of 800 kg/m^3 the corresponding calm condition size limit is from 2.5 x 10 x 10 cm (190 g) and at 35 m/s the size is 2 x 8 x 8 cm (95 g).

III. ICEFALL FROM THE TRYVANN COMMUNICATION MAST

The IceRisk model is linked to a hindcast archive with time series of meteorological parameters such as icing, wind speed, wind direction and temperature from the 35 year period 1979-2013. For the 209 m tall communication mast at Tryvann [23][26], this archive was used to define the periods of icing and the associated ice amount in the structure.

During the average winter 8 800 kg of ice is shed from the construction (L>1.0 kg/m). 4 200 kg of the ice fall is calculated above the 40 J energy limits For episodes with an ice load minimum of 1 kg/m the strongest winds during melting were 27 m/s and during ice present 30 m/s for the 35 year period.

Ice cubes (rime ice) with a weight of more than 150 g falling from the mast were considered dangerous, as the impact energy can exceed 40 Joules (see Table 2 and Figure 14). The furthest drift distance for a dangerous ice piece at Tryvann was calculated to be 1.5 times the height of the construction for the strongest wind episode.

The size distribution and fall parameters for the period is presented in Table 2 and we observe with the given discretization in the Cd*A/M parameter that the longest horizontal drift distance is 280 m during the strongest winds (30 m/s), which is 70 m longer than the total mast height. Using the safety distance curve we get 300 m as a safety distance for the worst size ice cube in the 40 J limit.

[1] average density: ρ=500 kg/m^3, freely rotating ice piece[19], Cd*A/M=Cd*(ab+ac+bc)/(2*ρ*a*b*c), where a,b,c are the average side lengths for the ice piece. Cd is taken as 1.0. a=b=c=(L/ ρ)$^{0.5}$

[2] The drag coefficient can vary quite a lot depending on the shape of an object. For flow across a long straight cylinder the drag coefficient is 1.2, for a perfect sphere it is 0.5, while it for cubes varies between 1.05 for flow against a face and 0.8 for flow oriented against an edge. For oblong boxes it can be 2.05 for flow on a face and 1.55 for flow oriented against an edge.

D. Validation and verification of the model

During the winter of 2013-2014, the telecom mast experienced extreme icing conditions and both the mast and area surrounding the mast were inspected. Based on the inspections we consider the model as qualitatively validated yielding zones for ice fall with a high degree of accuracy. A quantitative comparison between the number of ice pieces and larger craters found on the ground in given areas against the calculated probability maps was also found favourable with a logarithmic decrease in the number of strikes per square meter with distance. The kinetic energy of impact is an important parameter in the risk assessment; this could however not be directly compared.

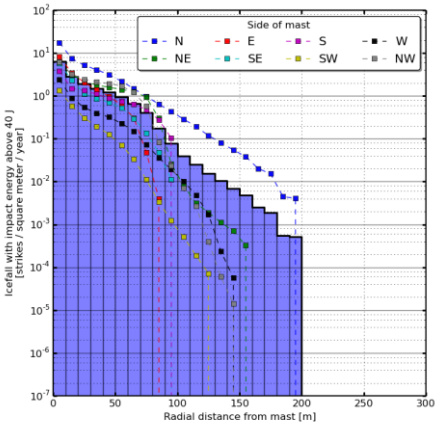

Figure 3: Probability map [#/per square meter] showing combined numbers of ice strikes (E>40J) for each size class together with combined statistics on radial distribution of dangerous ice fall for the 2013-2014 winter. The blue bars show the statistics for all sectors combined, while the colored markers are averages for 8 sectors relative to the mast center described in the legend. (N is north side etc.)

For the ice cube classes with weights of 4 kg, 1.2 kg, 500 g, 250 g, and 150 g the respective furthest drift distance for this winter was calculated to 99 m, 128 m, 156 m, 179 m, and 199 m. The calculated number of dangerous ice fall strikes for the 2013-2014 winter were 3 times of the average for the 1979-2013 period. The calculated mass for the dangerous ice fall was 6 times larger. Both 160 m north of the mast and in the intersection 90 m northwest of the mast the calculated probability for a dangerous strike is 0.02. This corresponds to 1 dangerous strike every 50th m^2.

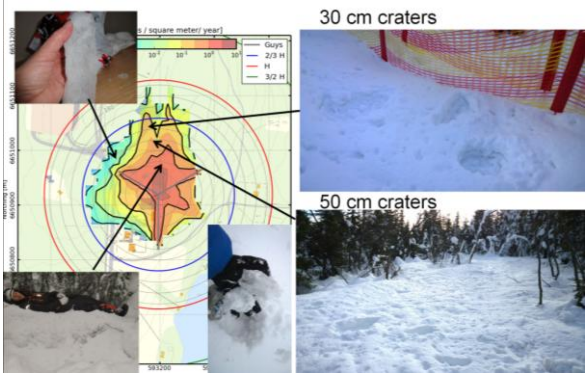

Figure 4: Probability map [#/per square meter] showing combined numbers of ice strikes (E>40J) for each size class together with pictures showing ice fall of different sizes (craters and ice pieces) and probabilities (# craters/ice pieces). The probabilities are based on a simulation for the winter 2013-2014.

The largest ice amount accumulated in the construction this winter was shed in one melting episode with simulated southerly winds of 23 m/s in the top of the mast (16-17th of February 2014). After the event 5-20 cm craters could be observed at a distance of 160 m north of the mast (not shown). On a parking lot 140 m north of the mast 30 cm craters (shown) were observed. In a ski track at distances between 80 and 140 m north of the mast the craters were typically between 5 cm (as showers) and 70 cm (fewer). The 50 cm craters 100 m north of the mast compares with the furthest calculated drift distance for the 4 kg (20 cm) ice cubes while the 30 cm craters at 120 m distance compares with 1.2 kg (13.3 cm) ice cube drift distances. The 500 g (10 cm), 250 g (8 cm) ice cube distributions can both reach the roof of the building at 160 m distance. The 150 g (7 cm) ice cubes reached the 40 J limit only for the strong wind episode yielding a band starting 70 m north of the mast extending to 200 m north of the mast.

Both pictures on the left are from another episode on the 11.02.2014. The coffin hole has a horizontal size of (2m x 1m). The ice piece shown in the upper left of the figure was from a 3 m long section evidently from a guy because of metal thread cast on the inside. It was split in half along the length direction, with a diameter of ~5 cm, and with a density of 800 kg/m3.

E. Forecast system and observations of ice fall as a thin plate

A warning system, coupled to automated forecasts of risk zones for the following 48 hours, was installed before the winter 2014-2015. A total of 6 separate cases with dangerous amounts of ice were forecasted during the winter, which resulted in warnings issued. After each episode, inspections were performed before the warning system was de-activated.

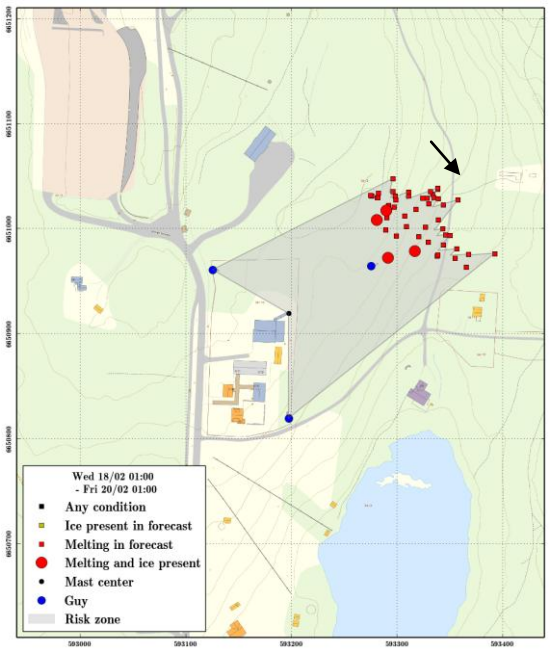

Figure 5: Forecast showing the forecasted risk zone and the safety distance function evaluated for hourly values of wind speed and direction in the 48 hours forecast assuming flat terrain. The red large circles show the combination of melting at the top of the mast when dangerous ice mounts still are present. The smaller red squares indicate positive temperatures for hours after the model has shed the dangerous ice amounts (The closest shown safety distance of 203 m was forecasted for a later time in the same day.

In one of the inspections (2015-02-18 10:00 UTC) observations were made of a large thin plate the size of a news paper that was shed from the glass-fibre reinforced plastics (GRP) top antenna, which is shaped as a 20 m high cylinder in

the upper part of the mast with a diameter of 1.6 m. The observed landing position was 210 m northeast of the mast at a terrain height 20 m lower than the mast. At the time of the inspection the modeled wind speed at 209 m were 20 m/s (corresponding to a safety distance for freely rotating ice cubes of 185 m for flat terrain). With a calculated safety distance of 185+20=205 m for the 500 kg/m^3 density freely rotating ice cube safety distance this agrees well with the observed distance of 210 m.

Figure 6: Icefall as 1 cm thin plate (22 cm x 38.5 cm) shed from the round top antenna of diameter 1.6 m. Picture by Amundsen, K., Norkring.

Calculating for the densities of 900 and 800 kg/m^3 we get horizontal drift distances for the regular ice piece of 220-234 m, weights of 680 g-760 g and impact kinetic energies of 130-160 J corresponding to an impact velocity of 20 m/s (72km/h). The same ice piece shedded from the lowest possible position in the top antenna yields a drift distance of 192-204 m for the respective densities assuming flat terrain. These results suggest that the safety distance for freely rotating plates, which are formed from frozen water film on rounder objects such as wind turbine blades and GRP antennas, could be revised and extended with up to 10-20 % depending on future observations. However, at this time we still consider the presented safety distance as valid (ref section B).

IV. ICETHROW FROM WIND TURBINES

For wind turbines, IceRisk calculates the impact position and impact energy of the ice pieces released from various positions on the blades. Heavier ice pieces can be thrown further than light pieces, however light pieces may drift longer distances in strong winds. When ice that has built up on a turbine blade is released it can be thrown hundreds of meters in the worst cases. Calculations with the IceRisk model suggest that safety distances are dependent on the local wind conditions and may in the worst cases with modern turbines exceed the general rule of 1.5 * (H+D), where H is hub height and D is the rotor diameter [11]. If the turbine is located at an elevated position compared to the surrounding, we also recommend adding the overheight, dZ, to H in the above formula for screening purposes.

For the global average in-cloud icing conditions [39] ice accretes at a rate of roughly 1 kg/m/hour on a typical wind turbine blade airfoil section at 85 % blade span for wind speeds of 7 m/s corresponding to a airfoil section velocity of 60 m/s.

F. Calculated ice throw from a V112 3.3 MW coastal wind farm in Northern Norway

For wind turbines the longest safety distances are associated with ice throw of larger ice pieces and not necessarily the drift distance for the smallest dangerous ice piece with the furthest drift distance in strong winds. For ice throw the longest safety distances are related to the performance curves of the turbine, showing peak wing tip velocity during iced conditions [14], and the maximum ice accumulation (e.g. [35][36][37][38]) as larger ice pieces can be thrown further than smaller ones.

The considered turbine has a hub height of 80 m, a rotor diameter of 112 m, and a peak rotational velocity of 17.7 rpm corresponding to a peak wing tip velocity of 103.8 m/s for 25 m/s winds. The considered site is classified as an IEA Wind Ice Class 3 site [15] with light to moderate icing. Expected production losses due to icing for sites in the class is between 3 and 12 %. The highest iceload on a standard body (vertical rotating cylinder with a diameter of 30 mm) is for a 15 year period calculated to 3.4 kg for the considered location varying between 1 and 4.7 kg/m for the turbines in the farm. Based on the ice map for Norway [20] the considered site has between 350 and 550 hours per year with meteorological icing 80 m.a.g.l.

The ice accumulation on the blades have for this site been calculated, using the IceLoss model calibrated against observed ice throw from another operational Norwegian wind farm with similar icing conditions, resulting in the ice throw distribution shown in Figure 7. For an average year the turbine throws 6 000 kg with ice. The highest modelled ice accretion at 75 % of the blade length measured from the hub is 27 kg/m for the 15 year period.

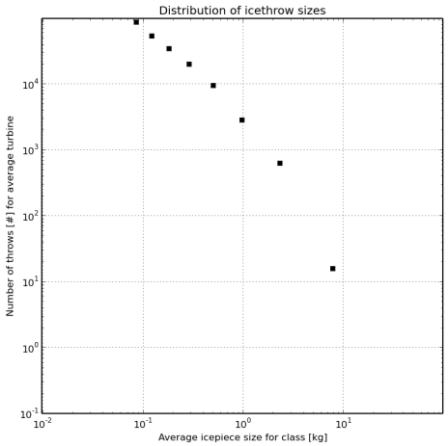

Figure 7 Calculated ice throw size distribution for a 15 year period from 3 blades on a turbine. Number of throws are given in the range of 10^{-1} - 10^5 and sizes in the range of 10 g - 100 kg.

For the considered turbine and location we see from Figure 15 that the calculated ice throw zone extends to 330 m but with

most of the ice throw within the general safety distance of 294 m. Smaller ice pieces than shown are not considered harmful while larger ice pieces are considered unrealistic at the given location. We note that the largest and most dangerous ice pieces can be thrown furthest to the side while the lightest ice pieces can drift furthest downwind.

When the wind speed is 30 m/s at the hub height the turbine will stop and the furthest drift distance for this wind velocity is shown in blue with a distance of 220 m in Figure 15. Another general safety rule for a stopped turbine states that the safety distance for ice fall is linear with the wind speed and corresponds to the total height of the construction when the hub wind speed is 15 m/s. Utilizing this rule we get a safety distance of 280 m for ice fall which can be reduced with 20 % to match our results for the longest drift distance for a dangerous ice cube during 30 m/s winds. However, for ice pieces shaped as plates and rods the drift distance is a little higher than for the ice cube in the 40 J limit. Also note that if the stopped turbine is kept oriented against the wind with one blade pointing downward the total height is reduced with another 20 % compared to when one blade is oriented upwards.

The resulting probability distribution calculated with the trajectory model is shown in Figure 8 on a logarithmic scale. Of the 6 000 kg/year of ice thrown we end up with 800 dangerous ice pieces being thrown for the average year from the turbine (E>40 J and M>0.1kg). We observe that the dangerous ice throw occurs within 330 m from the turbine and that the expected return period for at dangerous ice throw on a square meter in the 290-300 m distance range on average is 2 500 000 years. At distances of 150, 75, and 25 m from the turbine the corresponding return periods are 1000, 100, and 10 years respectively for the dangerous ice throw.

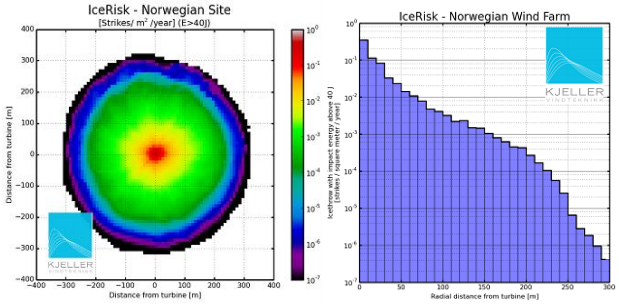

Figure 8: Probabilities for ice throw [strike / square meter/ year] with impact kinetic energy above 40 J from a wind turbine plotted on a logarithmic scale from 10^{-0} to 10^{-7} as a function of distance [m]. The spatial distribution in a 400 m zone around the turbine is shown to the left while the average radial distribution is shown to the right for distances up to 300 m from the turbine. The safety distance using the generic formula is 294 m for this site [8].

G. *Comparison with other studies of ice throw*

In a comparison between thrown ice pieces and ice loads on a standard body [13] (here located at hub height) at the TechnoCentre éolien in Canada indicates that only small ice fragments can accrete on the blade when the ice load on a standard body is below 500 g/m for a REpower MM92 CCV Turbine with hub height of 80 m and rotor diameter of 92 m [16]. The furthest observed throw distance for this turbine is 100 m [8] and the safety distance from the general formula is 258 m. The longest documented icethrow (92 m) relative to the safety distance (135 m) is from Gütch [7]. The furthest observed ice throw known to the author of 140 m is from the EU-project Icethrower[3] for a Vestas V90 turbine with a hub height 100 m. The largest found ice weights are 0.4-0.9 kg but only for a few occurrences. The correlation between distance and wind speed was weak, but the hub wind speed was in the range 9-15 m/s for the observation periods.

A comparison of the IceRisk throw zones for the V90 turbine, using similar figures such as those presented in Figure 15, confirms 140 m as a likely throw distance for 15 m/s winds and an ice cube of size 10 cm (600 g).

V. Wet snow icing on 420 kV power lines crossing a Norwegian fjord

In Norway, crossing fjord spans can have length scales in the order of kilometers with corresponding elevations hundreds of meters above the ground. On these power lines wet snow can accrete for a narrow temperature region around 0 °C [40][41] [42].

For the IceRisk analyses the fjord affected wind field has to be modeled with care because of the steep terrain surrounding the fjord. The horizontal displacement of conductors under wind loading toward buildings etc. should also be considered as well as the line sag. The effect of Joule-heating from the conductor is also being considered in an ongoing analysis as it may play a role for the shed time and the maximum wet snow accumulation.

H. *Terrain model: drift distance above steep terrain*

In Figure 9 a directional sensitivity analysis is performed for a 200 g ice cube released during 200 m winds of 20 m/s. This wind speed corresponds roughly to the highest winds occurring in combination with concurrent wet snow icing for this site during the analysis period. As seen from the figure, the horizontal drift distances for the indicated release position vary between 120 and 240 m depending on the wind direction.

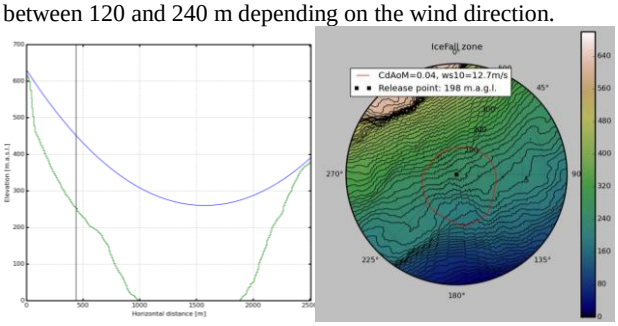

Figure 9: Left: 2.5 km fjord crossing span (blue) above terrain between 0-740 m.a.s.l. (green). The considered position is shown with the black vertical line. Right: Ice piece landing position (red) in 500 m radial zone for different wind directions given indicated release position (black square). 10 m wind speeds are 12.7 m/s, the form factor is CdAoM=0.04 and the terrain is given as black contour with an equidistance of 10 m and corresponding colors in the range 0-700 m.a.s.l.

I. *On the lower limit ice load for a dangerous ice piece and the associated uncertainties*

In the presented analysis wet snow accretions on 6 cm electric conductors crossing a fjord is considered where the 50 year return period ice load is 3 kg/m corresponding to an ice coat with a radial thickness of 2.5 cm. The typical ice densities for wet snow at this site is between 350 and 500 kg/m^3 with increasing density with load.

For this site we observe that snow accretions above a chosen threshold of 1.75 kg/m are rare (5-10 year event). The combination of low ice loads and lack of community experience on icefall from power lines, and the large uncertainly in the size distribution of the falling ice debris, make the IceRisk analyses especially sensitive for this site. Other key questions are on the ice amounts that can shed without breaking, on the limiting thickness and length for a falling rod before the dynamic

3 Preliminary information from project manager Bengt Göransson, Pöyry, from Swedish Energy Agency research project Icethrower (29.08.2014).

pressure exerted will erode and break the debris into smaller pieces. As the wet snow accretion events are associated with positive temperatures it is also a key question if the ice has time to freeze before it is shed. We are currently working on improving the wet snow modeling which includes ice erosion and shedding as part of an ongoing research project with Statnett as a partner (FRonTLINES). In the current model setup, ice is assumed to shed within 24 hours after the active icing event or when the wet bulb temperature of the snow reaches 2 °C whichever comes first. We also expect the modeled ice load at this site to be conservative and that it can be reduced with model improvements [43][44][45][46][47][48][49][50][51][52].

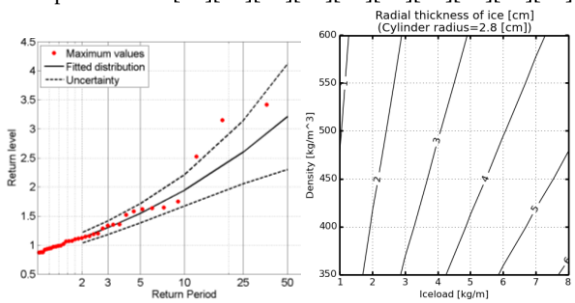

Figure 10: Return period [years] for wet snow ice load [kg/m] on conductor (left) and the relation between density and radial thickness as function of ice load (right).

VI. RISK ASSESSMENT

J. *Relation between impact kinetic energy for an ice piece and probability of survival*

From [18] the relation between impact kinetic energy and fatality for debris (weight between 100 g and 4.5 kg) thrown from explosions are given. The relation is based on a probit function matching skull-base fracture criteria for fragments with weights between 0.1 and 4.5 kg. For debris between 100 g and 4.5 kg, thrown from explosions the 1%, 50 % and 99 % probabilities of death are matched to the kinetic energies of 46, 71 and 110 J.

For the impact kinetic energy of 40 J, the probability of survival is evaluated to 99.9 % [18]. Since the band between certain death and 40 J is narrow, we have in our analyses mainly assumed 40 J as a sharp limit between dangerous (fatal) and non dangerous ice pieces [2][4]. With an ice density of 500 kg/m^3, the 40 J limit compares roughly to 200 g of ice falling from 30-50 m or 500 g of ice falling from 5-6 m for freely rotating ice cubes. If a 500 g freely rotating ice cube of size 10x10x10cm (500g) reaches terminal velocity of 23 m/s (given by Cd*A/M=0.03), the impact kinetic energy will be above 120 J. Evaluating the risk function we get that the probability of survival is 81.7 % for 60 J, 26 % for 80 J, and 0.25 % for an impact kinetic energy of 120 J.

K. *Guidelines for acceptable risk levels*

Currently there are no internationally recognized standards for safety distances or methods for assessing the risk caused by ice fall or ice throw. Guidelines, rules and regulations vary significantly by country [5].

Lloyd's Register Consulting has proposed safety zones around wind turbines, met masts, towers and similar installations that may case risk of ice throw or ice fall [2], based on Norwegian Directorate for Civil Protection (DSB) guidelines for acceptable risk outside industrial facilities [17]. The result is a map showing safety zones, i.e. what type of activities are acceptable within the vicinity of the wind turbine or similar installation.

The key guiding principle for determining safety zones is that the facility should not increase risk to public significantly compared to daily risk in society.

Exposure time is factored into the acceptance criteria, resulting in different zones for different type of activities. A zone with low activity, will have a higher risk acceptance criteria than a zone with high public activity. Higher risk may also be accepted for personnel operating the facility, when taking into account that this will be professional personnel with understanding, knowledge, and routines to handle the risk.

L. *Suggested risk acceptance criteria*

Guidelines for acceptable risk level, both for personnel operating the facility and third parties, are proposed and shown in Figure 10. The calculated risk for any specific site may take into account local risk reducing measures, and calculate individual risk for different exposure, such as pedestrians and vehicle passengers, separately [26][27].

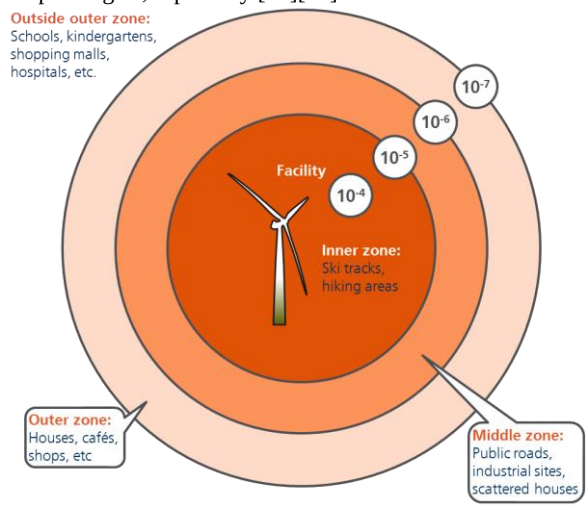

Figure 11: Lloyd's Register Consulting's suggested safety zones around installation that may case risk of ice throw or ice fall. The numbers indicate the iso-risk contours for localised individual risk (LIRA), the probability that an average unprotected person, permanently present at a specified location, is killed during one year due to ice fall or throw from the facility.

Lloyd's Register Consulting's suggested safety zones and acceptance criteria for localized individual risk (LIRA) is in line with the IEA Task 19's suggestion [3]. While IEA Task 19 suggests a general approach based on the ALARP principle (As Low As Reasonably Practicable), Lloyd's Register Consulting propose more detailed limits, and acceptable activity within each safety zone.

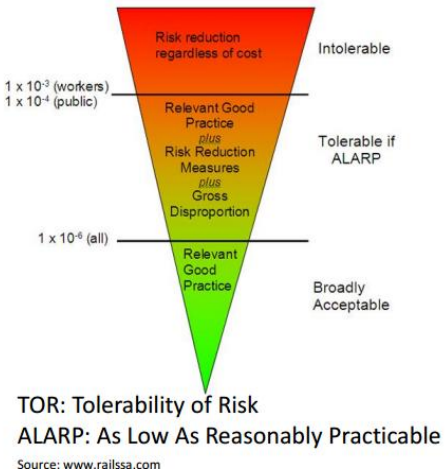

Figure 12: Risk reduction according to the ALARP principle as presented by IEA Task 19 suggestion [3].

The principle of minimising impact on the surroundings and risks imposed by the facility, is a common denominator in most international guidelines and regulations. In cases where there are no clear guidelines or rules regulating the dangers associated with ice fall and ice throw, it rests on the installation owner to document safe operation. In for example UK, there are strict requirements to document that risks are acceptable according to the ALARP principle [33].

To put the risks of fatality due to ice fall or ice throw in perspective, in line with the key principle that the facility should not increase the risk to public significantly, we can compare to the risk of fatality from any accident in Norway ($3.7 * 10^{-4}$), and the top three risks: Fall accident ($1.6 * 10^{-4}$), transportation excl. railway ($6.5 * 10^{-5}$), and poisoning ($3.6 * 10^{-5}$) [34]. The total increase in risk due to risk posed by the facility (from ice fall, ice throw or anything else) should be negligible compared to these figures.

M. Localised individual risk (LIRA)

LIRA is the probability that an average unprotected person, permanently present at a specified location, is killed in a period of one year due to an accident at a hazardous installation [31]. The term corresponds to individual risk as presented in [17].

For evaluating the risk we are considering a person, of size 20 cm x 50 cm = 0.1 m^2, standing permanently at a fixed position. Assuming that all strikes with impact energy above 40 J as 100 % fatal. The LIRA statistic is found by dividing the probability of strike per square meter with impact energy above 40 J per year with 10.

N. Risk assessment for the 209 m telecom mast at Tryvann, Oslo

If we apply the Lloyd's Register Consulting's suggested safety zones, for a third person of size 0.1 m^2 standing permanently in a fixed position, on the LIRA statistic for Tryvann shown in we get the following distances for the respective inner, middle, outer, and outside outer safety zones:

-Ski tracks and footpaths	110-200 m from mast
-Public roads and scattered houses	135-235 m from mast
-Cafe, ski lifts, and houses	170-260 m from mast
-Kindergarden	260 m from mast

The safety limit for allowing a person walking along the road (middle safety zone) is then at a 190 distance west of the mast (220 m south-west).

In addition to risk for pedestrians at Tryvann we have also analyzed the risk for car drivers and passengers on the road 80 m west of the mast [26][27]. With the assumption that[4] applies to cars in general it was found that the roof construction can withstand even the largest ice piece that can reach the road at Tryvann, which is a 4 kg cube with an impact kinetic energy below 2700 J. Since the impact angle for ice pieces hitting the road 80 m from the mast was calculated to be 70 degrees to the horizontal the weak side windows were not considered further in the analysis. However, 10 % of the cars projected horizontal area consist of laminated front windows[5], which are designed to stand impacts[6] of up to 140 J. The relation between LIRA and strike probability above the given energy limit for a car driver was combined to 0.01. Strikes on the rear window were not considered in the analysis.

At Tryvann the calculated risk for car drivers was not within the 140 J limit, but if the energy for penetrating the window (140 J) was added to the limit for fatality for an unprotected person of (40 J), then the calculated risk was equal to the combined alternative accept criteria of 180 J for the road.

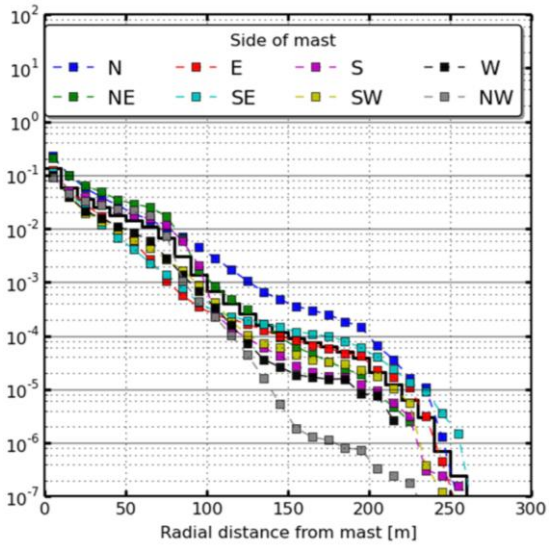

Figure 13 Localized individual risk calculated for the period 1979-2013. [1/year] assuming flat terrain. The black line shows the all-sector average in radial intervals of 10 m. The colored lines shows averages for the sectors described in the legend. Since terrain wasn't not included in the calculations we recommend subtracting the overheight for the lookup distances when there is overheight between the mast location and the considered area.

O. ISO 12494 indicate 2/3 structure height as the maximum distance for falling ice in R6 rime ice class (Tryvann)

The ISO-12494 – Atmospheric Icing of Structures Rime classes are [13]: R1: 0.5 kg/m, R2: 0.9, R3:1.6, R4:2.8, R5:5.0, R6: 8.9, R7: 16, R8: 28, R9:50 kg/m as 50 years return ice mass 10 m.a.g.l. on a standard body.

For Tryvann the 50-year iceload is 10 kg/m [24] at the 10 m level corresponding to ice class R6. The indicated [13] maximum distance for falling ice is at 2/3 of the structure height. We note that the standard remarks on the large uncertainty associated with the indicated safety distance.

[4] An American study [28] has shown that cars that are tested according to the NHTSA compliance program can stand a load on the roof corresponding to 1.5 times the cars dry weight in a simulated roll-over.

[5] A typical automobile covers a horizontal area of 6-7 m^2 (1.5 m wide x 4.2 m long = 6.3 m^2). The front window is typically 1.5 m wide and 0.7 m high with a 30 degree angle to the horizontal (projection of 0.42) covers a horizontal projected area of 0.63 m^2.

[6] The minimum energy required for a steel ball of 2.25 kg to break and penetrate a laminated wind screen was 138.6 J [29]. Firstly, we note that the 140 J limits for dangerous ice fall is conservative since steel (and concrete) are denser than ice and therefore smaller objects in these materials have a higher penetration ability. Secondly, the probability for ice crushing is larger than for the other materials. Hence, the area for spreading the impact kinetic energy is larger for ice.

Table 1: ISO 12494 indicated maximum distance given ice class and structure height (h). The presented risk are calculated at the given distances for 209 m mast at Tryvann (Oslo), which is in the Ice class R6. The DSB safety zone class is given to the right for the indicated distances.

ISO Ice class	ISO maximum distance	All sector risk	Risk north sector	DSB average zone	DSB zone north sector
R0-R3, G0-G1	Normally not considered				
R4-R6, G2-G3	2/3h (140m)	$1x10^{-4}$	$7x10^{-4}$	Touching inner limit inner zone	Inside inner limit inner zone
R7-R8, G4-G5	H (210m)	$2x10^{-5}$	$1x10^{-4}$	Middle zone	Touching inner limit inner zone
R9-R10	3/2h (315m)	$<10^{-7}$	$<10^{-7}$	Outside outer zone	Outside outer zone

P. *Risk assessment for the wind turbine*

The outer safety zones where housing is accepted is at the 10^{-5} contour and is located on average 250 m from the turbine (280 m away on east side; not shown) . Since the projected size of a person is 0.2 m x 0.5 m and all strikes with an impact kinetic energy above 40 J is considered fatal this corresponds to the 10^{-6} [1/year] LIRA contour. The inner safety zones where ski tracks and hiking areas are excepted is on average located 150 m from the turbine (10^{-3} strikes/year/m^2). The middle safety zone is on average located 230 m from the considered turbine. (public roads etc.).

VII. Examples with icicles from rooftops, hydrometeors (hail), and icefall from bridges

In an urban environment icicles falling from poorly insulated roofs have caused injuries in Norway[7] and fatalities in other countries[8]. In Norway landlords are responsible for clearing ice and court has ruled that owners are liable for damages.

In rare violent hailstorms, Large hail (2-2.75") reach the 40 J limit for sizes between eggs and tennisballs (5.1-6.4 cm, Cd=0.65, rho=700-910 kg/m^3 [53]).[9] The largest hailstone recorded fell in Vivian, South Dakota on July 30, 2010. It measured 8" in diameter (20 cm), 18.5" in circumference (47 cm), and weighed almost 2 pounds (880 g). Hail stones of this size are extremely rare. A hailstorm in the Moradabad and Beheri districts of India killed 246 people on April 30, 1888, the deadliest hailstorm on record in modern history[10].

In Vancouver, Canada, the newly built Port Mann bridge had a design flaw leading to formation of large ice pieces directly above the traffic lanes.[11]

[7] http://www.newsinenglish.no/2011/07/07/icicles-led-to-injury-and-prison-term/

[8] Falling icicles have killed five and injured 150 people in St Petersburg following Russia's coldest winter in three decades. Regional figures show icicles kill dozens of Russians each year. http://www.telegraph.co.uk/news/worldnews/europe/russia/7512865/Falling-icicles-kill-record-numbers-in-St-Petersburg.html)

[9] http://www.washingtonpost.com/posttv/national/severe-thunderstorms-hail-strike-denver-area/2015/06/04/9f1fd370-0ac0-11e5-951e-8e15090d64ae_video.html

[10] http://www.dailymail.co.uk/news/article-2271147/Nine-people-killed-freak-hailstorm-rains-massive-boulders-Indian-villages.html#ixzz3c8fYSDzt

[11] http://www.news1130.com/2014/12/22/port-mann-bridge-ready-to-tackle-ice-bombs-ti-corp

VIII. Summary

A trajectory model is used together with the energy limit of 40 J to differentiate dangerous ice throw or fall from other ice debris. Safety zones based on calculated risks are suggested based on similar criteria for other industries. For the icefall from the Tryvann communication mast we assumed freely rotating ice cubes of density 500 kg/m^3 where the length of the ice piece (l) in each class is dimensioned after the accreted ice load (L) and density (rho), $l = (L/rho)^{0.5}$

Based on current observations of differently shaped ice pieces with varying densities the safety distances calculated for the freely rotating ice cube holds and we consider the calculated ice fall risk zones as highly accurate.

For ice throw, the safety zones have been calculated using a density of 800 kg/m^3 since denser ice pieces can be thrown further than lighter ones and ice gets denser when accreted at high speeds which is the case for a moving turbine blade.

Acknowledgment

The authors would like to thank Norkring, Torvald Trondsen, Knut Kjennerud, Kjell Amundsen, Malmfrid Kjørri, Rasmus Nikolai Nes, Knut Harstveit, Bjørn Egil Nygaard, Øyvind Byrkjedal, Bengt Göransson, Ville Lehtomäki, and the IEA Task 19 sub-commite [3] lead by Matthew Wadham-Gagnon with Collaborators, Tomas Wallenius, Bjørn Montgomery, Kathleen F. Jones, Statnett, Finnmark Kraft, Austri Vind, Lyse., and Vattenfall for contributions to the presented IceRisk methodology. The work has been partly funded by the FRonTLINES project from the Norwegian Research Council (245370/E20).

References

[1] Biswas, S., Tayler, P. and Salmon, J.: Wind Energy nr 15. 2012. A modell of ice throw trajectories from wind turbines.

[2] Refsum, H.A., Bredesen, R.E., (2015), Methods for evaluating risk caused by ice throw from wind turbines, Lloyd's Register Consulting, NO. Winterwind 2015. http://windren.se/WW2015/WW2015_39_521_Refsum_Lloyd_Ice_throw_evaluating_risk.pdf

[3] Wadham-Gagnon et al., 2015. IEA Task 19 - Ice Throw Guidelines. Winterwind 2015. http://windren.se/WW2015/WW2015_52_621_Wadham_TCE_IEAT19_IceThrowGuidelines.pdf

[4] Bredesen, R.E., Refsum, H.A. (2014). IceRisk: Assessment of risks associated with ice throw and ice fall. Kjeller Vindteknikk AS. Winterwind 2014.

[5] Krenn, A., Claussen, N.-E., Wadham-Gagnon, M., Wallenius, T., Cattin, R., Ronsten, G., Klintrström, R., Durstewitz, M., Qiying, Z., 2014. Risk of icefall in the international context. Winterwind 2014.

[6] Battisti, L., Fedrizzi, R., Dell`Anna, S., Rialti., M. (2005). Ice Risk Assessment for Wind Turbine Rotors Equipped with De-Icing Systems, BOREAS VII. FMI, Saariselkä, Finland.

[7] Cattin, R. (2012). Ice throw studies, Gütch and St.Brais. *Winterwind 2012*

[8] Hutton, G. (2014) Validating an ice throw model: A collaborative approach. RES. Winterwind 2014.

[9] Morgan, C. (1997). Assessement of safety risks arising from wind turbine icing. *EWEC*. Dublin.

[10] Morgan, C., Bossanyi, E., & Seifert, H. (1998). Assessement of safety risks arising from wind turbine icing. *Boreas IV* (ss. 113-121). Hetta: VTT.

[11] Seifert, H., Westerhellweg, A., & Krönig, J. (2003). Risk Analysis of Ice throw from wind turbines. *Boreas IV*. Pyhätunturi: VTT.

[12] IEA Wind (International Energy Agency) (2012) Recommended practice 13: Wind energy in cold climate (1. Edition 2011)

[13] ISO/TC98/SC3/WG6: Atmospheric icing of structures, International Standard, ISO 12494, 2000

[14] IEC 61400-1 ed4 draft for Cold Climate. IEC 61400 is an International Standard published by the International Electrotechnical Commission regarding wind turbines.

[15] IEA Wind (International Energy Agency) (2012) Recommended practice 13: Wind energy in cold climate (1. Edition 2011)

[16] Wadham-Gagnon, M., (2013). Ice profile Classification Based on ISO 12494. TechnoCentre éolien (Wind Energy TechnoCentre). Winterwind 2013.

[17] DSB Temaveileder "Sikkerheten rundt anlegg som håndterer brannfarlige, reaksjonsfarlige, trykksatte og eksplosjonsfarlige stoffer: Kriterier for akseptabel risiko", Mai 2013.

[18] TNO Greenbook, Methods for the determination of possible damage, to people and objects resulting from release of hazardous materials, CPR 16E, TNO – The Netherlands Organisation of Applied Scientific Research, first edition 1992.

[19] Montgomerie, B., 2014. Ice ejection from rotating wind turbine blades. Appendix: Derivation of effective dynamic reference area.. ProgramoGrafik HB Report 141. Winterwind 2014.

[20] Byrkjedal, Ø., & Åkervik, E. (2009). *Vindkart for Norge, Isingskart i 80m høyde. NVE, 2009*. Kjeller: Kjeller Vindteknikk AS.

[21] Bredesen, R.E.,(2014). IceRisk: Assessment of risks associated with ice throw and ice fall. Presentation on Vattenfall Wind Icing Day 2014. 2014-10-2014. Vattenfall, Solna, Stockholm.

[22] Kjennerud, K, 2013. Falling ice from lattice guyed tower. International Association for Shell and Spatial Structures (IASS) Working Group 4: Masts and Towers. 26th Meeting in Paris, France, 9th-12th September 2013.

[23] Bredesen, R.E.: Antennemast Tryvann, Oslo kommune – IceRisk - Beregninger av isnedfall med validering. KVT Report, KVT/KH/2013/R079, Revisjon 15.5.2014, Kjeller Vindteknikk, 2014.

[24] Harstveit, K.: Antennemast Tryvann. Klimalaster. DNMI Rapport 33/95, Oslo 1995.

[25] Refsum, H.A.: "Risikoanalyse – Antennemast Tryvann – Vurdering av risiko tilknyttet isnedfall", 104282/R1a, Lloyd's Register Consulting, 2014.

[26] Bredesen, R.E.: Antennemast Tryvann, Oslo kommune – IceRisk - Beregninger av isnedfall på bilvei. KVT Report, KVT/REB/2014/R071, Kjeller Vindteknikk, 2014

[27] Kjørri, M.: "Vurdering av risiko for bilister på Tryvannsveien i forbindelse med isnedfall fra antennemast Tryvann", 105226/R1, Lloyd's Register Consulting, 2014

[28] Federal Motor Vehicle Safety Standards; Roof Crush Resistance, doc no NHTSA-2005-22143 for National Highway Traffic Safety Administration.

[29] Queensland Government, department of Main Roads: "Report on testing to determine impact resistance of vehicle windscreens – overpass screening project" 2001 by John Spathonis.

[30] Norsk standard NS 5814:2008, Krav til risikovurderinger.

[31] Rausand, Marvin: Risk Assessment – Theory, Methods and Applications, 2011,ISBN: 978-0-470-63764-7

[32] Forskrift om tekniske krav til byggverk (Byggteknisk forskrift), § 10-3. Nedfall fra og sammenstøt med byggverk, 2010, http://www.lovdata.no/ltavd1/filer/sf-20100326-0489.html.

[33] Health and safety executive, ALARP "at a glance", http://www.hse.gov.uk/risk/theory/alarpglance.htm

[34] SSBs report "Dødsårsaker for personer bosatt i Norge", 1992-2008.

[35] Adrian Ilinca (2011). Analysis and Mitigation of Icing Effects on Wind Turbines, Wind Turbines, Dr. Ibrahim AlBahadly (Ed.), ISBN: 978-953-307-221-0, InTech, Available from: http://www.intechopen.com/books/windturbines/analysis-and-mitigation-of-icing-effects-on-wind-turbines

[36] Homola, M. C., Wallenius, T., Makkonen, L., Nicklasson, P. J., and Sundsbo, P. A.: The relationship between chord length and rime icing on wind turbines, Wind Energy, 13, 627-632, 2010.

[37] Homola, M. C., Wallenius, T., Makkonen, L., Nicklasson, P. J., and Sundsbø, P. A. Turbine Size and Temperature Dependence of Icing on Wind Turbine Blades. WIND ENGINEERING VOLUME 34, NO. 6, 615-628, 2010.

[38] Homola, M. C., Virk, M. S., Wallenius, T., Nicklasson, P. J., and Sundsbø, P. A. Effect of atmospheric temperature and droplet size variation on ice accretion of wind turbine blades. Journal of Wind Engineering and Industrial Aerodynamics, volume 98, p.724-729, 2010.

[39] Lehtomäki, V. & Rissanen, S. *Simple methodology to map and forecast icing for wind power*. WinterWind 2014 conference proceedings, Sundsvall, Sweden (http://windren.se/WW2014/08_03_047_Simple%20methodology%20to%20map%20and%20forecast%20icing.pdf

[40] Kuroiwa, D. 1965. Icing and Snow Accretion on Electric Wires. Research Report 123 January 1965. U.S. Army Materiel Command. Cold Regions Research & Engineering Laboratory. Hanover, New Hampshire.

[41] Nygaard, Bjørn Egil Kringlebotn, Hálfdán Ágústsson, and Katalin Somfalvi-Tóth. "Modeling Wet Snow Accretion on Power Lines: Improvements to Previous Methods Using 50 Years of Observations." Journal of Applied Meteorology and Climatology 2013 (2013).

[42] Farzaneh, M. (Editor, 2008). Atmospheric Icing of Power Networks. Springer Book.

[43] Ballard, G.E.H., Feldt, E.D. 1965. A theoretical consideration of the strength of snow. U.S. Army Cold Regions Research and Engineering Laboratory, Hanover, New Hampshire, U.S.A.

[44] Ballard, G.E.H., and McGaw, R. W. 1965. A theory of snow failure. U.S. Cold Regions Research and Engineering Laboratory. Research report 137.

[45] Fonyó, András, Kollar, László E., Farzaneh, Masoud and Montpellier, Patrice (2009) Experimental Simulation of Wet-Snow Shedding from Sagged Cables. In: 13th International Workshop on Atmospheric Icing of Structures, 8th - 11th September 2009, Andermatt, Switzerland. http://eprints.hud.ac.uk/16647/

[46] Hefny, R.M.H., Kollár, L.E., Farzaneh, M. (2012): Experimental Investigation of Dynamic Force on The Performance of Wet Snow Shedding. International Journal of Mechanical Engineering and Mechatronics. Volume 1, Issue 2 - Year 2012 - Pages 72-79. DOI: 10.11159/ijmem.2012.009. ISSN: 1929-2724. http://ijmem.avestia.com/2012/009.html

[47] Kollár, László E., Olqma, Ossama, and Farzaneh, Masoud (2010). Natural Wet-Snow Shedding from Overhead Cables. Cold Regions Science and Technologiy, 60(1). pp 40-50. ISSN 0165-232X. http://eprints.hud.ac.uk/16079/1/2010_CRST_Natural_wet-snow_shedding_from_overhead_cables.pdf

[48] Olqma, O., Kollár, L.,E. , Farzaneh, M., Pellet, L., 2009. Modeling Wet-snow shedding from current carrying conductors. IWAIS 2009. http://www.iwais2009.ch/fileadmin/user_upload/pictures/Session_2_powerlines.zip

[49] Rehman, M.H.H,. Kollár, L.E., Farzaneh, M., 2012. Experimental Investigation of Dynamic Force on The Performance of Wet Snow Shedding. International Journal of Mechanical Engineering and Mechatronics Volume 1, Issue 1, Year 2012 Avestia Publishing.

[50] Roberge, Mathieu, (2006). A Study of Wet Snow Shedding from an Overhead Cable. Department of Civil Engineering and Applied Mechanics McGill University, Montreal December 2006. A thesis submitted to McGill University in partial fulfillment of the requirements of the degree of Master of Engineering. http://digitool.library.mcgill.ca/R/-?func=dbin-jump-full&object_id=99790&silo_library=GEN01

[51] Roberge, M., Farzaneh, M., McClure, G. Peyrard, C., 2007. Wet Snow Shedding from an Overhead Cable Part 1: Experimental Study. IWAIS 2007. http://iwais.compusult.net/html/IWAIS_Proceedings/IWAIS_2007/Category8%20Others/Lecture/Roberge_1.pdf

[52] Zhan, C., et al (2011). A wet snow failure model for predicting snow shedding from an overhead cable. IWAIS 2011. http://iwais.compusult.net/html/IWAIS_Proceedings/IWAIS_2011/Papers/A5_3_179.pdf

[53] Knight, N. C., Heymsfield, A. J., 1983. Measurement and interpretation of hailstone density and terminal velocity. Journal of atmospheric sciences. Volume 40 page 1510-1516 http://journals.ametsoc.org/doi/pdf/10.1175/1520-0469%281983%29040%3C1510%3AMAIOHD%3E2.0.CO%3B2

Table 2 Statistics on dangerous icefall for the period 1979-2013 released from mast and guy positions in Tryvann telecom mast, Oslo. Note that the Cd*A/M parameter is increased with 50 % for a freely rotating ice cube compared to an ice cube falling with the flat side oriented against the wind and falling direction. The drag coefficient, Cd, is taken as 1.0. Note that the given terminal velocities and impact kinetic energies are valid for calm wind conditions are therefore taken as lower limits for the falling ice pieces. In the IceRisk calculation, the contribution to the kinetic energy from the horizontal ice piece velocity is included. With the wind conditions at Tryvann the smallest ice piece with impact kinetic energy above 40 J is 7 cm weighing 150 g.

Ice cube size [m]	Ice cube weight [kg]	Terminal velocity [m/s]	Kinetic energy at terminal velocity [J]	Cd*A/M [m^2/kg]	Maximum distance [m]	Ice fall with energy > 40 J [cubes/year]	Ice fall with energy > 40 J [kg/year]
0.050	0.063	16.3	8	0.040*1.5	(329)	-	-
0.057	0.093	17.5	14	0.035*1.5	(307)	-	-
0.067	0.148	18.9	26	0.030*1.5	283	80	12
0.080	0.256	20.7	55	0.025*1.5	256	4902	1255
0.100	0.500	23.1	133	0.020*1.5	225	2495	1247
0.133	1.185	26.7	422	0.015*1.5	188	936	1110
0.200	4.000	32.7	2136	0.010*1.5	142	151	603
Sum						**8566**	**4227**

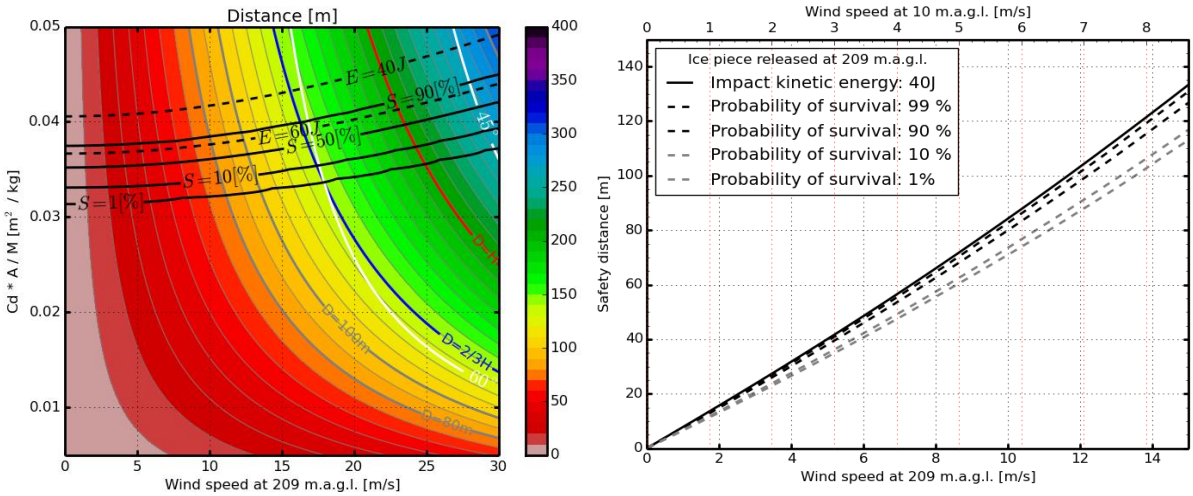

Figure 14: Left: Distances for impact of icefall released at 209 m.a.g.l.. The parameters that dimension the ice fall distances are the drag-coefficient (Cd), the effective frontal area of an ice piece (A) and the weight of the ice piece (M) in addition to the wind speed and shear. A wind shear coefficient alpha=0.18 is used based on a high resolution simulation of the local wind condition. Freely rotating ice cubes with a density of 500 kg/m^3 and a drag-coefficient of 1 is used in the presented results. The distances that correspond to the mast height of 209 m, as well as 2/3 of this height is marked as thicker red and blue lines. The distances of 80 and 100 m is marked by thicker grey lines to ease the reading. The dashed black lines shows the greatest distances freely rotating ice cubes with impact kinetic energies of 40 and 60 J can drift at the given wind velocities. The solid black lines shows the probability of surving (S) being hit by the ice piece given impact kinetic energy and mass (assuming all energy is trasfered on impact). The levels of 90, 50, 10 and, 1 % probability of surving impact of the smallest ice cube with sufficient impact energy (the worst case) is given. The white lines shows the impact angles relative to the ground. (60° and 45°). **Right:** Safety distance for smallest ice cubes (worst case with size depending on wind speed) reaching the impact kinetic energy limit of 40 J. The ice cubes are released from the top of the construction as function of given windspeed at 10 m and 209 m heights (x-axis above and below). The safety distance curve (40J) is nonlinear and can be fitted with the following representation: D = A+B*C*(exp(WS/B)-1). Here WS is the wind velocity at 209 m, A=-3.4, B=63.5 , C=8.1, and D is the safety distance.

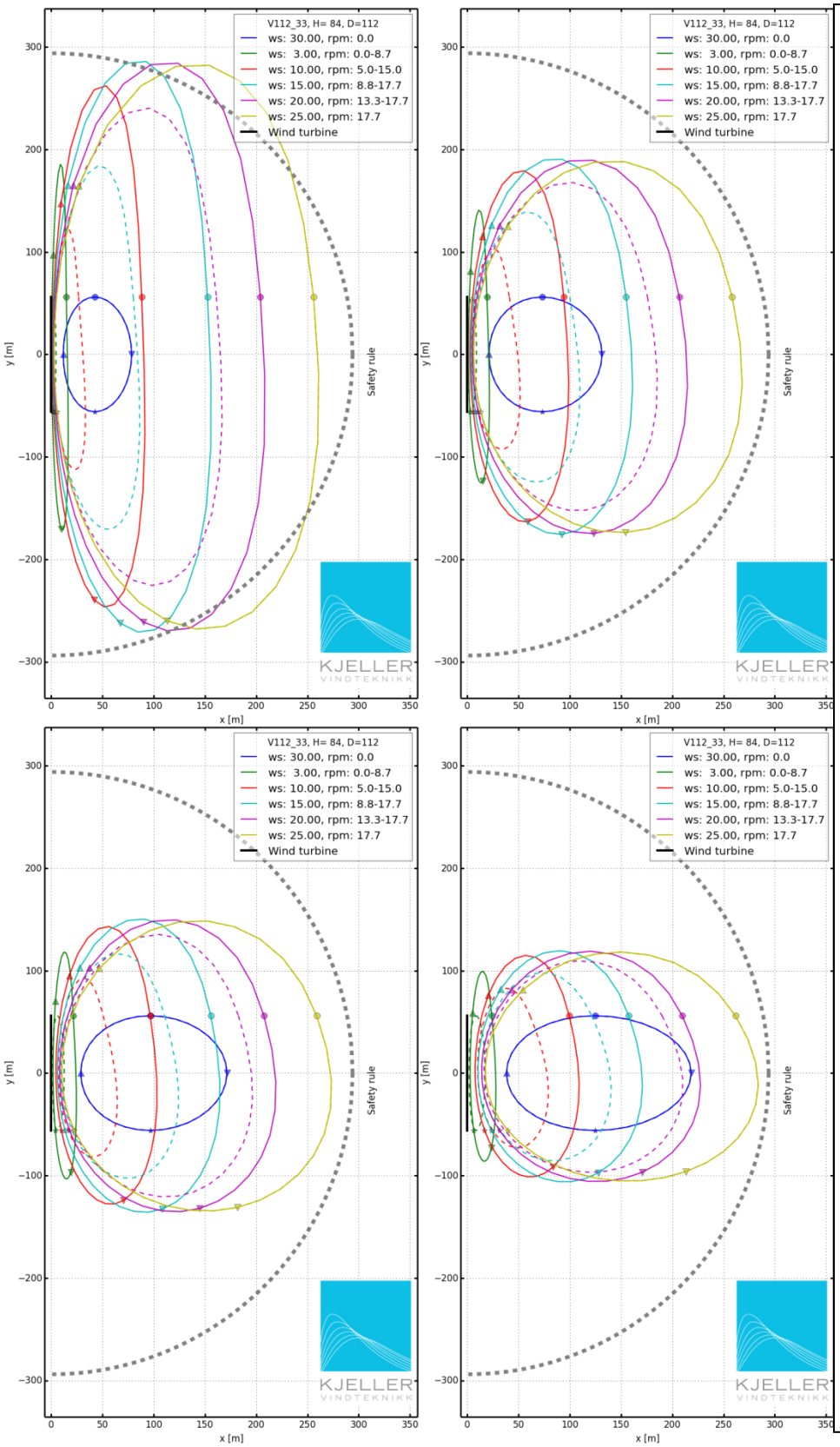

The wind direction is from left to right and the black line shows the turbine position and extent viewed from above (positive z-direction). The ice throw zones for 4 different ice piece sizes are shown in 4 separate plots with in order of decreasing size and weight for regular ice cubes. The blue circles shows the ice fall distance from a stopped turbine during hub wind speed of 30 m/s. The full lines shows where the ice cubes that are thrown from the wind tip will land when turbine is operating without performance reduction giving lowered rpm at given velocities. The dashed lines shows corresponding ice throw zones when icing has caused a performance reduction due to the icing. The rpm values and wind speed are shown in the legend. The markers shows the release orientation and directional movement of the blade (the blade moves along the +y-axis at the lowest position (shown with the upward triangle marker). The gray dashed line shows the general safety distance rule: (H+D)*3/2 (294 m) [8],. Red, light blue, purple and yellow colors shows the ice throw zones when the hub velocity is respectively 10, 15, 20 and 25 m/s. For an ice density of 800 kg/m^3 the icethrow zones shown in the 4 figures correspond to ice cubes of sizes 5 kg (19 cm), 600 g (10 cm), 200 g (6 cm) and 60 g (4 cm). For an ice density of 500 kg/m^3 the ice throw zones corresponds to ice cubes with respective sizes of 13.5 kg (30 cm), 1.7 kg (cm), 500 g (10 cm), og 150 g (6.7 cm). Since flat terrain is assumed in this calculation ice pieces can be thrown a longer distance if there is overheight between the turbine position and the surroundings.

Figure 15: Calculated ice throw zones for different ice piece sizes thrown from the wing tip of a Vestas V112 - 3.3 MW turbine. This turbine has a rotor diamater of 112 m and a hub height of 84 m.

Ice Detection Methods and Measurement of Atmospheric Icing

M. Wadham-Gagnon[1], N. Swytink-Binnema[1], D. Bolduc[1], K. Tété[1], C. Arbez[1]
[1] TechnoCentre éolien, Québec, Canada
mgagnon@eolien.qc.ca

***Abstract*: Accurate and reliable ice detection is essential for operators in the wind energy, aerospace, power transmission and transportation industries. Since these different operating conditions require different information about an event or site, it is useful to be able to directly compare multiple detectors under identical conditions.**

This paper presents the results of a comparative study with 9 ice detection methods from a single test site in moderate icing conditions. These include three instrumental ice detection methods (a Combitech IceMonitor, double anemometry, and wind vane variation test), five meteorological ice detection methods (a horizontal visibility sensor, relative humidity sensor for dew point estimation, liquid water content from a Metek MRR, a Goodrich Ice Detector, and a Labkotech Ice Detector), and an ice accretion measurement from camera images.

The Goodrich and Labkotek produced good indications of meteorological icing while overestimating the duration compared to the methods based on horizontal visibility or liquid water content. The relative humidity method did not provide a good estimate of icing (indicating false positives more than 75% of the time). The Combitech provided instrumental icing estimations comparable to the double anemometry and wind vane variation methods with the added value of providing ice load measurements.

Images from a remote camera installed on the met mast, provide indisputable evidence of the presence (or not) of ice (provided there is good visibility of the structure being monitored). The image processing algorithm developed by the TechnoCentre éolien shows promising results for integration as an automated ice detection method.

Keywords: icing, ice detection sensors and methods, field study

Legend and Abbreviations

AGL	*Above Ground Level*
CBH	*Cloud Base Height measured from a ceilometer*
HR	*Horizontal Visibility*
HUA	*Heated Ultrasonic Anemometer*
HV	*Horizontal Visibility*
LWC	*Liquid Water Content*
MRR	*Micro Rain Radar*
MVD	*Median Volume Diameter*
SNEEC	*Site Nordique Expérimental en Éolien Corus*
SR	*Solar Radiation*
T	*Temperature*
T_{dew}	*Dew point temperature*
TCE	*TechnoCentre éolien*
UCA	*Unheated Cup Anemometer*
WD	*Wind Direction*
WS	*Wind Speed*
WV	*Wind Vane*
σ	*Standard deviation*

Introduction

From power transmission to wind energy, ice detection methods provide total ice load, icing conditions, persistence, or other information depending on which limiting factor is most relevant [1].

Most detection methods provide an indication of meteorological icing, i.e. the period of active ice accretion, and/or instrumental icing, i.e. the period of time where ice is present on a structure or instrument. Few sensors or methods provide information regarding severity (ice load) or intensity (icing rate).

In the wind energy industry, some turbines may be equipped with ice protection systems while others may have preventive shut down strategies during icing events [2], [3]. Both strategies attempt to reduce icing-related production losses and both could greatly benefit from reliable ice detection.

A previous study, conducted in moderate to severe icing conditions in Sweden, compared the IceMonitor, Goodrich, Labkotech, and Holooptics ice detectors with a camera and heated/unheated anemometer measurements [4]. The intent of the present paper is to extend the comparative analysis to tests based on dedicated ice detectors, standard meteorological instruments, and novel detection methods during light to moderate icing conditions.

I. Site, Sensors and Methods

In order to compare the performance of different ice detection methods, a measurement campaign was conducted by TechnoCentre éolien (TCE) using sensors installed at the Site Nordic Expérimental Éolien Corus (SNEEC). The measurement campaign was conducted on a 126 m meteorological mast at the SNEEC test site, based in Rivière-au-Renard, Québec, Canada.

The sensors and methods discussed in this paper are described in Table 1. Each method will be referred to hereinafter by the acronym/abbreviation defined in this table. All methods are intended to detect ice at 80m above ground level which represents the hub height of the wind turbines installed on the same site.

The criteria used to determine the presence of ice for each method are provided in Table 2.

The LID, GID and CIM methods are based on simple criteria defined to interpret the signal of the specialised ice detection sensors. Note, however, that the thickness measured by the GID is in fact a pre-set linear calibration based on a vibration frequency; it was not calibrated after installation.

The RHT, WDD and WSD methods are based on standard data quality control tests [8].

The CAM method in the context of this study consists of analysing images taken from a camera installed on the meteorological mast. The thickness of ice is measured on the vertical section of the boom that supports an anemometer using an automatic image analysis algorithm developed by TCE.

Table 1: Description of ice detection methods

Method	Sensor	Description
CAM	Camera	Ice thickness measured from images of vertical anemometer support
CIM	Combitech Ice Monitor	Freely rotating ISO cylinder with load sensor [5]
GID	Goodrich 0872F1	Specialised ice detection sensor based on ultrasonic frequency change [6]
HVT	HV, T	Based on Horizontal Visibility and Temperature criteria
LID	Labkotek LID-3300IP	Specialised ice detection sensor based on ultrasonic frequency change [7]
LWCT	MRR & T	Atmospheric icing based on LWC measured from MRR and T
RHT	RH, T	Based on relative humidity and temperature criteria
WDD	WV	Detects ice from the variation in standard deviation of WD
WSD	HUA, UCA	WS difference between HUA and UCA

Table 2: Ice detection criteria for the different methods

Method	Icing Criteria
CAM	N/A
CIM	Load > 0.2 kg/m
GID	Thickness > 1 mm
HVT	HV < 300m T < 1°C
LID	Signal < 60% within past 30 min
LWCT	LWC > 0.1g/m^3 at 75m AGL T < 0°C WS > 4 m/s
RHT[1]	$\lvert T - 0.9T_{dew} \rvert < 1°C$ T < 1°C
WDD	$\sigma_{WV} < 3°$ Or: $\sigma_{WV} < 1/3\ \sigma_{WV(ref)}$ T < 1°C
WSD	$(WS_{HUA}-WS_{UCA})/WS_{HUA} < 80\%$ $WS_{HUA} > 4$ m/s T < 0°C

1. T_{dew} is calculated with the Magnus-Tetens equation [9], which is a function of relative humidity.

The camera images were recorded every 10 minutes at low resolution as they were initially not intended to be used for ice detection by image analysis. An example of non-iced and iced anemometer and vertical support structure is given in Figure 1.

As the direction of ice accretion on the anemometer's boom depends on the wind direction, the image analysis algorithm may not measure the maximum thickness of ice on the structure. Due to this, the measured ice thickness was an estimate provided for qualitative purposes only in the present study; no ice detection criterion was associated. For the same reason, the ice load, which may be estimated using ISO 12494 [10], was not calculated.

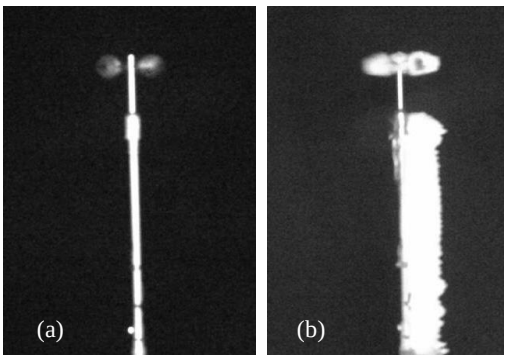

Figure 1: CAM image of (a) a non-iced anemometer, and (b) an iced anemometer and shaft

The HVT method is based on the horizontal visibility as measured by a CS120 visibility sensor at 18 m AGL.

Finally, the LWCT method uses LWC measured from a Metek Micro Rain Radar (MRR) installed next to the met mast. An example of LWC measurement is shown in Figure 2. This method detects ice when LWC greater than 0.1g/m^3 is measured at 75m above ground level and temperature measured at the same level (from a thermometer on the met mast) is below 0°C. Note that the MRR measures precipitating water content but not cloud water content. This is due to the water droplet diameter range it is capable of registering. Hence, this method was used as a preliminary test of the potential of the equipment.

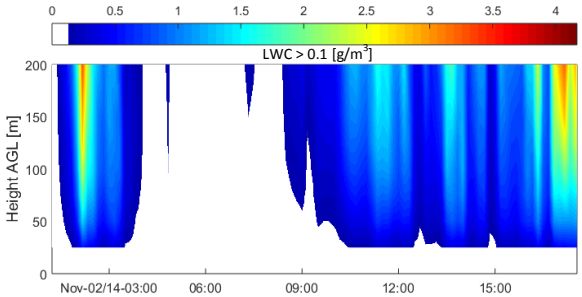

Figure 2: Sample LWC time series measured from an MRR sensor between 25 m and 200 m above ground

II. Icing Duration

A. *Annual Statistics*

Total icing duration over the winter 2014-2015 months is shown in Figure 3, with each method identified as indicating either meteorological (met) or instrumental (ins) icing. The GID and LID methods estimate durations of meteorological icing close to the durations of instrumental icing estimated by the CIM, WSD and WDD. This is unexpected as the instrumental-to-meteorological icing ratio on this site has previously been observed to be of the order of 2 to 1 [11]. The HVT method for meteorological icing compared to the CIM or WSD methods for instrumental icing are closer to reflecting this ratio. It is noted that the LID method relies on a criteria that is based on the heating cycle of the sensor (30-40 minutes). The heating cycle of the sensor may cause this method to overestimate meteorological icing. Meanwhile the GID method tests whether a single point has surpassed its threshold. While this has a more rapid response time, a low threshold may be too sensitive while a high threshold results in numerous "on-off" cycles within a single event. For the present analysis, a low threshold was used, which may explain the higher-than-expected hour count. Further investigation is required.

The duration of meteorological icing based on the RHT method is at least 4 times greater than any other method (instrumental icing included). This suggests that the RHT method is false-positive at least 75% of the time, supporting earlier reports that the method is unreliable [12].

The CIM and WSD methods estimate just over 400 instrumental icing hours each. The HVT method indicates the lowest number of meteorological icing hours yet is within the expected ratio compared to instrumental icing of the CIM and WSD methods.

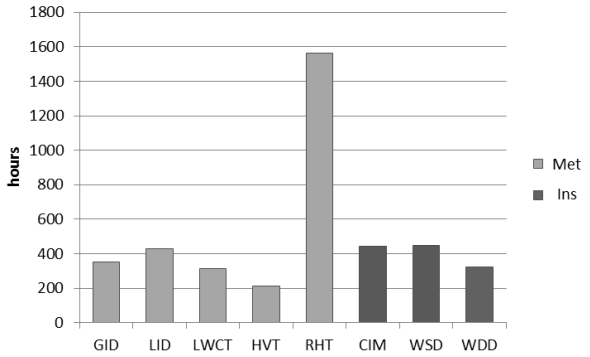

Figure 3: Duration of icing detected by different methods over the course of winter 2014–2015 (Nov to Apr)

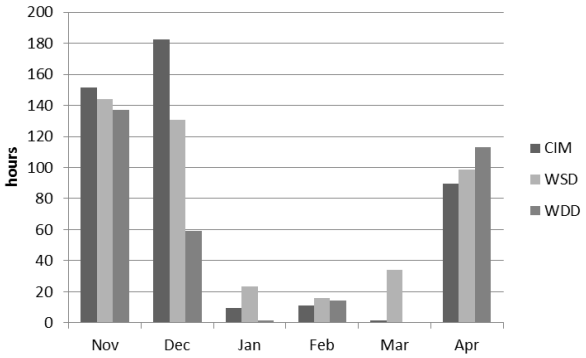

Figure 5: Monthly duration of instrumental icing detected by different methods during winter 2014–2015

B. Monthly Statistics

The number of hours of icing per month is shown in Figure 4 for methods intended to detect meteorological icing and in Figure 5 for methods intended to detect instrumental icing. Figure 4 illustrates how the RHT method greatly exceeds all other method estimations in every month. The other methods are comparable with the exception of the months of January when the HVT method suggested almost no icing hours, and February when both the GID and HVT methods suggested almost no icing hours.

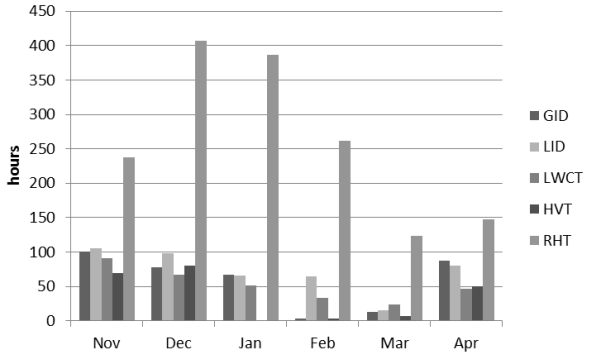

Figure 4: Monthly duration of meteorological icing detected by different methods during winter 2014–2015

The methods intended to detect instrumental icing are in good agreement in November, February, and April (Figure 5). The large difference between the methods in December is likely due to the low wind speeds during the main icing event of that month (see the following section). WSD excludes possible false positives at low wind speeds when cup anemometers underestimate the wind speed. Similarly for WDD, readings at low winds are unreliable due to the cut-in speed of the wind vane. Periods of low winds were therefore excluded from the analysis yielding a significantly lower icing duration than the other instrumental methods in December.

III. Icing Events of Interest

Of 20 icing events identified based on the GID method during the winter, three are presented in this paper.

A. Event 1 (Nov 2-5, 2014)

The first event (Figure 6) is a "text book example" with all sensors and methods (except RHT) working as expected. Active ice accretion in the beginning observed with CAM coincides with a higher frequency of heating cycles with the GID method. The raw LID data may be seen to decrease below its heating threshold (60% signal level) implying that ice was still accumulating at least one sampling period – 30 s – after it started heating.

Inspection of the CAM images reveals that ice was shed from part of the support around 22:40 on Nov 2. The anemometer itself remained iced, however, as is also confirmed by WSD (which uses different anemometers). The camera lens was covered in ice for a period, preventing good CAM data. Ice was then shed along the same section of the support around 18:00 on Nov 3 but remained on the anemometer rotor until the temperature had risen above 0°C around 6:40 Nov 5.

The WSD and WDD returned to the non-iced condition when the temperature rose. In contrast, the CIM took 6 hours longer. Since the anemometer did not completely freeze during the event, slightly higher vibrations and relative wind vectors may have quickened the ice shed compared with the static CIM sensor.

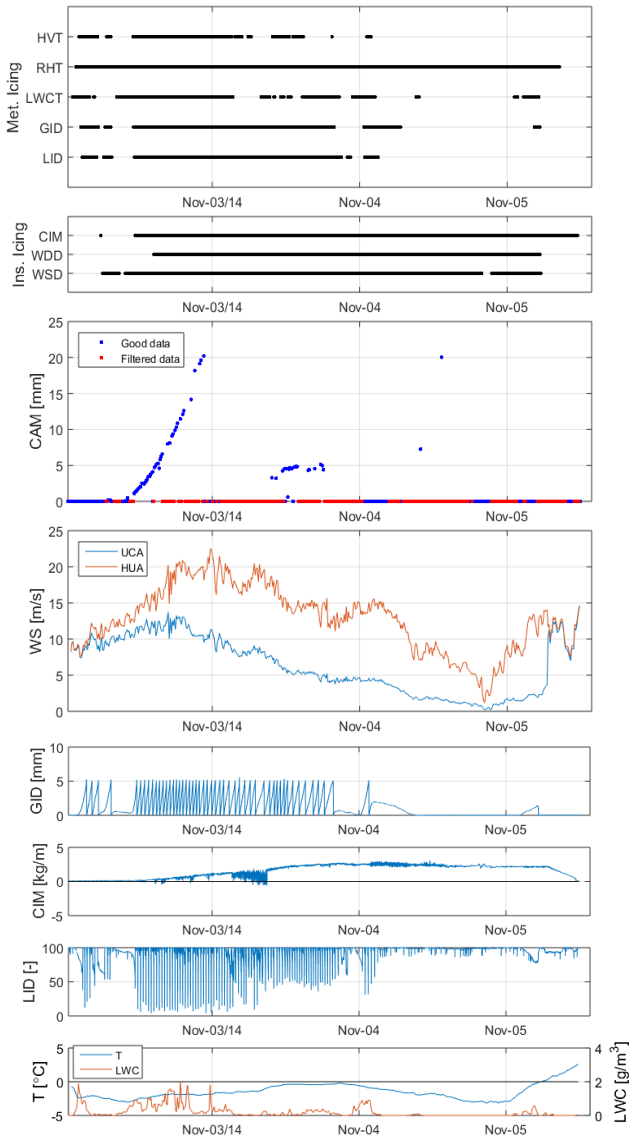

Figure 6: Ice detection methods and raw data – Event 1

B. *Event 2 (Dec 17-25, 2014)*

The second event, seen in Figure 7, lasted over 7 days with a single day of meteorological icing. Once again, the meteorological methods coincide with CAM accretion, though they have some offset in their start and finish times. The LID algorithm requires that a heating cycle is initiated and so is less sensitive than a visual inspection of the raw data would suggest – LID therefore appears later than GID despite both raw data time series showing signs of ice at the same time. GID stopped indicating ice the first time it reached its heating threshold because further ice accretion was not sufficient to attain its icing threshold after that point. In contrast, LID raw data suggest that a strong icing event continued after GID and CAM indicate no additional accretion. This behaviour for the LID sensor was observed at other instances during the winter when observations indicated very minimal ice accretion, and may be caused by non-icing precipitations.

CIM, CAM, and WSD raw data indicate a five-day period of instrumental icing which is not fully accounted for by the WSD and WDD methods. This is likely caused by each method's threshold criteria. The WSD method requires winds above 4 m/s measured by the HUA to prevent false positives. It is also likely that the standard deviation criteria of the WDD method are not met at low wind speeds but this needs to be verified.

On Dec 24, freezing rain appears to have caused a short event and some ice accretion though it is uncertain why the CAM method did not measure it as the images were reasonably clear..

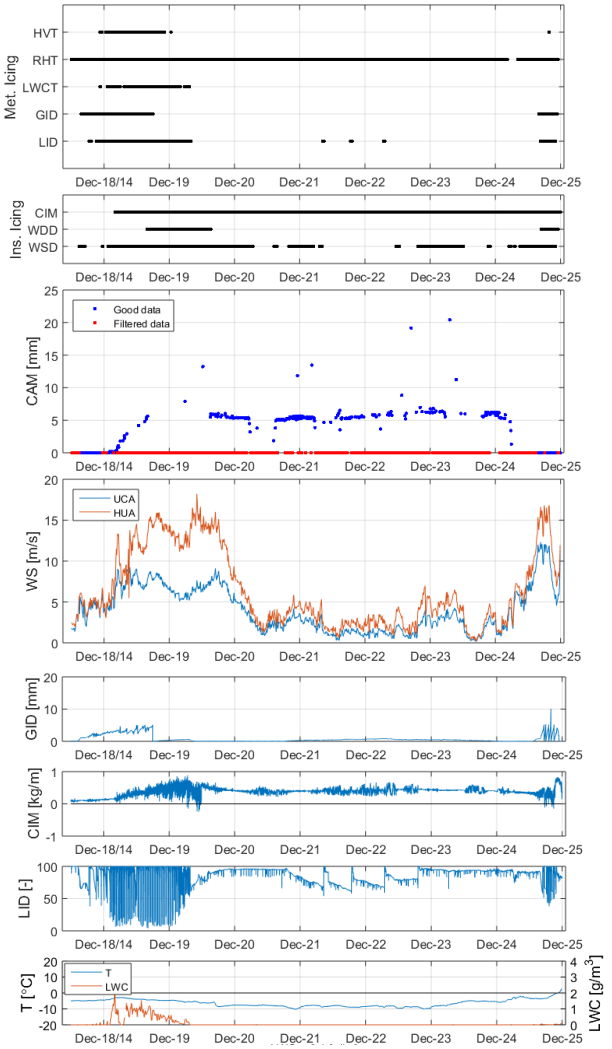

Figure 7: Ice detection methods and raw data – Event 2

C. *Event 3 (Apr 21-27, 2015)*

Event 3, a 4-day icing event shown in Figure 8, began in higher winds than the previous two but the winds decreased as the event intensified (seen in the higher cycle frequency of the GID raw data); this may have caused the UCA to freeze completely in early morning Apr 22. Ice accreted intermittently for the remainder of the event, though once again the LID raw data indicated a much more severe event than the GID in the latter half.

The instrumental icing methods indicate similar trends to one another except the CIM start time, which is approximately 12 hours behind the WDD and WSD methods. The raw CIM data indicates a negative load during this time; this is an occasional issue which tends to occur at the beginning of icing events. Note that the noise in the raw CIM data in Figure 8 is significantly reduced compared with the first two events because 10 minute average data acquisition was implemented in March 2015 in place of the 30 s single samples taken before.

There is a significant difference between the meteorological icing methods for this event. The GID suggests ice is accreting during the majority of the event. The raw GID data suggest that

ice accretion was slow or even reversed during some of the time; this behaviour is not accounted for by the single threshold which assumes a positive ice accretion *rate* above a 1 mm ice accretion signal level. In contrast, the LID method matches its raw signal more closely. Whereas the GID method uses a threshold based on a single point, the LID method requires the threshold to be passed at some point in the previous 30 minutes (about the time of a heating cycle during an icing event).

In early morning Apr 26, a small event with temperatures at or just above 0°C and no measured LWC caused the UCA to freeze again soon after its ice was shed. During the previous period, however, all methods correctly indicated an absence of ice formation conditions.

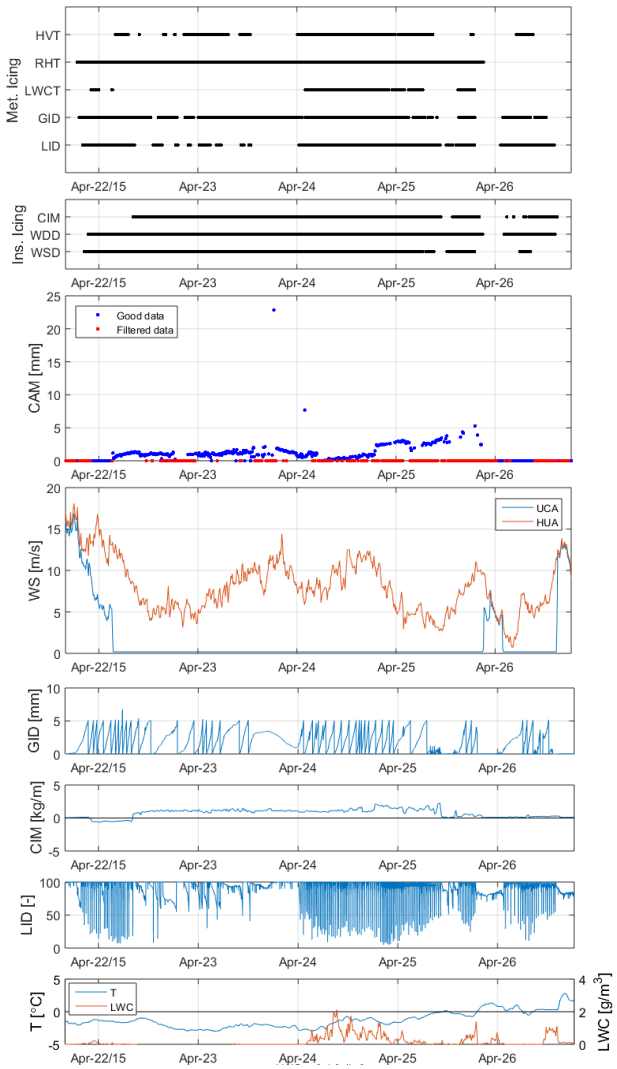

Figure 8: Ice detection methods and raw data – Event 3

IV. Icing Severity

Icing severity may be interpreted through further processing of several of the methods presented. A quantitative analysis will be presented in a future paper, but some discussion is included here by way of introduction.

Heating cycle frequency may be counted with cyclically-heated ice detectors such as the LID and GID. Higher frequencies therefore indicate more severe icing. In Event 3, for example, the GID heating cycle which begins at midnight Apr 26 lasts 6 hours whereas the one immediately following lasts one hour, thereby suggesting a six-fold increase in severity. Both the GID and LID detectors have adjustable parameters which would enable shorter heating cycle times: the current 30 min or greater cycles are not conducive to (wind) industry-standard 10 min averaging. Using the GID raw data, the events may be classified in order of most to least severe as: Event 1, 3, and 2.

Using accumulating instrumental icing methods, such as CAM and CIM, the icing severity may be estimated based on the total accretion, either in mm (camera), kg/m (CIM), or by converting to a standard ice class using Annex A of [10]. With these methods, the derivative of the data yields the accretion rate. As discussed previously regarding Figure 7, the CAM method (and CIM) may indicate both the meteorological and instrumental icing in this way. The CIM suggests that, in terms of total ice accretion, Event 1 was most severe, followed by Event 3 and Event 2. Icing severity could not be estimated from the CAM method as implemented in this setup: as discussed in Section I, the maximum ice thickness was not measured.

Finally, the LWCT method may be extended into an ice accretion model using WS, LWC, and T [10]. This would estimate the ice load (kg/m) or accretion (mm) during an icing event on a standard reference tube.

V. Conclusion and Future Work

A comprehensive study of 9 ice detection methods was presented for a single test site in Québec, Canada over the winter 2014–2015. It has provided a means of direct comparison between methods overall (icing hours) and for specific events (sensitivity of each instrument from beginning of accretion to ice shed). The following conclusions could be drawn:

- The LID method shows ice accretion after the heating cycle is initiated providing an indication of icing intensity.
- The GID method also provides an indication of icing intensity as the sensor increases the frequency of heating cycles during periods of active ice accretion.
- The HVT method followed the LID quite closely for all three events, but reported half the total icing hours. HVT may be the more accurate measurement of the two since the LID method was found to overestimate ice accretion during small icing events.
- The RHT method provides excessive false positive results.
- The CAM method provides the most information on the icing event but relies on the camera lens not being obstructed by ice. This can be managed with adequate heating and protection from ice. The algorithm also relies on the quality of the images and may not be capable of detecting ice when there are not sufficient contrasts in the images.
- The WSD and WDD methods provide reliable indication of instrumental icing but may need to be refined for low wind speeds.
- With 10 minute averaging, the CIM method yielded a consistent instrumental icing response though its load measurement was not validated and it occasionally reported negative load values.
- The LWCT method followed meteorological icing of other methods, but is incomplete as it does not capture in-cloud icing. Its suitability for ice detection and forecasting needs to be investigated further.
- The LID and GID methods measured a high number of meteorological icing hours relative to instrumental icing hours measured with WSD and WDD methods. Further investigation is warranted.

Many of the sensors used in this analysis were installed in 2014 and have only experienced a single (relatively mild) winter. The researchers plan to continue the study into the winter 2015–2016 in the hopes of increasing the number and severity of observed icing events.

An ice accretion model based on LWC, WS and T may be developed and algorithms for ice severity based on the LID and GID methods may be completed in the future.

As well, ice detection based on cloud base height and temperature has shown promising results in previous studies. Data from a ceilometer sensor is available and will be included in a future paper.

ACKNOWLEDGMENT

The authors would like to thank their colleague Charles Godreau for running the image analysis for the CAM method. TCE operations and the SNEEC wind farm infrastructure are made possible with the support of the Québec Government's "Ministère Finance et Économie" and Canada Economic Development. The met mast was installed with funding from the Canada Foundation for Innovation, Renewable NRG Systems and RES Canada. Finally, the TCE mandate as a college centre for technology transfer in wind energy is provided by the "Cégep de la Gaspésie et les Îles".

REFERENCES

[1] S. Fikke, et al., "COST 727: Atmospheric Icing on Structures Measurements and data collection on icing: State of the Art", Publication of MeteoSwiss, 2006

[2] J. Nelson, "L'expérience de TransAlta avec le givrage des pales", 6th Quebec Wind Energy Conference, Carleton-sur-mer, 2012

[3] S. Trudel, "Les arrêts préventifs: solution face au givre", 8th Quebec Wind Energy Conference, Gaspé, 2014

[4] H. Wickman, et al., "Experiences of different ice measurement methods," Elforsk Report 13:15, 2013

[5] Combitech, "The Ice Load Surveillance Sensor IceMonitor™", Product Sheet, 2013

[6] Campbell Scientific (Canada) Corp., "0872F1 Ice Detector Instruction Manual", 2014

[7] Labkotec Indutrade Group, "LID-3300IP Ice Detector - Installation and Operating Instructions", 2014

[8] TechnoCentre Éolien, "PRO-REC 002: Procédure de contrôle qualité des données", Gaspé (Québec) Canada, 2014.

[9] D.R. Heldman, "Encyclopedia of Agricultrual, Food, and Biological Engineering", CRC Press, p. 188, 2003.

[10] ISO. Atmospheric Icing of Structures. Standard ISO 12494:2001(E). Geneva, 2001

[11] D. Bolduc, et al., "Field Measurement of Wind Turbine Icing", IWAIS XV, St-John's, 2013

[12] R. Cattin, "Icing of Wind Turbines", Elforsk, Stockholm, 2012.

Wet snow icing - Comparing simulated accretion with observational experience

Árni Jón Elíasson [1], Sigurjón Páll Ísaksson[2], Hálfdán Ágústsson [3], Egill Þorsteins[2]
[1] Landsnet, [2] EFLA Consulting Engineers, [3] Belgingur
arnije@landsnet.is, sigurjon.pall.isaksson@efla.is, halfdana@gmail.com, egill.thorsteins@efla.is

***Abstract*: Coupled icing and mesoscale atmospheric models are a valuable tool for assessing ice loading for overhead power lines. This paper presents an analysis of how well icing model captures wet snow accumulation in areas that are historically known to be exposed to wet snow icing in Iceland. Wet snow icing maps were prepared using a snow accretion model with 21 years of data. The weather parameters used in the accretion model, i.e., wind speed, temperature, precipitation rate and snowflake liquid water fraction, were derived by simulating the state of the atmosphere with WRF model at a horizontal resolution of 3 km. The icing maps were compared to data from an icing database that contains long term historical information on icing events on the overhead power lines in Iceland.**

Keywords: wet snow accretion, modelling, icing observations

I. Introduction

Wet snow accretion on overhead power lines can cause mechanical overloading and can lead to a failure of the supporting structures. Historically, wet snow accumulation has led to many severe failures of power lines in the distribution grid in Iceland. Especially before adequate knowledge and experience had been obtained regarding the most severe icing areas and the main icing directions. An important step in the quantification of the risk was taken in 1977 when a systematic registration of known icing events on all overhead power lines in the country was initiated.

In recent years a huge step has been taken in further understanding of the wet snow accretion risk with use of icing models. The improved icing accretion models combined with weather parameters that are derived by simulating the state of the atmosphere, for example with the WRF model, are very powerful tools to gain further understanding and quantification of the wet snow accretion risk. Especially in complex orography and in areas where no prior operational experience of power lines exists. An increased use of icing models to assess the risk of wet snow accretion is foreseen in coming years.

The paper presents an analysis of icing model performance based on a comparison with observed wet snow icing. Icing maps containing maximum predicted accretion mass in the period 1994-2014 were prepared for the analysis. The main focus of the study is on how well the predicted wet snow accumulation reflects areas prone to icing as well as how icing in complex terrain is reproduced.

II. Historical observations of wet snow accretion

In a global context, wet snow accretion is a frequent occurrence on overhead power lines in Iceland. It may occur in all regions but some parts are more exposed than others and the frequency and the amount has varied greatly between locations. Experience from the overhead network reveals a dependence of accretion on predominant icing directions. Power lines oriented favourably with regard to the predominant icing directions often experienced far less and minimal accretion compared to nearby lines with a more unfavourable orientation.

A systematic collection of data and registration of all icing events on power lines was started in 1977 due to the impact of the icing on the operational reliability of the power lines. The registration has been continuous from the start and an effort has also been made to find information on events prior to 1977. A reasonable good overview is now reaching back to 1930, with the database containing data from power lines of all voltages as well as on some older telephone lines. The largest part of the records is related to wet snow accretion on the 11-33 kV distribution net. Records of individual icing events are done for all affected line sections and contain estimates, and in some cases actual measurements, of typical and maximum ice diameters on the section, type of accretion, information on wind and eventual failures. Figure 1 shows the number of broken poles from 1960 that have been registered in the database in relation to icing, with most failures due to wet snow icing. The reduction in failures rate from 1995 is related to a program where distribution lines exposed to severe wet snow icing were put underground. The data is collected, organized and hosted by Landsnet, the transmission system operator in Iceland, and has previously been described in [1].

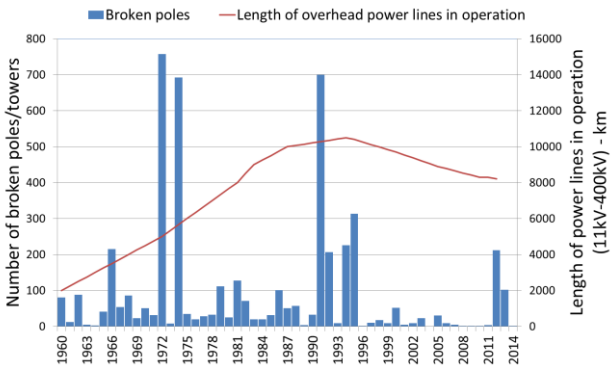

Figure 1: Number of broken poles registered in the database since 1960. Most failures are due to wet snow icing on 11-33 kV lines.

Figure 2 shows the location of overhead power lines in Iceland. Most of the power lines, and especially those in the distribution grid, are located in coastal regions. Some of the 132 kV and 220/400 kV lines are located inland and on the boundary of the central highlands. No overhead power lines have so far been built in the central part of the country, but several test spans have been installed. All power lines can be expected to get wet snow accretion but the amount and frequency varies greatly. Line sections of where the highest and most extreme wet snow loads have been observed are marked in Figure 2. Wet snow accretion has been observed on many line sections not marked, but to a lesser extent.

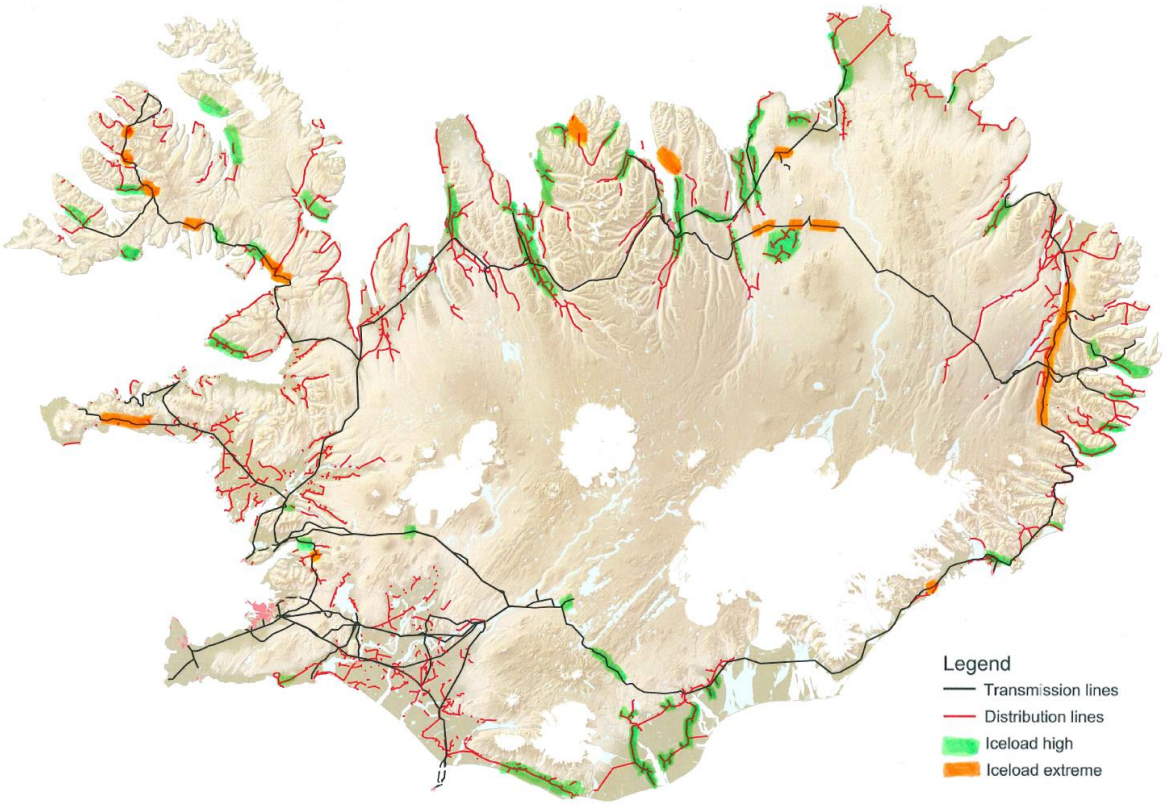

Figure 2: Power lines where high and extreme wet snow accretion has been observed.

III. ICING MODEL

The atmospheric parameters needed as input for the wet snow accretion models are obtained from the RÁV-project [2]. In the project, weather in Iceland during 1994-2014 was dynamically downscaled using version 3.0 of the non-hydrostatic mesoscale Advanced Research WRF-model (ARW, [3]). This state of the art numerical atmospheric model is used extensively both in research and in operational weather forecasting throughout the world, including Iceland. The atmospheric modelling is done at high resolution, 9 km (1957-2014) and 3 km (1994-2014) in the horizontal and 55 levels in the vertical, with the 3 km dataset employed in this study. The model is forced by atmospheric analysis from the European Centre for Medium-Range Weather Forecasts (ECMWF). The model takes full account of atmospheric physics and dynamics, and the relevant parameterization scheme for this study is the moisture scheme of [4], with other details of the setup of the model found in [5]. One of the key aspects of the dataset is its high spatial resolution, but as resolution is increased, the atmospheric flow and its interaction with the complex orography are in general better reproduced. In short, the readily available RÁV-dataset is currently the most accurate and detailed dataset describing the state of the atmosphere above Iceland, at high temporal and spatial resolutions in 4 dimensions. The dataset has previously been used in a number of studies of weather and climate in Iceland, including studies of orographic winds and precipitation, as well as the climatology of wet snow accretion in Southeast-Iceland [6].

Wet snow icing accretion is calculated based on the cylindrical accretion model approach ([7], [8]) where sticking efficiency is calculated with the equation from Nygaard et. al. [6]. Two different icing model setups are employed in this study: (i) vertical cylinder approach, (ii) horizontal cylinder approach. In the vertical cylinder approach the particle impact speed is always perpendicular to the object and hence the accretion is independent of wind direction. In the horizontal cylinder approach, eight different span directions are considered, with a 22,5° interval. Hence, accretion is reduced proportionally when the snow flux is not perpendicular to the spans. Ice shedding is assessed to take place as soon as the air temperature exceeds 3°C or when no accretion has occurred for 24 hours.

IV. WET SNOW ICING MAPS BASED ON ICING MODEL

Wet snow icing maps were made using the icing model and 21 years of simulated atmospheric data. The results from the vertical cylinder icing model are shown in Figure 3 where the maximum modelled icing in the period is presented in kg/m.

Wet snow icing in Iceland is usually combined with strong winds which enhance the accretion intensity and density. Extreme wet snow accretion has in few cases been measured or observed in range of 15-20 kg/m in Iceland.

Figure 4 shows a box-plot (histogram) of wet snow icing events classified based on elevation above sea level, total area of land for each class is also presented. Figure 5 shows the median values of wet snow icing in different regions of the country (SW, NW, NE and SE), also based on elevation.

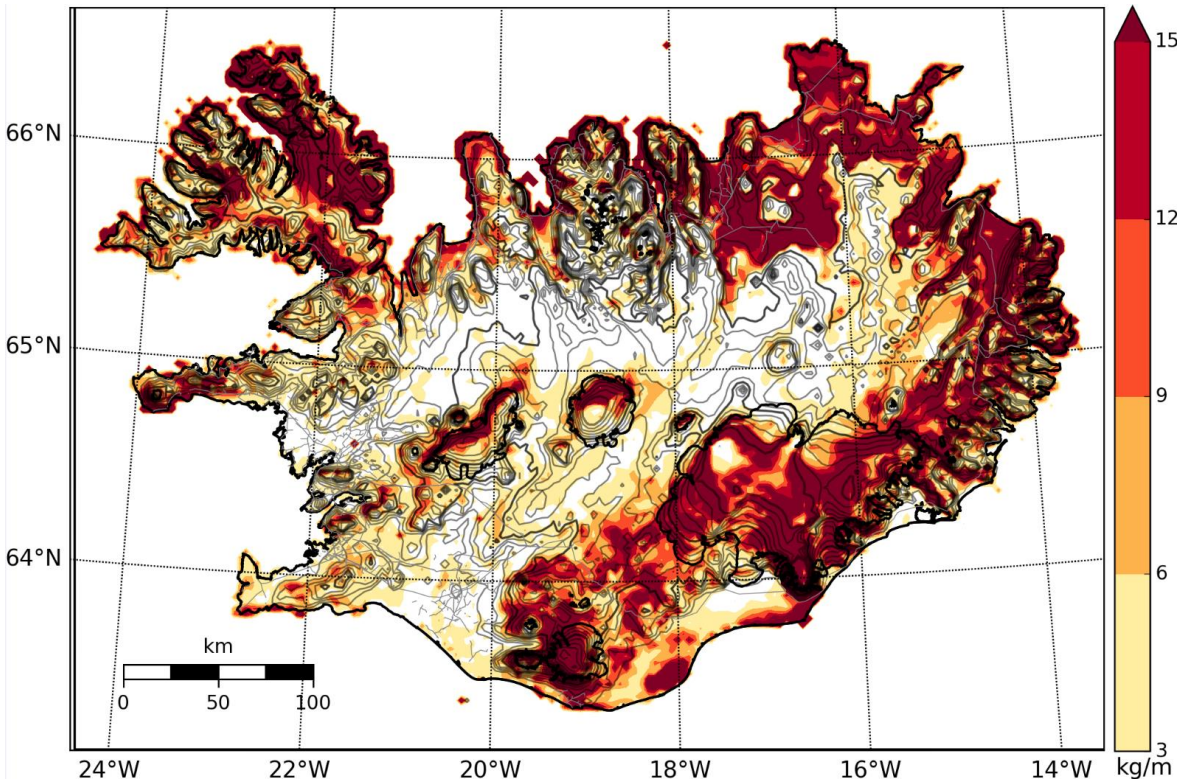

Figure 3: Estimated maximum wet snow load in the period 1994-2014, based on the vertical cylinder model approach.

The following remarks can be made on the estimated maximum wet snow load in the period 1994-2014 presented in Figure 3. In this context it should be noted that the figure presents icing based on the vertical cylinder approach and does not necessarily resemble to what would accrete on a horizontal span.

- The expected wet snow accretion is very site dependent.
- The most severe icing is usually relatively close to the coast.
- The wet snow ice load can be quite high, in most severe cases it can be well above 15 kg/m
- The central highlands experience low loads in the icing model, especially in the precipitation shadow north of the glaciers.
- High wet snow icing loads inland are often associated with a relatively gentle upwards slope of the land, or where there is an upstream mountain barrier.
- Extreme wet snow maxima are found at the foot of high mountains and massifs in parts of the country.
- High accumulation occurs on the glaciers. Most of the severe accretion in higher altitude occurs on glaciers.
- Southwest-Iceland has relatively little wet snow accretion except in localized areas.

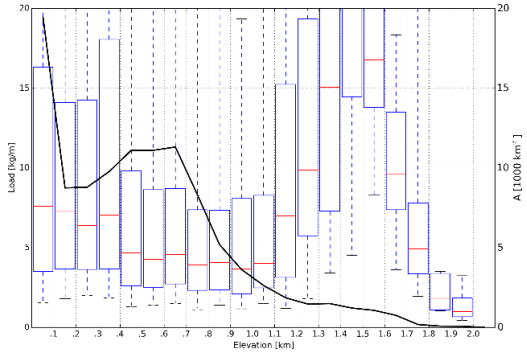

Figure 4: Box-plot of wet snow icing classified on elevation above sea level. Total land area is given on Y2 axis.

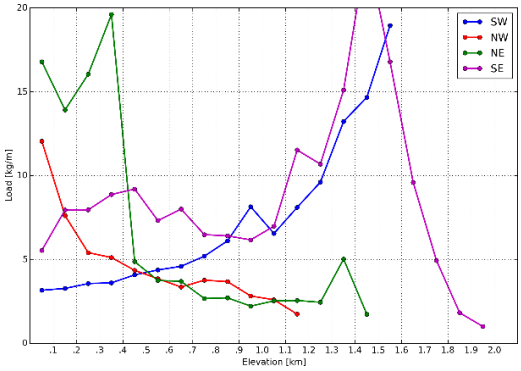

Figure 5: Median values of wet snow icing in different regions.

The complex spatial structure of the simulated ice loading depends strongly on regional differences in atmospheric and topographic factors. Those include, the complexity and shape of the orography, prevalent precipitation directions, average air temperature and its typical evolution during precipitation events.

Accretion downstream in complex orography, especially in the mountains in N and E

The interaction of atmospheric flow with complex orography may create favourable conditions for wet snow accretion on the lee slopes, and immediately downstream, of large mountains, such as in the mountains in north- and east-Iceland, see [9], [10] and [11]. Three key factors are relevant here.

- Heavy precipitation may occur as a result of the orographic uplift experienced by the air mass as it passes above the mountain. The precipitation is partly carried downstream with the flow and to the lowlands in the lee of the mountains.
- In a stable stratified air mass gravity (mountain) waves may be excited in the flow above the mountain. As a result, the wind accelerates in the descending part of the wave and a local wind speed maximum is created over the lee slopes of the mountain. Furthermore, previous studies [11] and [12]

indicate that enhanced cloud water amounts created in the ascending part of the wave may strongly influence the total atmospheric water content in the lee.

- The plunging airflow on the lee side warms slightly due to adiabatic heating in the descending air. When the adiabatic heating is sufficient to bring sub-zero temperatures up to 1-2°C, partial melting of snowflakes will occur, while orographically enhanced precipitation and downslope accelerated winds guarantee an abundant in-flux of wet snow.

Gently sloping terrain in N and NE

When it comes to wet snow accretion, several locations in gently sloping terrain in North- and Northeast-Iceland seem to be favoured over similar locations in other parts of Iceland. A possible explanation is as follows: When the temperature at sea level is only several degrees over freezing, the 0°C isotherm will inevitably intersect the topography at some level, say few hundred metres above sea level. Hence, in gently sloping terrain there will always be a large region somewhere inland, where temperatures are favourable for wet snow formation, i.e. in the range 0.5-2°C. The adiabatic cooling associated with the forced uplift of the impinging air mass is also of relevance here and may contribute towards heavy precipitation by destabilizing the layers aloft. Such conditions are more likely to occur in the north than in South-Iceland as precipitation during winter in north- and northeast-Iceland generally falls in colder weather than during precipitation events in the south. This is mostly associated with different origins of the air masses and their mixing with cold air advection from the north, but colder sea surfaces are also relevant.

Accretion upstream of mountains in SE

Previous observational and modelling studies of wet snow in southeast-Iceland ([13], [14]) revealed that catastrophic events are related to eastward moving extratropical cyclones of the south coast of Iceland, which is presumably also the case for other significant icing events [6]. These synoptic systems are often associated with slowly moving precipitating fronts at or off the coast and temperatures of 0-2°C ahead of the fronts. The role of the topography (Vatnajökull glacier, Mýrdalsjökull ice cap and surrounding highlands) in creating favourable icing conditions is at least twofold; it blocks the impinging flow and channels a cold northeasterly flow ahead of the front, along the low-lands and perpendicular to many distribution lines in the region. The flow accelerates when it is forced to turn further to the south as it approaches Mýrdalsjökull glacier. The precipitation is furthermore increased as the warmer impinging flow is cooled in a forced ascent above the colder northeasterly flow, which furthermore destabilizes the layers aloft and may cause heavy precipitation. The stability and speed of the cold low level flow is enhanced, which with the heavy precipitation creates ideal conditions for rapid accretion of wet snow icing of high density compared to reports from many other countries.

V. EXAMPLE OF DIRECTIONAL INFLUENCE OF ACCRETION

Experience shows that in most areas the risk of wet snow accretion is related to specific icing- and wind directions. There are numerous cases where repeated failures of distribution lines due to wet snow accretion were solved by changing the orientation of the lines to being as much as possible parallel to the predominant accretion direction. The southeast coast between Mýrdalsjökull and Vatnajökull ice caps is an example of a region with great difference in wet snow accretion on power lines depending on the line direction. Icing events in this area have previously been described and studied in [13], [14] and [6].

Figure 6: Observing and measuring a diameter of wet snow accretion in southeast-Iceland.

Figure 7 shows that the maximum observed icing on power lines in the area varies greatly with the line direction. Figure 8 shows the maximum simulated accretion in the period 1994-2014 using the vertical cylinder approach, i.e. assuming accretion from all directions, while Figures 9 to 16 shows accretion on differently oriented horizontal spans, stepwise with a 22,5° interval, during the same period. There is a clear dependence of ice loading on the span direction. The span direction 67,5°/247,5° is most favourable while span directions: 0°/180°, 22,5°/202,5°, 135°/315° and 157,5°/337,5° accrete a far greater load.

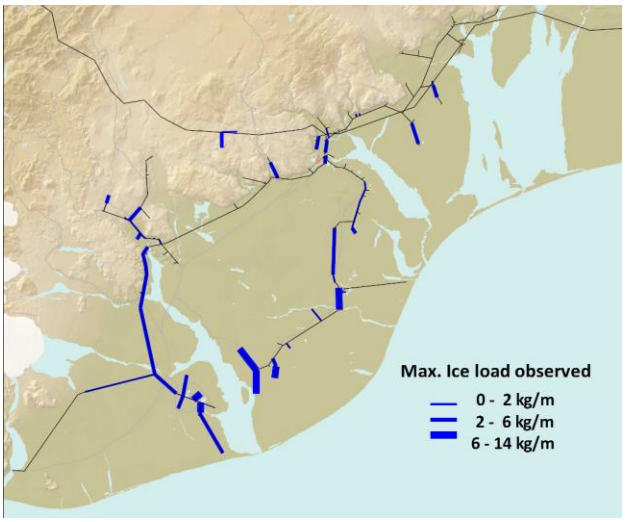

Figure 7: Observed icing in part of southeast-Iceland.

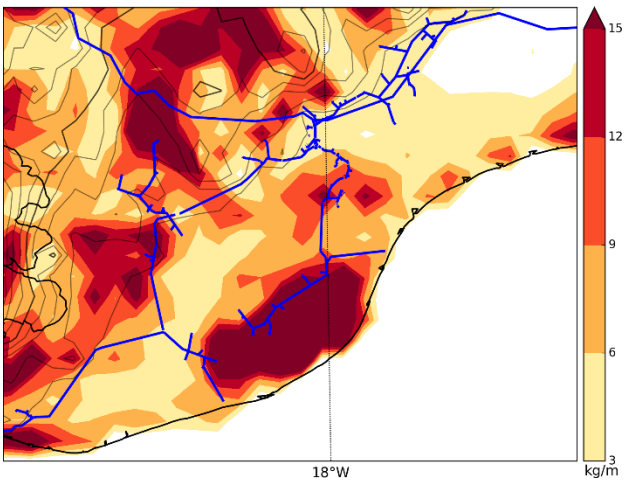

Figure 8: Wet snow accretion, vertical cylinder.

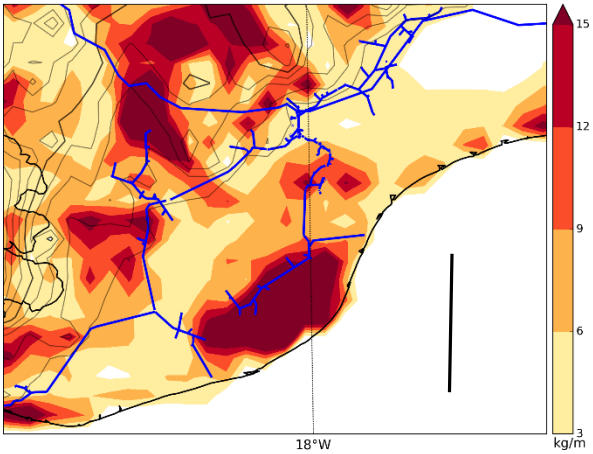

Figure 9: Span direction 0°/180°.

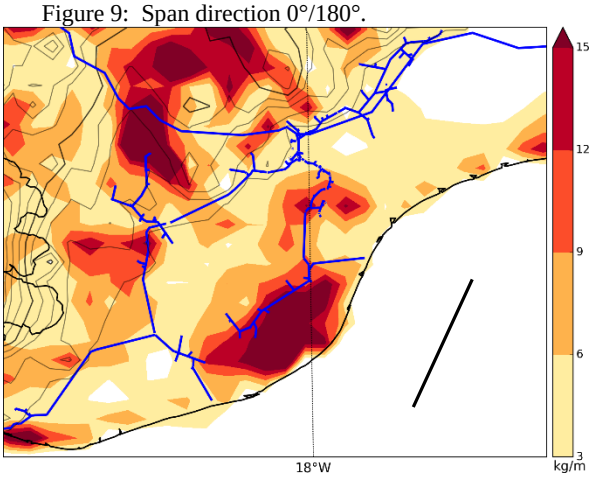

Figure 10: Span direction 22,5°/202,5°.

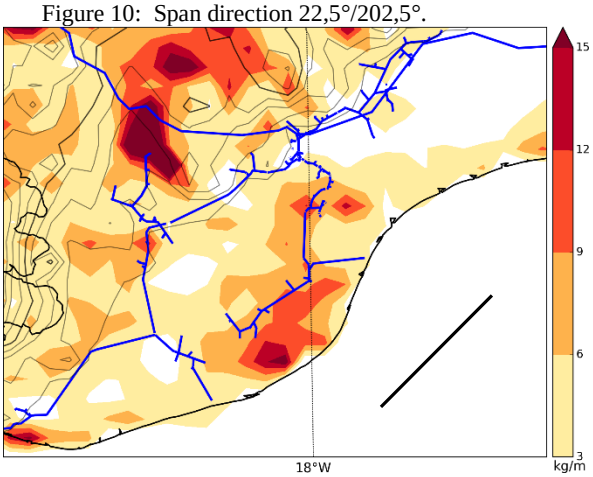

Figure 11: horizontal span direction 45°/225°

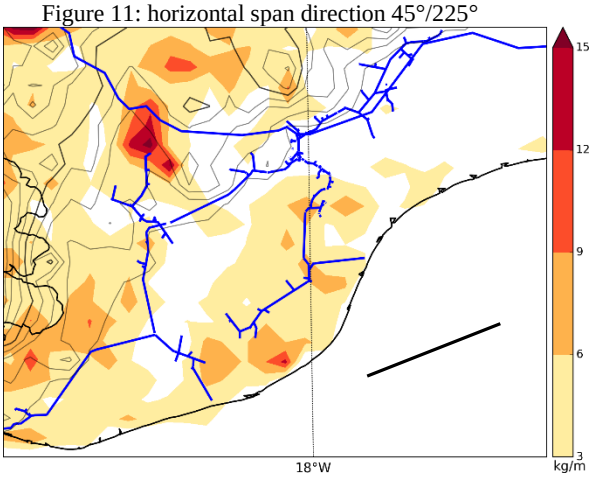

Figure 12: horizontal span direction 67,5°/247,5°

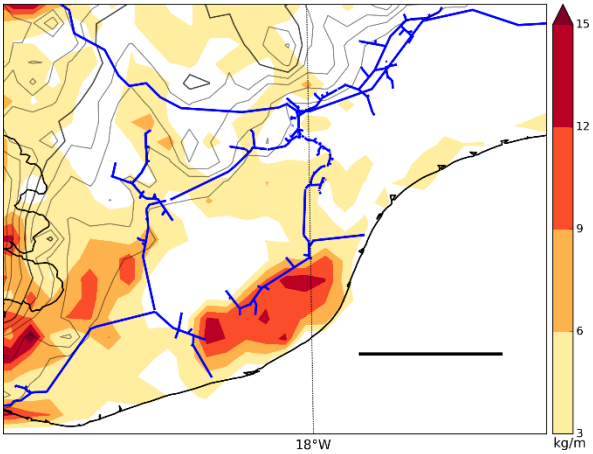

Figure 13: Span direction 90°/270°

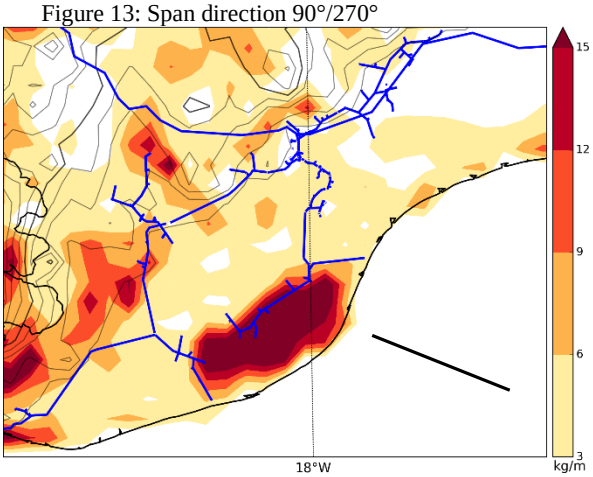

Figure 14: Span direction 112,5°/292,5°

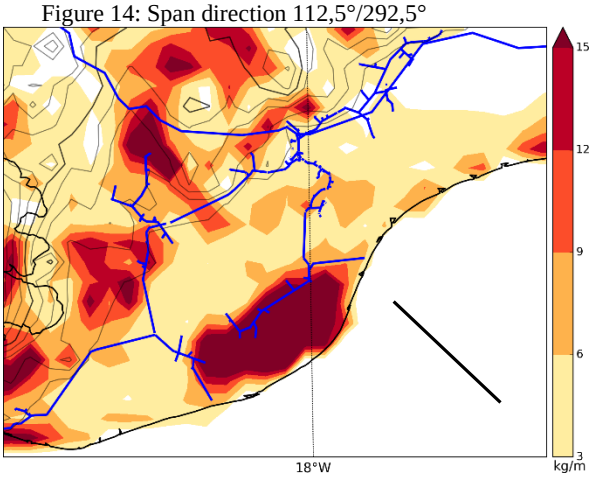

Figure 15: Span direction 135°/315°

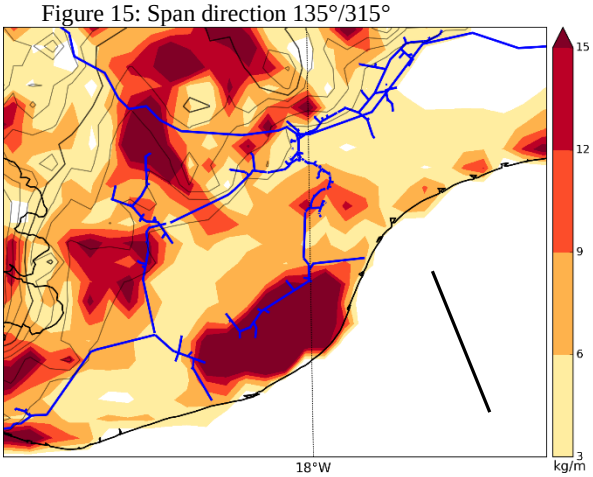

Figure 16: Span direction 157,5°/337,5°

VI. Comparison of observed accretion with icing map

It can be concluded that, qualitatively, there is in general a good correlation between areas with observed accretion and areas with modelled icing. High ice load is simulated in areas where the most severe accretion has been observed. In some cases high loads are simulated where high loads have not been observed. These cases can most often be explained by the strong dependence on the actual line direction compared to main icing direction. In fact, the icing model needs to be analysed with the actual direction of the power line instead of the vertical cylinder model, as is exemplified in paragraph V. There are no power lines operated in the central parts of the country but there is, however, data available from many test spans located there. Those test sites have generally observed little wet snow accretion, fitting well with the low values in the model.

There are indications that the icing model may be predicting too high loading in the higher end of the loading. Extreme wet snow accretion has in few cases been measured or observed in the range of 15-20 kg/m in Iceland but larger values may be possible. The icing model predicts considerably higher values at some locations. It is believed that there is a considerable uncertainty in those cases since the icing model has not been calibrated or verified for so high values.

Wet snow accretion depends on a critical combination of strong winds and large precipitation amounts in a narrow temperature interval, and small deviations in temperature can have a large effect on the overall accreted load. The simulated ice accretion based on the atmospheric RÁV data does not capture all events correctly. It does sometimes underestimate and in other cases overestimate the load. The deviation can often be explained by small errors in the temperature rather than due to errors in wind speed or precipitation amounts. Better atmospheric input data can be prepared, given adequate computational resources, based on a more recent version of the atmospheric model, higher horizontal resolution (1 km) as well as improved descriptions of necessary input and forcing data. Simulated icing based on improved atmospheric data for chosen events gave better and more realistic results and highlights the high sensitivity of ice accretion to small deviations in the atmospheric parameters.

A closer inspection of accretion events at sites with high loading, revealed that in some cases only one or two events gave extreme loading while other events were much smaller. This raises the question if the 21 years long data series is long enough and how to take model errors into account. Sensitivity analysis may be performed, e.g. based on shifting the temperature and the liquid water content of the snow in the icing model slightly compared to the dataset and evaluate icing assuming unchanged precipitation and wind speed.

Overall the performance of the wet snow icing model has been found to give relatively reliable results compared to observations, i.e. it correctly identifies main icing directions and locations of high observed loads as well as locations with no or little ice loading. If correctly used and interpreted then it can be of great use for identifying areas prone to wet snow accretion and assessing main icing directions in the areas.

References

[1] S. P. Ísaksson, Á. J. Elíasson and E. Thorsteins, "Icing Database—Acquisition and registration of data," in *Proc. Eighth Int. Workshop on Atmospheric Icing of Structures (IWAIS)*, Reykjavik, 1998.

[2] Ó. Rögnvaldsson, H. Ágústsson and H. Ólafsson, "Stöðuskýrsla vegna þriðja árs RÁVandar verkefnisins," 2009.

[3] W. C. K. J. Skamarock, J. Dudhia, G. D. O., D. M. Barker, M. G. Duda, X. Y. Huang, W. Wang and J. G. Powers, A description of the advanced research WRF version 3, NCAR: Boulder, 2008.

[4] G. Thompson, R. Rasmussen and K. Manning, "Explicit forecasts of winter precipitation using an improved bulk microphysics scheme. Part I: Description and sensitivity analysis," *Mon. Wea. Rev.*, vol. 132, pp. 519-542, 2004.

[5] Ó. Rögnvaldsson, J. W. Bao, H. Ágústsson and H. Ólafsson, "Downslope windstorm in Iceland – WRF/MM5 model comparison," *Atmos. Chem. Phys.*, no. 11, pp. 103-120, 2011.

[6] B. E. K. Nygaard, H. Ágústsson and K. Somfalvi-Tóth, "Modeling wet snow accretion on power lines: Improvements to previous methods using 50 years of observations," *Journal of Applied Meteorology and Climatology*, vol. 52, no. 10, pp. 2189-2203, 2013.

[7] ISO 12494, "Atmospheric icing of structures," Geneva, 2001.

[8] L. Makkonen, "Models for the growth of rime, glaze, icicles and wet snow on structures," *Phil. Trans. R. Soc. London*, vol. 358, pp. 2913-2939, 2000.

[9] Á. J. Elíasson and E. Thorsteins, "Field measurements of wet snow icing accumulation," in *IWAIS 2000*, Chester, UK, 2000.

[10] H. Ólafsson, Á. J. Elíasson and E. Thorsteins, "Orographic influence on wet snow icing - Part II: Downstream of mountains," in *IWAIS 2002*, 2002.

[11] H. Ágústsson, Á. J. Elíasson, G. M. Hannesson and E. Thorsteins, "Modeling wet-snow accretion -- Comparison of cylindrical model to field measurements," in *Proc. 15th International Workshop on*, Canada, 2013.

[12] Á. J. Elíasson, H. Ágústsson and G. M. Hannesson, "Wet snow accumulation - A study of two severe events in complex terrain in Iceland," in *IWAIS 2013*, St. John's, 2013.

[13] Á. J. Elíasson, E. Thorsteins and H. Ólafsson, "Study of wet snow events on the south coast of Iceland," in *IWAIS 2000*, Chester, UK, 2000.

[14] H. Ólafsson, Á. J. Elíasson and E. Thorsteins, "Orographic creation of wet snow icing conditions, Part I: Upstream of mountains.," in *IWAIS 2002*, 2002.

[15] G. Thompson, P. Field, R. Rasmussen and W. Hal, "Explicit forecasts of winter precipitation using an improved bulk microphysics scheme. Part II: Implementation of a new snow parameterization," *Mon. Wea. Rev.*, vol. 136, pp. 5095-5115, 2008.

[16] G. Thompson, N. B. E., L. Makkonen and S. Dierer, "Using the Weather Reserach and Forecasting (WRF) Model to Predict Ground/Structural Icing," in *13th IWAIS*, Andermatt, 2009.

Comparison of measured and simulated icing in 28 test spans during a severe icing episode

Árni Jón Elíasson [1], Hálfdán Ágústsson [2], Guðmundur Hannesson[3], Egill Thorsteins[3]
[1] Landsnet, [2] Belgingur, [3] EFLA Consulting Engineers
arnije@landsnet.is, halfdana@gmail.com, gudmundur.m.hannesson@efla.is, egill.thorsteins@efla.is

***Abstract*: This paper presents an analysis of simulated in-cloud icing and a comparison of the results with detailed field measurements from 28 test spans at 19 test sites in North- and East-Iceland for a period of 99 days during the winter of 2013-2014. Ice accretion was extensive with the maximum ice load measured equal to 47 kg/m, the greatest total accumulation in one test span was 177 kg/m/winter and the total accumulation at the 28 test spans was 1076 kg/m/winter. The icing simulations are based on cylindrical accretion model using atmospheric data from a high resolution atmospheric model as an input.**

Model results are presented as time-series of icing at locations of test spans, as well as summaries of total accretion loads and intensities at the spans. Results are highly sensitive to the performance of the atmospheric model, while the timing of individual icing periods is nevertheless on average correctly captured. Small and medium size accretion events are generally better captured than more extreme events which are often underestimated due to too weak accretion intensity. In an attempt to remove the complicating and random effect of ice-shedding, the icing model is forced to shed ice in unison with the observations, with total simulated accretion compiled for each span during periods when accretion is actually observed.

Keywords: ***In-cloud icing, measurements, modelling, test spans***

INTRODUCTION

Long time series of systematic observations of atmospheric icing events are invaluable for mapping the icing climate and developing methods to parameterize icing. Accurate observations of extreme events are particularly important, especially within the framework of overhead power lines where appropriate design loads are critically dependent upon an accurate estimate of the maximum expected ice load for a given return period. Although, the observational sites are typically too few and far apart to describe adequately the spatial structure of the icing climate in complex orography, their data can be corroborated with parameterized icing based on simulated atmospheric data and numerical accretion models, as done for in-cloud icing in the USA, Japan and Iceland [1], [2], [3], [4].

In this light, the extreme icing winter of 2013-2014 presents an invaluable opportunity to test the current methods for parameterizing ice accretion and explore their strength and weaknesses. Special attention is given to the accretion process and the complicating influence of ice-shedding on the analysis is eliminated by forcing the accretion model to shed ice simultaneously with observed icing.

I. ICING MEASUREMENTS

Iceland has an extensive network of nearly 60 operational test spans at more than 40 locations, measuring ice accretion in real-time. Locations of test spans used in this study are shown in Figure 1.

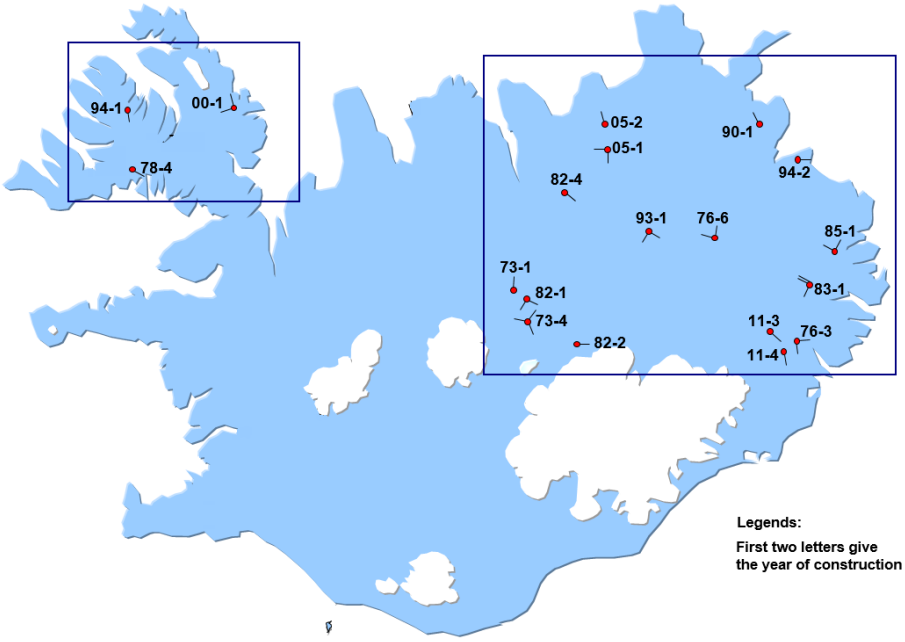

Figure 1: Locations of test span used in this paper, with black lines indicating the direction of each test span. Boundaries of the 1 km model domains are shown with black boxes.

In short, a test span consists of two poles with a conductor strung between them, in which the tension is measured in real-time with a load cell. A detailed description of the test setup is given in [5] and [6]. This setup may result in an overestimation of actual ice loading as the load cells measures the total load from both vertical (ice) and horizontal (wind) components. Other possible sources of uncertainty include calibration range of the load cells described in more detail in [7] or a change in base stringing during icing events.

Measurements from a sub-set of 28 test spans, in Northwest- and Northeast-Iceland (locations in Figure 1), are analyzed and compared with simulated icing. In short, the winter of 2013-2014 was characterized by extensive and more or less continuous ice accretion for 99 days from December to March in North- and East-Iceland, with two intense accretion periods from mid-December to mid-January, and again in February to early March. The maximum in-cloud ice load measured during the winter in a test span was 47 kg/m, the greatest total accumulation in a span during the period was 177 kg/m/winter and the total accumulation at the 28 test spans was 1076 kg/m/winter. The ice accretion was chiefly due to rime ice (in-cloud) and accreted wet-snow amounts were presumably minimal. The atmospheric and icing conditions are described in more detail in [7].

Four spans are located at an elevation of 500-600 m in the northwestern highlands. The orography is relatively simple with spans mostly located near the edges of a relatively flat plateau. Here the greatest ice accretion is expected at the northeastern margin of the plateau during northerly and northeasterly flow. Indeed, extreme icing was observed at test site 00-1 (Figure 2 and Figure 3) and caused a failure in early January, before the end of the accretion period. The remaining spans (23) are located in the northeastern part of Iceland. Those along the coast are generally located in complex orography while those in the highlands are in less complex orography. Here the main icing direction is from the northeast and east, with the highest loads expected at exposed mountain stations at the seaside. Three coastal sites; 90-1, 94-2 and 76-3, did indeed fail in early January due to the extreme ice loads.

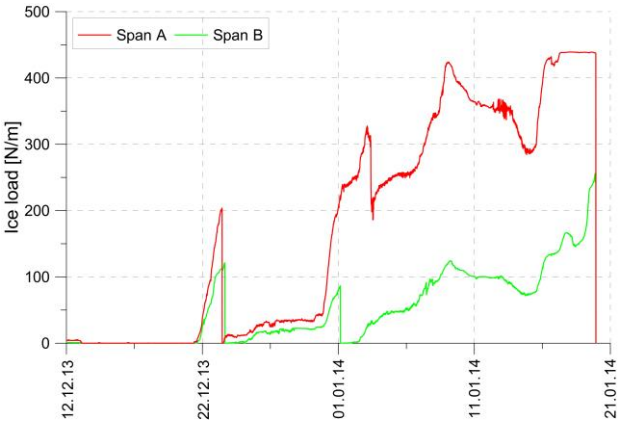

Figure 2: Ice load at test site 00-1. Both spans (00-1-A and 00-1-B) failed due to ice overload in January.

Figure 3: Ice on a guy wire in test span 00-1 after failure, the measured diameter was 47 cm.

II. PARAMETERIZATION OF ATMOSPHERIC ICING

Typically, in studies involving simulated icing, atmospheric models are used to simulate the state of the atmosphere at high resolution in complex terrain, making available all the necessary atmospheric parameters needed for estimating ice accumulation at any given location, based on numerical accretion models. For rime (in-cloud) icing these variables are the wind speed, air temperature as well as all the relevant atmospheric water species, namely cloud water and drizzle/rain.

A. Atmospheric data

Here, the atmospheric data is prepared with version 3.6.1 of the WRF model which is a state-of-the-art mesoscale atmospheric model [8] and has previously been used in a number of icing studies ([2], [5], [9]). The model was run with 55 layers in the vertical and a horizontal resolution of 9, 3 and 1 km, with the complex orography mostly resolved at a 1 km resolution. Results from the two 1~km model domains covering the two main regions of interest are used in the accretion modelling (cf. Figure 1 for domain locations).

The model was initialized and forced at its boundaries using the Interim atmospheric re-analysis data from the ECMWF ([10], resolution ~80 km). The most relevant parameterization schemes for studies of icing are the moisture physics scheme of Thompson ([11], [12]) which gives the necessary detail in the atmospheric water distribution needed to calculate both wet-snow and in-cloud accretion. The ETA planetary boundary layer scheme [13] is the second most relevant parameterization scheme employed and it should be noted that atmospheric stability and uplift, hence atmospheric water and precipitation distributions, are strongly linked to both the moisture physics scheme and the boundary layer scheme.

Since the actual orography is smoothed considerably at the resolution of the atmospheric model, the atmospheric data is interpolated linearly upwards at each grid point to the true elevation of the orography. As the aim is to seek an upper bound on maximum icing loads, no attempt is made to correct for overestimated terrain elevation.

The performance of the atmospheric model is analyzed based on a comparison with observations of weather from a dense network of automatic weather stations. Many of the stations are located in the lowlands and/or in coastal regions while some are located in the mountains with a few mountain top stations. As is frequently the case during icing episodes, observational data is lost, or it is unreliable, at many mountain stations. The model captures well the observations, with a mean temperature / wind speed bias of -0.1°C / 0.3 m/s and -0.6°C / 0.4 m/s in the northwestern and eastern domains, respectively. The mean bias is mostly well within ±1°C and ±1

m/s at individual stations but higher errors are generally found at stations where the orography is not well resolved by the model. There is significant temporal variability in the errors with the period after mid-February generally captured worse than earlier during the icing period. The overall accuracy of simulated data is considered adequate for input into the accretion model.

B. *The accretion model*

The simulated data described above is used as input to a time dependent numerical cylindrical ice accretion model, based on the model of Makkonen described in [14] and the methodology in [15]. The current study includes rime icing (in-cloud) as well as freezing drizzle and rain, but wet-snow is not considered. The icing rate is described by (1)

$$\frac{dM}{dt} = \alpha_1 \cdot \alpha_2 \cdot \alpha_3 \cdot w \cdot A \cdot V \qquad (1)$$

where M(t) is the accreted ice mass (kg), V is particle velocity (m/s), A is the cross-sectional area (m^2) of the cylinder as seen by an impinging particle, and w is the liquid water content (kg/m^3) of the particle and is chiefly due to cloud water but also due to drizzle and rain. V is here taken as the wind speed, with the size dependent fall speed of rain and drizzle particles taken into account. The three α-coefficients can generally take values between 0 and 1, and are given by: α_1 which is the collision efficiency and is calculated based on [16] and a median volume diameter (MVD) of the impinging water particles and a fixed droplet number N_d = 50 droplets/cm^3. α_2 is the sticking efficiency and is taken as 1 as it is generally assumed that all impinging particles will stick to a wet as well as a dry accretion surface. α_3 is the accretion efficiency and is calculated based on estimates of the heat balance at the accretion surface (see in [15] and references therein), and may deviate significantly from 1 during wet growth when the latent heat released at the accretion surface is not removed efficiently enough (generally occurs at high accretion intensity, during weak winds and when temperatures are only slightly negative). The density of the accreted cloud water (rime ice) is parameterized based on equation (4.1) in [15] while for freezing drizzle/rain the density is taken as 917 kg/m^3 (clear ice).

Icing calculations are done for a horizontal cylinder representing the conductor at 28 test spans and at 19 locations, taking into account individual span direction and conductor diameter. Furthermore, at each span an account is kept of simulated ice accretion concurrent with observed accretion (type A), as well as of accretion simulated when none is observed (type B).

C. *Ice shedding*

Ice shedding must be taken into account in modeling of in-cloud icing, especially in areas characterized by extreme and frequent icing conditions and where the temperature is on average near or below freezing. Main factors for ice shedding are: (i) melting, (ii) sublimation and (iii) mechanical ice break. Some attempts have been made to model ice shedding but no widely accepted model exists that has been validated with sufficient field data. Some models ignore (iii) but they can severely underestimate the intensity of ice loss processes.

Ice shedding is partly a stochastic process as can be seen in Figure 4, which shows measurements from three spans at the test site 83-1. Two spans (A and C) are parallel and have different conductor diameters while the third span (B) is oriented perpendicular to them and has the same conductor diameter as span A. A visual comparison shows that the ice shedding is occurring at different times in the spans.

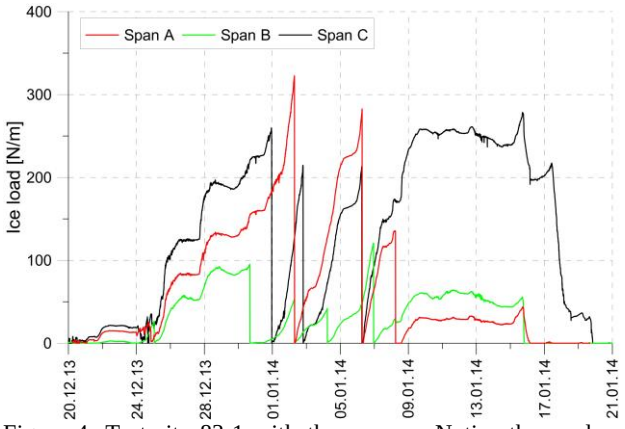

Figure 4: Test site 83-1 with three spans. Notice the random nature of ice-shedding.

The effect of ice-shedding is eliminated from the analysis of the simulated accretion process by forcing the accretion model to shed ice in unison with observed ice shedding at individual spans. During periods when there is no observed ice accretion, and hence no observed shedding, ice shedding within one hour (dm_{shed}) is simply parameterized as in (2), which has previously given reasonable results in studies of in-cloud icing.

$$dm_{shed} = max \begin{cases} k_{break} \cdot M_{ice} \\ k_{sublim} \cdot \pi \cdot D \end{cases} \qquad (2)$$

with the shedding factor associated with ice fall given by

$$k_{break} = \begin{cases} \frac{1}{3}(1 + 0.075 \cdot V) \;\; if \; T > 0°C \\ \frac{1}{3} \; if \; T + 0.05 \cdot V > 0 \; and \; T \leq 0 \\ 0 \; otherwise \end{cases} \qquad (3)$$

Here M_{ice} is the accreted mass of ice (kg), D_{ice} is the icing diameter (m), T is the air temperature (C) and k_{sublim} is an estimated shedding factor associated with sublimation (0.00125 gr/m^2/hour).

III. Results of Accretion Calculations

Ice accretion was simulated at 28 test spans, with 4 spans located in Northwest Iceland and 24 located in Northeast-Iceland. Figure 5 to 12 show examples of observations and ice modelling at eight of the test spans:

- The figures illustrate clearly how the model is forced to shed the accreted ice in unison with the observations.
- The timing of observed accretion is usually well captured.
- While some accretion periods are well captured there are cases where the observed accretion intensity and the ice load are either overestimated or underestimated.
- Large biases in overall accretion are found at some spans, including 83-1-A where smaller accretion events are very well predicted but the accretion intensity is too weak in the three largest events

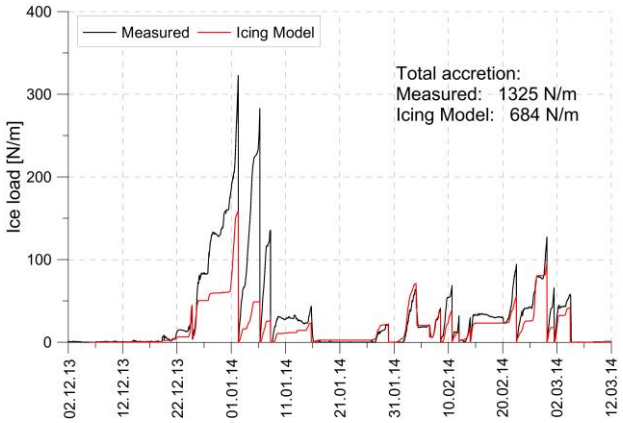

Figure 5: Measured and modelled icing in test span 83-1-A.

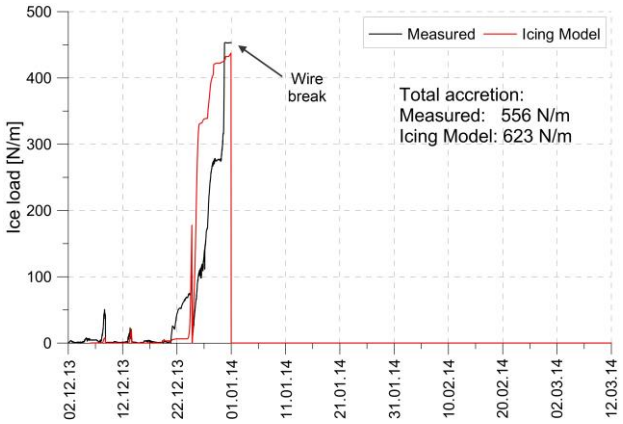

Figure 6: Measured and modelled icing in test span 94-2-A.

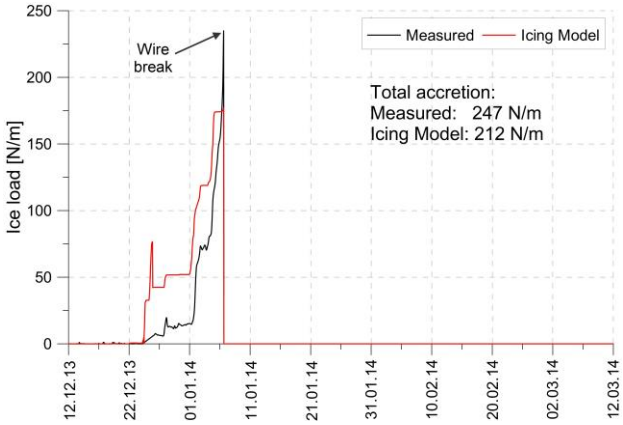

Figure 7: Measured and modelled icing in test span 76-3-B.

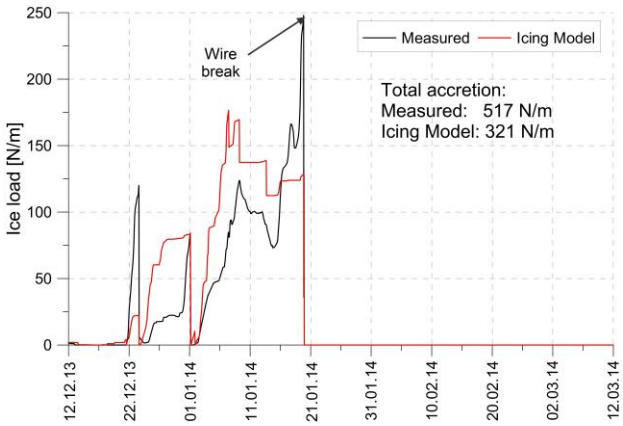

Figure 8: Measured and modelled icing in test span 00-1-B.

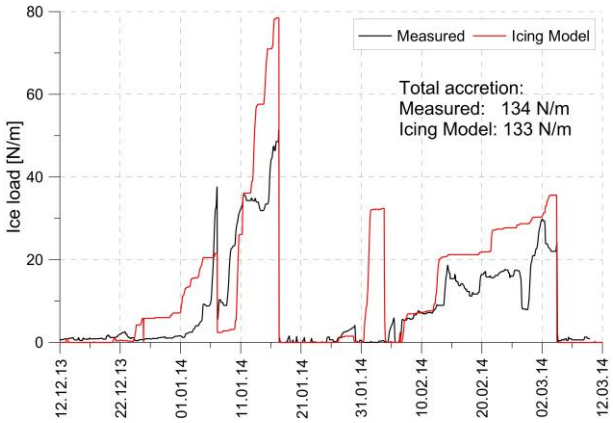

Figure 9: Measured and modelled icing in test span 11-4-A.

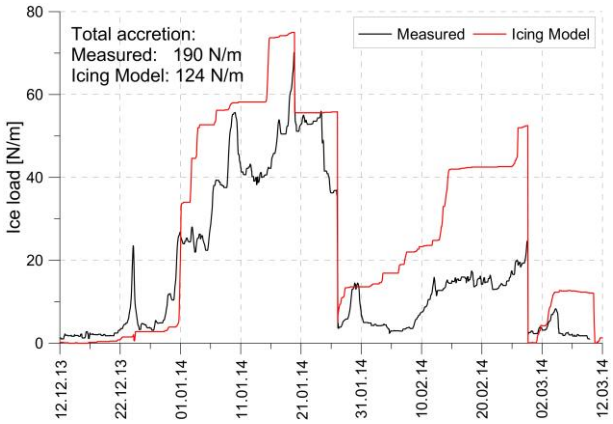

Figure 10: Measured and modelled icing in test span 73-4-A.

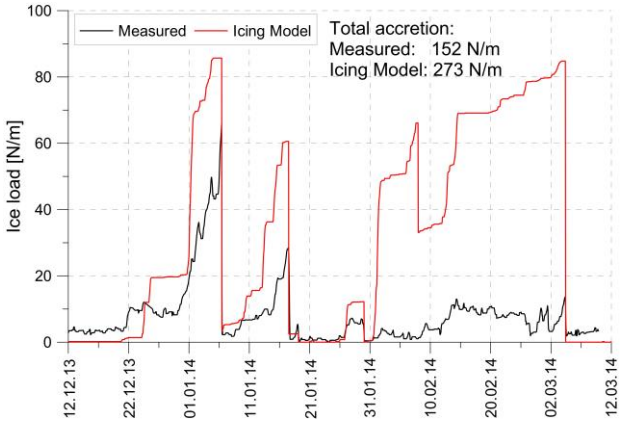

Figure 11: Measured and modelled icing in test span 11-3-A.

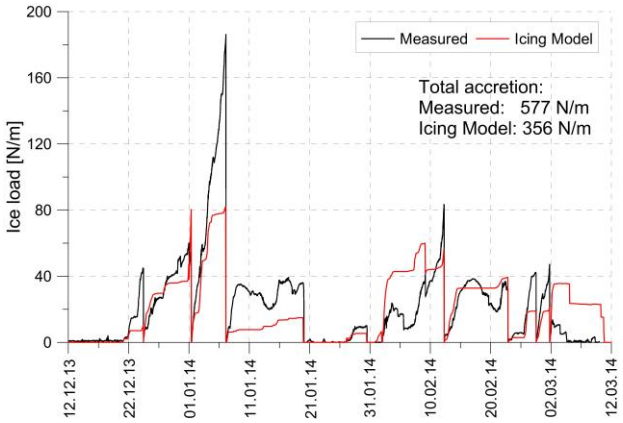

Figure 12: Measured and modelled icing in test span 82-4-A.

Figure 13 shows the overall observed icing and accretion simulated during periods when icing is observed (type A), i.e. ignoring accretion in the icing model when no ice is on the test span. The total accumulated observed and simulated loads at individual test spans generally compare favorably at locations where icing amounts are small or moderate. There is, however, a tendency towards underestimating the observed icing, especially at large icing amounts. The most significant outliers include test site 83-1 (3 spans) where only about half of the total accumulation is simulated and test site 85-1 where the accretion is significantly overestimated.

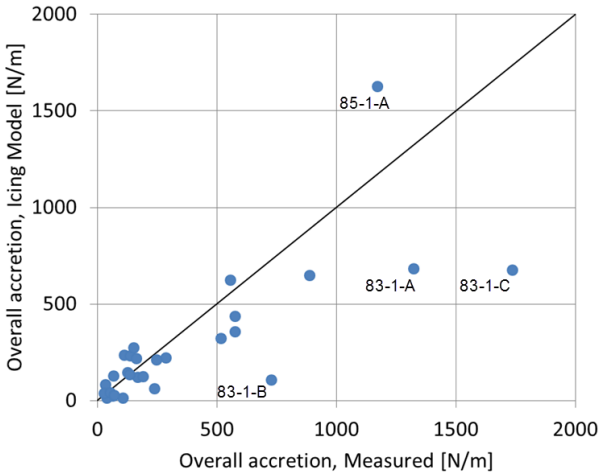

Figure 13: Observed and simulated total accumulation during the winter.

A comparison of the maximum icing observed and modelled in the period reveals that the maximum observed load is on average reasonably captured (Figure 14).

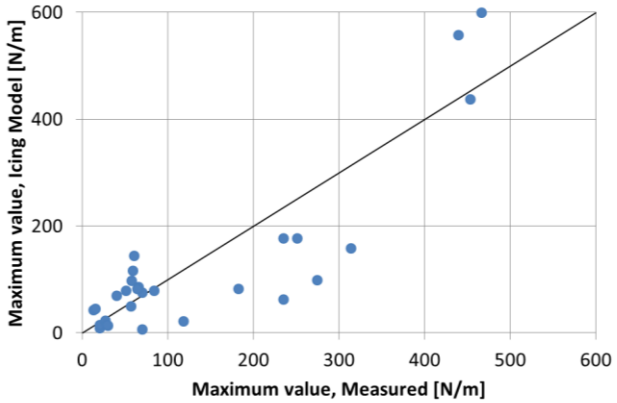

Figure 14: Comparison of calculated and measured maximum ice load over the winter 2013-2014.

Figure 15 presents a different method of assessing the overall performance than is presented in Figure 13. The time series of accumulated accretion are summarized over all the spans and simulated accretion is shown for periods when accretion is observed (type A) and also including periods when none is observed (type A+B), i.e. A is accretion at same time as ice is observed and B is when no ice is observed. Ice accretion starts in December and the first intense accretion period are in late December 2013. There is an apparent decrease in accretion intensity in early January 2015, after which the intensity is approximately half of what it was before. This decrease is associated with a mechanical failure of 5 spans and hence the subsequent analysis includes a reduced number of operational test spans. The greatest accretion intensities and largest ice loads were measured at some of the test spans that failed.

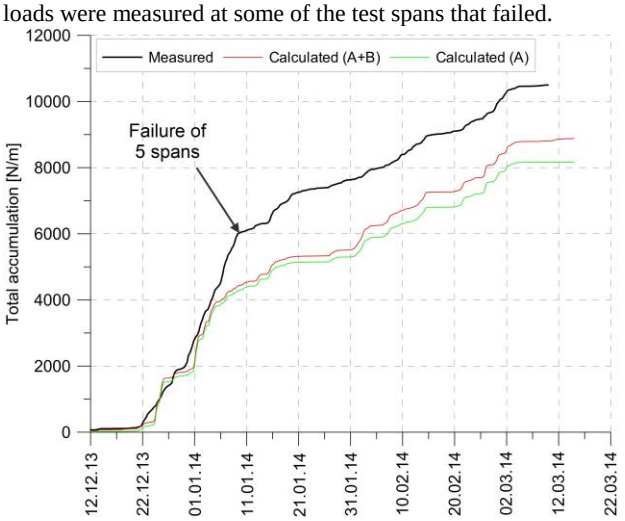

Figure 15: Total ice accretion in all spans, during the winter 2013-2014.

Figure 15 reveals that the total amount of modelled icing is following the measured icing reasonably well. The exception is the period 05-09 January 2014 when it is underestimating the accretion. The underestimation is largely related to the three test spans at test site 83-1, Figure 5 shows test span 83-1-A.

A sensitivity test was made, where icing conditions were modified to enhance the ice accretion. The atmospheric water content and wind speed were increased by 10% and the observed temperature was lowered by 1°C and used instead of simulated temperature. This analysis (not shown) reveals that the total amount of ice accretion increases and exceeds the observed accretion in Figure 15. Accretion has increased at test site 83-1 in the period 05-09 January 2014 although it is still lower than measured.

In the context of analyzing sensitivity to small variability in the atmospheric parameters then it should be noted that the icing model was analyzed assuming a fixed droplet number N_d = 50 droplets/cm^3. This implies rather large droplets sizes and consequently a relatively high accretion rate due to an enhanced collision efficiency factor (α_1), compared to larger values of Nd.

IV. Discussion and Concluding Remarks

Overall the results of the study are promising and show that coupled atmospheric and accretion models can be used to quantify and analyze atmospheric icing in complex terrain. The onset of ice accretion is generally correctly captured and the performance of the accretion model is on average good, both in a regional context as well as locally. The size of the observed ice load at individual spans varies greatly and includes eight test spans with loading in range of 20 to 46 kg/m. No systematic deviations were found at different magnitude of modelled accretion. Before discussing the most relevant deviations in more detail then it should be noted that there is, as previously mentioned, some uncertainty in the measured ice load which may partly explain the difference between measured and modelled ice load. It is however unlikely that the largest errors, e.g. at test site 83-1 (Figure 5) can be explained by complications in the measurement process.

The largest part of the negative bias seen in the accretion series presented in Figure 15 is obviously associated with the outliers in Figure 13, where the large observed accretion amounts are in some cases not as well captured. A large part of the bias is related to the three test spans at site 83-1 in the period 05-09 January 2014. Many of the smaller icing accretion

periods are well modelled in 83-1 (see Figure 5) but the most intense accretion is underestimated. The local topography at test site 83-1 is not too complex and the state of the atmosphere should therefore be reasonably well captured. Here, as well as at most other locations, the air temperature is on average reasonably captured and the icing model performance does not change significantly when observed temperatures are used instead of simulated temperatures. Comparison with lowland locations where instrumental icing is not a problem reveal that wind speeds are generally well reproduced but this is not necessarily true for nearby mountain stations. Significant and realistic quantities of atmospheric water are simulated at test site 83-1 but unfortunately no observational data is available for verification purposes. A sensitivity test, where icing conditions were made more favorable, reveals that realistic errors in the atmospheric conditions can explain a part of the poor performance in the period 05-09 January 2014. With respect to the accretion sensitivity it should be noted that the selected value of droplet size (N_d=50 droplets/cm^3) leads to a rather high accretion rate.

Test site 85-1 shows the largest overestimation of modelled ice accretion. It is located in very complex terrain which cannot be reproduced in the 1 km numerical domain. The temporal structure of the ice accretion at the site furthermore differs significantly from most of the other sites in the region. Thus it is not unexpected that test site 85-1 performs badly.

In general, errors in simulated atmospheric data can mainly be traced back to three factors:

- Inaccuracies in the input data from the courser model, i.e. in this case the boundary and initial data from the ECMWF. However, this does not seem to be of importance here, except possibly during the period 5-9 January 2015.
- Errors in the parameterizations of physical processes, e.g. boundary layer effects and precipitation processes. This may be relevant but is hard to verify due to the lack of observational data, e.g. of atmospheric water content.
- Local and small scale effects not resolved at the resolution of the atmospheric model. This is presumably the main source of error at many locations in complex terrain and may also be valid in simpler terrain if very small scale features disrupt the local flow.

Modelling of ice-shedding is an important factor when assessing extreme ice load in areas prone to frequent in-cloud icing. Here, the effect of the ice-shedding can be eliminated from the analysis by forcing the accretion model to shed ice in unison with observed ice shedding at individual spans. Example of the importance of the ice-shedding can been seen in Figure 5, where the largest ice load would be much higher, in early January, if there were not three cases of ice-shedding in the period.

The analysis presented in this study is made possible by the detailed observations available from a large number of test spans. The overall performance of icing model is good at the observational sites. This indicates that the accretion model is in general also reliable at other locations and its results can be used to assess ice loads in complex terrain where observational data is generally sparse or missing.

REFERENCES

[1] G. Thompson, Nygaardm B. E., L. Makkonen, and S. Dierer, "Using the Weather Reserach and Forecasting (WRF) Model to Predict Ground/Structural Icing," in *13th IWAIS*, Andermatt, 2009.

[2] Á. J. Elíasson, H. Ágústsson E. Þorsteins, and Ó. Rögnvaldsson, "Comparison between simulations and measurements of in-cloud icing in test spans," in *Proc. 14th Int. workshop on atmospheric Icing on structures*, China, 2011, p. 7.

[3] B. E. K. Nygaard, Kristjánsson. J. E., and L. Makkonen, "Prediction of In-Cloud Icing Conditions at Ground Level Using the WRF Model," *J. Appl. Meteor. Climatol.*, vol. 50, pp. 2445-2459, 2011.

[4] E. A. Podolskiy, B. E. K. Nygaard, K. Nishimura, L. Makkonen, and E. P. Lozowski, "Study of unusual atmospheric icing at Mount Zao, Japan, using the Weather Research and Forecasting model," *J. Geophys. Res.*, vol. 117, p. 12106, 2012.

[5] H. Ágústsson, Á. J. Elíasson, G. M. Hannesson, and E. Thorsteins, "Modeling wet-snow accretion -- Comparison of cylindrical models to field measurements," in *Proc. 15th International Workshop on*, Canada, 2013, p. 9.

[6] Á. J. Elíasson and E. Thorsteins, "Ice loadmeasurements in test spans for 30 years," in *Proc. 12th Int. Workshop on Atmospheric Icing of Structures (IWAIS)*, Yokohama, 2007, p. 6.

[7] Á. J. Elíasson and E. Sveinbjörnsson, "A severe In-cloud Icing Episode Mid-winter 2013-2014 in Northern and Northeastern Iceland ," in *Proc. 16th International Workshop on Atmospheric Icing of Structures*, Uppsala, 2015.

[8] W. C.: Klemp, J.B. Skamarock et al., *A description of the advanced research WRF version 3*.: NCAR: Boulder, 2008.

[9] B. E. K. Nygaard, H. Ágústsson, and K, Somfalvi-Tóth, "Modeling wet snow accretion on power lines: Improvements to previous methods using 50 years of observations," *Journal of Applied Meteorology and Climatology*, vol. 52, no. 10, pp. 2189-2203, 2013.

[10] D. P. Dee, S. M. Simmons, A. J. Berrisford, P. Poli, and co-authors, "The ERA-Interim reanalysis: configuration and performance of the data assimilation system," *Q. J. Roy. Meteorol. Soc.*, vol. 137, no. 656, pp. 553-597, 2011.

[11] G. Thompson, R. Rasmussen, and K. Manning, "Explicit forecasts of winter precipitation using an improved bulk microphysics scheme. Part I: Description and sensitivity analysis," *Mon. Wea. Rev.*, vol. 132, pp. 519-542, 2004.

[12] G. Thompson, P Field, R. Rasmussen, and W.l Hal, "Explicit forecasts of winter precipitation using an improved bulk microphysics scheme. Part II: Implementation of a new snow parameterization," *Mon. Wea. Rev.*, vol. 136, pp. 5095-5115, 2008.

[13] Z. I. Janjic, "Nonsingular implementation of the Mellor–Yamada level 2.5 scheme in the NCEP Meso model," in *NCEP Office Note 437*, 2002, p. 61.

[14] ISO 12494, "Atmospheric icing of structures," Geneva, Switzerland, ISO 12494, 2001.

[15] L. Makkonen, "Models for the growth of rime, glaze, icicles and wet snow on structures," *Phil. Trans. R. Soc. London*, vol. 358, pp. 2913-2939, 2000.

[16] K. J. Finstad, E. P. Lozowski, and E. M. Gates, "A computational investigation of water droplet trajectories," *J. Atmos. Oceanic Technol.*, vol. 5, no. 1, pp. 160-170, 1988.

[17] S. P. Ísaksson, Á. J. Elíasson, and E. Thorsteins, "Icing Database—Acquisition and registration of data," in *Proc. Eighth Int. Workshop on Atmospheric Icing of Structures (IWAIS)*, Reykjavik, 1998, pp. 235-240.

[18] Ó. Rögnvaldsson, H. Ágústsson, and H. Ólafsson. (2009) Stöðuskýrsla vegna þriðja árs RÁVandar verkefnisins. [Online]. ftp://ftp.betravedur.is/pub/publications/RAV-stoduskyrsla2009.pdf

[19] F. H. Sigurðsson, "Ísingarhætta og háspennulína yfir hálendið," *Veðrið*, vol. 16, no. 2, pp. 53-58, 1971.

[20] Á. J. Eliasson and E. Thorsteins, "Ice load measurements in test spans for 30 years," in *12th IWAIS*, Yokohama, Japan, October 2007.

Development of operational forecasting for icing and wind power at cold climate sites

Øyvind Byrkjedal, Johan Hansson and Henrik van der Velde
Kjeller Vindteknikk AS, Postboks 122, 2027 Kjeller, Norway
oyvind.byrkjedal@vindteknikk.no

***Abstract*: Based on icing measurements from 12 meteorological stations in Sweden a methodology for calculating icing from meso scale model data has been developed over the past 5 years. Operational data from seven wind farms in cold climate regions in Sweden (total of 272 MW and 111 individual turbines) have in addition been utilized to develop a state-of-the-art model for estimating production losses due to icing (IceLoss).**

Operational forecasting of energy production, icing and production losses due to icing has been carried out for the four wind farms which all experiences losses due to icing. The forecast simulations are run 4 times daily, each with a lead time of 48 hours. It is shown that the method is able to realistically describe the periods when ice is influencing the energy production for the wind farms. 63-82% of the time periods when icing is influencing the energy production are captured by the forecasts.

Essential to forecast icing events is the ability to forecast the events at the correct time. For 67-71 % of the strongest icing events the timing was correctly forecasted. These icing events accounted for approximately 90 % of the production losses from the wind farms.

The power forecasts with and without losses due to icing are compared to the hourly production data from the wind farm. It is evident that the accuracy of the forecasts is improved when the power losses caused by icing are taken into account, resulting in a reduction of the mean absolute error (MAE), reduction of the average bias and increase of hourly correlation coefficients. The results show that the number of cases when the produced energy is over-predicted is reduced when including power losses due to icing, while the cases of under-prediction the produced energy is somewhat increased.

Keywords: icing, wind power, forecast, production losses, validation

INTRODUCTION

As the number of wind farms installed in Sweden has increased over the recent years wind farms has also been developed in cold climate regions on exposed hills. At these hills the wind conditions are often quite favourable for wind energy generation, but also quite exposed to in-cloud icing which can disrupt the energy generation during the winter months.

The typical wind energy forecasts are dependent on the wind conditions only. If the icing is not considered these forecasts will be biased during the winter time. A high accuracy forecast can also be valuable information to be used for the control of wind turbine blade heating systems.

In this paper we present the validation of icing forecasts for four wind farms in Sweden. The validation considers the instrumental icing periods, timing of icing events and wind energy forecasts.

I. METHODOLOGY

This chapter describes the model setup of the forecasts, the calculation of the ice load, the IceLoss methodology and identification of icing periods from SCADA data.

A. Meso-scale model data

In this work we have used the Weather Research and Forecasting (WRF) model (version 3.2.1) run both with a hindcast setup, with input data from Final Global Data Assimilation System (FNL), and for forecasting using GFS (Global Forecast System) data as input.

The area covered by a 4 km x 4 km resolution grid is given as the inner domain showed in Figure 1. The simulations are setup with 32 layers in the vertical with four layers in the lower 200 m. We have used the Thompson microphysics scheme [1] and the Yonsei University Scheme [2] for boundary layer mixing.

In forecast mode the model is initiated 4 times daily and run for a period of 48 hours. Hourly data is stored for the simulation periods.

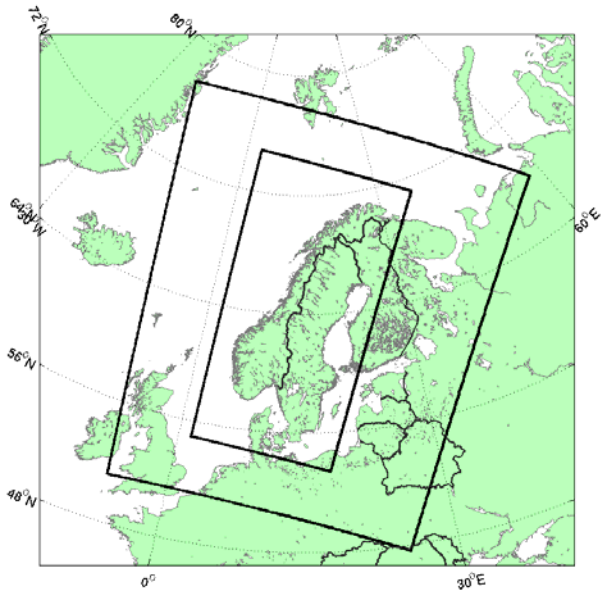

Figure 1 The model setup used. The inner rectangle shows the area covered by 4 km x 4 km simulations.

B. *Ice load calculations*

According to the standard ISO 12494 [3] icing has been calculated from:

$$\frac{dM}{dt} = \alpha_1 \alpha_2 \alpha_3 \cdot w \cdot A \cdot V$$

Here *dM/dt* is the icing rate on a standard cylindrical icing collector (defined by ISO 12494 as a cylinder of 1 m length and 30 mm diameter), w is the liquid water content (LWC), and A is the collision area of the exposed object. V is the wind speed and α_1, α_2 and α_3 are the collision efficiency, sticking efficiency and accretion efficiency, respectively.

The topography in the simulations is represented by a computational grid that is too coarse to represent the real height of the mountain peaks. This means that the mountain tops in the model often are lower than in the real world. This discrepancy can lead to an underestimation of the icing amounts particularly for coarse model grids. The discrepancy in height is corrected for by lifting the air in the model to the correct terrain height. This lifting will contribute to lower the pressure and temperature in the air, and will lead to condensation in the cases when the air when reaching the saturation water vapor pressure. The lifting is performed according to the vertical profile of temperature and moisture locally in the model.

The modelled ice load at a given time, t, is defined as a function of the icing rate, melting rate (dM_{melt}/dt) and sublimation rate ($dM_{sublimation}/dt$) according to:

$$M(t) = \sum_{t=t_0}^{t} \left(\frac{dM}{dt}(t) + \frac{dM_{melt}}{dt}(t) + \frac{dM_{sublimation}}{dt}(t) \right) \Delta t$$

The time step, Δt, used in the calculations of icing are 3600 s. A detailed description of the terms for the melting rate is given in [4]. Sublimation is defined as the transfer of ice from solid state directly to water vapour, which occurs in situations with dry and cold air. The sublimation rate increases with wind speed as the ventilation of the iced object is high. This can allow for a faster ice removal from a rotating turbine blade compared to other fixed objects. The sublimation rate is calculated by evaluating the energy balance between outgoing long wave radiation and latent heat release from the sublimation process. Sublimation has been included in the icing calculations. During the process of sublimation we have observed that the accreted ice becomes brittle and that small ice-pieces are continuously shed from the cylinder. The shedding is included by multiplying the sublimation rate with a factor of 2.5.

C. *Production losses caused by icing*

To estimate the production loss we assume that energy production will continue with ice on the rotor blades, and that there is a direct relation between the ice load on the standard ISO cylinder and the production loss experienced by the turbines. Ice on the blades will disrupt the aerodynamic structure of the blades which leads to a lower energy yield at any wind speed. The energy production follows the principle of a two-dimensional power curve as shown in Figure 2 The methodology is denoted IceLoss.

The curve is adjusted based on the operational data gathered for 3 wind farms in Sweden during 2009-2011. The power curve is adjusted using the ice load data calculated from WRF (and not the observed ice load data) to adapt the power loss calculation to WRF data.

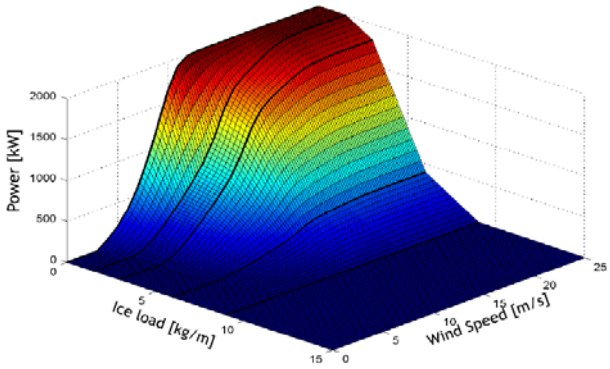

Figure 2 Two-parameter power curve P(V,M), function of ice load and wind speed.

Observed weekly production losses from one of the wind farms are shown together with the modelled production losses using the IceLoss methodology in Figure 3. We note a high correlation between the observed and modelled production losses, but also a small underestimation of the losses for some winters.

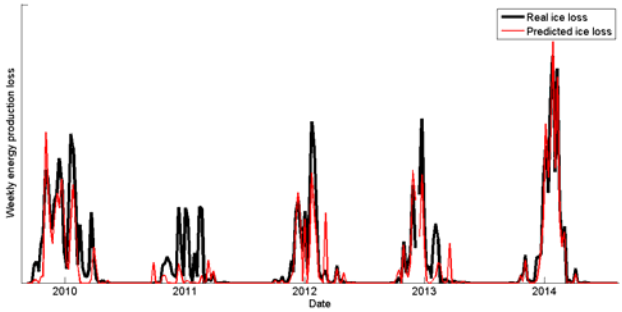

Figure 3 Observed (black curve) and modelled (red curve) weekly production loss values for one wind farm.

D. *Identification of icing from wind turbine SCADA data*

For each of the turbines in the available wind farms a power curve representative for the winter season has been calculated from the nacelle anemometer and power data. The power curve has been calculated using the median power values for wind speeds binned with 0.5 m/s intervals. When an alarm code is given the data is removed along with the pro- and preceding 10 minute time steps. Data for periods with curtailed power output is also removed in the analyses.

A threshold power curve has also been defined based on the associated 10-percentile value in each wind speed bin. When the power output from the turbine is below the threshold power curve, then the period is flagged as icing given that the operational codes also indicates normal operation and that the temperature measured at the nacelle is below 3 ºC. Only indications that are lasting more than 3 consecutive time steps (30 minutes) are used.

According to [5] this is the preferred method for defining periods of icing based on power data from the wind farm SCADA system.

II. WIND FARM DATA

In this work data from four wind farms in Sweden have been used. All four wind farms experiences considerable amounts of icing and icing losses during the winter. For all wind farms more than 2 years of data has been available for the analyses. The four wind farms are denoted A, B, C and D.

III. RESULTS

E. *Validation of icing periods*

According to [6] the periods of meteorological icing is defined as the periods when the meteorological conditions result in buildup of ice on structures, instruments, turbine blades etc. In the model these periods are defined by dM/dt > 0 g/hr. Instrumental icing is defined as the period when icing is influencing the wind measurements or the wind turbine production. Typically for modelled ice loads, M, larger than 100 g/m on the standard ISO cylinder we often observe that ice is influencing the energy production. In these analyses we compare the periods with ice loads larger than 100 g/m from the model with icing identified from the wind turbine SCADA data.

In Table 1 the percentages of time when ice was detected from the SCADA data for the four wind farms are displayed in the first line. We note that wind farm A has clearly a higher percentage of icing compared to the other 3. For wind farm A icing is found to influence energy production 22 % of the time. The probability of the model to also detect the periods when ice was found to influence wind power production was found to be 63-82% of the time for the four wind farms. The cases when the model falsely detected icing although no icing was detected from the SCADA data were 5-7 % of the time.

Note also that there are considerable uncertainties in the method for detecting icing from the SCADA data. During periods with low wind speeds it can be difficult to identify icing from the method described above. By reducing the threshold value of 100 g/m used for the modelled icing we were able to detect a higher number of the icing periods, but resulting also in a larger number of false alarms. An increase of the icing threshold had the opposite effect. The duration of the instrumental icing periods is also influenced by ice shedding that is difficult to model due to its stochastic behaviour. This also influences the probability of detection and false alarm percentages given.

Table 1 Percentage of time when instrumental icing is detected from SCADA data, the probability of detection of instrumental icing from the forecasts, and percentage of false alarm cases from the forecasts

	A	B	C	D
Ice detected from SCADA	22 %	9%	10 %	13 %
Probability of detection	74 %	82 %	79 %	63 %
False alarm percentage	6 %	7 %	6 %	5 %

F. *Timing of icing events*

Timing is essential in order to forecast icing and when the influence wind energy production is expected to start. If icing is successfully forecasted this can be valuable information to be used for the control of blade heating systems to be able to heat up the blade before the meteorological icing occurs.

For each icing event identified from the wind farms we perform a check to see if the event starts within a period when meteorological icing is forecasted. The meteorological icing events can last from 1hr events to events lasting for 3 days or more. The average durability for the forecasted icing events are 12 hours. The forecast is shifted 6 hours as the observed icing event is more likely to start in the middle of the modelled icing period. If the observed icing event starts within the time period of the forecasted event we denote it as successful at forecasting the particular event. Otherwise we report the time lag between the forecasted icing period and the onset of the observed icing period.

In Table 2 the number of individual icing episodes for each of the wind farms is reported. We see that for wind farm A and C a higher number of icing episodes were identified. These are also the wind farms where the longest time series are available. The table also shows how many of these icing episodes the model was able to correctly forecast the timing of when the icing started to influence the energy production

Table 2 The number of individual icing episodes identified for each of the four wind farms. The probability of the forecast model to correctly detect when the icing episode starts is also given. The number of severe episodes is also given along with the probability of the forecast model to detect when the severe icing episodes starts.

	A	B	C	D
Total number of icing episodes	273	161	254	122
Probability of detection	52 %	63 %	63 %	42 %
Number of severe episodes	109	57	115	27
Probability of detection	67 %	70 %	71 %	70 %

For wind farm B and C the forecast model was able to correctly describe the timing for 63 % of all icing episodes. For wind farm A and D a lower number is found. A large number of the identified icing episodes results only in minor losses, influences only a few turbines in the wind farm or only last for a short time period. For the four wind farms studied the 55-80 % of the icing episodes are related to such minor episodes. The total losses during these minor icing episodes equals to only around 10 % of the total production losses observed in these wind farms.

The individual cases when icing causes the aggregated production losses in the wind farm to be higher than 20% as an average over a period of 12 hours is then identified and defined as “severe” icing episodes. The remaining events includes only around 20-45 % of the total individual cases, but equals a total of 90 % of the total production losses in the wind farms and are therefore the events that are most important to capture with the icing forecasts. From Table 2 the number of severe events and the probability of detection are given as the third and fourth row. We note that the probabilities for the model to forecast the timing of these events are starting are 67-71 % for the four wind farms.

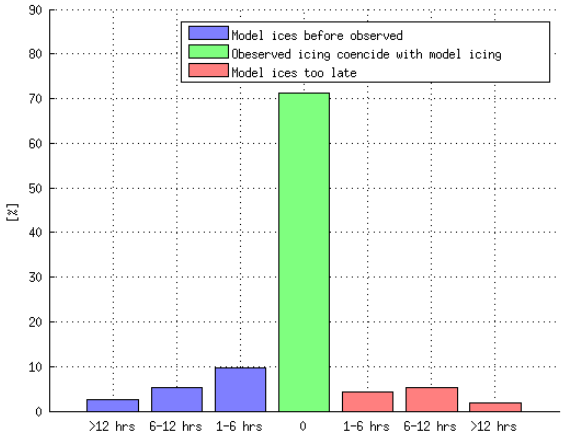

Figure 4 Percentage of observed severe icing episodes forecasted with corrects timing (green bar), percentage of observed icing episodes when the model forecast icing too early (blue bars) and percentage of observed icing episodes when the model forecast icing too late (red bars). The figure displays the results for site C.

For the cases when the model is unable to correctly forecast the timing the icing event will either be forecasted too late, too soon or not at all. For wind farm C a histogram showing the percentage of timing biases in the forecast is shown in Figure 4. The blue bars denote the cases when the icing event is

forecasted too soon, while the red bars denote the number of cases when the icing event is forecasted too late.

G. *Forecasting of wind energy production*

The wind energy production for each of the four wind farms have been forecasted on a daily basis during the last two winter seasons. The forecast have been delivered at 10:00 every day in time to make use of the forecasts for bids at the NordPool spot market for the next day. The forecasts are made both for energy production assuming clean blades, depending only on the forecasted wind conditions, and for ice reduced forecast where we assume the icing influences the energy production according to the IceLoss model described in Section C.

The change in mean absolute error (MAE), bias and correlation coefficient in the forecasts when we include the IceLoss model is shown for one of the four sites in Figure 5. The MAE for this site is reduced by from an average of 22.5 % to 15 %. The negative bias is also clearly reduced, while the correlation coefficient between the forecasted energy production and the actual production is increased. Similar statistics for all the sites (as an average of the two winters 2013/2014 and 2014/2015) is given in Table 3. The values given are the average errors for +6 h to +48 h lead time. It is clear that the forecasts using the IceLoss model reduces the errors for all wind farms and increases the correlation coefficient. The largest improvement is found for wind farm A.

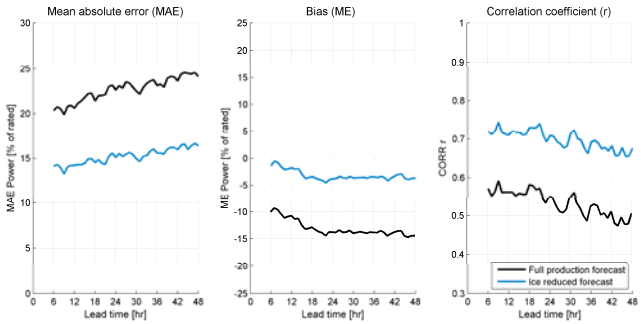

Figure 5 Mean absolute error, bias and correlation coefficient for the forecasts. The forecasts assuming clean blades are shown in black curves, while forecasts using the IceLoss model are shown as blue curves. The forecast lead time is displayed on the horizontal axis. The results shown are for site A during the winter 2013-2014.

Table 3 Mean absolute error, bias, and correlation coefficient, r, in the forecast of energy production for 4 wind farms as an average over the two winters 2013/2014 and 2014/2015.

	A	B	C	D
MAE clean blades	23 %	17 %	21 %	16 %
MAE IceLoss	16 %	15 %	17 %	15 %
BIAS clean blades	- 14 %	-5 %	-5 %	-8 %
BIAS IceLoss	-5 %	-2 %	-1 %	-5 %
r clean blades	0.60	0.78	0.72	0.80
r IceLoss	0.70	0.79	0.78	0.80

The distribution of forecast errors for site A is shown in Figure 6. The number of cases when the produced energy is forecasted within +/- 12.5 % is clearly higher when the IceLoss model is applied (ice reduced forecast) compared to the full production forecast derived using information about the wind conditions only. The number of cases when the forecast over-predicts the energy produced is also clearly reduced for the ice reduced forecast. On the other hand we see a somewhat larger number of cases when the forecast under-predicts the produced energy in the wind farm.

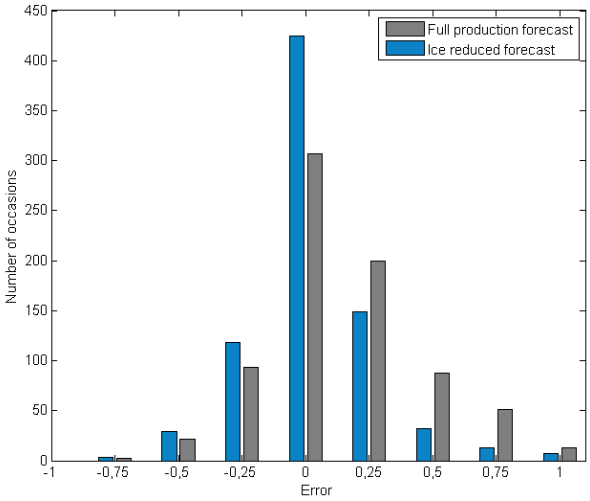

Figure 6 Distribution of forecast errors. The results shown are for site A during the winter 2013-2014.

IV. Conclusions

The WRF model has been configured to run operational 48 hour forecasts, initiated four times per day, in order to predict icing and wind farm energy production for wind farms located at exposed locations for icing in Sweden. The results of the analysis described show that the modelling system is able to correctly predict the periods when ice influences wind energy production in 63-82 % of the time of observed production losses in the considered wind farms. In 68-71 % of the severe icing events, which accounts for approximately 90 % of the observed production losses, the forecasted onset of the icing episodes were correct.

For all four wind farms the IceLoss model improved the energy forecasts and the associated icing losses.

Acknowledgment

The work has been supported by the project “Large scale, cost effective wind energy development in icing environments” which is financed through the Swedish Energy Agency and by the Top-Level Research Initiative (TFI) project, Improved Forecast of Wind, Waves and Icing (IceWind). The simulations were performed on the Abel Cluster, operated by the Department for Research Computing at USIT, University of Oslo.

References

[1] Thompson, G. R. M. Rasmussen and K. Manning (2004). “Explicit forecasts of winter precipitation using an improved bulk microphysics scheme. Part 1: Description and sensitivity analysis.” Monthly Weather Review, 117, 231-235

[2] Hong S-Y, Noh Y and J. Dudhia 2006: A new vertical diffusion package with an explicit treatment of entrainment processes. Monthly Weather Review 134: 2318-2341

[3] ISO 12494 2000: Atmospheric Icing of structures, International Standard, ISO/TC98/SC3/WG6

[4] Harstveit K. (2009) “Using Metar - Data to Calculate In-Cloud Icing Mountain Site near by the Airport” in proceedings of IWAIS XIII, Andermatt, Switzerland, September 8 to 11, 2009.

[5] Neil N. Davis, Øyvind Byrkjedal, Andrea N. Hahmann, Niels-Erik Clausen, Mark Zagar (2015): *Ice detection on wind turbines using the observed power curve*, accepted for publication in Wind Energy

[6] Expert Group Study on Recommended Practices for Wind Energy Projects in Cold Climates. IEA Wind Recommended practices no. 13. 201

Comparison of ice accumulation on simplex and duplex conductors in parallel overhead transmission lines in Iceland.

Árni Jón Elíasson[1], Árni Björn Jónasson[2] and Pétur Thor Gunnlaugsson[3]
[1] Landsnet, [2] ARA Engineering, [3] ARA Engineering,
arnije@landsnet.is, arni@araengineering.is, petur@araengineering.is

Abstract: **This paper presents results from icing measurements which have been operated for more than 8 years in two parallel OHTLs. The two OHTLs are built for 400 kV but are currently operated on 220 kV. The measurements are made in suspension towers with load cells in one phase conductor attachment points.**

The ice accumulation at the measuring site from November 2006 to May 2015 is analysed. The lines were energised January 2007. A diagram of icing on simplex and duplex conductors is published. Icing periods are recorded and the icing accumulation calculated for each period. Timing of the beginning of ice shedding is evaluated. Icing accumulation on simplex and duplex conductors is investigated with regards to estimated torsional stiffness of the conductors.

Keywords: **Icing measurements, icing on duplex conductor, icing on simplex conductor, torsional stiffness, ice shedding, energised OHTL.**

I. Introduction

Since autumn 2006 load measuring cells have been in operation in side-by-side towers in two parallel transmission lines at Hallormsstaðaháls in the eastern part of Iceland (Fig. 1, Fig. 2 and Fig. 6). Test measuring spans have been operated at the same site since 1983 [1].

The measuring site Hallormsstaðaháls is a mountain ridge, located 575 m a. s. l. between two narrow valleys. Most icing events at the site occur when wind is blowing from north to northeast. The distance from the site to the east coast of Iceland is approximately 65 km in this direction. One of the OHTLs has simplex conductors (49.9 mm in diameter). The other OHTL has duplex conductors (2x39.2 mm in diameter).

Icing is frequent every year at the site which in most cases is due to in-cloud icing events, although wet snow icing events also occur. 300 m away from the location of the measuring towers there is a test span where icing has been measured continuously for more than 30 years. Also there is a long experience of

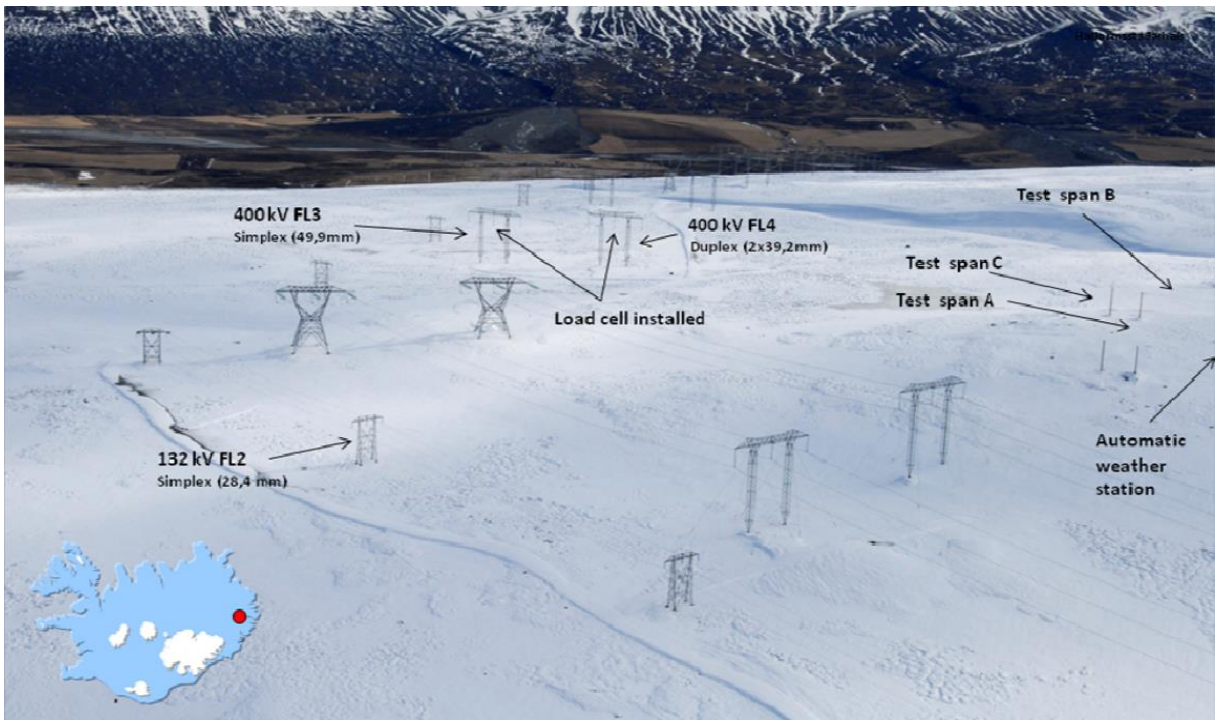

Fig. 1. Hallormsstaðaháls measuring site.

Fig. 2 The towers with measuring cells. The test spans and the automatic weather station can be seen in the background.

operating a 132 kV transmission line parallel to the two 400/220 kV lines. An automatic weather station has been in operation close to the test span for 19 years.

II. Setup and measurements

Detailed information on the measurement site is given in [1].

The parallel OHTLs Fljótsdalslína 3 and Fljótsdalslína 4 have centre spacing of 60 m and direction of the lines at the measuring site is 117° (True).

Fljótsdalslína 3 is fitted with a simplex conductor, Austria, d=49.9 mm (Table 1). Height is 540 m a. s. l. with conductor attachment 19 m above ground. Adjacent spans are 205 m and 192 m and weight of the suspension chain is 435 kg. The OHTL was energized in January 2007.

Fljótsdalslína 4 is fitted with a duplex conductor, AACSR, d=39.16 mm (Table 1) with 0.45 m conductor spacing. Height is 545 m a. s. l. with conductor attachment 19 m above ground. Adjacent spans are 175 m and 192 m and weight of the suspension chain is 525 kg. The 175 m span has the following sub spans between spacers: 30, 36, 42, 37 and 30 m. The 192 m span has the following sub spans between spacers: 33, 40, 46, 40 and 33 m.

Table 1

Parameter	*Unit*	*Austria 49.9 mm*	*AACSR 39.16 mm*
Diameter, d	[mm]	49.9	39.16
Cross section area, A	[mm^2]	1470.9	905.8
Modulus of elasticity, E	[N/mm^2]	70533	81099
Weight, g	[kg/m]	5.24	3.7
Tensile strength, Pu	[kN]	613	453
Temperature expansion coefficient, α_T	[$°C^{-1}$]	1.9 E-5	1.8 E-5
No wind and ice reading, $P_{LOAD\ CELL,0}$	[kg]	1452	1768

An on-line monitoring system was installed in one suspension tower in each line. It consists of load cells with data loggers and video cameras (Fig. 3). The load cells are fitted between the tower bridge and the insulator string in the middle phases. A reading is taken and recorded every 5 minutes.

Fig 3. Measurement equipment in one of the OTHLs.

The ice accumulation at Hallormsstaðaháls measuring site on simplex and duplex conductors from November 2006 to May 2015 is analysed. Due to some instrumental or communication failures during this period some of the data acquired could not be used. Thus, data from mid-January 2007 to spring 2008 and from March 2012 to spring 2013 could not be included in the analysis.

III. Observed icing events

During the recording periods 61 icing events were observed. Fig. 4 shows the plot of the maximum ice load in the events. The figure shows the general tendency of the duplex line to have lower maximum unit ice load on each sub conductor than the simplex line. However the larger load cases have a greater scattering.

Considering two extreme points, marked with 1 and 2 respectively (Fig. 4), the first was observed during an icing event from 13-28 November 2006 (Fig. 5), before the OHPL's were energized. The temperature at the beginning of this event was just

below 0°C and became gradually lower during the first three days to a minimum of –14 °C. It then raised a little and then remained low, mostly between –4 °C and –9 °C, during the remainder of the event. Ice shedding occurred first after about one day on the duplex and occurred again a few times during the period. Ice shedding did not occur on the simplex until the end of the event.

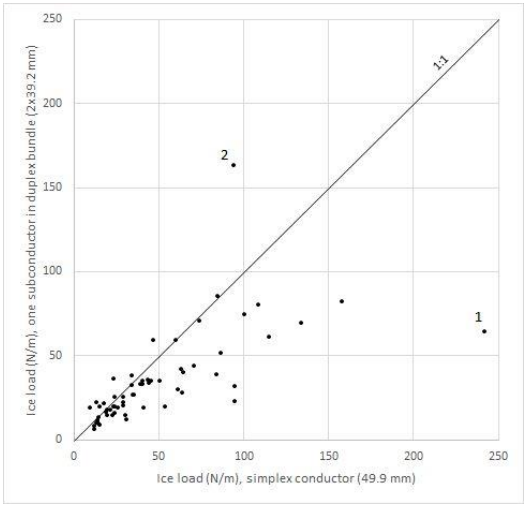

Fig. 4. Comparison of maximum ice load during each icing event on simplex conductor (49.9 mm) and one sub-conductor in duplex conductor (2x39.2 mm).

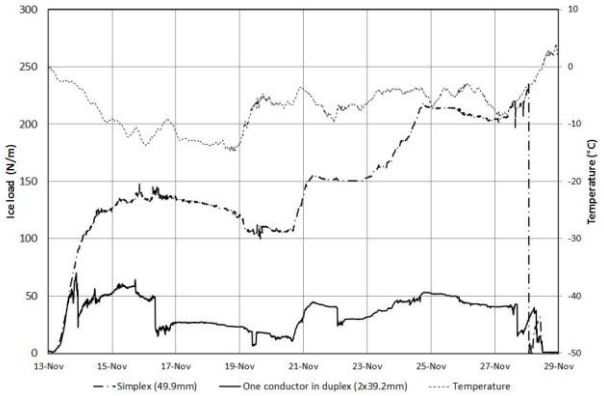

Fig. 5. Ice load on simplex conductor (49.9 mm) and one sub-conductor in a duplex conductor (2x39.2 mm) during the period 13-28 Nov.2006.

Point 2 (Fig. 4) was observed during an icing event from 18-21 March 2010 (Fig. 7). The temperature at the beginning is just below 0°C becoming gradually lower and remains at -2 °C for a day, then lowering down to -6 °C during the day after. Ice shedding starts on the simplex after approximately half a day. The icing falls off the duplex after a little less than two days, but no shedding until that time.

Fig. 6. Fljótsdalslína 3 and Fljótsdalslína 4 parallel at Hallormsstaðaháls, view to the east.

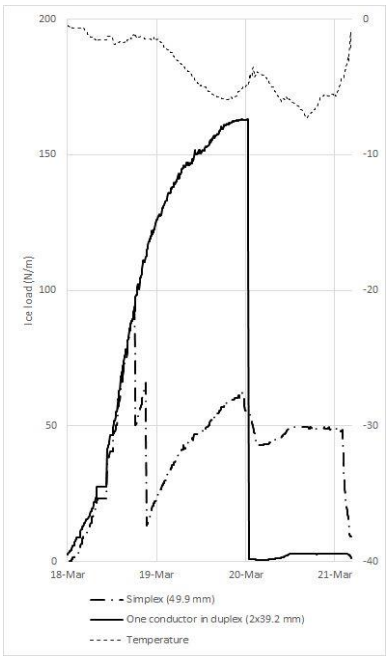

Fig. 7. Ice load on simplex conductor (49.9 mm) and one sub-conductor in a duplex conductor (2x39.2 mm) during the period 18-21 March 2010.

IV. EFFECT OF TORSIONAL STIFFNESS

While studying the load diagrams of the ice load events it became evident that ice shedding has a great effect on the resulting maximum ice load values. However, the effect of differences in the torsional stiffness of the two systems could only be investigated by selecting loads up to the occurrence of the first shedding in cases where no evident disturbances (such as wind fluctuations) occur during the ice accumulation period. 26 such cases were observed. The relation between the two power lines is shown in Fig. 8.

It can be seen from Fig. 8 that by applying a linear trend line, on average the unit ice load on one sub-conductor of the duplex is about 93% that of the simplex conductor.

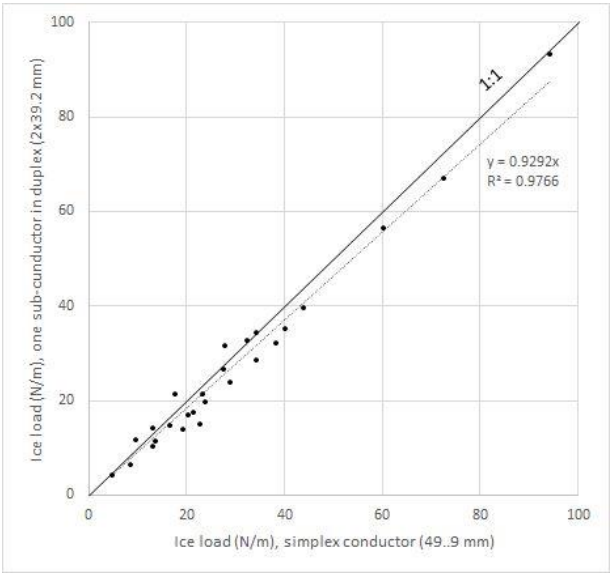

Fig. 8. Comparison of undisturbed ice load on simplex conductor (49.9 mm) and one sub-conductor in duplex conductor (2x39.2 mm).

In [2] a model for the theoretical assessment of ice loading depending on torsional stiffness is presented. A precipitation

direction of 45° is assumed. Figure 6 in [2] shows relation between precipitation and accumulated ice volume for cylinders with different torsional stiffness. In order to compare the results in Fig. 8 to the model presented in [2] the following assumptions and calculations were made:

The torsional stiffness can be approximately calculated as 20% of the stiffness of an equivalent solid bar [2]. The stiffness ratio of the duplex conductor system to simplex conductor, k_{bundle}/k_{single}, = He^2/GJ +2, is half of that given in [2] for a quad bundled conductor. Further assuming that the higher shear modulus of the relatively narrow steel core may be omitted, with a load of 50 N/m resulting in horizontal tension of H = 103860 N and with e = 0.45 m:

The shear modulus of aluminium is G = 27 GPa. Therefore, for the simplex $GJ_{simplex}$ = 1860 Nm^2/rad and for one conductor in duplex $GJ_{1\text{-in-duplex}}$ =705 Nm^2/rad and k_{bundle}/k_{single} = 31.8, $k_{eq,simplex}$ = 112 Nm/rad, $k_{eq,duplex}$ = 1468 Nm/rad and then for the duplex line $k^*_{eq,duplex}$ = 182, and for the simplex line $k^*_{eq,simplex}$ = 15.

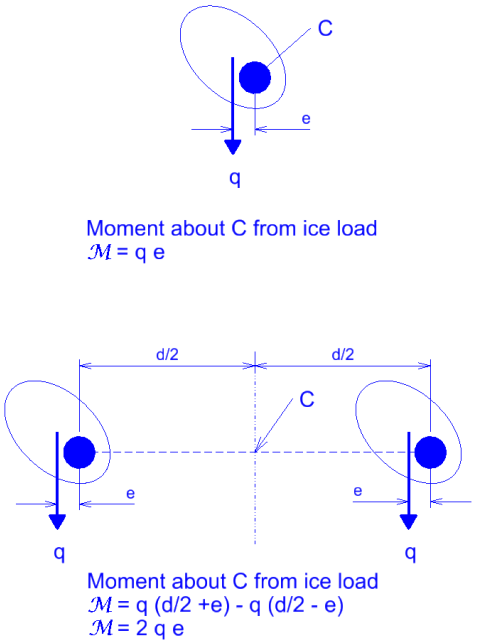

Fig 9. Eccentric ice load on a simplex conductor (upper figure) and on a duplex conductor (lower figure).

Looking closer at how the duplex system rotates (Fig. 10), the bundle system rotates ϕ_1 about its axis due to $2\mathcal{M}$ moment (Fig. 9), but the sub spans between spacers will rotate additionally ϕ_2 due to the $\mathcal{M}$ moment.

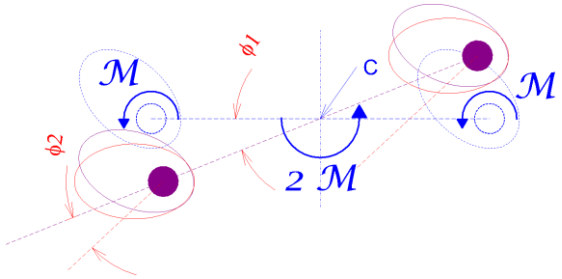

Fig 10. Rotation of the duplex system due to eccentric ice load.

Sum of the rotations gives with local stiffness of the sub spans (on average L_{sub} = 36.7 m, and $k_{eq,sub}$ = 12*705/36.7 = 231 Nm^2/rad).

$$\mathcal{M}/k_{eq,duplex,mod} = \phi = \phi_1 + \phi_2 = 2\mathcal{M}/k_{eq,duplex} + \mathcal{M}/\ k_{eq,sub}$$

$$k_{eq,duplex,mod} = k_{eq,duplex}\ k_{eq,sub}\ /(2\ k_{eq,sub} + k_{eq,duplex})$$

$$= 1468 \cdot 231/(2 \cdot 231 + 1468) = 176 \text{ Nm/rad}$$

and $k^*_{eq,duplex}$ = 2, which is considerably lower that calculating the torsional stiffness of just the bundle system.

Reading and calculating through the rather small Figure 6 in [2] applying the k* = 16 curve for $k^*_{eq,simplex}$ = 15 simplex, and between k* = 16 and k* = 32 curves for the $k^*_{eq,duplex}$ = 24 for the duplex assuming that the same precipitation applies for both conductors, then Figure 6 in [2] gives that the duplex line should have about 87% of the load on the simplex line compared with 93% obtained from the observations.

This is a considerable difference. One or more of the following reasons could explain this:

(a) The precipitation direction may vary from the assumed 45° in [2] and could in fact vary throughout the icing event.

(b) The ice might accumulate on the conductors differently from just setting on the face it hits directly and may set on the leeward side as well, similar to snow that blows over a mountain edge (see Fig. 11 with downward pointing ice tail on the leeward side). Thus the eccentricity of the ice will be less or even zero.

(c) The estimated stiffness of the system with respect to ice accumulation may be inaccurate (too high). It is a little unclear how the torsional stiffness of the bundled system is to be calculated. In [3] it is clear that the sub span configuration, i.e. distance between spacers, does not have an effect on the torsional stiffness of the bundle as such. In the calculations above the torsional stiffness calculated for the bundle has been lowered in order to compensate for additional rotation of the sub spans caused by the eccentric ice load.

Fig. 11. In-cloud icing on duplex conductor in FL4 (400 kV OHTL) in Dec. 2006.

V. Effect of Ice Shedding

It is evident that ice shedding has great effect on the resulting load on the conductors in the two power lines.

In the study here it was assumed that an ice shedding event started with a 2 N/m over 10 minutes load decrement and stopped when load decrement became lower than 2 N/m again. For the simplex conductor the lowest load decrement during a shedding event was 4.6 N/m and the highest observed was 236.7 N/m. For one conductor in duplex the lowest load decrement during a shedding event was 5.6 N/m and the highest observed was 161.9 N/m.

It was observed that on average ice started to fall off the duplex line at lower unit load (35.5 N/m) than observed for the simplex conductor (54.9 N/m), as shown in Fig. 12. It was also noted that the period of ice shedding from the simplex conductor

often lasted a little longer than observed for the duplex conductor. Thus 53% of ice shedding events for the duplex were over in less than 10 minutes, but 33% in case of the simplex conductor.

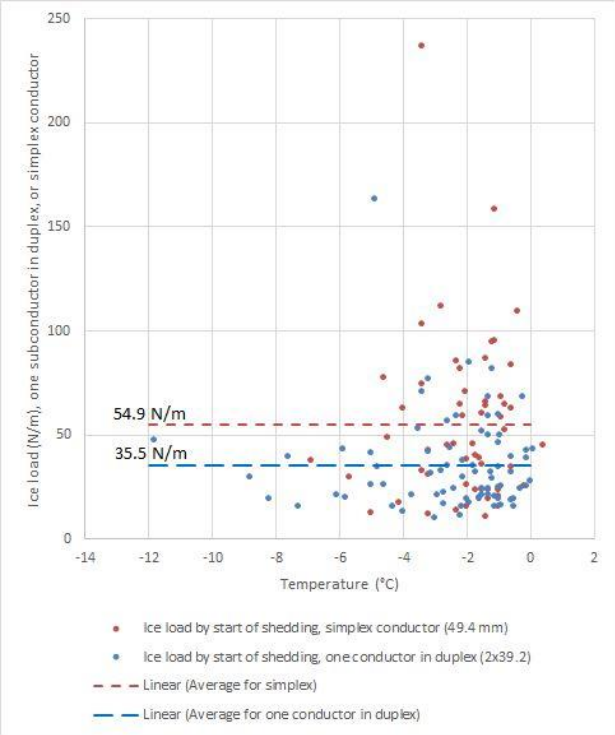

Fig 12. Ice load by the start of a shedding episode.

More ice shedding events were observed for the duplex conductor (75) than for the simplex conductor (55).

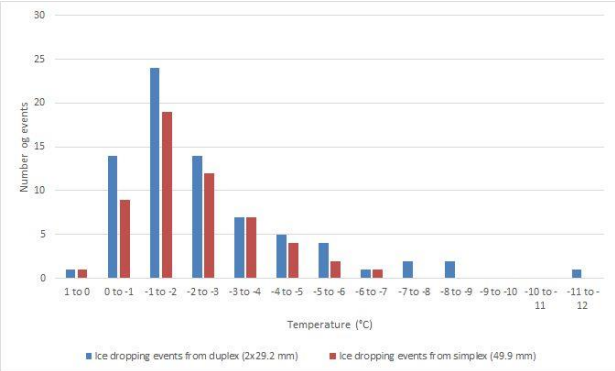

Fig 13. Temperature at the start of ice shedding events.

It is difficult to pinpoint any specific rule for the ice shedding process. The ice shedding events start at different temperatures and at different, very scattered ice load intensities.

Weaknesses in the ice formations are probably more in the case of the duplex conductors, i.e. larger leeward area due to difference in torsional stiffness and weaker ice (thinner ice or less compact) on the leeward side. Weaknesses by the spacers as can be seen on Fig. 11 where the ice has begun to fall off by the spacer.

The measurements showed that wind excitement was more frequent in case of the duplex conductor and dynamic forces due to that excitement could lead to an earlier ice shedding.

The effect of temperature is important when considering causes of ice shedding. Ambient temperature, solar radiation and energy transfer in the power lines can all have an effect to raise the temperature of the conductors and thereby weaken the bond between ice and conductor. It can be seen in Fig 14 that when ambient temperature rises close to or above -2°C, ice begins to fall of the duplex line. Ice falls off the simplex line more seldom, but at similar time points. The energy transport on the lines during the period shown in Fig. 14 was rather steady and generated heat energy of 6 W/m for each conductor in the duplex and 13.7 W/m in the simplex.

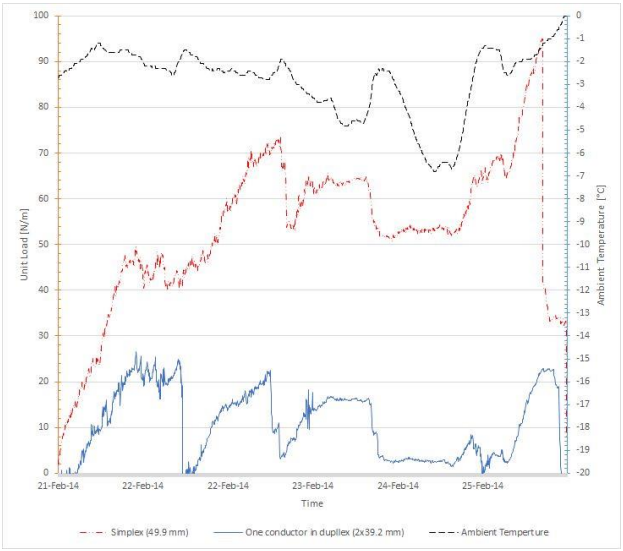

Fig. 14. Unit Ice Loads and Temperature for Fljótsdalslína 3 and Fljótsdalslína 4 OHPL: February 21 5:10 – February 26 11:10 2014.

VI. Conclusion

The case studied showed that ice load accumulated on one conductor in duplex was about 7% less than ice load accumulated on the simplex conductor. It could not be verified if this was due to variations on torsional stiffness alone.

It was observed for both the simplex and duplex OHTLs that ice shedding had considerable lowering effect on the ice load. The ice shedding had more effect on the duplex OHTL where the ice shedding began on average at lower load intensities and was more frequent.

VII. References

[1] Á. J. Elíasson, P. Th. Gunnlaugsson and E. Thorsteins, „Ice accumulation at measuring site Hallormsstadahals, IWAIS XIII, Andermatt, September 2009.

[2] C. Hardy, A. Leblond and D. Gagnon, „Theoretical Assessment of Ice Loading of Cables as a Function of their Torsional Stiffness, IWAIS XI, Montreal, June 2005.

[3] O. Nigal, G. J. Clarke and D. G. Havard, „Torsional Stability of Bundle Conductors“, Ontario Hydro Research Division, Toronto, Canada, 1976.

A severe in-cloud icing episode in Iceland 2013-2014

- Weather pattern background -

Árni Jón Elíasson[1], Einar Sveinbjörnsson[2]
[1] Landsnet, Reykjavík, Iceland, [2] Veðurvaktin ehf, Garðabær, Iceland.
arnije@landnet.is

Abstract: **A severe in-cloud icing episode from mid-winter 2013-2014 which lasted 80 to 90 days is analysed. A reoccuring weather pattern characterized by low pressure system tracking from west to east south of Iceland towards the British Isles. As the systems passed slowly or became quasi stationary. The repetitive pattern resulted in high amounts of precipitation, high humidity and relatively mild air circulated towards the eastern part of Iceland as the wind direction was almost uniformaly between E and NE. This unusual weather pattern resulted high accumulation of in-cloud icing. In the affected area, of elevation interval from 350 to 700m in N- and NE-part of Iceland, the TSO of Iceland operates many test spans for icing accumulation.**

Data from ECMWF reanalysis from 1961 to 2013 are analysed. The so called Hovmøller method of analysis of large scale pattern of the 500 hPa pressure level near Iceland is imposed for estimating the anomaly of the winter of 2013-14 compared to more than 50 seasons from 1961. The severe and long lasting icing episodes during this winter was caused by abnormal weather pattern where the normal west component of the 500 hPa over Iceland was shifted to extraordinary strong east component.

Keywords: In-cloud icing, test spans, icing measurments, circulation pattern, reanalysis. Hovmøller analyses method.

I. INTRODUCTION

The severe in-cloud icing episode during mid-winter 2013-2014 in Iceland is obviously linked to abnormal weather pattern in the North Atlantic. The period of ice accumulation on several test spans was recorded almost continuously from 23. December to 2. March as the prevailing E- and NE-winds brought humid and relatively mild air towards east and north parts of Iceland. The ice accumulation is assumed to been in most part due to rime ice (in-cloud icing), but short periods of wet snow cannot be excluded [1]. Following is a discussion on how the simple parameterisation of the 500hPa pressure field correlates to this long continuous episode of rime icing in N and NE Iceland. The aim of this study is to connect the upper level wind where icing occurs repeatedly to the surface weather pattern. A large scale weather pattern controls rather diffuse feature as in-cloud icing. Its rate is as expected sensitive to meteorological variables such as air temperature, wind speed, cloud water, cloud droplet size and also highly to the complexity of the terrain.

Figure 1: At the test site Náttmálahæðir (00.1) after the severe icing episode.

II. A LINKAGE BETWEEN UPPER AIR STATE TO LOCAL VARIABLES

The state of the middle-troposphere is indicated by the 500 hPa atmospheric pressure field. On average the elevation of this pressure level is around 5.300 m in sub-polar areas in the boreal winter. Higher elevation of this standard pressure field is associated with warmer column of the air between surface and the 500 hPa, while lower elevations indicates colder column of air. The 500 hPa is often referred to as a steering level to the weather systems of synoptic scale such as the mid-latitude low pressures and ridges. On average, Iceland is situated on the eastern edge of cold higher level trough over eastern Canada. This trough maintains an average WSW wind at 500 hPa level over Iceland [2]. Fluctuations are of all dimensions in both temporal and spatial fields. The formation, movements and dissipation of mid-latitude systems are strongly connected to the horizontal east propagating planetary Rossby waves near the level of 500 hPa as well. Depending also to the higher level associated North Atlantic jet stream.

A multitude of circulation classification methods have been introduced in the literature. In the 1950´s the Swedish meteorologist Ernst Hovmøller classified how to use weather types based on the circulation pattern to forecast parameters such as temperature or precipitation. In Iceland the original parameters were first used by Hovmøller as part of weather classification scheme [3]. Recently, as reanalysis of

standardized upper air data is available, there is again focus on such simple statistical methods. Gridded reanalysis is particularly well suited for studies based on statistical down scaling method where one single surface variable is correlated to the 500 hPa field over and around Iceland.

There are three conceivable Hovmøller parameters:

A. Zonal (west) component of the wind at 500 hPa in a cross section 70°N-60N along the 20°W longitude.
B. Meridional (south) component of the wind at 500 hPa in a cross section 30°W-10°W along the 65°N latitude.
C. Height of the 500 hPa at 65°N-20°W.

By these definations, the fields are categorized into three very simple components which form a parameter space (Figure 2). The zonal component and how it advects humid air towards N and NE Iceland is of main concern in this study, as well as parameters influencing the weather during the periods of days or weeks where in-cloud icing occurs repeatedly in NE and N Iceland.

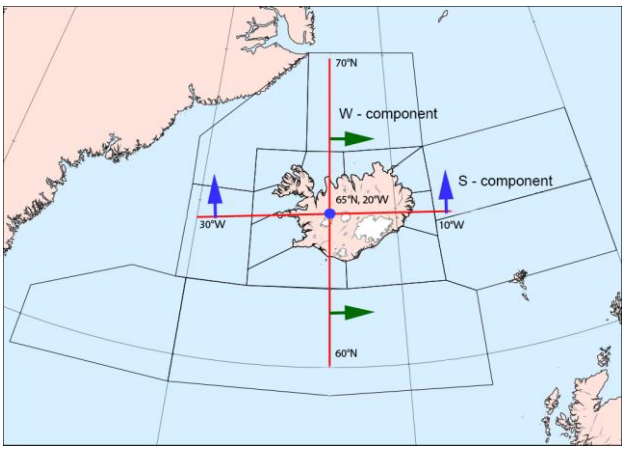

Figure 2: Figuration to the Hovmøller parameters. A: West-component, B: South-component and C: Hight of the 500 hPa at 65°N-20°W.

A set of daily data for the three Hovmøller parameters was extrected from ECMWF´s ERA-20C global reanalyses [4]. The data set contain fully comparable 55 years to the three 500 hPa parameters; A,B,C with a temporal resolution of 6 hours.

III. PARAMETERS OF THE WINTER 2013-2014

Zonal component of the 500 hPa

Figure 3 shows the average zonal component of the 500 hPa wind for each winter in the data set (December to February). As expected the positive zonal component (W-wind) is prevailing, but the variability is large. The 2014 winter (Dec. 2013 - Feb. 2014) is a clear outlier. It is the only single winter where negative component (E-wind) is more frequent than positive (W-wind). Another outlier of this 55 years dataset is the winter of 1977, in which longer periods of E-component where measured, although the combined component for the whole period is slightly positive. This winter (1976-1977) there was extensive damage experienced on transmission lines in NE and E Iceland.

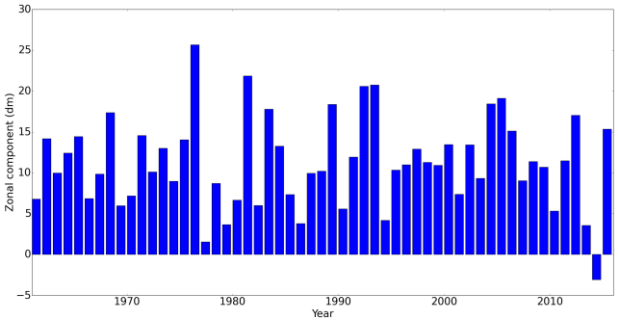

Figure 3: Zonal component (A) in dekameters (dm). The extraordinary value of the winter 2013-2014 is -3.1 dm.

On figure 4 the zonal component is calculated each 6 hours from 1st. Dec 2013 until 28th. Feb. 2014. A weather pattern that led to significant negative zonal component started on 21st of December and lasted more or less until 3d of March when the component shifted completely. The mean value of the zonal component during December to February (1961-2015) is +11,5 dm The lower tercile is calculated as +3,5 dm and during most of the period 21st Dec. to 3d March the zonal component remain constant.

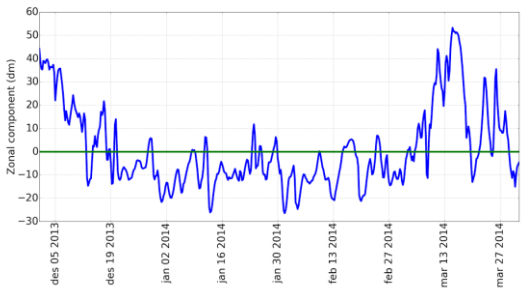

Figure 4: The Zonal component of the 500 hPa wind in cross section over Iceland. Negative values indicate east wind.

The test span Heiðarhnjúkur

Heiðarhnjúkur is one of Landsnet´s test spans, located in East-Iceland at a mountain ridge ~900 m.a.s.l (Figures 5,6). Severe in-cloud icing has been measured frequently at this location since the beginning of measurements in the mid 1980´s.

Figure 5: Heiðarhnjúkur test site (85-1)

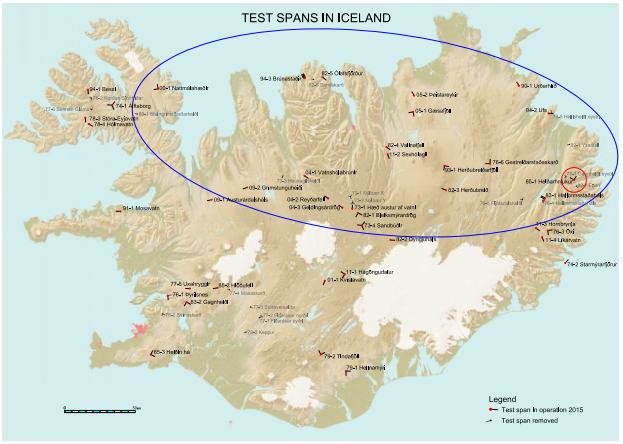

Figure 6: Location of all the test spans. Test site Heiðarnjúkur is marked in the red circle and the affected area in the blue circle.

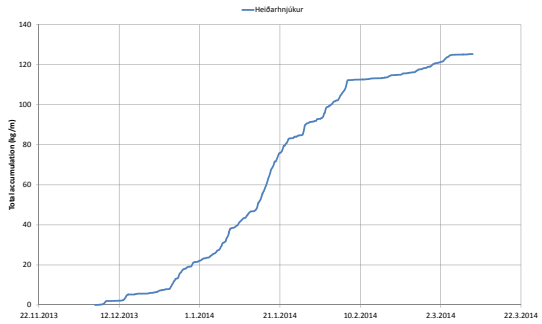

Figure 8: Measured ice accumulation at Heiðarnhjúkur in the unit of kg/m/h. The calibration limit (see Figure 7) is not taken into account.

Figure 7 shows the measured ice load at Heiðarnhjúkur (A) from 1. Dec 2013 to 12. March 2014. Significant ice accumulation began 23.-24. December and icing events where frequent until March. During longer periods the accretion was recorded constantly. Ice shedding is occasional, mainly caused by wind conditions, but sometimes it happens randomly. The ice load period from 20. January until 16. February is extreme compared to Heiðarnhjúkur´s records, but also absolutely in combination to the network of nearly 60 operational test spans measuring ice accumulation in real-time. However ice accumulation has once before been measured 600 N/m [5].

The flat top of the curve in February is due to the fact that the measuring equipment is calibrated for certain range. If the measured load is above the range of the instrument it is recorded as the maximum. It is not possible to determine accurately how much the actual accumulation was during this period but has been estimated close to 60 kg/m (dashed line) based on nearby test spans and icing calculation from WRF modelling [1].

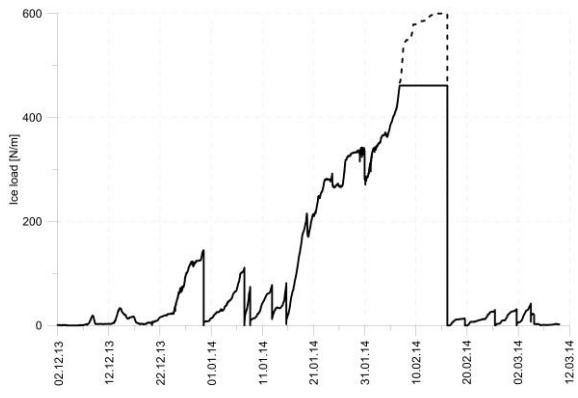

Figure 7: Measured Ice accretion at test span Heiðarnhjúkur (A) at E Iceland from December 2nd 2013 to March 12th 2014. Dashed line is estimate when calibration was out of range.

The rate of the accumulation at Heiðarnhjúkur is show in figure 8. In-cloud icing was strong and nearly continuous. Very short periods of light or negligible icing are measured. The rate of accumulation was extremely high from ~15th to 22nd January. The sharp brake on the line is due to the equipment calibration limit (10.000 kg).

IV. Results and Dicussions

The 500 hPa Zonal wind crossing Iceland mainly has a westerly component. In that situation in-cloud icing is rare and normally not of any importance at N and NE Iceland. When low pressure systems are dissipating towards east south of Iceland the Zonal component shifts to negative for a while. Sometimes even for a periods of days. During these periods, measurements have shown that in-cloud icing can accumulate on test spans. There are no instances in the 55 year period analysed where the zonal component is negative continuously for weeks or months as 2013-2014. Figure 9 shows 500 hPa mean and anomalies for January 2014. A dipole anomaly appears where large negative anomaly is observed over Ireland and an opposite anomaly is found over the Norwegian Sea and Spitzbergen. February was modeled and a map of Sea level pressure is shown on Figure 10. Anomaly up to 27 hPa below the average on monthly base is extraordinary in all cases. Such a pattern leads to strong and persistent E- and NE- surface winds generally in Iceland which is similar to the January anomaly shown at figure 9.

The severe and long lasting icing during the winter months of 2013 – 2014 was caused by succession of numerous vigorous low pressure systems moving eastward south of Iceland toward the British Isles. UK experienced both the wettest winter on record as well as the stormiest since records began in 1910 [6]. The global causes for this extraordinary winter are still under debate. Some publications associated its occurrence with extraordinarily low temperature occurring over the North American continent, generating recurrent cold air outbreaks. At the same time, the subtropical Atlantic was comparatively warm. This combination lead to strong temperature gradients and created ideal conditions for the generation of storm systems. over the North Atlantic [7]. The cold air outbreak is related to North-America circulation anomalies. Characterized as a dipole with amplified upper-level ridge over the Pacific coast and deepening through over the central-eastern parts of U.S and Canada [8]. The abnormal winter 2013-2014 also emphasizes the necessity of a better understanding of the drivers of extreme weather pattern and this is particularly relevant within the scope of climate change.

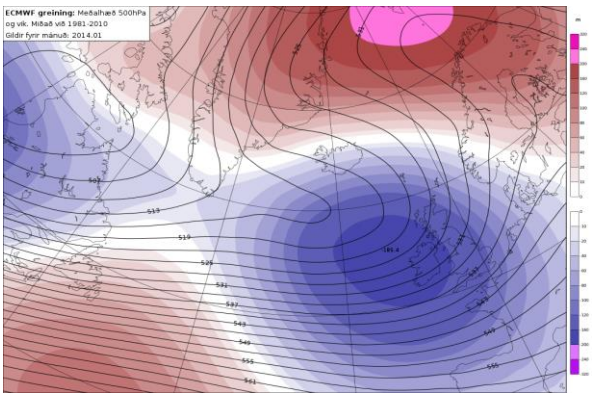

Figure 8: January 2014. 500 hPa mean in dekameters (contours) and anomaly from 1981-2010 average. Red: positive and blue: negative. From IMO (Icelandic Meteorological Office)

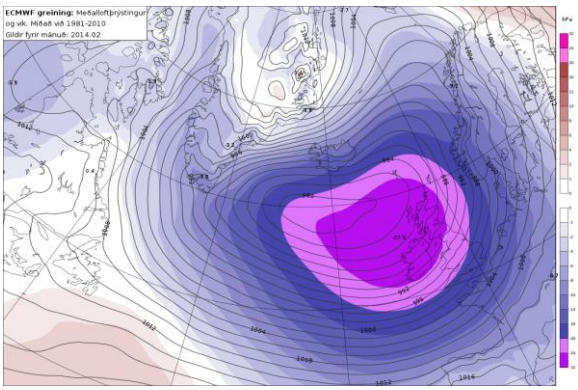

Figure 9: February 2014. Sea surface pressure in hPa (contours) and anomaly from 1981-2010 average. Red: positive, blue and violet: negative anomaly.

V. ACKNOWLEDGMENT

The author´s would like to thank Guðmundur Hannesson at EFLA Consulting Engineers for preparing the ice load recording and for creating figures 4 and 5. Also Elín Björk Jónasdóttir meteorologist at IMO for valuable comments.

VI. REFERENCES

[1] Elíasson, A.E, Ágústsson,H.,Hannesson G. and Þorsteins E, "Comparison of measured and simulated icing in 29 test spans during the extreme icing episode in Iceland." In 16th IWAIS, Uppsala, 2015.

[2] von Storch, H., P. Jones (ed.) (2001) ACCORD Atmospheric Circulation Classification and Regional Downscaling E.U. Project number ENV4-CT97-0530, CR SPECIAL 9, Volume 17, Number 3, August 29 2001.

[3] http://www.cru.uea.ac.uk/cru/projects/accord/vi.pdf

[4] Hovmøller, E. "Climaological information on Iceland." United Nations report no. TAO/ICE/4, 115 p. 1960.

[5] Dee, D.P. et.al. "The ERA-Interim reanalysis: configuration and performance of the data assimilation system." Q. J. Roy. Meteorol. Soc., vol. 137, no. 656, pp. 553-597. 2011.

[6] Elíasson, A.E and Þorsteins E, "Ice load measurements in test spans for 30 years." In 12th IWAIS, Yokohama, 2007.

[7] Muchan, K. et.al. "The winter storms of 2013/2014 in the UK: hydrological responses and impacts." Weather. Special Issue: The storms of winter 2013/2014 in the UK. Volume 70, Issue 2, p.55-59, February 2015.

[8] Mike Kendon and Mark McCarthy. "The UK´s wet and stormy winter of 2013/2014." Weather. Special Issue: The storms of winter 2013/2014 in the UK. Volume 70, Issue 2, p.40-47, February 2015.

[9] Wang, Shih-Yu Simon et.al. "The North American winter "dipole" and extremes activity: a CMIP5 assesment." Atmos. Sci. Lett. DOI: 10.1002/asl2.565. 2015

[10]

Research on icing behavior and ice adhesion testing of icephobic surfaces

Heli Koivuluoto[1], Christian Stenroos[1], Riku Ruohomaa[1], Giovanni Bolelli[2], Luca Lusvarghi[2], Petri Vuoristo[1]
[1]Tampere University of Technology (TUT), Department of Materials Science, Tampere, Finland, [2]University of Modena and Reggio Emilia (UNIMORE), Department of Engineering "Enzo Ferrari", Modena ,Italy
heli.koivuluoto@tut.fi

***Abstract*: Surface engineering shows potential to provide sustainable approach to icing problems. Currently several passive anti-ice mechanisms adoptable to coatings are known but further research is required to proceed for practical applications. Icing wind tunnel and centrifugal ice adhesion test equipment enable the evaluation and development of anti-ice and icephobic coatings for e.g., wind turbine applications but also other growing players in arctic environment e.g. oil, extractive and logistic industries. This research is focused on the evaluation of icing properties of various surfaces.**

Keywords: ice adhesion, icing wind tunnel, ice accretion, coatings, surface properties

LEGEND AND ABBREVIATIONS

CA	*Contact angle*
F	*Fluorine*
FEP	*Fluorinated ethylene propylene*
IA	*Ice adhesion*
LWC	*Liquid Water Content*
PTFE	*Polytetrafluoroethylene*
PU	*Polyurethane*
VMD	*Volume median diameter*

INTRODUCTION

On-going climate change, opening of new logistic routes, energy and mineral resources as well as increasing tourism feed the growing activity in cold climate regions. One of the major challenges for operations in these areas is ice and snow accretion. Icing reduces safety, operational tempo, productivity and reliability of logistics, industry and infrastructure. Figure 1 shows examples of an ice accretion on the problematic parts such as on wind turbine blade leading edge and on vessel.

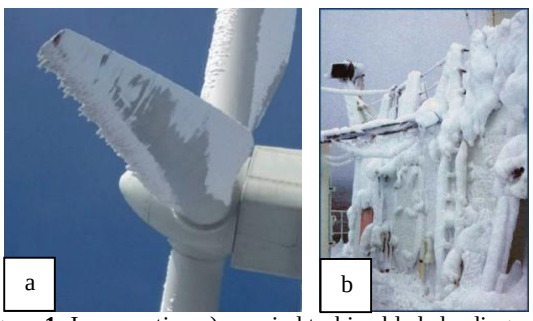

Figure 1: Ice accretion a) on wind turbine blade leading edge [1] and b) on vessel [2].

Surface engineering shows potential to sustainable approach to icing problems. Passive anti-ice coatings can hinder ice formation and icephobic surfaces reduce the adhesion of accreted ice. Current commercial coatings with icephobic characteristics rely on hydrophobicity, releasing of lubricant or melting point depressants and ablation. Currently, research is additionally carried out on icephobic potential of superhydrophobic surfaces [3], phase change materials [4], slippery liquid infused surfaces [5], anti-freeze proteins [6] and surface morphology [3,7]. All these anti-ice mechanisms show promising results in reducing ice accretion and adhesion. Nevertheless, so far these are functional only in specific icing conditions for a limited amount of time. However, the wear resistance of these coatings is poor and thus, the current coatings are practical only in limited applications or the icephobic effect is insufficiently significant [8]. Ideal icephobic surface should have also anti-ice characteristics. It should work in three different stages of ice formation. Ideal icephobic surface should 1) minimize accumulation of water on the surface by reducing interactions of the surface and incoming water, 2) inhibit heterogeneous ice nucleation and 3) weaken the adhesion of ice on the surface [9].

As an example, there are three main icing mechanisms for wind turbine applications: 1) in-cloud icing, 2) precipitation icing (wet snow, freezing rain) and 3) frost formation [10]. The first two mechanisms include supercooled liquid water and the third one condensing water vapor. In-cloud icing is the most detrimental icing mechanism for wind turbines [11]. It occurs when supercooled water droplets, contained in cloud or fog, hit a surface below 0 ºC and freeze upon impact. In-cloud icing can be divided in two sub-mechanisms based on the macrostructure of resulting ice: rime (soft and hard) icing and glaze icing. In rime icing, water droplets freeze immediately upon impact contact with the surface and form porous ice with white appearance [12]. Soft rime has a feathery appearance, it is formed at cold temperatures, from small droplets, low liquid water content (LWC) and its adhesion is low. Hard rime has more icy appearance but it has still high porosity. Hard rime has higher adhesion and it is formed after slower freezing which, in turn, is due to larger droplets, higher liquid water content, or higher temperature. On the other hand, in glaze icing, part of the water droplets freeze upon impact and the remainder run along the surface before freezing and form smooth and non-porous clear ice.

In order to develop anti-ice or icephobic coatings, test equipment was designed and constructed. Several icing tests have been introduced in literature [13-15]. However, often these tests either include heavy wind tunnels used by aerospace and automotive industry or the tests are extremely simplified and far from practical conditions. Even more, icing tests are not standardized. To make affordable and compact but truthful test facilities for evaluation of icing, it was decided that a small scale icing wind tunnel and an ice adhesion test apparatus be constructed. Both of these items are placed in a climatic room to guarantee constant atmospheric conditions throughout testing.

An icing wind tunnel has a capability to simulate the ice accretion by both in-cloud mechanism (glaze and rime icing) and precipitation icing. With centrifugal ice adhesion test, it is possible to test either bulk-formed ice or atmospherically accreted ice. These test devices enable evaluation and development of anti-ice and icephobic coatings not only for wind turbine applications but also other application fields in arctic environment.

This research focuses on the evaluation of icing properties of various coatings and surfaces. Furthermore, the stress distribution in the ice block during the centrifugal ice adhesion test was modelled by finite elements method in order to understand the interfacial behavior of ice and surface. In addition to ice adhesion, wettability and surface roughness were characterized.

I. Experimental procedure

A. *Icing tests*

For ice testing, an icing wind tunnel was designed and constructed. After ice accretion, the ice adhesion was measured with centrifugal ice adhesion test. Icing behavior is compared with wettability and roughness of the surfaces. Icing tests therefore include ice accretion through a wind tunnel in a cold climate room and ice adhesion measurements by using a centrifugal ice adhesion test, Fig. 2. The ice adhesion test equipment is based on the description by Laforte and Beisswenger [16].

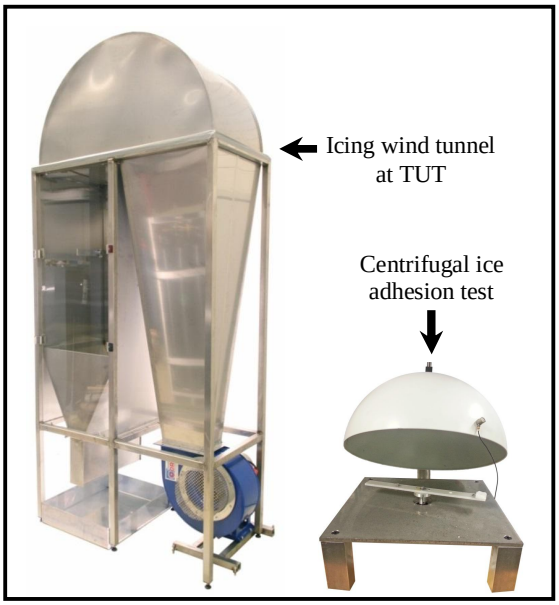

Figure 2: Icing wind tunnel and centrifugal ice adhesion test at TUT.

In the centrifugal ice adhesion test, a plate (340 x 30 mm) with iced area (30 x 30 mm) is rotated with a constant acceleration rate until the ice detaches. Detachment is observed by acceleration sensor. The iced test plate is weighted before and after the test in order to measure the mass of detached ice. When adhesion area is measured and the speed of rotation at the moment of detachment is known, the maximum adhesive shear strength can be calculated. The centrifugal force F can be written as:

$$F = mr\omega^2 = wLhpr\omega^2 \quad (1)$$

Where m is the mass, w is the width, L is length, h is the height and ρ is the density of ice, r is the radius of rotation and ω is angular velocity. It can be seen that centrifugal force is directly proportional to all specimen dimensions. However, width and length do not effect on shear stress τ:

$$\tau = \frac{F}{A} = \frac{wLhpr\omega^2}{wL} = hpr\omega^2 \quad (2)$$

Specification of the icing wind tunnel at TUT is presented in Table 1. Several parameters e.g. nozzle parameters, water droplet size and liquid water content can be varied. By this way, the ice formation can be modified (e.g., rime and glaze ice). The critical factor affecting on the quality and type of ice are the spraying parameters.

Table 1: Specification of the icing wind tunnel at TUT.

Parameters		Min	Max	
Nozzle parameters	P (Liquid)	0	5	bar
	Q (liquid)	0	0.3	l/min
	P (Gas)	0	5	bar
	Q (Gas)	0	150	l/min
Volume median diameter (VMD)	D(V0.5)	25	1000	µm
Flow velocity	v	0	25	m/s
Temperature	T	0	-40	˚C
Nozzle-specimen distance	H	0	1.9	m
Liquid water content	LWC	0	4.2	g/m^3

In this study, icing conditions were selected as rime, normal and glaze ice can be formed. Normal test ice refers to ice which is as close to glaze ice as possible without containing icicles or runback ice. This kind of ice is easy to test due to regular shape of the ice block. It contains approximately 3 vol-% of porosity resulting in translucent appearance.

Rime ice is formed, when clouds or fog containing supercooled droplets freeze immediately upon contact to a surface preserving their spherical form. The glaze ice is formed from larger droplets caused by wet in-cloud icing, freezing rain or drizzle. The droplets that create glaze ice will stay in the liquid state momentary in the contact of the surface, before freezing.

In the present ice accretions, the temperature was chosen as –10 ºC and the flow velocity was set to the maximum 25 m/s. In addition, the nozzle-specimen distance was set to 1.5 m. The different ice types were created by altering the gas pressure. By increasing the pressure to 5.5 bar, the 25 µm VMD for droplets could be achieved (according to nozzle manufacturer: Spraying system Co.) and rime ice created. The glaze ice was accreted with the 2.3 bar corresponding to 40 µm VMD of the droplets. The normal ice was accreted with the 3.5 bar pressure corresponding to 31 µm VMD of the droplets.

B. *Finite element modeling of the centrifugal ice adhesion test*

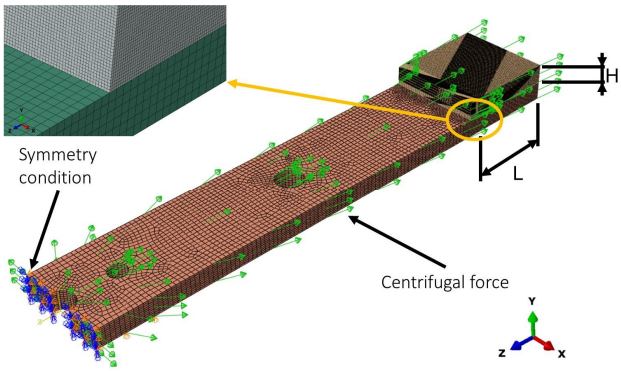

Figure 3: Finite element model of the centrifugal ice adhesion test.

Stress-strain distributions in the centrifugal ice adhesion test were modelled by the finite elements method. As shown in Fig. 3, the model reproduces the test geometry and dimensions as shown in Fig. 2. Both the ice and the substrate were assumed as linear elastic materials; plasticization of ordinary substrates during the test is indeed not expected. Among the various simulation runs performed in this research, the case for steel and aluminum substrates are presented in this contribution. Additional models were run by assuming the existence of a thin coating layer (modelled as a 200 µm-thick shell) in order to reproduce the actual test conditions as summarized in Table 3. Material properties are summarized in Table 2. The models were meshed using reduced-integration, bilinear, 8-node hexahedral elements and were run using Simulia-Abaqus 6.12-3 and later versions.

Table 2: Material properties for finite element simulations.

Properties	Al	Steel	Coating	Ice [17]
E [GPa]	70	210	0.225	9.332
ν	0.34	0.30	0.40	0.325
ρ [kg/m^3]	2700	7890	4700	919

C. *Other research methods*

Contact angle (CA) measurements were done by using distilled water and KSV CAM200 equipment. A droplet volume of 10 µl was used for static contact angles of superhydrophobic surfaces whereas a volume of 5 µl was used for other surfaces. At least five droplets were used for determining the static contact angle. For dynamic contact angle measurement, the droplets were filled up to 30 µl in 30 s and unfilled at the same rate. The dynamic angles were analyzed once a second. One droplet was used for each sample determining the dynamic contact angles resulting in three parallel measurements for each type of specimen.

Surface properties (surface profile, Ra, Sa values) were analyzed by Alicona Infinite Focus G5 optical profilometer with the 20x objective magnification, resulting in a measurement field size of 0.81 mm x 0.81 mm on the xy-plane. Vertical resolution achieved with this magnification is 50 nm. Ra- and Sa-values were measured from areas as large as possible.

D. *Tested materials*

Several materials and surfaces were selected for the testing. Three hydrophobic and two superhydrophobic coatings were studied (Table 3). Steel was used as a substrate material. Aluminium bulk material was chosen as reference material. It is typical material used in atmospheric conditions and also mainly studied in icing testing by other researchers. PTFE (as a form of tape, making it possible to use a fresh surface for each test) was selected as other reference due to its good non-sticking behaviour.

Table 3: Deposited surfaces and reference materials.

Sample	Coating/surface
H1	PTFE-based hydrophobic coating, Alu Releco
H2	FEP-based hydrophobic coating, Alu Releco
H3	PTFE-based hydrophobic coating, CeraFlon, Alu Releco
SH1	F-containing superhydrophobic hybrid coating, Millidyne
SH2	Superhydrophobic coating, Ultra-Ever Dry®
Al	Reference: Polished aluminum bulk surface
PTFE	Reference: Teflon tape, smooth surface

II. Results and Discussion

Icing behavior of selected coatings and surfaces was studied. Ice adhesion was evaluated and different types of ice were formed. Ice adhesion was compared to the wettability and surface roughness of the surfaces in order to find correlations between icing properties and surface properties.

A. *Icing behavior and ice formation*

Ice was formed in the temperature of -10 ºC. Different ice types were produced by changing icing conditions. Figure 4 presents rime, normal and glaze ice. Soft rime is named as rime ice, glaze ice with no other features than transparency is named as normal ice and glaze ice with distinctive features such as icicles and runback ice is named as a glaze ice.

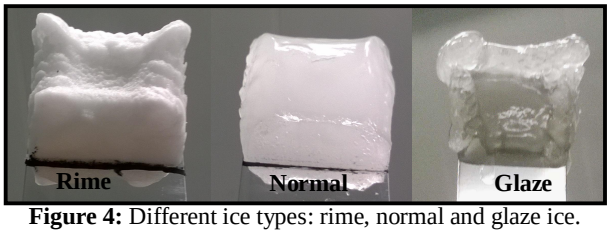

Figure 4: Different ice types: rime, normal and glaze ice.

The different ice types have some characteristic properties, and the types are classified based on their density. According to the standard "ISO-12494", density of soft rime ice varies between 300-600 kg/m^3, hard rime 600-900 kg/m^3 and glaze ice around 900 kg/m^3 [18]. The appearance of soft rime is white, irregularly shaped ice, which has grown against the wind direction. Glaze ice is transparent evenly shaped ice that has runback ice and icicles. The normal ice does not have icicles or runback ice and it is translucent unlike transparent glaze ice.

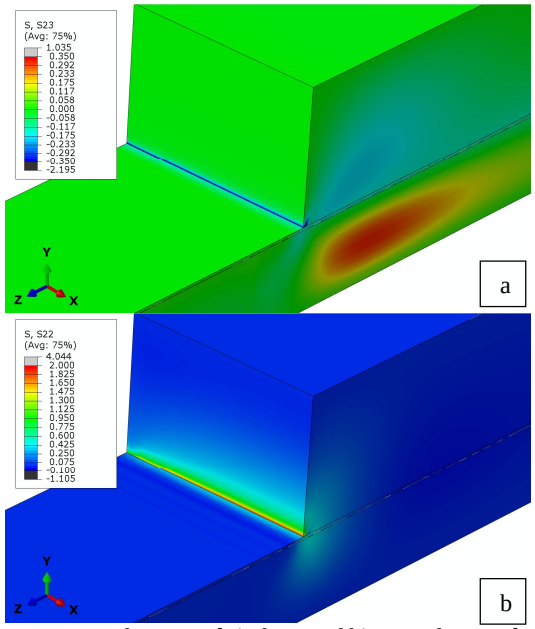

Figure 5: Distributions of a) shear and b) normal stress for an ice block on coated Al substrate.

Finite element simulations confirm that the test method generates maxima of both in-plane shear stress (τ_{23}, Fig. 5a) and out-of-plane normal stress (σ_{22}, Fig. 5b) at the ice-plate interface, regardless of the plate material and of the presence of a thin coating shell. Adhesive failure will therefore occur along such interface, thus minimizing the risks of cohesive failure events, which would act as confounding factors on the test results. It is anyway important to account for the fact that stress maxima along the ice block edge are much larger than they

would be predicted by simple application of the beam theory. This means the detachment of the ice block occurs at larger stress values than those predicted by the analytical equation (2). The actual magnitude of such stresses is a function of the mechanical properties of the involved materials, as these will affect the overall deformation under the action of the centrifugal force. For instance, an elastically compliant substrate (e.g. Al) allows larger elastic bending of the beam under the action of the centrifugal force (Fig. 6a) than a stiffer one (e.g. steel, Fig. 6b) does. The average interface shear stress value at rupture computed according to equation (2) can therefore be assumed as a comparative value, but care should be taken in using this value for quantitative design purposes. Most importantly, the centrifugal ice adhesion test must be run using identical plate material for all samples to be compared, to avoid additional confounding effects on the measured ice adhesion values.

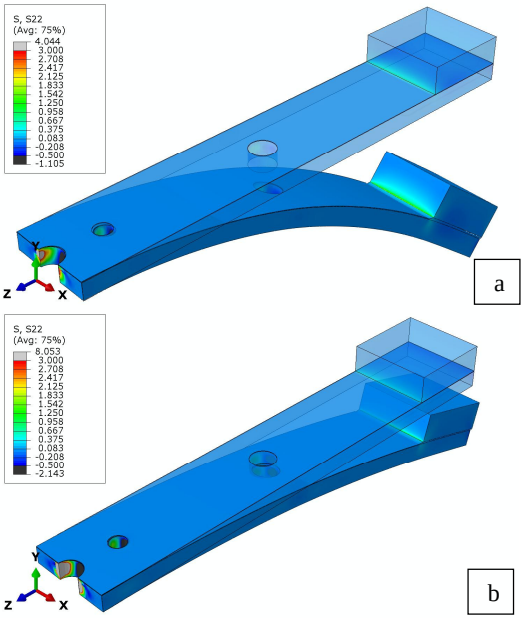

Figure 6: Plots of σ_{22} on original and deformed configuration in the case of a) Al and b) steel substrates. Deformation is enhanced x200 times in both cases.

B. Surface properties

The surface is said to be hydrophobic if the contact angle (CA) is greater than 90º and hydrophilic if the CA is less than 90º. The maximum CA is 180º and minimum 0º. Surfaces with CAs close to these extremes are called either superhydrophobic (>150º) or superhydrophilic (<5º) [19]. The mobility of the droplet may be described by dynamic contact angle parameters: 1) advancing CA is the CA observed at the front end of a moving droplet, 2) receding CA is the CA at the rear end of a droplet and 3) CA hysteresis is the remainder between advancing and receding CAs. A surface with advancing and receding CAs close together has a low CA hysteresis and the droplet easily slides or rolls on the surface.

Table 4 summarizes the static and dynamic CA values. Superhydrophobic SH1 and SH2 coatings had the highest CA values and the lowest hysteresis, which indicates the high mobility of the water droplet. The PTFE reference sample also has relatively low hysteresis although it behaves hydrophobically. Hydrophobic coatings H1 and H2 have similar water droplet behavior whereas H3 has higher CA and also higher hysteresis. H1, H2 and H3 are all fluorine containing polymers, which have been considered to provide low surface energy values. Various fluorine containing coatings have been studied e.g., in [20-22].

Table 4: Contact angle values (CA_Stat: static, CA_Adv: advancing, CA_Rec: receding and Hysteresis) of surfaces.

Ice adhesion increases	Sample	CA_Stat (°)	CA_Adv (°)	CA_Rec (°)	Hysteresis (°)
	PTFE	100	108	92	16
	SH2	165	166	164	2
	SH1	159	165	155	10
	H2	114	123	98	25
	H1	113	116	91	25
	H3	139	148	104	44
	Al	66	80	20	60
Superhydrophobic		Hydrophobic		Hydrophilic	

In addition to the wettability, surface roughness was evaluated. Table 5 presents roughness values Ra (2D values) and Sa (3D values) for the studied samples. Hydrophobic coatings (H1, H2, H3) have different the roughness values. Furthermore, the superhydrophobic coating SH1 has higher roughness compared with the SH2 coating. The surface roughness (Sa) of very smooth Al and PTFE was not measured.

Table 5: Surface roughness values Ra and Sa for the samples measured by using optical profilometer.

Sample	Ra (µm)	Sa (µm)
H1	1.08	3.01
H2	0.61	0.85
H3	9.45	14.28
SH1	2.89	6.84
SH2	0.34	0.7
PTFE	0.14	N/A
Al	0.17	N/A

Figures 7 and 8 present the 3D-surface profiles. In Fig. 7, the surface profiles of the hydrophobic samples, H1, H2 and H3, are presented from the smoothest to coarser surface. The H2 coating has relatively smooth surface containing only fine asperities. The H1 coating has larger variation in the shape of asperities and its surface is consisting of small cavities, which are surrounded by elevated areas creating golf ball-like surface structure. The H3 coating, in turn, has a large variety of different shapes of asperities and its surface is relatively coarse.

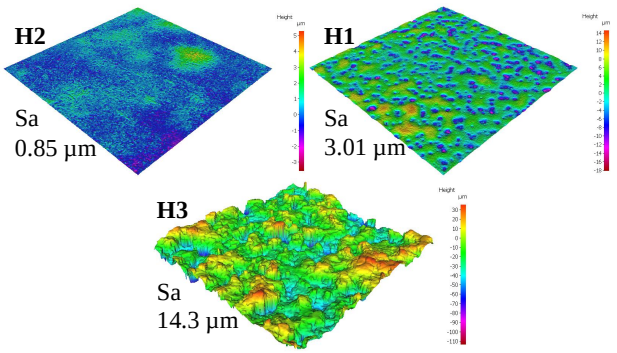

Figure 7: Surface profiles of hydrophobic coatings (H2, H1 and H3).

The 3D-surface profiles of superhydrophobic surfaces are presented in Fig. 8. The surface topographies of these surfaces differ rather significantly from each other. The SH2 coating has relatively smooth surface with only a few higher asperities whereas the topography of the SH1 coating is much coarser, and its surface consists of deep valleys surrounded by either flat or elevated areas. Furthermore, the coarseness of SH1 might have influence on the CA hysteresis of the sample because the water droplet might impinge on the valleys of the surface,

which decreases its mobility (the CA hysteresis of SH1 and SH2 are 10° and 2°, respectively).

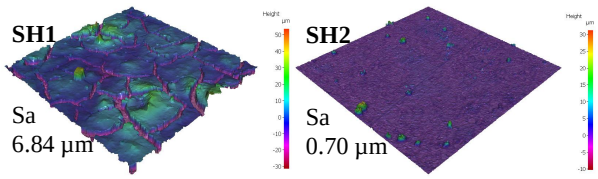

Figure 8: Surface profiles of superhydrophobic coatings (SH1 and SH2).

C. Ice adhesion

Ice adhesion was measured as an average of five measurements. The ice adhesion values with standard deviations are presented in Figure 9. Normal ice was used in this test, which results in the experimental conditions matching closely with the modelled geometry and material properties (Figs. 3,5,6). The uncoated Al plate has the highest ice adhesion whereas PTFE has the lowest. Ice adhesion of superhydrophobic coatings (SH1 and SH2) is close to that of PTFE, indicating good icephobic behavior of superhydrophobic coatings. Icing behavior of hydrophobic coatings H1 and H2 is similar whereas H3 has much higher ice adhesion value.

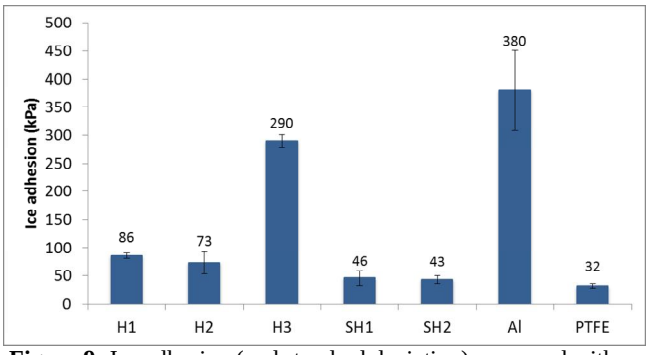

Figure 9: Ice adhesion (and standard deviation) measured with centrifugal ice adhesion test of surfaces.

Relationships between ice adhesion and other surface properties (static CA, hysteresis and surface roughness Ra) are shown in Figure 10. As Fig. 10a indicates, there is no clear relationship between ice adhesion and contact angle (CA). Both superhydrophobic and hydrophobic surfaces can have low ice adhesion values, indicating good icephobicity. Hysteresis vs. ice adhesion, in turn, has clearer connection. This was also noticed in other studies [21, 23]. Surfaces with low hysteresis have lower ice adhesion values (Fig. 10b).

Surface roughness and ice adhesion are also connected. Lower surface roughness usually leads to lower ice adhesion. However, in this study, the surface of the smooth Al plate has low roughness but high ice adhesion, which is due to the material properties. Smooth surface alone does not guarantee low ice adhesion, because other factors such as wettability and surface energy also have impact on adhesion [20,24,25]. PTFE and other fluorine containing polymers are known as low surface energy materials. On the other hand, aluminum has significantly higher surface energy value, which causes high difference in ice adhesion values. [22]

Hydrophobic H1 and H2 coatings showed roughly two times higher ice adhesion values compared to superhydrophobic SH1 and SH2 coatings. Wetting behavior of the droplets has been typically described by Cassie, Wenzel or mixed Cassie-Wenzel states. These tell how the droplets will settle on the surface. In Wenzel state, the liquid will penetrate into the surface roughness whereas in Cassie state, the air will entrapped in the roughness of the surface. The mixed Wenzel-Cassie state is the combination of these two states. [26,27] SH1 and SH2 surfaces are in the Cassie wetting mode due to their high CA and low CA hysteresis. In the Cassie wetting state, the droplets are placed on atop of surface roughness peaks which decrease the ice-solid contact area. The wetting mode of hydrophobic H1 and H2 coatings is, in turn, the mixed Wenzel-Cassie. In this mixed Wenzel-Cassie mode, the droplets can penetrate deeper into cavities of the surfaces creating larger ice-solid contact area. It has been discussed that the larger ice-solid contact area inflicts higher ice adhesion strengths. [19,28,29].

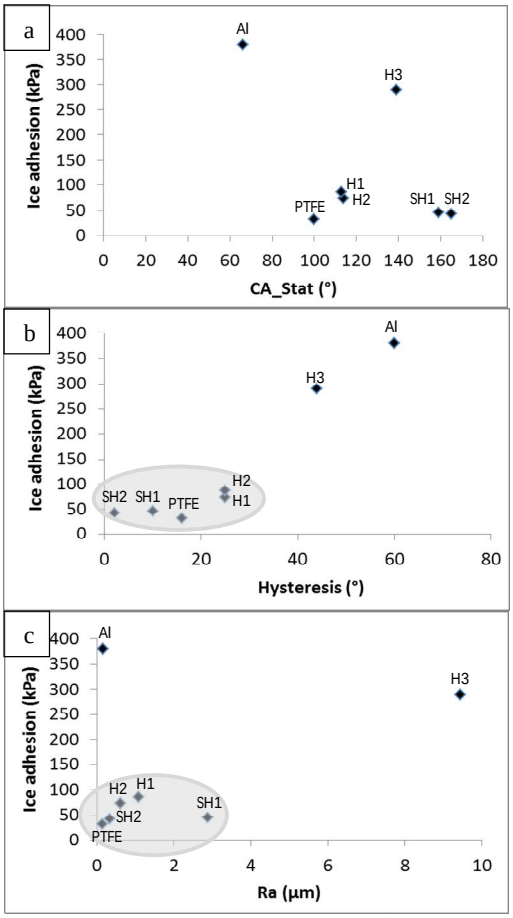

Figure 10: Ice adhesion (IA) versus surface properties: a) IA vs. static contact angle (CA_Stat), b) IA vs. Hysteresis and c) IA vs. surface roughness (Ra).

In literature, one major research approach has been the study of superhydrophobic coatings for the prevention of icing or the minimization of ice adhesion on the surfaces, e.g., in [24,30]. However, opposite opinions have been presented for the speculations of the effectiveness of superhydrophobicity in ice prevention [31,32]. In this study, superhydrophobic coatings showed good icephobic behaviour comparable with PTFE material. However, hydrophobic coatings with low roughness had also relatively good icing behaviour with relatively low ice adhesion values. The surface roughness is a complex phenomenon and suitable texture is dependent on the icing mechanism. Similar to the observations in this study, usually a decrease in roughness reportedly leads to a decrease in ice adhesion [25,33,34].

III. Conclusions

Icing wind tunnel and centrifugal ice adhesion measuring equipment were designed and constructed at TUT. One benefit

of this equipment is that icing conditions can be varied. In addition, different types of ice (rime and glaze ice) can be formed.

In this study, fluoropolymeric coatings taken as examples of hydrophobic and superhydrophobic behavior showed reasonable or low ice adhesion values. These results showed no clear connection between static contact angle and ice adhesion, whereas hysteresis and surface roughness have clearer connection to the ice adhesion. Surfaces with low hysteresis had low ice adhesion. In addition, low surface roughness (except for the smooth Al plate) enables to get lower ice adhesion and thus, better icephobic behavior.

The next research step is to study the effect of different icing conditions and the ice type on the icing properties of the selected surfaces. In the future, the research will be focused on the improvement of wear properties of icephobic coatings.

ACKNOWLEDGMENT

The author would like to thank the staff of the Department of Materials Science, Tampere University of Technology (Tampere, Finland) for helping with a construction of the icing test facilities. This research was done partly in the frame of Hydrobond project (EU, FP7, NMP3-SL-20012-3100531).

REFERENCES

[1] Windpower Engineering and Development, website: http://www.windpowerengineering.com/maintenance/detecting-ice-on-wind-turbine-blades/, cited 6/2015.

[2] P. Guest, Vessel Icing, Mariners Weather Log, 49(3), 2005, 1 p.

[3] L. Cao, A.K. Jones, V.K. Sikka, J. Wu, D. Gao, Anti-Icing Superhydrophobic Coatings, Langmuir, 25(21), 2009, p. 12444–12448.

[4] C.C. Ryerson, Assessment of Superstructure Ice Protection as Applied to Offshore Oil Operations Safety, ERDC/CRREL TR-09-4, 2009, p. 344

[5] P. Kim, T.-S. Wong, J. Alvarenga, M.J. Kreder, W.E. Adorno-Martinez, J. Aizenberg, Liquid-Infused Nanostructured Surfaces with Extreme Anti-Ice and Anti-Frost Performance, ACS Nano, 6(8), 2012, p. 6569–6577.

[6] J. Lv, Y. Song, L. Jiang, J. Wang, Bio-Inspired Strategies for Anti-Icing, ACS Nano, 2014, p. 18.

[7] S. Jung, M. Dorrestijn, D. Raps, A. Das, C.M. Megaridis, D. Poulikakos, Are Superhydrophobic Surfaces Best for Icephobicity?, Langmuir, 27, 2011, p. 3059–3066.

[8] C.C. Ryerson, Ice protection of offshore platforms, Cold Regions Science and Technology, 65, 2011, p. 97–110.

[9] V. Hejazi, K. Sobolev, M. Nosonovsky, From superhydrophobicity to icephobicity: forces and interaction analysis, Scientific Reports, 3(2194), 2013, 6 p.

[10] M.C. Homola, P.J. Nicklasson, P.A. Sundsbø, Ice sensors for wind turbines, Cold Regions Science and Technology, 46, 2006, p. 125–131.

[11] B. Tammelin, K. Säntti, Icing in Europe, BOREAS IV, 1998, p. 125-132.

[12] A.G. Kraj, E.L. Bibeau, Phases of icing on wind turbine blades characterized by ice accumulation, Renewable Energy, 35, 2010, p. 966–972.

[13] C. Peng, S. Xing, Z. Yuan, J. Xiao, C. Wang, J. Zeng, Preparation and anti-icing of supehydrophobic PVDF coating on a wind turbine blade, Applied Surface Science, 259, 2012, p. 764–768.

[14] P. Tourkine, M. Le Merrer, D. Quere, Delayed Freezing on Water Repellent Materials, Langmuir, 25(13), 2009, p. 7214–7216.

[15] F. Arianpour, M. Farzaneh, S.A. Kulinich, Hydrophobic and ice-retarding properties of doped silicone rubber coatings, Applied Surface Science, 265, 2013, p. 546– 552.

[16] C. Laforte, A. Beisswenger, Icephobic Material Centrifuge Adhesion Test, International Workshop on Atmospheric Icing of Structures (IWAIS) XI, Montreal, June 2005, 4 p.

[17] P.H. Gammon, H. Kiefte, J.M. Clouter, W.W. Denner, Elastic Constants of Artificial and Natural Ice Samples by Brillouin Spectroscopy, Journal of Glaciology, 29(103), 1983, p. 433-460.

[18] ISO-12494 standard, Atmospheric icing of structures, The Internatiol Standardization Organization, 2001, p. 56.

[19] X. Zhou, X. Guo, W. Ding, Y. Chen, Superhydrophobic or superhydrophilic surfaces regulated by micro-nano structured ZnO powders, Applied Surface Science, 255, 2008, p. 3371–3374.

[20] S. Farhadi, M. Farzaneh, S. Simard, On Stability and Ice-Releasing Performance of Nanostructured Fluoro-Alkylsilane-Based Superhydrophobic Al alloy2024 Surfaces, International Journal of Theoretical and Applied Nanotechnology, 1(1), 2012, p. 38-44.

[21] S. Kulinich, M. Farzaneh, How wetting hysteresis influences ice adhesion strength on superhydrophobic surfaces, Langmuir , The ACS Journal of Surfaces and Colloids, 25(16), 2009, p. 8854-8856.

[22] S. Yang, Q. Xia, L. Zhu, J. Xue, Q. Wang, Q. Chen, Research on the icephobic properties of fluoropolymer-based materials, Applied Surface Science, 257(11), 2011, p. 4956–4962.

[23] G. Momen, R. Jafari, M. Farzaneh, Ice repellency behaviour of superhydrophobic surfaces: Effects of atmospheric icing conditions and surface roughness, Applied Surface Science, 349, 2015, p. 211–218.

[24] L. Makkonen, Ice Adhesion - Theory, Measurements and Countermeasures, Journal of Adhesion Science Technology, 26, 2012, p. 413–445.

[25] M. Zou, S. Beckford, R. Wei, C. Ellis, G. Hatton, M.A. Miller, Effects of surface roughness and energy on ice adhesion strength, Applied Surface Science, 257, 2011, p. 3786–3792.

[26] R.N. Wenzel, Resistance of solid surfaces to wetting by water, Industrial and Engineering Chemistry, 28, 1936, p. 988-994.

[27] A.B.D. Cassie, S. Baxter, Wettability of porous surfaces, Transactions of the Faraday Society, 40, 1944, p. 546-551.

[28] S. Farhadi, M. Farzaneh, S.A. Kulinich, Anti-icing performance of superhydrophobic surfaces, Applied Surface Science, 257(14), 2011, p. 6264–6269.

[29] G. Fortin, J. Perron, Ice Adhesion Models to Predict Shear Stress at Shedding, Journal of Adhesion Science and Technology, 26(4-5), 2012, p. 523–553.

[30] O. Parent, A. Ilinca, Anti-icing and de-icing techniques for wind turbines: Critical review, Cold Regions Science Technology, 65(1), 2011, p. 88–96.

[31] T. Bharathidasan, S. V. Kumar, M. S. Bobji, R. P. S. Chakradhar, and B. J. Basu, Effect of wettability and surface roughness on ice-adhesion strength of hydrophilic, hydrophobic and superhydrophobic surfaces, Applied Surface Science, 314, 2014, p. 241–250.

[32] S. Kulinich, S. Farhadi, K. Nose, X. W. Du, Superhydrophobic surfaces: are they really ice-repellent?, Langmuir, 27(1), 2011, p. 25-29.

[33] M. F. Hassan, H. P. Lee, S. P. Lim. The variation of ice adhesion strength with substrate surface roughness, Measurement Science and Technology, 21, 2010, 9 p.

[34] M. Susoff, K. Siegmann, C. Pfaffenroth, M. Hirayama, Evaluation of icephobic coatings - Screening of different coatings and influence of roughness, Applied Surface Science, 282, 2013, p. 870–879.

A Comparison of Three Different Anti- and De-Icing Techniques Based on SCADA-Data

Kolar S[1]
[1] Uppsala University
sandra.j.kolar@gmail.com

***Abstract*: This work is a master thesis done within the master program in energy systems engineering at Uppsala University and in cooperation with OX2. The aim is to compare the operation and performance of three different anti- and de-icing systems (ADIS) for wind turbines (WTGs) during the winter 2014/2015. The systems evaluated are de-icing with heating resistances, de-icing with warm air and anti-icing with heating resistances.**

Inconsistency in the operation of the wind WTGs and the ADISs as well as lack of information made it hard to compare the efficiencies of the systems. The systems showed tendencies to improve the production. Especially examples during single ice events where the systems increased the power output were found, but the examples also showed possible improvements regarding the size of the systems and the duration of the de- or anti-icing cycles. Based on the approximated gain in production, during the studied time period, none of the systems could be determined to be profitable. The gain in production does however not have to be especially large for the systems to become profitable, and the results could be very different in a year with more ice, higher electricity prices or a more consistent operation of the systems.

Important characteristics of the systems were found to be the duration of a cycle, the energy required for the operation of the system and the trigger-point for activation of the system. Additional benefits like for instance decreased loads, risk for standstill and ice throws could also be provided by the systems.

Keywords: ice, anti-icing, de-icing, losses

Legend and Abbreviations

ADIS	*Anti- and De-Icing Systems.*
Anti-icing systems	*Systems that prevents ice accretion on the blades of the WTG.*
De-icing systems	*Systems that aims to remove ice from the blades once already formed.*
Overproduction	*Production higher than expected, due to for instance frozen anemometers.*
Production Loss	*Output lower than expected according to the power curves.*
Wind Farm 1	*Wind farm with a de-icing system based on heating resistances.*
Wind Farm 2	*Reference to Wind Farm 1.*
Wind Farm 3	*Wind farm with a de-icing system based on warm air.*
Wind Farm 4	*Reference to Wind Farm 3.*
Wind Farm 5	*Wind farm with an anti-icing system based on heating resistances.*
Wind Farm 6	*Reference to Wind Farm 5.*
WTG	*Wind Turbine Generator*

Introduction

A. Background

Ice accretion on the blades of the Wind Turbine (WTG) causes a lower energy production compared to the energy production in the same wind conditions with no ice, and thereby results in a loss of income for the owner of the WTG. WTGs in cold climates, like the climate in the north of Sweden, could have an anti- or de-icing system (ADIS) installed to prevent losses due to ice. In this report anti-icing refers to systems that aim to prevent ice from forming on the blades of the turbine whereas de-icing refers to systems with the strategy to remove ice once it already has been formed on the surface. Since there is no general technique for ADIS, it is of interest to learn more about the operation and efficiency of different de- and anti-icing systems, in order to minimize the losses and maximize the income of a wind farm.

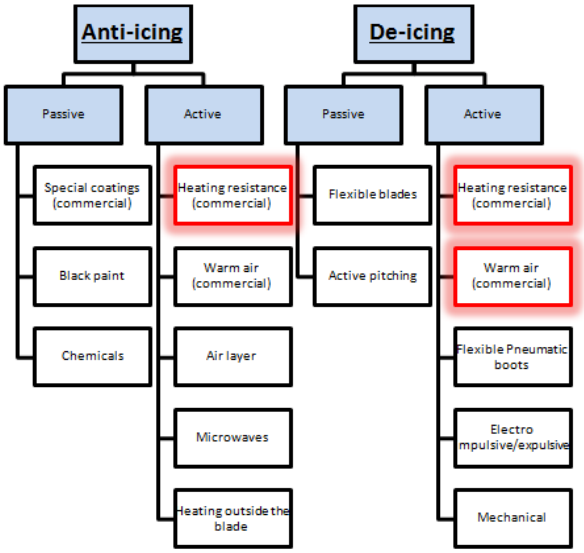

Figure 1: Overview of different de- and anti-icing strategies. The evaluated techniques in the report are marked in red (anti-icing with heating resistancs, de-icing with heating resistances and de-icing with warm air).

B. Aim

This work is a master thesis within the master program in energy systems engineering at Uppsala University and covers 30 credits. The thesis is done in cooperation with OX2, a privately held Swedish company active within the renewable energy sector. The aim of the work was to compare the operation and efficiency of three different ADISs installed in three wind farms operated by OX2 in Sweden. The de- and anti-icing techniques that were evaluated are de-icing with heating resistances, anti-icing with heating resistances and

de-icing with warm air (in red in Figure 1). The main focus has been to evaluate the production of the wind farms during the winter 2014/2015. The performance was evaluated against the production in conditions considered to be free from ice, against a wind farm nearby the evaluated wind farm without an ADIS installed (reference farms) and against the other ADISs studied.

I. Method

Today production losses due to icing are calculated with many different methods. IEA Task 19 - Wind energy in cold climates, a working group within IEA Wind, are currently working on a standard method (T19IceLossMethod) to evaluate the production losses due to icing [1]. In this work a MATLAB-code was produced based on the main outlines in the proposed standard, with some alterations.

The parameters being used for the evaluation are wind speed, wind direction, ambient temperature, the power output and the state of operation of the turbine. The power output is compared to the output in conditions considered to be ice free, as a first approximation by constructing turbine specific power curves from measurements corresponding to temperatures above +3 °C [1]. In this work wind bins of 1 m/s and 90 ^{O} were used to construct the power curves.

Three types of icing events are identified in the evaluation:

- ***Type A)*** Loss of production
- ***Type B)*** Turbine standstill due to icing or operation of the de- or anti-icing system
- ***Type C)*** Ice influenced wind anemometer resulting in overproduction compared to the power curve.

For all three types of icing events to start, a temperature below 0 $^{\circ}$C is required. There are no temperature requirements for the rest of the ice event. Ice events of type A (production losses) occur if three following measurements (10-minute averages) of the power output are below the 10th percentile (P10) and last until three following measurements are above the P10. Ice event of type B (stand still) start if one measurement is below P10 and the following two measurements indicate a stop of the WTG, i.e. the mean power output is less than 0.5 % of the rated power. The event stops when three following measurements are above P10. Ice event C (overproduction) begins when three following measurements are above the 90th percentile (P90) and ends if three following measurements are below P90 [1]. In the code used, stops of the WTG are identified by the operation state of the WTG instead of limits in the power output as proposed in the standard. The reason for this was to make the calculation of the losses more manageable later on.

The identified ice events are removed from the complete data set and new power curves are constructed. Based on the new power curves, which contain "winter conditions", the final ice events are identified as above. Losses in the production are calculated for icing events of type A and B. The reference production during icing event C cannot be estimated since there is no knowledge about the accurate wind speed [1]. The loss of production during ice event A is defined as the difference between the reference production according to the reference power curve and the actual output and the loss during ice event B is defined as the reference output according to the power curve together with the power input for running the de- or anti-icing system.

A. Validation of the model

In order to validate the estimation of ice losses, data from one summer month (July) and one winter month (December) were compared, see **Error! Reference source not found.**2. Because of lack of data and time this was only done for one evaluated wind farm (Wind Farm 1). It can be seen that the data in July (blue) is much less spread than the data in December (red). The losses for both months were calculated for each WTG by taking the difference between the power curve and the output for all values under P10 for December (green). In July the loss was then found to be 0.7 % of the monthly production on average for the WTGs with a standard deviation of 0.6 % between the WTGs. In December the losses was 5.0 % on average, with a standard deviation of 0.7 %. All WTG stops were removed from the data sets.

Since there are few measurements from July under the power curve, the most common cause for the measurements under the curve in December is probably ice. Deviations could however also be caused for instance by increased turbulence etc. According to the result there are some measurements that will be treated as ice losses that are caused by other factors. For Wind Farm 1 this is about 1 % of the monthly production. This is however without considering the requirement for three following measurements to indicate the start of an ice event, which possibly could reduce the number further. The results are also without the requirement of a temperature below 0 $^{\circ}$C for an ice event to begin, since this obviously would result in no losses during the summer.

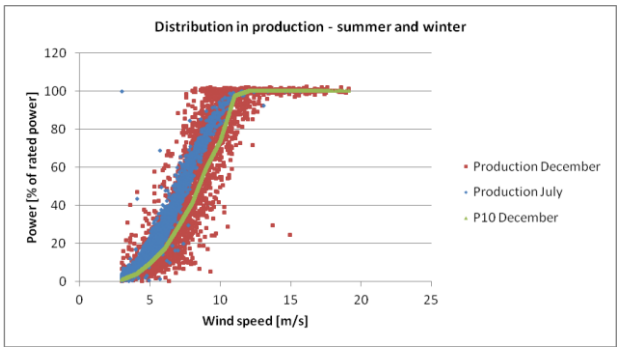

Figure 2: Distribution in production for summer (blue) and winter (red) measurements. The figure shows that most measurements under the P10 (green), in December, probably are due to ice. About 1 % of the measurements in July are however also under the P10 for December, indicating that there are some measurements that will be wrongly identified as ice losses.

II. Results

A. Characteristics of the Studied Systems

Wind Farm 3 (de-icing with warm air) has the lowest installed power for operation of the system in relation to rated power, whereas the system in Wind Farm 5 (anti-icing with heating resistances) has the highest installed power as well as the highest range of power installed. The de-icing system in Wind Farm 3 is the only system using warm air, and the thermal efficiency could therefore be expected to be lower compared to the other two systems according to theory. The de-icing cycle in Wind Farm 3 was found to often be about 5 hours longer in comparison to Wind Farm 1 (de-icing with heating resistances), and the de-icing system in Wind Farm 3 is the only system which treats one blade at the time. Due to the longer de-icing cycle in Wind Farm 3, the availability could be decreased, which would be important if wind conditions are good. Since the winter is the time of year with most wind, according to theory, availability is therefore important. If the duration of a cycle can be altered through the control system this would be avoided, but this doesn't seem to be the case in the examples found. The fact that one blade at the time is de-iced in Wind Farm 3, also speaks

against this, since stopping the de-icing cycle probably could cause imbalances. The system in Wind Farm 1 had a lot more starts per WTG during all months except March compared to Wind Farm 3, which probably is because the studied time period was a test period in Wind Farm 3. Information about the length of the anti-icing cycles and the number of starts during the studied months was not available or possible to identify based on the given information in Wind Farm 5.

B. Impact of Having the De- and Anti-Icing Systems Installed

Based on the approximated losses calculated for each wind farm, the possible "gain" of having the de- or anti-icing systems installed during the evaluated winter (in relation to the reference wind farms) are illustrated in Figure 3. The error bars are describing a confidence interval of 95 %, which means that the difference between the average losses of the two wind farms will be found within the extremes ("lowest gain" and "highest gain") with a certainty of 95 %.

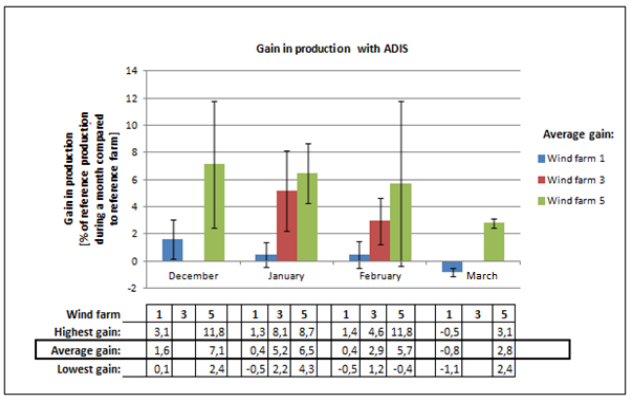

Wind farm	1	3	5	1	3	5	1	3	5	1	3	5
Highest gain:	3,1		11,8	1,3	8,1	8,7	1,4	4,6	11,8	-0,5		3,1
Average gain:	1,6		7,1	0,4	5,2	6,5	0,4	2,9	5,7	-0,8		2,8
Lowest gain:	0,1		2,4	-0,5	2,2	4,3	-0,5	1,2	-0,4	-1,1		2,4

Figure 3: Outcome of having the de- and anti-icing systems installed during the winter 2014/2015. The colored bars show the average production gain in relation to reference wind farms. The error bars are illustrating a confidence interval of 95 %. Energy for operation of the systems is not included for Wind Farms 3 and 5

It can be seen that in the "lowest gain- scenario" i.e. the lower end of the confidence interval, there is no gain of having the system in Wind Farm 1 (de-icing with heated resistances) during the studied period compared to the reference wind farm. This is probably partly because the losses in the reference wind farm (Wind Farm 2) were small as well. In the "lowest gain scenario" the systems in Wind Farms 3 and 5 (de-icing with warm air and anti-icing with heating resistances) show a small gain compared to the reference wind farms, in all cases except Wind Farm 5 in February probably because of the large variation in the corresponding reference wind farm (Wind Farm 6). Energy for operation of the systems in Wind Farms 3 and 5 is however not included, and the bars should be somewhat lower. Since the gain is small, none of the systems can, for certain, be said to be advantageous in this scenario when considering the energy for the operation of the systems. In both the "average gain-" and the "highest gain-scenario" all systems perform better than the reference wind farms, except Wind Farm 1 in March, since the loss in the corresponding reference wind farm was close to zero.

The system in Wind Farm 5 appears to have the highest gain of all systems, but has at the same time the largest variation, which is probably due to a large uncertainty due to lack of data and information. Also Wind Farm 3 is showing a large variation, which could be due to the large uncertainty due to a small number of WTGs and inconsistent operation of the de-icing system. The WTGs in Wind Farm 1 do not show an apparent gain during the studied time period, the confidence intervals are however small, indicating a small variation between the WTGs.

B. Examples of Production During Single Days

Below, the production from one WTG in each wind farm is compared during a day. The purpose with these examples is to get an understanding of the operation of the de-icing system during single ice events.

B.1 Example - Wind Farms 1 & 2

During the 22nd of December the losses during the day for the studied WTG in Wind Farm 1 (de-icing with heating resistances) were about 50 % compared to the reference output, and the losses for the WTG in Wind Farm 2 (reference) about 81 %. It can be seen in Figure 5 that the WTG in Wind Farm 2 was still for 16 hours and the reference output was not achieved during the day. Since there were no error messages or manual stops and the wind speed was above cut-in wind speed, the stop was probably due to ice. The de-icing system of the WTG in Wind Farm 1 was activated 9 times, marked 1-9 in Figure 4, and for each de-icing cycle about 3 % of the rated power was used for the operation of the de-icing system. The de-icing cycles lasted for 40 minutes in all cases but one, where it lasted for 60 minutes. Between cycles 2 and 9 the de-icing system was reactivated within 20-40 minutes after the end of a cycle. The reference power was achieved about 1.5 hours after de-icing cycle 9. The many starts of the system indicate that one de-icing cycle does not ensure that the production reaches the reference output and perhaps there is room for improvement regarding power, control etc.

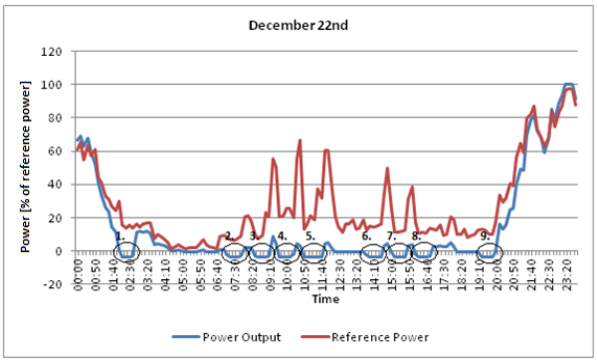

Figure 4: Output of a WTG with de-icing, during the 22nd of December. The de-icing system was started 9 times, marked 1-9 in the figure. The loss was about 50 % compared to the reference output. At 21:30 the production was 87 % of the reference output.

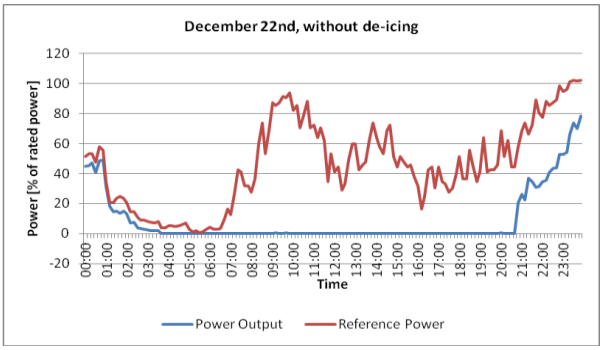

Figure 5: Output of a WTG without de-icing, during the 22nd of December. The WTG was at standstill for about 16 hours and the loss was about 81 % of the reference output. At 21:30 the production was 48 % of the reference output.

B.2 Example - Wind Farms 3 & 4

During the 1st of February the loss for the WTG in Wind Farm 4 (reference) was about 34 % during the day, see Figure 7. The de-icing system of the WTG in Wind Farm 3 (de-icing with warm air) was started 3 times during the day, see Figure 6, and the loss was about 76 %. If the energy for running the de-icing system is included the loss is about 77 % instead. Each de-icing cycle takes about 6 hours. After the first cycle the output is a maximum 45 % of the reference output and after the second de-icing cycle 55 % of the reference output. This indicates that the de-icing system was not able to remove the ice.

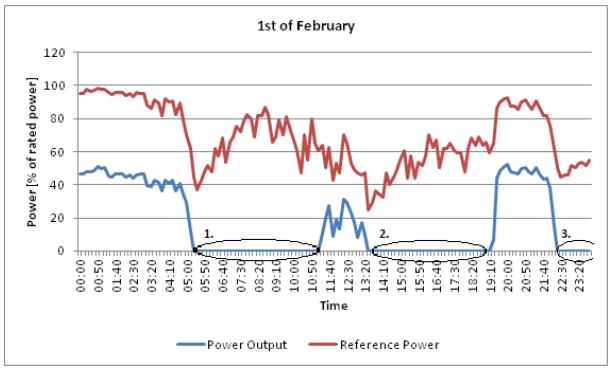

Figure 6: Output with de-icing system, 1st of February. The losses during the day are about 77-76 % of the reference output. At 20:50 the output is about 55 % of the reference output.

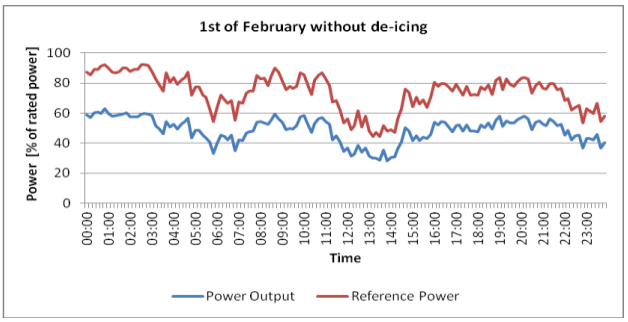

Figure 7: Output without de-icing, 1st of February. The losses during the day are about 34 % of the reference output. At 20:50 the output is about 68 % of the reference output.

B.3 Example - Wind Farms 5 & 6

There is no information about the operation of the anti-icing system in Wind Farm 5 and the length of the anti-icing cycles and the number of starts during the studied months was not possible to identify. It was therefore not found to be of interest to illustrate the production with an example

III. Conclussions

In this work a MATLAB-script for evaluating losses in production of WTGs due to ice was created according to the main outlines in a standard proposed by IEA task 19. The losses due to ice, between December 2014 and March 2015, were then estimated in three wind farms with de- or anti-icing installed and three additional wind farms without any de-or anti-icing installed.

From the evaluation, it is evident that all studied sites are subject to ice. Based on the results obtained the three wind farms with a de- or anti-icing system installed show a tendency to improve the production in comparison to the evaluated reference parks. The quantification of the losses are however influenced by the model for evaluation, inconsistent operation of the systems and the WTGs, inconsistent data reporting and lack of information about the studied systems. It was therefore not possible to compare the efficiencies of the three systems.

In particular, one of the studied systems (de-icing with heating resistances) could be shown to improve the production during single ice events, which shows the potential of having a de- or anti-icing system installed. The results also indicate that the de-icing system with warm air not is sufficient enough, this could however partly be because the studied time period was a testing period of the system. The information about the anti-icing system with heating resistances was too sparse to evaluate the system. The studied examples showed possible improvements regarding for instance size and duration of the de-icing cycles, reflecting the limited experience of the operation of the systems. With a couple of more years of experience, the operation of the systems may become more efficient and profitable.

Based on the approximated gain (between December and March) none of the studied systems can, for certain, be said to be profitable with today's electricity prices. The evaluation is however entirely based on the difference in losses compared to the reference wind farms and is very uncertain. The conditions could be very different in a year with more icing and higher electricity- and certificates prices. A longer time period therefore needs to be studied and more information about the operation of the systems is needed in order to determine the profitability and efficiency of the systems. Considering de- or anti-icing systems when establishing wind farms at locations with similar ice conditions is recommended. Important characteristics are then energy for operation of the system, duration of one de- or anti-icing cycle and when the systems are activated. Important to consider is also possible additional benefits of the systems as for instance increased availability, decreased risk for stops, loads and fatigue of WTG components as well as safety aspects.

It is clear from the work that a standard method for evaluating losses due to ice is needed. The main guidelines should contain a method of how to form the reference output (i.e. the ice free production) and definitions of what to consider as losses due to ice, which is handled in the proposed standard. In addition information about how to handle overlapping ice events and how to take the operation of a de- or anti-icing system into account when calculating the losses needs to be included.

C. *7.2 Future Work*

Most important in order to evaluate the performance of the systems is to study a longer time period, so that different icing conditions are included and a more acceptable statistical basis is given. In addition more information about the operation of the systems needs to be known to evaluate the systems, in particular knowledge about signals for when the systems are activated, in operation and measurements of the energy required to run the systems is needed. It is also important to study the production during the summer months in order to gain knowledge about normal occurring variations in output, both within the evaluated wind farms and in relation to the reference wind farms.

It would also be recommended, if possible, to do evaluations where the de- or anti-icing systems of some WTGs within the studied wind farms are turned off during known time periods. This would result in better references, than the reference wind farms used in this work, and therefore give a better and more accurate estimation of the efficiency. It would also be advantageous to study known ice events, not only identified by deviations in the power curve.

Suggested studies would then be to evaluate in which conditions the systems are able to remove ice and when they are profitable to run, and which improvements that can be made regarding starts of the system, the duration of the de-icing cycles and if the power of the system, in particular in Wind Farm 3, could be improved.

The MATLAB-code created to estimate the losses had some flaws that would have to be improved if used in further studies. First of all using another smoothing function is advisable since the power curves and percentiles tended to be underestimated. It would be beneficial to see evaluations of the approach of using P10 and P90 compared to other statistical measurements and also the impact of evaluating all months together, since by evaluating the months separately there will always exist a P10 and P90, even during summer months, and ice events probably risk to be under- or overestimated in years with much or little ice respectively.

ACKNOWLEDGMENT

I would like to thank all the people that in some way have contributed to this work with knowledge, advice or encouragement. I would especially like to thank my supervisor at OX2, Martin Löfstrand, for commitment, guidance and a positive attitude throughout the work and my subject reader, Anders Goude, at Uppsala University for advice and thorough reading. I would also like to thank the coworkers at OX2 for a pleasant working environment and Göran Ronsten and the other members of IEA task 19 for contributing with information and discussion.

REFERENCES

[1] IEA Task 19 - Wind energy in cold climates, "Standardized method to assess production losses due to icing from wind turbine SCADA data (T19IceLossMethod)", IEA Wind (rev 0.5), 2014

Effect of alkyl chain length on the hydro/ice-phobic properties of self-assembled monolayers (*SAM*s) coatings on aluminum alloy 6061 surfaces

F. Arianpour*, M. Farzaneh, R. Jafari,
Canada Research Chair on Atmospheric Icing Engineering of Power Networks (INGIVRE) www.cigele.ca
Université du Québec à Chicoutimi, Canada
*Email: faranak.arianpour@uqac.ca

Abstract- The effects of alkyl chain length on hydro/ice-phobic properties were studied through self-assembled monolayers (SAMs) thin films of an alkylsilane compound, OT (trichloro(octyl)silane, 8C) and OD (trichloro(octadecyl)silane, 18C), on a flat aluminum alloy (AA6061) substrate. The contact angle (CA) values for OD and OT coatings after a 12-hours immersion time (IT) were ~140° and ~120°, respectively. The contact angle hysteresis (CAH) for the OD sample was ~38° and ~55° for the OT sample after the 12-hour immersion. The ice adhesion reduction factor (ARF) of the OD and OT samples showed that the ice adhesion strength values are ~1.24 and ~1.05 times smaller than those obtained on a polished Al sample, respectively. It was shown that the hydro/ice-phobic properties of the OD sample was more improved compared to the OT sample. This behavior could be explained by the reduction of the molecular reactivity caused by the *steric effect* in case of the OT sample on a polished Al surface. The surface morphology of the surfaces was analyzed by scanning electron microscopy (SEM). The SEM micrographs of the coated surfaces demonstrated the presence of a rough structure at micro/nanoscale levels on the mirror-polished Al substrate.

Keywords: self-assembled monolayers (*SAM*s); hydro/ice-phobic properties; scanning electron microscopy (SEM); ice adhesion reduction factor (*ARF*); steric effect.

INTRODUCTION

Atmospheric icing occurs when surfaces of exposed structures are hit with supercooled water droplets or snow particles. For instance, overhead transmission lines and their substations can be subjected to ice accumulations for an extended period of time each year [1,2]. These may cause damage to power network equipment [3-5]. Reducing or preventing ice accumulation on exposed surfaces can be accomplished by developing ice-phobic coatings [6-10]. The wetting behavior of a surface can be determined by the contact angle (CA) which is the angle between the surface and a water liquid drop [11]. Development of self-assembled monolayer (*SAM*) coatings with $-CH_3$ or $-CF_3$ groups oriented outward from the ice surface is one of the most successful approaches to chemically modified hydrophilic surfaces [12]. The *SAM*s through processes involving adsorption, hydrolysis, and polymerization can lead to spontaneously assembled low energy surfaces on many solids and oxides (Al_2O_3, SiO_2, etc.) [13-16]. In the present study, the effects of alkyl chain length on the hydrophobic and ice-phobic properties of *SAM*s coatings of OT (trichloro(octyl)silane, 8C) and OD (trichloro(octadecyl)silane, 18C) on polished aluminum alloy 6061 (AA6061) will be investigated.

I. EXPERIMENTAL PROCEDURE

Aluminum alloy 6061 composed of Al 97.9 wt.%, Mg 1.0 wt.%, Si 0.60 wt.%, Cu 0.28 wt.%, Cr 0.20 wt.% from industrial rolled sheets was cut into 5.1 × 3.2 cm samples, that were used as substrates. This alloy is widely used for power transmission and distribution line conductors. Organic molecules providing low surface energy, Trichloro(octadecyl)silane ($C_{18}H_{37}Cl_3Si$) and Trichloro(octyl)silane ($C_8H_{17}C_{l3}Si$), were purchased from Sigma-Aldrich®. The as-received AA6061 samples were ultrasonically cleaned in acetone and distilled water each for 5 minutes. Subsequently, the cleaned samples were first mechanically polished using 320-800-1200 and 4000-grit sand paper, then with successively finer SiC abrasive. Finally, they were mirror-polished with aqueous 1.0 μm alumina slurry. The polished substrate were then cleaned and degreased ultrasonically in organic solvents of methanol (99.8%), acetone (99.5%) and finally de-ionized water. The cleaned and polished Al plates were then blow-dried in a N_2 gas flow followed by a 1-hour post-treatment in oven at 70 °C. Later, they were placed in *SAM*s baths of octadecyltrichlorosilane (OD) in toluene (1 mM) and octyltrichlorosilane (OT) in toluene (1 mM) by the dip coating method. The substrates were then removed from their respective solutions after 15 minutes, 2, 6, and 12 hours. They were then rinsed with toluene and blow dried under nitrogen gas. Finally, they were post-treated in an oven for 2 hours, drying at 70 °C.

The dried samples were characterized by measuring their hydrophobic and ice-phobic properties. The wetting characteristics reported in this study were obtained following the standard sessile drop method on a fully automated contact angle goniometer (DSA100 from Krüss) with controllable volume (4 μl) of water droplets. Surface topographies were studied via scanning electron microscopy (SEM, Hitachi S-4700 Field-Emission SEM with accelerating voltages from 500 V to 25 kV) to take surface images of the coated samples and therefore reveal their surface characteristics. The ice-repellent performance of bare as well as prepared coatings was evaluated using a home-made centrifugal apparatus which was placed in a climate room at subzero temperature (-10°C). The detail of the ice preparation procedure has been described previously [7].

II. RESULTS AND DISCUSSION

Figure 1 shows the IT effect of alkylsilane with short chains (OT) on the hydrophobic properties. The concentration of OT in this series of experiments was 1 mM OT diluted in toluene. By increasing IT from 2 h

to 12 h, the CA value of aluminum coated with OT increased from ~ 90° to ~ 121° while the CAH values decreased from ~ 77° to ~50°.

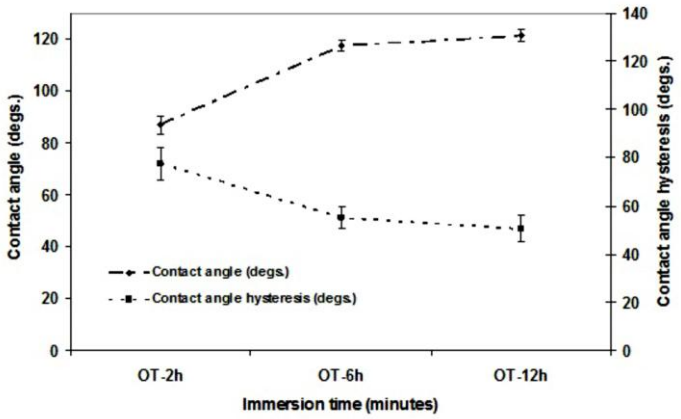

Figure 1: Contact angle and contact angle hysteresis values of coated samples with OT (1mM) for different ITs.

In order to study the effect of chain length on wetting characteristics and ice-phobic properties, dissimilar alkylsilanes in term of chain length were chosen, i.e. 18 carbon (trichloro(octadecyl)silane, OD) with similar chemical component to 8 carbons (trichloro(octyl)silane, OT). Figure 2 shows the CA and CAH values of sample surfaces coated with OD (1 mM). By increasing the IT from 15 min to 12 hours, the CA values of the coated samples increased, in such a way that, a remarkable enhancement of CA to ~152° was observed after 12-h IT, with regards to superhydrophobic characteristics. As seen from Figure 2, CAH decreased over time, as IT increased from 15 minutes to 12 hours. A CAH decrease of ~ 32° was also obtained in the case of coatings with 12-h IT, whereas the CAH of other coatings was ~40-70° (for samples with15 min, 2 and 6 h IT).

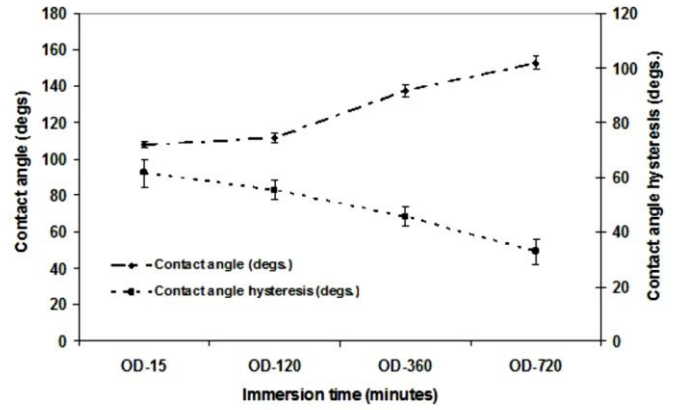

Figure 2: CA and CAH values of coated samples with OD (1mM) for different ITs.

As observed earlier, increasing IT from 15 min to 12h resulted in a significant enhancement of the hydrophobic properties of the samples coated with OD (1 mM) as compared to the short chain alkylsilane (OT). Thus, the IT parameter plays a very important role on the self-assembly process [17]. The reason of the observed results concerning the wetting properties of OD coatings as well as the remarkable increase in CA by increasing the IT is probably due to well-ordered *SAM* structure on the aluminum oxide layer compared to that of the shorter IT [18, 19]. However, in case of short chain alkylsilane, this is probably due to the rise of the *steric effect* that prevents *SAM*s molecule structures on the aluminum oxide layer from ordering well [20].

Figure 3 shows scanning electron microscopy (SEM) analysis for the OT coated Al surface (1 mM). The SEM images of the surface coated with OT shows a distribution of white points and trenches at the micrometer scale, as seen in Figure 3 (a and b).

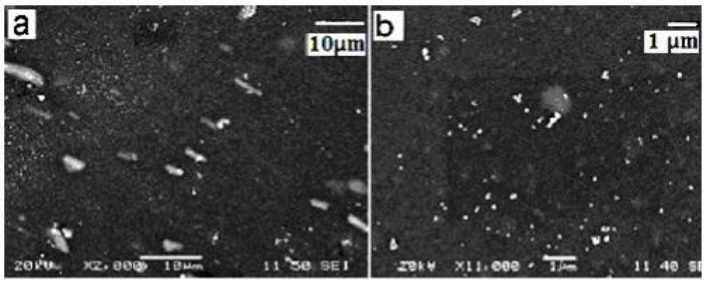

Figure 3: Scanning electron microscopy (SEM) images of sample coated with OT (12 hours). Magnification is (a) 2000X, (b) 11000X.

Figure 4 shows SEM images of the Al sample coated with OD (1 mM) for a 12-hour IT with 2000X and 11000X magnifications. Rough structure at micro-/nano-metre scale as well as the distribution of some branches in several parts on the polished aluminium surface were observed in the case of coated samples with OD (1 mM) (Fig.4 a and b). This micro/nanoscale roughness was obtained following the immersion of aluminium samples in a chemical solution bath, which corresponds to the hydrolysis step of the *SAM*s process, where chloride ions are released to form hydrochloric acid (HCl). More precisely, as HCl contains aggressive ions of Cl^-, the aluminium surface sample are subjected to erosion as IT Is increased. This reaction is expressed by the following equation [21]:

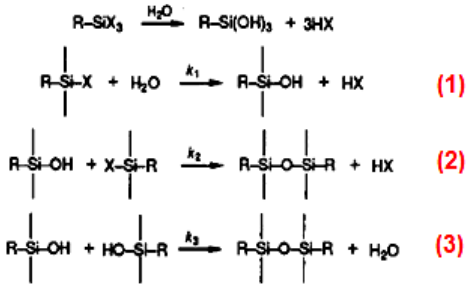

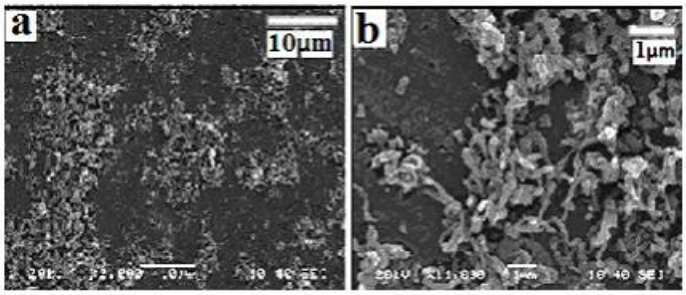

Figure 4: Scanning electron microscopy (SEM) images of sample coated with OD (12 h). Magnification is (a) 2000X and (b) 11000X.

In order to study the effect of IT on the ice-repellent properties of the coatings, the ice adhesion tests were carried out on samples coated with OD. These samples were selected with regards to enhanced hydrophobic properties of long alkyl chain coatings (OD) compared to short alkyl chain OT coated samples. In other words, the first value of shear stress of ice detachment, for sample coated with OT-12h was 220.5 ± 12 compared to 242.5 ± 25 which was obtained on the polished bare Al sample. These two sets of values are very close to each other.

Table 1 presents the first values of shear stress of ice detachment and ice adhesion reduction factor (*ARF*) of coated samples of OD (1 mM) for different IT.

Table 1: Ice adhesion strength and ARF values of OD samples for different IT.

Sample-IT	Ice adhesion strength (kPa)	*ARF*
Polished Al	242.5 ± 26.1 ± 27	1
OD-15	241.3 ± 25.2	1.005
OD-120	237.3 ± 15.9	1.02
OD-360	202.0 ± 10.1	1.2
OD-720	181.7 ± 8.0	1.33

The difference of ice adhesion strength between the 12-h OD sample and other ones is due to the superhydrophobic characteristics and lower wetting hysteresis (CAH) of this sample. As well, the *ARF* of the prepared sample for 12-h IT showed ice adhesion strength of at least ~ 1.33 times lower than that obtained on the polished bare Al sample.

III. Conclusions

In this study, the effect of alkylsilane chain length on the formation, wetting behavior and anti-ice performance of prepared *SAM*s coatings on flat aluminum alloy (AA6061) surfaces were investigated. For this purpose, self-assembled monolayers of alkylsilane compounds with ITs of 15 min, 2, 6 and 12 hours were elaborated on polished aluminum substrates. It was observed that, by increasing the IT from 15 min to 12h, the hydrophobic properties of the samples coated with OD (1 mM) were significantly enhanced compared to those of the short chain alkylsilane. The *ARF* of the OD sample with 12-h IT demonstrated values of ice adhesion strength ~1.33 times lower than those obtained on a polished bare Al sample. The SEM images of the samples coated with OD and OT (12-hour IT) showed the presence of micro/nano scale roughness which was obtained following aluminum sample immersion in their corresponding chemical baths resulting in the erosion of the aluminum substrate during the *SAM*s process.

IV. Acknowledgements

This research work has been conducted within the framework of the NSERC/Hydro-Quebec/UQAC Industrial Chair on Atmospheric Icing of Power Network Equipment (CIGELE) and the Canada Research Chair on Atmospheric Icing Engineering of Power Networks (INGIVRE) at Université du Québec à Chicoutimi. The authors would like to thank the CIGELE partners (Hydro-Québec, Hydro One, Réseau Transport d'Électricité (RTE), Rio Tinto Alcan, General Cable, K-Line Insulators, Dual-ADE, and FUQAC) whose financial support made this research possible.

V. References

[1] M. Farzaneh, J. Zhang and C. Volat, "Effect of Insulator Diameter on AC Flashover Voltage of an Ice-covered Insulator String", IEEE Trans. Diel. El. Ins., vol. 13, pp. 264, 2006.

[2] M. Farzaneh, I. Fofana, I. Ndiaye, and K.D. Srivastava, "Experimental studies of ice surface discharde inception and development", J.Int. Elec.. Power., vol. 26, pp. 34, 2006.

[3] M. Farzaneh (Chair), "IEEE standard 1783 – guide for test methods and procedures to evaluate the electrical performance of insulators in freezing conditions". IEEE Press, New York, 2009.

[4] M. Farzaneh, "Ice accretion on H.V. conductors and insulators and related phenomena", Philos. Trans. R. Soc. London, Ser. A. vol. 358, pp. 1, 2000.

[5] M. Farzaneh, W.A. Chisholm, "Insulators for icing and polluted environments", IEEE Press series on Power Engineering, IEEE/John Wiley, New York, ISBN 9780470282342, pp. 680, 2009.

[6] C. Laforte, J. L. Laforte, J. C. Carrier, "How a solid coating can reduce the adhesion of ice on a structure", Proceedings of the International Workshop on Atmospheric Icing of Structures (IWAIS), pp. 1-5, 2002.

[7] F. Arianpour, M. Farzaneh, S. A. kulinich, "Hydrophobic and ice-retarding properties of doped silicon rubber coatings", Appl. Surf. Sci., vol. 265, pp. 546-552, 2013.

[8] R. Jafari, R. Menini, M. Farzaneh, "Superhydrophobic and icephobic surfaces prepared by RF-sputtered polytetrafluoroethylene coatings Appl. Surf. Sci. vol. 257, pp. 1540–1543, 2010.

[9] V. F. Petrenko and S. Peng, "Reduction of ice adhesion to metal by using self assembling monolayers (SAMs)", J. Phys. vol. 81, pp. 387, 2003.

[10] J. L. Laforte, M. A. Allaire and J. Laflamme, "State-of-the-art on power line de-icing", Atm. Res. vol. 46, pp. 143, 1998.

[11] V. K. Croutch and R. A. Hartley, "Adhesion of ice to coatings and the performance of ice release coatings", J. Coat. Technol., vol. 64, pp. 41, 1992.

[12] S. A. Kulinich and M. Farzaneh, "Hydrophobic properties of surfaces coated with fluoroalkylsiloxane and alkylsiloxane monolayers '', Surf. Sci., vol. 573, pp. 379, 2004.

[13] R. Menini and M. Farzaneh, "Advanced icephobic coatings", J. Adhe. Sci. Tech. vol. 25, pp. 971, 2011.

[14] D. Quéré, "Non-sticking drops", Rep. Prog. Phys. vol. 68, pp. 2495, 2005.

[15] S. Farhadi, M. Farzaneh, S.A. Kulinich, "Anti-icing performance of superhydrophobic surfaces", Surf. Sci., vol. 257, pp. 6264, 2011.

[16] V. Subramanian, and W. J. van Ooij, "Silane based metal pretreatments as alternatives to choromating" Surface Eng., vol. 15, pp. 168, 1999.

[17] W. Limbut, P. Kanatharana, B. Mattiasson et al., "A comparative study of capacitive immunosensors based on self-assembled monolayers formed from thiourea, thioctic acid, and 3-mercaptopropionic acid" , J. Biosens. Bioelectron., vol. 22, pp. 233, 2006.

[18] A. Franquet, J. De Laet, T. Schram, et al., "Determination of the thickness of thin silane films on aluminium surfaces by means of spectroscopic ellipsometry", Thin Solid Films, vol. 384, pp. 37, 2001.

[19] M. J. Pellerite, T. D. Dunbar, L. D. Boardman et al., "Effects of Fluorination on Self-Assembled Monolayer Formation from Alkanephosphonic Acids on Aluminum: Kinetics and Structure", J. Phys. Chem., vol. 107, pp. 11726, 2003.

[20] M. Jin, S. Li, J. Wanga, M. Liao, Y. Zhao, "Controllable fabrication of organosilane nano-architectured surfaces with tunable wettability", Appl. Surf. Sci. vol. 258, pp. 7552-7555 2012.

[21] C. R. Kessel and S. Granick, "Formation and Characterization of a Highly Ordered and Well- Anchored Alkylsilane Monolayer on Mica by Self –Assembly", Langmuir, vol. 7, pp. 532-538, 1991.

How the Steric Effect Affects Ice Repellency, UV Stability and Corrosion Resistance of Dissimilar *SAMs* Coatings on Al 2024

S. Farhadi[1], M. Farzaneh[1] and S. Simard[2]

[1] Canada Research Chair on Atmospheric Icing Engineering of Power Networks (INGIVRE), Université du Québec à Chicoutimi, QC, Canada

[2]Aluminum Technology Centre, Industrial Materials Institute, National Research Council Canada (CNRC) 501, boul. de l'Université Est, Chicoutimi, QC, Canada

Email: shahram.farhadi@uqac.ca

Abstract: Ice adhesion on outdoor structures is an important issue in cold climate regions. Passive approaches to the problem, e.g. anti-icing or icephobic coatings that inhibit or retard ice accumulation on surfaces, are gaining in popularity. The development of ice-releasing coatings on metallic structures, e.g. Al alloys, is closely related to anti-corrosive protection of that metal, since they must be durable enough when placed in humid environments. In the present study, icephobic stability against UV irradiation and anti-corrosive performance of three dissimilar alkyl-terminated *SAMs* thin films on an aluminium alloy 2024 (AA2024) substrate were investigated. The samples were prepared following wet-chemistry technique by depositing three alkylsilane-based *SAMs* of triethoxy(octyl)silane [$CH_3(CH_2)_7Si(OC_2H_5)_3$, 8C], octadecyltrimethoxysilane [$C_{18}H_{37}Si(OCH_3)_3$, 18C], and trichlorooctadecylsilane [$(CH_3(CH_2)_{17}SiCl_3$, 18C+Cl] on the Al substrate. The influence of the steric effects on coating formation and performance, as well as hydrophobicity and durability versus different pH and/or against UV-irradiation were investigated by means of contact angle measurements, and hydrophobicity losses over time. Glaze ice was artificially deposited on the coated surfaces by spraying supercooled water microdroplets (~65 µm) in a wind tunnel at subzero temperature (-10 °C) to simulate most severe natural atmospheric icing. All samples initially demonstrated ice detachment shear stress values ~ 1.68 to 2 times lower than those of as-received Al surfaces. However, following successive icing/de-icing cycles, different degree of coating degradation was observed. In addition, surface hydrophobicity was studied after icing/de-icing tests to study its stability, showing decreases in contact angle values. Hydrophobicity losses and ice adhesion increase were indeed dramatically and completely different for coated samples with 8C and 18C+Cl *SAMs* compared to 18C *SAMs* thin films. This is probably due to the fact that the 18C *SAMs* was the most ordered thin film among the other two, which is due to the significant influence of the *steric effect*. Meanwhile, potentiodynamic polarization revealed that the corrosion resistance of the coated sample with 18C *SAMs* is slightly improved if compared to the 8C, 18C+Cl and bare samples.

Keywords: steric effects; self-assembling; UV-irradiation; ice adhesion strength; potentiodynamic polarization; coating stability.

INTRODUCTION

Ice and wet snow accumulation hinders the operation and efficiency of infrastructural components, mechanisms and machines, including aircraft, power transmission lines, telecoms equipment, etc. Atmospheric icing occurs when surfaces of exposed structures come into contact with supercooled water droplets or snow particles [1]. Prevention of the icing process requires reducing adhesive strength of ice onto the surface, and therefore, various de-icing and anti-icing techniques have been developed so far, e.g. hydrophobic and superhydrophobic coatings on metallic and non-metallic substrates [2-9]. The ideal solution would be using durable, inexpensive and easy to apply coatings which would reduce ice adhesion to such an extent that ice would fall off under the pull of gravity, e.g. alkyl-terminated coatings [3, 10, 11]. Meanwhile, reasonable correlation between hydrophobicity and ice repellecy was reported earlier [2, 3, 6, 8, 10]. Hydrophobicity can also improve anti-corrosive performance of coated metallic substrates such as Al, as it can prevent penetration of water/aggressive molecules underneath the metallic surface [6-9, 12, 13]. In most studies, ice adhesion on a solid was evaluated by freezing the water artificially on the surface sample under unrealistic icing conditions [14, 15]. Meanwhile, no systematic study on their durability as well as their anti-corrosive performance has been yet reported. Consequently, testing adhesion of glaze ice prepared by spraying supercooled water droplets is expected to give more reliable results [5, 6, 8, 16].

In the present study, icephobicity, stability against UV-irradiation and other aggressive conditions as well as anti-corrosive performance of three dissimilar alkyl-terminated *SAMs* thin films on a aluminium alloy 2024 (AA2024) substrate were investigated. The hydrophobic Al samples were prepared via *"wet-chemistry"* technique, known as an easy-to-apply method, by depositing three alkylsilane-based *SAM*s coatings, as potential ice and snow-repellent layers. The influences of the steric effect on coating performance, their hydrophobicity and durability versus different pH and against UV-irradiation over time were studied by means of contact angle (CA) measurements. Furthermore, a potentiodynamic polarization test was conducted to study corrosion resistance of such prepared coated samples.

I. Experimental procedure

A. *Sample Preparation*

The AA2024-T3 with chemical composition of Al 90.7-94.7wt.%, Si 0.5wt.%, Fe 0.5wt.%, Cu 3.8–4.9wt.%, Mn 0.3-0.9wt.%, Zn 0.25wt.%, Mg 1.2–1.8wt.%, other impurity 0.15wt.% [17] was used as substrate. This alloy is used extensively in applications that require high strength to weight ratio as well as good fatigue resistance. The as-received 2-mm thick Al substrates were ultrasonically cleaned and degreased in water and organic solvents (acetone and ethanol), each for 3 min, followed by cleaning in a *Turco Redoline 53D* alkaline solution (pH~10) for 2-3 min. The alkaline solution was used to create a freshly cleaned Al oxide layer on each surface substrate [18, 19]. The cleaned and polished Al samples were then blow-dried in a N_2 gas flow, and were dried in an oven at 80 °C in air for 3 hrs. They were subsequently placed in corresponding chemical baths of 1% (V/V%) triethoxy(octyl)silane, octadecyltrimethoxysilane, and trichlorooctadecylsilane (from SIGMA-ALDRICH®) at room temperature, abbreviated as 8C, 18C and 18C+Cl *SAMs* coatings (see Fig.1). The solvent was isopropanol, ACS grade, purchased from EMD® .

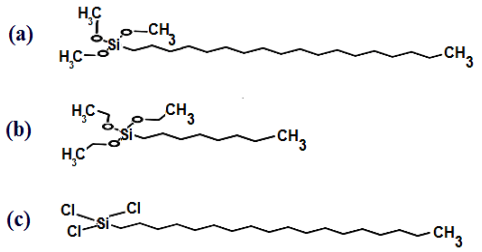

Figure 1: Chemical structure of a) Octadecyltrimethoxysilane (18C), b) Triethoxy(octyl)silane (8C), and c) Trichlorooctadecylsilane (18C+Cl).

Prior to tests or surface characterization, all the coated samples were rinsed ultrasonically with copious amounts of the relevant solvent, isopropanol for 5 sec, followed by blow-drying with N_2. They were finally post-dried in oven at 80 ^oC for 3 hrs and then at 50 ^oC for 5 hrs to remove any volatile components or residual solvents and to improve layer cross-linking [20]. Different concentrations of the silane solutions were tested, but no significant difference was found within a few mM range. The characterization procedures were conducted immediately following sample preparation. While the smaller samples (2 × 2 cm^2) were used to evaluate coatings stability in different conditions, the larger ones (3.2 × 5.2 cm^2) were used to study their ice-repellent performance and corrosion measurements.

B. *Sample charactrization*

Sample stability in water, basic and acidic conditions was studied by means of CA measurements on the samples after immersion in nano-pure water, tap water, as well as in basic (pH: 10.1) and acidic (pH:4) buffer solutions at ~18-20 ^oC. The wetting characteristics, reported in Fig. 2, were obtained following the standard sessile drop method on a DSA100 goniometer from Krüss [4, 6, 16]. For each sample, at least three different spots were randomly measured and the CA reported was the average value of about 5 measurements. Surface topographies were studied by means of scanning electron microscopy (SEM, Hitachi FEGSEM-SU 70) in high-vacuum mode. The X-ray photoelectron spectroscopy (XPS) was performed with a Quantum-2000 instrument from PHI and X-Ray source of achromatic Al Kα. (1486.6 eV). The ice adhesion test was conducted by creating glaze ice (up to ~1 cm thick and ~4-5 gr weight) over a ~3.2 × 3.0 cm^2 surface area and prepared by spraying supercooled micro-droplets of water (average size of ~65 µm) in a wind tunnel at subzero temperature (-10 ^oC), wind speed of 11 ms^{-1}, water pressure of 325 kPa, and water feed rate of 6.3 gm^{-3}. The iced samples were then spun in the centrifuge at constantly increasing speed. Degradation due to UV illumination was assessed using QUV/Accelerated Weathering

Tester in accordance with ASTM G154 and by exposition to a UVA-340 fluorescent lamp to simulate damaging in outdoors conditions in a controlled laboratory environment. Finally, potentiodynamic polarization was used to examine the overall corrosion behaviour of the bare and coated Al samples. The working cell was a standard three-electrode cell with a 1-cm^2 area of the working electrode. A platinized platinum net and saturated calomel electrode (SCE) were used as counter and reference electrode, respectively. The setup used to control the experiments was a potentiostat system composed of a Solartron SI1287A electrochemical interface (controlled by Corrware® software). Measurements were performed in 3.5 wt.% NaCl solutions at room temperature. Potentiodynamic polarization curves were established and the corrosion potential (E_{corr}) and corrosion current density (i_{corr}) were determined using the *Tafel* extrapolation method. The polarization scan was started from 250 mV below the open circuit potential (OCP) in the cathodic region, through the corrosion potential, and 250 mV above the open circuit potential in the anodic region, with a constant scan rate of 1 mVs^{-1}.

II. Results and Discussion

A. Hydrophobicity and Icephobicity of Disimillar SAMs Coatings

Table 1 presents the CA and surface energy values of three dissimilar organosilanes in alkyl chain length and molecular structure on Al substrates. These results were calculated according to Young–Laplace method, as the most theoretically accurate method [16]. It is worthy to mention that prior to use, all baths were vigorously stirred for 3 hrs to allow adequate dissolution/hydrolysis. The hydrolysis/condensation reactions were, indeed, catalyzed by amount of water added to the chemical bath solutions. As it is well known, Al is extremely reactive to atmospheric oxygen, and so has a thin native oxidized surface layer (~4 nm). Thus, it showed water CA and surface energy values of ~41.5±3° (hydrophilic substance) and 46.36±1.64 (mNm^{-1}), respectively. Organosilanes can be easily grafted to a surface by chemical bond (Si-O-Al) demonstrating low surface energy and chemical stability. The XPS signals of C, O and Si, not shown here, showed that the Al surfaces were covered with corresponding *SAMs* coatings. Evidently, by increasing the alkyl chain length, the surface hydrophobicity, CA, was also changed in the following order: 18C+Cl *SAM*s > 18C-*SAM*s > 8C-*SAM*s. The immersion time also plays a significant role in the self-assembly process in terms of surface coverage [21, 22]. Different immersion time periods of 1 min to 120 min were tested. However, the CA corresponding to immersion time of 60 min provided the optimum condition, demonstrating improved wetting properties on the Al substrates.

Table 1: Contact angle and free surface energy [ε (mNm^{-1})] of AA2024 coated with different *SAM*s coatings.

Applied *SAM*s / Experimental conditions	**As-received AA2024**	**8C-*SAM*s**	**18C-*SAM*s**	**18C+Cl *SAM*s**
Immersed for 15 min in diluted bath	------	102.2 ± 1° ε: 12.14 (±0.60)	111.4 ± 2° ε: 6.03 (±1.14)	117.1 ± 1° ε: 4.77 (±0.54)
No *SAM*s coating	41.5 ± 3° ε: 46.36 (±1.64)	------	------	------

After coating deposition, all samples demonstrated initial values of contact angle, CA ≥ 100° (Figs.1 and 2), which indicates hydrophobic characteristics. Among these three compounds, the 18C+Cl *SAM*s showed the highest values of CA, which is probably due to erosion of the Al substrate during the *SAM*s process. The CAs of the samples coated with 18C-*SAM*s and 18C+Cl *SAM*s were very close. In contrast, the CA of 8C-coated Al was remarkably smaller than the other two samples. This result suggests that 18C-*SAM*s formed more packed self-assembled thin film on the substrate compared to the 8C-*SAM*s coating. It is also possible that 8C-*SAM*s molecules form film on Al with alkyl chains anchored onto the substrate and that the functional moieties are oriented towards the solution phase, i.e. opposite molecular orientation (formation of -Si-OH bond). This results in more hydrophilicity. Meanwhile, between each layer, the functional trichlorosilane or trimethoxysilane groups can polymerize together through hydrolysis and condensation reaction. This polymer network would provide extra strength to stabilize layer-to-layer interactions. By increasing the alkyl length, the steric effect rises and thus the movement of organosilane moleculs freely decreases. Subsequently, the organosilane hydrolysis/polycondensation becomes more difficult causing the number of organosilane molecules forming a network structure to decrease. Therefore, the network structure becomes thin and the corresponding CAs decreases. When the aliphatic tail is small, the steric effect is dominant. In other words, by increasing the alkyl

chain length, the competition between decrease of reactivity due to the steric effect and the increase of alkyl hydrophobicity caused the difference observed in sample wettability [23]. Now the question is that are these *SAM*s coatings dense enough to prevent aggressive molecules from penetrating through the coatings? Figure 1 shows the CA values of Al samples coated with different silanes as a function of immersion time in nano-pure and tap water as well as basic and acidic media. While these samples initially demonstrated hydrophobicity, however, the CA values decrease over time and lose their hydrophobicity. The coated surfaces were found to gradually lose their hydrophobic properties completely over ~1100-h immersion in different media, associated with a decrease of water CA. This tendency to lose surface hydrophobicity is probably due to a rupture in the Si-O-Al bond between silane molecules and the Al oxide layer due to their hydrolysis. Hydrolysis of Al-O-Si bonds is one of the possible reasons for the silane coatings degradation when they are exposed to aggressive media. This caused hydration of the network and disruption of siloxane and alkyl moieties. The trichlorosilanes contains the corrosive Cl^- ions after hydrolysis. Between the two trimethoxysilane compounds, 18C-*SAM*s has a longer alkyl chain of 18 carbons, while 8C-*SAM*s has a shorter alkyl chain of 8 carbons. This chain length difference may lead to some variations in the structures and properties of the formed thin films. Packing density is expected to increase with chain length [24].

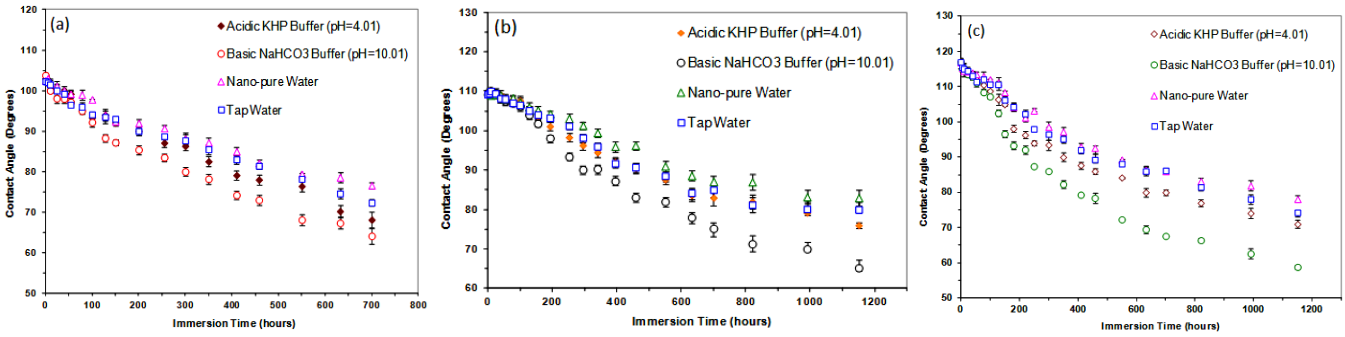

Figure 1: Contact angle of Al sample coated with a) 8C, b) 18C and c) 18C+Cl *SAM*s vs. immersion time in acidic (pH=4.01), basic (pH=10.01), nano-pure and tap water.

It is clear from Figs. 1 and 2 that losing hydrophobicity was faster in the case of samples coated with 8C-*SAM*s and 18C+Cl *SAM*s compared to 18C-*SAM*s. Meanwhile, in all cases, decrease of CA was quiet fast in the case of samples immersed in basic solution in comparison with samples immersed in other media in counterpart. The reason for this observation is attributed to the influence of basic conditions on Al oxide layer stability and the rate of Al corrosion in basic media. Meanwhile, losing hydrophobicity was slightly faster for samples immersed in tap water compared to nano-pure water which is most likely due to influence of salts dissolved in tap water, resulting in accelerated coating deterioration. These *SAM*s layers, indeed, are believed to be not dense enough or too thin with insufficiently cross-linked networks to prevent water molecules/aggressive ions from penetrating through the coating to the surface beneath. In aggressive conditions, the silane layers undergo degradation, and hence, alkylsilane molecules were removed from the surface, resulting in a decrease of surface hydrophobicity.

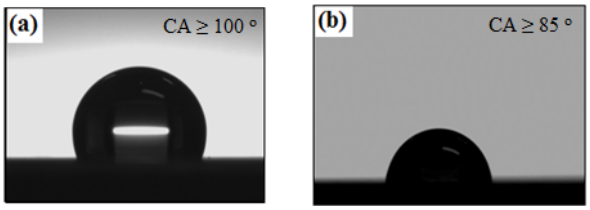

Figure 2: Water droplet on Al surface coated with18C-*SAM*s: a) before and b) after 700-h immersion in nano-pure water.

B) Effect of UV Radiation on Hydrophobic Properties of Prepared SAMs Coatings

Any icephobic coatings must necessarily accomplish both of the following requirements: first, they must efficiently reduce snow/ice adhesion, and second, have a reasonably long service-life (durability). In order to study the durability of coatings in a simulated natural weathering process for potential outdoor applications, their aging performance was studied against UV exposure. The samples were exposed to UVA-340 fluorescent lamp according to ASTM G154. Almost each 537-h of artificial UV exposure is equivalent to one year of sunlight exposure [26]. Figure 3 presents CA values of coated Al samples with different *SAM*s following UV exposure. It is obvious that all samples lost their hydrophobicity associated with a decrease of CA while the number of UV cycles increased. No significant

difference was observed from one sample to another one. Meanwhile, the CA remains almost constant between the 12th to the 20th cycles where the CA slightly decreased. However, after the 20th cycle, the CA reduced dramatically, especially in the case of the sample coated with 8C-*SAM*s where it turns completely hydrophilic. Therefore, based on UV exposure results, it is possible to conclude that a realistic stability was observed for Al coated with 18C-*SAM*s and 18C+Cl *SAM*s over almost six months of natural sunlight exposure. The 8C-*SAM*s exhibits a remarkable UV-induced degradation (reached to ~80^{o} water CA).

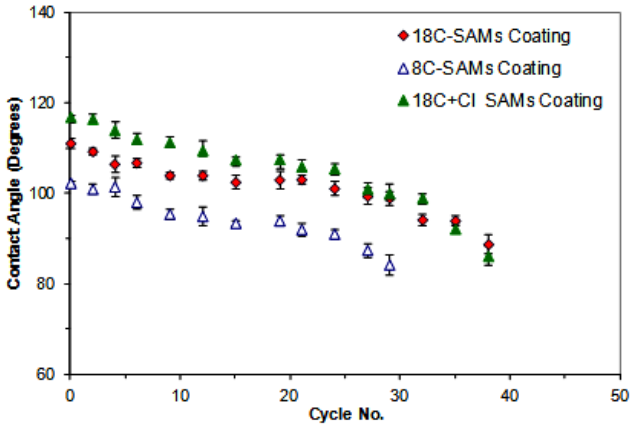

Figure 3: Coating durability (CA vs. UV cycle) for Al coated with different *SAM*s.

C. Ice Adhesion Strength

Each coated Al sample was subjected to 9 successive icing/de-icing cycles. Ice adhesion strength was evaluated as a function of the number of icing/de-icing cycles (Fig.4). While uncoated as-received Al samples showed initial values of ice adhesion strength of ~370±30 kPa, its coated counterparts with 8C-*SAM*s, 18C-*SAM*s and 18C+Cl *SAM*s layers showed reduced values of ~ 220, ~ 190 and ~ 185 kPa, respectively.

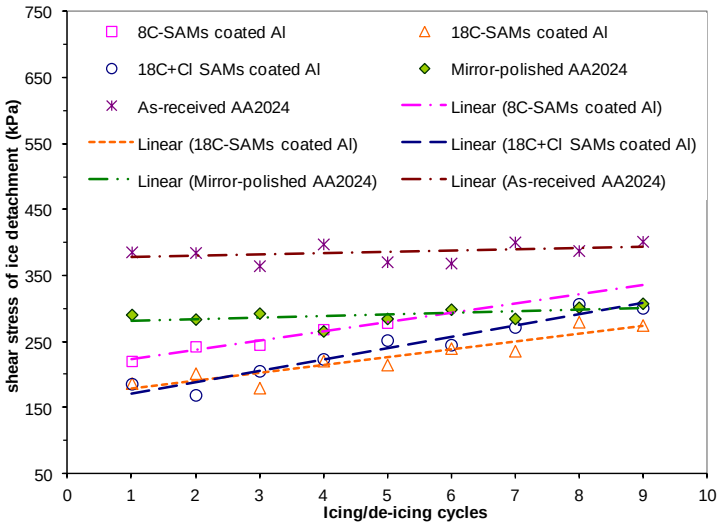

Figure 4: Shear stress of ice detachment *vs.* icing/de-icing for Al surfaces coated with 8C, 18C and 18C+Cl *SAM*s layers.

This reduction can be attributed to the presence of the low surface energy coatings on Al samples. All flat coated surfaces demonstrated shear stress of ice detachment values of ~ 1.68 to 2 times lower than as-received Al surfaces. However, ice adhesion strength increased for both samples, 18C-*SAM*s and 18C+Cl *SAM*s, after as many as 9 icing/de-icing cycles in a similar manner, as shown in Fig.4. This increase in ice adhesion is believed to be associated with partial decay of the coatings caused by their contact with freezing water. The XPS analysis showed that while all coatings demonstrated a peak of Si 2p before test (silane layer(s) on Al), its atomic concentration decreased significantly after ice detachments. Increase in ice adhesion strength was completely different in the case of sample coated with 8C-*SAM*s. It raised the fact that well-ordered 18C-*SAM*s was created on Al surface if compared to *SAM*s of 8C. This decrease was even worse in the case of the sample coated with 8C-*SAM*s. This supports the above mentioned assumption according to

which water molecules hydrolyzed the -O-Si-R bond and gradually destroyed the silane layers on the Al substrate. Meanwhile, the wettability of these samples after several icing/de-icing cycles were studied, showing a gradual decrease in CA values over repeated icing/de-icing cycles.

D. Corrosion resistance of hydrophobic coatings

The potentiodynamic polarization curves of bare and coated AA2024 in 3.5 wt.% NaCl solution are presented in Fig. 5. The $E_{corr.}$, $j_{corr.}$ and R_p values derived from corresponding polarization curves, using Tafel extrapolation, are summarized in Table 2. It is evident in Fig.5 and Table 2 that the value of E_{corr} positively increases from -0.68±0.03V for bare AA2024 to -0.60±0.03V in the case of hydrophobic 18C-*SAM*s coating. However, it shifts slightly to positive values for samples coated with 8C-*SAMs* and 18C+Cl *SAMs*, i.e. -0.64±0.03V and -0.65±0.04V, respectively. This shift obviously corresponds to the improvement in the protective performance of the hydrophobic coating formed on the Al substrate. The 18C-*SAMs* film also showed decrease in $j_{corr.}$ in the cathodic and anodic regions, which suggests a cross-linked network firmly attached to the metallic substrate, leading to protecting the surface against corrosion.

Table 2: Potentiodynamic results of bare and coated AA2024 with 8C-, 18C- and 18C+Cl *SAM*s in 3.5 wt.% NaCl solution.

Specimen	$E_{corr.}$ (V *vs.* SCE)	$j_{corr.}$ (μAcm^{-2})	R_p ($k\Omega cm^2$)
Standard AA2024	-0.68 (±0.03)	22.89 (±.9.06)	2.96 (±2.71)
8C-*SAMs*	-0.64 (±0.03)	4.07 (±1.12)	21.45 (±2.11)
18C+Cl *SAMs*	-0.65 (±0.04)	5.65 (±0.83)	39.24 (±1.21)
18C-*SAMs*	-0.60 (±0.03)	0.90 (±0.11)	248.11 (±2.55)

The slope of anodic current versus E was smaller for 18C-*SAM*s than for the other two coatings that support the fact that this film protects Al surface more effectively.

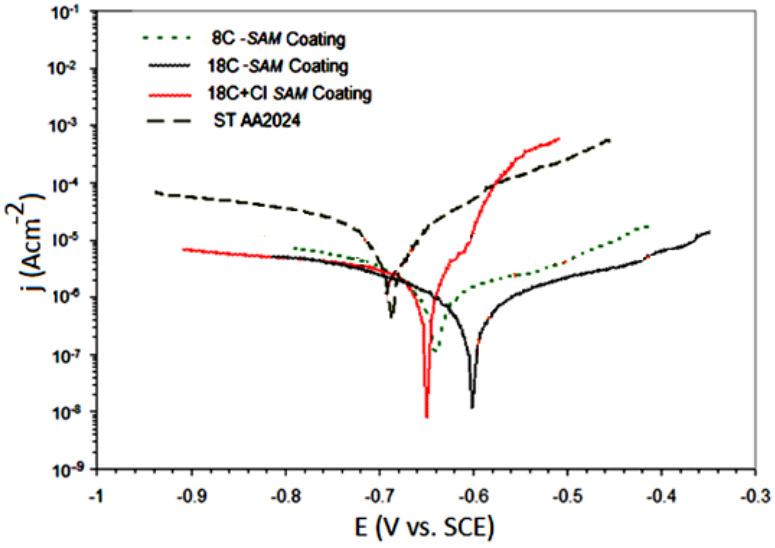

Figure 5: Polarization curves of bare and coated AA2024 with 8C-, 18C- and 18C+Cl *SAMs* coating.

This difference is attributed to the bonding of silane groups to the oxide surface, resulting in enhanced corrosion inhibition. In other words, the corrosion inhibition of 18C-*SAM*s film was superior to those observed for 8C- and 18C+Cl *SAM*s films. It is possible to conclude that according to the polarization results, the 18C-*SAMs* provided a good coverage of the Cu-enriched parts of the AA2024 surface. The Al_2O_3 layer is permeable to electrolytes or moisture and is prone to undergo dissolution in a humid environment, leading to accelerated corrosion. In contrast, the film formed from 18C-*SAMs* is less permeable to corrosion accelerants and thus presents good barrier protection. This is possibly due to presence of less defects in the *SAMs* film of 18C.

IV. Conclusions

In this study, icephobicity, stability in different conditions and against UV-irradiation and anti-corrosive performance of three dissimilar alkyl-terminated *SAMs* thin films on AA2024 were investigated. The hydrophobicity and durability of such coatings in different conditions were tested by means of CA measurements, showing gradual loss of hydrophobicity over time. This was associated with a decrease in CA values of the coated samples. All coated surfaces initially demonstrated shear stress of ice detachment values lower than as-received samples. However, it gradually increased after as many as 5 to 9 successive icing/de-icing cycles due to degradation of coatings upon their contact with freezing water. In addition, the hydrophobic properties of coated surfaces following each ice release presented a slight decrease in CA values. It was showed that hydrophobicity loss and ice adhesion increase were completely different for coated samples with 8C- and 18C+Cl *SAMs* compared to 18C-*SAMs* thin films. It raised the fact that 18C-*SAMs* was more well-ordered than the other *SAMs* mainly due to the significant steric effect on surface properties. Electrochemical measurements showed that the corrosion potential of 18C-*SAMs* increased and its corrosion current density decreased more significantly as compared to that of bare samples. This supports the fact that 18C-*SAMs* demonstrates enhanced corrosion resistance if compared to the 8C- and 18C+Cl *SAMs*.

Acknowledgements

This research work has been conducted within the framework of the NSERC/Hydro-Quebec/UQAC Industrial Chair on Atmospheric Icing of Power Network Equipment (CIGELE) and the Canada Research Chair on Atmospheric Icing Engineering of Power Networks (INGIVRE) at Université du Québec à Chicoutimi. The authors would like to thank the CIGELE partners (Hydro-Québec, Hydro One, Réseau Transport d'Électricité (RTE), Rio Tinto Alcan, General Cable, K-Line Insulators, Dual-ADE, and FUQAC) whose financial support made this research possible.

References

[1] M. Farzaneh, "Atmospheric Icing of Power Networks", Ed., Springer, Berlin, pp. 320, August 2008.
[2] H. Saito, K. Takai, G. Yamauchi, "Water- and ice-repellent coatings". Surface Coatings International, vol. 80, pp. 168–171, 1997.
[3] S. A. Kulinich, M. Farzaneh, "Hydrophobic properties of surfaces coated with fluoroalkylsiloxane and alkylsiloxane monolayers", Surface Science vol. 573, pp. 379–390, 2004.
[4] S. Farhadi, M. Farzaneh, S. Simard, "Nanostructured ultra superhydrophobic Al surfaces: stability and icephobic properties", International Journal of Theoretical and Applied Nanotechnology, vol. 1, pp. 38-44, 2013.
[5] S. A. Kulinich, M. Farzaneh, "How wetting hysteresis influences ice adhesion strength on superhydrophobic surfaces", Langmuir, vol. 25, pp. 8854–8856, 2009.
[6] S. Farhadi, M. Farzaneh, S. A. Kulinich, "Anti-Icing Performance of Superhydrophobic Surfaces", Applied Surface Science, vol. 257, pp. 6264–6269, 2011.
[7] Z. Ghalmi, R. Menini, M. Farzaneh, "Effect of different aluminium surface treatments on ice adhesion strength", Advanced Materials Research, vol. 409, pp. 788-792, 2012.
[8] F. Arianpour, M. Farzaneh, S. Kulinich, "Hydrophobic and ice-retarding properties of doped silicone rubber coatings", Applied Surface Science, vol. 265, pp. 546-552, 2013.
[9] F. Arianpour, M. Farzaneh and S. A. Kulinich, "Nanopowder-Doped Silicone Rubber Coatings for Anti-Ice Applications", Scanning Electron Microscopy, 497 (2010)4.
[10] V. F. Petrenko and S. Peng, "Reduction of ice adhesion to metal by using self-assembling monolayers (*SAMs*)", Can. J. Phys, vol. 8, pp. 387-393, 2003.
[11] M. Farzaneh, "Systems for prediction and monitoring of ice shedding, anti-icing and de-icing for overhead lines", CIGRÉ WG B2.29, CIGRE Publications, Technical Brochure #438, pp. 100, 2010.
[12] Z. Guo, F. Zhou, J. Hao, W. Liu, "Stable Biomimetic super-hydrophobic engineering materials", Journal of the American Chemical Society, vol. 127, pp.15670–15671, 2005.
[13] Y. Shaojun, S. O. Pehkonenb, L. Bin, Y. P. Ting, K.G. Neoh, E. T. Kang, "Superhydrophobic fluoropolymer-modified copper surface via surface graft polymerisation for corrosion protection", Corrosion Science, vol. 53, pp. 2738–2747, 2011.
[14] E. H. Andrews, H. A. Majid, N. A. Lockington, "Adhesion of ice to a flexible substrate", Journal Materials Science, vol. 19, pp. 73-81, 19984.
[15] V. K. Croutch and R. A. Hartley, "Adhesion of ice to coatings and the performance of ice release coatings", *J. Coat. Technol*.**,** vol. 64, pp. 41-52, 1992.
[16] S. Farhadi, M. Farzaneh and S. Simard "On Stability and Ice-Releasing Performance of Nanostructured Fluoro-Alkylsilane-Based Superhydrophobic AA2024 Surfaces", Inter. J. Theor. and Appl. Nanotechnology, 2012.
[17] http://www.matweb.com/search/DataSheet.aspx?MatGUID=57483b4d782940faaf12964a1821fb61.
[18] L. Thomsen, B. Watts, D. Cotton, J. Quinton and P. Dastoor, Surf. Interface Anal., 37 (2005) 472.
[19] X. Yao, Q. W. Chen, L. Xu, Q. K. Li, Y. L. Song, X. F. Gao, D. Quere and L. Jiang, Adv. Funct. Mater., 20 (2010) 656.
[20] S. Farhadi, M. Farzaneh and S. A. kulinich, "Preventing Corrosion and Ice Accretion on Aluminium Surfaces Applying Organic and Inorganic Thin Films", MSc thesis, UQAC, Dec. 2010.
[21] M. J. Pellerite, T. D. Dunbar, L. D. Boardman et al., "Effects of Fluorination on Self-Assembled Monolayer Formation from Alkanephosphonic Acids on Aluminum: Kinetics and Structure", J. Phys. Chem., 107 (2003)11726.
[22] W. Limbut, P. Kanatharana, B. Mattiasson et al., "A comparative study of capacitive immunosensors based on self-assembled monolayers formed from thiourea, thioctic acid, and 3-mercaptopropionic acid" , J. Biosens. Bioelectron., 22 (2006) 233.
[23] M. Jin, S. Li, J. Wanga, et al., Appl. Surf. Sci., 258 (2012) 7552.
[24] M. D. Porter, T. B. Bright, D. L. Allara, C. E. D. Chidsey, J. Am. Chem. Soc. 109 (1987) 3559.
[25] http://www.iso.org/iso/home/store/catalogue_tc/catalogue_detail.htm?csnumber=24372.
[26] ATLAS Weathering Testing Guidebook.

On Self-cleaning and Anti-ice Performance of Double-layer*SAMs* Coatings with Enhanced Corrosion Resistance on an Al Alloy Substrate

S. Farhadi[1], M. Farzaneh[1] and S. Simard[2]

[1] Canada Research Chair on Atmospheric Icing Engineering of Power Networks (INGIVRE), Université du Québec à Chicoutimi, QC, Canada

[2]Aluminum Technology Centre, Industrial Materials Institute, National Research Council Canada (CNRC) 501, boul. de l'Université Est, Chicoutimi, QC, Canada

Email: shahram.farhadi@uqac.ca

Abstract: In cold climate regions, outdoor structures including transmission lines and telecommunication networks are exposed to ice and/or snow accretions which may result in damage and malfunctions. Superhydrophobic coatings were introduced and developed over the past decades as a passive technique to reduce or prevent ice accumulation on outdoor structures. At the same time, corrosion protection of metallic substrates such as aluminium and its alloys is another important issue when they are used in environments in close contact with water or other aggressive molecules. The present study, therefore, aims at systematically studying a double-layer *SAMs* coating terminated with surface alkyl groups that are expected to reduce ice adhesion and corrosion rates on an Al surface. More precisely, thin films of 1,2-bis-trioxymethyl-silyl-ethane [$C_{14}H_{34}O_6Si_2$] and octadecyltrimethoxysilane [$C_{18}H_{37}Si(OCH_3)_3$] were deposited layer by layer on etched Al alloy (AA2024-T3) substrates. The first layer was used as an underlayer expecting to improve the anti-corrosive performance for the top-layer providing surface water and ice repellency (surface hydrophobization). The prepared coated samples demonstrated good superhydrophobic and self-cleaning properties providing a static water contact angle of CA>155° and a hysteresis angle of CAH≤5°. The low CAH causes the water droplets to roll off the surface easily carrying away surface contamination by water droplets passing by. The coating stability was studied by immersing the coated samples into water, with basic and acidic conditions (different pH), showing gradual loss of superhydrophobicity over time. In the meantime, while bare mirror-polished and as-received Al showed average ice detachment shear stress values of ~270 ± 20 kPa and ~370±30 kPa, respectively, their counterparts coated samples showed reduced values of ~182±15 kPa. This reduction is ascribed to the presence of engineered micro-/nano-hierarchical surface asperities along with the applied low surface energy top-layer on the sample surface. The ice-releasing performance, however, gradually decreased over repeated icing/de-icing cycles. Potentiodynamic polarization studies revealed that the corrosion resistance of modified aluminium alloy improved remarkably compared to the unmodified samples. Meanwhile, cyclic corrosion exposure tests demonstrated that while extensive corrosion appeared on bare Al after only 8 cycles of salt spray exposure, trace of corrosion was observed for the double-layer *SAMs* coating after 81 cycles of exposure.

Keywords: superhydrophobicity; self-cleaning; anti-corrosive performance; nanostructured aluminum; double-layer coating; durability; ice repellency; wetting hysteresis.

INTRODUCTION

Atmospheric icing occurs when the surface of exposed structures comes into contact with supercooled water droplets or snow particles. Ice and wet snow accumulation and adhesion on outdoor structures or equipment are well known to be a serious issue in cold climate countries [1]. In the specific case of power transmission lines, ice/wet snow may cause serious damage due to their high adherence to both metallic and insulator surfaces [1]. Each year, numerous failures due to ice accumulation are reported in Canada, USA, Iceland, Japan and so forth. Prevention of icing requires reducing its adhesive strength. Therefore, a variety of de-icing and anti-icing techniques were developed over the last decades [2]. Most of the efforts in recent years have been devoted to develop more efficient systems to prevent icing. While most of the techniques currently in use are active de-icing methods, e.g. thermal, electrical, chemical or mechanical techniques, all are used where accumulations are considerable and therefore, they consume a great deal of energy. Passive approaches, e.g. development of anti-icing or icephobic coatings that inhibit ice accumulation, are gaining in popularity [2, 3, 4]. Alkyl-terminated coatings, e.g. alkylsilane-based layers, were previously proposed as potentially ice-releasing coatings [4, 5, 6]. Reasonable correlation between hydrophobicity and ice repellecy has been reported earlier [3, 6-8]. Superhydrophobic surfaces defined as surfaces with static water contact

angle larger than 150^o and low hysteresis, CAH<6, have attracted considerable interest in this area. It is well known that the key factors underlying superhydrophobicity is the chemical composition of the surface along with a micro-/nano-hierarchical texture [3, 5, 6, 9]. Superhydrophobicity can also improve self-cleaning and anti-corrosive properties of Al alloys [4, 10-12] as it can prevent penetration of water molecules or other aggressive moieties into the metallic surface underneath [11, 12]. Arianpour *et al.* [9] reported delayed water freezing on rough superhydrophobic surfaces. In the meantime, metal corrosion should also be taken into account since metal or metallic alloys are subject to corrosion problems when exposed to aggressive environments. For this reason, in the development of anti-ice coatings on Al surface, they must not only be durable enough, but also provide anti-corrosive protection of that specific metal. It would be interesting for industrial applications to introduce new coatings which would be more specifically environmentally friendly alternatives to the currently used toxic chromate-based coatings and which would be anticorrosive.

In the present study, organic coatings terminated with alkyl groups were prepared as potential ice/snow-repellent layers on the surface of etched aluminium alloy 2024 (AA2024) for one-layer and multilayer approaches. More precisely, a thin film of octadecyltrimethoxysilane [ODTMS] as top-layer (water repellent coating) on an underlayer of 1,2-bis-trioxymethyl-silyl-ethane [BTSE] (providing a high density of -OH groups on the surface for the top-layer of ODTMS), were applied on Al substrates. These nanostructured surfaces were characterized and their coating stability (in water, basic and acidic conditions) and ice-repellent performance were carefully studied. To study their anti-corrosive performance, potentiodynamic polarization tests as well as cyclic corrosion exposure tests were carried out.

I. Experimental procedure

A. Sample Preparation

The AA2024-T3 panels from industrial rolled sheets were cut into smaller plates with dimensions of 2 × 2 and 5.1 × 3.2 cm^2 and were used as substrates. This Al alloy, whose Cu content as the primary alloying element is typically between 3.8-4.9 % (wt. %) [13, 14], is used extensively in applications that require high strength to weight ratio as well as good fatigue resistance. The as-received Al substrates, 2-mm thick, were ultrasonically cleaned and degreased in water and organic solvents (acetone and absolute ethanol), each for 5 min. The unpolished cleaned samples were then etched in ~9 wt % HCl at room temperature for 3 min. This was followed by ultrasonically rinsing 2-3 times in deionized water to remove any unstable particles on the surface resulting from the etching process. The etched samples were dried in a N_2 flow and were kept in oven at 80°C for 3 hrs. The pre-treated samples were then placed in baths with different chemicals at room temperature. The deposition baths for the top layer was ODTMS 1% (V/V%) from SIGMA-ALDRICH® in isopropanol (ACS grade with water content of <0.2%)-deionized water, as solvent. Prior to use, the bath were vigorously stirred for 3 hrs to allow for dissolution/hydrolysis. A BTSE solution (4.7 ml in isopropanol-water) for silane deposition was prepared to deposit the underlayer. These conditions could offer the best compromise between silane hydrolysis and condensation [15]. Rough Al samples were dipped into the BTSE solution for 1 min followed by blow-drying in N_2 and were then immersed into the ODTMS-isopropanol bath solution for 15 min. Upon coating and prior to tests, the modified samples were removed from their corresponding solutions, rinsed with copious amounts of isopropanol and blown-dried with N_2. They were then annealed in ambient atmosphere at 80 ^{o}C for 5hrs to remove any volatile components or residual solvents and to improve coating cross-linking [16]. Sample characterizations were done immediately following sample preparation. While the smaller samples were used to test stability of the coatings in various conditions, the larger ones were further used to evaluate their ice-repellent and anti-corrosive performance.

B. Sample charactrization

The sample stability in water, basic and acidic conditions was studied by means of CA measurements on samples immersed in nanopure water, tap water as well as basic (pH: 10.1) and acidic (pH:4) buffer solutions at ~18-20 ^{o}C. The wetting characteristics, reported in Fig. 2, were obtained following the standard sessile drop method on a DSA100 goniometer from Krüss [4, 6, 16]. For each sample, at least three different spots were randomly measured and the CA reported was the average value of about 5 measurements. Surface topographies were studied by means of scanning electron microscopy (SEM, Hitachi FEGSEM-SU 70) in high-vacuum mode. X-ray photoelectron spectroscopy (XPS) was performed with a Quantum-2000 instrument from PHI and an X-Ray source of achromatic Al Kα. (1486.6 eV). The ice adhesion test was conducted by creating glaze ice (up to ~1 cm thick and ~4-5 gr weight) over ~3.2 × 3.0 cm^2 surface

area and prepared by spraying supercooled micro-droplets of water (average size of ~65 μm) in a wind tunnel at subzero temperature (-10 ^{o}C), wind speed of 11 ms^{-1}, water pressure of 325 kPa, and water feed rate of 6.3 gm^{-3}. The iced samples were then spun in the centrifuge at constantly increasing speed. Potentiodynamic polarization was used to examine the overall corrosion behaviour of the bare and coated Al samples. The working cell was a standard three-electrode cell with working electrode area of 1 cm^2. A platinized net and saturated calomel electrode (SCE) were used as counter and reference electrodes, respectively. The setup used to control the experiments was a potentiostat system composed of a Solartron SI1287A electrochemical interface (controlled by Corrware® software). Measurements were performed in 3.5 wt.% NaCl solutions at room temperature. Potentiodynamic polarization curves were established and the corrosion potential (E_{corr}) and corrosion current density (i_{corr}) were determined using the *Tafel* extrapolation method. The polarization scan was started from 250 mV below the open circuit potential (OCP) in the cathodic region, through the corrosion potential, and 250 mV above the open circuit potential in the anodic region and with a constant scan rate of 1 mVs^{-1}. Finally, the Al panels were placed into a cyclic corrosion test chamber (*Ascott*) with the unmodified surface protected by a scotch tape and the the modified surfaces exposed alternatively to salt mist, dry and wet conditions in accordance with ISO14993-Corrosion of Netals and Alloys [17].

II. Results and discussion

A. Coating durability in different pH condition

The aluminium alloy is a hydrophilic material with a native oxidized thin layer (~4 nm thickness) demonstrating water CA and surface energy of ~41.5±3^{o} and 46.36±1.64 (mNm^{-1}), respectively. The Al substrates were etched in diluted HCl for 3 minutes followed by immersion in a BTSE or ODTMS solution. By immersing the Al samples in HCl, they react with HCl and $AlCl_3$ is produced while H_2↑is released. Bare etched Al showed water CA and surface energy of ~21.2±5^{o} and 68.30±1.16 (mNm^{-1}), respectively. Prior to deposition, the baths were vigorously stirred for 3 h to allow adequate dissolution/hydrolysis according to the following reaction:

$$\mathbf{R\text{-}Si(OMe)_3 + 3\ H_2O \rightarrow R\text{-}Si(OH)_3 + 3\ MeOH} \qquad \mathbf{(1)}$$

The freshly formed thin layer of metal oxide on the Al surface reacted with precursor molecules (BTSE) to form a covalently bound coating on the Al substrate. The CA value at this step was measured after the BTSE deposition was ~41^{o}. After ODTMS deposition, however, the double layer coating (BTSE/ODTMS) demonstrated initial values of CA>150^{o} (Figures 2 and 3a) and CAH<6° indicating the presence of well-coated rough Al surfaces. The CA measured on a flat Al sample coated with ODTMS alone is ~111±2^{o}. However, if the the sample is etched for 5 min, it shows hydrophobic properties as its CA and CAH values are ~143.4^{o}±2 and ~12.1°, respectively. These CA and CAH values imply that water droplets rest at the top of rough asperities on the solid-air composite surface (Cassie-Baxter wetting regime). In this regime, CA can be expressed as follows:

$$\mathbf{Cos\theta^* = \mathit{f}\ (1+Cos\theta) - 1} \qquad \mathbf{(2)}$$

where θ^* and θ are the CA of rough and flat surfaces with the same surface chemistry, respectively, and f is the area fraction of the solid surface that contacts water [4, 18]. The Cassie-Baxter model assumes that a water droplet is suspended on rough asperities and allows air trapping between asperities on a surface underneath the droplet, as shown in Fig. 1.

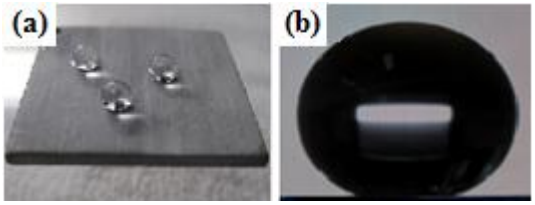

Figure 1: (a) Water droplets on as-prepared superhydrophobic Al surface, (b) water droplet profile on Al surface with CA>150°.

The XPS signals of C, O and Si, not shown here, of prepared superhydrophobic samples show that the Al samples were well covered with a low surface energy coating of ODTMS. Water droplets easily roll off from coated surface even when the surface is not tilted much (sliding angle of <5^{o}). Based on CA values and applying the Cassie-Baxter equation, a solid fraction (%) area of 11.48 is obtained for the BTSE/ODTMS samples (large amount of air trapped beneath the water droplets). The root-mean-square roughness (R_{rms}), skewness (Ssk) and kurtosis (Sku) of coated Al samples were measured using the AFM technique. While the first parameter represents the standard

deviation of surface profile from its mean value, the second parameter (S_{sk}) measures the asymmetry of the profile about its mean plane (being positive for surfaces with peaks and negative for surfaces with valleys), and last parameter (S_{ku}) is a measure of the "spikiness" of the surface [8]. The values of R_{rms}, S_{sk} and S_{ku} were 418±12, 2.8±0.2 and 12.5±3, respectively. While the value of R_{rms} measured automatically by AFM was <420 nm, the R_{rms} values measured for the as-received and mirror-polished samples were ~109 and ~25 nm, respectively. A hydrophobic surface with higher roughness, with more "spiky" peaks, should show improved water repellency and therefore, lower CAH values [8]. The water-solid contact area on this sample was expected to be small, which is consistent with small CAH (<6°) and high CA values (≥150°), characteristic of superhydrophobic surfaces. Also, the high CA and low CAH values observed suggest good surface coverage with ODTMS molecules. Scanning electron micrographs (SEM) images of etched Al sample coated with BTSE/ODTMS at different magnifications are shown in Figure 2, showing rough samples at micro/nanoscales. Both superhydrophobic samples demonstrated good self-cleaning properties as soil mesh was easily carried away by water droplets passing by.

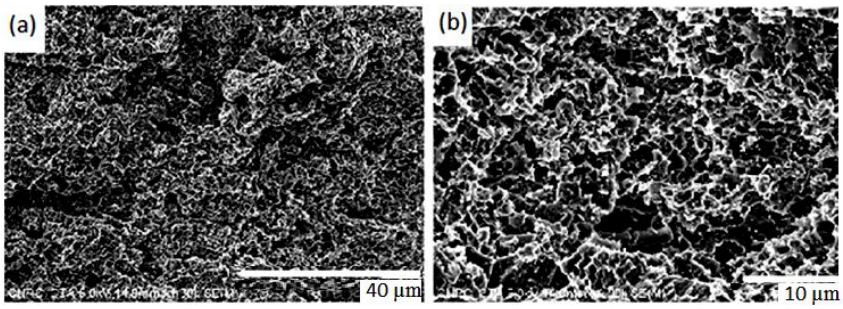

Figure 2: (a and b) Low and high magnification SEM images of 3-min-etched Al sample coated with BTSE/ODTMS.

Figure 3 shows CA and CAH of Al samples coated with BTSE/ODTMS layers as a function of immersion time in nanopure and tap water as well as in basic and acidic solutions. It is obvious that while this sample showed superhydrophobicity, indicating well-coated nano-structured superhydrophobic surfaces, they were found to gradually lose their superhydrophobicity, and completely so after ~720 to ~1000-h of immersion in basic and nanopure media, respectively.

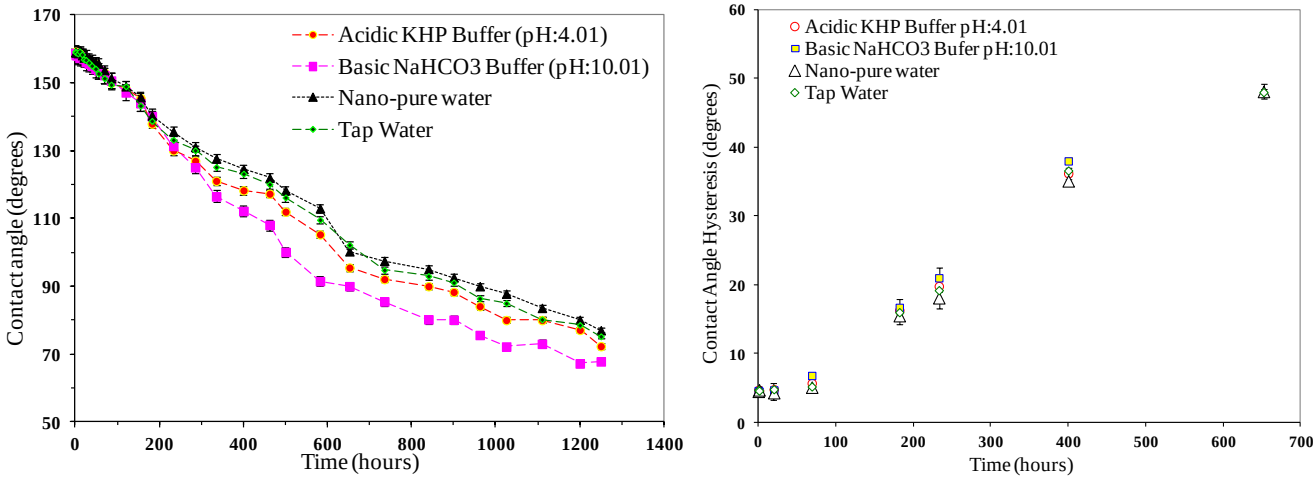

Figure 3: The CA (left) and CAH (right) vs. immersion time for Al coated with BTSE/ODTMS in different conditions.

This is associated with a decrease in CA and an increase in CAH. This tendency to lose surface hydrophobicity is most likely due to the rupture of the Si-O-Si bond between the ODTMS molecules and the BTSE layer caused by hydrolysis of these bonds. By immersing coated Al samples in aggressive media, the ~2-nm ODTMS layer undergoes some degree of degradation initially, as compared to the BTSE layer which is thicker, i.e., ~100 nm [19]. Therefore, alkylsilane molecules were removed from the surface, resulting in a decrease in surface superhydrophobicity. The top layer was not believed to be dense enough to prevent water molecules from penetrating through the coating and reaching the coating-substrate interface. This caused hydrolysis of the Si-O-Si bond, through which the ODTMS molecules were attached to the surface. However, the BTSE underlayer created a dense coating on Al surface to prevent corrosion acceleration, e.g. water going through underlayer coating and reaching the underneath metallic substrate.

B. Ice-repellent performance

Since dynamic hydrophobicity may play an important role in ice repellency, more specially for nanostructured substrates, glaze ice was prepared in a wind tunnel at subzero temperature (-10 ^{o}C) by spraying water micro-droplets with an average size of ~65µm to simulate outdoor icing condition [3-10, 16]. The procedure to evaluate ice adhesion strength was previously reported in detail elsewhere [3-10, 16]. Figure 4 shows the shear stress of ice detachment as a function of icing/de-icing cycles on coated Al samples. For each coating studied, one sample was subjected to 12 successive de-icing tests. Due to high mobility of water (low CAH), the ice accretion process was delayed on these surfaces. Both ODTMS and BTSE/ODTMS samples showed close values of shear stress, with very similar ice adhesion strength (*IAS*) on alkyl-grafted samples.

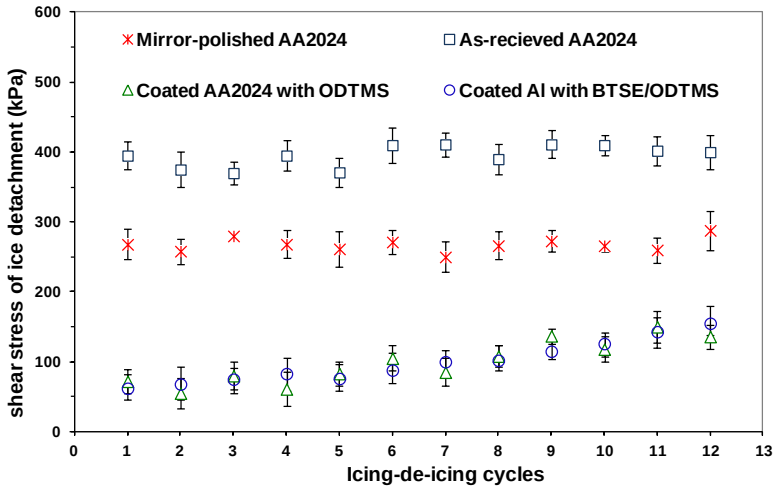

Figure 4: Shear stress of ice detachment *vs.* icing/de-icing cycle for Al surface coated with ODTMS and BTSE/ODTMS.

While as-received and mirror-polished Al was used as standard reference showing initial values of shear stress of ice detachment of ~370±30 kPa and ~270±20 kPa, respectively, its coated counterparts with ODTMS or BTSE/ODTMS coatings showed reduced values of ~62 kPa which is ~6 times lower than those on as-received Al standard (low CAH). This reduction is attributed to the presence of micro-/nano-hierarchical surface structures and low surface energy layers. However, superhydrophobic samples demonstrated increase of ice adhesion strength if compared to the as-prepared surfaces. The observed increase in ice adhesion strength is believed to be associated with both a decay of the ODTMS layer and of a larger ice-solid contact area, after 12 icing/de-icing cycles [5]. Meanwhile, water repellency of the coated sample gradually decreased over repeated icing/de-icing cycles (CA decreased and CAH increased). The top layer degraded on the BTSE underlayer in a manner similar to what happened on Al surfaces. Water molecules can attack the R-Si-O- bond to hydrolyze it, resulting in hydrophilic –OH groups on the surface.

C. *Anti-corrosive performance of double layer superhydrophobic coating*

Aluminium alloy 2024 is an alloy with Cu as major element and thus, with poor corrosion resistance. Therefore, developing anti-icing coatings on Al substrates highlights the necessity of improving their anticorrosive resistance. The potentiodynamic polarization curves of (a) bare AA2024 and the superhydrophobic coatings of (b) ODTMS and (c) BTSE/ODTMS on the Al alloy in 3.5 wt.% NaCl solution are presented in Fig. 5. The $E_{corr.}$and $j_{corr.}$ values derived from corresponding polarization curves, using *Tafel* extrapolation, are summarized in Table 2. It is evident in Fig. 5 and Table 2 that the value of E_{corr} positively increases from -0.71±0.03 V for bare Al to -0.62±0.02 V and -0.53±0.02 V for the superhydrophobic coatings of ODTMS and BTSE/ODTMS, respectively.

Table 2: Potentiodynamic results of bare and coated AA2024 with ODTMS and BTSE/ODTMS in 3.5 wt.% NaCl solution.

Sample	$E_{corr.}$ (V *vs.* SCE)	$j_{corr.}$ (µAcm^{-2})
Bare AA2024	-0.71±0.03	24.4
ODTMS Coating	-0.62±0.02	1.12
BTSE/ODTMS Coating	-0.53±0.02	0.008

The positive shift observed in E_{corr} is obviously due to the improvement of the protective performance of the superhydrophobic coating formed on the AA2024 substrate. In the meantime, the corrosion current density, j_{corr}, of the superhydrophobic coating of BTSE/ODTMS (8.04E−9 Acm^{-2}) had a decrease of about 4 orders of magnitude as compared to that of bare (2.44E-5 Acm^{-2}) and a decrease of 3 orders of magnitude as compared to ODTMS (1.12-6 Acm^{-2}). These results indicate that the double-layered superhydrophobic coating of BTSE/ODTMS improved corrosion resistance of Al surfaces as compared to bare Al on which the Al oxide layer is permeable to moisture and is prone to undergo dissolution in humid environment (accelerated corrosion). Therefore, the barrier property of the BTSE/ODTMS-modified Al sample was improved significantly as compared to an unmodified sample or even to an Al surface coated with ODTMS (single layer).

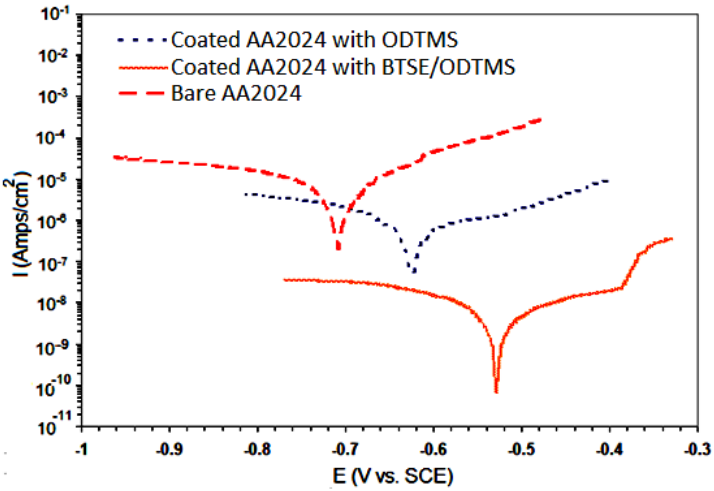

Figure 5: Polarization curves of AA2024 with and without coating.

The anti-corrosive properties of coated and bare samples were further studied by cyclic corrosion test. These samples were exposed alternatively to salt mist, dry and wet conditions in accordance with ISO14993 [17], following 3 repeating step: 2-hr exposure to a continuous indirect spray of neutral (pH: 6.5-7.2) salt water solution at a rate of 2ml-80cm^{-2}/hour at 35 ^{o}C, then, 4 hrs of air drying in a climate of >30 % RH at 60 ^{o}C and finally a 2-hr exposure to a wetting (95 to 100 % RH) at 50 ^{o}C. The bare Al samples exhibited extensive corrosion after only 8 cyclic corrosion cycles with appearance of numerous black dots (pits) in micrometer scale. Meanwhile, the size and density of the black dots increased as the number of salt spray cycles increased, which was due to increasing localized corrosion expansion.

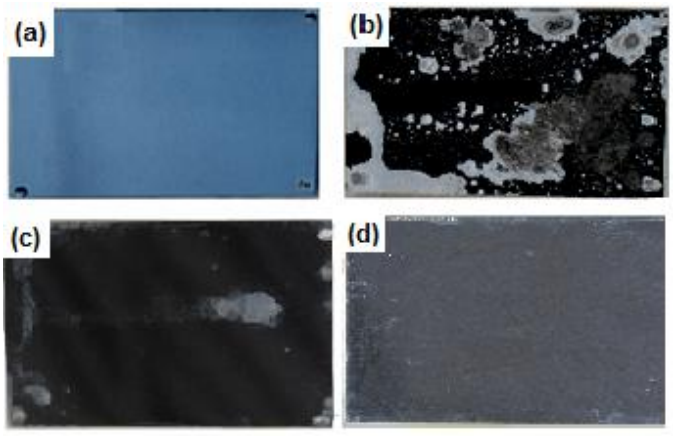

Figure 6: Optical images of bare AA2024 before (a) and after (b) an 18-cycle corrosion test for ODTMS coated AA2024 alloy (c) and for BTSE/TMSOD coated alloy (d) after test.

However, the earlier stage of corrosion was observed after 18 cycles of exposure in the case of samples coated with ODTMS. Small traces of corrosion were observed in the case of the Al sample coated with BTSE/ODTMS, even after 81 cycles of exposure (Fig.6). These observations confirm the results presented earlier in Fig. 5 by the potentiodynamic polarization curves showing the corrosion resistance improvement of samples modified with BTSE layers (less defect areas and dense enough) compared to bare or sample coated with ODTMS.

IV. Conclusions

In this study, alkyl-terminated nano-structured superhydrophobic surfaces were prepared by depositing a layer of ODTMS on BTSE-grafted AA2024 or rough AA2024 substrate. Both samples demonstrated excellent superhydrophobic and self-cleaning properties. Their durability in different conditions was tested by means of CA measurements, demonstrating gradual loss of hydrophobicity after ~720 to ~1000-h of immersion in basic and nanopure media, respectively, associated with a decrease of water CA. Ice-releasing properties of the coated surfaces were investigated by accumulating glaze ice in a wind tunnel at subzero temperature. While bare Al showed average ice detachment shear stress of ~370±30 kPa, its counterparts coated with ODTMS or BTSE/ODTMS showed reduced values of ~62 kPa which is ~6 times lower than those of the as-received Al standard (low CAH). This reduction is attributed to the presence of micro-/nano-hierarchical surface structures and low surface energy layers. These values gradually increased after as many as 12 successive icing/de-icing cycles. The increase in ice adhesion strength is believed to be associated with both a decay of the ODTMS layer and a larger ice-solid contact area after 12 icing/de-icing cycles. The electrochemical measurement results demonstrated that corrosion potential of the BTSE/ODTMS coating increased significantly, and its corrosion current density decreased by 4 orders of magnitude as compared to those on bare samples. These results showed that the BTSE underlayer on the AA2024 substrate provides particularly enhanced corrosion resistance which would be an excellent approach to improving anti-corrosive performance of metallic surfaces for outdoor applications instead of the toxic chromate-based coatings currently in use.

Acknowledgements

This research work has been conducted within the framework of the NSERC/Hydro-Quebec/UQAC Industrial Chair on Atmospheric Icing of Power Network Equipment (CIGELE) and the Canada Research Chair on Atmospheric Icing Engineering of Power Networks (INGIVRE) at Université du Québec à Chicoutimi. The authors would like to thank the CIGELE partners (Hydro-Québec, Hydro One, Réseau Transport d'Électricité (RTE), Rio Tinto Alcan, General Cable, K-Line Insulators, Dual-ADE, and FUQAC) whose financial support made this research possible.

References

[1] M. Farzaneh, "Atmospheric Icing of Power Networks", Ed., Springer, Berlin, pp. 320, August 2008.
[2] H. Saito, K. Takai, G. Yamauchi, "Water- and ice-repellent coatings". Surface Coatings International, vol. 80, pp. 168, 1997.
[3] S. A. Kulinich, M. Farzaneh, "Hydrophobic properties of surfaces coated with fluoroalkylsiloxane and alkylsiloxane monolayers", Surface Science vol. 573, pp. 379, 2004.
[4] S. Farhadi, M. Farzaneh, S. Simard, "Nanostructured ultra superhydrophobic Al surfaces: stability and icephobic properties", International Journal of Theoretical and Applied Nanotechnology, vol. 1, pp. 38, 2013.
[5] S. A. Kulinich, M. Farzaneh, "How wetting hysteresis influences ice adhesion strength on superhydrophobic surfaces", Langmuir, vol. 25, pp. 8854, 2009.
[6] S. Farhadi, M. Farzaneh, S. A. Kulinich, "Anti-Icing Performance of Superhydrophobic Surfaces", Applied Surface Science, vol. 257, pp. 6264, 2011.
[7] Z. Ghalmi, R. Menini, M. Farzaneh, "Effect of different aluminium surface treatments on ice adhesion strength", Advanced Materials Research, vol. 409, pp. 788, 2012.
[8] F. Arianpour, M. Farzaneh, S. Kulinich, "Hydrophobic and ice-retarding properties of doped silicone rubber coatings", Applied Surface Science, vol. 265, pp. 546, 2013.
[9] F. Arianpour, M. Farzaneh and S. A. Kulinich, "Nanopowder-Doped Silicone Rubber Coatings for Anti-Ice Applications", Scanning Electron Microscopy, 497, 4, 2010.
[10] S. Farhadi, M. Farzaneh and S. Simard "On Stability and Ice-Releasing Performance of Nanostructured Fluoro-Alkylsilane-Based Superhydrophobic AA2024 Surfaces", Inter. J. Theor. and Appl. Nanotechnology, 2012.
[11] Z. Guo, F. Zhou, J. Hao, W. Liu, "Stable Biomimetic super-hydrophobic engineering materials", Journal of the American Chemical Society, vol. 127, pp.15670, 2005.
[12] Y. Shaojun, S. O. Pehkonenb, L. Bin, Y. P. Ting, K.G. Neoh, E. T. Kang, "Superhydrophobic fluoropolymer-modified copper surface via surface graft polymerisation for corrosion protection", Corrosion Science, vol. 53, pp. 2738, 2011
[13] V. F. Petrenko and S. Peng, "Reduction of ice adhesion to metal by using self-assembling monolayers (*SAMs*)", Can. J. Phys, vol. 8, pp. 387-393, 2003.
[14] M. Farzaneh, "Systems for prediction and monitoring of ice shedding, anti-icing and de-icing for overhead lines", CIGRÉ WG B2.29, CIGRE Publications, Technical Brochure #438, pp. 100, 2010.
[15] E. H. Andrews, H. A. Majid, N. A. Lockington, "Adhesion of ice to a flexible substrate", Journal Materials Science, vol. 19, pp. 73, 19984.
[16] V. K. Croutch and R. A. Hartley, "Adhesion of ice to coatings and the performance of ice release coatings", *J. Coat. Technol*.**,** vol. 64, pp. 41, 1992.
[17] http://www.matweb.com/search/DataSheet.aspx?MatGUID=57483b4d782940faaf12964a1821fb61.
[18] L. Thomsen, B. Watts, D. Cotton, J. Quinton and P. Dastoor, Surf. Interface Anal., 37, 472, 2005.
[19] X. Yao, Q. W. Chen, L. Xu, Q. K. Li, Y. L. Song, X. F. Gao, D. Quere and L. Jiang, Adv. Funct. Mater., 20, 656, 2010.
[20] S. Farhadi, M. Farzaneh and S. A. kulinich, "Preventing Corrosion and Ice Accretion on Aluminium Surfaces Applying Organic and Inorganic Thin Films", MSc thesis, UQAC, Dec. 2010.
[21] http://www.iso.org/iso/home/store/catalogue_tc/catalogue_detail.htm?csnumber=24372.
[22] ATLAS Weathering Testing Guidebook.
[23] A. Franquet, C. Le Pen, H. Terryn, et al., "Effect of bath concentration and curing time on the structure of nonfunctional thin organosilane layers on aluminium", Electrochim. Acta, vol. 48, pp. 1245, 2003.

Hydrophobic and anti-ice properties of homogeneous and heterogeneous nanoparticle coatings on Al 6061 substrates

F. Arianpour*, M. Farzaneh, R. Jafari,
Canada Research Chair on Atmospheric Icing Engineering of Power Networks (INGIVRE) www.cigele.ca
Université du Québec à Chicoutimi, Canada
*Email: faranak.arianpour@uqac.ca

Abstract- In this study, chemically homogeneous and heterogeneous nanoparticles coatings of low surface-energy materials on Al surface were investigated. Experimental work has demonstrated the existence of the heterogeneity effect on an Al surface by applying different hydrophobic functions (C-H and C-F). More precisely, for homogeneous coatings, the contact angle (CA) values were ~100° while it was ~134° for heterogeneous coating (HC). Contact angle hysteresis (CAH) was smaller for HC (~32°) than homogeneous coatings (~46° and ~56°). Icing tests showed delayed ice formation and lower adhesion strength on HC. The chemical composition of the surfaces was analyzed by X-ray photoelectron spectroscopy (XPS). The scanning electron microscopy (SEM) and atomic force microscopy (AFM) analysis of the coated surfaces demonstrated the presence of a rough structure at micro/nanoscale levels on the mirror polished Al substrate.

Keywords: homogeneous coating, heterogeneous coating; contact angle (CA); contact angle hysteresis (CAH); hydrophobic; Ice Adhesion Strength; X-ray photoelectron spectroscopy (XPS); scanning electron microscopy (SEM); atomic force microscopy (AFM).

INTRODUCTION

In cold climate regions, ice and wet snow accumulations on overhead power transmission lines are sometimes the source of damage and malfunctions which may lead to mechanical line failures, insulator flashovers, etc. [1-4]. Reducing or preventing ice accumulation on exposed surfaces can be accomplished by developing ice-phobic coatings [5-8]. There is extensive research on hydro/ice-phobic properties of various nanoparticles incorporated in polymer coatings [9-12]. However, the low surface energy heterogeneous coatings (HCs) or surfaces including both hydrocarbons and fluorocarbons have drawn less attention. These types of coatings are a very attractive alternative because they show lower ice adhesion as compared to homogeneous coatings. Important papers related to this work have been published in the field of heterogeneous polymer coatings, where the authors tried to decrease ice adhesion by applying a heterogeneous effect [13-17]. Therefore, the aim of this work is to study of the heterogeneity effect on the hydrophobic and ice-phobic properties of coatings on polished aluminum alloy 6061 (AA6061).

I. EXPERIMENTAL PROCEDURE

Aluminum alloy 6061 composed of Al 97.9 wt.%, Mg 1.0 wt.%, Si 0.60 wt.%, Cu 0.28 wt.%, Cr 0.20 wt.% from industrial rolled sheets was cut into 5.1 × 3.2 cm samples used as substrates. Prior to coating, the plates were mechanically polished. The polished Al plates were then cleaned in acetone and distilled water each for 5 minutes. The organic polyethylene (PE) and polytetrafluoroethylene (PTFE) providing low surface energy were purchased from Good-fellow and Sigma-Aldrich® companies, respectively. A one-gram (1 g) solution of polyethylene (PE) in 50 ml of toluene was prepared as a first layer for the homogeneous coating. For HC, suspension of 1 g of dispersed nanoparticles with different surface energy such as polytetrafluoroethylene (PTFE) and Al_2O_3 in 50 ml of methanol were prepared. These suspensions were shaken by ultrasonic waves for 5 minutes followed by magnetic stirring during 20 minutes. The suspensions were used to elaborate several series of HCs on polished Al surfaces, in order to study the effect of different surface energy and surface roughness. The homogeneous and heterogeneous nanoparticle coatings were prepared using a spin-coater from Laurel (WS-400B-6NPP). Spin coating is a commonly used technique for preparing uniform thin films on flat substrates which involves the controlled precipitation from the solution of a compound on a suitable substrate while spinning with specific parameters. The spinning rate was set at 500 rpm (15 s). Upon coating, all samples were heat-treated at 70 °C in oven for 2 hours to remove residual solvents. Table 1 shows the procedure for preparing homogenous and heterogeneous nanoparticle coatings.

Table1: Detail information for prepararing homo/heterogeneous coatings.

Material	Quantity	Solvent	Method	Company	Abbreviate
PE	1 g	50 ml Toluene (at 110° cc)	Spin coating	Good-fellow	PE-spin
PTFE	1 g	50 ml Methanol	Spin coating	Sigma-Aldrich	PTFE-spin
PE, PTFE	1g, 1g	100 ml Toluene	Spin coating	Good-fellow, Sigma	PE-PTFE
PE, PTFE	1g, 1g	100 ml Toluene	Spin coating	Good-fellow, Sigma	PE+PTFE

The dried samples were stored in clean Petri dishes at ambient conditions and characterization was conducted immediately after. The coated samples were characterized by measuring their hydrophobic and ice-phobic properties. The wetting characteristics reported in this study were obtained following the standard sessile drop method on a fully automated contact angle goniometer (DSA100 from Krüss) with controllable volume (4 µl) of water droplets. These measurements were performed with the Young–Laplace method. Surface topographies were studied using scanning electron microscopy (SEM, Hitachi S-4700 Field-Emission SEM with accelerating voltages from 500 V to 25 kV) to take surface images of coated samples and therefore reveal their surface characteristics. The ice-repellent performance of bare as well as prepared coatings was evaluated using a home-made centrifugal apparatus which was placed in a climate room at subzero temperature (-10^{o}C). The detail of ice preparation procedure has been described previously [9].

II. Results and discussion

Figure 1 shows the CA and CAH for the PE-spin, PTFE-spin, PE-PTFE and PE+PTFE coatings. For the homogeneous coatings PE-spin and PTFE-spin on a polished Al surface, the CA values were ~100^{o} and ~98^{o}, respectively. A significant enhancement of CA values (~134^{o}) was observed for the heterogeneous coating of PE-PTFE. In the case of HCs, the presence of PTFE nanoparticles on a PE-coated Al surface resulted in surface roughening. Therefore, to exclusively focus on the heterogeneity effect and to avoid the surface roughening, a PE+PTFE coating on Al sample was also prepared. More precisely, the PE+PTFE sample was prepared from the deposition of a mixture of PE and PTFE nanoparticles on an Al surface. This sample was only prepared to investigate the effect of the surface roughening and heterogeneity effect. As shown in Figure 1, the existence of surface roughening in case of PE+PTFE coated Al sample resulted in a bigger CA value of ~129^{o} compared to homogeneous coatings. This observation is due to surface roughening. However, the CA value of PE-PTFE (~134^{o}) was greater than that of PE+PTFE (~129^{o}). This may be due to the heterogeneity effect. Moreover, the CAH values are smaller for PE-PTFE (~32^{o}) than for homogeneous PE-spin and PTFE-immersion coatings and even for the PE+PTFE sample (~64^{o}). Therefore, a small value of CAH is the most important factor in the heterogeneity effect [14].

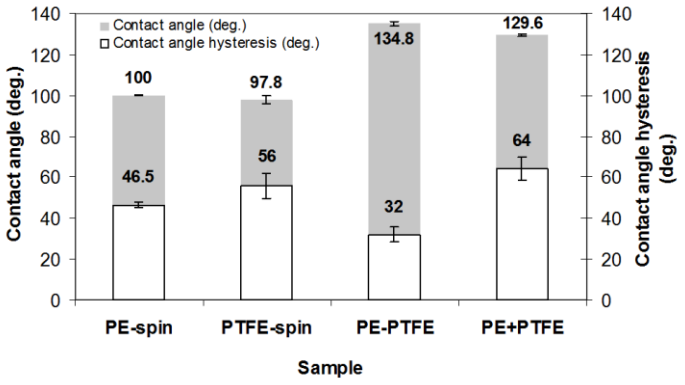

Figure 1: Contact angle and contact angle hysteresis values of homo/heterogeneous coatings.

To further support and confirm the presence of surface roughening on Al samples coated with PTFE nanoparticles, an AFM analysis was conducted. Table 2 shows the root mean square (Rms) roughness values for the PTFE-spin, PE+PTFE and PE-PTFE coatings. It is obvious that the Rms values of the PE+PTFE and PE-PTFE coatings are close together, although they are somewhat bigger for PE+PTFE than for PE-PTFE. However, the CA value of a PE+PTFE coated Al sample was smaller than what was observed in the case of a PE-PTFE coating. Meanwhile, the CAH value for a PE+PTFE coated Al sample was much bigger than that of a PE-PTFE coating. The observed difference in CAH values of such coatings was about 32^{o}. Therefore, it is possible to say that in an AFM analysis, contact angle and contact angle hysteresis measurements confirm again the effect of heterogeneity or dissimilar functions (C-H and C-F) on polished Al surfaces.

Table 2: The Rms (nm) of homogeneous and HCs samples.

Sample	Root mean square (nm)
PTFE-spin	165.5 ± 68.58
PE+PTFE	284.79 ± 173.14
PE-PTFE	239.85 ± 145

Ice adhesion tests were carried out on homo/heterogeneous nanoparticle coatings. The results showed that the ice detachment shear stress value for the HC of PE-PTFE is smaller than that for homogeneous PE-spin. Also, the ice adhesion reduction factor (*ARF*) of homogeneous and heterogeneous coatings showed that the ice adhesion strength values are ~1.13 and ~1.3 times lower than those obtained on a polished Al sample, respectively. It is worthy to mention that the shear stress values of ice detachment for the PE+PTFE sample was generally greater than that obtained on a polished Al sample. This fact is obvious from the CAH values of homogeneous PE-spin and heterogeneous PE-PTFE coatings. Since, the CAH value for the HC of PE+PTFE sample was greater than for the homogeneous and heterogeneous coatings of PE-spin and PE-PTFE, respectively. This is in agreement with the values of the shear stress of ice detachment [18]. The reason for the enhancement of CAH values in the case of the PE+PTFE compared to the homogeneous sample is the topological nature of the surface roughness, which is of prime importance in determining hydrophobicity [20-23].

III. Conclusions

In this research work, homogeneous and heterogeneous nanoparticle coatings of low surface-energy materials with hydro/ice-phobic properties were prepared by the spin coating method. The contact angle, contact angle hysteresis measurements, and AFM analysis results demonstrated the effect of heterogeneity on Al substrates. Also, the obtained results showed that the HCs prepared from dissimilar hydrophobic functions of C-H and C-F can affect the hydro/ice-phobic characteristics of such coatings. The anti-ice performance of HC, confirmed the heterogeneousity effect on Al surfaces, since the ice-phobic properties of HC improved upon those of homogeneous coatings and polished Al substrate.

IV. Acknowledgements

This research work has been conducted within the framework of the NSERC/Hydro-Quebec/UQAC Industrial Chair on Atmospheric Icing of Power Network Equipment (CIGELE) and the Canada Research Chair on Atmospheric Icing Engineering of Power Networks (INGIVRE) at Université du Québec à Chicoutimi. The authors would like to thank the CIGELE partners (Hydro-Québec, Hydro One, Réseau Transport d'Électricité (RTE), Rio Tinto Alcan, General Cable, K-Line Insulators, Dual-ADE, and FUQAC) whose financial support made this research possible.

V. References

[1] M. Farzaneh, "Atmospheric Icing of Power Networks", Springer, Berlin, 381 pp, 2008.

[2] M. Farzaneh, "guide for test methods and procedures to evaluate the electrical performance of insulators in freezing conditions", IEEE standard 1783. IEEE Press, New York, 2009.

[3] M. Farzaneh, W. A. Chisholm, "Insulators for icing and polluted environments", IEEE Press series on Power Engineering, IEEE/John Wiley, New York, pp. 680, 2009.

[4] M. Farzaneh. O. T. Melo, "Flashover performance of insulators in the presence of short icicles", Int. J. Offshore Polar Eng, vol.4, pp.112, 1994.

[5] C. Laforte, J. L. Laforte, J. C. Carrier, "How a solid coating can reduce the adhesion of ice on a structure", Proceedings of the International Workshop on Atmospheric Icing of Structures (IWAIS), pp. 1-5, 2002.

[6] R. Jafari, R. Menini, M. Farzaneh, "Superhydrophobic and icephobic surfaces prepared by RF-sputtered polytetrafluoroethylene coatings Appl. Surf. Sci. vol. 257, pp. 1540–1543, 2010.

[7] V. F. Petrenko and S. Peng, "Reduction of ice adhesion to metal by using selfassembling monolayers (SAMs)", J. Phys. vol. 81, pp. 387, 2003.

[8] J. L. Laforte, M. A. Allaire and J. Laflamme, "State-of-the-art on power line de-icing", Atm. Res. vol. 46, pp. 143, 1998.

[9] F. Arianpour, M. Farzaneh, S.A. Kulinich, "Hydrophobic and ice-retarding properties of doped silicone rubber coatings", Appl. Surf. Sci. vol. 265, pp. 546, 2013.

[10] R. Jafari and M. Farzaneh, "A simple method to create superhydrophobic aluminium surfaces", Mater. Sci. Forum., vol. 706, pp. 2874, 2012.

[11] G. Momen, M. Farzaneh, R. Jafari, "Wettability behaviour of RTV silicone rubber coated on nanostructured aluminium surface", J. Appl. Surf. Sci., vol. 257, pp. 6489–6493, 2011.

[12] A. Safaee, D.K. Sarkar, M. Farzaneh, "Superhydrophobic properties of silver-coated films on copper surface by galvanic exchange reaction", vol. 254, pp. 2493–2498, 2008.

[13] H. Murase, and T. Fujibayashi, "characterization of molecular interfaces in hydrophobic systems", Prog. Org. Coat.., vol. 31, pp. 97, 1997.

[14] H. Murase, K. Nanishi, H. Kogure, T. Fujibayashi, K. Tamura, N. Haruta, "Intraction between heterogeneous surfaces of polymers and water", J. Appl. Polym. Sci., vol. 54, pp. 2051, 1994.

[15] N.R. Byrd, "Polysiloxane (Amide-ureide) anti-ice coating", US 6,797,795, 2004.

[16] R. Menini and M. Farzaneh "Advanced Icephobic Coatings". J. Adhes. Sci. Tech. vol. 25, pp. 971, 2011.

[17] X. Lia, Y. Zhao, H. Li, X. Yuan, Preparation and icephobic properties of polymethyltrifluoropropylsiloxane-polyacrylate block copolymers, Appl. Surf. Sci. vol. 316, pp. 222–231, 2014.

[18] S.A. Kulinich, M. Farzaneh, "How wetting hysteresis influences ice adhesion strength on superhydrophobic surfaces", Langmuir, vol. 25, pp. 8854, 2009.

[19] S. A. Kulinich, M. Farzaneh, "Hydrophobic properties of surfaces coated with fluoroalkylsiloxane and alkylsiloxane monolayers", Appl. Surf. Sci., vol. 573, pp. 379–390, 2004.

[20] S. A. Kulinich, M. Farzaneh, "On ice-releasing properties of rough hydrophobic coatings", J. Cold Reg. Sci. Technol., vol. 65, pp. 60-64, 2011.

[21] M. Miwa, A. Nakajima, A. Fujishima, K. Hashimoto, T. Watanabe, "Effects of surface roughness on sliding angles of water droplets on superhydrophobic surfaces", Langmuir, vol. 16, pp. 5754, 2000.

[22] W. Chen, A.Y. Fadeev, M.C. Hsieh, D. Oner, J. Youngblood, T.J. McCarthy, "Ultrahydrophilic and ultrahydrophobic surfaces: Some comments and examples", Langmuir, vol. 15, pp. 3395, 1999.

[23] H. Nakae, R. Inui, Y. Hirata, H. Saito, "Effects of surface roughness on wettability", Acta Mater. Vol. 46, pp. 2313, 1998.

Lessons learned from "Large scale, cost-effective deployment of wind energy in icing climates"

Göran Ronsten
OX2 & WindREN
goranronsten@windren.se

***Abstract*: The two primary goals of this project have been to a) support the development and installation of 40 de-icing systems and b) for 4 competing meteorological entities to develop and improve methods to assess production losses caused by icing. Funding, some 7,25 MEuro (72,5 MSEK), was provided by Swedish Energy Agency between 2008 and 2015. The activities carried out include synoptic icing measurements, mapping of icing, daily production forecasts with a focus on losses caused by icing, seasonal reports, de-icing of wind turbine blades and the evaluation of performance and loads with respect to icing. In a European perspective, the support for development of wind energy technologies adapted to icing climates has improved since 2008. Initially to be blamed for the lack of interest was a Catch-22-like situation where a lack of mapping of icing had prevented market studies to be carried out. A milestone market study, [1] is available since early 2013.**

Keywords: wind energy, icing, measurements, mapping of icing, de-icing, production losses

LEGEND AND ABBREVIATIONS

CC	*Cold Climate, both LT and icing*
IEA	*International Energy Agency*
EM	*Swedish Energy Agency*
LT	*Low Temperature (not icing)*
LWC	*Liquid Water Content*
MVD	*Median Volume Diameter*
RD&D	*Research, Development & Demonstration*
Task 19	*IEA WG dealing with CC challenges*
WG	*Working Group*
WT	*Wind Turbine*
10 SEK	*1 Euro (exchange rate used in this paper)*

INTRODUCTION

A. Wind energy in Sweden – present and future

By the end of 2014, Sweden had a growing, installed wind power capacity of 5 425 MW, [2], that produced 11.5 TWh, equaling 8% of the electricity consumed in the country, [3]. A scenario with 100% renewable energy has been studied by Söder, [4], where 60 TWh of electricity come from wind and photo voltage.

How much is 60 TWh compared to electricity produced by nuclear power in Sweden? Until 1999, Sweden had 12 nuclear reactors in operation. One of two units in Barsebäck ceased production in 1999 and the other was shut down in 2005. The majority owners of the reactors in Oskarshamn (E.ON) and Ringhals (Vattenfall) recently (June 2015) announced their intentions to, with reference to current and forecasted low electricity prices, close down another four units before 2020. The average annual production from nuclear power in Sweden between 2005-2014 was 59.6 TWh. Statistics for 2001-2013 can be found in [5].

B. Wind energy in icing climates

The goal of any wind farm owner is to keep the wind turbines (WT) ready to operate when there's wind, i.e. maintain a high availability. Iced up WT blades poses a significant challenge to WT manufacturers as well as wind farm developers and owners in cold climate regions around the world. The main reasons for the concern are: personal safety, loss of production, increased noise and an expected reduction of the life of components.

I. MOTIVATION

A. Not producing when expected is expensive

Electricity produced by Swedish wind farms is sold either through long-term contracts at fixed prices or on the Nordic spot market to the marginal price from the most expensive, currently needed, production unit. Not producing due to iced up wind turbine blades when production has been forecasted, based on wind only, isn't a major problem if the installed wind energy production capacity is small (low penetration). However, a large increase in wind capacity in N Sweden requires commercially available de- and anti-icing systems. De-icing systems were, likely due to a lack of market studies, only available from one single manufacturer when this project was initiated in 2008.

B. Icing reduces the reimbursement for electricity in long-term contracts

Before a standard wind farm has been built, the developer focuses on four issues; wind, wind, wind (power is proportional to the third power of the wind speed) and infrastructure.

Once the wind farm has been built and the normalized annual energy production is known, the income will be dependent on wind speed, electricity price and, in the case of Sweden and Norway, the price of the green certificates. On a liberalized electricity market the most stable parameter of wind, electricity price and reimbursement for green certificates is… the wind resource and thereby the energy production.

Icing will in the near future, unless a large-scale deployment of de-icing systems is carried out, reduce the payment for electricity in long-term contracts, as the cost for balance of power will be indirectly charged through a lower reimbursement. Luckily, icing doesn't influence the

price of the green certificates, which can be saved over the years and sold anytime.

II. Why didn't we start mapping of icing earlier?

Before the start of COST Action 727 (Atmospheric icing of structures) in April 2004 Sweden had carried out a number of cold climate wind energy evaluation projects, participated in IEA RD&D Task 19 and been involved in the EU-project NEW ICETOOLS. No new cold climate projects could be foreseen by the Swedish Energy Agency (EM) as the plans for large scale offshore wind energy were ambitious.

The wind turbine manufacturers were only seemingly interested in adapting the turbines to cold climates until early 2005 when long backlogs at the wind turbine manufacturers made niche segments like wind energy in icing climates uninteresting for all but Enercon. Only one cold climate wind pilot project was ordered by EM as offshore was at focus until March 2007. At this time, the utility E.ON announced that the compensation for offshore wind farms in Sweden was insufficient and surprisingly handed 70 MSEK (7 MEuro) in wind pilot project support back to the EM.

One challenge encountered in European wind energy research development, from an icing point of view, has been the one-sided focus on offshore. A Catch-22 situation appears when European funding for the development of de-/anti-icing systems requires market studies, which require mapping of icing, which requires the development and verification of icing forecasts. All of a sudden we're, no surprise, once again back at the core of IWAIS, i.e. measuring and modeling atmospheric icing on structures.

III. National funding was made available based on intuition rather than on a market study

In March 2007, the message from E.ON to the EM was clear, "offshore is too expensive". EM ordered another 4 cold climate related wind pilot projects with a total budget exceeding 200 MSEK (20 MEuro). The wind turbine manufacturers' backlogs shrank when the financial crises hit also the wind turbine manufacturers in August 2008. Additionally, an increased international competition has since made many more wind turbine manufacturers that are active in areas prone to significant icing interested in finding cost-effective de-/anti-icing solutions.

Living in a cold climate makes people, at least in the wintertime, aware of the challenges associated with iced up objects. During the winters, the hit, near-hit or even the risk of falling ice from tall buildings, are in the news multiple times per week. It is therefore no wonder if the EM in 2009 decided to promote the development of wind energy in icing conditions, in four separate projects through its wind pilot project program, without having access to either a market study or a national icing map. EM's best option was to encourage the WT manufacturers to provide WT equipped with de-icing systems.

IV. The wind pilot project

OX2 Wind (7.25 MEuro) – The main objective for OX2's wind pilot project has been to promote the development and installation of de-icing systems.

For all reports provided to EM, OX2 has requested confidentiality with reference to commercial interests. By Sep 15, 2015, some of the reports produced within this project will be made publicly available. Results from the project has been continuously presented at conferences in general and at Winterwind, [6] and [7], in particular.

A. De-icing systems

In this project alone, more than 40 de-icing systems were to be installed. As commercial de-icing systems were largely unavailable, 3rd party development was initially encouraged with an aim to catch the interest of the WT manufacturers.

Starting in the fall of 2008, **Kelly Aerospace Thermal Systems (US)** installed three de-icing systems on Vestas V90-2MW. Three de-icing systems from **EcoTEMP (CA)** were deployed on Vestas V90-2MW and one system was installed on a Siemens SWT 2.3 with a rotor diameter of 101 m. Later, **Siemens** developed a first and a second generation de-icing systems for OX2. The former was installed on a wind turbine on Brahehus. The latter system was installed in 9 turbines on Korpfjäll in 2011. In 2014, **Vestas** erected 30 of its V90-2MW wind turbines, all equipped with a newly developed de-icing system. Described above are 47 de-icing systems. Additionally, funding from the project, for the development of de-icing systems, has been made available to a wind turbine manufacturer for testing the performance of a de-icing system. De-icing systems from all four providers mentioned above have been presented at the Winterwind conferences, [6] and [7].

Figure 1 shows a significant amount; several hundred kg, of ice collected on a non-de-iced wind turbine blade.

Figure 1: Ice collected on a wind turbine blade, which was taken down for the removal of a de-icing system.

B. Synoptic icing measurements

Measurements have been carried out in four tall masts from N to S and at neighboring wind farms or planned sites.

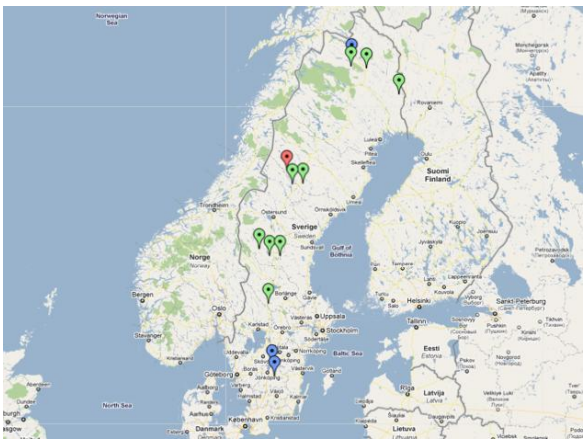

Figure 2: Distribution of ice measurement stations in OX2's wind pilot project.

At most of the measurement stations there's been a camera installed to enable verification of the icing measurements. The cameras have provided valuable empirical data not only for ice build-up, but also for ice ablation (melting, sublimation and breaking off). Inherently difficult to calculate, the cameras have captured when brittle ice has braked into pieces at low temperatures.

Figure 3: A view of the instruments at the Sjisjka icing measurement station. This particular mast is 60 m tall.

Monthly evaluations of icing measurements and production have been carried out by **a)** Weathertech (SE), **b)** Kjeller Vindteknikk (NO, **c)** Leading Edge Atmospherics (US)/Finnish Meteorological Institute FMI (FI) and **d)** The Swedish Meteorological and Hydrological Institute SMHI (SE). These executors have also provided daily forecasts as well as seasonal reports. Results have been presented at five Winterwind conferences, i.e. Winterwind 2011 to 2015, [6] and [7].

V. RESULTS AND DISCUSSION

A. De-icing systems

Since 2008, the Swedish Energy Agency has been using significant resources to actively promote a rapid development of wind energy in cold climates. A major hurdle for the developers has been overcome as WT manufacturers have developed and made de-icing systems available. It still remains, however, to include icing in the guaranteed availability.

Knowledge regarding the surprisingly large energy production losses caused by icing comprises sensitive information for the WT owners and is therefore generally kept confidential. The initial, major drawback of this secrecy made developers in general unable to put sufficient pressure on the WT manufacturers to offer de-icing systems. Another drawback of the secrecy has been that authorities, for better and worse, have been largely unaware of the challenges associated with wind farming in icing conditions. Authorities might want to interfere if ice is causing an unacceptable increase of noise and risk of ice throw.

At Winterwind 2014, Madsen presented examples of the performance of Siemens de-icing systems, [8]. No results were presented by Siemens at Winterwind 2015, [9]. Siemens has announced large orders, several hundred units, for wind turbines equipped with de-icing systems.

The 30 Vestas de-icing systems funded by the project were deployed in late 2014 and no information regarding the performance of these de-icing systems is yet publicly available. The performance has, however, been evaluated by the meteorologists involved in the wind pilot project. The results will be made available, likely in confidential reports, to EM by Aug 15, 2015. Since 2012, a general description of Vestas de-icing system has been made annually at Winterwind, the latest by Nielsen at Winterwind 2015, [10]. Nielsen provided examples of the performance of the system and mentioned orders of 72 wind turbines equipped with de-icing systems.

B. Mapping of icing

If the anti-/de-icing systems would be capable of handling light, medium and severe icing conditions as required according to local site conditions, mapping of icing and an increased cost of balancing of power with respect to icing would be of little concern.

Evaluations of modeled and measured icing and power performance show a) icing periods to be captured relatively well in time, b) the magnitude of icing to be difficult to estimate correctly and c) the actual production losses due to iced up wind turbine blades to be surprisingly large, although d) generally smaller than the initially modeled losses. Results from the evaluation of performance of wind farms exposed to icing using data from OX2's wind pilot project were presented at Winterwind 2015 by

Weathertech, [11] and [12]: *"Much can be learned by careful analysis of SCADA data from existing wind farms"* and *"The variability coefficient for icing hours is an order of magnitude larger than for wind speed"*,

Kjeller Vindteknikk, [13]: *"General improvement of the power forecasts when the icing is included."* and

The Swedish Meteorological and Hydrological Institute SMHI, [14]: *"Production loss forecast a bit too pessimistic, needs tuning"*.

Leading Edge Atmospherics & the Finnish Meteorological Institute FMI presented [15] at

Winterwind 2014: *"Each of the 4 [analysis] systems "wins" some of the time"*.

At IWAIS 2015, there will be ten presentations from the wind pilot project, [16]-[25].

VI. Conclusions

Significant progress has since 2008 been made both with respect to the development and commercial availability of de-icing systems as well as the ability to map and forecast icing.

The wind turbine manufacturers were, mainly due to a large order backlog, initially hesitant to develop de-icing systems. A developer ordering third party de-icing systems was a drastic call for help. This project has, according to at least one manufacturer, played an important role in making the importance of de-icing capability catch the manufacturer's attention.

Mapping of icing, forecasting of icing and verification of production losses has been carried out by the four executors in an atmosphere of close cooperation, in spite of being competitors. This has been in line with OX2's goal to raise the standards to a level from which all stakeholders of wind energy in icing climates can benefit.

Acknowledgment

The author would like to thank all those involved in various cold climate related projects in Sweden for contributing, actively or passively, to the content of this paper. It's also worth mentioning that the Swedish Energy Agency luckily didn't need a market study to realize that icing of WT blades can be a showstopper.

References

[1] "World Market Update 2012", Navigant Research, March 26, 2013

[2] "New Record in Worldwide Wind Installations", World Wind Energy Association, February 5, 2015, http://www.wwindea.org/new-record-in-worldwide-wind-installations/ (2015-06-27)

[3] "Global Wind Report – Annual Market Update 2014", Global Wind Energy Council, March, 2015, p.70, http://www.gwec.net/wp-content/uploads/2015/03/GWEC_Global_Wind_2014_Report_LR.pdf (2015-06-27)

[4] Söder L., "På väg mot en elförsörjning baserad på enbart förnybar el i Sverige - En studie om behov av reglerkraft och överföringskapacitet", Version 4.0 (in Swedish), 2014-06-22, http://kth.diva-portal.org/smash/get/diva2:727697/FULLTEXT01.pdf (2015-06-27)

[5] "Electricity supply and use 2001–2013", http://www.scb.se/en_/Finding-statistics/Statistics-by-subject-area/Energy/Energy-supply-and-use/Annual-energy-statistics-electricity-gas-and-district-heating/Aktuell-Pong/6321/24270/ (2015-06-27)

[6] Winterwind presentations, previous conferences, 2008-2014 http://winterwind.se/about-the-conference/previous-conferences/ (2015-06-27)

[7] Winterwind 2015, presentations, http://winterwind.se/about-the-conference/presentations/ (2015-06-27)

[8] Madsen F.D., "Siemens Wind Power Blade De-Icing - 25 years of experience with turbines in cold climate", presented at Winterwind 2014, Sundsvall, Feb, 2014, http://www.winterwind.se/sundsvall-2014/presentations-2014/?edmc=2860 (2015-06-27)

[9] Birkemose B., "Siemens Wind Power Blade De-icing", presented at Winterwind 2015, Piteå, Feb, 2015, http://windren.se/WW2015/WW2015_57_711_Birkemose_Siemens_Deicing.pdf (2015-06-27)

[10] Nielsen,B.D., "Vestas De-icing System", presented at Winterwind 2015, Piteå, Feb, 2015, http://windren.se/WW2015/WW2015_61_715_Nielsen_Vestas_Deicing.pdf (2015-06-27)

[11] Baltscheffsky M., Söderberg S., "Towards an increased understanding of icing conditions within a wind farm through visualisation of SCADA data in a topographic context", presented at Winterwind 2015, Piteå, Feb, 2015, http://windren.se/WW2015/WW2015_34_433_Baltscheffsky_Weathertech_Ice_intrafarm.pdf (2015-06-27)

[12] Söderberg S., Baltscheffsky M., "Analysis of spatial and temporal variability in icing conditions and production losses due to icing using a new long-term icing climate database", presented at Winterwind 2015, Piteå, Feb, 2015, http://windren.se/WW2015/WW2015_36_512_Soderberg_Weathertech_Icewind_Production_losses.pdf (2015-06-28)

[13] Byrkjedal Ø. Et al, "Validation of icing and wind power forecasts at cold climate sites", presented at Winterwind 2015, Piteå, Feb, 2015, http://windren.se/WW2015/WW2015_37_513_Byrkjedal_Kjeller_Icewind_Forecast_validation.pdf (2015-06-28)

[14] Olsson E., "High resolution forecast maps of production loss due to icing", presented at Winterwind 2015, Piteå, Feb, 2015, http://windren.se/WW2015/WW2015_42_531_Olsson_SMHI_Icing_forecast_maps.pdf (2015-06-28)

[15] Bernstein B. C., "Validation of Icing and Power Predictions for the O2 Wind Pilot Program", presented at Winterwind 2014, Sundsvall, Feb, 2014, http://windren.se/WW2014/02_03_053_Validation%20of%20icing%20and%20power%20predictions%20for%20the%20O2%20wind%20pilot%20program.pdf (2015-06-28)

[16] Ronsten G., "Lessons learned from "Large scale, cost-effective deployment of wind energy in icing climates"", (This paper), IWAIS 2015, Uppsala, July, 2015, http://iwais.org/. (To be published, 2015-06-28)

[17] Bernstein B. C. et al, " Innovations in F-LOWICE real-time forecasts of wind power and icing effects, IWAIS 2015, Uppsala, July, 2015, http://iwais.org/. (To be published, 2015-06-28)

[18] Byrkjedal Ø., "Development of operational forecasting for icing and wind power at cold climate sites", IWAIS 2015, Uppsala, July, 2015, http://iwais.org/. (To be published, 2015-06-28)

[19] "Vestas de-icing system", IWAIS 2015, Uppsala, July, 2015, http://iwais.org/. (To be published, 2015-06-28)

[20] Levati D., "Siemens de-icing system", IWAIS 2015, Uppsala, July, 2015, http://iwais.org/. (To be published, 2015-06-28)

[21] Norén B., "What we learned – Adaption and development of measurement technique and camera supervision for icing conditions", IWAIS 2015, Uppsala, July, 2015, http://iwais.org/. (To be published, 2015-06-28)

[22] Söderberg S., "Experiences from studies of icing and production losses due to icing in OX2's Vindpilot project", IWAIS 2015, Uppsala, July, 2015, http://iwais.org/. (To be published, 2015-06-28)

[23] Olsson E., "Modelling icing conditions for a selection of Swedish wind farms during winter 2014–2015", IWAIS 2015, Uppsala, July, 2015, http://iwais.org/. (To be published, 2015-06-28)

[24] Westerlund R., "Controller for Surface heating", IWAIS 2015, Uppsala, July, 2015, http://iwais.org/. (To be published, 2015-06-28)

[25] Kolar S., " Comparison of three different anti and de-icing techniques based on SCADA-data", IWAIS 2015, Uppsala, July, 2015, http://iwais.org/. (To be published, 2015-06-28

Experimental research on the icing progress of insulators at Xuefeng Mountain Natural Icing Test Base

Xingliang Jiang[1], Yuyao Hu[1], Zhijin Zhang[1], Quanlin Wang[1]， Yang Pan[1] and Chengzhi Zhu[2]

1. State Key Laboratory of Power Transmission Equipment & System Security and New Technology，Chongqing University，Chongqing 400030，China
2. State Grid Zhejiang Electric Power Company, Hangzhou 310007, China

***Abstract*—The environmental parameters can be controlled and the ice test is not limited by season in the artificial climate chamber. Therefore, the experimental research on the icing progress of insulators is mainly carried out in the artificial climate chamber. However, there are considerable differences between the icing formed under artificial environment and that formed under natural environment. To explore the characteristics of the icing growth under natural environment, the different type of insulators were suspended on glaze tower at Xuefeng Mountain Natural Icing Test Base and the key factors affecting the icing growth were analyzed. The research results indicate that icing is influenced by many factors, such as the meteorological parameters, the arrangement positing and structure of insulator. The lower of temperature and the greater of wind speed, the more icing accretion on the surface of insulator will be. The ice mass of insulators and the thickness of insulator surface grow nonlinearly with the increasing of time, while the growing degree of ice thickness slows down with the increasing of time. Icing of insulators arranged on the windward side is somewhat more serious than that arranged on the leeward side. Under natural condition, ice mainly exits on windward side of insulator and there is almost no ice on leeward side.**

***Key words*—Natural icing test base, insulator icing, icing growth, mass of ice, thickness of ice.**

I. INTRODUCTION

In recent years, "EI Nino" and "La Nina" and other extreme weather events frequently occur, which result in transmission lines covered by ice. When ice load exceeds the design value of transmission lines, tower falling down, icing flashover and even large area power outages will happen. Icing is a serious threat to the safe operation of power system. China is one of the countries which are frequently attacked by icing [1-2]. In 1954, China recorded the first icing disaster of transmission lines. In the following decades, icing accidents have reached up to thousands of times [3]. In particularly, the freezing rain, rare in the history, attacked the south of China in early 2008. An average ice thickness of transmission lines was up to 30 mm and the maximum icing thickness was more than 100 mm, which was far more than the design value. This icing disaster brought great economic losses.

So far, the domestic and foreign scholars have carried out extensive studies on the icing accretion on the surface of conductor and the icing forecast models, mainly based on meteorological parameters and characteristics of collision, have been built [5-11]. However, the shape and structure of insulators are complex. Therefore, it is difficult to build a model to predict the icing growth of insulators. Literatures [12-13] experimentally research on the icing process of LXP-160 and composite insulators under different environment parameters and analyze the influence of these parameters, such as temperature, mean diameter of water droplet and wind velocity, etc.

Icing is a common natural phenomenon. There are four meteorological parameters affecting the outdoor insulator icing, namely, air temperature, wind velocity and wind direction, super-cooled water droplet diameter and liquid water content in the air. Nevertheless, insulators at service are also influenced by other factors, such as the local geography, altitude, condensation level, the structure of insulator, electric field strength and load current, etc. [14-18]. Due to natural conditions, test equipment and other reasons, the current study for icing is mainly carried out in artificial climate chamber rather than in field. Whether or not the results obtained in artificial climate chamber should directly guide the design of external insulation is worth discussing. This paper experimentally studies the icing accretion on the surface of insulators at Xuefeng Mountain Natural Icing Test Base (XMNITB) and analyzes the factors influencing icing.

II. TEST BASE AND SPECIMENS

A. Xuefeng Mountain Natural Icing Test Base

The field tests are conducted at XMNITB (seen Figure 1) where there are the characteristics of the typical local topography and local meteorology with 150 days icing period a year, more than 1800 mm rainfall per year, maximum wind velocity of 35 m/s, the lowest temperature of -15 ℃ and maximum glaze ice thickness of up to 500 mm. The two glaze towers (9 m (width)×9 m (length)×9 m (height)) are set up to

suspend different types of insulator strings and conductors at XMNITB.

Figure 1 Xuefeng Mountain Natural Icing Test Base

B. *Test specimens*

As shown in Figure 2, different types of insulator strings are suspended at the top of glaze tower, which include three porcelain insulator strings with seven units and two glass insulator strings with seven units. Each of insulator strings is fixed on the glaze tower by the drawing force transducer. Four types of composite insulators with different shed configurations are arranged on the bottom of the glaze tower. The basic technical parameters and structure diagrams of all insulators are shown in Table 1 and Figure 3. In Table 1, *H* is the length of insulator, mm; *L* is the creepage distance, mm; and *D* is the diameter of the shed, mm. PortLog is used to measure the meteorological parameters during the ice period, including: temperature, relative temperature, wind speed and direction, atmospheric pressure, and so on.

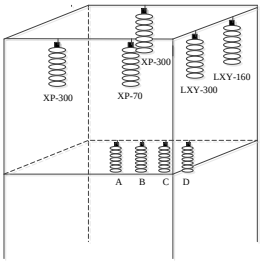

Figure 2 Diagram of insulator strings arrangement

Table 1 Dimensions and profiles of porcelain and glass insulators

Types	*D*	*H*	*L*	Profile
XP-300	320	195	370	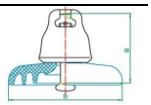
XP-70	255	146	295	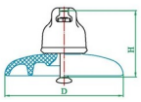
LXY-300	320	195	485	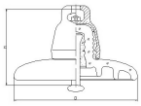
LXY-160	280	170	400	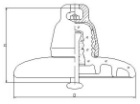

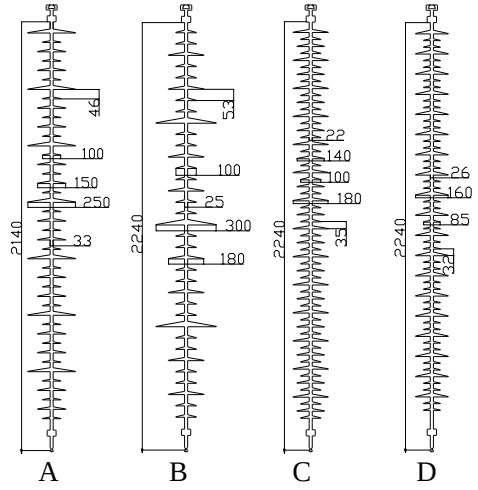

Figure 3 Profiles of composite insulators

III. Test Results And Analysis

A. *Meteorological parameters during the ice period*

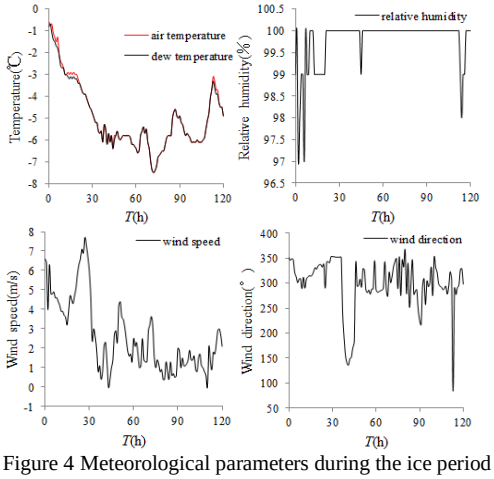

Figure 4 Meteorological parameters during the ice period

When the air temperature dropped to below 0 ℃, ProtLog started to record the data of meteorological parameters for the following 120 hours. Figure 4 shows the change tendency of air temperature, dew temperature, relative humidity, wind velocity and wind direction with the time increasing during the icing period.

Although air temperature was somewhat higher in initial and final stage, it was always below 0℃ throughout the icing period. Due to effect of wind, temperature declines linearly at early stage and dropped to -7.5℃ after 70 hours. The dew temperature had the same change trend with air temperature. Although relative humidity fluctuated at the beginning, it remained at 100% in the following rest of the icing period and provided sufficient super-cooled water droplets for the atmospheric structure icing. Wind velocity was higher at the early stage and the maximum reached up to 7.7m/s. Wind velocity fluctuated with alternative day and night. The overall trend was that wind speed during the night was higher than that during the day. During most time of the ice period, wind blew from the northwest and north. When it blew from southeast, it blew at lower speed and lasts only a short time.

B. Air flow field characteristics and water droplets collision characteristics near insulator

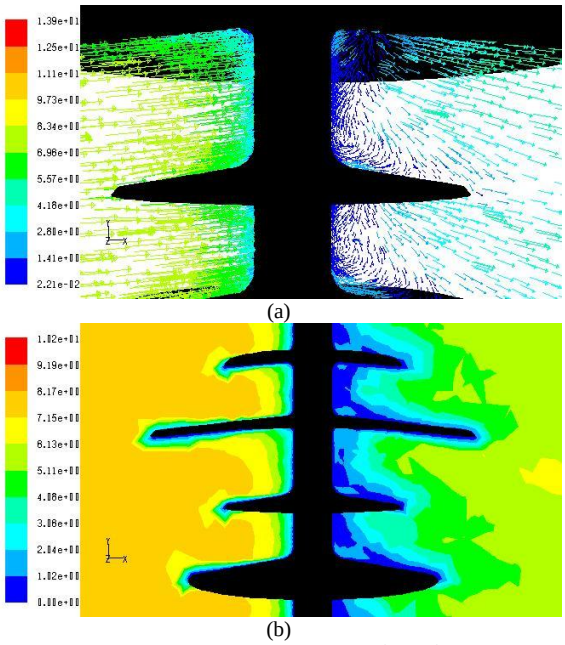

(a)

(b)

Figure 5 (a) Velocity vectors near the surface of insulaotor
(b) Velocity magnitude near the surface of insulator

This paper obtains velocity magnitude, velocity vectors and water droplets collision characteristics near the surface of the insulator for Type C without icing by using CFD software to simulate air flow field. As shown in Figure 5, a boundary layer, changing with gradient, exists on the surface of insulator. Due to the viscous effect, air velocity near the surface of insulator approximates zero, then increases gradually along with normal direction of the wall. Air flow velocity drops greatly near the bottom surface of insulator, where there is obvious vortex resulting in icing.

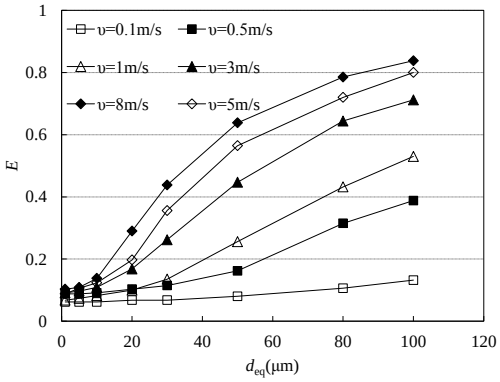

Figure 6 Influence of wind velocity on E

As shown in Figure 6, the collision efficient (E) increases with the increase of mean diameter of water droplet (d_{eq}) or wind velocity (v). When d_{eq} is less than 10 μm, E changes slowly. While d_{eq} is more than 10 μm, E changes quickly. This is mainly because that with the increase of wind velocity, the inertial effect of water droplets is greater than the air drag force, and the number of water droplets colliding with the surface of insulator increases.

C. Difference in icing appearance

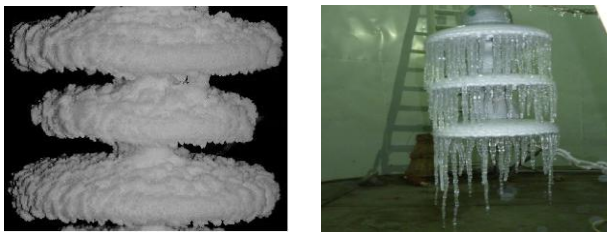

(a) Rime (b) Glaze

Figure 7 Appearance of ice-covered insulator in artificial climate chamber

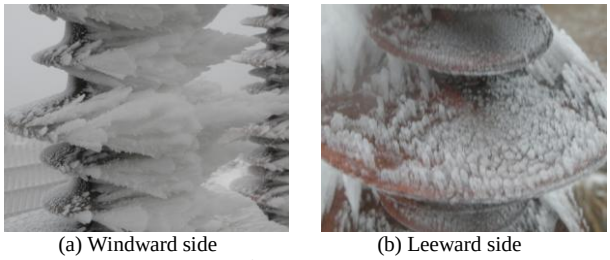

(a) Windward side (b) Leeward side

Figure 8 Appearance of ice-covered insulatorat XMNITB

It can be seen from Figure 7 and 8 that the different test environments have a great influence on the icing appearance. As shown in Figure 7, two types of icing (glaze and rime) are uniform in the artificial climate chamber. However, for field experiment, it is totally different. As shown in Figure 8, ice mainly exists on windward side of insulator and there is almost no ice on leeward side. There is a clear dividing line between the both. Although a variety of meteorological parameters can be simulated and the ice tests are not limited by season in artificial climate chamber, using the results obtained to guide engineering design still has many limitations. Therefore, carrying out the field tests is an indispensable part.

D. Growth of ice mass

The ice mass of four types of insulator strings are measured by drawing force transducer and the results are shown in Figure 9.

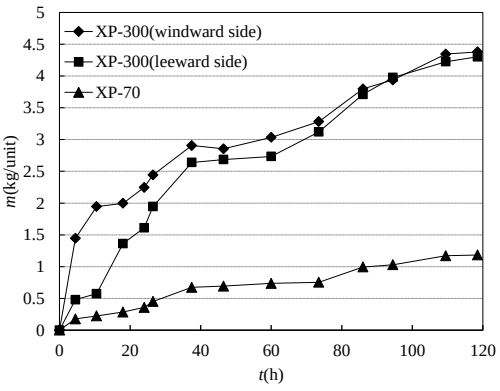

(a)

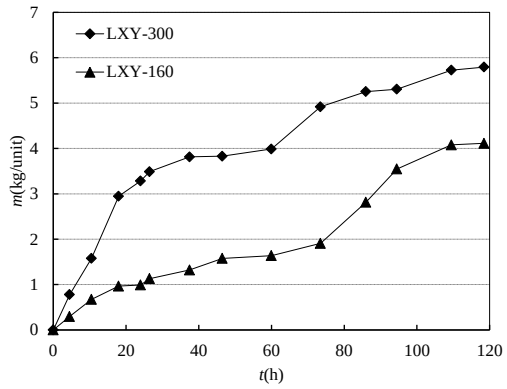

(b)

Figure 9 Relationship between the ice mass of insulators and the icing time. (a) porcelain insulator strings; (b) glass insulator strings

According to the results shown in Figure 9, the following conclusions can be drawn.

(1) The ice mass of insulator strings grows nonlinearly with the increasing of time, while the growing degree is varied with the increasing of time. Within 40 hours from the beginning of icing, the ice mass grow rapidly. The ice mass of insulators per unit is up to 2.9, 2.6, 0.67, 3.81, 1.32 kg, respectively, accounting for 66.4, 61.4, 47, 65.8, 32.2 % of total ice mass. At this stage, the temperature decreases from 0 to -6 ℃ and wind speed is more than 3 m/s. Due to low environmental temperature and high air humidity, a part of super-cooled water droplets are frozen on the surface of insulators, which resulted in the increase of the roughness. When a number of super-cooled water droplets carried by the wind collide with insulators, the ability to capture the water droplets is enhanced. The wind speed accelerates heat exchange process and water droplets freeze rapidly. With the increase of time, the ice growth rate slows down. The reason might be that the windward side of insulator has been bridged by ice after 40 hours, which results in the change of turbulent flow field near insulator and the decrease of *E*.

(2) For porcelain insulator strings with same structure, Icing of insulators arranged on the windward side is somewhat more serious than that arranged on the leeward side. This is mainly because that due to effect of the rest of insulator strings and glaze tower, the airflow and water droplets lose a part of momentum energy causing the speed decrease of the air flow and water droplets, which results in the decrease of collision coefficient. As time increases, icing changes the shape of the insulator and *E* tends to be the same. Therefore, the difference of the ice mass becomes smaller and smaller and finally tends to be saturated.

(3) There is considerable difference in the ice mass between two types of porcelain insulator stings. The ice mass of XP-300 is as high as 4.3 kg, while there is only 1.2 kg for XP-70. However, the ice mass of LXY-300 and LXY-160 is 5.8kg and 4.1 kg, respectively, with a difference of 1.7 kg. The reason might be that the larger diameters of the shed of XP-300 and LXY-300 with the larger windward area could capture more super-cooled water droplets leading to more severe icing.

E. Growth characteristics of ice-covered insulators

To analyze the growth characteristics of ice-covered insulator over time, the icing period is averagely divided into three stages, namely the early stage, the middle stage and the later stage. As is shown in Figure 10, this paper selects the extended length of icicle attached on the surface of insulator (l), the ice thickness of the shed (d_0) and the ice thickness of insulator's leeward side (d_1) as ice characteristics of ice-covered insulators.

Figure 10 Schematic diagram of experimental measurement

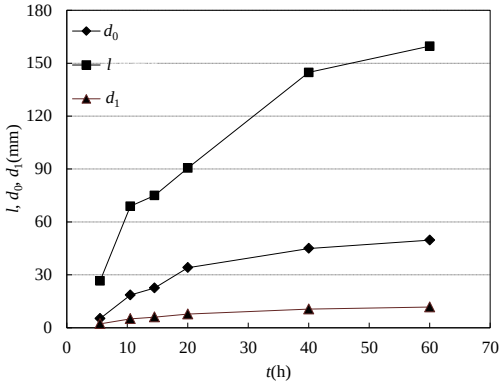

Figure 11 Relationship between ice characteristics of ice-covered insulators and icing time.

There is a similar ice growth process among four types of composite insulators, so the ice characteristics of Type C are only chosen to be analyzed. As is shown in Figure 11, d_0 increases by 34.05, 10.87 mm and 11.75 mm and d_1 increases by 7.72, 2.83 mm and 2.31 mm at each stage, respectively. It is obvious that the ice growth rate of d_0 is significantly faster than that of d_1 and then both grow slowly. This can be explained by the fact that the shape of insulators is changed by ice, which results in *E* reducing.

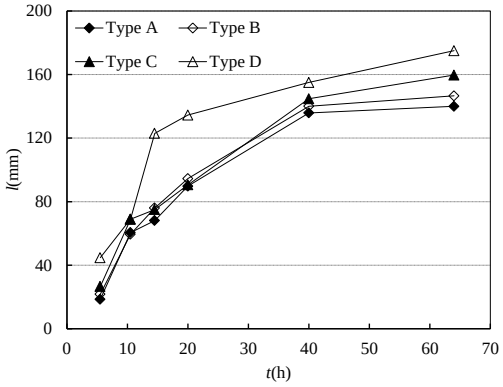

(a)

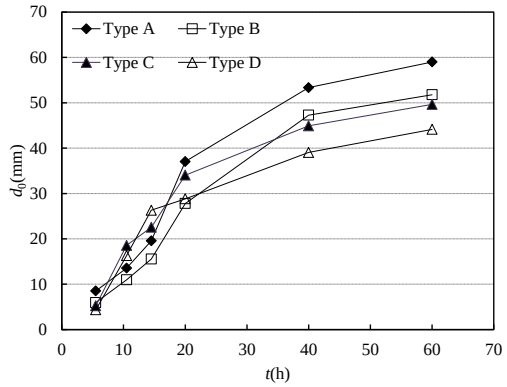

(b)

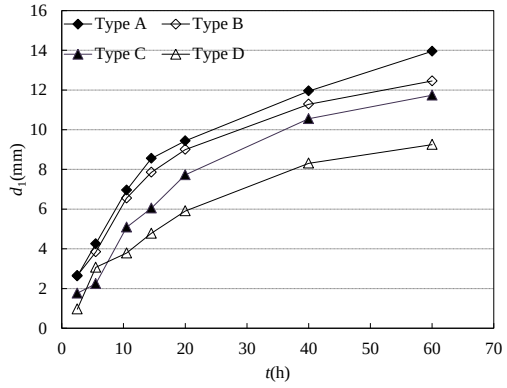

(c)

Figure 12 Relationship between ice characteristics of ice-covered insulators and icing time. (a) l; (b) d_0; (c) d_1.

According to Figure 12, it can be observed that:

(1) From Figure 12(a), it can be seen that the increase of l is nonlinear. At the initial period of icing, the extended length of type A~C is 89.76, 94.5 mm and 90.56 mm respectively, however, Type D gain a faster increase of 134.5 mm. The simulation analysis of previous research concludes that E decreases with increasing of top surface inclination and diameter of shed [19].The disturbance degree increases with the shed diameter increasing, which results in increasing the bend degree of the flow line, enhances the drag force of water droplet applied by the flow and reduces E. As icing continues, the shape of insulator has been changed and the equivalent diameter of insulator is larger. Thus, E further reduces. Then, l tends to be saturated, which is also affected by the decrease of wind speed in the later stage.

(2) As shown in Figure 12(b), for all four types of composite insulators with different shed configurations, d_0 will first increase with an increase in the icing time, and then change very slowly. At initial period of icing stage, d_0 of different type insulators grows rapidly with increasing by 37.05, 27.8, 34.05 mm and 28.83 mm, respectively. The reason can be explained by following two factors. Firstly, in this stage, the wind speed remains above 3.5m/s and super-cooled water droplets obtain larger kinetic energy and are more likely to collide with the insulator. Meanwhile, the increase of wind speed accelerates the process of heat exchange of water droplets, which is more conductive to the freezing of water droplets and accelerates the growth of ice. The growth rate of d_0 becomes slower with the increase of icing time. Taking d_0 in final stage for example, d_0 of insulators is 5.66, 4, 4.72 mm and 5.07 mm. The reason for this is that with the increase of d_0, the damping effect of super-cooled water droplets carried by the air flow rises and reduces the air velocity on the surface of the insulators. Therefore, the momentum of water droplets also decreases, which weakens icing growth.

(3) d_1 of four types of insulators demonstrates a nonlinear growth with the increase of time, but the growth degree will slow down along with the increase of time. d_1 of four types of insulators is only 13.95, 12.46, 11.74 mm and 9.25 mm respectively, which is far less than that shown in Figure 12(b). The reason can be explained by the fact that ice accretion on the surface of insulators on the leeward side forms by super-cooled water droplets which bypass the rod of insulator and collide with insulator. When water droplets carried by wind bypass the rod of insulator, the velocity dramatically drops leading to the decrease of E, thus there is little ice existed on the leeward side.

IV. Conclusions

(1) There are considerable differences between the icing formed under artificial environment and that formed under natural environment. The icing formed under the field test is not uniform. And ice mainly exists on windward side of insulator and there is almost no ice on leeward side.

(2) With the increase of time, the ice mass will grow nonlinearly, while the grow degree slows down. Icing of insulators arranged on the windward side is somewhat more serious than that arranged on the leeward side.

(3) The increase of the extended length icicle attached on the surface of insulator shows a nonlinearly growth with the increase of time. The growth degree at the first stage is rapid, while it slows down at other two stages. The increase of the ice thickness of the edge of sheds and the ice thickness of leeward side shows the same trend.

References

[1] X. Jiang, L. Shu, C. Sun, *The insulation of power system under pollution and icing*, Beijing, China Electric Power Press, 2009 (in Chinese).

[2] Y. Hu, "Analysis and countermeasures discussion for large area icing accident on power grid," High Voltage Engineering, vol. 34, no. 2, pp. 215-216, 2008.

[3] D. Huang, Y. Hu, Q. Wan, et al, "Review on flashover characteristics and measures to improve flashover voltage of the ice-coasted insulators," Power System Technology, vol. 34, no. 5, pp. 46-54, 2010.W.-K. Chen, *Linear Networks and Systems*. Belmont, CA: Wadsworth, 1993, pp. 123–135.

[4] S. Xu, J. Zhao, "Review of ice storm cases impacted seriously on power systems and de-icing technology," Southern Power System Technology, no. 2, pp. 1-6, 2008.

[5] Lenhard R W, "An indirect method for estimating the weight of glaze on wires," Bulletin of the American Meteorological Society, vol. 36, no. 3, pp. 1-5,1955.

[6] Makkonen L, "Modeling of ice accretion on wires," Journal of Climate Applied Meteorology, vol. 23, no. 6, pp. 929-939, 1984.

[7] Imai, "Studies on ice accretion," Researches on Snow and Ice, vol. 3, no. 1, pp. 34-35, 1953.

[8] Fistad K J, Lozowski E P, Gates E M, "A computational investigation of water droplet trajectories," Journal of Atmospheric and Oceanic Technology, vol. 5, pp. 160-170, 1988.

[9] Chaine P M, Casfonguay G, *New approach to radial ice thickness concept applied to bundle-like conductors*, Toronto, Environment Canada, 1974.

[10] L. Yang, Y. Hao, W. Li, et al, "Relationships among transmission line icing, conductor temperature and local meteorology using grey relation analysis," High Voltage Engineering, vol. 36, no. 3, pp. 775-781, 2010.

[11] H. Liu, D. Zhou, J. Fu, et al, "A simple model for predicting glaze loads on wire," Proceeding of the CSEE, vol. 21, no. 4, pp. 44-47, 2001.*Examples:*

[12] *Z. Zhang, X. Jiang, J. Hu, "Influence of environment parameters on the icing accretion on the surface of insulator," High Voltage Engineering, vol. 36, no. 10, pp. 2418-2423, 2010.Motorola Semiconductor Data Manual*, Motorola Semiconductor Products Inc., Phoenix, AZ, 1989.

[13] S. Zhao, X. Jiang, Z. Zhang, et al, "Impact of environmental parameters on the icing process of 110 kV composite insulators," High Voltage Engineering, vol. 38, no. 10, pp. 2575-2581, 2012. *Example:*

[14] X. Jiang, F. Zhou, J. Hu, "Effects of pre-polluting manners on artificial icing DC flashover characteristics of composite insulator," High Voltage Engineering, vol. 35, no. 3, pp. 551-556, 2009.

[15] X. Jiang, Q. Shen, "Experimental research on influence of environmental parameters on the conductor icing thickness," High voltage Engineering, vol. 36, no. 5, pp. 1096-1100, 2010.*Example:*

[16] L. Chen, X. Jiang, Q. Hu, "Evaluation of ice mass on insulator under natural icing condition base on the ice thickness accumulated on rotating multi-cylinder," High Voltage Engineering, vol. 37, no. 6, pp. 1371-1376, 2011.

[17] B. Huang, S. Xu, W. Su , "Summary of research on icing of transmission lines," Insulators and Surge Arresters, no. 1, pp. 27-32, 2012.

[18] L. Yang, Y. Hao, L. Li, "Fuzzy expert system for condition assessment of overhead transmission line icing," High Voltage Engineering, vol. 37, no. 12, pp. 3028-3035, 2011.

[19] X. Jiang, Z. Wen, C. Sun, "Numerical simulation of water droplet impingement on composite insulator surface and analysis of shed configuration," Proceeding of the CSEE, vol. 28, no. 19, pp. 7-12, 2008.

Effect of Surface Roughness of Wind Turbine Blade on its Ice Accretion

Jian Liang[1], Lichun Shu[1], Xingliang Jiang[1], Qin Hu[1], Xiaokai Ren[1], Chengzhi Zhu[2]

1State Key Laboratory of Power Transmission Equipment and System Safety and New Technology, College of Electrical Engineering, Chongqing University, Shapingba District, Chongqing, China

2 State Grid Zhejiang Electric Power Corporation, Hangzhou 3100017, China

***Abstract*— The wind turbine blades' icing often occurs under cold climates when the blades suffer from super-cooling droplets. Ice on blades changes the airfoil profile, reducing the efficiency of wind turbine. In this paper, the icing characteristic of the miniature horizontal-axis rotating wind turbine blade under the conditions of different surface roughness is experimentally studied by establishing the platform of ice wind tunnel in artificial climate chamber. A simulation is performed to reflect the flow field characteristics of the blade profile and different icing conditions. By measuring the ice mass, ice thickness and ice type of the blades, it is found that rough surface significantly increases the ice mass of blades; Ice mass of blades hardly changes under different roughness of rough surface, but a rougher surface leads to a more non-uniform distribution of ice on blades; Surface roughness cannot change the ice type of blades. Surface roughness is largely relative to the collision coefficient and heat transfer coefficient by simulation and numerical calculation.**

Key words: wind turbine blade, surface roughness, flow field, ice mass, ice type, CFD.

I. INTRODUCTION

As the global environment deteriorated, renewable energy, especially wind energy is widely used around the world. Wind energy is rich in north China, but most areas are suffered from icing problem. The super-cooling droplets fall down on the cold wind turbine blades and freeze, which seriously affects the normal operation of wind turbine. Bose[1] experimentally studied the ice of the miniature horizontal-axis wind turbine blade under stationary state. Han[2] studied the ice of a rotating wind turbine by experiment under different environment conditions. His team developed the device AERTS to predict the ice model of wind turbine. Most research institutes tended to pay more attention to the simulation by CFD. The ice model of Turbice[3] from VTT and Lewice[4] from NASA were relatively systematic to study the icing problem. Virk[5] simulated the droplet trajectory to get the collision coefficient of water droplet onto the blade profile and studied the effect of angle of attack(AOA) and profile size on the ice.

At present, studies on surface roughness of wind turbine were few reported. Etemaddar[6] took the ice roughness of the blade into consideration, but he did not focus on the blade surface roughness itself. In this paper, the platform of ice wind tunnel is established in the artificial climate chamber. The icing characteristic of the miniature horizontal-axis rotating wind turbine blade is experimentally studied under the condition of different surface roughness of the blade and large angle of attack. A simulation of flow field characteristics of icing blade profiles is performed as well.

II. EXPERIMENTAL FACILITY AND EXPERIMENTAL PROCEDURE

As shown in Fig. 1, a multifunctional artificial climate chamber, with an internal diameter of approximately 7.6m and an internal height of approximately 11m, can simulate different atmospheric environments. The lowest temperature T can reach −45 ℃. Inside the climate chamber, the water nozzle can simulate different Median Volume Diameter (*MVD*) and Liquid Water Content (*LWC*). An ice wind tunnel is designed for the miniature wind turbine, which can provide the maximum wind velocity V 10m/s. The miniature horizontal-axis wind turbine is with an output power of 100W, the blade radius R of 0.5m, the maximum chord c of 0.102m and the minimum chord of 0.028m. To change the output loads keeps the rotate speed of wind turbine in 60r/min.

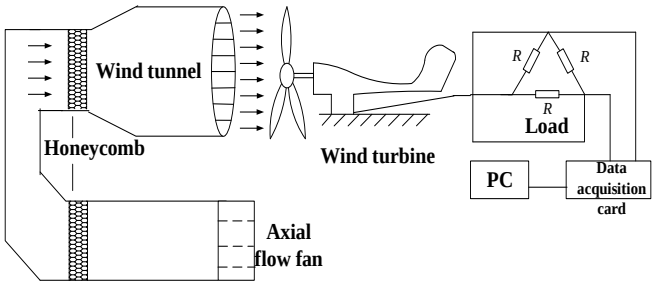

Fig. 1. Experimental schematic diagram

The surface roughness is defined by the equivalent sand grain roughness k_s[7]. The surface roughness of three blades is 0、0.035mm、0.2mm in the experiment. The experimental environment is show in TABLE I.

TABLE I

PARAMETER OF ICING EXPERIMENT IN 30MIN

Test	LWC(g/m^3)	MVD(μm)	T(℃)	V(m/s)	AOA (°)	Ice type
1	1.42	100	-3	5	26.82	Glaze ice
2	1.42	100	-6	5	26.82	Mixed ice
3	1.42	100	-9	5	26.82	Rime ice
4	1.42	100	-6	3	14.80	Glaze ice
5	1.42	100	-6	7	36.03	Glaze ice

III. EXPERIMENTAL RESULTS

A. Influence of Surface Roughness on Ice Type

The ice type of each group is recorded in TABLE II, which indicates that the surface roughness is hardly relative to the ice type of the blade. Compared with test 1, test 2 and test 3, it is concluded that the ice type is mainly influenced by ambient temperature. If the temperature is around 0℃, it tends to be glaze ice. If the temperature reduces to about or lower than -10℃, it tends to be rime ice.

B. Influence of Surface Roughness on Ice Load

Fig. 2 shows the changes of ice thickness and ice mass on the blades with the icing test going on. Both the ice thickness and ice mass on the rough blade are much greater than those on the smooth blade. However, the two rough blades have the same ice mass and different ice thickness. Fig. 3 shows the ice shape at the blade tip under the conditions of different surface roughness when icing time is 30min. It can be seen that the rougher the blade surface is, the less uniformly the distribution of ice on the blade profile exhibits. The ice tends to be uniformly covered on the windward of the smooth blade profile. However, in the condition of 0.2mm surface roughness of the blade, the ice mainly accretes at the leading edge of the windward of the blade profile. This also explains why the two rough blades have the different ice thickness. The non-uniformity of ice distribution keeps rising with the process of ice accretion, and it leads to greater ice thickness. It is noticed that a rougher surface seems not to contribute to more ice accretion.

In addition, when the icing time reaches 10min, most parts of the blades have been covered with ice. It can be seen in Fig.2 that each group has the same ice accretion rate in 10~30min, which means the surface roughness of the blade only influences the ice accretion at the beginning. The surface roughness turns into ice roughness after the blade is covered with ice, and the ice roughness seems to be weakly relative to surface roughness.

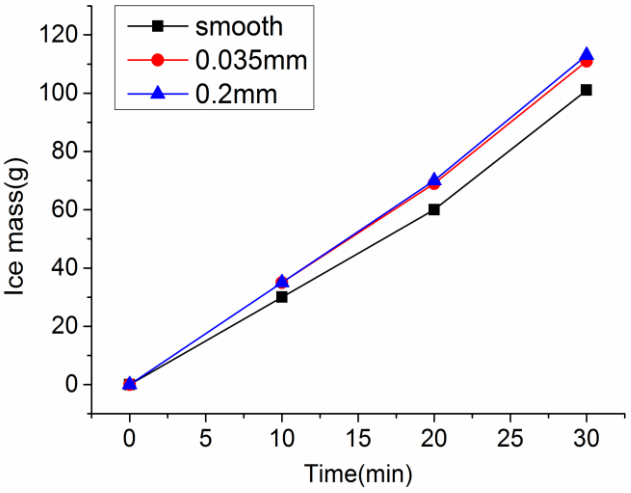

(a) Ice mass

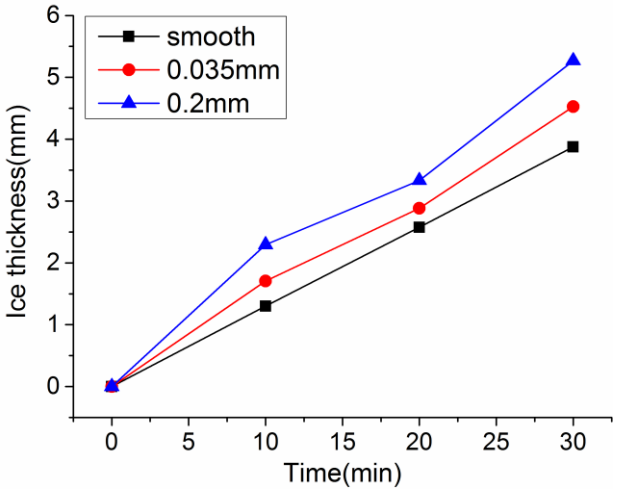

(b) Ice thickness

Fig.2. Ice characteristic of wind turbine blade under different surface roughness

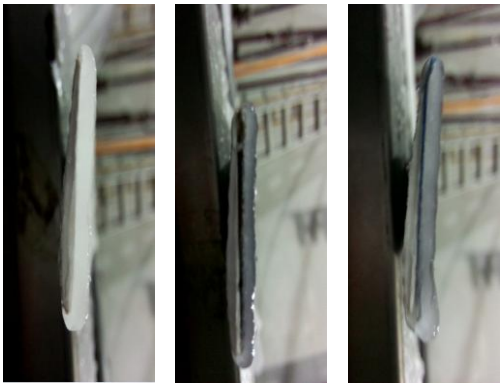

(a) smooth (b) 0.035mm (c) 0.2mm

Fig.3. Ice shape of blade tip under different surface roughness (icing time: 30min)

IV. DISCUSSION

The rate of ice accretion on the blade can be described as[8]:

$$\frac{dM}{dt} = \alpha_1 \cdot \alpha_2 \cdot \alpha_3 \cdot LWC \cdot U_e \cdot A \quad (1)$$

Where, U_e is the relative velocity, A is the cross-sectional area of the object relative to U_e, and α_1, α_2, α_3 are the correction factors with the values ranging from 0 to 1. α_1 is the collision coefficient of the droplet. α_2 is the sticking coefficient. α_3 is the accretion coefficient.

A. Influence of Surface Roughness on the Collision Coefficient

To further explain the experiment phenomenon, a simulation is performed to reflect the pathlines of droplets in the flow field in the cases of different surface roughness.

Numerical studies of the flow field show a significant change in the pathlines of flow field by FLUENT. The flow separation and vortex occur at the leading edge of the leeward of the NACA 2308 profiles under 26 AOA. The vortex area grows larger and moves to the trailing edge as the surface roughness increases. The length of vortex is 0.5c in the flow field of the smooth profile, 0.9c in that of 0.035mm profile and 2c in that of 0.2mm profile.

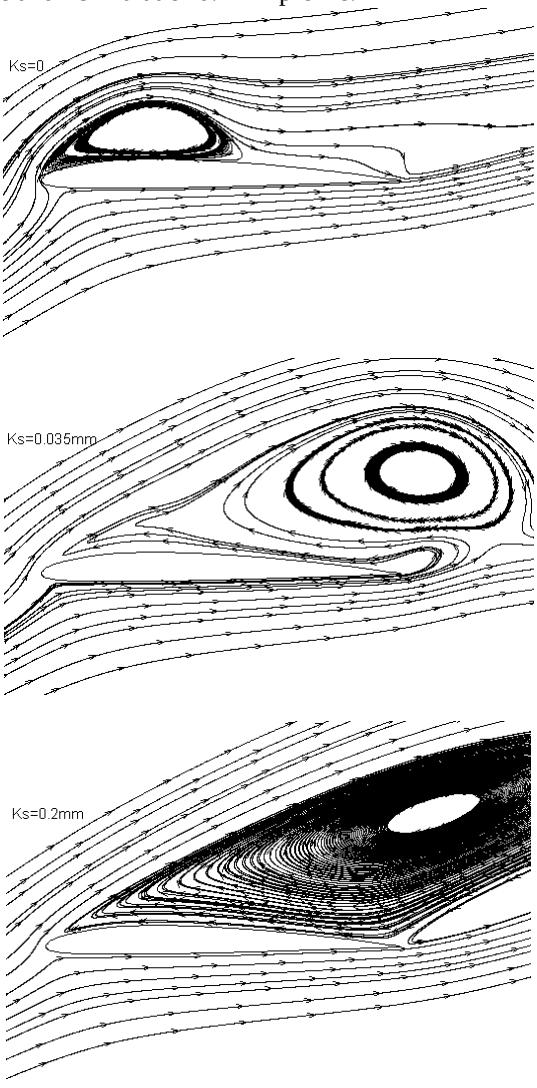

(a) The pathlines of flow field

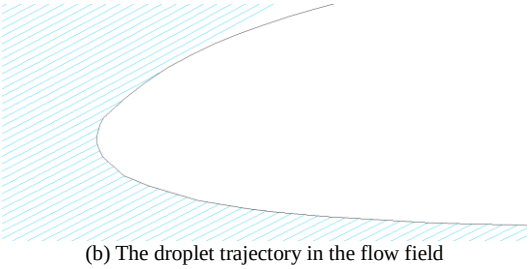

(b) The droplet trajectory in the flow field

Fig.4. The pathlines and droplet trajectory in the flow field of NACA 2308 profiles with roughness 0, 0.2mm, 0.035mm

The different flow field changes the droplets trajectory, which leads to different collision coefficient. The local collision coefficient of droplets is defined as[9]:

$$\alpha_1 = dY/dL \quad (2)$$

Where dY is the initial distance of two adjacent droplets, and dL is their distance on the profile.

It is found that a rougher surface has a lager collision area, especially at the leading edge of the leeward of the profile. The local collision coefficient increases at the leading edge and decreases on the other parts of the profile, as the surface roughness increases.

TABLE II

SIMULATION RESULTS ON COLLISION LOCATION

k_s(mm)	The maximum collision location of windward(x/c)	The maximum collision location of leeward(x/c)
0	1	0.0037
0.035	1	0.0105
0.2	1	0.0173

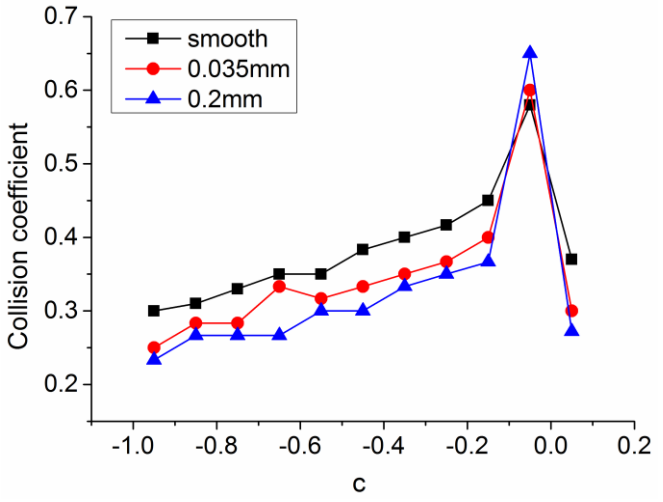

Fig.5. The local collision coefficient of NACA 2308 profiles under AOA 26°(c=0 presents the peak point, c<0 presents the point of the windward)

B. Influence of Surface Roughness on the Accretion Coefficient

The accretion coefficient of the droplet is related to the heat transfer coefficient in the boundary-layer. According to

Chilton-Colburn [10], the heat convection of rough surface is expressed as follows:

$$h = \rho_a \cdot c_a \cdot U_e \cdot St \tag{3}$$

Where ρ_a is the air density, c_a is the specific heat of air, St is the Stanton number. Whether the boundary-layer is in the turbulent area is determined by the roughness Reynolds number Re_k:

$$\mathrm{Re}_k = \frac{U_k k_s}{\upsilon} \geq 600 \tag{4}$$

Where U_k is the speed at the roughness level, v is the kinematic viscosity of air. The heat transfer coefficient could be written respectively in laminar boundary and turbulent boundary as follows:

In laminar boundary-layer:

$$h_c = 0.296 \cdot \frac{\lambda}{\upsilon} [U_e^{-2.88} \int_0^s U_e^{1.88}\, ds]^{-1/2} \tag{5}$$

In turbulent boundary-layer:

$$h_c = \frac{\rho_a \cdot c_a \cdot U_e \cdot C_f}{0.8 + 1.13 \cdot C_f^{0.6} \cdot (\frac{U_e k_s}{\upsilon})^{0.2}} \tag{6}$$

Where λ is the thermal conductivity coefficient of air, the friction coefficient C_f is related to k_s and can be obtained by the empirical formula as follows

$$C_f = [0.707 \ln(\frac{x}{k_s}) + 3.476]^{-2.46} \tag{7}$$

Where, x is the arc length from the point of leading edge to the stagnation point. It is concluded from Eqs. (5), (6) that the surface roughness mainly influences the heat transfer coefficient in the turbulent boundary-layer, which is in accordance with the air flow of wind turbine with large AOA. This leads to a lager heat transfer coefficient and a lager rate of ice accretion at the leading edge.

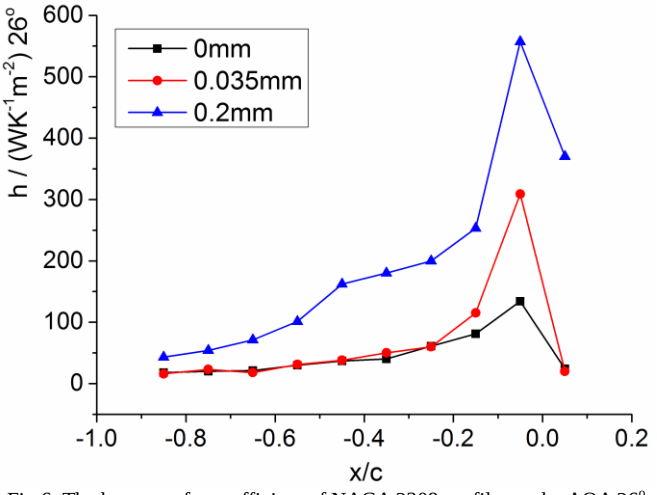

Fig.6. The heat transfer coefficient of NACA 2308 profiles under AOA 26°

V. CONCLUSION

The influence of surface roughness of wind turbine blade with large AOA on icing characteristic is experimentally studied in artificial climate chamber. Surface roughness cannot change the ice type. Rough surface causes more serious ice accretion. Surface roughness hardly changes the ice mass on blades, but it can significantly influence the ice distribution especially at the leading edge of the profile.

A theoretical analysis is made based on the ice accretion model. The collision coefficient and accretion coefficient are related to surface roughness. The collision coefficient decreases while the local collision coefficient of the leading edge increases, in case that roughness grows greater, which causes more serious ice accretion at the leading edge. The heat transfer coefficient in turbulent boundary-layer increases with the rise of surface roughness. Surface roughness does not change the heat transfer coefficient in laminar boundary-layer.

ACKNOWLEDGMENTS

This work was supported by the Central University Basic Scientific Research Business Expenses (CDJZR12150015), National Natural Science Foundation of China (51107151) and the Funds for Innovative Research Groups of China (51021005).

REFERENCES

[1]. Bose, N., Icing on a small horizontal-axis wind turbine — Part 1: Glaze ice profiles. Journal of Wind Engineering and Industrial Aerodynamics, 1992. 45(1): p. 75-85.

[2]. Han, Y., J. Palacios and S. Schmitz, Scaled ice accretion experiments on a rotating wind turbine blade. Journal of Wind Engineering and Industrial Aerodynamics, 2012. 109: p. 55-67.

[3]. Marjaniemi, M., L. Makkonen and T. Laakso. Turbice-the wind turbine blade icing model. in Proceedings of the BOREAS V conference, Finnish Meteorological Institute. 2000.

[4]. Kwon, O.J. and L.N. Sankar, Numerical investigation of performance degradation of wings and rotors due to icing. 1992.

[5]. Muhammad S. Virk, M.C.H.P., Atmospheric icing on large wind turbine blades. International Journal of Energy and Environment, 2012. 3(1): p. 1 - 8.

[6]. Etemaddar, M., M.O.L. Hansen and T. Moan, Wind turbine aerodynamic response under atmospheric icing conditions. Wind Energy, 2014. 17(2): p. 241-265.

[7]. Shin, J., Characteristics of surface roughness associated with leading-edge ice accretion. Journal of aircraft, 1996. 33(2): p. 316-321.

[8]. Makkonen, L., Models for the growth of rime, glaze, icicles and wet snow on structures. Philosophical Transactions of the Royal Society of London A: Mathematical, Physical and Engineering Sciences, 2000. 358(1776): p. 2913-2939.

[9]. Finstad, K.J., E.P. Lozowski and E.M. Gates, A Computational Investigation of Water Droplet Trajectories. Journal of Atmospheric and Oceanic Technology, 1988. 5(1): p. 160 - 170.

[10]. Kays, W.M., M.E. Crawford and B. Weigand, Convective heat and mass transfer. 2012: Tata McGraw-Hill Education.

Study on Icing Characteristics of Bundle Conductors Based on Xuefeng Mountain Natural Icing Station

Xingliang Jiang[1], Quanlin Wang[1], Zhijin Zhang[1], Yuyao Hu[1]， Yang Pan[1] and Chengzhi Zhu[2]

1. State Key Laboratory of Power Transmission Equipment & System Security and New Technology，Chongqing University，Chongqing 400030，China
2. State Grid Zhejiang Electric Power Company, Hangzhou 310007, China

Abstract—**Icing on electric transmission line is one key factor which threatens the security and reliability of power grid. With wider application of bundle conductors in UHV or EHV transmission lines, however, there is no in-depth analysis of growth characteristics of icing on bundle conductors in the natural environment so far. Most researches are based on the methods of artificial simulation, which have big differences from engineering practice. In order to study the icing characteristics of bundled conductor, the icing tests on three kinds of bundle conductors have been done at Xuefeng Mountain Natural Icing Stations (XMNIS). Based on the testing results, this paper concludes: the growth rate of icing on windward site of conductors is faster than that of leeside, and the thickness of transverse direction is about ten times as much as that of lengthways direction; The growth of icing weight is nonlinear process, which is large at preliminary stage and saturated at last period; There is obvious stratification phenomenon in the icicles of hard rime, which is quite different from icing on short conductor in the artificial simulation experiments; Through the observation in the experiments, the ice shape, ice weight and ice thickness have no obvious differences among the single conductor, 3-bundle conductor and 4-bundle conductor. The conclusions can provide references for design and selection of overhead transmission lines in the region of hard rime.**

***Index Terms*—bundle conductor; icing; shape feature; ice thickness; ice weight**

I. INTRODUCTION

China is one of the countries in the world that has the most serious icing on transmission line[1]. Icing leads to mechanical and electrical properties of transmission line, which cause the ice accidents and have a strong impact on the security and reliability of power network. According to the incomplete statistics, the number of accidents has exceeded for 1000 times since there was a record of ice accidents on the transmission line[2]. In the period between January of 2006 and June of 2007, the number of 500kv line tripping caused by icing is 13, which is accounting for 8.84% of total line tripping [3]. The year of 2008 is the most memorable among recent years. Many areas in southern China have suffered extreme freezing natural disaster[4]. About 14 provincial power network and user from 570 counties are suffered varying influences. Over 100 of 220kV and above 220kv substation and hundreds of EHV line are outage in ice disaster. Icing on transmission line has been one key reason which influences the security operation of power network in the world.

With the accelerating pace of economic development and increasing of power requirement, bundled conductor has been a main style of erection in order to restrain corona development and reduce the line impedance, especially in the EHV and UHV[5]. Therefore, it is necessary to do further research on the characteristics of bundled conductor in icing environment.

The mechanism of ice accretion, formation conditions and the calculation method of ice and wind load are explored in the countries that have serious icing. Meanwhile, they have done significant research on icing protection. Research in [6] proposes that the temperature decide whether it can be iced, speed of icing and the types of ice. When conductors are in 0℃, the grow rate speed of icing is the fastest. Research in [7] shows that the growth rate of icing on transmission line has not totally direct ratio relations with wind speed. The speed of icing is fastest when the wind speed is between 3 and 6 meter per second. Research in [8-9] proposes that icing windward slope of mountains from east to west has a stronger icing degree than leeward slope. So far, researchers from domestic and overseas have studied many kinds of forecast model of ice, including empirical model from Lenhard [10], easy conceptual model from Goodwin [11], complex conceptual model from Makkonen [12],and numerical calculation model of freezing mixture between rime and glaze.

In order to pursue the natural character of bundle conductors, this paper chooses 3 kinds of conductors, including single conductor, 3-bundle conductor, and 4-bundle conductor, and conducts natural icing experiments at XMNIS. Characteristic parameters in the process of icing growth of hard rime are based on ice thickness, ice shape and ice weight. The key research point is the character of 3 kinds of bundle conductors in icing conditions, and compare with each other. Research results are a very important theoretical value for mechanism study of bundle conductor in rime and buildup of forecast model.

II. Test platform, Samples and Methods

A. Test platform

XMNIS is located in Xuefeng Moutain of Huaihua City, Hunan province. The altitude is 1400 meters high. The icing station has typical micro-topographic climate and microclimate character. The period ice is between November and March in next year; the maximum of wind speed can reach 25m/s; annual precipitation is over 1800mm; the ice duration is as long as 50 days; the max ice thickness is above 500mm.The panorama of Xuefeng Mountain Natural Icing Station is shown is Fig.1.

Fig. 1 Panorama of Xuefeng Mountain Natural Icing Station

In the meantime, automatic meteorology is used to monitor the meteorological changes of the period of ice in real time, including wind speed, wind direction, temperature, humidity, air pressure and so on.

B. Samples and Methods

Samples are set up between two experimental towers in Natural Icing Station, and the line length is about 120 meters. Parameters of samples are shown in Tab.1. Characteristic parameters in the process of icing growth of hard rime are based on ice thickness, ice shape and ice weight. Ice thickness is measured by vernier caliper along ice growth direction of conductor, including the length of horizontal axis and vertical axis. Average is taken via multiple measurements. The procedures for measuring ice cross-section shape and ice thickness at the field station are summarized as follows. Firstly, an incision on the ice layer should be made, so the ice cross-section shape can be observed conveniently. Secondly, a hole with the same diameter as the conductor on the paper should be taken. And then, a channel from the edge of the paper toward the hole should be cut. The ice conductor through the hole on the paper should be inserted. Thirdly, sketch the outline of the ice layer on the paper. Finally, the area of the ice layer can be easily obtained using AutoCAD software based on the sketch. Ice weight is measured through cutting out ice on 1m of conductor.

Tab.1 Basic parameters of conductors

No	Types of wire	Diameter of wire(mm)	Material
1	single conductor	16.36	ACSR
2	3-bundle conductor	18.77/19.03 18.64	ACSR
3	4-bundle conductor	24.06/24.05 24.18/24.14	ACSR

III. Result and Analysis

A. meteorological condition

Portlog was used to monitor the meteorological changes of the period of ice in real time, including wind speed, wind direction, temperature, humidity, air pressure and so on. Based on the data acquired by automatic meteorology, the temperature at 19 o'clock on January 27th of 2015 was below zero, so this experiment regarded this moment as the beginning time and start to record the environment parameters in 120 hours of ice period. Temperature, dew point temperature, relative humidity, wind speed and wind direction in ice duration changed over time, and the changing curve is shown in Fig.2. As is shown in Fig.2(a), temperature and dew point temperature were always below zero in entire time. Temperature decreased with linear trend at the beginning. Temperature of third day fluctuated with day-night cycle, and fluctuation range had obvious increase with increasing ice time. When the ice time got 70 hours, temperature reached the minimum which was -7.5℃. Dew point temperature had the same trend with temperature. As is shown is Fig2(b), relative humidity was always too high, which kept 100 percent in most of time and its minimum value was 97 percent, which provided sufficient supercooled water droplets for ice of atmospheric structure. Fig2(c) shows that the wind was high at the beginning of ice, and it came to the maximum 7.7 m/s in the nighttime of January 28th. After that, it began to fluctuate with day-night cycle. Wind speed in the daytime and night were below 2 m/s and above 4m/s respectively. As is shown in Fig2 (d), wind direction was northwest or north in most of time, only southeast in the afternoon of January 29th, but the wind speed at that time was low.

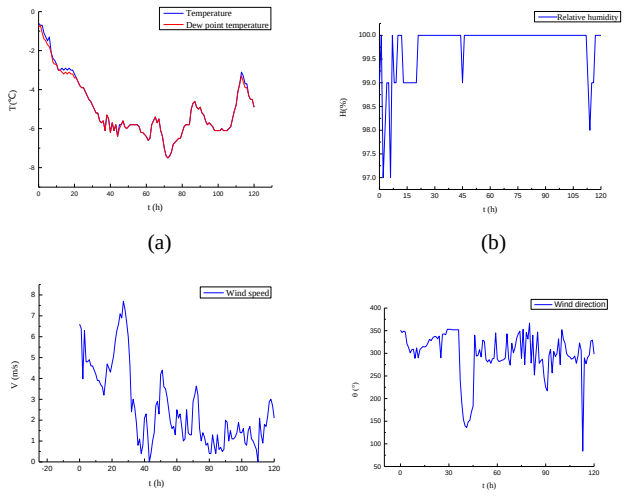

Fig. 2 Relationship between meteorological parameter and time

B. Icing Characteristics of Bundle Conductors

1、 Ice thickness of Bundle Conductors

In order to study thickness growth rule of bundled conductor, two axles were chosen to represent the thickness growth, which were horizontal axis and vertical axis respectively. As is shown in Fig.3, ice growth of horizontal axis was measured by the length of ice at windward side. Similarly,

ice growth of vertical axis was measured by the length of ice at the direction which was perpendicular to the wind. As is shown in Fig.4 and Fig.5, conductor coated hard rime changed with time.

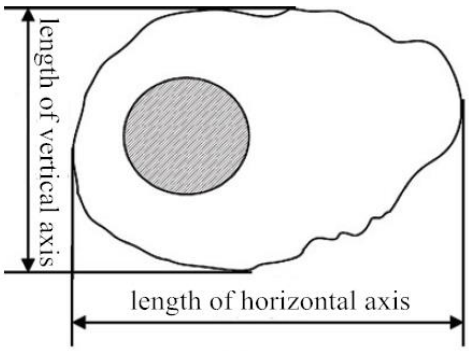

Fig. 3 Length of the horizontal and vertical axis

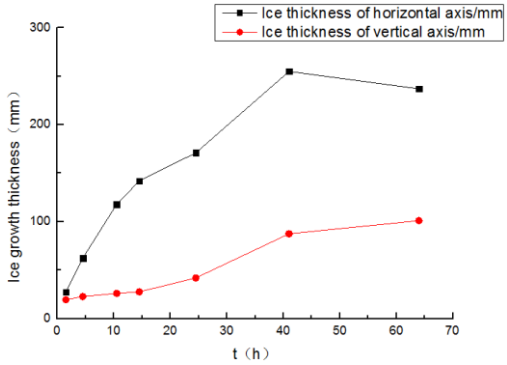

Fig. 4 Relationship between icing thickness of single conductor and time

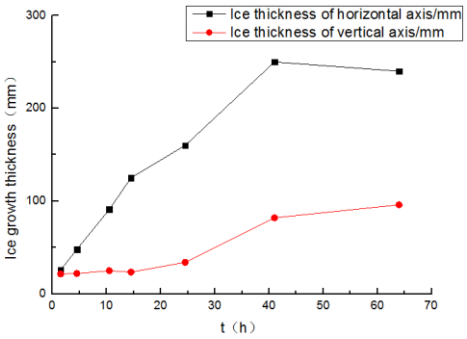

(a) d=18.77mm

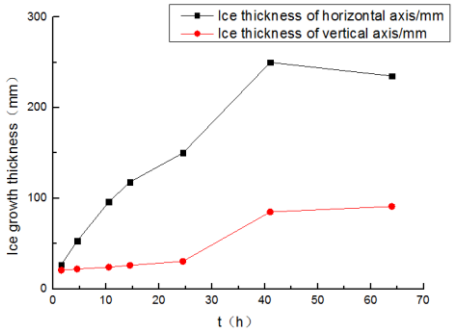

(b) d=19.03mm

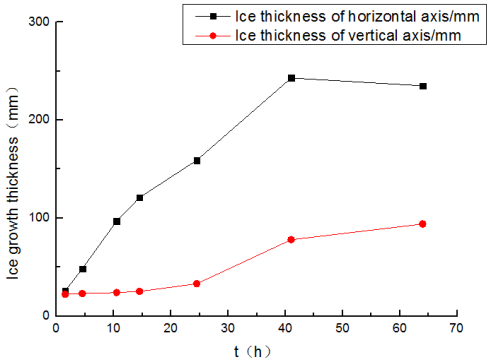

(c) d=18.64mm

Fig. 5 Relationship between icing thickness of 3-bundle conductor and time

As is shown in Fig.4 and Fig.5, when comparing 3-bundle conductor with single conductor, there was no obvious difference in growth trend and ice process. Specific representation is shown as below:

(1) Growth speed of horizontal axis is distinctly different with which of vertical axis for both 3-bundle conductor and single conductor in the process of ice. This is because wind direction plays a decisive role in ice growth.

(2) The growth of ice thickness is a nonlinear process. In the first 15 hours of ice period, temperature of environment decrease sharply, and both humidity and wind speed are very high. In the meteorological condition, airflow with large numbers of supercooling water drop and conductor collide, water drop which is captured and stays on the conductor are freezing, thereby accelerating the rapid growth of ice on conductor.

(3) In the period between 15 hours and 41 hours, speed of ice decrease slightly but ice still grows with a certain speed. Because collision rate of water drop on surface of conductor changes with the increase of ice thickness. For the hard rime in this paper, ice thickness enlarges with the passing of time. When the sectional area on windward becomes bigger, viscous force in airflow makes component of the flow direction which is perpendicular to acceleration more bigger. Then distance of deviation movement is bigger, hence collision rate between small water drop and conductor decreases. However, windward area expands and decrement of collision rate is big, so some influence caused by decreased collision rate can be counteracted. After a period of time, with continuous thickness growth, collision rate rapidly decreases and icing speed is also lower accordingly.

(4) Ice period from forty-second hours, ice thickness of vertical axis increases slightly, while that of horizontal axis decreases slightly. This is due to twisting of conductor and further speed up the ice growth in direction of vertical axis, which decrease the ice growth in direction of horizontal axis accordingly. When the ice period approaches or exceeds 70 hours, ice on conductor reach saturation in direction of both vertical and horizontal axis. It can be seen clearly that the specific value of ice thickness between vertical and horizontal axis is above 5. The value in saturation is about 2.5.

(5) As in shown in Fig.5, No.1 and No.2 sub-conductor which in vertical direction had almost no difference. However, No.3 sub-conductor located in lee side was slightly lower than No.2

sub-conductor located in windward from the horizontal direction. It may be that wake flow of upper conductor may affect collision characteristics of lee conductor, resulting that ice on No.3 conductor was less serious. There was similar feature in 4-bundle conductor, which showed that ice growth in upper conductor is faster than lee conductor. However, there was no difference on ice thickness among all the sub-conductor in the period of saturation.

2、 Ice shape of bundle conductor

In order to study change of ice shape in bundle conductor, because there was almost no difference in ice shape among all the sub-conductors of 3-bundle conductor and 4-bundle conductor, one sub-conductor to state was chosen. As is shown in Fig.6, Fig.7 and Fig.8, icing morphologic change between multiconductor bundles and single conductor was basically the same in the process of icing.

(1)In initial stage, icing on windward of conductor was relatively uniform, but icing on lee side of conductor was rare, which was thin and nonuniform and even without ice in some places. This is because air offers glutinousness, which makes large numbers of water drops hamper windward of conductor, and turbulent vortex is formed at leeside. Momentum of supercooling water drop was bigger than that of airflow at windward of conductor, which made supercooling water drop separate from airflow and conductor collide, thereby form icing on windward of conductor.

(2)Ice period from seventeen hours, ice on windward of conductor grows rapidly. There is layered phenomenon in ice, the length of which under layer is 3 times longer than that of upper layer. The reason: if the wind during that period didn't turn rapidly, ice thickness on windward would grow. When ice reached some thickness, the weight of ice was able to make the conductor twist, the phenomenon of stratification was found. Ice thickness on leeside also increased continuously, but the twist of conductor is limited, in comparison with ice on windward, that on lee side is still less. However, short conductor used for simulation in laboratory didn't have stratification in ice environment, for the 刚矩 of conductor is bigger than twist. This is an obvious difference between ice on practical transmission line and short conductor in lab.

(3)Ice period from forty-second hour, there was obvious dent in stratification of ice. The reason: ice under layer was influenced by air flow, and collision efficiency between small water drop and ice under layer increased, then ice thickness under layer obviously grew. Ice period over sixty-fourth hour, both ice under layer and ice on upper layer was thickened, and the dent of stratification was much deeper than before.

(a)10h

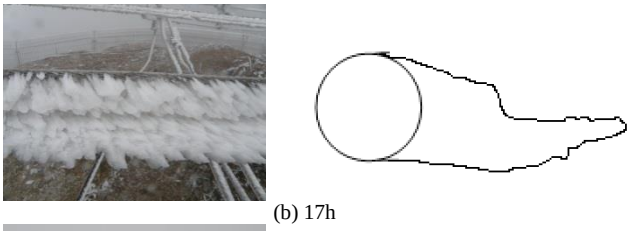

(b) 17h

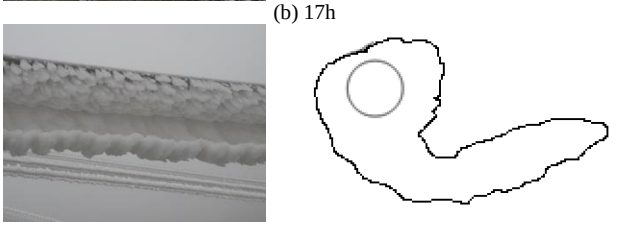

(c) 38h

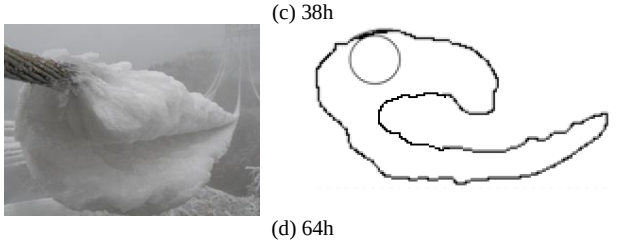

(d) 64h

Fig. 6 Relationship between ice shape of single conductor and time

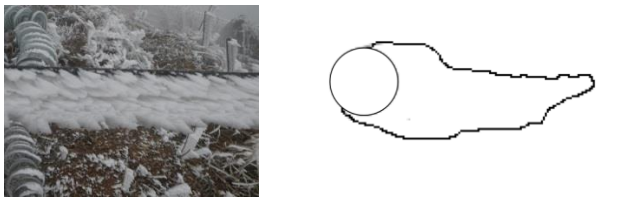

(a)17h

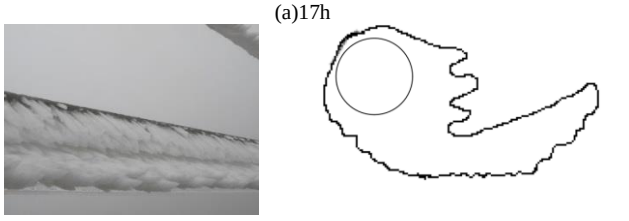

(b)38h

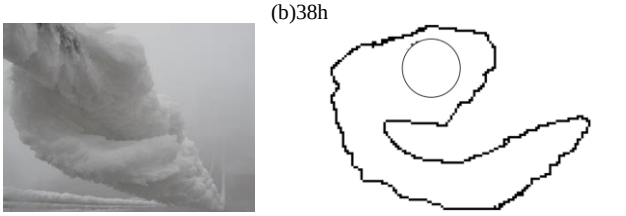

(c)64h

Fig. 7 Relationship between ice shape of 3-bound conductor and time

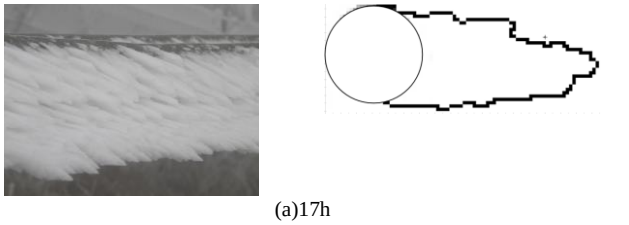

(a)17h

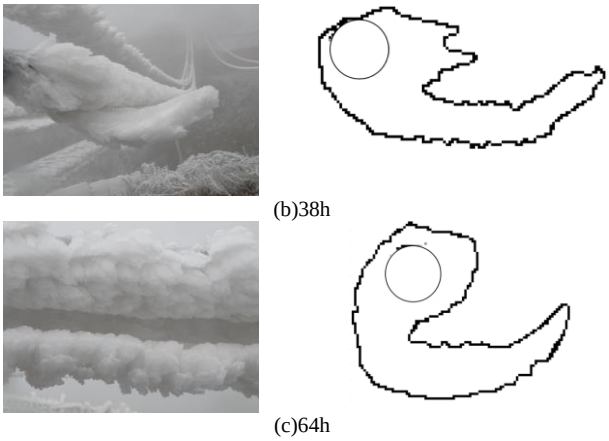

(b)38h

(c)64h

Fig. 7 Relationship between ice shape of 4-bound conductor and time

In order to study change of ice weight in bundle conductor, ice weight at the initial stages and metaphase grew fast, while it tended to saturation in later period for its light variation. As in shown in Tab.2, the difference of ice weight among 3 kinds of bundle conductors is quite small, which even can be negligible. The reason: the bundle conductors which has different diameter located in parallel position mainly influenced the initial stage of icing. When the icing in metaphase, both ice shape and area on windward were approached, and the ability to capture the supercooling water drop is same, so the ice weight at last almost had no difference.

Tab.2 Ice weight of bundle conductor

Types	Single conductor	3-bundle conductor	4-bundle conductor
Ice weight (kg/m)	5.8	5.83	5.93

IV. CONCLUSION

(1) Growth speed of horizontal axis is distinctly different with which of vertical axis for bundle conductor in the process of ice. The specific value of ice thickness between vertical and horizontal axis is above 5. The value in saturation is about 2.5.
(2) The growth of ice thickness is a nonlinear process. Icing on conductor at the initial stages and metaphase grew fast, while it tended to saturation in later period.
(3) When ice reached some thickness, the weight of ice was able to make the conductor twist, the phenomenon of stratification was found. While short conductor used for simulation in laboratory didn't have stratification in ice environment.
(4) Through the observation in the experiments, the ice shape, ice weight and ice thickness have no obvious differences among the single conductor, 3-bundle conductor and 4-bundle conductor.

REFERENCES

[1] Yuan Jiehe, Jiang Xingliang, Yi Hui, et al. The Present Study on Conductor Icing of Transmission Lines [J]. High Voltage Engineering, 2003, 30(1):6-9.
[2] Yi Hui. Analysis and Countermeasures for Large Area Accident Cause by Icing on Transmission Line [J]. High Voltage Engineering, 2005, 31(4): 14-15.
[3] Hu Yi. Analysis and Countermeasures Discussion for Large Area Icing Accident on Power Grid [J]. High Voltage Engineering, 2008, 34(2): 215-219.
[4] Huang Xinbo， Liu Jiabing， Cai Wei， Wang Xiaojing. Present Research Situation of Icing and Snowing of Overhead Transmission Lines in China and Foreign Countries [J]. Power System Technology, 2008, 32(4): 23-28.
[5] Lu Yao, Gan Zheyuan, Chen Yuchao, et al. Consistency analysis between the electric field and audible noise caused by UHV test line and UHV transmission line[J]. High Voltage Engineering, 2011, 37(2):354-360.
[6] Jiang Xiangliang, Yi Hui, Transmission line icing and its protection[M].Beijing, China: China Electric Power Press,2002
[7] Jiang Xingliang. Mechanism of ice on transmission line, the law of the coagulated ice and influence factor in San Xia[D].Sichuan：University of Chongqing，1997.
[8] The meteorological research institute in Gunzhou, Ice corpus [M]. Guizhou: Electric power tech in Guizhou, 1992.
[9] The meteorological research institute in Yunan,icing on line in high elevation regions of Yunan[M].Yunan:Yunnan Science and Technology Press,1993.
[10] Lenhard R W. An indirect method for estimating the weight of glaze on wires [J]. Bulletin of the American Meteorogical Society, 1955, 36(3): 1-5.
[11] Goodwin E J. Predicting ice and snow loads for transmission lines[C]// Proceedings of the first International Workshop on Atmospheric icing of structures. Hampshire, England: [s.n.],1983:267-273
[12] Makkonen L. Model for the growth of rime, glaze, icicles and wet snow on structures[J].Philosiphical Transactions of the Royal Society A, 2000, 358:2913-2939

Study on characterization method of icing degree of Porcelain and Glass insulators based on icing thickness of equivalent diameter

Zhang Zhijin[1], Zheng Qiang[1], Jiang Xingliang[1], Zhu Chengzhi[2]

1. State Key laboratory of Power Transmission Equipment& System Security and New Technology Chongqing University, Chongqing 400030, China
2. State Gird Zhejiang Electric Power Company, Hangzhou 310007, China

***Abstract*-The structure of insulator is more complicated than that of transmission line and the shape and distribution of icing on the surface of insulators are different to each other. So the method of using icing mass, which is dissimilar to current characterization methods of icing degree of transmission lines, is hard to exactly characterize icing degree of insulators. Based on typical Porcelain and Glass insulators, this paper studied the measurement method of the equivalent diameter of insulators with configuration parameters and did the icing experiments in Xuefeng Mountain Natural Icing Station (XMNIS). The icing thickness of the equivalent diameter of insulators is investigated and compared to verify the characterization method of the equivalent diameter of insulators. The results show that:**

(1) Based on equation of the equivalent diameter of insulators deduced by equal-area method, the equivalent diameter of insulators is related to configuration parameters. The larger the sheds and areas of insulators are, the bigger the equivalent diameter of insulators is.

(2) There are obvious windward side and leeside on the surface of icing insulators in natural icing environment. Meanwhile, the icing of insulator is related to icing time, meteorological parameters and its structure.

(3) The icing thickness of the equivalent diameter of insulators is concluded from equal icing volume. More serious the icing on insulator surface is, the thicker the icing thickness of the equivalent diameter of insulator is.

***Key words*: insulator, the equivalent diameter, natural icing, icing thickness, icing degree, characterization method**

I. INTRODUCTION

Flashover of iced insulator string is a kind of transmission line icing disaster. Power grid accident caused by flashover of iced insulator could destroy the network structure and threaten the safety operation of power system [1-3]. With the development of UHV engineering projects in China, higher requirements are demanded for the reliability service of power system. Researches on icing insulators would provide engineering significance and value to it.

Average ice thickness and ice mass are commonly used to characterize ice degree of insulators. Different researchers would adopt different ice degree characterization parameter while studying icing performances. Reference [4] proposed an evaluation method for icing severity of insulator string through statistical analysis of icicle bridging degree. Test results show that, under a certain operating voltage, as icing time increases, the icicle bridging degree of insulator string increases sharply at first till it reaches and keeps at saturation. Reference [5] used the ice mass of insulators, the ice thickness of insulator surface, and the length and diameter of ice ridge to do researches on icing process. The results indicate that these parameters grow nonlinearly with the increasing of time, and the growing degree of ice mass slows down with the increasing of time. Reference [6] analyzed the influences of both wind velocity and electric field on the variations of icicle growth, ice weight, ice density, ice thickness while studying influence of wind velocity and electric field on ice accretion of composite insulators. Scholars at home and abroad also select ice thickness of rolling conductor monitoring to describe ice degree of insulators [7-8]. Reference [9] deduced the relation between ice thickness of rolling conductor monitoring and ice mass of insulator string.

Structure of insulator is more complicated than that of transmission line and icing shape and distribution on insulators surface are different to each other. So it is hard to accurately characterize the real icing process of insulators through ice thickness of rolling conductor monitoring, ice mass and average ice thickness. A standard characterization parameter of icing degree is essential. By taking typical porcelain and glass insulators as research objects, this paper proposed a method of calculating equivalent diameter of insulator which is based on structure parameters of insulator. And the icing experiments was conducted in Xuefeng Mountain Natural Icing Station to research icing thickness of the equivalent diameter of insulator

II. CHARACTERIZATION METHOD OF INSULATOR ICINGDEGREE

A. Test Samples and Facilities

Two string of XP-300 porcelain insulators and LXY-300 glass insulators are selected in this paper. The parameters and sketch of tested insulators are shown in Table 1 and Figure 1.

Table 1. The structure parameters of tested insulators

Type	D/mm	L/mm	H/mm	S/cm^2	M/kg
XP-300	322	385	192	2455	13.5
LXY-300	320	485	195	3138	10.7

D-shed diameter, *L*-creepage distance, *H*-structure height, S-surface area, M- insulator mass

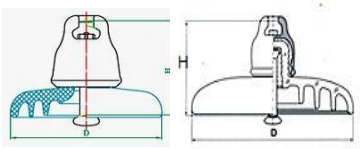

(a) XP-300 (b) LXY-300

Figure1. Sketch maps of the tested insulators

The icing experiments of these two insulator strings were conducted in Xuefeng Mountain Natural Icing Station. Before the experiment, clean tested insulators and install them on the top of steel shelf for glaze icing. The arrangement of insulators is displayed in Figure 2. It is hard to measure ice mass variation directly so an indirect way with strain gauge load cell was adopted to regulate the variation of ice mass. It is necessary to calculate the original mass of insulators. Taking weights of insulators into consideration, 300kg strain gauge load cell was selected to record the variation of ice mass of insulator string. The PortLog is a compact rugged industrial grade data logging weather station which would automatically measure temperature, wind speed, wind direction and relative humidity and other parameters during icing process. It would record real-time data and logging interval could vary from 1min to 60 min according to user's need. Logging interval was set as 1 min during the experiment and the maximum recording time is 64 Days. Export the data file of weather parameters after the experiment.

Figure 2. Arrangement of insulators

B. Equivalent Diameter of Insulators

The irregular shape and complex structure of insulators on transmission lines lead to different ice accretion process and ice shape. In order to study the icing growth process of different insulator, a standard variable that relates to insulator structure parameters is needed.

In engineering applications, the equivalent diameter of an object with irregular cross section is often used to characterize its physical characterization [10], as is shown in Figure 3. The cylinder with the equivalent diameter of D can be taken to describe the physical size of an irregular object with the cross section area of S, and the relationship between the equivalent diameter D and the cross section area Scan be described as:

$$D=2\sqrt{\frac{S}{\pi}} \tag{1}$$

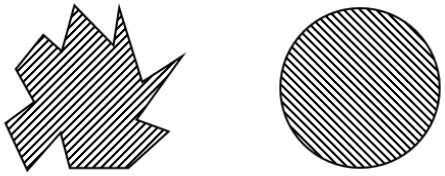

(a) Cross section of irregular sample

(b) Cross section of equivalent diameter cylinder

Figure 3. Equivalent diameter of irregular sample

The calculating method of the equivalent diameter depends on the practical research problem. Icing on insulator is actually a process in which over cooling water droplets in the air, under the influence of airflow, collides with the surface of insulator and then be captured and frozen in the surface. Therefore, for insulators in gas liquid two-phase flow, more attention should be paid to their surface area. Based on thoughts above, the insulator can be equivalent to a cylinder whose surface area is identical with that of the insulator and height is the creepage distance. As is shown in Figure 4, the diameter of the cylinder is the equivalent diameter of the insulator. The expression of equivalent diameter of insulator is:

$$D_{eq} = \frac{S}{\pi \times L} \tag{2}$$

Where S is the surface area of the insulator and the L is the creepage distance.

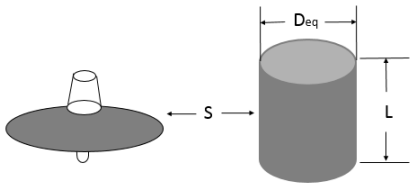

Figure 4. The equivalent diameter of the tested insulators

According to Equation (2), the equivalent diameters of two types of insulators are calculated and shown in Table 2.Compared to insulator structure parameters, it is concluded that the equivalent diameter of insulator increases with its surface area and shed diameter.

Table 2. Equivalent diameter of different insulators

Type	Equivalent diameter D_{eq}/mm
XP-300	203.0
LXY-300	205.9

C. Ice Thickness of Equivalent Diameter of Insulators

The insulator has been equivalent to a cylinder with the same surface area and the height of the creepage distance. Since icing of the cylinder is similar with conductor icing and both are icing around the column, the ice thickness of the equivalent diameter of insulator is

defined as the thickness of ice with equivalent weight to insulator icing amount evenly distributing on the cylinder body. According to its definition, the equation of ice thickness of the equivalent diameter of the insulator is derived as:

$$d = \frac{1}{2}\left(\sqrt{\frac{4V}{L\pi} + D_{eq}^2} - D_{eq}\right) \quad (3)$$

Where V is the volume of coated ice, L is the creepage distance of the insulator and D_{eq} is the equivalent diameter.

III. TEST RESULT AND ANALYSIS

A. *Performance of Icing Accretion on Insulators*

Ice accretion on two type of insulators is shown in Figure 5 and Figure 6.

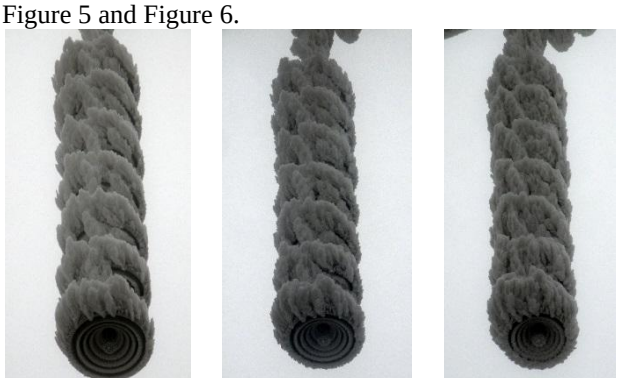

(a) time: 21 h (b) time: 40 h (c) time: 88 h

Figure 5. Ice shape of XP-300 porcelain insulators

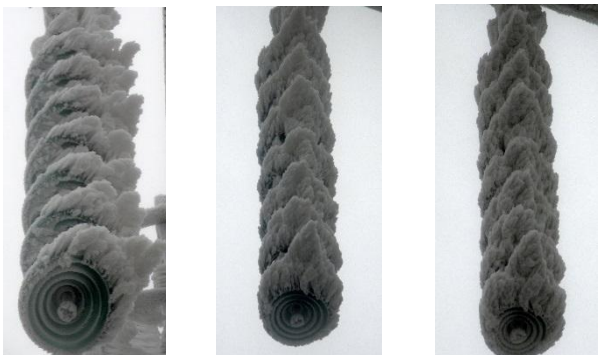

(a) time: 21 h (b) time: 40 h (c) time: 88 h

Figure 6. Ice shape of LXY-300 glass insulators

Figure 5 and Figure 6 show that, ice shapes on two types of insulators are similar. There are big differences in ice shape and accretion process between windward side and leeward side. Moreover, icing on windward side is much more serious than that on leeward side. Icing on the windward side grew against the wind and formed ice bridge connection gradually, while icing on the leeward side was well-distributed and would not form ice bridge connection. There are also some ice in the flute of insulators. The reasons for these are: the flow fields in windward side and leeward side are disparate, which contribute to differences in the way and amount of capturing over cooling water droplets on both sides. Inflow in the air impinged the surface of windward side directly, so windward side of insulators could capture a lot of over cooling water droplets. However, over cooling water droplets captured by leeward side mostly came from air flow around surface of insulator and vortex backflow. And only part of droplets in the air flow would impinge on the surface of leeward side. Furthermore, ice bridge connection on the windward side would make it hard for air flow around the insulators. So the leeward side would capture little over cooling water droplets.

Average ice mass variations of one insulator of two types are presented in Figure 7. It is known from Figure 7 that: ice mass of insulator grew nonlinearly with the time and growth rate is high at first and then slow down. The increased ice mass of XP-300 porcelain insulator every 30 hours is respectively about 1946，788，1243，326 g and that of LXY-300 glass insulator every 30 hours is respectively about 3489，500，1317，488 g。

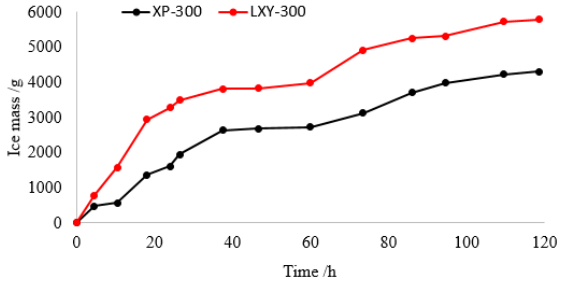

Figure 7. Average ice mass of one insulator vs. time

The PortLog weather station recorded data of weather parameters in 120h icing period. Figure 8 shows variation of environment temperature, dew temperature, relative humidity, wind speed, and wind direction.

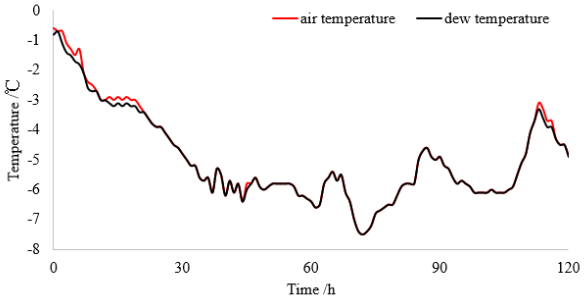

(a) Environment temperature and dew temperature

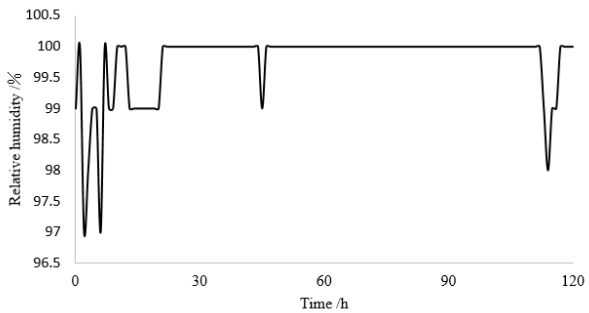

(b)Relative humidity

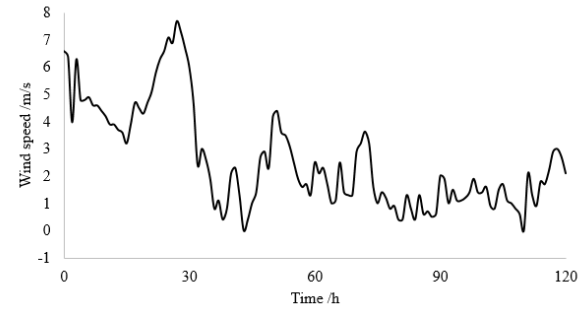

(c) Wind speed

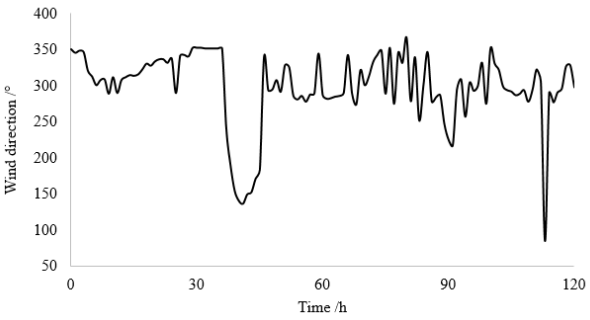

(d) Wind direction

Figure 8. Variation of weather parameters

The whole icing period could be divided into three phases. In the first phase, ice mass of insulators grows heavily. The environment temperature started falling gradually and remain under -3℃ in a long time. The average wind speed in this phase is higher than1 m/s and the maximum wind speed is 7.6 m/s. The relative humidity is above 97%. In the middle phase, growth of ice mass of insulators slows down. The environment temperature declined till it reaches the lowest point and then increased a little. The relative humidity is still above 98%. Wind speed in this phase is obviously lower than that in the first phase. Moreover, wind speed fluctuated severely with the time and is under 2 m/s in most of time. In the last phase, ice mass of insulators still grows a little. Environment temperature at night declines again and varies from -4.6 to -6℃. Wind speed is less than 2 m/s but still higher than 1 m/s, which is beneficial to ice accretion. In the day time, environment temperature rises a lot but is less than -2℃. The average wind speed is about 1 m/s and relative humidity is almost 100% in most of this period.

In the whole icing period, wind speed and environment temperature have great influences on ice accretion. The larger wind speed is, the bigger collision coefficient and freezing coefficient are. On the one hand, large wind speed increased droplets' momentum, which make it easier for droplets impinging the surface of insulator. On the other hand, large wind speed intense heat interchange of droplets and would be helpful to freezing of droplets on insulator surface. When environment temperature is high, the latent heat of droplets released slowly. It takes more time for droplets to be frozen on the surface of insulators. In the first icing phase, environment temperature is low and wind speed is high, so ice accretion is fast. In the middle icing phase, wind speed declines seriously and is not good to impingement and frozen of droplets. Therefore, ice growth slows down and is not as much as that in the first phase. In the last icing phase, although wind speed and environment temperature is not as high as those in the first phase, they would still promote impingement and frozen of droplets. And ice mass on insulators still grows a little.

B. Icing Thickness of the Equivalent Diameter of Insulator

Ice density was measured several times during icing period. It did not change a lot. The average ice density is 0.725 g/cm^3. Ice volume could be derived from ice mass and ice density. Assuming that ice is equally distributed around the equivalent cylinder, based on equal volume method, icing thickness of equivalent diameter of insulator could be calculated from Equation (3). Figure 9 shows variation of icing thickness of equivalent diameter of different insulator.

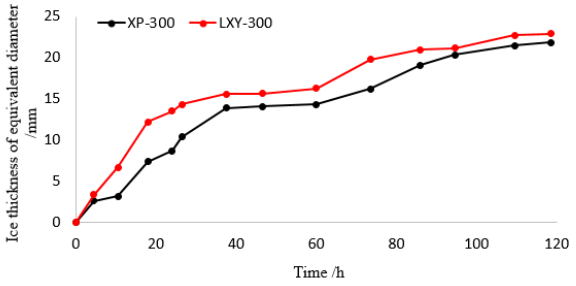

Figure 9. Ice thickness of equivalent diameter of different insulators

It could be concluded from Figure 8 that: with time varying, more serious the icing degree is, the thicker icing thickness of equivalent diameter of insulator is. For XP-300 porcelain insulator and LXY-300 glass insulator, their equivalent diameter are pretty much the same and variation of icing thickness of equivalent diameter of insulator are similar. In the first icing phase, icing thickness of equivalent diameter of both insulators have larger dispersion degree and fluctuation while they become more stable in the middle and last icing phase. This is because: ice mass is far smaller than the mass of insulator in the first icing phase, and wind speed is high (the maximum wind speed reached 7.6 m/s). Wind load has to some extent influence on ice mass so icing thickness of equivalent diameter have large dispersion degree. While wind speed reduced a lot in the middle and last phase, effects of wind load on ice mass is little. Ice accretion on insulators make the measurement results steadier. And variation tendency of icing thickness of equivalent diameter of both insulators looks alike.

IV. CONCLUSIONS

(1) Based on equation of the equivalent diameter of insulators deduced by equal-area method, the equivalent diameter of insulators is related to configuration parameters. The larger the sheds and areas of insulators are, the bigger the equivalent diameter of insulators is.

(2)There are obvious windward side and leeside on the surface of icing insulators in natural icing

environment. Meanwhile, the icing of insulator is related to icing time, meteorological parameters and its structure. The greater the wind speed is and the lower the temperature is, the faster the insulator icing accretion is.

(3)The icing thickness of the equivalent diameter of insulators is obtained from equal icing volume. More serious the icing on insulator surface is, the thicker the icing thickness of the equivalent diameter of insulator is.

REFERENCE

[1] Huang Qiang，Wang Jiahong，Ou Mingyong. Analysis on accidents caused by icing damage in Hunan power grid in 2005 and its countermeasures[J]. Power System Technology，2005，29(24)：16-19.

[2] Li Qingfeng, Fan Zheng, Wu Qiong, et al. Investigation of ice-covered transmission lines and analysis on transmission line failures caused by ice- coating in China[J]. Power System Technology，2008，32(9)：33-36.

[3] Hu Yi. Analysis and countermeasures discussion for large area icing accident on power grid[J]. High Voltage Engineering，2008，34(2)：215-219.

[4] YU Xinzhe，ZHOU Jun，LIU Bo，*et al*. Icing Flashover Characteristic of Full-scale EHV and UHV AC Insulators Strings[J]. High Voltage Engineering，2013，39（6）：1454-1459.

[5] ZHAO Shihua，JIANG Xingliang，ZHANG Zhijin，*et al*. Impact of Environmental Parameters on the icing Process of 110 kV Composite Insulators[J]. High Voltage Engineering，2012，38(10)：2575-2581.

[6] SHU Lichun，WANG Shijing，YE Kaiyan，*et al*. Influence of Wing Velocity on Ice Accretion and Flashover Performance of Composite Insulators[J]. Proceeding of the CSEE. 2015，35(6)：1533-1540.

[7] CHENG Deng-feng，JIANG Xing-liang，GUO Shouxian，*et al*. DC flashover performances of different types of ice-coated insulators[J]. High Voltage Engineering，2009，35（4）：965-970.

[8] Farzaneh M，Kiernicki J. Flashover performance of IEEE standard insulators under ice conditions[J]. IEEE Transactions on Power Delivery，1997，12(4)：1602-1613.

[9] WEN Xishan，JIANG Rikun，JIANG Xingliang，*et al*. Influence of Iced Level of Porcelain and Glass Insulators on DC Flashover Performance[J]. High Voltage Engineering，2010，36(3)：565-571.

[10] Huang Yongwei. Calculation of equivalent diameter of a workpiece[J]. Nondestructive Testing. 2000，22(12)：570-573.

Automated Icing Monitoring System on the territory of the Czech and Slovak Republic

Jaroslav Šabata[1], Petr Lehký[1], Lubomír Zeman[1], Petr Vaculík[2]
[1] EGÚ Brno, a. s., [2] E.ON Česká republika, s.r.o.
jaroslav.sabata@egubrno.cz

***Abstract*: Ice load on overhead lines is a major concern of the distribution utilities as it influences their operational reliability significantly. Real-time information about current ice load and also the knowledge of its recent development can be, in some situations, crucial for the dispatchers and their fast reaction.**

Building of an automated icing monitoring system started in the Czech Republic in 1999, when the first monitoring stations were put in operation on overhead lines. In recent years (2011-2012) a new generation of monitoring stations were deployed in the south part of the Czech Republic and the west part of the Slovak Republic. Within the next two years more than twenty monitoring stations will be installed in other parts of the Czech Republic.

The paper will describe the performance of these ice monitors, their present deployment and also the intended future development of the whole monitoring system.

Keywords: Icing, Overhead lines, Automated icing monitoring system

LEGEND AND ABBREVIATIONS

PMS	*Meteorological monitoring station*
SCADA	*Supervisory Control And Data Acquisition*

INTRODUCTION

EGÚ Brno in cooperation with distribution companies has been involved in solving the problems of icing of overhead lines since its establishment in 1952. The experience obtained during the years of icing measurement and monitoring has been used for designing a measuring device which enables a continuous measurement of some meteorological quantities.

I. PROJECT "METEO"

EGÚ Brno started this project in 1999, when the first prototype of a measuring device called Meteo was tested on the territory of distribution company VCE. Two years later, in autumn 2001 12 Meteo devices were installed on the territory of distribution company JME. In February 2003 second Meteo device was installed on the territory of VCE.

II. PROJECT "PMS"

The project of a new generation of meteorological monitoring station (called PMS) was started at the beginning of 2006. The new generation was based on the concept of Meteo device, new features have been supplemented.

A. Design

PMS is compact equipment for monitoring and processing meteorological data. The object is monitoring of the main climatic quantities which affect in terms of the reliability the operation of overhead electric lines.

The PMS station consists of two basic parts:

- Box of the central unit and of the source part including the accumulator
- Support arm with sensors measuring climatic quantities.

The constructional parts are made either of stainless steel or of steel protected against corrosion by zinc coating.

The PMS may be supplied in three ways:
- in LV networks directly
- in MV networks across a voltage transformer
- in UHV/HV networks across a solar panels.

The disposition of the automated monitoring equipment on a separate pole can be seen in Figure 1.

Figure 1: Monitoring station PMS installed on MV line

The body of the measuring device also includes the electronic part for processing the measured data and for communicating with superior SW or with the system.

B. The measurement

The following quantities are monitored by the PMS station:
- air temperature
- relative humidity
- ice mass
- wind speed and direction (on the measuring rod or by the external ultrasonic anemometer)
- irradiance (external sensor, optional).

The measuring device PMS is made of stainless steel and it has no moving parts requiring any maintenance. It consists of a body with sensors for the measurement of temperature, ice mass and the velocity and direction of wind, and of a measuring rod (length 0,5 m, diameter 30 mm) fixed vertically downwards.

For measuring wind speed and wind direction we mostly use external Gill ultrasonic anemometer (heated if possible). Irradiance is measured by external pyranometer Kipp &

Zonnen. Both external sensors are suitable for such routine field measurements.

The measured data are evaluated, processed (with 1 minute time interval), archived (in daily files, the capacity of the flash memory is 5 years) and can be sent to a superior system.

Figure 2: Support arm with sensors

C. *Communication*

It is possible to communicate with the PMS either remotely via GPRS, optic cable or on the spot from the computer via Ethernet.

Distribution companies mostly use SCADA system. To allow communication PMS directly with SCADA, protocol IEC 60870-5-101/104 was implemented.

The PMS station is also able to send warning messages when the set parameters of quantities monitored have been exceeded. The warning messages can indicate:

- exceeding the set up ice mass value
- exceeding the set up steepness of ice growing
- exceeding the value of wind velocity
- outage of supply and its restoration
- foreign intervention into the monitoring equipment.

III. PMS INSTALLATIONS

So far we have installed 53 PMS in total. As can be seen from the table below, most of them were mounted into the distribution networks, on mv lines.

Company	State		Nr. installed	Place of installation
ČEPS	Czech Republic	TSO	10	Lines 400 and 220 kV, substations 400/110 kV
	Slovenia	TSO	1	Line 380 kV
E.ON Distribuce	Czech Republic	DSO	19	MV lines
E.ON Thüringen	Germany	DSO	13	MV lines & hv/mv substations
ZSE Distribuce	Slovak Republic	DSO	8	MV lines
NKT	Germany	-	1	testing
SEPS	Slovak Republic	TSO	1	400 kV line

In next two years we plan to install 24 PMS on the territory, which is supplied by the biggest Czech DSO ČEZ Distribuce. All PMS locations have been checked out regarding condition of poles, accessibility from public communications, acceptable quality of signal etc. This year we plan to install 8 PMS stations, next year the remaining PMS stations will be put in operation. When finished, the significant area of the Czech Republic, where icing can occur, will be covered and monitored by PMS.

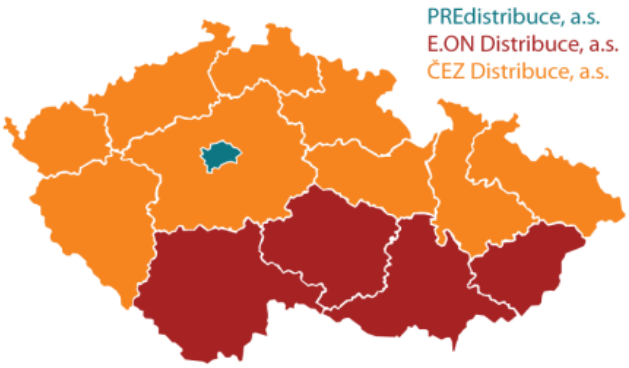

Figure 3: Map of the Czech Republic with areas supplied by DSOs

IV. USABILITY OF MEASURE METEOROLOGICAL DATA

Meteorological data, measured by PMS stations, can be used not only by dispatchers when operating the networks, but there are other fields they can be used in.

A. *Operation of the networks*

By dislocating PMS in areas which are important from the icing, dispatchers are obtaining sufficient information for the operative control of the distribution networks.

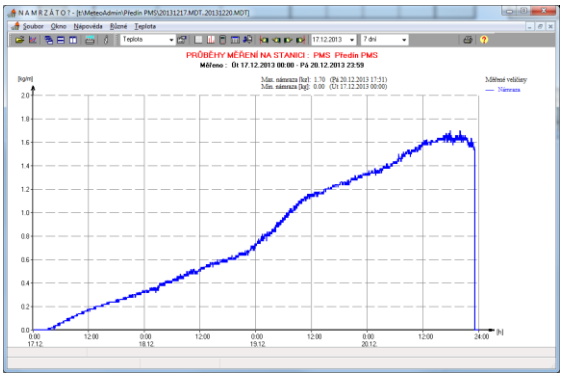

Figure 4: Example of icing cycle recorded by PMS

But for dispatchers not only information about icing is valuable. From experience we know measured wind speed is also of high interest to them, especially when wind speed exceeds limits set up and possible break downs in the networks can be expected (e. g, falling branches or trees).

Information from pyranometers can be used for evaluating energy produced by photovoltaics in the given region.

B. *Desing of OH lines and statistics*

Another very important effect is gathering all the data for further statistical evaluation. Information obtaiined about icing (and wind speed) is used when designing overhead lines. Determination of loading conditions on overhead lines (not only) and dimensioning of towers and overhead lines can result in possible savings on investment costs.

Knowledge about ice loads can then be used for further of icing maps and standards for designing overhead lines.

C. *Icing prediction*

Also seems to be important for cooperation with meteorological institution as far as the prediction of situations with icing occurrence and its verification are concerned. Such cooperation may result in making the prognoses more accurate from the point of view of the real occurrence of icing, of its size and the length of the icing cycle.

D. *Determination of dynamic line capacity*

Besides monitoring and processing meteorological data from PMS stations for control centres we used the data to verify a computational model for dynamic line rating on transmission lines (400 and 220 kV). PMS were used as a source of current meteorological data.

The project was divided into several phases and was finished last year, when the model of dynamic line rating was introduced into the dispatcher control system. The transmission capacity of some lines is now calculated based on current meteorological conditions. For these lines capacity for intraday, day ahead and two days ahead is also calculated.

V. AUTOMATED MONITORING SYSTEM

It was mentioned the PMS can be operated separately or can be connected to a superior system. It is obvious that the connection of PMS stations into the network of the monitoring system give the users additional benefits.

A. *Present state*

PMS stations operated on the territory of a utility are connected (mostly) to its SCADA system and data measured are downloaded into the SCADA database.

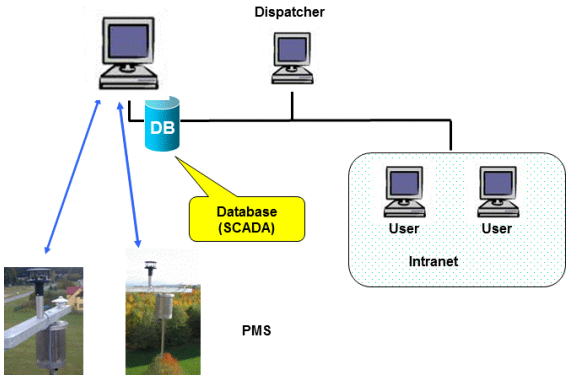

Figure 5: Scheme of processing data measured

A special software application displays the data measured to the dispatchers in table form or graphically. The dispatcher can see current values of meteorological quantities as well as the history of each quantity. When icing occurs, the dispatcher decides, based on current ice load and the recent development, how to cope with the situation (to start preparing a line for heating, for example).

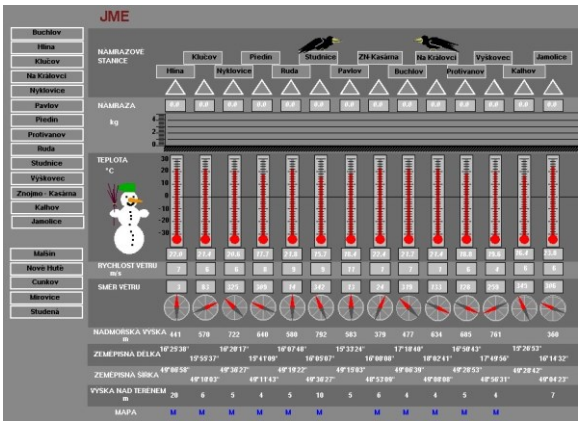

Figure 6: Values displayed to the dispatcher (E.ON)

At E.ON Distribuce, some data are also provided to Intranet where they are available for selected workers. Current values and history of meteorological quantities are presented in a simplified table or graph form.

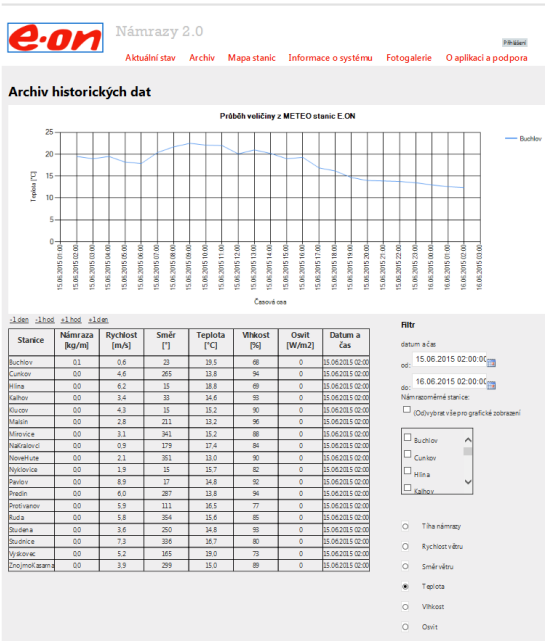

Figure 7: Displaying values on the E.ON Intranet

B. *Concept of a new project*

At the moment the data obtained from PMSs are "visible" and utilizable only within the utility itself. As a larger area of the Czech Republic is or soon will be covered with PMS stations we have decided to come up with a project which would enable us to share the data from PMS stations among utilities.

The first issue, which had to be solved, was to obtain content from all potential participants (DSOs, TSO) to provide the data to other entities. When the agreement was made we started preparing the technical solution. Discussions with other participants indicated that due to (cyber) safety reasons and other technical obstacles it would very difficult to exchange the data in a simple way. The solution, which will be implemented, is divided into following steps:

- Setting up a new data server in EGÚ Brno which will communicate to all PMS stations, download and store the data. It means each PMS station will communicate in two channels: to a utility SCADA system and server at EGÚ Brno.

- Creating parallel communication channel from PMS stations to data server in EGÚ Brno
- Creating a data format in which the data will be provided to other participants (DSOs, TSO, …)
- Testing phase of providing the data
- Visualisation data from "new" PMS stations for the dispatchers on side of DSOs and TSO respectively.

The first step has already been completed, last month we built the data server and installed special software for communication and storing the data into SQL database. A communication link from the server was established to a small number of PMS stations, which had been chosen for testing purposes. In the near future the communication will be spread up with remaining PMS station.

C. Outlook

We plan to gradually connect all PMS stations (E.ON, ČEPS) into this system and later on, when put in operation, also PMS stations from the territory supplied by ČEZ Distribuce.

In the title of this paper the territory of the Slovak Republic is mentioned. As the area, which is supplied by ZSE, borders the area supplied by E.ON Distribuce, it would make sense to connect to the system PMS stations from its territory. We believe that in near future we will be able to connect PMS stations installed on the area supplied by ZSE distribution utility to the data server and thus extend the area where meteorological data are measured and make them available to other parties.

We also intend to allow access to the data on the server to special users (planners from utilities e.g.) to see the current data and history. The access will be via a special Internet application. The first version of the application is being tested now.

VI. CONCLUSION

In recent years 29 PMS stations have been deployed on territory of the Czech Republic. Another 24 PMS stations will be mounted in the next two years. Then significant area of the Czech Republic, where icing occurs, will be monitored by PMS stations.

To allow utilities access to data from PMS stations we have proposed a project which would enable sharing of data among Czech utilities and TSO.

We consider this project very useful and challenging. It is obvious this solution will bring mutual profit to all parties involved as it would allow them to "see" the meteorological situation beyond their region with little cost and effort.

REFERENCES

[1] Lehký, Z. Zálešák, H. Kváčová, "Automated system for icing monitoring - supply area of VČE" (in Czech). EGÚ Brno, a.s. - 020, 1998

[2] P. Lehký, Z. Zálešák, H. Kváčová, "Automated system for icing monitoring - supply area of JME" (in Czech). EGÚ Brno, a.s. - 020, 1999

[3] P. Lehký, J. Šabata, Z. Zálešák, "Automated icing monitoring system" in Proc. 2002 IWAIS

[4] PMS Manual, EGÚ Brno, .a.s., 2008